Multiscale Response of Granular Materials under Cyclic Shear: Packing State, Force Chains, and Stress Transmission

Thesis by
Amanda Patricia Toledo Barrios

In Partial Fulfillment of the Requirements for the
Degree of
Doctor of Philosophy



CALIFORNIA INSTITUTE OF TECHNOLOGY
Pasadena, California

2026
Defended May 4, 2026

© 2026

Amanda Patricia Toledo Barrios
ORCID: 0009-0000-2018-7616

All rights reserved except where otherwise noted

ACKNOWLEDGEMENTS

My PhD journey was not linear. I encountered many setbacks and frustrations, but ultimately it was my support system that helped me reach the finish line.

First, I would like to thank my advisor, Professor Ravichandran, who, despite my slow progress in research, was very understanding and only continued to cheer me on after every small win. I also thank the other members of the dissertation committee, Professor Andrade, Professor Bhattacharya, and Professor Shaikeea, for their inspiring discussions throughout the years.

I would also like to thank current and former members of the Ravi and Kaushik groups, especially Dr. Barry Lawlor, Dr. Vatsa Gandhi, Dr. Eric Ocegueda, and Dr. Harkirat Singh, who were my sounding board for all ideas, big and small.

Next, I am truly grateful for my family and my fiancé, Andrew. Their continued love and encouragement carried me through all the difficult and happy moments during my PhD. I would not be the person I am today without them. This big achievement is as much theirs as it is mine.

I am also incredibly grateful to the Women in GALCIT (WiGALIT), the GALCIT Graduate Student Council (GGSC), Women in Engineering and Applied Science (Women in EAS), Club Latino, and the Caltech Center for Inclusion & Diversity (CCID) for all of the incredible individuals who helped Caltech feel like home. In particular, Yazmin Gonzalez and Christine Ramirez provided me with nonstop support. Overall, whenever research felt overbearing, the Caltech community always picked me up.

Regarding my experimental methodology, I would like to give a shout-out to Micah Simonsen at Correlated Solutions Inc. and Bill Porcaro at Allied Visions Technologies, Inc., both of whom helped me troubleshoot and configure solutions for my research-specific problems. Micah helped me automate Digital Image Correlation (DIC) processes, while Bill helped me develop a robust method for processing large image series. I appreciate their time and effort.

None of this research would have been possible without the funding from the Department of Defense Multidisciplinary University Research Initiative (MURI) titled *Predicting and Controlling the Response of Particulate Systems through Grain-Scale Engineering* (grant #W911NF-19-1-0245). I thoroughly enjoyed meeting and discussing with the other collaborators at the MURI workshop in 2023.

Lastly, I would like to acknowledge the National Defense Science and Engineering Graduate Fellowship (NDSEG) for funding three years of my research, connecting me with my ARL mentor, Dr. Ryan Emerson, and providing me with valuable information and connections during the 2024 NDSEG conference.

ABSTRACT

Granular materials are widely encountered in natural and engineered systems, yet their behavior under cyclic loading remains difficult to predict because bulk response emerges from complex grain-scale interactions. Repeated loading can produce irreversible deformation, history dependence, and evolving internal load-transfer mechanisms that are not fully captured by macroscopic measurements alone. Although cyclic behavior has been studied extensively at the continuum scale, direct experimental characterization of the grain-scale processes governing cyclic response remains limited.

This thesis investigates the multiscale behavior of dry, cohesionless granular materials subjected to quasi-static cyclic simple shear loading through laboratory experiments coupled with the Granular Element Method (GEM), a mechanics-based force-inference framework for estimating interparticle contact forces from experimentally measurable grain-scale data. An experimental framework was developed by upgrading an existing simple shear apparatus to enable controlled cyclic loading and by integrating imaging, tracking, and post-processing methods for multiscale measurements.

At the macroscale, the experiments show that cyclic simple shear produces direction-dependent and history-dependent behavior. Repeated loading generates asymmetric stress and deformation responses, incomplete recovery of the initial state, and progressive changes that depend on packing condition and confinement level. Densely packed and loosely packed assemblies exhibit qualitatively different cyclic responses, while normal confinement primarily influences the strength and persistence of those responses.

At the grain-scale, the results show that cyclic behavior is governed largely by the reorganization of the internal force network rather than by large changes in overall contact connectivity. Force chains evolve continuously with loading direction and cycle history, while anisotropy plays a central role in linking internal structure to bulk shear resistance. Dense systems initially develop stronger, more coherent load-bearing structures that weaken with repeated cycling, whereas loose systems deform via more distributed force transmission and progressive compaction.

Overall, this work provides a mechanistic framework for understanding how granular materials accumulate history, weaken, and reorganize under repeated shear. The

combined experimental and GEM results also provide benchmark data to calibrate and validate physics-based particle models for broader granular systems and relevant engineering applications.

TABLE OF CONTENTS

Acknowledgements . . . iii
Abstract . . . v
Table of Contents . . . vii
List of Illustrations . . . x
List of Tables . . . xxxii
Chapter I: Introduction . . . 1
1.1 Objectives . . . 1
1.2 Granular Materials under Cyclic Loading . . . 1
1.3 Common Test Devices for Studying Granular Media . . . 3
1.4 Granular Media Across Length Scales . . . 5
1.4.1 Macroscale Properties . . . 6
1.4.2 Microscale and Mesoscale Properties . . . 7
1.5 Multiscale Approaches to Characterizing Granular Material Behavior 8
1.5.1 Modeling Approaches . . . 8
1.5.2 Force-Inference Techniques . . . 10
1.6 Research Gap and Thesis Scope . . . 11
Chapter II: Granular Element Method . . . 13
2.1 Introduction . . . 13
2.2 Experimental measurements . . . 15
2.3 Mathematical Framework . . . 16
2.4 Summary . . . 22
Chapter III: Micro-to macroscopic Response of Granular Materials under Cyclic Simple Shear: A One-Cycle Experimental Study . . . 23
3.1 Introduction . . . 23
3.2 Experimental Setup: Cyclic Shear Apparatus . . . 24
3.2.1 Design Overview . . . 24
3.2.2 Measurements . . . 27
3.2.3 Granular Samples . . . 30
3.2.4 Experimental Procedure and Image Analysis . . . 30
3.3 One Cycle Response of a Densely Packed Granular Assembly . . . 35
3.3.1 Macroscopic Response . . . 35
3.3.2 Grain-Scale Response . . . 42
3.4 Summary . . . 74
Chapter IV: Multiscale Response of Granular Materials under Cyclic Simple Shear: Effects of Packing State and Confinement . . . 76
4.1 Introduction . . . 76
4.2 Experiment # 1: Densely Packed, $\sigma_n = -44.1$ kPa . . . 78
4.2.1 Macroscopic Response . . . 78
4.2.2 Grain-scale Response . . . 85

4.3 Experiment # 2: Densely Packed, $\sigma_n = -29.6$ kPa 118
4.3.1 Macroscopic Response 119
4.3.2 Grain-Scale Response 130
4.4 Experiment # 3: Loosely Packed, $\sigma_n = -44.1$ kPa 162
4.4.1 Macroscopic Response 162
4.4.2 Grain-Scale Response 175
4.5 Experiment # 4: Loosely Packed, $\sigma_n = -29.6$ kPa 211
4.5.1 Macroscopic Response 212
4.5.2 Grain-Scale Response 220
4.6 Macroscopic Response Across Experiments: Influence of Packing State and Normal Stress 257
4.7 Grain-Scale Response Across Experiments: Influence of Packing State and Normal Stress 259
4.8 Summary 262
Chapter V: Conclusions and Future Work 264
5.1 Summary of Research Objectives 264
5.2 Major Findings 264
5.2.1 Cyclic Simple Shear Produces Directional and History-Dependent Response 265
5.2.2 Macroscopic Behavior is Governed by Evolving Grain-scale Force Transmission 265
5.2.3 Packing State Controls the Dominant Cyclic Deformation Mechanism 265
5.2.4 Force Chains and Anisotropy as Effective Internal Descriptors 266
5.2.5 Multiscale Experimental Methods Provide New Insight into Cyclic Behavior 267
5.2.6 Summary 267
5.3 Thesis Contributions 267
5.3.1 Development of a Cyclic Simple Shear Framework 267
5.3.2 Application of GEM to Cyclic Loading 268
5.3.3 Experimental Force Chain Characterization from Inferred Contact Forces 268
5.3.4 Multiscale Linkage Between Internal Structure and Bulk Response 268
5.3.5 Multiscale Insight into the Role of Packing State and Confinement 268
5.3.6 Creation of a Multiscale Experimental Dataset 269
5.4 Limitations on the Present Study 269
5.4.1 Two-Dimensional Experimental Representation 269
5.4.2 Data Acquisition and Tracking Demands 269
5.4.3 Motion Control Precision 270
5.4.4 Finite Experimental Scope 270
5.4.5 Force Inference Uncertainty 270
5.4.6 Summary 270
5.5 Future Work 271

5.5.1 Improved Motion Control . . . 271
5.5.2 Automated Tracking and Computational Efficiency . . . 271
5.5.3 Additional Cyclic Loading Experiments with Varying Parameters . . . 271
5.5.4 Broader Material Conditions . . . 271
5.5.5 Model Validation and Multi-Scale Modeling . . . 271
5.5.6 Closing Remark . . . 272
Bibliography . . . 273
Appendix A: Force Chain Detection Algorithm: α Selection . . . 281
Appendix B: Three-Cycle Experiments: Dilatancy Per Cycle . . . 283
B.1 Densely Packed Granular Assembly . . . 283
B.2 Loosely Packed Granular Assembly . . . 284
Appendix C: Three-Cycle Experiments: Macroscopic Comparison Plots . . . 285
C.1 Stress Ratio . . . 285
C.2 Volumetric Strain . . . 286
C.3 Dilatancy . . . 287
C.4 Void Ratio . . . 288
Appendix D: Three-Cycle Experiments: Grain-scale Comparison Plots . . . 289
D.1 Coordination Number . . . 289
D.2 The Number of Detected Force Chains . . . 290
D.3 Accumulated Force Chain Network Content . . . 291
D.4 Force Chain Participation . . . 293
D.5 Strong Network Participation and Strong Network Chain Participation 294
D.6 Micro-Macro Comparison . . . 295
D.7 Temporal Evolution of Fabric and Force Anisotropy Magnitudes . . . 296
D.8 Verification of the Stress-Force-Fabric Relationship . . . 297
D.9 Force Transmission . . . 298
Appendix E: Three-Cycle Experiments: Strong Network Participation and Strong Network Chain Participation Statistics Tables . . . 304
E.1 Experiment # 1: Densely Packed, $\sigma_n = -44.1$ kPa . . . 304
E.2 Experiment # 2: Densely Packed, $\sigma_n = -29.6$ kPa . . . 305
E.3 Experiment # 3: Loosely Packed, $\sigma_n = -44.1$ kPa . . . 306
E.4 Experiment # 4: Loosely Packed, $\sigma_n = -29.6$ kPa . . . 307

LIST OF ILLUSTRATIONS

Number *Page*

1.1 Liquefaction-induced damage during the 1964 Niigata, Japan earthquake. Image reproduced from [3] and accessed via Wikimedia Commons. 2

1.2 Vehicle mobility examples in granular terrain. (a) A Humvee traversing rugged terrain in Khowst Province, Afghanistan. U.S. Marine Corps image, public domain [8]. (b) NASA's Mars Exploration Rover Spirit partially embedded in loose Martian regolith [9]. Image credit: NASA/JPL-Caltech. 3

1.3 Characteristic length scales in granular media: macroscale (km), mesoscale (mm), and microscale (μm). Example behavior at each scale includes bulk landslide flow, a representative volume element (RVE) of grains deforming within that flow, and individual grain interactions within the RVE. The macroscale panel includes a photograph by Timo Volz from Unsplash [18]. The mesoscale panel was adapted from Hurley et al. [19], with permission from Springer Nature. 6

1.4 Early experimental visualization of force chains in a granular assembly of discs using photoelasticity. Adapted from Drescher and de Josselin de Jong [38], with permission from Elsevier. 11

2.1 GEM methodology for contact force inference (Reproduced from Marteau [56]). 15

2.2 Schematic of particles p and q in contact at point α. The position vector $\boldsymbol{x}^{\alpha}$ locates the contact point relative to the reference basis $\boldsymbol{e} = [e_1 \quad e_2]^{\top}$. 17

2.3 Illustration of particle-particle contacts (index i) and particle-boundary contacts (index j). 18

2.4 Local contact coordinate system for contact i, showing the unit normal vector, $\boldsymbol{e}^i$, and unit tangential vector, $\boldsymbol{t}^i$, used to resolve the contact force exerted by particle q on particle p. 20

3.1 Three-dimensional computer-aided design (CAD) model illustrating an exploded view of the components of the simple shear apparatus. Reproduced from Marteau and Andrade [63], Fig. 1a, with permission from Springer Nature. 25
3.2 Top-view photograph of the cyclic simple shear apparatus during testing. The shear cell is a deformable parallelogram consisting of four rigid arms: A-B (bottom arm), C-B (right arm), C-D (top arm), and A-D (left arm). The shear cell is shown in a left-sheared configuration, with the LED illumination system, hanging normal-load weights, and microcontroller wiring visible. Scale bar = 20 cm. . 25
3.3 Rapid grain rearrangement resulting in localized motion blur. Data from these transient images are excluded from all results. Scale bar = 20 mm. 27
3.4 Shear cell state of deformation under a prescribed shear angle, γ, and an external compressive normal load, σ_n. 28
3.5 Detected shear cell position from AprilTags via the MATLAB® Computer Vision Toolbox. 29
3.6 Displacement, u, versus time, t, schematic for $N = 1$ cycle. τ represents the duration between shear stages. In the experimental results, these stages are called: shear-right-forward ($2 \rightarrow 3$), shear-right-reverse ($3 \rightarrow 4$), shear-left-forward ($4 \rightarrow 5$), and shear-left-reverse ($5 \rightarrow 6$). The normal loading stage (segment $1 \rightarrow 2$) of the experiment is not shown. 32
3.7 Close-up view of the circular grain boundaries generated in MATLAB®. The larger grains ($D_2 = 30\,mm$) are outlined in red, the smaller grains ($D_1 = 20\,mm$) in blue, and the corresponding polygonal approximations in green. The polygonal boundaries were slightly inset relative to the true grain edges to reduce spurious overlap between adjacent AOIs during the DIC analysis. Scale bar = 10 mm. . . 33
3.8 Visualization of the grain-tracking procedure in VIC-2D. (a) Enlarged view of the speckle pattern with the 11 × 11 pixel correlation subsets overlaid on grains within the assembly. (b) Snapshot of the full DIC workspace showing the granular assembly with all grain areas of interest (AOIs) and manually assigned seed points. The foreground panel illustrates manual adjustment of the initial guess for a selected seed point during frame-to-frame grain tracking. 34

3.9 Macroscopic behavior of the one-cycle, densely packed granular assembly under $\sigma_n = -44.1$ kPa. (a) Stress ratio, μ, (b) volumetric strain, ϵ_V, (c) void ratio, e, and (d) dilatancy, β, as functions of shear strain, γ. 36
3.10 Force chain visualization at the start and end of the pronounced stress ratio, μ, drop during shear-right-forward, corresponding to (a) $\gamma = 0.147$ rad and (b) $\gamma = 0.151$ rad 37
3.11 Assemblies of highly stressed grains that (a) do not and (b) do form a force chain. Adapted from Peters et al. [73]. Reprinted with permission from A. Peters, H. A. Makse, and H. J. Herrmann, *Physical Review E*, Vol. 72, 041307 (2005). Copyright 2005 by the American Physical Society. 43
3.12 Force chain detection at $\gamma = 0.0756$ rad.(a) |Max.compressivestress| and corresponding directions shown as lines through grain centers. Red lines indicate grains that are part of force chains. (b) Detected force chains, categorized by chain length (number of grains). (c) Tresca strain field (from DIC) overlaid with the magnitude of the normal component of contact forces, $|f_n|$, in magenta, and the detected force chains in white. 45
3.13 Evolution of the number of force chains. 46
3.14 Evolution of the number of force chains per cycle stage. The trend line (red) is for visual purposes only. 47
3.15 Evolution of the coordination number, Z_c, the average number of contacts per particle. 49
3.16 Evolution of the total chain length (number of grains). 50
3.17 Evolution of the total chain length per cycle stage. The trend line (red) is for visual purposes only. 51
3.18 Bar chart of the normalized area under the curve (AUC) of the total chain length for each shear stage (**S**hear-**R**ight-**F**orward, **S**hear-**R**ight-**R**everse, **S**hear-**L**eft-**F**orward, **S**hear-**L**eft-**R**everse). The normalized AUC represents the average size of the force chain network sustained per unit shear deformation within each stage. 52
3.19 Violin plot of the total chain length for each cycle stage, used to visualize force chain structure size distribution. Red vertical bars mark the median of the distribution. Blue vertical bars mark the Q1 and Q3 quartiles of the distribution. 54

3.20 Violin plot of the chain density for each cycle stage, used to visualize the distribution of force chain network participation. Red vertical bars mark the median of the distribution. Blue vertical bars mark the Q1 and Q3 quartiles of the distribution. 55
3.21 Evolution of the percentage of strong network grains and the percentage of strong network grains in force chains. Strong network grains are those whose maximum compressive stress is greater than the average grain stress in the assembly. 56
3.22 Stage-wise medians of the macroscopic shear stress [kPa] and the total chain length [number of grains]. Error bars represent one-half of the interquartile range, centered about the median. 59
3.23 Polar histograms showing the normalized angular distributions of contact fabric orientation, $P(\theta)$, the mean normal contact force, $\bar{f}_n(\theta)$, and the mean tangential contact force $\bar{f}_t(\theta)$, at the midpoint of each stage in the loading cycle (i.e., mid-normal loading, and mid-shear). The solid curve shows the distribution, the dash-dotted curve shows the Fourier fit of the distribution, and the red dashed line is the maximum compressive stress axis. 63
3.24 Evolution of the fabric anisotropy magnitude, a, mean normal force anisotropy magnitude, a_n, and mean tangential force anisotropy magnitude, a_t, per stage in the loading cycle. 65
3.25 Verification of the stress-force-fabric relationship. 67
3.26 Scatter plots comparing the theoretical stress-force-fabric (SFF) relation with the experimental invariant stress ratio, q/p, which indicates internal stress anisotropy. The simplified (a) and full (b) SFF expressions are shown. Points below the red $y = x$ line indicate that the theory overpredicts q/p, and vice versa. 69
3.27 Probability density function of the normal force, f_n, normalized by the mean normal force, $\langle f_n \rangle$, for each stage in the loading cycle, on a semi-log scale. 70
3.28 Probability density function of the tangential force magnitude, $|f_t|$, normalized by the mean normal force, $\langle f_n \rangle$, for each stage in the loading cycle, on a semi-log scale. 71
3.29 Probability density function of the mobilized friction, $S = |f_t|/\mu f_n$, where μ is the interparticle friction coefficient. This variable reveals how close a contact is to sliding (Coulomb failure criterion). 72

4.1 Macroscopic response of the three-cycle, densely packed granular assembly under $\sigma_n = -44.1$ kPa: (a) stress ratio, μ; (b) volumetric strain, ϵ_V; (c) void ratio, e; and (d) dilatancy, β, versus shear strain, γ. Solid curves denote forward shearing (SRF, SRR), dash-dotted curves denote reverse shearing (SLF, SLR), and gray vertical dashed lines indicate stage transitions. Yellow and green stars mark the start and end of cyclic loading, respectively. 78
4.2 Dilatancy evolution per stage for the three-cycle, densely packed granular assembly under $\sigma_n = -44.1$ kPa. Stage markers are shown only for Cycle 1. 81
4.3 Evolution of the coordination number, Z_c, for the dense granular assembly ($\sigma_n = -44.1$ kPa). Z_c is the average number of contacts per particle. Curve style indicates shearing direction (solid: forward, dash-dotted: reverse), gray dashed lines mark stage transitions, and stars mark the start (yellow) and end (green) of cyclic loading. 86
4.4 Per-stage evolution of the coordination number, Z_c, for the dense granular assembly ($\sigma_n = -44.1$ kPa). Stage markers are shown only for Cycle 1. 86
4.5 Evolution of the detected number of force chains, for the dense granular assembly ($\sigma_n = -44.1$ kPa). Curve style indicates shearing direction (solid: forward, dash-dotted: reverse), gray dashed lines mark stage transitions, and stars mark the start (yellow) and end (green) of cyclic loading. 89
4.6 Per-stage evolution of the detected number of force chains for the dense granular assembly ($\sigma_n = -44.1$ kPa). Stage markers are shown only for Cycle 1. 89
4.7 Evolution of the total force chain length, in number of grains, for the dense granular assembly ($\sigma_n = -44.1$ kPa). Curve style indicates shearing direction (solid: forward, dash-dotted: reverse), gray dashed lines mark stage transitions, and stars mark the start (yellow) and end (green) of cyclic loading. 91
4.8 Per-stage evolution of the total force chain length, in number of grains, for the dense granular assembly ($\sigma_n = -44.1$ kPa). Stage markers are shown only for Cycle 1. 92

4.9 Bar chart of the normalized area under the curve (AUC) of the total force chain length for each cycle and shear stage for the dense assembly ($\sigma_n = -44.1$ kPa). The normalized AUC represents the average extent and persistence of the force chain network sustained per unit shear deformation within each stage. 93
4.10 Violin plots of the force chain density for each cycle and shear stage for the dense assembly ($\sigma_n = -44.1$ kPa). Force chain density is defined as the fraction of grains participating in the force chain network relative to the total number of interior grains. The bottom x-axis shows the normalized chain density, while the top x-axis shows the equivalent total force chain length in number of grains. The width of each violin indicates the relative frequency of occurrence of a given chain density during that stage. 95
4.11 Stage-wise medians of the strong network participation [%] (top) and the strong network chain participation [%] (bottom) for each cycle and shear stage for the dense assembly ($\sigma_n = -44.1$ kPa). Error bars represent one-half of the interquartile range, centered about the median. 97
4.12 Stage-wise medians of the shear stress [kPa] (top) and total chain length [number of grains] (bottom) for each cycle and shear stage for the dense assembly ($\sigma_n = -44.1$ kPa). Error bars represent one-half of the interquartile range, centered about the median. 99
4.13 Polar histograms of the normalized angular distributions of the contact fabric orientation, $P(\theta)$, arranged by cycle (rows) and midpoint of each shear stage (columns) for the dense assembly ($\sigma_n = -44.1$ kPa). The solid curve represents the distribution, the dash-dotted curve shows its Fourier fit, and the red dashed line denotes the principal compressive stress axis. 101
4.14 Polar histograms of the mean contact normal force, $\bar{f}_n(\theta)$, arranged by cycle (rows) and midpoint of each shear stage (columns) for the dense assembly ($\sigma_n = -44.1$ kPa). The solid curve represents the distribution, the dash-dotted curve shows its Fourier fit, and the red dashed line denotes the principal compressive stress axis. 103

4.15 Polar histograms of the mean contact tangential force, $\bar{f}_t(\theta)$, arranged by cycle (rows) and midpoint of each shear stage (columns) for the dense assembly ($\sigma_n = -44.1$ kPa). The solid curve represents the distribution, the dash-dotted curve shows its Fourier fit, and the red dashed line denotes the principal compressive stress axis. 105

4.16 Per cycle evolution of the anisotropy magnitudes as functions of shear strain for the dense assembly ($\sigma_n = -44.1$ kPa): fabric anisotropy magnitude, a, and normal and tangential force anisotropy magnitudes, a_n and a_t, respectively. Curve style indicates shearing direction (solid: forward, dash-dotted: reverse), gray dashed lines mark stage transitions. 108

4.17 Per cycle evolution of the invariant stress ratio, q/p, as a function of shear strain for the dense assembly ($\sigma_n = -44.1$ kPa). The experimental response is compared with the predictions of the full and simplified stress-force-fabric (SFF) relationships. Curve style indicates shearing direction (solid: forward, dash-dotted: reverse), gray dashed lines mark stage transitions. 111

4.18 Per-cycle evolution of the probability density function (PDF) of the normalized normal contact force, $f_n / \langle f_n \rangle$, for the dense assembly ($\sigma_n = -44.1$ kPa). Each panel shows one loading cycle, with all stages on a semi-log scale. 113

4.19 Per-cycle evolution of the probability density function (PDF) of the normalized tangential contact force, $f_t / \langle f_n \rangle$, for the dense assembly ($\sigma_n = -44.1$ kPa). Each panel shows one loading cycle, with all stages on a semi-log scale. 114

4.20 Per cycle evolution of the probability density function (PDF) of the mobilized friction, $S = |f_t|/\mu f_n$, for the dense assembly ($\sigma_n = -44.1$ kPa). Each panel shows one loading cycle, with all stages on a semi-log scale. Here, μ is the interparticle friction coefficient, and S indicates the proximity of a contact to sliding (Coulomb failure criterion). 116

4.21 Macroscopic behavior of the three-cycle, densely packed granular assembly under $\sigma_n = -29.6$ kPa. (a) Stress ratio, μ, (b) volumetric strain, ϵ_V, (c) void ratio, e, and (d) dilatancy, β, as functions of shear strain, γ. Solid curves indicate forward shearing stages (SRF, SRR), whereas dash-dotted curves indicate reverse shearing stages (SLF, SLR). Furthermore, gray vertical dashed lines indicate shear-stage transitions. The yellow and green stars mark the start and end of the cyclic loading, respectively. 119

4.22 Stress ratio evolution for the two three-cycle, dense experiments. Left: higher-confinement ($\sigma_n = -44.1$ kPa $\approx$ 122 lb). Right: lower-confinement ($\sigma_n = -29.6$ kPa $\approx$ 82 lb). Curve style indicates shearing direction (solid: forward, dash-dotted: reverse), gray dashed lines mark stage transitions, and stars mark the start (yellow) and end (green) of cyclic loading. 120

4.23 Volumetric strain evolution for the two three-cycle, dense experiments. Left: higher-confinement ($\sigma_n = -44.1$ kPa $\approx$ 122 lb). Right: lower-confinement ($\sigma_n = -29.6$ kPa $\approx$ 82 lb). Curve style indicates shearing direction (solid: forward, dash-dotted: reverse), gray dashed lines mark stage transitions, and stars mark the start (yellow) and end (green) of cyclic loading. 122

4.24 Dilatancy evolution for the two three-cycle, dense experiments. Left: higher-confinement ($\sigma_n = -44.1$ kPa $\approx$ 122 lb). Right: lower-confinement ($\sigma_n = -29.6$ kPa $\approx$ 82 lb). Curve style indicates shearing direction (solid: forward, dash-dotted: reverse), gray dashed lines mark stage transitions, and stars mark the start (yellow) and end (green) of cyclic loading. 125

4.25 Void ratio evolution for the two three-cycle, dense experiments. Left: higher-confinement ($\sigma_n = -44.1$ kPa $\approx$ 122 lb). Right: lower-confinement ($\sigma_n = -29.6$ kPa $\approx$ 82 lb). Curve style indicates shearing direction (solid: forward, dash-dotted: reverse), gray dashed lines mark stage transitions, and stars mark the start (yellow) and end (green) of cyclic loading. 127

4.26 Evolution of the coordination number, Z_c, for the dense granular assembly ($\sigma_n = -29.6$ kPa). Z_c is the average number of contacts per particle. Curve style indicates shearing direction (solid: forward, dash-dotted: reverse), gray dashed lines mark stage transitions, and stars mark the start (yellow) and end (green) of cyclic loading. 130
4.27 Per-stage evolution of the coordination number, Z_c, for the dense granular assembly ($\sigma_n = -29.6$ kPa). Stage markers are shown only for Cycle 1. 131
4.28 Evolution of the detected number of force chains for the dense granular assembly ($\sigma_n = -29.6$ kPa). Curve style indicates shearing direction (solid: forward, dash-dotted: reverse), gray dashed lines mark stage transitions, and stars mark the start (yellow) and end (green) of cyclic loading. 133
4.29 Per-stage evolution of the detected number of force chains for the dense granular assembly ($\sigma_n = -29.6$ kPa). Stage markers are shown only for Cycle 1. 133
4.30 Evolution of the total force chain length, in number of grains, for the dense granular assembly ($\sigma_n = -29.6$ kPa). Curve style indicates shearing direction (solid: forward, dash-dotted: reverse), gray dashed lines mark stage transitions, and stars mark the start (yellow) and end (green) of cyclic loading. 135
4.31 Per-stage evolution of the total force chain length, in number of grains, for the dense granular assembly ($\sigma_n = -29.6$ kPa). Stage markers are shown only for Cycle 1. 136
4.32 Bar chart of the normalized area under the curve (AUC) of the total force chain length for each cycle and shear stage for the dense assembly ($\sigma_n = -29.6$ kPa). The normalized AUC represents the average extent and persistence of the force chain network sustained per unit shear deformation within each stage. 137

4.33 Violin plots of the force chain density for each cycle and shear stage for the dense assembly ($\sigma_n = -29.6$ kPa). Force chain density is defined as the fraction of grains participating in the force chain network relative to the total number of interior grains. The bottom x-axis shows the normalized chain density, while the top x-axis shows the equivalent total force chain length in number of grains. The width of each violin indicates the relative frequency of occurrence of a given chain density during that stage. 139

4.34 Stage-wise medians of the strong network participation [%] (top) and the strong network chain participation [%] (bottom) for each cycle and shear stage for the dense assembly ($\sigma_n = -29.6$ kPa). Error bars represent one-half of the interquartile range, centered about the median. 141

4.35 Stage-wise medians of the shear stress [kPa] (top) and total chain length [number of grains] (bottom) for each cycle and shear stage for the dense assembly ($\sigma_n = -29.6$ kPa). Error bars represent one-half of the interquartile range, centered about the median. 143

4.36 Polar histograms of the normalized angular distributions of the contact fabric orientation, $P(\theta)$, arranged by cycle (rows) and midpoint of each shear stage (columns) for the dense assembly ($\sigma_n = -29.6$ kPa). The solid curve represents the distribution, the dash-dotted curve shows its Fourier fit, and the red dashed line denotes the principal compressive stress axis. 145

4.37 Polar histograms of the mean contact normal force, $\bar{f}_n(\theta)$, arranged by cycle (rows) and midpoint of each shear stage (columns) for the dense assembly ($\sigma_n = -29.6$ kPa). The solid curve represents the distribution, the dash-dotted curve shows its Fourier fit, and the red dashed line denotes the principal compressive stress axis. 147

4.38 Polar histograms of the mean contact tangential force, $\bar{f}_t(\theta)$, arranged by cycle (rows) and midpoint of each shear stage (columns) for the dense assembly ($\sigma_n = -29.6$ kPa). The solid curve represents the distribution, the dash-dotted curve shows its Fourier fit, and the red dashed line denotes the principal compressive stress axis. 149

4.39 Per cycle evolution of the anisotropy magnitudes as functions of shear strain for the dense assembly ($\sigma_n = -29.6$ kPa): fabric anisotropy magnitude, a, and normal and tangential force anisotropy magnitudes, a_n and a_t, respectively. Curve style indicates shearing direction (solid: forward, dash-dotted: reverse), gray dashed lines mark stage transitions. 151

4.40 Per cycle evolution of the invariant stress ratio, q/p, as a function of shear strain for the dense assembly ($\sigma_n = -29.6$ kPa). The experimental response is compared with the predictions of the full and simplified stress-force-fabric (SFF) relationships. Curve style indicates shearing direction (solid: forward, dash-dotted: reverse), gray dashed lines mark stage transitions. 154

4.41 Per-cycle evolution of the probability density function (PDF) of the normalized normal contact force, $f_n / \langle f_n \rangle$, for the dense assembly ($\sigma_n = -29.6$ kPa). Each panel shows one loading cycle, with all stages on a semi-log scale. 157

4.42 Per-cycle evolution of the probability density function (PDF) of the normalized tangential contact force, $f_t / \langle f_n \rangle$, for the dense assembly ($\sigma_n = -29.6$ kPa). Each panel shows one loading cycle, with all stages on a semi-log scale. 158

4.43 Per cycle evolution of the probability density function (PDF) of the mobilized friction, $S = |f_t|/\mu f_n$, for the dense assembly ($\sigma_n = -29.6$ kPa). Each panel shows one loading cycle, with all stages on a semi-log scale. Here, μ is the interparticle friction coefficient, and S indicates the proximity of a contact to sliding (Coulomb failure criterion). 160

4.44 Macroscopic behavior of the three-cycle, loosely packed granular assembly under $\sigma_n = -44.1$ kPa. (a) Stress ratio, μ, (b) volumetric strain, ϵ_v, (c) void ratio, e, and (d) dilatancy, β, as functions of shear strain, γ. Solid curves indicate forward shearing stages (SRF, SRR), whereas dash-dotted curves indicate reverse shearing stages (SLF, SLR). Furthermore, gray vertical dashed lines indicate shear-stage transitions. The yellow and green stars mark the start and end of the cyclic loading, respectively. 163

4.45 Stress ratio evolution for the three-cycle, dense (left) and loose (right) experiments subjected to a normal load of $\sigma_n = -44.1$ kPa. Curve style indicates shearing direction (solid: forward, dash-dotted: reverse), gray dashed lines mark stage transitions, and stars mark the start (yellow) and end (green) of cyclic loading. 164
4.46 Volumetric strain evolution for the three-cycle, dense (left) and loose (right) experiments subjected to a normal load of $\sigma_n = -44.1$ kPa. Curve style indicates shearing direction (solid: forward, dash-dotted: reverse), gray dashed lines mark stage transitions, and stars mark the start (yellow) and end (green) of cyclic loading. 166
4.47 Volumetric strain evolution per stage for the three-cycle, loosely packed, assembly under $\sigma_n = -44.1$ kPa. Stage markers are shown only for Cycle 1. 166
4.48 Void ratio evolution for the three-cycle, dense (left) and loose (right) experiments subjected to a normal load of $\sigma_n = -44.1$ kPa. Curve style indicates shearing direction (solid: forward, dash-dotted: reverse), gray dashed lines mark stage transitions, and stars mark the start (yellow) and end (green) of cyclic loading. 169
4.49 Dilatancy per stage for the three-cycle, loosely packed, assembly under $\sigma_n = -44.1$ kPa. Stage markers are shown only for Cycle 1. . . 169
4.50 Void ratio evolution for the three-cycle, dense (left) and loose (right) experiments subjected to a normal load of $\sigma_n = -44.1$ kPa. Curve style indicates shearing direction (solid: forward, dash-dotted: reverse), gray dashed lines mark stage transitions, and stars mark the start (yellow) and end (green) of cyclic loading. 172
4.51 Void ratio evolution per stage for the three-cycle, loosely packed, assembly under $\sigma_n = -44.1$ kPa. Stage markers are shown only for Cycle 1. 173
4.52 Evolution of the coordination number, Z_c, for the loose granular assembly ($\sigma_n = -44.1$ kPa). Z_c is the average number of contacts per particle. Curve style indicates shearing direction (solid: forward, dash-dotted: reverse), gray dashed lines mark stage transitions, and stars mark the start (yellow) and end (green) of cyclic loading. 176
4.53 Per-stage evolution of the coordination number, Z_c, for the loose granular assembly ($\sigma_n = -44.1$ kPa). Stage markers are shown only for Cycle 1. 176

4.54 Evolution of the detected number of force chains, for the loose granular assembly (σ_n = −44.1 kPa). Curve style indicates shearing direction (solid: forward, dash-dotted: reverse), gray dashed lines mark stage transitions, and stars mark the start (yellow) and end (green) of cyclic loading. 179
4.55 Per-stage evolution of the detected number of force chains for the loose granular assembly (σ_n = −44.1 kPa). Stage markers are shown only for Cycle 1. 179
4.56 Evolution of the total force chain length, in number of grains, for the loose granular assembly (σ_n = −44.1 kPa). Curve style indicates shearing direction (solid: forward, dash-dotted: reverse), gray dashed lines mark stage transitions, and stars mark the start (yellow) and end (green) of cyclic loading. 182
4.57 Per-stage evolution of the total force chain length, in number of grains, for the loose granular assembly (σ_n = −44.1 kPa). Stage markers are shown only for Cycle 1. 183
4.58 Bar chart of the normalized area under the curve (AUC) of the total force chain length for each cycle and shear stage for the loose assembly (σ_n = −44.1 kPa). The normalized AUC represents the average extent and persistence of the force chain network sustained per unit shear deformation within each stage. 185
4.59 Violin plots of the force chain density for each cycle and shear stage for the loose assembly (σ_n = −44.1 kPa). Force chain density is defined as the fraction of grains participating in the force chain network relative to the total number of interior grains. The bottom x-axis shows the normalized chain density, while the top x-axis shows the equivalent total force chain length in number of grains. The width of each violin indicates the relative frequency of occurrence of a given chain density during that stage. 187
4.60 Stage-wise medians of the strong network participation [%] (top) and the strong network chain participation [%] (bottom) for each cycle and shear stage for the loose assembly (σ_n = −44.1 kPa). Error bars represent one-half of the interquartile range, centered about the median. 190

4.61 Stage-wise medians of the shear stress [kPa] (top) and total chain length [number of grains] (bottom) for each cycle and shear stage for the loose assembly ($\sigma_n = -44.1$ kPa). Error bars represent one-half of the interquartile range, centered about the median. 192
4.62 Polar histograms of the normalized angular distributions of the contact fabric orientation, $P(\theta)$, arranged by cycle (rows) and midpoint of each shear stage (columns) for the loose assembly ($\sigma_n = -44.1$ kPa). The solid curve represents the distribution, the dash-dotted curve shows its Fourier fit, and the red dashed line denotes the principal compressive stress axis. 195
4.63 Polar histograms of the mean contact normal force, $\bar{f}_n(\theta)$, arranged by cycle (rows) and midpoint of each shear stage (columns) for the loose assembly ($\sigma_n = -44.1$ kPa). The solid curve represents the distribution, the dash-dotted curve shows its Fourier fit, and the red dashed line denotes the principal compressive stress axis. 196
4.64 Polar histograms of the mean contact tangential force, $\bar{f}_t(\theta)$, arranged by cycle (rows) and midpoint of each shear stage (columns) for the loose assembly ($\sigma_n = -44.1$ kPa). The solid curve represents the distribution, the dash-dotted curve shows its Fourier fit, and the red dashed line denotes the principal compressive stress axis. 197
4.65 Per cycle evolution of the anisotropy magnitudes as functions of shear strain for the loose assembly ($\sigma_n = -44.1$ kPa): fabric anisotropy magnitude, a, and normal and tangential force anisotropy magnitudes, a_n and a_t, respectively. Curve style indicates shearing direction (solid: forward, dash-dotted: reverse), gray dashed lines mark stage transitions. 199
4.66 Per cycle evolution of the invariant stress ratio, q/p, as a function of shear strain for the loose assembly ($\sigma_n = -44.1$ kPa). The experimental response is compared with the predictions of the full and simplified stress-force-fabric (SFF) relationships. Curve style indicates shearing direction (solid: forward, dash-dotted: reverse), gray dashed lines mark stage transitions. 203
4.67 Per-cycle evolution of the probability density function (PDF) of the normalized normal contact force, $f_n / \langle f_n \rangle$, for the loose assembly ($\sigma_n = -44.1$ kPa). Each panel shows one loading cycle, with all stages on a semi-log scale. 206

4.68 Per-cycle evolution of the probability density function (PDF) of the normalized tangential contact force, $f_t / \langle f_n \rangle$, for the loose assembly ($\sigma_n = -44.1$ kPa). Each panel shows one loading cycle, with all stages on a semi-log scale. 207
4.69 Per cycle evolution of the probability density function (PDF) of the mobilized friction, $S = |f_t|/\mu f_n$, for the loose assembly ($\sigma_n = -44.1$ kPa). Each panel shows one loading cycle, with all stages on a semi-log scale. Here, μ is the interparticle friction coefficient, and S indicates the proximity of a contact to sliding (Coulomb failure criterion). 208
4.70 Macroscopic behavior of the three-cycle, loosely packed granular assembly under $\sigma_n = -44.1$ kPa. (a) Stress ratio, μ, (b) volumetric strain, ϵ_v, (c) void ratio, e, and (d) dilatancy, β, as functions of shear strain, γ. Solid curves indicate forward shearing stages (SRF, SRR), whereas dash-dotted curves indicate reverse shearing stages (SLF, SLR). Furthermore, gray vertical dashed lines indicate shear-stage transitions. The yellow and green stars mark the start and end of the cyclic loading, respectively. 212
4.71 Stress ratio evolution for the two three-cycle, loose experiments subjected to a normal load of $\sigma_n = -29.6$ kPa. Curve style indicates shearing direction (solid: forward, dash-dotted: reverse), gray dashed lines mark stage transitions, and stars mark the start (yellow) and end (green) of cyclic loading. 213
4.72 Volumetric strain evolution for the two three-cycle, loose experiments subjected to a normal load of $\sigma_n = -29.6$ kPa. Curve style indicates shearing direction (solid: forward, dash-dotted: reverse), gray dashed lines mark stage transitions, and stars mark the start (yellow) and end (green) of cyclic loading. 215
4.73 Dilatancy evolution for the two three-cycle, loose experiments subjected to a normal load of $\sigma_n = -29.6$ kPa. Curve style indicates shearing direction (solid: forward, dash-dotted: reverse), gray dashed lines mark stage transitions, and stars mark the start (yellow) and end (green) of cyclic loading. 217

4.74 Void ratio evolution for the two three-cycle, loose experiments subjected to a normal load of $\sigma_n = -29.6$ kPa. Curve style indicates shearing direction (solid: forward, dash-dotted: reverse), gray dashed lines mark stage transitions, and stars mark the start (yellow) and end (green) of cyclic loading. 219
4.75 Evolution of the coordination number, Z_c, for the loose granular assembly ($\sigma_n = -29.6$ kPa). Z_c is the average number of contacts per particle. Curve style indicates shearing direction (solid: forward, dash-dotted: reverse), gray dashed lines mark stage transitions, and stars mark the start (yellow) and end (green) of cyclic loading. 221
4.76 Per-stage evolution of the coordination number, Z_c, for the loose granular assembly ($\sigma_n = -29.6$ kPa). Stage markers are shown only for Cycle 1. 221
4.77 Evolution of the detected number of force chains, for the loose granular assembly ($\sigma_n = -29.6$ kPa). Curve style indicates shearing direction (solid: forward, dash-dotted: reverse), gray dashed lines mark stage transitions, and stars mark the start (yellow) and end (green) of cyclic loading. 224
4.78 Per-stage evolution of the detected number of force chains for the loose granular assembly ($\sigma_n = -29.6$ kPa). Stage markers are shown only for Cycle 1. 224
4.79 Evolution of the total force chain length, in number of grains, for the loose granular assembly ($\sigma_n = -29.6$ kPa). Curve style indicates shearing direction (solid: forward, dash-dotted: reverse), gray dashed lines mark stage transitions, and stars mark the start (yellow) and end (green) of cyclic loading. 227
4.80 Per-stage evolution of the total force chain length, in number of grains, for the loose granular assembly ($\sigma_n = -29.6$ kPa). Stage markers are shown only for Cycle 1. 227
4.81 Bar chart of the normalized area under the curve (AUC) of the total force chain length for each cycle and shear stage for the loose assembly ($\sigma_n = -29.6$ kPa). The normalized AUC represents the average extent and persistence of the force chain network sustained per unit shear deformation within each stage. 230

4.82 Violin plots of the force chain density for each cycle and shear stage for the loose assembly ($\sigma_n = -29.6$ kPa). Force chain density is defined as the fraction of grains participating in the force chain network relative to the total number of interior grains. The bottom x-axis shows the normalized chain density, while the top x-axis shows the equivalent total force chain length in number of grains. The width of each violin indicates the relative frequency of occurrence of a given chain density during that stage. 232

4.83 Stage-wise medians of the strong network participation [%] (top) and the strong network chain participation [%] (bottom) for each cycle and shear stage for the loose assembly ($\sigma_n = -29.6$ kPa). Error bars represent one-half of the interquartile range, centered about the median. 235

4.84 Stage-wise medians of the shear stress [kPa] (top) and total chain length [number of grains] (bottom) for each cycle and shear stage for the loose assembly ($\sigma_n = -29.6$ kPa). Error bars represent one-half of the interquartile range, centered about the median. 237

4.85 Polar histograms of the normalized angular distributions of the contact fabric orientation, $P(\theta)$, arranged by cycle (rows) and midpoint of each shear stage (columns) for the loose assembly ($\sigma_n = -29.6$ kPa). The solid curve represents the distribution, the dash-dotted curve shows its Fourier fit, and the red dashed line denotes the principal compressive stress axis. 240

4.86 Polar histograms of the mean contact normal force, $\bar{f}_n(\theta)$, arranged by cycle (rows) and midpoint of each shear stage (columns) for the loose assembly ($\sigma_n = -29.6$ kPa). The solid curve represents the distribution, the dash-dotted curve shows its Fourier fit, and the red dashed line denotes the principal compressive stress axis. 241

4.87 Polar histograms of the mean contact tangential force, $\bar{f}_t(\theta)$, arranged by cycle (rows) and midpoint of each shear stage (columns) for the loose assembly ($\sigma_n = -29.6$ kPa). The solid curve represents the distribution, the dash-dotted curve shows its Fourier fit, and the red dashed line denotes the principal compressive stress axis. 242

4.88 Per cycle evolution of the anisotropy magnitudes as functions of shear strain for the loose assembly ($\sigma_n = -29.6$ kPa): fabric anisotropy magnitude, a, and normal and tangential force anisotropy magnitudes, a_n and a_t, respectively. Curve style indicates shearing direction (solid: forward, dash-dotted: reverse), gray dashed lines mark stage transitions. 244

4.89 Per cycle evolution of the invariant stress ratio, q/p, as a function of shear strain for the loose assembly ($\sigma_n = -29.6$ kPa). The experimental response is compared with the predictions of the full and simplified stress-force-fabric (SFF) relationships. Curve style indicates shearing direction (solid: forward, dash-dotted: reverse), gray dashed lines mark stage transitions. 248

4.90 Per-cycle evolution of the probability density function (PDF) of the normalized normal contact force, $f_n / \langle f_n \rangle$, for the loose assembly ($\sigma_n = -29.6$ kPa). Each panel shows one loading cycle, with all stages on a semi-log scale. 251

4.91 Per-cycle evolution of the probability density function (PDF) of the normalized tangential contact force, $f_t / \langle f_n \rangle$, for the loose assembly ($\sigma_n = -29.6$ kPa). Each panel shows one loading cycle, with all stages on a semi-log scale. 252

4.92 Per cycle evolution of the probability density function (PDF) of the mobilized friction, $S = |f_t|/\mu f_n$, for the loose assembly ($\sigma_n = -29.6$ kPa). Each panel shows one loading cycle, with all stages on a semi-log scale. Here, μ is the interparticle friction coefficient, and S indicates the proximity of a contact to sliding (Coulomb failure criterion). 254

A.1 Three frames analyzed for α selection from the densely-packed, -44.1 [kPa] normally loaded, $N = 1$ cyclic simple shear experiment. 282

B.1 Dilatancy evolution per cycle for the three-cycle, dense experiments. Left column: higher-confinement ($\sigma_n = -44.1$ kPa ≈ 122 lb). Right column: lower-confinement ($\sigma_n = -29.6$ kPa ≈ 82 lb). Curve style indicates shearing direction (solid: forward, dash-dotted: reverse), gray dashed lines mark stage transitions, stars mark the start (orange) and end (green) of cyclic loading, and filled circles indicate where cycles connect. 283

B.2 Dilatancy evolution per cycle for the three-cycle, loose experiments. Left column: higher-confinement ($\sigma_n = -44.1$ kPa ≈ 122 lb). Right column: lower-confinement ($\sigma_n = -29.6$ kPa ≈ 82 lb). Curve style indicates shearing direction (solid: forward, dash-dotted: reverse), gray dashed lines mark stage transitions, stars mark the start (orange) and end (green) of cyclic loading, and filled circles indicate where cycles connect. 284

C.1 Stress ratio evolution for the three-cycle experiments. Columns indicate the applied normal stress: (left) $\sigma_n = -44.1$ kPa ≈ 122 lb, and (right) $\sigma_n = -29.6$ kPa ≈ 82 lb. Rows indicate (top) densely packed and (bottom) loosely packed granular assemblies. Curve style indicates shearing direction (solid: forward, dash-dotted: reverse), gray dashed lines mark stage transitions, and stars mark the start (yellow) and end (green) of cyclic loading. 285

C.2 Volumetric strain evolution for the three-cycle experiments. Columns indicate the applied normal stress: (left) $\sigma_n = -44.1$ kPa ≈ 122 lb, and (right) $\sigma_n = -29.6$ kPa ≈ 82 lb. Rows indicate (top) densely packed and (bottom) loosely packed granular assemblies. Curve style indicates shearing direction (solid: forward, dash-dotted: reverse), gray dashed lines mark stage transitions, and stars mark the start (yellow) and end (green) of cyclic loading. 286

C.3 Dilatancy evolution for the three-cycle experiments. Columns indicate the applied normal stress: (left) $\sigma_n = -44.1$ kPa ≈ 122 lb, and (right) $\sigma_n = -29.6$ kPa ≈ 82 lb. Rows indicate (top) densely packed and (bottom) loosely packed granular assemblies. Curve style indicates shearing direction (solid: forward, dash-dotted: reverse), gray dashed lines mark stage transitions, and stars mark the start (yellow) and end (green) of cyclic loading. 287

C.4 Void ratio evolution for the three-cycle experiments. Columns indicate the applied normal stress: (left) $\sigma_n = -44.1$ kPa ≈ 122 lb, and (right) $\sigma_n = -29.6$ kPa ≈ 82 lb. Rows indicate (top) densely packed and (bottom) loosely packed granular assemblies. Curve style indicates shearing direction (solid: forward, dash-dotted: reverse), gray dashed lines mark stage transitions, and stars mark the start (yellow) and end (green) of cyclic loading. 288

D.1 Coordination number evolution for the three-cycle experiments. Columns indicate (left) densely packed and (right) loosely packed granular assemblies. Rows indicate the applied normal stress: (top) $\sigma_n = -44.1$ kPa ≈ 122 lb, and (bottom) $\sigma_n = -29.6$ kPa ≈ 82 lb. Curve style indicates shearing direction (solid: forward, dash-dotted: reverse), gray dashed lines mark stage transitions, and stars mark the start (yellow) and end (green) of cyclic loading. 289

D.2 Number of force chains evolution for the three-cycle experiments. Columns indicate (left) densely packed and (right) loosely packed granular assemblies. Rows indicate the applied normal stress: (top) $\sigma_n = -44.1$ kPa ≈ 122 lb, and (bottom) $\sigma_n = -29.6$ kPa ≈ 82 lb. Curve style indicates shearing direction (solid: forward, dash-dotted: reverse), gray dashed lines mark stage transitions, and stars mark the start (yellow) and end (green) of cyclic loading. 290

D.3 Bar chart of the normalized area under the curve (AUC) of the total force chain length for each cycle and shear stage for the dense assembly. (a) Higher confinement ($\sigma_n = -44.1$ kPa), and (b) lower confinement ($\sigma_n = -29.6$ kPa ≈ 82 lb) . The normalized AUC represents the average extent and persistence of the force chain network sustained per unit shear deformation within each stage. 291

D.4 Bar chart of the normalized area under the curve (AUC) of the total force chain length for each cycle and shear stage for the loose assembly. (a) Higher confinement ($\sigma_n = -44.1$ kPa), and (b) lower confinement ($\sigma_n = -29.6$ kPa ≈ 82 lb) . The normalized AUC represents the average extent and persistence of the force chain network sustained per unit shear deformation within each stage. 292

D.5 Violin plots of the force chain density for each cycle and shear stage. Force chain density is defined as the fraction of grains participating in the force chain network relative to the total number of interior grains. The bottom x-axis shows the normalized chain density, while the top x-axis shows the equivalent total force chain length in number of grains. The width of each violin indicates the relative frequency of occurrence of a given chain density during that stage. 293

D.6 Stage-wise medians of the strong network participation [%] (top) and the strong network chain participation [%] (bottom) for each cycle and shear stage for the dense assembly (left) and loose assembly (right). The first metric is the fraction of high-stress grains among all interior grains (Eq. (3.5)), and the second metric is the fraction of high-stress grains that are organized into force chains (Eq. (3.6)). Error bars represent one-half of the interquartile range, centered about the median. 294

D.7 Stage-wise medians of the shear stress [kPa] (top) and total chain length [number of grains] (bottom) for each cycle and shear stage for the dense assembly (left) and loose assembly (right). Error bars represent one-half of the interquartile range, centered about the median. 295

D.8 Per cycle evolution of the anisotropy magnitudes as functions of shear strain: fabric anisotropy magnitude, a, and normal and tangential force anisotropy magnitudes, a_n and a_t, respectively. Curve style indicates shearing direction (solid: forward, dash-dotted: reverse), gray dashed lines mark stage transitions. 296

D.9 Per cycle evolution of the invariant stress ratio, q/p, as a function of shear strain. The experimental response is compared with the predictions of the full and simplified stress-force-fabric (SFF) relationships (Eqs. (3.10) and (3.13)). Curve style indicates shearing direction (solid: forward, dash-dotted: reverse), gray dashed lines mark stage transitions. 297

D.10 Probability density functions (PDFs) of the normalized normal contact force, $f_n / \langle f_n \rangle$, for the dense assembly, where each panel shows one loading cycle, with all stages on a semi-log scale. (a) Higher confinement ($\sigma_n = -44.1$ kPa $\approx$ 122 lb load), and (b) lower confinement ($\sigma_n = -29.6$ kPa $\approx$ 82 lb load). 298

D.11 Probability density functions (PDFs) of the normalized normal contact force, $f_n / \langle f_n \rangle$, for the loose assembly, where each panel shows one loading cycle, with all stages on a semi-log scale. (a) Higher confinement ($\sigma_n = -44.1$ kPa $\approx$ 122 lb load), and (b) lower confinement ($\sigma_n = -29.6$ kPa $\approx$ 82 lb load).. 299

D.12 Probability density functions (PDFs) of the normalized tangential contact force, $f_t / \langle f_n \rangle$, for the dense assembly, where each panel shows one loading cycle, with all stages on a semi-log scale. (a) Higher confinement ($\sigma_n = -44.1$ kPa $\approx$ 122 lb load), and (b) lower confinement ($\sigma_n = -29.6$ kPa $\approx$ 82 lb load). 300

D.13 Probability density functions (PDFs) of the normalized tangential contact force, $f_t / \langle f_n \rangle$, for the loose assembly, where each panel shows one loading cycle, with all stages on a semi-log scale. (a) Higher confinement ($\sigma_n = -44.1$ kPa $\approx$ 122 lb load), and (b) lower confinement ($\sigma_n = -29.6$ kPa $\approx$ 82 lb load). 301

D.14 Probability density functions (PDFs) of the mobilized friction, $S = |f_t|/\mu f_n$, for the dense assembly, where each panel shows one loading cycle, with all stages on a semi-log scale. Here, μ is the interparticle friction coefficient, and S indicates the proximity of a contact to sliding (Coulomb failure criterion). (a) Higher confinement ($\sigma_n = -44.1$ kPa $\approx$ 122 lb load), and (b) lower confinement ($\sigma_n = -29.6$ kPa $\approx$ 82 lb load). 302

D.15 Probability density functions (PDFs) of the mobilized friction, $S = |f_t|/\mu f_n$, for the loose assembly, where each panel shows one loading cycle, with all stages on a semi-log scale. Here, μ is the interparticle friction coefficient, and S indicates the proximity of a contact to sliding (Coulomb failure criterion). (a) Higher confinement ($\sigma_n = -44.1$ kPa $\approx$ 122 lb load), and (b) lower confinement ($\sigma_n = -29.6$ kPa $\approx$ 82 lb load). 303

LIST OF TABLES

Number *Page*

1.1 Comparison of common laboratory apparatuses used to investigate cyclic loading behavior in granular materials. The triaxial, hollow cylinder, and simple shear tests are evaluated with respect to loading-path control, principal stress rotation, boundary conditions, and suitability for cyclic shear studies. Based on these criteria, the simple shear apparatus was selected for the experiments in this thesis. 5

3.1 Percentage of strong network grains median and mean absolute deviation (MAD) 57

3.2 Percentage of strong network grains in force chains median and MAD 57

A.1 Mid-stage frame (Img 176). 282

A.2 Strongest force chain frame (Img 210). 282

A.3 Near shear-reversal frame (Img 549). 282

E.1 Percentage of strong network grains: median and MAD 304

E.2 Percentage of strong network grains in force chains: median and MAD 305

E.3 Percentage of strong network grains: median and MAD 305

E.4 Percentage of strong network grains in force chains: median and MAD 306

E.5 % of strong network grains median and mean absolute deviation (MAD) 306

E.6 % of strong network grains in force chains median and MAD 307

E.7 % of strong network grains median and mean absolute deviation (MAD) 307

E.8 % of strong network grains in force chains median and MAD 308

Chapter 1

INTRODUCTION

1.1 Objectives

This thesis investigates the multiscale behavior of dry, cohesionless granular materials subjected to quasi-static cyclic simple shear loading through laboratory experiments coupled with the Granular Element Method (GEM), a force-inference framework for estimating interparticle contact forces.

The primary objectives of this research are:

1. To develop and implement an experimental framework for controlled cyclic simple shear loading by upgrading an existing simple shear apparatus.
2. To determine how grain-scale mechanisms – including force chain evolution, contact network reorganization, and anisotropy development – govern the macroscopic cyclic response of granular materials.
3. To evaluate how repeated loading, packing density, and normal confinement influence the multiscale behavior of granular assemblies under cyclic shear.

1.2 Granular Materials under Cyclic Loading

Granular materials are among the most abundant materials encountered in nature and engineering, second only to fluids in everyday occurrence, and are defined as collections of solid frictional particles of size greater than one micron. Common examples include sand, rice, pharmaceutical pills, railway ballast, and snow [1, 2]. Despite their prevalence, the mechanical behavior of granular materials under cyclic loading remains incompletely understood, particularly when examined across multiple length scales.

Cyclic loading arises from a wide range of natural and man-made sources. In nature, wind and waves impose repeated loading on onshore and offshore structures. Earthquakes generate shear waves that induce cyclic shearing of soils that can lead to catastrophic soil liquefaction. Soil liquefaction during earthquakes, such as the infamous 1964 Niigata 7.5-magnitude earthquake, has caused severe damage to foundations, embankments, retaining structures, and transportation infrastructure

(Figure 1.1) [3]. Repeated loading also occurs in engineered systems, including traffic loads from railways and highways, crane rails, vibrating machinery, the repeated filling and emptying of watergates and silos, and the mechanical compaction of surfaces [4].

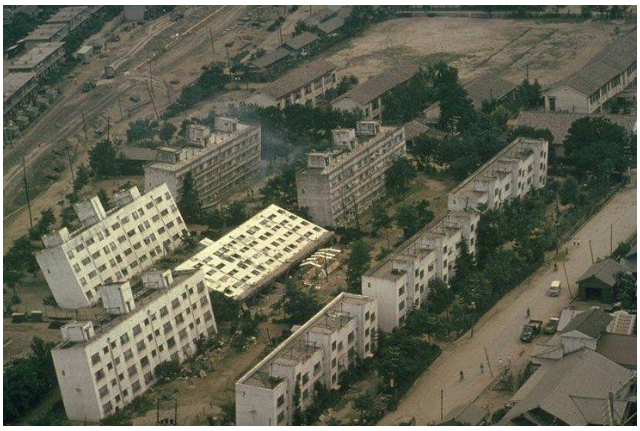


Figure 1.1: Liquefaction-induced damage during the 1964 Niigata, Japan earthquake. Image reproduced from [3] and accessed via Wikimedia Commons.

At the macroscale, it is well known that cyclic loading can produce behavior that differs significantly from monotonic loading. Repeated cycles may reduce bearing capacity, induce uneven settlement, alter stiffness, and cause permanent deformation beneath structures. In offshore energy applications, for instance, excessive foundation rotation can reduce turbine serviceability once tilt exceeds 2 to 5 degrees [5]. Repeated loading on already-deformed granular terrain, commonly referred to as multi-pass loading, is also particularly important in vehicle mobility problems (Figure 1.2). In military operations, successive wheel and track passes can progressively alter the density and internal structure of granular terrain, leading to excessive sinkage, reduced drawbar pull, and eventual vehicle immobilization. These effects are critical in go/no-go mobility assessments for convoys operating on unpaved terrain [6]. Similar challenges arise in planetary exploration, where rover wheels or tracks are subjected to repeated loading as they traverse loose regolith. A well-known example is the entrapment of the Mars Exploration Rover Spirit, which became embedded in weak soil deposits within Troy crater in 2009 [7]. These examples demonstrate that cyclic loading is not simply repeated monotonic loading, but a distinct loading condition in which history effects and progressive internal changes become important.



(a) (b)

Figure 1.2: Vehicle mobility examples in granular terrain. (a) A Humvee traversing rugged terrain in Khowst Province, Afghanistan. U.S. Marine Corps image, public domain [8]. (b) NASA's Mars Exploration Rover Spirit partially embedded in loose Martian regolith [9]. Image credit: NASA/JPL-Caltech.

Although the macroscopic effects of cyclic loading are well documented, the grain-scale mechanisms underlying this behavior are less well understood experimentally. Processes such as contact rearrangement, force chain evolution, anisotropy development, and localized particle sliding are believed to influence the bulk response strongly, yet are difficult to observe directly during loading [2, 10, 11]. For this reason, a variety of laboratory test devices were developed to reproduce cyclic loading conditions and to study granular media behavior in controlled environments.

1.3 Common Test Devices for Studying Granular Media

Several laboratory devices are commonly used to study the response of granular materials under cyclic loading, including: (1) the consolidation (oedometer) test, (2) the axisymmetric triaxial test, (3) the hollow cylinder torsional shear test, and (4) the simple shear test [4]. Each apparatus offers different advantages depending on the loading path and material behavior of interest.

The oedometer test, introduced by Terzaghi in 1925 [12], has long been used to evaluate the compressibility and swelling behavior of soils under one-dimensional loading. It remains widely used in geotechnical practice for estimating settlement beneath foundations and earth structures. However, because loading is restricted to one dimension, the oedometer test is not well-suited to studying cyclic shear deformation or more complex stress paths [13].

For this reason, the most relevant devices for the present study are the axisymmetric triaxial test, the hollow cylinder torsional shear test, and the direct simple shear test, all of which permit shear loading under controlled confinement.

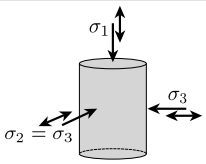
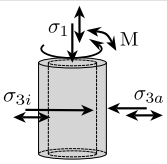
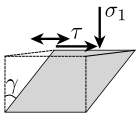
In the axisymmetric triaxial test, a cylindrical specimen enclosed within a latex membrane is subjected to an all-around confining pressure while axial loading is applied vertically. Shearing develops due to the difference between axial stress and confining stress. The triaxial test is widely available, relatively simple to operate, and extensively used for monotonic and cyclic soil testing. However, true simple shear stresses cannot be applied, the compliant membrane permits radial deformations, and the principal stress directions rotate rapidly rather than gradually during loading. Since many geotechnical problems involve progressive rotation of the principal stress directions during loading, this limitation can be significant [4, 14].

The hollow cylinder torsional shear test addresses several of these limitations. In this apparatus, a hollow cylindrical specimen enclosed by a membrane can be subjected to axial loading, torsional shear, and independently controlled inner and outer pressures. This allows complex stress paths and gradual rotation of the principal stress directions [4, 14]. However, the test remains mechanically complex, and membrane effects can produce stress and strain nonuniformities that vary with radius. Additional nonuniform stresses may arise from the simultaneous application of torque and pressure gradients [15].

In the simple shear test, the specimen is laterally confined by rigid rings or rigid walls while a normal load is applied vertically. Shearing is then induced by horizontal displacement of either the top or bottom boundary. As in the hollow cylinder test, the principal stress directions rotate continuously during loading [4, 14]. More importantly, the simple shear test closely reproduces field conditions associated with horizontal ground motion, such as earthquake-induced soil shearing [16]. The main limitations of the test are nonuniform stress and strain fields near boundaries and the possible pinching of material at corners or wall interfaces. In practice, nonuniform stresses and strains are avoided by focusing the analysis on the specimen's central region, often referred to as the sample core [17].

Table 1.1 summarizes the main advantages and limitations of the triaxial, torsional shear, hollow cylinder, and simple shear devices. After considering the loading paths relevant to this study, the need for gradual stress rotation, and the desire to simulate field-like cyclic shearing conditions, the simple shear apparatus was selected for the experiments presented in this thesis.

Table 1.1: Comparison of common laboratory apparatuses used to investigate cyclic loading behavior in granular materials. The triaxial, hollow cylinder, and simple shear tests are evaluated with respect to loading-path control, principal stress rotation, boundary conditions, and suitability for cyclic shear studies. Based on these criteria, the simple shear apparatus was selected for the experiments in this thesis.

Criterion	**Triaxial Test**	**Hollow Cylinder Test**	**Simple Shear Test**
			
Stress Path Control	Moderate	**High**	Moderate–High
Principal Stress Rotation	Limited/sudden	**Continuous**	**Continuous**
Ability to Simulate Cyclic Shear	Moderate	**High**	**High**
Boundary Conditions	Membrane confinement	Membrane confinement	Rigid lateral confinement
Main Advantages	Widely available, simple, standardized	Complex loading paths, independent stress control	**Closely simulates field shearing, continuous stress rotation**
Main Limitations	No true simple shear, radial deformation	Complex apparatus, radial stress/strain gradients	Boundary non-uniformity near walls/corners

1.4 Granular Media Across Length Scales

As shown schematically in Figure 1.3, granular materials can be studied across three primary length scales: microscale, mesoscale, and macroscale. The macroscale describes the overall behavior of the full specimen or bulk material. For example, one may be interested in the motion of a landslide, the settlement beneath a foundation, or the shear resistance of an entire laboratory sample. The microscale, also known as the grain-scale, focuses on individual grains and their local interactions, such as contacts, rotations, and contact forces. Between these two is the mesoscale, where behavior is examined within a smaller representative volume of material containing many particles. Studying all three scales helps explain how local grain behavior gives rise to the granular assembly's overall response.

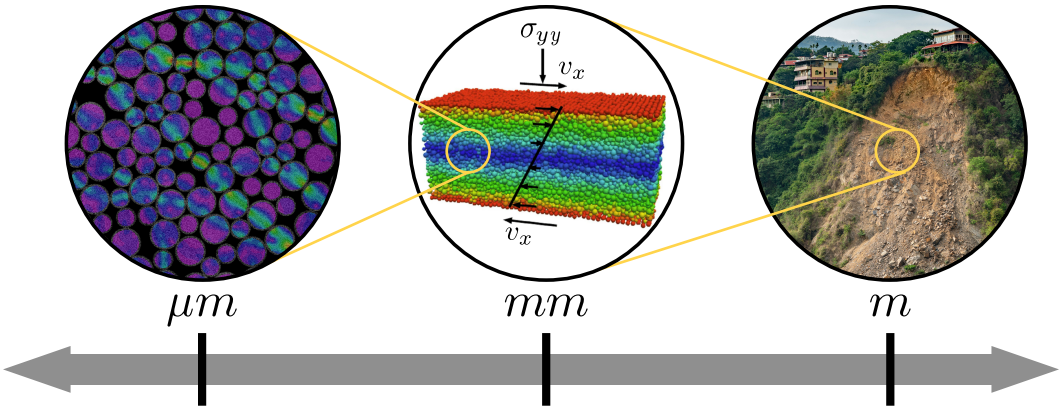


Figure 1.3: Characteristic length scales in granular media: macroscale (km), mesoscale (mm), and microscale (μm). Example behavior at each scale includes bulk landslide flow, a representative volume element (RVE) of grains deforming within that flow, and individual grain interactions within the RVE. The macroscale panel includes a photograph by Timo Volz from Unsplash [18]. The mesoscale panel was adapted from Hurley et al. [19], with permission from Springer Nature.

1.4.1 Macroscale Properties

In this thesis, the four macroscopic quantities of interest are: (1) stress ratio, (2) shear strain, (3) volumetric strain, and (4) void ratio. Together, these quantities describe the overall strength, deformation, and packing state of the granular assembly during cyclic loading.

The first is the **stress ratio**, μ, defined as the ratio of shear stress to applied normal load, $\mu = \tau_{xy}/\sigma_{yy}$. The stress ratio indicates the level of shear resistance mobilized under the applied load. In general, a higher stress ratio corresponds to a stronger bulk response [20].

The next two quantities are **shear strain**, γ, and **volumetric strain**, ϵ_v. Shear strain describes the distortion of the sample during loading, while volumetric strain describes changes in specimen volume. A positive volumetric strain indicates dilation (i.e., the granular assembly expands), whereas a negative volumetric strain indicates contraction. These quantities are linked through Reynolds dilatancy, which describes the tendency of granular materials to change volume as they shear, $\dot{\epsilon_v} = \beta\dot{\gamma}$ [21].

The fourth quantity is the **void ratio**, e, which is the ratio of pore volume to solid particle volume. The void ratio is especially useful for distinguishing densely packed and loosely packed assemblies, since packing state strongly influences stiffness, strength, and deformation behavior [22].

With sufficient shearing, deformation may also localize into narrow zones known as **shear bands**. Shear bands are regions of concentrated strain that often precede failure, since the surrounding material loses the ability to bear load uniformly [23].

1.4.2 Microscale and Mesoscale Properties

At the microscale, five quantities are particularly important: (1) coordination number, (2) interparticle forces, (3) particle kinematics, (4) particle rearrangement mechanisms, and (5) anisotropy. Together, these quantities help describe how grains interact, reorganize, and transmit load during deformation.

The **coordination number**, Z_c, is the average number of contacts per grain. This property plays an important role in the stability and connectivity of a granular assembly. In general, a higher coordination number indicates more contact pathways available to transmit forces through the material [12].

Interparticle forces develop at contact point locations between grains. These forces are typically highly nonuniform and often organize into preferential load-bearing paths, forming chain-like structures called force chains. Force chains form the internal skeleton that carries much of the applied load [24, 25].

Particle kinematics describe how individual grains translate, rotate, and deform during loading. Tracking these motions provides direct insight into how the assembly accommodates shear and how contacts form and break over time [26].

Particle rearrangement mechanisms include sliding, rolling, and interlocking between neighboring grains. These local mechanisms strongly influence force transmission and bulk response. For example, an interlocked granular assembly can often sustain larger loads than one in which grains are freely rolling or sliding [26–28].

Another important concept is **anisotropy**. Anisotropy refers to the directional dependence of the material's internal structure or force transmission. In granular assemblies, contacts or forces may become preferentially aligned in certain directions during loading, thereby significantly influencing shear strength and deformation behavior [29, 30].

These same properties can also be examined at the mesoscale by measuring them within a representative volume element (RVE) rather than across the entire specimen or at the level of individual particles.

1.5 Multiscale Approaches to Characterizing Granular Material Behavior

The macroscopic and grain-scale quantities introduced in the previous section can be studied using both computational and experimental approaches. Over the past several decades, researchers have developed continuum constitutive models, particle-based numerical simulations, and laboratory force-inference techniques to better understand how granular materials deform, transmit loads, and fail. These approaches are especially valuable because they help relate bulk material response to the evolving mechanics of individual grains and contacts. Together, they provide complementary perspectives for linking behavior across length scales.

1.5.1 Modeling Approaches

Granular materials have been studied using two broad modeling approaches: continuum constitutive models and physics-based particle methods. These approaches differ mainly in how they represent the material. Continuum models treat a granular assembly as an equivalent homogeneous medium described by averaged stress, strain, and density fields. In contrast, particle methods represent the material as a collection of individual grains that interact through contact forces. Both approaches have contributed significantly to understanding granular behavior, but they provide different levels of insight into the mechanisms governing deformation and failure. Continuum models are especially useful for engineering-scale prediction, whereas particle-based methods are better suited for studying how grain-scale interactions produce the observed bulk response.

1.5.1.1 Continuum (Constitutive) Modeling

Granular materials have traditionally been described using continuum constitutive frameworks that relate macroscopic stresses, strains, and volume change through phenomenological or semi-empirical laws. These approaches have been highly effective in representing bulk behavior across a wide range of loading paths and in establishing widely used concepts such as yielding, dilatancy, and failure. In geomechanics, models based on the Mohr–Coulomb failure criterion and critical-state theory have provided the foundation for interpreting shear strength, stress-strain response, and density-dependent behavior in sands and other cohesionless materials [31, 32]. Because these frameworks are formulated in terms of averaged field quantities, they are well-suited to engineering-scale analyses in which the material can be treated as a continuum.

However, cyclic loading introduces additional complexity that is difficult to capture using purely phenomenological descriptions. Repeated loading can produce irreversible deformation, stiffness evolution, anisotropy development, and memory effects, all of which depend strongly on loading history and internal structural rearrangement [4, 5]. Numerous constitutive extensions have therefore been proposed to describe cyclic ratcheting, stiffness degradation, and liquefaction resistance in sands. Ratcheting refers to the progressive accumulation of permanent deformation over repeated loading cycles, even when each cycle is bounded [33]. While these models often improve engineering predictions, they still rely on internal state variables–such as fabric, density state, hardening parameters, and accumulated plastic strain–that are usually inferred from macroscopic response rather than measured directly [34].

This limitation is especially important for cyclic simple shear, where the gradual rotation of principal stress directions and repeated reversals in loading produce strongly path-dependent behavior. Experimental studies have shown that the response of granular assemblies evolves with cycle count, loading amplitude, and stress path, rather than remaining fixed by a single constitutive relation [10, 35]. Consequently, although continuum models remain indispensable for practical engineering analysis, they do not directly reveal the grain-scale mechanisms responsible for the observed macroscopic response. This limitation has motivated the continued development of particle-based and experimentally informed approaches that link bulk response to the mechanics of individual grains and contacts.

1.5.1.2 Physics-Based Modeling

To address the limitations of continuum-only descriptions, physics-based particle methods have been developed to represent granular materials as assemblies of interacting grains. Rather than averaging the material response over the full specimen, these approaches track the motion of individual particles and resolve contact interactions directly using force and moment balance. As a result, they provide access to grain-scale quantities that are difficult to obtain from continuum models alone, including contact forces, contact orientations, particle rotations, coordination number, and internal load-bearing structures.

The most widely used of these methods is the Discrete Element Method (DEM), first introduced by Cundall and Strack [24]. In DEM, particles interact via prescribed normal and tangential contact laws, and their translational and rotational motions are updated over time. Since its development, DEM has become a powerful tool for studying granular materials under monotonic, cyclic, and dynamic

loading conditions. By explicitly resolving particle interactions, DEM has shown that macroscopic behavior emerges from collective grain-scale processes rather than intrinsic continuum properties alone.

DEM studies have provided important insight into the response of granular materials under cyclic loading. Repeated shearing has been shown to cause continuous reorganization of the contact network, breakage and reformation of force chains, evolving anisotropy, and highly heterogeneous force transmission [11, 36, 37]. These studies have also shown that irreversible deformation, hysteresis, cyclic mobility, and strength evolution are closely tied to changes in the internal force network. In many cases, force anisotropy has been found to play a stronger role than fabric anisotropy in controlling stress transmission, indicating that the mechanical state of a granular assembly depends not only on particle arrangement but also on the distribution of forces among contacts.

Despite these advantages, DEM also has important limitations. Simulations can be computationally expensive, particularly for large assemblies or long loading histories, and they often rely on simplified particle shapes and idealized contact laws. While these simplifications are useful for isolating key mechanisms, they may reduce fidelity when compared with natural materials composed of irregular grains under realistic boundary conditions. Consequently, DEM is most powerful when used alongside experiments that can validate its predicted grain-scale behavior. These challenges have motivated the development of experimental techniques to directly characterize internal force transmission in granular materials.

1.5.2 Force-Inference Techniques

While modeling approaches provide valuable predictions of granular behavior, experimental techniques are needed to directly examine how forces are transmitted through real granular assemblies. This remains challenging because most experimental methods measure particle motion, geometry, or boundary response, while the internal contact force network is not directly observable.

1.5.2.1 Photoelasticity

An influential experimental approach for studying granular force transmission is photoelasticity. In this method, birefringent particles develop stress-dependent fringe patterns that can be used to visualize contact forces, force chains, arching, and stress heterogeneity (Figure 1.4). However, photoelasticity is generally limited to transparent birefringent materials with relatively simple particle shapes [38, 39].

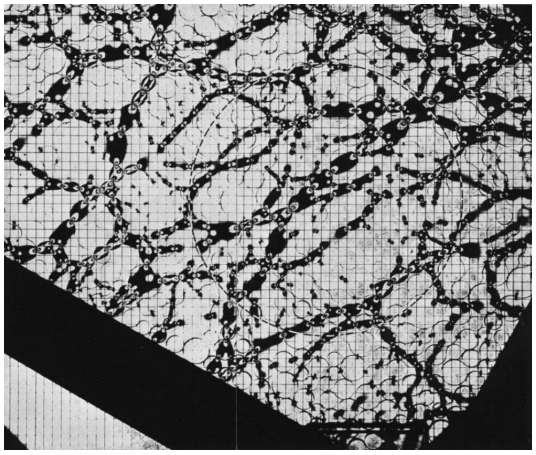


Figure 1.4: Early experimental visualization of force chains in a granular assembly of discs using photoelasticity. Adapted from Drescher and de Josselin de Jong [38], with permission from Elsevier.

1.5.2.2 Granular Element Method

To address these limitations, Andrade and Avila introduced the Granular Element Method (GEM), a mechanics-based inverse framework for estimating interparticle contact forces from experimentally measurable grain-scale data [40]. GEM uses information such as particle geometry, contact locations, and grain kinematics, along with equilibrium and contact constraints, to reconstruct the internal force network. Unlike photoelasticity, GEM can be applied to opaque materials and irregular grain shapes.

Since its introduction, GEM has been extended to a variety of loading conditions and specimen configurations, demonstrating its usefulness as a multiscale experimental tool. In this thesis, GEM is used to investigate the grain-scale mechanics of granular materials under cyclic simple shear loading. A detailed review of the GEM framework is provided in Chapter 2.

1.6 Research Gap and Thesis Scope

Although the cyclic behavior of granular materials has been studied extensively, much of the existing work has focused on macroscopic quantities such as settlement, stiffness degradation, liquefaction resistance, and strength evolution. These studies have provided important engineering insight, but they offer limited information about the internal grain-scale mechanisms responsible for the observed bulk response. More recent DEM studies have improved understanding of contact-network evolution, force chain reorganization, and anisotropy development during cyclic loading. However, experimental grain-scale characterization remains com-

paratively limited, particularly for opaque materials and irregular grain geometries.

This thesis addresses that gap through laboratory experiments coupled with the Granular Element Method (GEM), which enables estimation of interparticle contact forces from experimentally measurable grain-scale data. Using an upgraded cyclic simple shear apparatus, this work investigates how internal force transmission, structural evolution, packing density, and confinement influence the macroscopic cyclic response of granular materials.

The layout for this thesis is as follows. **Chapter 2** presents the Granular Element Method (GEM), outlines the experimental inputs required by the method, and develops the inverse problem for inferring interparticle contact forces from measurable grain-scale data. **Chapter 3** describes the upgraded cyclic simple shear apparatus, experimental procedures, imaging methods, and a baseline one-cycle experiment on a densely packed granular assembly. Macroscopic and grain-scale responses are analyzed to establish the system's fundamental behavior under cyclic loading. **Chapter 4** extends the study to three-cycle experiments performed at two normal confinement levels and two initial packing densities (dense and loose). Emphasis is placed on how the loading history, packing density, and confinement level affect force chain evolution, anisotropy, contact connectivity (coordination number), and the resulting bulk response. **Chapter 5** summarizes the major findings of this thesis, discusses their implications for granular mechanics, and provides recommendations for future work. Supporting procedures and supplementary figures are provided in the appendices.

Chapter 2

GRANULAR ELEMENT METHOD

2.1 Introduction

Granular materials exhibit complex behavior because their macroscopic response emerges from interactions occurring at the grain scale. Phenomena such as shear strength, dilatancy, strain localization (i.e., shear band formation), and anisotropy are governed by the creation, loss, and reorganization of interparticle contacts, as well as by the heterogeneous transmission of forces through the granular assembly [2, 39, 41, 42]. For this reason, understanding granular material behavior requires methods capable of resolving not only macroscopic quantities, but also the internal grain-scale mechanics that generate them.

Both computational and experimental advances have significantly improved access to grain-scale behavior. On the computational side, the Discrete Element Method (DEM) is the most widely used physics-based approach for modeling granular materials as interacting particles governed by contact laws and Newtonian mechanics [24]. DEM can provide detailed micromechanical information, including contact forces, particle kinematics, force chain evolution, and bulk stress response, making it a valuable tool for studying multiscale behavior. More recently, the Level-Set Discrete Element Method (LS-DEM) has extended this framework by representing realistic particle morphologies more accurately than conventional sphere- or polyhedron-based DEM formulations [43]. However, despite their predictive power, DEM and LS-DEM remain computationally expensive, often limiting the number of particles, loading duration, or parameter studies that can be practically analyzed. In addition, the model predictions depend on assumptions regarding contact constitutive laws, friction, damping, and boundary conditions. Consequently, experimental measurements remain essential for calibration, validation, and assessment of model fidelity.

On the experimental side, substantial progress has improved direct observation of granular kinematics, fabric, and particle-scale response. Optical techniques such as digital image correlation (DIC) enable measurements of full-field displacements, rotations, and strains from image sequences [44], while X-ray computed tomography provides three-dimensional characterization of particle geometry, fabric, and

internal rearrangements within opaque assemblies [45, 46]. Building on these developments, XRCT combined with particle image velocimetry (PIV) has also been used to characterize soil flow kinematics beneath running gears, enabling measurements of velocity and strain fields during wheel-soil interaction [47]. More recently, synchrotron microcomputed tomography (SMT) combined with three-dimensional X-ray diffraction microscopy (3DXRT) has enabled in-situ measurements of the internal structure, particle kinematics, lattice strains, and evolving force structures of thousands of natural sand grains under compression, representing a major advance in 3D experimental characterization of granular mechanics [48]. These techniques have greatly expanded the ability to observe how granular systems deform during loading.

Despite this progress, direct measurement of interparticle contact forces remains considerably more challenging. Most available experimental techniques provide kinematic, geometric, or averaged motion information, while the internal force network responsible for load transmission often remains hidden. Photoelasticity has historically provided one of the most influential approaches for visualizing force transmission in granular assemblies. By using birefringent particles, contact forces can be inferred from stress-induced fringe patterns, allowing direct observation of force chains, arching, and stress heterogeneity [38, 39]. However, photoelastic methods are generally limited to birefringent materials with relatively simple grain shapes, and often require detailed knowledge of boundary and contact conditions to obtain high-fidelity force reconstructions [49, 50].

The Granular Element Method (GEM), introduced by Andrade and Avila [40], was developed to help bridge this gap. GEM combines experimentally measurable grain-scale information – such as particle geometry, contact locations, and average particle stress or strain states – with governing equations for force and moment equilibrium, along with contact constraints, to infer the unknown interparticle contact forces. Hence, GEM provides a mechanics-based inverse framework that converts observable kinematic and geometric data into estimates of the hidden internal force network. An advantage of GEM is that it can be applied to opaque materials and irregular grain morphologies that are difficult to study using traditional force-measurement techniques. Moreover, GEM provides a quantitative experimental benchmark for assessing and improving DEM-based simulations.

Since its introduction, GEM has been successfully applied to two-dimensional granular systems under quasi-static loading, extended to dynamic loading conditions,

and adapted to three-dimensional assemblies [51–53]. These developments demonstrate that GEM is a versatile framework for linking grain-scale force transmission to macroscopic loading across a range of materials and boundary conditions. In particular, previous studies have used GEM to investigate monotonic quasi-static shear behavior and to compare experimental force networks against DEM and LS-DEM predictions [54, 55].

Motivated by these limitations and opportunities, the remainder of this chapter presents the Granular Element Method (GEM) in detail. The GEM methodology (Figure 2.1) can be decomposed into two main stages: (1) imaging techniques for extracting grain strain fields and material fabric (position of contact points and centroids), and (2) the constrained optimization problem for inferring contact forces by solving an inverse problem. For the first stage, any experimental technique capable of extracting strain fields and fabric can be coupled with GEM. In the second stage, GEM can locally infer contact forces in regions of interest, such as shear bands, without solving an inverse problem for the entire granular assembly.

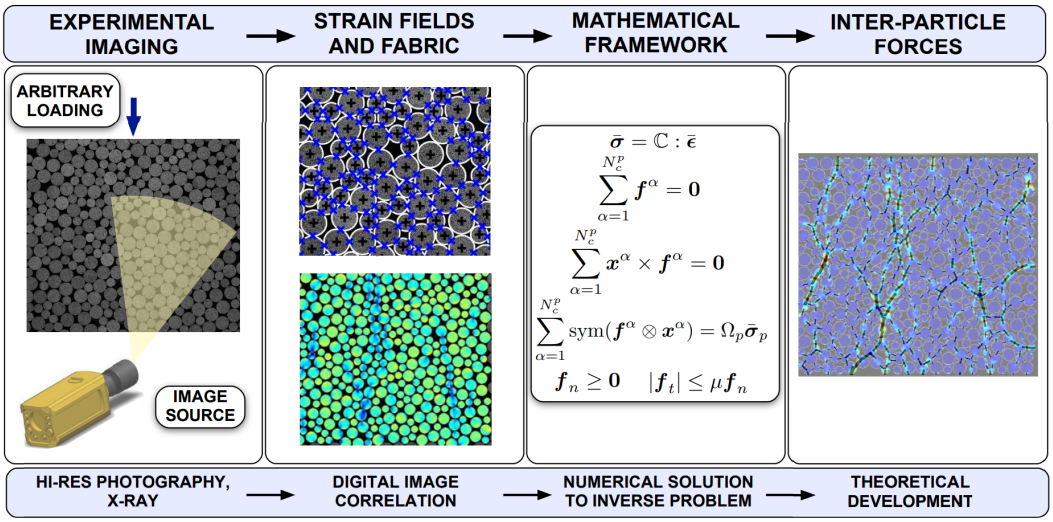


Figure 2.1: GEM methodology for contact force inference (Reproduced from Marteau [56]).

2.2 Experimental measurements

The first step of GEM is to acquire a set of digital images from a granular assembly under arbitrary loading conditions. The next step is to extract fabric information at each time step. In the present context, fabric encompasses grain boundaries, centroid locations, particle orientations, and contact network connectivity. Grain contours and centroids are obtained from digital images using segmentation algorithms that separate grains from voids and adjacent particles. Typically, the Circular

Hough Transform algorithm is used for circular grains, and the Watershed Segmentation algorithm is used for arbitrarily shaped grains. Once particle boundaries are identified, contact locations are determined from the minimum Euclidean distance between neighboring contours. Pairs of particles whose boundary separation falls below a prescribed tolerance are considered to be in contact. Repeating this procedure for each image frame yields the evolving contact network during loading.

Once the fabric is determined, the next task is to measure grain kinematics and deformation. In principle, GEM may be coupled with any experimental technique that provides displacement or strain files at the particle scale. In this thesis, we use Digital Image Correlation (DIC). DIC is a non-contact optical technique that partitions an image into small subsets and tracks each subset between successive frames. Each subset is matched by maximizing the correlation of its grayscale intensity pattern, yielding a full-field displacement field over the specimen surface. The accuracy of these measurements depends on a high-contrast random speckle pattern, stable illumination, and sufficient image resolution to clearly resolve the surface texture [44]. From the displacement field, rigid body motion of each grain can be separated to obtain particle translations and rotations, while spatial gradients of displacements provide the corresponding strain field. Because measurements are obtained over the full image rather than at discrete points, DIC is well suited for granular systems where deformation is spatially nonuniform.

Next, the measured strain field within each grain is averaged to obtain an average particle strain tensor, $\bar{\boldsymbol{\epsilon}}$. For grains undergoing small elastic deformations, the corresponding average stress tensor, $\bar{\boldsymbol{\sigma}}$, is computed using the generalized Hooke's law linearly elastic constitutive relation using the known material properties. Each grain, therefore, acts as a local strain gauge, with the measured deformation providing an estimate of its average internal stress state. These average particle stresses, together with the measured fabric and applied boundary conditions, form the principal experimental inputs to GEM.

2.3 Mathematical Framework

The constrained optimization problem used in GEM to infer contact forces from experimental measurements is governed by three sets of equations: (1) momentum balance, (2) a force-stress compatibility relationship, and (3) contact constraint equations. The formulation of these governing equations adopts a point-contact idealization between neighboring grains. This approximation is well-suited for stiff

granular materials, such as sands, powders, and many pharmaceutical particulates, where contact areas remain small relative to particle size. For more compliant particles, the point-contact assumption may still be appropriate when loading levels are sufficiently low such that contact deformations remain localized [51].

Consider an individual grain p within a granular assembly in static equilibrium. Let N_c^p be the number of contact points associated with particle p, with each contact labeled by α. At each contact, a force vector $\boldsymbol{f}^\alpha$ acts on the particle at position $\boldsymbol{x}^\alpha$, measured relative to a convenient reference frame (Figure 2.2).

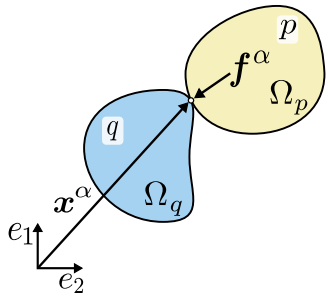


Figure 2.2: Schematic of particles p and q in contact at point α. The position vector $\boldsymbol{x}^\alpha$ locates the contact point relative to the reference basis $\boldsymbol{e} = [e_1 \quad e_2]^\top$.

Static equilibrium requires that both the resultant force and the resultant moment acting on the grain vanish. This gives the local balance equations for each particle.

$$\sum_{\alpha=1}^{N_c^p} \boldsymbol{f}^\alpha = \boldsymbol{0} \tag{2.1}$$

$$\sum_{\alpha=1}^{N_c^p} \boldsymbol{x}^\alpha \times \boldsymbol{f}^\alpha = \boldsymbol{0} \tag{2.2}$$

The local force and moment balance equations, Eq. (2.1) and Eq. (2.2), are assembled over all particles to obtain the global equilibrium system,

$$\boldsymbol{K}_{eq}\boldsymbol{f} = \boldsymbol{0}\,,$$

where $\boldsymbol{f}$ is the vector of unknown contact force components, and matrix $\boldsymbol{K}_{eq}$ is constructed from the measured contact locations and particle connectivity. In two

dimensions, this system takes the following form:

$$
\begin{array}{c} \\ p \\ \\ q \\ \\ \end{array}
\begin{array}{c}
\begin{array}{ccccc} & & i & & j \end{array} \\
\begin{pmatrix}
\ddots & \mathbf{0} & \cdots & \mathbf{0} & \cdots \\
\mathbf{0} & \boldsymbol{K}^i_{eq} & \mathbf{0} & \boldsymbol{K}^j_{eq} & \mathbf{0} \\
\vdots & \mathbf{0} & \ddots & \mathbf{0} & \vdots \\
\mathbf{0} & -\boldsymbol{K}^i_{eq} & \mathbf{0} & \mathbf{0} & \mathbf{0} \\
\vdots & \mathbf{0} & \vdots & \mathbf{0} & \ddots
\end{pmatrix}
\end{array}
\begin{pmatrix} \vdots \\ \boldsymbol{f}^i \\ \vdots \\ \boldsymbol{f}^j \\ \vdots \end{pmatrix}
=
\begin{pmatrix} \vdots \\ 0 \\ \vdots \\ 0 \\ \vdots \end{pmatrix}
\tag{2.3}
$$

with

$$
\boldsymbol{K}^i_{eq} = \begin{bmatrix} 1 & 0 \\ 0 & 1 \\ -x^i_2 & x^i_1 \end{bmatrix}; \quad \boldsymbol{f}^i = \begin{pmatrix} f^i_1 \\ f^i_2 \end{pmatrix}
\tag{2.4}
$$

where p and q represent different particles, i represents particle-particle contacts, and j represents particle-boundary contacts (Figure 2.3). The dimension of the $\boldsymbol{K}_{eq}$ matrix is $N_p\, d(d+1)/2$ rows and $N_c\, d$ columns, where N_p is the total number of particles in the granular assembly, d is the spatial dimension ($d = 2$ for two dimensions), and N_c is the total number of contact points.

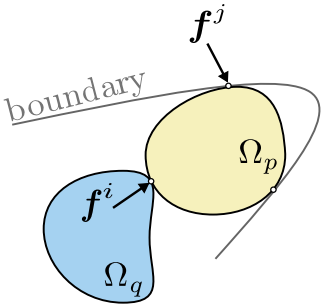


Figure 2.3: Illustration of particle-particle contacts (index i) and particle-boundary contacts (index j).

Although the present formulation is discrete rather than continuous, the same fundamental principle arises as in continuum mechanics: equilibrium conditions alone are insufficient to uniquely determine the internal force state. Additional constitutive or compatibility constraints are therefore required. In GEM, this additional information is provided by experimentally measured particle stresses, which can be related to the contact forces at each grain boundary.

The average Cauchy stress within a particle p is defined as

$$
\bar{\boldsymbol{\sigma}}^p = \frac{1}{\Omega_p} \int_{\Omega_p} \boldsymbol{\sigma}^p \, \mathrm{d}\Omega \,,
\tag{2.5}
$$

where Ω_p is the particle area (or volume in 3D). Using equilibrium, boundary tractions, and standard micromechanical homogenization arguments, this quantity can be written in terms of discrete contact forces acting on the particle boundary as

$$\bar{\boldsymbol{\sigma}}^p = \frac{1}{\Omega_p} \sum_{\alpha=1}^{N_c^p} \mathrm{sym}(\boldsymbol{f}^\alpha \otimes \boldsymbol{x}^\alpha)\,, \tag{2.6}$$

where $\mathrm{sym}(\cdot)$ denotes the symmetric part of the tensor product. This micromechanical force-stress relation is commonly associated with the work of Christoffersen et al. [57] and provides the key link between experimentally measured particle stresses and unknown interparticle contact forces used in GEM.

Analogous to the equilibrium equations, Eq. (2.6) is assembled over all particles into the global matrix system

$$\boldsymbol{K}_{st}\boldsymbol{f} = \boldsymbol{b}_{st}\,,$$

where $\boldsymbol{K}_{st}$ is constructed using measured contact locations and particle connectivity, and $\boldsymbol{b}_{st}$ contains the experimentally measured average stress components of all grains. In two dimensions, this system takes the following form:

$$\begin{array}{c} \\ p \\ \\ q \\ \\ \end{array} \begin{array}{c} \begin{array}{ccccc} & & i & & j & \\ \end{array} \\ \begin{pmatrix} \ddots & \mathbf{0} & \cdots & \mathbf{0} & \cdots \\ \mathbf{0} & \boldsymbol{K}_{st}^i & \mathbf{0} & \boldsymbol{K}_{st}^j & \mathbf{0} \\ \vdots & \mathbf{0} & \ddots & \mathbf{0} & \vdots \\ \mathbf{0} & -\boldsymbol{K}_{st}^i & \mathbf{0} & \mathbf{0} & \mathbf{0} \\ \vdots & \mathbf{0} & \vdots & \mathbf{0} & \ddots \end{pmatrix} \end{array} \begin{pmatrix} \vdots \\ \boldsymbol{f}^i \\ \vdots \\ \boldsymbol{f}^j \\ \vdots \end{pmatrix} = \begin{pmatrix} \vdots \\ \boldsymbol{b}_{st}^p \\ \vdots \\ \boldsymbol{b}_{st}^q \\ \vdots \end{pmatrix} \tag{2.7}$$

with

$$\boldsymbol{K}_{st}^i = \begin{bmatrix} x_1^i & 0 \\ 0 & x_2^i \\ x_2^i & x_1^i \end{bmatrix}; \quad \boldsymbol{b}_{st}^p = \begin{bmatrix} \Omega_p \bar{\sigma}_{11}^p \\ \Omega_p \bar{\sigma}_{22}^p \\ 2\Omega_p \bar{\sigma}_{12}^p \end{bmatrix}. \tag{2.8}$$

Similar to $\boldsymbol{K}_{eq}$, the dimension of the $\boldsymbol{K}_{st}$ matrix is $N_p\, d(d+1)/2$ rows and $d\, N_c$ columns.

Collectively, the global equilibrium and force-stress compatibility systems,

$$\boldsymbol{K}_{eq}\boldsymbol{f} = \mathbf{0} \tag{2.9}$$

$$\boldsymbol{K}_{st}\boldsymbol{f} = \boldsymbol{b}_{st}\,, \tag{2.10}$$

define the primary equality constraints governing the unknown interparticle contact forces. To obtain a physically admissible solution for a cohesionless granular material, additional contact constraints must also be enforced.

Normal contact forces (f_n) must remain compressive, and tangential contact forces (f_t) must satisfy the Coulomb friction limit, such that $|f_t| \leq \mu |f_n|$, where μ is the interparticle coefficient of friction.

For any contact point i associated with particle p, these constraints are expressed as

$$-\boldsymbol{e}^i \cdot \boldsymbol{f}^i \geq 0 \tag{2.11}$$

$$-(\boldsymbol{e}^i + \frac{1}{\mu}\boldsymbol{t}^i) \cdot \boldsymbol{f}^i \geq 0 \tag{2.12}$$

$$-(\boldsymbol{e}^i - \frac{1}{\mu}\boldsymbol{t}^i) \cdot \boldsymbol{f}^i \geq 0\,, \tag{2.13}$$

where $\boldsymbol{e}^i$ and $\boldsymbol{t}^i$ denote the unit normal and tangential vectors, respectively, associated with contact i (Figure 2.4). The first inequality enforces a compressive normal force, whereas the latter two inequalities define the lower and upper bounds of the Coulomb friction criterion.

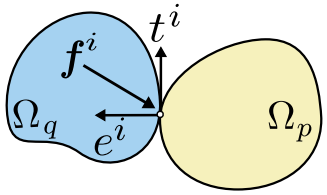


Figure 2.4: Local contact coordinate system for contact i, showing the unit normal vector, $\boldsymbol{e}^i$, and unit tangential vector, $\boldsymbol{t}^i$, used to resolve the contact force exerted by particle q on particle p.

Applying these conditions (Eqs. (2.11), (2.12), (2.13)) to every active contact in the assembly yields the global inequality system

$$\boldsymbol{B}\boldsymbol{f} \geq \boldsymbol{0}\,, \tag{2.14}$$

where $\boldsymbol{B}$ contains the contact normal and tangential directions, particle connectivity, and friction coefficients associated with all measured contacts.

In two dimensions, this system takes the following form:

$$
\begin{array}{c}
\\
i \\
\vdots \\
j \\
i \\
\vdots \\
j \\
i \\
\vdots \\
j
\end{array}
\begin{array}{c}
\begin{array}{ccccc} i & i & & j & j \end{array} \\
\begin{pmatrix}
-e_1^i & -e_2^i & 0 & 0 & 0 \\
0 & 0 & \ddots & 0 & 0 \\
0 & 0 & 0 & -e_1^j & -e_2^j \\
-e_1^i - \frac{1}{\mu} t_1^i & -e_2^i - \frac{1}{\mu} t_2^i & 0 & 0 & 0 \\
0 & 0 & \ddots & 0 & 0 \\
0 & 0 & 0 & -e_1^j - \frac{1}{\mu} t_1^j & -e_2^j - \frac{1}{\mu} t_2^j \\
-e_1^i + \frac{1}{\mu} t_1^i & -e_2^i + \frac{1}{\mu} t_2^i & 0 & 0 & 0 \\
0 & 0 & \ddots & 0 & 0 \\
0 & 0 & 0 & -e_1^j + \frac{1}{\mu} t_1^j & -e_2^j + \frac{1}{\mu} t_2^j
\end{pmatrix}
\end{array}
\begin{pmatrix} f_1^i \\ f_2^i \\ \vdots \\ f_1^j \\ f_2^j \end{pmatrix}
\geq
\begin{bmatrix} 0 \\ \vdots \\ \vdots \\ \vdots \\ 0 \end{bmatrix},
\tag{2.15}
$$

where subscripts denote vector components, and superscripts identify individual contact points. The dimension of $\boldsymbol{B}$ is $3N_c$ rows and $d\,N_c$ columns.

Having established the governing equations of the system, Eq. (2.9), Eq. (2.10), and Eq. (2.14), the remaining objective is to determine the unknown interparticle contact force vector, $\boldsymbol{f}$. Since all other terms in the formulation are obtained from experimental measurements or material parameters, the resulting inverse problem is formulated as the constrained optimization problem:

$$
\boldsymbol{f} = \arg\min_{\boldsymbol{f}} \left(\lambda \left\| \boldsymbol{K}_{eq} \right\|_2 + (1-\lambda) \left\| \boldsymbol{K}_{st} \boldsymbol{f} - \boldsymbol{b}_{st} \right\|_2 \right) \tag{2.16}
$$

$$
\text{subjected to: } \boldsymbol{B}\boldsymbol{f} \geq \boldsymbol{0}\,, \tag{2.17}
$$

where $\left\| \boldsymbol{K}_{eq} \right\|_2$ is the equilibrium objective function, $\left\| \boldsymbol{K}_{st} \boldsymbol{f} - \boldsymbol{b}_{st} \right\|_2$ is the stress objective function, and λ is a weighting parameter that controls the trade-off between the equilibrium and force-stress residuals.

The constrained optimization problem is solved in MATLAB using the CVX convex optimization solver [58]. Because the two objective functions are generally competing, varying λ yields a family of admissible trade-off solutions rather than a single universally optimal one. In previous GEM studies, this trade-off has been interpreted in terms of a Pareto front, and a preferred solution has been selected using a knee-point criterion [52, 59].

2.4 Summary

Although previous applications of GEM have primarily focused on monotonic or other quasi-static loading conditions, the response of granular materials under cyclic shear remains comparatively less understood. Repeated loading can produce memory effects, progressive rearrangement, path-dependent behavior, and evolving contact-force networks that differ substantially from those observed during monotonic deformation.

In the two-dimensional implementation adopted in this thesis, top-surface images of the granular assembly are processed to obtain particle boundaries, centroid locations, contact geometry, and in-plane strain fields, which serve as direct inputs to GEM. These measurements are then used to reconstruct the evolving interparticle contact force network throughout shear loading. The next chapter introduces the experimental apparatus, testing procedures, and baseline one-cycle simple shear experiment that establishes the foundation for the multi-cycle investigations presented thereafter.

Chapter 3

MICRO-TO MACROSCOPIC RESPONSE OF GRANULAR MATERIALS UNDER CYCLIC SIMPLE SHEAR: A ONE-CYCLE EXPERIMENTAL STUDY

3.1 Introduction

Granular media exhibit complex behavior at the macroscale, influenced by loading history, boundary conditions, and initial packing state. Unlike continuum materials, granular materials are discrete, and their collective grain interactions influence the overall macroscale behavior. A key challenge in granular mechanics is linking grain-scale processes—like contact rearrangement and force transmission—to the observed bulk response [1, 2].

Many models and theories exist, such as phenomenological and empirical approaches, which limit their predictive capabilities to the physical and environmental conditions under which they were calibrated [60]. In contrast, physics-based models, most notably the Discrete Element Method (DEM), extend predictive capabilities to a range of physical conditions across environments. Specifically, physics-based models use balance laws and particle kinematics to capture the multi-scale behavior of discrete particles. DEM has provided significant insight into micromechanical processes, including contact force distributions, fabric anisotropy, and force chain formation, highlighting the importance of grain-scale structure in controlling macroscopic behavior [24, 36].

Despite these advances, DEM simulations are computationally intensive and often rely on simplified grain geometries and contact laws that do not fully capture how real granular materials deform and fail [40, 61]. As a result, a gap remains between simulated micromechanics and experimentally observed behavior, particularly for irregular grain shapes and realistic boundary conditions. More importantly, direct experimental characterization of grain-scale quantities remains limited, especially under cyclic loading.

To address this gap, experimental techniques capable of resolving grain-scale mechanics are essential. One such approach is the Granular Element Method (GEM), which infers interparticle contact forces directly from experimental measurements. As described in Chapter 2, GEM's ability to extract realistic grain-scale data enables

quantitative comparison between experimental data and simulations (such as DEM) at the micro- and mesoscales, making it critical for validating micromechanical theories [40, 51].

Previously, GEM was coupled with a cyclic simple shear apparatus to study granular materials under monotonic shear [54, 56]. This chapter extends that work by investigating the deformation mechanisms of a densely packed granular assembly subjected to a single cyclic shear cycle. Central to this investigation is the evolution of force chains, which form the primary load-bearing skeleton of the material and govern transmission across the assembly [62]. This work provides a unified micro-to-macro interpretation of granular cyclic shear behavior by tracking the evolution of force chain structure, coordination number, and anisotropy alongside macroscopic measures such as the stress ratio, volumetric strain, and dilatancy.

This chapter serves as a baseline for understanding granular response under cyclic loading. The insights gained from this one-cycle, densely packed experiment establish a reference framework for the three-cycle, density-dependent, and stress-dependent behaviors examined in the following chapter.

This chapter is organized as follows. Section 3.2 presents the experimental setup and procedure. Section 3.3 details the macroscopic and grain-scale responses observed during a single shear cycle. Section 3.4 summarizes the key findings and their implications.

3.2 Experimental Setup: Cyclic Shear Apparatus

3.2.1 Design Overview

This thesis uses an apparatus for applying quasi-static cyclic simple shear to 2D analog granular materials, originally designed and built by Dr. Eloïse Marteau during her doctoral thesis work at Caltech [56]. While Dr. Marteau performed monotonic simple shear tests, this thesis examines the behavior of granular media under cyclic simple shear. Accordingly, a microcontroller was added to the original setup to impose programmed displacement cycles.

Figure 3.1 presents a detailed CAD drawing of the apparatus and its major components [63], while Figure 3.2 shows the corresponding top-view image of the experimental setup.

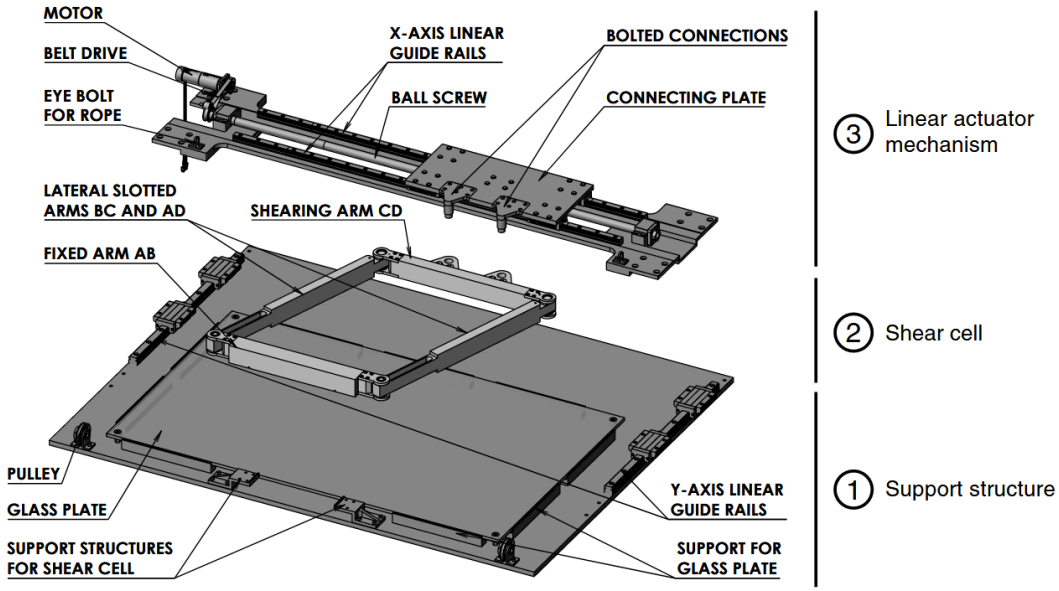


Figure 3.1: Three-dimensional computer-aided design (CAD) model illustrating an exploded view of the components of the simple shear apparatus. Reproduced from Marteau and Andrade [63], Fig. 1a, with permission from Springer Nature.

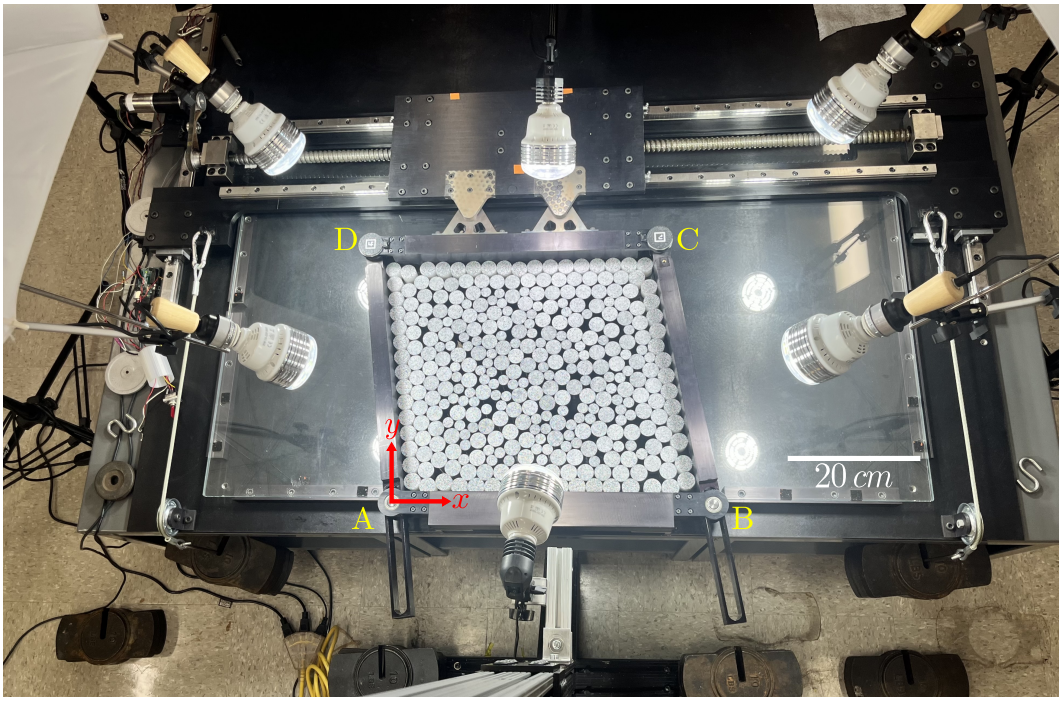


Figure 3.2: Top-view photograph of the cyclic simple shear apparatus during testing. The shear cell is a deformable parallelogram consisting of four rigid arms: A-B (bottom arm), C-B (right arm), C-D (top arm), and A-D (left arm). The shear cell is shown in a left-sheared configuration, with the LED illumination system, hanging normal-load weights, and microcontroller wiring visible. Scale bar = 20 cm.

The base of the apparatus is a 1630 mm x 1270 mm x 15.875 mm rectangular aluminum 7075 plate mounted on a steel table. Attached to the top surface of the base plate are two y-axis linear guide rails with carriages that provide vertical motion to the ball screw actuator system, two Z-shaped supports that fix the bottom of the shear cell, nine L-shaped supports that hold a glass sheet, and two pulleys for applying hanging masses. There is a small gap between the bottom plane of the shear cell and the glass sheet, allowing the shear cell to move freely while the samples glide on a frictionless surface.

The shear cell is a deformable parallelogram consisting of four rigid arms: A-B (bottom arm), C-B (right arm), C-D (top arm), and A-D (left arm). The bottom arm of the shear cell, arm A-B, is held fixed by the Z-shaped supports, while the top of the shear cell, arm C-D, is attached to the actuator carriage through an L-shaped bracket for left and right movement ($+x$ and $-x$ direction). The top and bottom arms are a constant length of $L_x = 525$ mm (20.67”). The corners of the shear cell (points A, B, C, and D) contain rotary systems, an arrangement of a rotary shaft, ball bearings (support radial loads), and thrust bearings (support axial loads) that allow arms C-B (right arm) and A-D (left arm) to rotate at a constant angular velocity about point A and point B, respectively. The bottom third of the right and left arms contains slots that allow the arms to change length, L_y, as the rotary shaft moves through the slotted section. The angle between the vertical (y-axis) and arm A-D is called the shear angle, γ. It can be positive (shearing in the $+x$ direction) or negative (shearing in the $-x$ direction), allowing for cyclic shearing.

The ball screw actuator system is driven by a belt-drive motor (Maxon® brushless DC electric motor) mounted on a platform constrained to vertical movement along the y-axis linear guide rails on the base plate. The motor uses a speed controller (Maxon® ESCON 50/5) with an added Arduino® Uno to control the shear cell’s positioning and speed, and to execute the programmed shear cycles.

The weight rigging system consists of shouldered steel eyebolts threaded through both ends of the platform (held in place with locknuts), connected to D-shackles, steel wire rope, weight hangers, and pulleys that guide the rope’s travel. The weight hangers and added disk weights hang off the side of the steel table, forming an approximately 90-degree deflection angle between the rope and the load. This gravity-weighted dead-load system applies a constant normal stress, σ_n, to the shear cell top arm (C-D), thereby transmitting it to the entire granular assembly.

Lastly, the experiments are digitally photographed with an Allied Vision® CCD camera (Prosilica GT 4907) attached to a Nikkor® 105mm f/2.8 Micro-Nikkor lens, mounted approximately 2.6 m (102.4") above the sample surface. The camera can run up to 7.6 frames per second at a resolution of 15.7 MP [64]; however, the average frame rate in the present experiments was 7.1 frames per second. The imaging parameters were set to an aperture of $f/11$, an exposure time of 8000 $[\mu s]$, and a gain of 0 [db]. The relatively small aperture was selected to provide sufficient depth of field and maintain sharp focus across the sample surface, but it also reduced the amount of light reaching the sensor. To compensate, six 5500 K LED lights were positioned around the apparatus to provide uniform illumination and adequate image brightness for digital image correlation (DIC) without increasing gain or exposure time. Based on the calibrated pixel resolution from DIC, these settings limit motion-induced displacement during exposure to approximately 0.47 pixels, ensuring minimal blur under typical conditions. Nevertheless, occasional rapid grain rearrangements exceeded this threshold, resulting in localized motion blur (Figure 3.3). Such transient frames were excluded from all results.

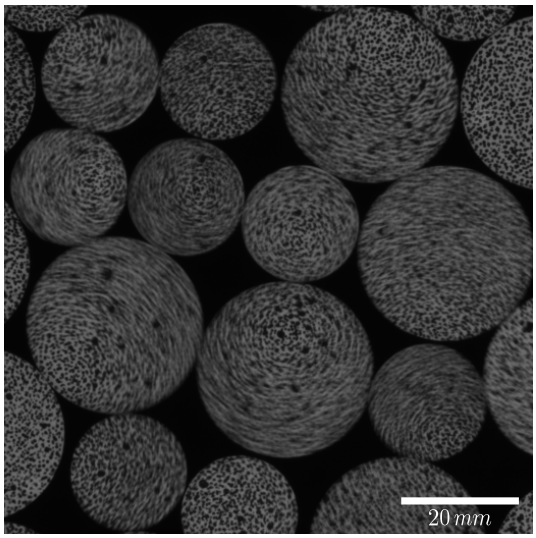


Figure 3.3: Rapid grain rearrangement resulting in localized motion blur. Data from these transient images are excluded from all results. Scale bar = 20 mm.

3.2.2 Measurements

Figure 3.4 shows the general state of deformation of the shear cell subjected to a shear angle, γ, and an external compressive normal load σ_n. The solid line schematic shows the shear cell in its initial configuration ($\gamma = 0°$), while the dotted line schematic shows the shear cell in a deformed state.

The two degrees of freedom that define the shear cell configuration are: (1) γ, the angle between the vertical (y-axis) and the A-D arm, and (2) $L_y = L_{y_0} + \Delta L_y$, the length in the y-direction of the slotted parallel arms (A-D and B-C). L_{y_0} is the initial length of A-D (equivalently B-C) when the shear cell is in its starting configuration, and ΔL_y is the change in length in the y-direction.

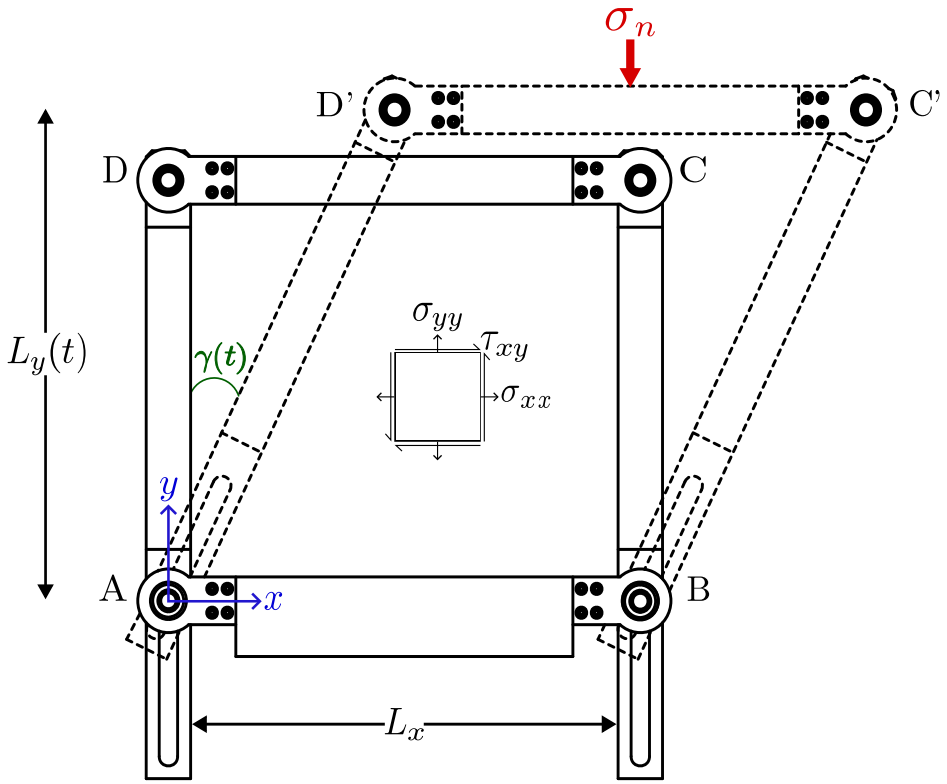


Figure 3.4: Shear cell state of deformation under a prescribed shear angle, γ, and an external compressive normal load, σ_n.

The limits of γ and L_y are:

$$-35^\circ < \gamma < 35^\circ$$

$$450 \text{ mm} < L_y < 630 \text{ mm}$$

3D-printed AprilTags mounted atop the C and D rotary centers are tracked using the MATLAB® Computer Vision Toolbox (Figure 3.5). Since points A and B are fixed, geometry is used to directly measure γ and L_y throughout the experiment.

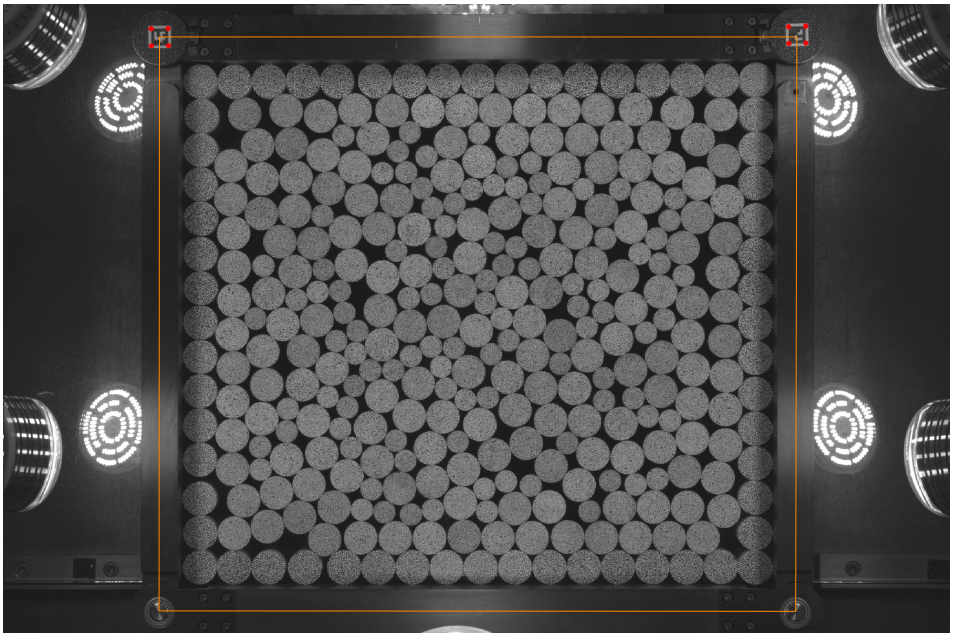


Figure 3.5: Detected shear cell position from AprilTags via the MATLAB® Computer Vision Toolbox.

The 2D macroscopic strain state is given by

$$\boldsymbol{\epsilon} = \begin{bmatrix} 0 & \epsilon_{xy} \\ \epsilon_{xy} & \epsilon_{yy} \end{bmatrix},$$

where $\epsilon_{xx} = 0$ (since L_x is constant), $\epsilon_{yy} = \Delta L_y / L_y$, and $\epsilon_{xy} = \tan\gamma/2$. The volumetric strain is therefore $\epsilon_V = \mathrm{tr}(\boldsymbol{\epsilon}) = \epsilon_{yy}$.

The preceding strain tensor characterizes the imposed in-plane deformation of the granular assembly. Separately, a plane-strain constitutive assumption is adopted when converting measured grain strains to stresses using linear elasticity, providing a practical two-dimensional approximation for the finite-thickness experimental system. This same assumption is used in the Granular Element Method formulation presented in Chapter 2.

The 2D macroscopic stress state (see Figure 3.4) is given by

$$\boldsymbol{\sigma} = \begin{bmatrix} \sigma_{xx} & \tau_{xy} \\ \tau_{xy} & \sigma_{yy} \end{bmatrix}.$$

This thesis uses the geomechanics convention of compression-positive and tension-negative for normal loads and stresses. The shear components of stress and strain remain unchanged from the normal convention.

3.2.3 Granular Samples

The cylindrical samples used in these cyclic simple shear experiments are the same as those used by Dr. Marteau during her first set of monotonic simple shear experiments [63]. The samples are made of two different materials: PTFE and polyurethane (PU).

The PTFE samples have a Young's Modulus of $E = 0.5$ GPa, Poisson's ratio of $\nu = 0.46$, and a kinetic friction coefficient of $\mu = 0.6$. These 30mm diameter stiff PTFE rods are placed along the inner perimeter of the shear cell walls. In addition to serving as a frictionless, rigid barrier between the interior polyurethane samples and the aluminum shear cell walls, the PTFE samples also occupy the location where stress and strain fields are the most inhomogeneous in simple shear tests [17]. Thus, the PTFE samples are excluded from DIC, and their contact forces are not inferred from GEM.

The polyurethane rubber samples have a Young's Modulus of $E = 50$ MPa, Poisson's ratio of $\nu = 0.5$, and kinetic friction coefficient of $\mu \approx 0.46$. The samples are of two different diameters: $D_1 = 20$ mm and $D_2 = 30$ mm. In the experimental images (4864 pixels x 3232 pixels), the smaller-diameter rods have a 59-pixel diameter, and the larger-diameter rods have an 87-pixel diameter. All samples have a height of 25 mm. These polyurethane samples are used to pack the interior of the shear cell.

It is essential to note that, although 3D samples are used in the experiments, only the top surface of the polyurethane samples (the surface visible to the camera) is speckle-patterned and analyzed using 2D DIC. Past monotonic simple shear studies packed with photoelastic rods [25, 65] and wooden rods [66] showed that the experimental behavior of the 2D rods (translation and rotation only along in-plane directions) exhibits similar deformation and strength behavior at the micro- and macro-scales as observed in similarly deformed sand. Hence, these 2D experiments are valid analogs for capturing the behavior of simple sheared real granular media.

3.2.4 Experimental Procedure and Image Analysis

The experimental procedure consisted of four stages: (1) granular assembly preparation, (2) application of normal confinement, (3) cyclic shearing, and (4) post-processing of images using digital image correlation (DIC).

3.2.4.1 Granular Assembly Preparation

The initial shear cell configuration corresponds to $\gamma = 0°$ (90° interior angles). Sixty PTFE cylinders are first placed around the inner perimeter of the shear cell, adjacent to the boundary walls. The remaining interior region was then randomly packed with the polyurethane samples.

This thesis examines the mechanical behavior of densely and loosely packed granular assemblies. The densely packed granular assembly consisted of 272 interior grains (100 D_1 and 172 D_2), whereas the loosely packed assembly used 258 interior grains (93 D_1 and 165 D_2). Further, because the shear cell lies horizontally, the initial packing process introduced no systematic bias in particle orientation or force distribution.

3.2.4.2 Normal Loading and Cyclic Shearing Protocol

After packing the shear cell with samples, it is gradually confined through 20 lb (9.07 kg) weight increments until the desired final normal stress, σ_n, is reached. In the following experimental results, this stage is termed 'normal loading'.

Following confinement, cyclic shearing was imposed at a constant shear strain rate of $\dot{\gamma} = 0.53\ °/s \approx 0.0093$ rad$/s$. One cycle begins from the initial configuration ($\gamma_0 = 0°$), followed by rightward shearing in the $+x$ direction for a duration τ ($\gamma_0 \rightarrow +\gamma_{max}$). The direction is then reversed, and the system is sheared leftward in the -x direction for a duration 2τ $\left(+\gamma_{max} \rightarrow -\gamma_{max}\right)$. Finally, rightward shearing is applied in the +x direction for an additional duration τ to return the shear cell to its initial configuration ($-\gamma_{max} \rightarrow \gamma_0$).

For experiments involving N cycles, this sequence was repeated N times. A schematic of the imposed displacement history for one cycle is shown in Figure 3.6.

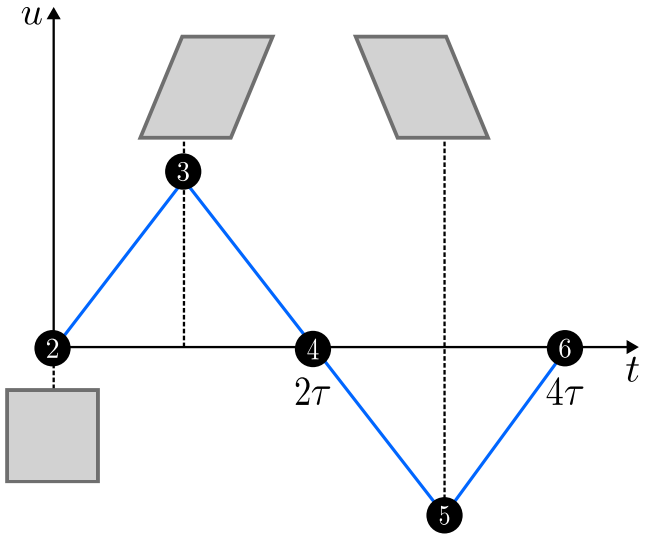


Figure 3.6: Displacement, u, versus time, t, schematic for $N = 1$ cycle. τ represents the duration between shear stages. In the experimental results, these stages are called: shear-right-forward ($2 \rightarrow 3$), shear-right-reverse ($3 \rightarrow 4$), shear-left-forward ($4 \rightarrow 5$), and shear-left-reverse ($5 \rightarrow 6$). The normal loading stage (segment $1 \rightarrow 2$) of the experiment is not shown.

3.2.4.3 Digital Image Correlation Processing

To provide the grain-scale displacement and strain data required for GEM, the raw images acquired throughout the loading history were processed with VIC-2D, a commercial DIC software developed by Correlation Solutions, Inc [67]. The image-processing workflow consisted of four main steps.

First, the reference image was analyzed in MATLAB® using the Hough Transform to identify grain centroids and boundaries. Each detected circular grain boundary was then represented by a polygonal approximation of a circle (Figure 3.7), using 26 vertices for the larger grains (D_2) and 22 vertices for the smaller grains (D_1). These polygonal boundaries match the circular area-of-interest (AOI) format used by VIC-2D. With initial guidance from Correlated Solutions, their Python batch-processing utility was modified to automate the generation and insertion of AOIs into an existing project file. Because a Vic-2D project file (.z2d) can be accessed as a compressed archive containing a `project.xml` file and associated metadata, the XML structure governing AOIs was used to programmatically insert the grain boundaries. This automation eliminated the need to draw hundreds of AOIs for each experiment manually and substantially reduced preprocessing time.

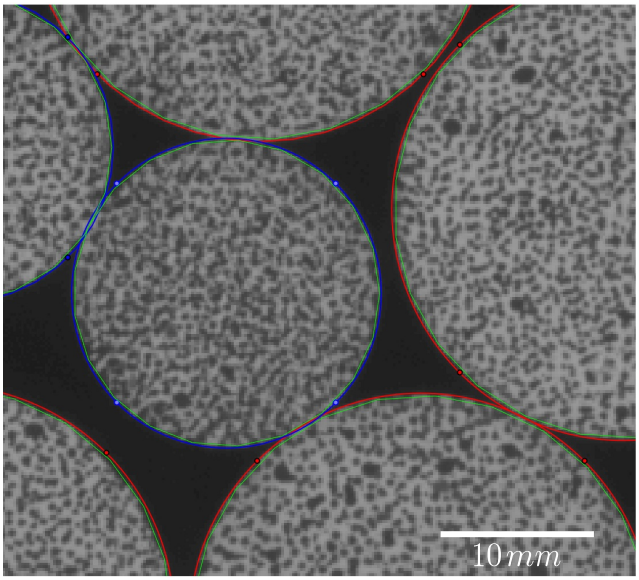


Figure 3.7: Close-up view of the circular grain boundaries generated in MATLAB®. The larger grains ($D_2 = 30\,mm$) are outlined in red, the smaller grains ($D_1 = 20\,mm$) in blue, and the corresponding polygonal approximations in green. The polygonal boundaries were slightly inset relative to the true grain edges to reduce spurious overlap between adjacent AOIs during the DIC analysis. Scale bar = $10\,mm$.

Second, as noted previously, rapid grain rearrangements during shearing often prevented fully automatic frame-to-frame tracking. Consequently, seed points were manually assigned within each AOI to maintain reliable grain tracking throughout the loading history. A subset size of 11 pixels was selected to ensure that each subset contained approximately 3–5 distinct speckles, which is generally sufficient for robust image correlation. A step size of 3 pixels was used to maximize spatial resolution, recognizing the associated increase in processing time. These parameters were held constant for all experiments to ensure consistency across datasets. Figure 3.8 illustrates the grain-tracking workflow, including seed-point placement and the 11×11 pixel correlation subsets used in the analysis.

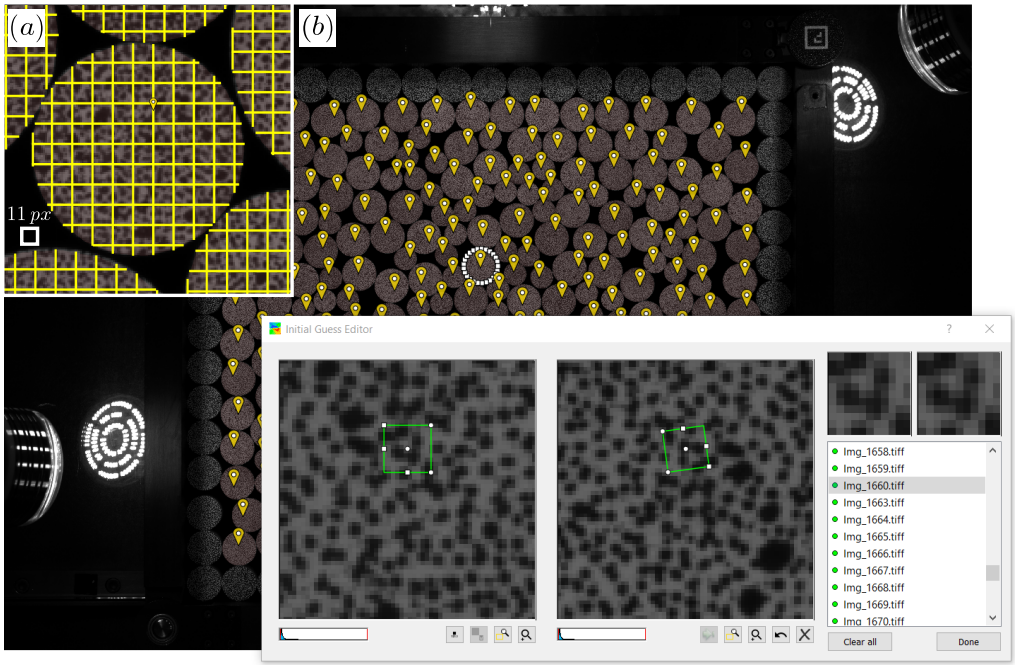


Figure 3.8: Visualization of the grain-tracking procedure in VIC-2D. (a) Enlarged view of the speckle pattern with the 11 × 11 pixel correlation subsets overlaid on grains within the assembly. (b) Snapshot of the full DIC workspace showing the granular assembly with all grain areas of interest (AOIs) and manually assigned seed points. The foreground panel illustrates manual adjustment of the initial guess for a selected seed point during frame-to-frame grain tracking.

Third, once grain tracking was completed, the displacement analysis was performed using the following settings for all experiments in this thesis: Gaussian weighting, optimized 8-tap interpolation, zero-normalized squared-difference correlation criterion, exhaustive search, and a 0.05-pixel threshold metric. These settings were selected to reject poor correlations while retaining as much valid data as possible. Additional implementation details are provided in the VIC-2D documentation [67].

Finally, strain fields were computed from the displacement data using a strain filter size of 11, corresponding to a virtual strain gauge length of 33 pixels (approximately 5.61 mm with a scale factor of 1.6994×10^{-4} m/pixel). This gauge length is approximately $0.28D_1$ for the smaller grains and $0.19D_2$ for the larger grains. In DIC, increasing the filter size reduces uncertainty and smooths the strain field, whereas decreasing it improves spatial localization at the expense of greater noise sensitivity [68]. Therefore, the selected value represents a practical compromise between resolving grain-scale strain heterogeneity and limiting noise amplification during numerical differentiation. This choice produced stable per-grain stress estimates for subsequent GEM analysis.

The reliability of these strain measurements, and consequently the contact forces inferred through GEM, depends strongly on the experimental noise floor. To quantify this baseline uncertainty, a DIC analysis was performed using 40 images of three grains undergoing rigid-body motion across the camera's field of view. Under ideal rigid-body motion, the true strain should be zero. In practice, however, all experimental systems introduce some degree of measurement noise arising from factors such as lighting variability, speckle pattern quality, interpolation error, and lens distortion. Establishing this baseline provides an objective threshold below which measured strains cannot be confidently distinguished from experimental error [68, 69]. This consideration is particularly important in granular materials, where grain-scale strains are often both small in magnitude and highly heterogeneous, causing some localized responses to approach the practical resolution limit of DIC [45]. For the experimental configuration used in this study, the strain noise floor was measured to be on the order of 10^{-3}, consistent with reported uncertainty levels for DIC-based strain measurements in rigid-body motion tests [68, 69].

3.3 One Cycle Response of a Densely Packed Granular Assembly

To obtain baseline results for higher cycle experiments, this section characterizes the response of a densely packed granular assembly, normally loaded by $\sigma_n = -44.1$kPa (corresponding to 122 lbs (9.07 kg)), and subjected to an $N = 1$ simple shear cycle. The dense granular assembly consists of 332 grains total, 60 of which are the boundary PTFE particles that do not contribute to the DIC or GEM analysis.

All evolution plots are plotted as a function of γ, where γ denotes the imposed shear angle of the shear cell in radians. For the maximum deformation applied during shear (up to 11.75°), the small-angle approximation $\tan\gamma \approx \gamma$ holds, so γ is effectively equivalent to the engineering shear strain. Hence, we will refer to γ as the shear strain throughout the thesis. Recall that all results assume the geomechanics convention of compression-positive and tension-negative. Hence, we negate the normal components of stress and strain from DIC and stresses computed from the micromechanical Christoffersen equation (Eq. (2.6)). The shear components of stress and strain remain unchanged.

3.3.1 Macroscopic Response

Figure 3.9 shows the macroscopic mechanical response of the one-cycle, densely packed experiment. In this figure, the stress ratio, μ, volumetric strain, ϵ_V, void ratio, e, and dilatancy, β, are plotted as functions of shear strain, γ.

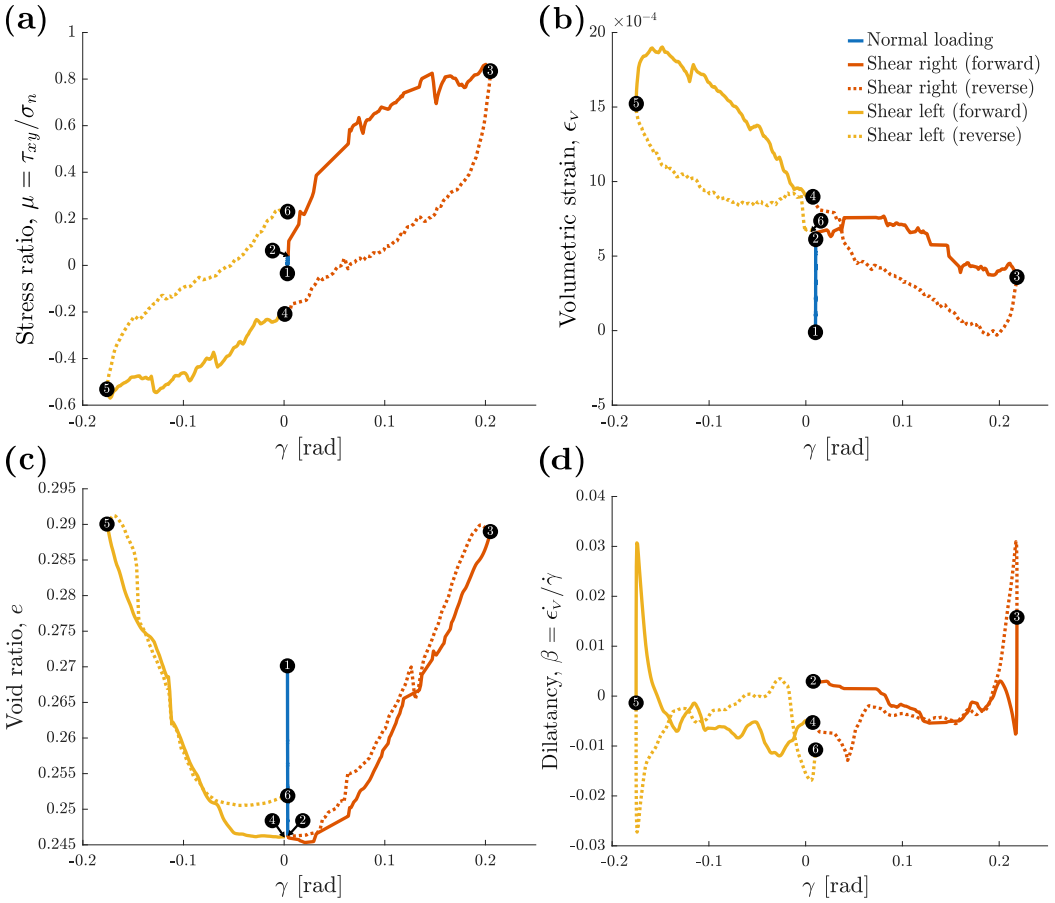


Figure 3.9: Macroscopic behavior of the one-cycle, densely packed granular assembly under $\sigma_n = -44.1$ kPa. (a) Stress ratio, μ, (b) volumetric strain, ϵ_V, (c) void ratio, e, and (d) dilatancy, β, as functions of shear strain, γ.

3.3.1.1 Stress Ratio

Figure 3.9a shows the stress ratio, $\mu = \tau_{xy}/\sigma_n$, as a function of shear strain, γ. The stress ratio quantifies the amount of shear resistance mobilized relative to the level of confinement imposed by the shear cell. It therefore serves as a macroscopic measure of friction at the boundary. During the initial forward shearing stage, μ gradually increases as friction is mobilized, and the contact network aligns with the imposed loading direction. Near the end of this stage, a pronounced fluctuation indicates a major internal restructuring event (Figure 3.10).

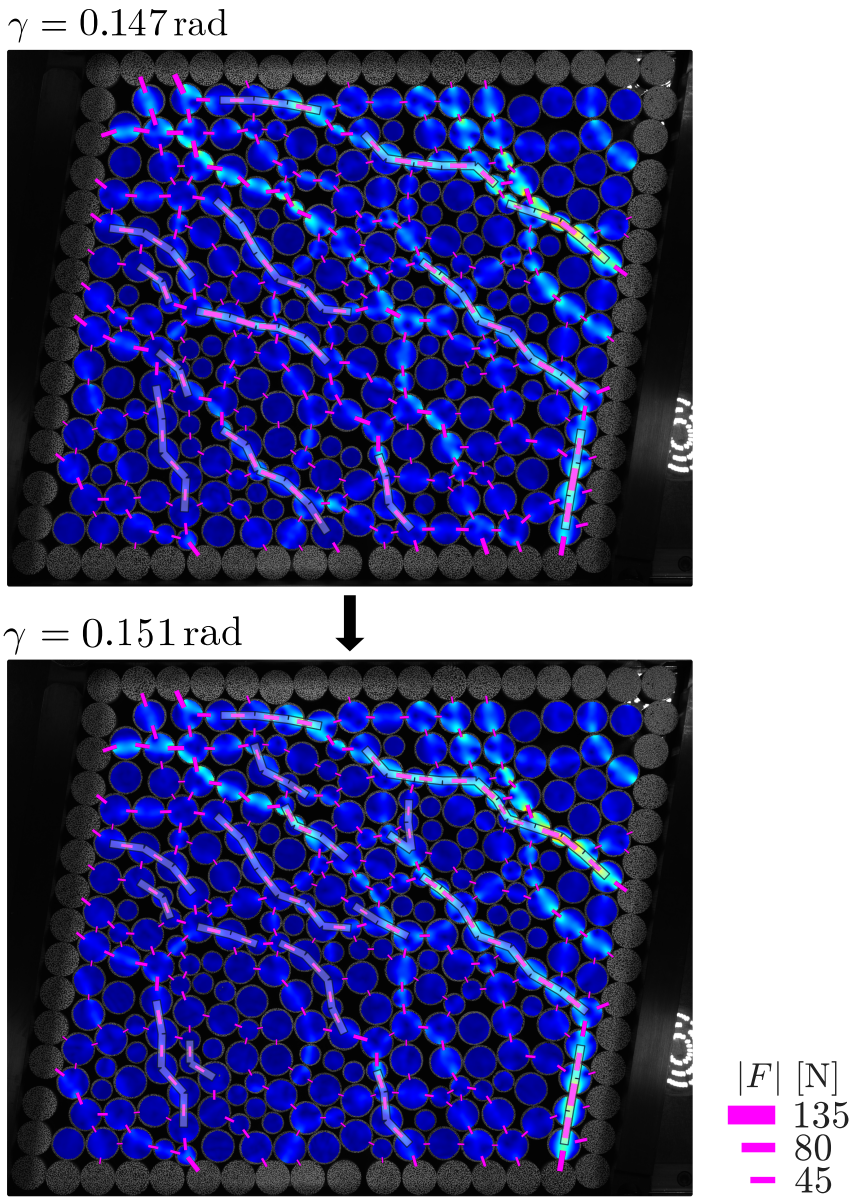


Figure 3.10: Force chain visualization at the start and end of the pronounced stress ratio, μ, drop during shear-right-forward, corresponding to (a) γ = 0.147 rad and (b) γ = 0.151 rad

Upon shear reversal, μ initially decreases as the previously developed force network collapses, followed by a gradual recovery as new load-bearing structures form. Similar behavior is observed during the shear-left stages, although the response in shear-left-forward is more fluctuating and the peak negative stress ratio is smaller in magnitude. Overall, the rightward branch is broader than the leftward branch, indicating directional asymmetry and structural memory in the cyclic response. These trends reflect the evolution and reorganization of the internal contact and force transmission during cyclic loading.

3.3.1.2 Volumetric Strain

Figure 3.9b shows the volumetric strain, ϵ_V, versus shear strain, γ. The volumetric strain tracks the bulk volume change of the granular assembly. An increase in ϵ_V indicates compression of the assembly, whereas a decrease in ϵ_V indicates dilation. Typically, in monotonically loaded soils, dense samples initially contract slightly, then dilate. In contrast, loose samples predominantly contract [31, 70].

During normal loading, ϵ_V increases substantially, reflecting significant densification of the granular assembly under the applied normal load. In the shear-right-forward stage, ϵ_V first increases in a stair-step manner, indicating continued incremental compression, before gradually decreasing as the assembly transitions to a dilatant response. This evolution reflects the increasing constraint imposed by the evolving contact network during shear, coincident with the increase in stress ratio shown in Figure 3.9a. It is consistent with the coupling between shear resistance and dilatancy characteristic of dense granular material behavior in critical-state soil mechanics [31, 70]. Although the present experiments do not reach a true critical state, the observed trends suggest that the assembly evolves toward this condition.

Upon shear reversal, ϵ_V decreases rapidly, consistent with a sudden dilation associated with internal restructuring, and then evolves more smoothly as the bulk adjusts to the reversed loading direction. Similar behavior is observed in the shear-left stages, although the shear-left-forward stage exhibits more pronounced fluctuations.

In contrast to the stress ratio evolution plot, ϵ_V produces a leftward branch that is broader than the rightward branch, suggesting that the directional asymmetry differs between strength and volumetric response. However, both measures exhibit greater fluctuations during the forward shearing stages, indicating that forward shearing is associated with more intermittent grain rearrangements and less smooth volumetric accommodation.

Another notable feature is that the shear-right-forward and shear-right-reverse (SRR) stages intersect towards the end of the SRR stage, indicating that the granular assembly partially recovers its prior volumetric state following reversal. In cyclic granular response, this may indicate memory and partial reversibility in the evolution of packing, even if the internal contact network is not identical.

3.3.1.3 Dilatancy

Dilatancy is the rate of volumetric strain change with respect to shear strain rate, $\beta = \dot{\epsilon_v}/\dot{\gamma}$. Figure 3.9d shows the evolution of dilatancy, highlighting the rate at which contraction and dilation occur during shear. Because γ remains nearly constant at shear direction reversals (i.e., $\dot{\gamma} \approx 0$), vertical segments appear at the reversal points in the loading cycle. Moreover, since dilatancy represents volume change induced by shear, the normal loading stage is excluded.

β is defined with respect to γ, so its sign depends on the shearing direction. Thus, contraction and dilation are interpreted in conjunction with the evolution of ϵ_v, not solely from the sign of β. Peaks in β indicate moments of significant internal rearrangement. In addition, increased dilation (as indicated by decreasing ϵ_v) typically correlates with higher shear resistance in granular materials, reflecting the link between volumetric expansion and friction mobilization [31, 71, 72].

During shear-right-forward, β gradually decreases, corresponding to a transition from compressive to dilatant behavior, consistent with the volumetric strain response. Near the end of the stage, β reaches a pronounced minimum, indicating strong dilation associated with significant internal restructuring. Upon shear reversal, β drops sharply, due to the change in shear direction. Following this, β then remains relatively stable, corresponding to a smooth, near-linear evolution of ϵ_v and indicating a stable deformation regime with minimal fluctuations. Toward the end of shear-right-reverse, β decreases noticeably; however, inspection of the volumetric strain response shows that this change mainly reflects a transition to a slightly steeper ϵ_v trend rather than the onset of a distinct dilatant episode.

The shear-left-forward stage exhibits more pronounced fluctuations while β trends upward overall, indicating contractive behavior (consistent with the increase in ϵ_v) interspersed with intermittent restructuring events. Following shear reversal, β reaches its most negative value (≈ -0.03), corresponding to the most dilated state of the assembly. The remainder of the shear-left-reverse stage is characterized by an initial rapid contraction, followed by continued contraction until a transition point where dilation resumes.

Another notable observation is that the maximum and minimum dilatancy occur during the shear-left stages. Additionally, the shear-right stages exhibit more retracing behavior (intersections), whereas the shear-left stages follow more distinct paths, further highlighting directional asymmetry in the cyclic response.

3.3.1.4 Void Ratio

The void ratio is the ratio of the volume of voids to that of the solids in the granular assembly, $e = V_{\text{voids}}/V_{\text{solids}}$. The void ratio was computed using the total specimen region bounded by the shear cell walls. The solid volume, V_{solids}, includes both interior and boundary grains contained in this region. Although only the interior grains are used in the GEM analysis, including the boundary grains in the void ratio calculation provides the appropriate bulk measure of the packing state, since these grains occupy part of the specimen volume and therefore are not part of the void space.

Figure 3.9c shows the evolution of the void ratio, which reveals changes in the internal structure. An increasing e signifies that the structure is loosening (dilating), whereas a decreasing e signifies that the structure is densifying (contracting). During normal loading, the void ratio decreases significantly, reflecting the collapse of initial void space as particles rearrange into more stable, load-bearing configurations under the applied normal stress.

During shear-right-forward, the gradual increase in void ratio indicates that the assembly transitions into a dilatant regime. As shear progresses, particle rearrangements become increasingly constrained by geometric interlocking, requiring the assembly to expand in order to accommodate continued deformation. The relatively small fluctuations during this stage suggest that this dilation occurs through distributed, incremental arrangements rather than large, discrete restructuring events.

Upon shear reversal, the brief increase followed by a decrease in void ratio reflects the breakdown of the previously formed load-bearing structure. The initial increase suggests a short-lived dilation as contacts become misaligned, followed by partial recompression as a new contact network forms in the reversed loading direction. The intersection of the shear-right-forward and reverse paths indicates that the assembly temporarily revisits a prior packing state, consistent with partial reversibility and memory in the contact configuration.

The near-constant void ratio observed toward the end of shear-right-reverse and into the shear-left-forward suggests a transient state in which grain rearrangements accommodate shear without significant net volume change. This behavior indicates a quasi-steady deformation regime in which competing mechanisms of dilation and contraction are approximately balanced. As shear continues beyond $\gamma \approx 0.05$ rad, the renewed increase in void ratio reflects a reactivation of dilatant behavior, likely

driven by the progressive development of anisotropic force-carrying structures that resist particle motion. The broad fluctuation observed during this stage suggests intermittent, larger-scale restructuring events.

During shear-left-reverse, the initial increase in void ratio once again reflects the disruption of the existing contact network, while the subsequent decrease indicates recompression as the assembly reorganizes. The rapid drop in e suggests a more efficient packing rearrangement compared to earlier stages, possibly due to accumulated structural memory from prior loading cycles. Near the end of the stage, e oscillates within a narrow range, suggesting that the system approaches a quasi-steady packing state.

The fact that the void ratio at the end of the cycle remains higher than at the onset of shearing indicates that the assembly does not fully recover its initial packing but instead evolves toward a slightly looser configuration. This net change reflects the irreversible rearrangements accumulated over the cycle. Additionally, the greater number of path intersections in the leftward branches compared to the rightward branches suggests stronger memory effects and more complex rearrangement pathways, further highlighting directional asymmetry in the cyclic response.

3.3.1.5 Macroscopic Response Summary

All macroscale measures reveal directional asymmetry resulting from the applied cyclic loading. The stress ratio response exhibits a broader rightward branch than leftward branch, whereas the volumetric strain response shows the opposite. For dilatancy, the shear-right stages exhibit more retracing behavior than the shear-left stages, whereas the opposite is observed for the void ratio, highlighting differences in memory response.

The forward shear stages of the stress ratio and volumetric strain exhibit greater fluctuations than the reverse stages, indicating that forward shear is associated with more intermittent rearrangement and less smooth bulk accommodation.

The stress ratio and the void ratio are both larger at the end of the cycle than at the onset of shear, indicating that the assembly does not fully recover its initial mechanical and packing state after one cycle. This suggests irreversible rearrangement and history-dependent behavior.

In contrast, the net change in volumetric strain over the full cycle is negligible, $|\delta\epsilon_V| \approx 5.5 \times 10^{-7}$ between the onset and end of shearing. Thus, although the assembly undergoes substantial stage-wise fluctuations in compression and dilation, its overall bulk volume is nearly recovered by the end of the loading cycle.

Altogether, the macroscopic response demonstrates that cyclic shearing produces a direction-dependent and history-dependent evolution of both strength and packing, while maintaining an almost unchanged net volumetric strain over one cycle.

The macroscopic response presented in this section reflects the boundary-driven behavior of the granular assembly, in which shear resistance and volumetric changes arise from collective particle rearrangements. However, these measures do not directly reveal the internal mechanisms governing this behavior. To understand how shear resistance is transmitted and how volume change develops, it is necessary to examine the grain-scale response, including force chain evolution, coordination number, and stress-force-fabric relationships.

3.3.2 Grain-Scale Response

3.3.2.1 Force Chain Detection

Inter-particle contact forces form two interdependent types of networks: weak and strong. In a weak network, contacts carry a force below the mean force. The weak network is analogous to fluid pressure in that it supports the structure. Most particles in the system (greater than 60%) fall into this category. In a strong network, contacts exert a force above the mean. It is these strong contacts that align along the most compressive principal stress direction to form force chains. These force chains act as the solid backbone of the granular medium, allowing it to sustain shear stresses [28, 73].

In 2005, Peters et al. devised a definition for identifying force chains using three criteria [73]:

1) *(3+ grains)* An assembly of three or more particles is needed to form a chain.

2) *(Strong network)* A force chain consists of only strong contacts.

3) *(Quasi-linearity)* Particle minor principal stress paths must line up within a reasonable degree of curvature, α.

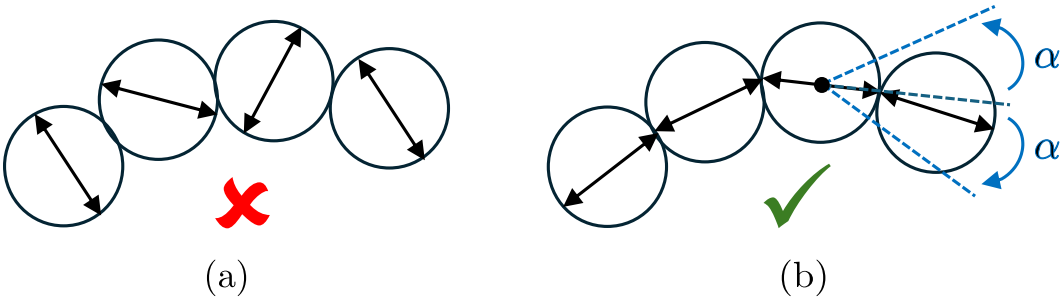


Figure 3.11: Assemblies of highly stressed grains that (a) do not and (b) do form a force chain. Adapted from Peters et al. [73]. Reprinted with permission from A. Peters, H. A. Makse, and H. J. Herrmann, *Physical Review E*, Vol. 72, 041307 (2005). Copyright 2005 by the American Physical Society.

These authors also created an algorithm that reads in grain contact and stress information to detect force chains. Ejtehad et al. further improved this algorithm by employing recursive graph traversal rather than the local pairwise rules used in the original [74]. As a result, this new force-chain finder algorithm better captures the full force network topology, including force-chain branching and self-intersections. This advancement is crucial for reliably linking microscale force chain evolution to the macroscale mechanical behavior of the granular medium.

For this thesis, a MATLAB® function for force chain detection was developed based on the force-chain finder algorithm. It takes as inputs the particle information (centroid positions, contact point locations, contact unit normal vectors), a connectivity map stating which grains are in contact, the inferred contact forces from GEM, and the α angle for the quasi-linearity metric. By default, this function identifies strong contacts as those that carry a force above the mean force. However, one can also select strong contacts based on a specified percentile threshold.

The results of the force chain detection algorithms all heavily depend on the choice of α. An α sweep analysis was performed to determine the best choice for the cyclic simple shear experiments. Four angles, $\alpha = 20°, 25°, 30°$, and $35°$, were tested over three images: (1) a mid-stage frame (about halfway through the forward shearing right motion), (2) the strongest force chain frame, and (3) a near-reversal shear frame (right after the shearing left motion switched directions from forward to reverse). Across the three images, all α choices produced stable results in that the number of detected chains and mean force chain lengths increased as you relaxed the angular alignment constraint. However, the $\alpha = 20°$ and $\alpha = 25°$ values were too restrictive, leading to under-connected, fragmented force chains, whereas $\alpha = 35°$ resulted in artificial force chain branching. Ultimately, $\alpha = 30°$ was selected because

it maximized chain continuity, achieving a tight angular distribution of permitted contacts aligned with the most compressive principal stress vectors. In simpler terms, across the three images, the median accepted angle is around 13°, far from the maximum limit of 30°, reflecting the true physical alignment of the force chains. More details on the alpha sweep are in Appendix A.

Figure 3.12 displays the results for the force chain detection function for the mid-stage image at $\gamma = 0.0756$ rad (4.33°). Figure 3.12a shows the absolute value of the maximum compressive stress of each grain in the assembly, along with their associated maximum compressive stress directions (visualized as lines through the grain centers). The grains with thicker red lines through their centers meet the force chain criteria. Figure 3.12b displays the detected force chains, categorized by length (number of grains in the chain). Lastly, Figure 3.12c shows the Tresca strain (maximum shear strain) field overlaid with the magnitude of the normal component of contact forces, $|f_n|$, in magenta, and the detected force chains in white. The thickness and length of the contact forces scale with their magnitude. In dry, frictional, granular media, the transmission of compressive forces is dominated by the normal component. Hence, we observe that the plotted $|f_n|$ segments align with the detected force chains [28, 39].

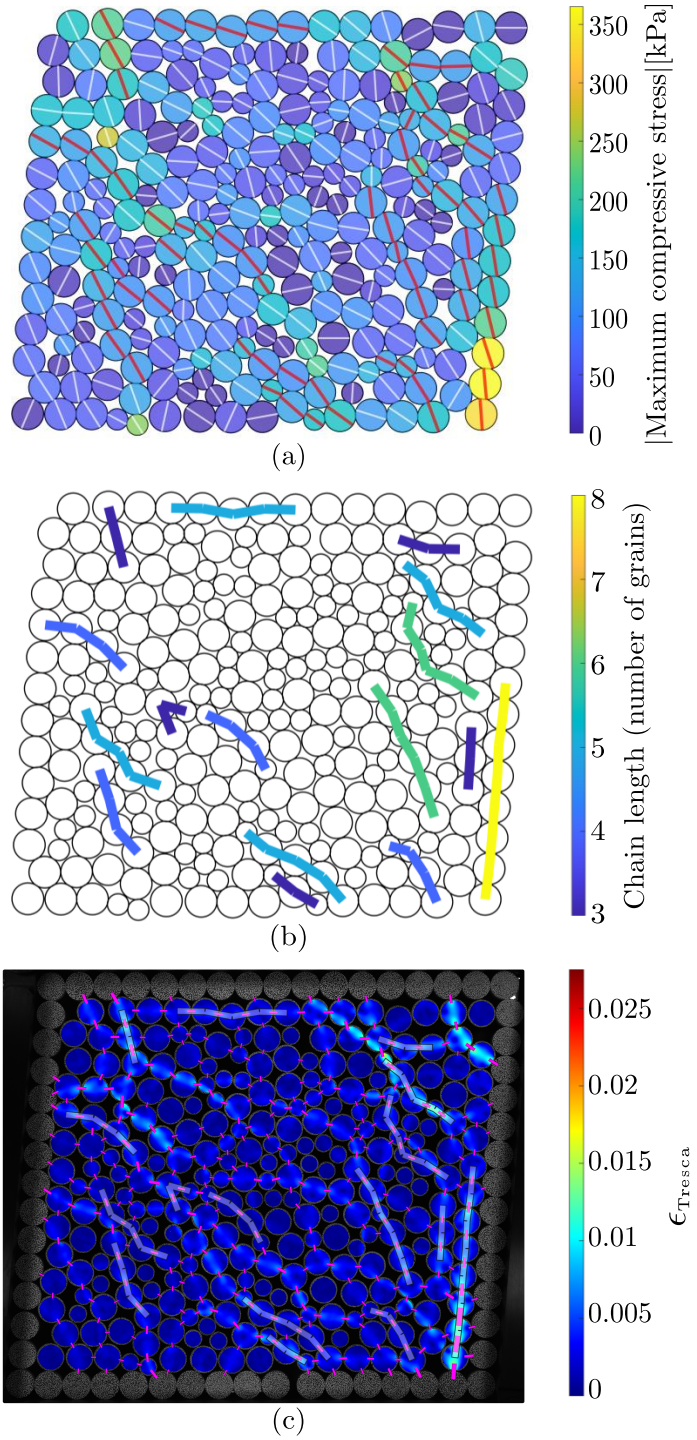


Figure 3.12: Force chain detection at $\gamma = 0.0756$ rad.(a) |Max.compressivestress| and corresponding directions shown as lines through grain centers. Red lines indicate grains that are part of force chains. (b) Detected force chains, categorized by chain length (number of grains). (c) Tresca strain field (from DIC) overlaid with the magnitude of the normal component of contact forces, $|f_n|$, in magenta, and the detected force chains in white.

Figure 3.13 shows the temporal evolution of the detected number of force chains, while Figure 3.14 shows the same data separated by cycle stage for clarity. During the initial loading stage, force chains form quickly and stabilize at approximately 14 chains. Once shearing begins (shear-right-forward), the number of force chains increases and stabilizes once more (~18). In contrast, the shear-right-reverse stage shows a gradual decline in the number of force chains, decreasing from roughly 18 to 13, with additional fluctuations near the end of the stage. During shear-left-forward, the number of chains briefly increases before stabilizing and gradually decreasing toward the next reversal. The last stage shows the greatest variability, with the number of force chains ranging from 18 at peak to 9 at minimum.

Overall, the number of force chains remains relatively stable across stages but shows greater variability near shear reversals, when the contact network reorganizes in response to changes in load direction. Notably, after the initial shearing stage, the number of force chains in subsequent stages does not fully recover to the same level. This behavior suggests history-dependent behavior in the force chain network, where previously formed chains become progressively misaligned as the principal stress direction rotates during cyclic shear, requiring increasing reorganization of the contact and force chain networks in later stages.

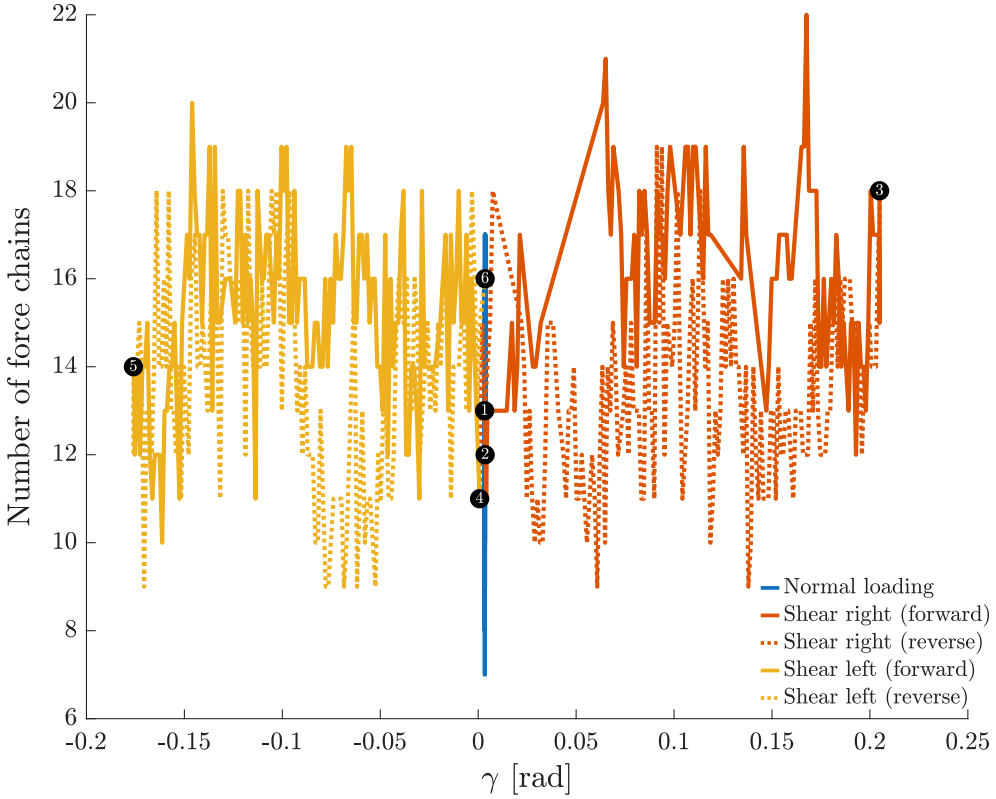


Figure 3.13: Evolution of the number of force chains.

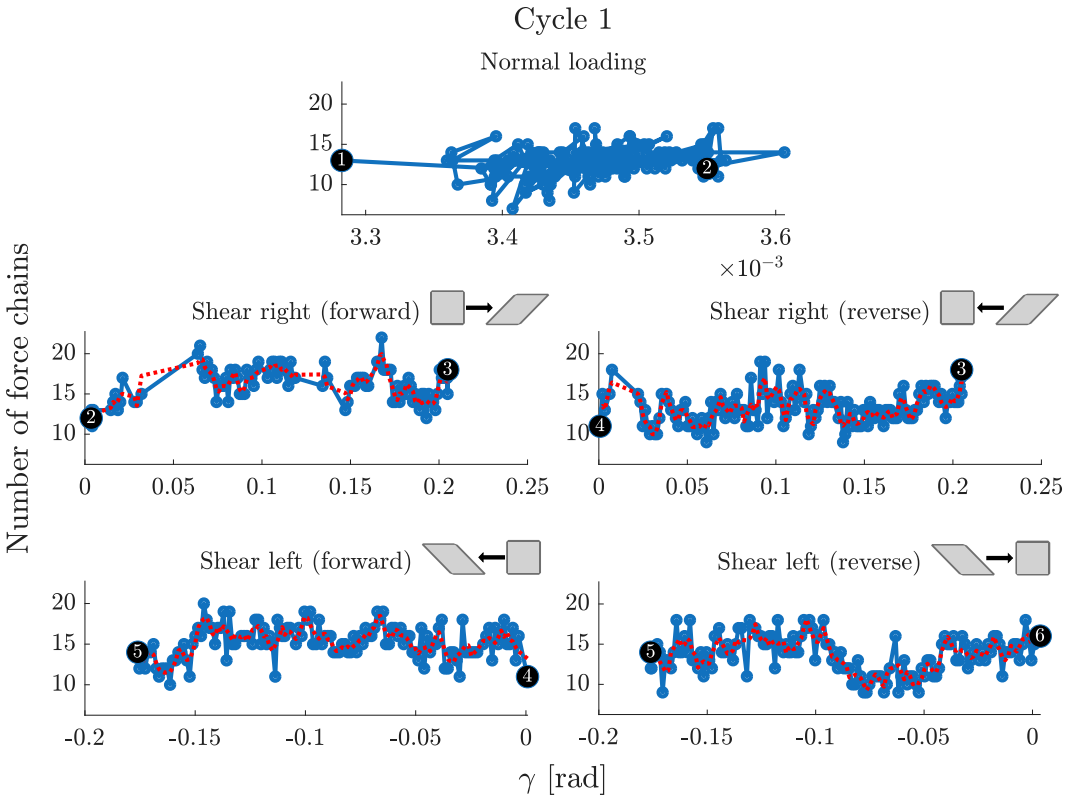


Figure 3.14: Evolution of the number of force chains per cycle stage. The trend line (red) is for visual purposes only.

3.3.2.2 Coordination Number

While the evolution of the force chain network reflects how stresses are transmitted through a subset of strong contacts, it is also important to consider how the underlying contact network evolves more broadly. Hence, we examine the coordination number, Z_c, defined as the average number of contacts per grain.

Figure 3.15 shows the temporal evolution of the coordination number throughout the loading cycle. Unlike the force chain network, which captures only the strong force-bearing structure, the coordination number reflects changes in the full contact network, including both strong and weak contacts. Variations in Z_c, therefore, indicate periods of contact creation and loss, offering insight into how the granular structure reorganizes during shear, particularly near stage transitions and shear reversals.

During the normal loading stage, we observe moderate growth in the coordination number from approximately 3.1 to 3.3, reflecting the formation of additional contacts as the granular assembly compacts. During the first shearing stage, shear-right-forward, Z_c, exhibits fluctuations but shows an overall decreasing trend, ultimately

reducing to about 3.15 as contacts are progressively lost due to shear-induced rearrangement. When shear switches directions, Z_c drops sharply to values below those observed during normal loading, indicating a rapid breakdown of the existing contact network as force chains become misaligned with the new loading direction. Following this drop, the coordination number partially recovers and remains relatively stable (~3.13) despite continuous contact restructuring, as evidenced by the significant fluctuations. Z_c only begins to increase towards the end of this shear-right-reverse stage, and then stabilizes well into the shear-left-forward stage at $Z_c \approx 3.2$.

The initially stable coordination number in the shear-left-forward stage is short-lived, first dropping, then gradually increasing until it peaks at about 3.32 near the end of the stage, indicating enhanced contact formation as the system adapts to the new loading direction. This is followed by a gradual decrease back to about 3.2. The next shear reversal once again results in a sharp drop in Z_c (to roughly 3.1), followed by a short recovery period as new contacts form and the network reorganizes.

As the shear-left-reverse stage ends, the coordination number gradually drops, eventually returning to a value nearly identical to its original state (3.126 at the end versus 3.129 at the start). This suggests that despite notable intermediate restructuring of the contact network, the overall connectivity is maintained over the full cyclic shear deformation. This nearly reversible global connectivity, however, does not imply that the internal force transmission structure remains unchanged. The force chain network, which governs stress propagation through the granular assembly, may undergo significant reorganization even when the total number of contacts is preserved. To quantify these changes, we now conduct a statistical analysis of the force chain network.

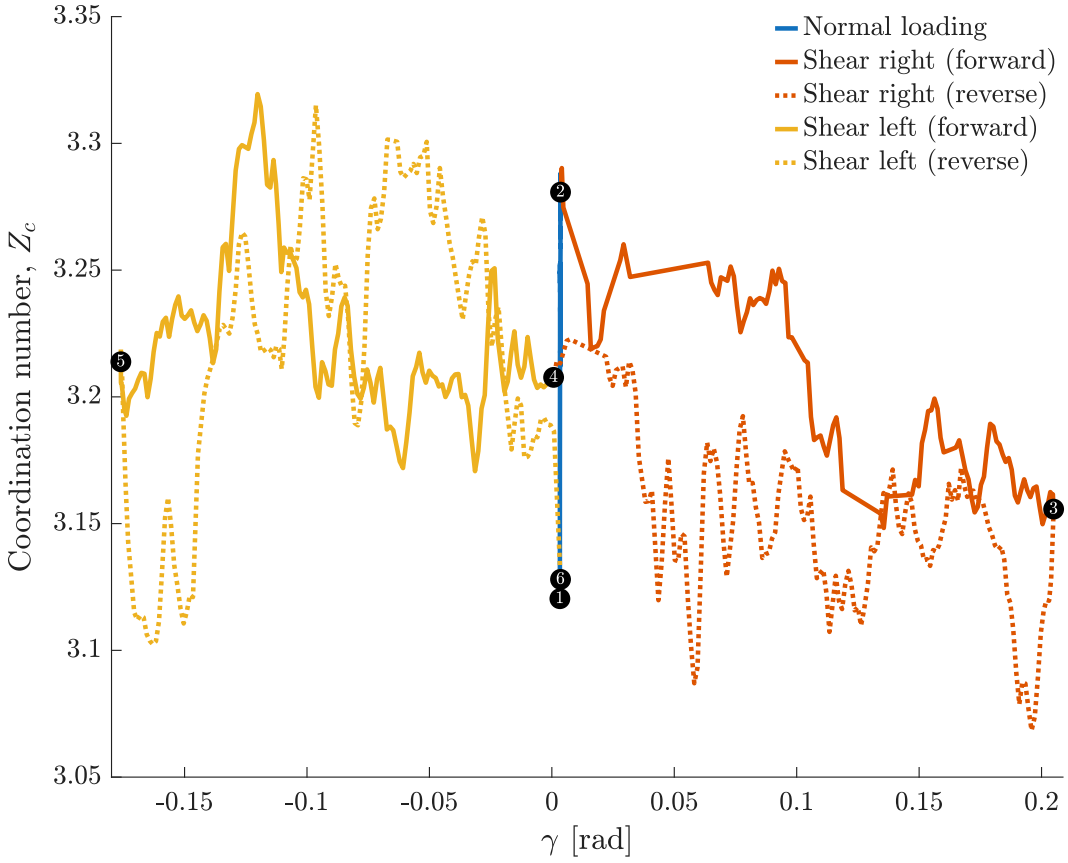


Figure 3.15: Evolution of the coordination number, Z_c, the average number of contacts per particle.

3.3.2.3 Force Chain Statistics and Evolution

Given the pronounced variability and continual reorganization of the force chain network, we identify trends in the data by first examining temporal evolution plots and then analyzing distributional summaries (median, interquartile range (IQR), 95th percentile, and area under the curve) for each stage of the simple shear cycle. The median describes the typical state, e.g., the typical chain network size, chain count, and chain length. IQR describes the typical variability in the data. High percentiles identify rare events such as occasional very strong force chains. The area under the curve (AUC) of the total force chain length evolution quantifies the accumulated extent and persistence of the force chain network during each stage of deformation. Taken together, these distributional summaries describe the full behavior of the force chain network.

Total force chain length (number of grains) The total chain length (in terms of number of grains) for a given frame, t, in the experiment is calculated as

$$S(t) = \sum_{k=1}^{N_{FC}(t)} L_k(t) \, , \tag{3.1}$$

where $N_{FC}(t)$ is the number of force chains and $Lk(t) = L_1(t), L_2(t), \ldots, L_{N_{fc}(t)}(t)$ is the different force chain lengths. Figure 3.16 shows the temporal evolution of the total chain length, and Figure 3.17 shows the same data per cycle stage. These plots closely resemble the temporal evolution of the number of force chains. This similarity arises because the total chain length depends on both the number of force chains and their individual lengths. Hence, when the typical chain length remains relatively consistent, changes in the number of force chains dominate the evolution of the total chain length. Therefore, we still observe rapid growth during the normal loading and shear-right-forward stages, followed by more variable behavior in the subsequent stages. However, the total chain length provides additional insight into changes in the sizes of individual force chains, reflecting the overall extent of the force chain network rather than simply the number of force chain structures present.

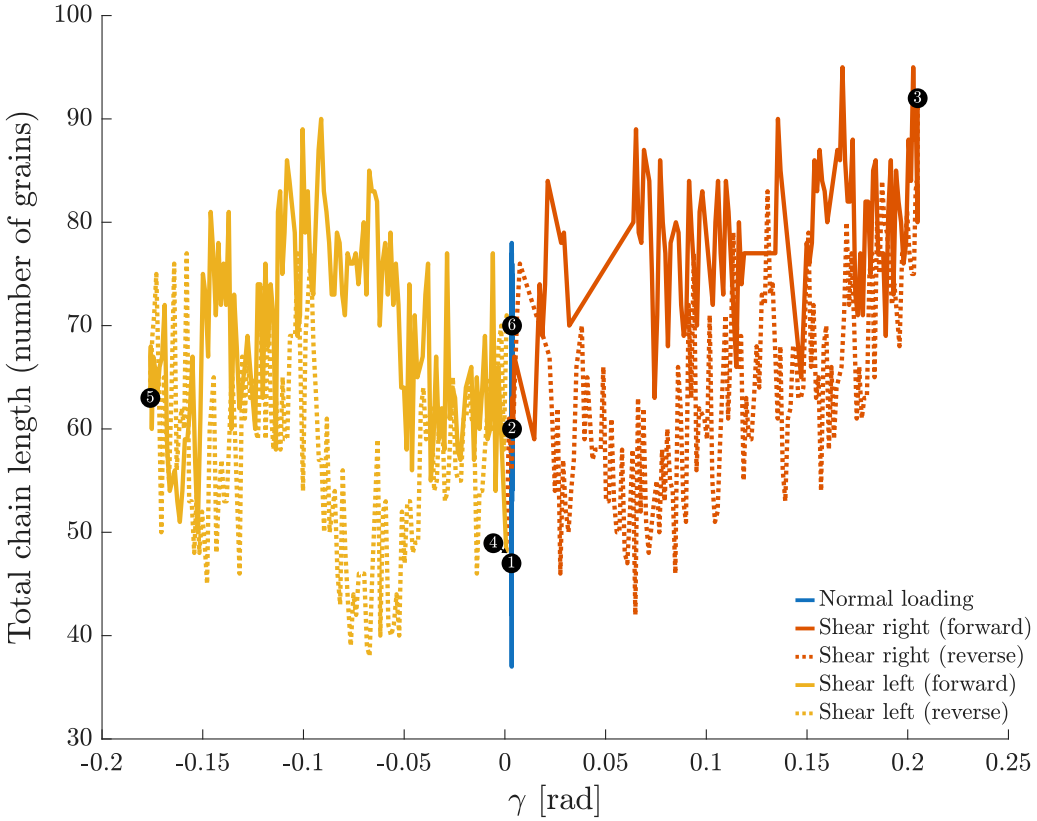


Figure 3.16: Evolution of the total chain length (number of grains).

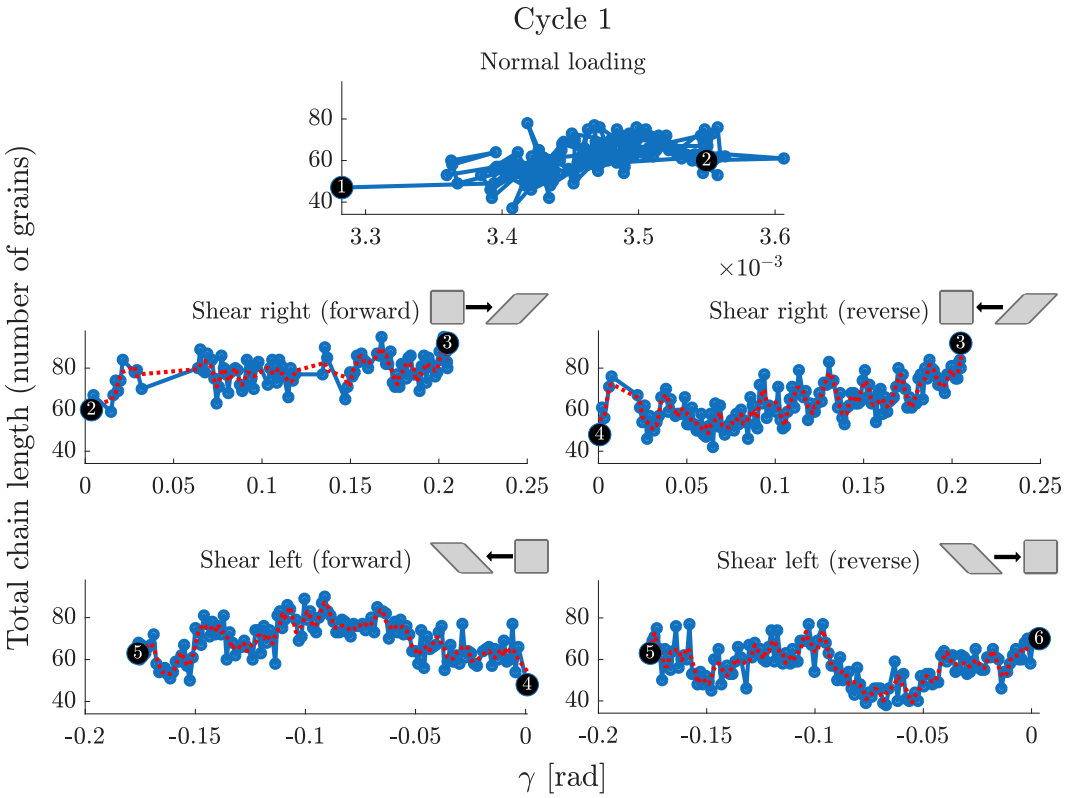


Figure 3.17: Evolution of the total chain length per cycle stage. The trend line (red) is for visual purposes only.

Accumulated Force Chain Network Content The normalized area under the curve (AUC) of the total chain length is calculated as

$$A = \frac{\int S(\gamma)\, d|\gamma|}{\Delta\gamma_{\text{stage}}}. \tag{3.2}$$

The absolute value of the shear angle, γ, makes it easier to interpret results since γ changes signs during left shear. Furthermore, since the shear span decreases a little with each stage (inherent to the experiment), normalizing the AUC by shear span per stage, $\Delta\gamma$, makes stage-to-stage comparisons across cycles fair. So, A represents the average force chain network size sustained per unit shear deformation. Intuitively, this metric captures both the size of the force chain network and the duration it remains large during shear deformation at that stage.

The bar chart (Figure 3.18) below shows the average chain-network size per unit of shear deformation for each cycle stage. From top to bottom, the y-axis shows the ordered stage names in the cycle. The first letter 'S' stands for "shear", the second letter 'R' or 'L' stands for "right" or "left", and the third letter 'F' or 'R' stands for "forward" or "reverse."

The data reveal that the first shearing stage (SRF) exhibits the highest average chain network size per unit deformation. Following reversal (SRR), the normalized AUC drops, indicating disruption of the existing chain structures. During SLF, the chain structure partially rebuilds but does not fully recover to the level of the first forward stage (SRF).

The next reversal (SLR) then causes the normalized AUC to drop again. Two main findings are apparent: (1) the data suggest that the initial shear-right stage (SRF) creates larger and more persistent chain structures, and (2) the forward stages have a higher normalized AUC than the reverse stages (specifically, 10.8% higher normalized AUC). Physically, this means that forward stages help the force chain network organize and grow, while the reverse stages disrupt that organization, leading to smaller, less persistent chain networks.

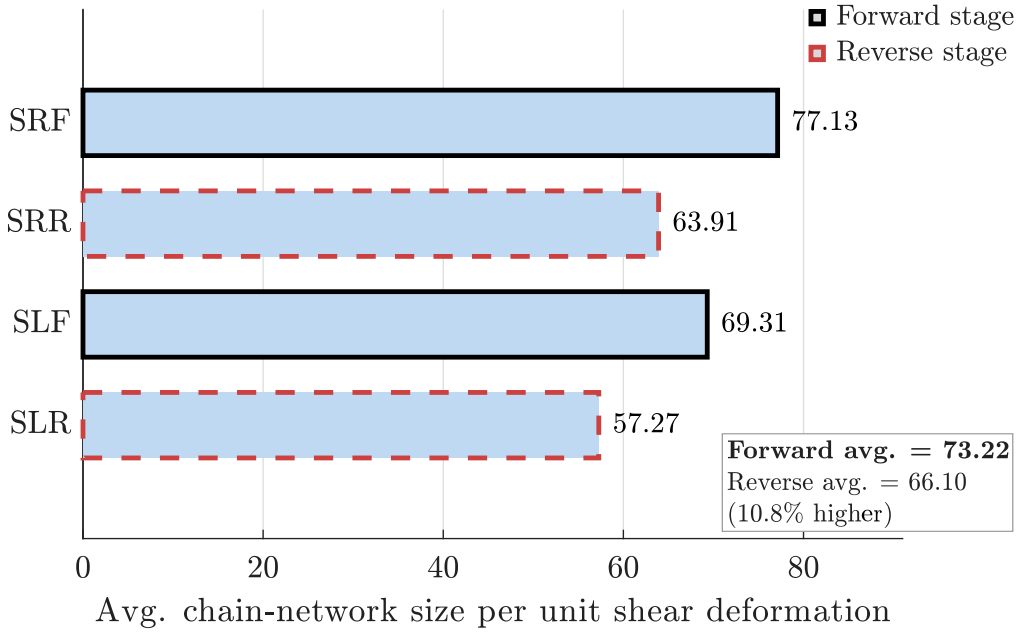


Figure 3.18: Bar chart of the normalized area under the curve (AUC) of the total chain length for each shear stage (**S**hear-**R**ight-**F**orward, **S**hear-**R**ight-**R**everse, **S**hear-**L**eft-**F**orward, **S**hear-**L**eft-**R**everse). The normalized AUC represents the average size of the force chain network sustained per unit shear deformation within each stage.

Force Chain Structure Distribution Next, we inspect a violin plot (Figure 3.19) of the total chain length (in terms of number of grains) for each cycle stage. The vertical red lines represent the median, and the vertical blue lines represent the lower and upper quartiles (Q1 and Q3). The width at any point on the violin shape indicates the frequency of data at that value. That is, wider sections represent a higher probability of that value occurring, whereas skinnier sections represent a lower probability. The tails of the violin plot represent extremes of the data distribution. The longer the tail, the more the distribution is skewed towards that direction. The distribution can also have multiple peaks, indicating possible multiple regimes in the data.

The normal loading violin plot serves as a baseline before the onset of shear, showing an intermediate total chain length size with occasional very small chain structures.

During the first shear stage, shear-right-forward (SRF), the distribution shifts towards larger chain networks, with a median total chain length of 79, the highest across all stages. The distribution is concentrated around the median, with short, narrow lower and upper tails, suggesting that this stage is dominated by comparatively large, consistent force chain structures. In the following stage, shear-right-reverse (SRR), the median total chain length decreases to 63. While the distribution is widest near the median, the very long tails suggest substantial variability, with occasional very short and very long chain structures. This broad spread suggests that force chain reorganization dominates this stage.

Next, during shear-left-forward (SLF), the total chain length again increases to a median of 70.5. However, the distribution shows a change in width near the center, suggesting two preferred ranges of chain length corresponding to moderately sized and larger sized chain structures. This pattern may reflect competing force chain configurations within the network. Finally, the last shearing stage, shear-left-reverse (SLR), has the smallest force chain structure size, indicating a more fragmented force chain than in the other stages. There is consistency between these distributional trends and the normalized AUC results: both indicate that the SRF stage produces larger and more persistent chain structures.

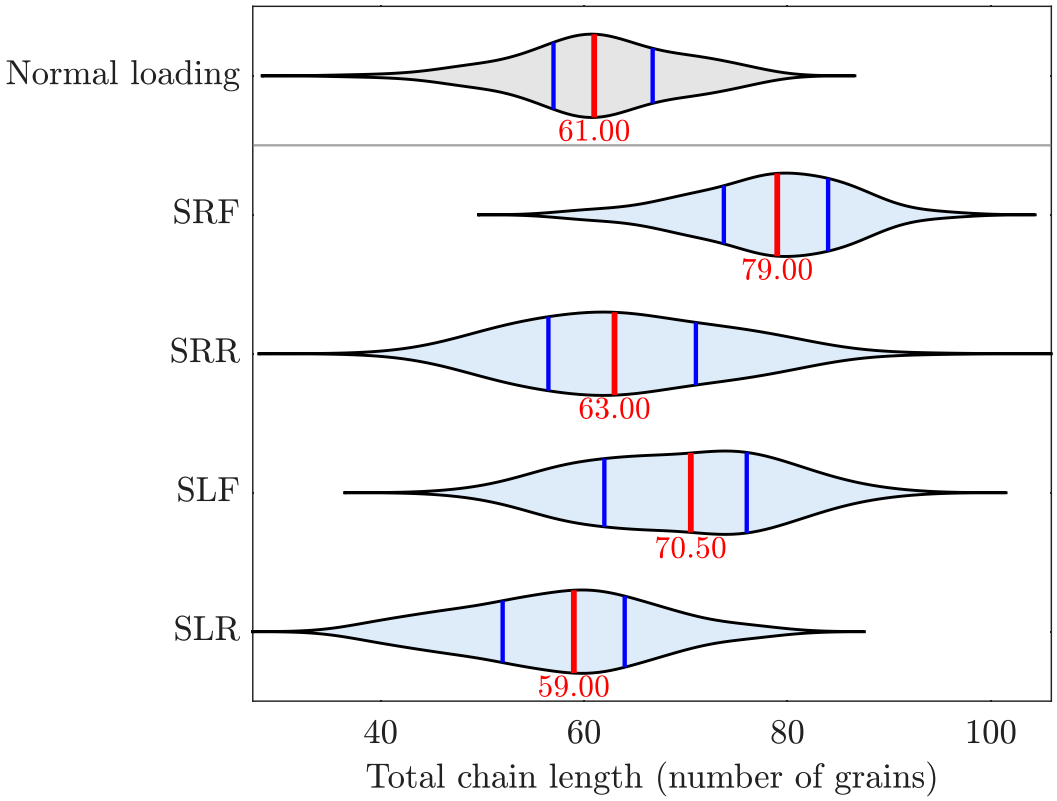


Figure 3.19: Violin plot of the total chain length for each cycle stage, used to visualize force chain structure size distribution. Red vertical bars mark the median of the distribution. Blue vertical bars mark the Q1 and Q3 quartiles of the distribution.

Force Chain Participation The chain density represents the fraction of all grains that participate in force chains and is calculated by

$$\text{Chain density} = \frac{S(t)}{N_g} \tag{3.3}$$

where $S(t)$ is the total chain length (in number of grains) and N_g is the total number of grains in the assembly. In this experiment, $N_g = 272$, corresponding to the number of interior grains in the densely packed granular assembly. A violin plot of the chain density is shown in Figure 3.20. As you can see, the chain density and total chain length plots look identical, because the chain density is the total chain length normalized by the total number of grains. However, the chain density is still reported because it will be more useful in the next chapter when comparing force chain network participation across experiments with different grain numbers (e.g., densely packed versus loosely packed granular assemblies). For context on interpreting the chain density, let us look at one example. The normal loading stage has a median chain density of 0.22, indicating that the equivalent of approximately 22% of the grains (about 60 grains) in the assembly participate in force chain

structures. Once shearing begins, force chain network participation increases to 29%, adding about 19 additional grains worth of chain structure during shear-right-forward (SRF).

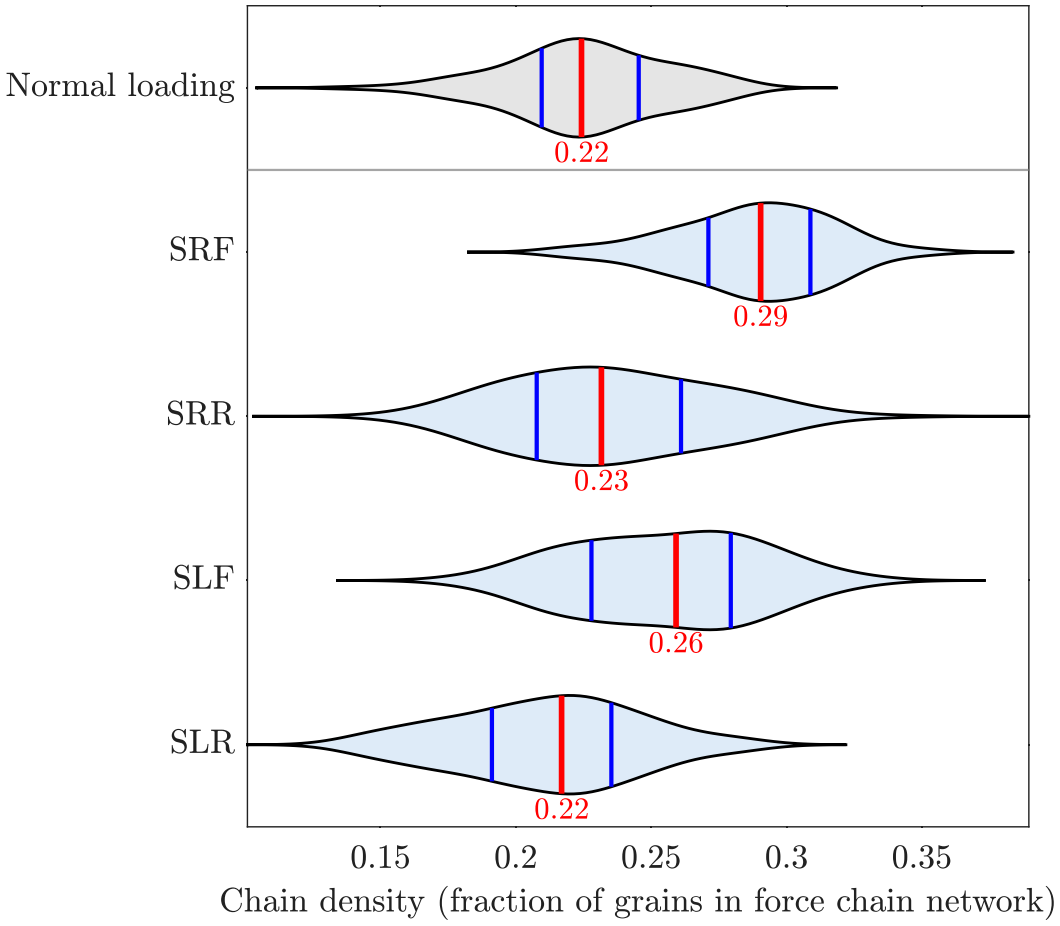


Figure 3.20: Violin plot of the chain density for each cycle stage, used to visualize the distribution of force chain network participation. Red vertical bars mark the median of the distribution. Blue vertical bars mark the Q1 and Q3 quartiles of the distribution.

Strong Network Participation and Strong Network Chain Participation

While the chain density violin plot is useful for understanding the fraction of the entire assembly that lies in force chains, it is also valuable to examine the size of the strong network and the extent to which it is organized into force chains. Strong network grains (high-stress grains) are those whose maximum compressive stress, σ_1 (note the compression-positive convention), is greater than the average in the assembly:

$$N_{\text{strong}} = |\sigma_1| > \langle|\sigma_1|\rangle \, . \tag{3.4}$$

The number of strong network grains that are part of force chains, which we already know, is the total chain length (in number of grains), S.

Figure 3.21 shows the evolution of the percent of strong network grains and the percent of strong network grains in force chains, where

$$\%\ \text{strong network grains} = \frac{N_{\text{strong}}}{N_g} \times 100 \tag{3.5}$$

and

$$\%\ \text{strong network grains in FC} = \frac{S}{N_{\text{strong}}} \times 100\ . \tag{3.6}$$

Across all cycle stages, roughly half of the granular assembly (41−47%) participates in the strong force network at any given time. Of these strong network grains, about 55 − 60% are part of force chains throughout the cycle. These findings suggest that while the strong network spans a considerable portion of the assembly, only about half of those grains are organized into chain-like bearing structures. Despite an entirely different loading condition, Peters et al. reported similar behavior in a flat punch indentation test where approximately half of the strong particles were found to belong to force chains [73].

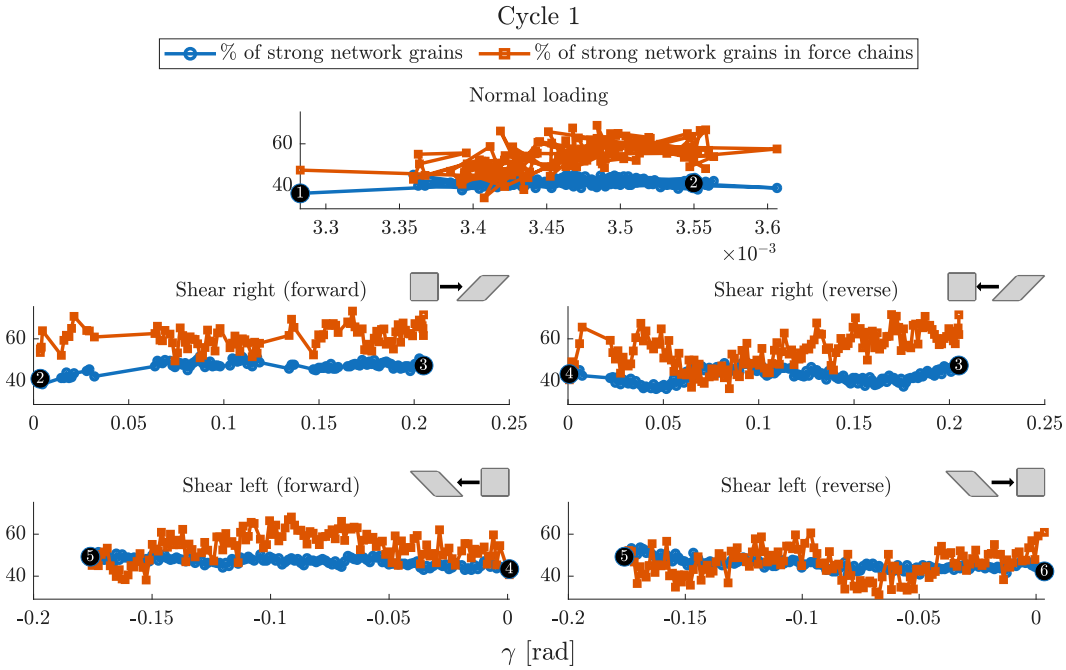


Figure 3.21: Evolution of the percentage of strong network grains and the percentage of strong network grains in force chains. Strong network grains are those whose maximum compressive stress is greater than the average grain stress in the assembly.

We can learn more by examining the median and mean absolute deviation (MAD) for each variable in Tables 1 and 2. MAD is used because it is a robust measure of statistical variability resistant to outliers and skewed data, in line with the sporadic nature of force chains [75]. Smaller MAD values indicate less variability, while larger values indicate more variability.

Table 3.1 reveals that the forward shear stages (SRF, SLF) have the largest fraction of strong grains in the assembly (median $\sim$ 47%), while the reverse shear stages (SRR, SLR) show smaller values. Furthermore, the strong network is quite stable (MAD $\sim$ 1 – 1.5% for most stages), except during SRF (MAD $\sim$ 2.6%), which shows the most variability. These results are consistent with the idea that shear reversal reorganizes the contact network.

Table 3.1: Percentage of strong network grains median and mean absolute deviation (MAD)

Cycle Stage	Median (%)	MAD (%)
Normal loading	41.54	1.10
Shear right (forward)	47.43	1.10
Shear right (reverse)	42.65	2.57
Shear left (forward)	47.43	1.47
Shear left (reverse)	45.59	1.47

The median values in Table 3.2 confirm that roughly half of the strong network grains form force chains, with SRF having the highest participation ($\sim$ 61%) and SLR the lowest ($\sim$ 46%). Compared to Table 1, the variability is higher (MAD $\sim$ 3 – 5% for most stages), with the highest variability at 6.5% during SRR (as indicated by the most force chain network). So, force chain organization is more dynamic than the strong network itself.

Table 3.2: Percentage of strong network grains in force chains median and MAD

Cycle Stage	Median (%)	MAD (%)
Normal loading	54.39	4.33
Shear right (forward)	61.42	3.43
Shear right (reverse)	55.60	6.52
Shear left (forward)	54.77	4.69
Shear left (reverse)	46.22	4.61

Combined, these results show that while the strong grain network occupies a consistent portion of the assembly, the organization of those grains into force chains is highly dependent on the shear direction and history. Forward shear (SRF) yields the highest and most stable participation of force chains. In contrast, larger fluctuations near shear reversals are indicative of repeated disruption and reformation of chain structures as the principal stress directions rotate towards a new shear direction.

Micro-Macro Comparison To place the force chain statistics in a broader context, the stage-wise medians of total chain length are compared with those of the macroscopic shear stress (Figure 3.22). The Q1 and Q3 quartile whiskers are also shown.

The stage with the highest median (SRF) also has the longest force chain length (in number of grains), indicating that the strongest internal resistance to deformation coincides with the most developed force chain network. However, this statement does not hold for the remaining stages, as the extent of the force chain network does not track shear stress in a monotonic manner. Hence, a longer force chain network does not necessarily imply a larger macroscopic shear stress. The shear stress depends on a variety of factors, such as chain connectivity, chain orientation relative to the principal load-bearing direction, and the magnitude of the force transmitted through the chains. This explains why, even though SLF has relatively longer chains compared to SLR, the median shear stress is higher in SLR.

During purely normal loading, the shear angle, γ, is essentially zero. Despite negligible shear stress, the total chain length increases to support the load imposed by downward normal compressive confinement. What distinguishes the shearing stages, especially SRF, is not merely the existence of force chains, but the development of force chains that are more effective at transmitting shear. The efficiency of stress transmission depends on the orientation of contacts and forces within the granular assembly. Therefore, the next section examines the anisotropy of the contact and force networks.

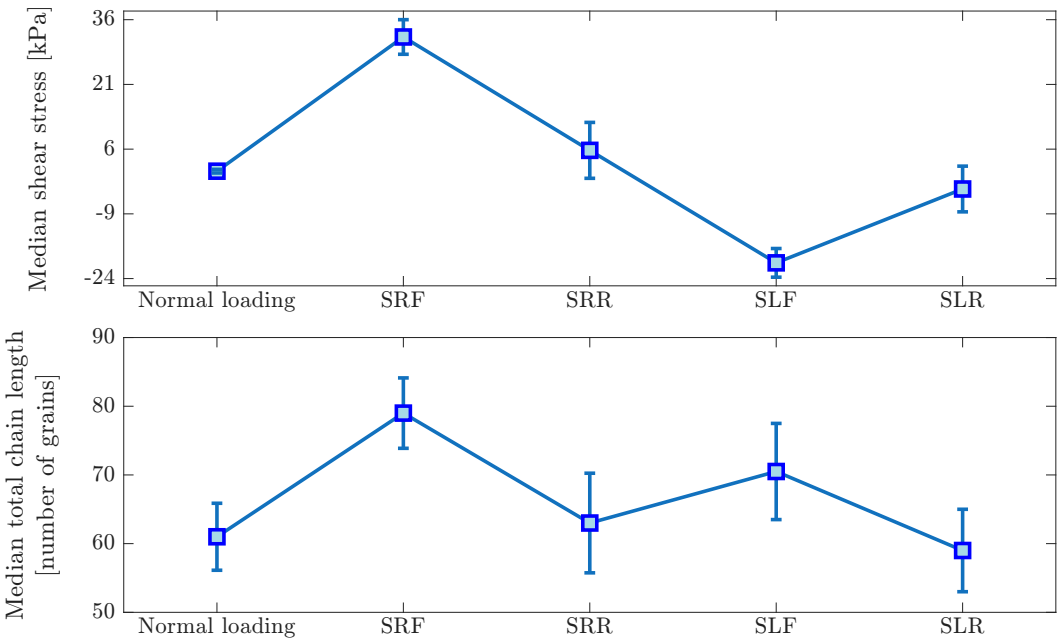


Figure 3.22: Stage-wise medians of the macroscopic shear stress [kPa] and the total chain length [number of grains]. Error bars represent one-half of the interquartile range, centered about the median.

3.3.2.4 Force Chain Structure and Anisotropy

The term fabric describes the internal structure of a granular material characterized by the geometric arrangement and orientation of particles and their contacts. Typically, granular materials exhibit an inherent anisotropic fabric even before deformation occurs. Several factors contribute to this initial anisotropy, including sample preparation methods (e.g., deposition under gravity, layered deposition, compaction) and grain shape, both of which influence particle settling and contact formation during assembly. Subsequent loading of the granular material, such as cyclic shear, produces additional anisotropy as contacts continuously rearrange throughout deformation. This evolution of the microscopic structure directly influences the macroscopic behavior of the granular material. In fact, these anisotropic structures are closely related to the formation of force chains, which act as the primary load-bearing pathways within granular materials [29, 30].

Thus, it is useful to track the nature and degree of anisotropy of a fabric measure. The nature of anisotropy refers to the directional preference of a fabric measure (e.g., the tendency of interparticle contacts to align with the major principal stress direction). The degree of anisotropy quantifies the strength of this directional bias [29]. In granular mechanics, fabric tensors and directional statistics of contact orientations are commonly used to measure anisotropy. In many granular systems,

these directional distributions are well approximated by second-order anisotropy, using a Fourier series ([29, 30, 57]) of the form,

$$g(\theta) = a_0 + a_1 \cos(2\theta) + b_1 \sin(2\theta) \ , \tag{3.7}$$

where a_0 is the isotropic component (mean) and a_1, b_1 capture the deviatoric (anisotropic) component. The harmonic coefficients are further interpreted in terms of the anisotropic magnitude,

$$a = \left(\sqrt{a_1^2 + b_1^2} \right) \Big/ a_0 \tag{3.8}$$

and the principal direction of anisotropy,

$$\theta_a = (1/2)\text{atan2}(b_1, a_1) \ . \tag{3.9}$$

The following subsections analyze the orientation distributions of both contacts (fabric anisotropy) and interparticle forces (force anisotropy), and their relationships with macroscale quantities through the stress-force-fabric framework established by Rothenburg and Bathurst [30]. Additionally, probability density functions (PDF) of normalized contact forces are examined to characterize how forces are transmitted through the granular assembly.

Fabric and Force Anisotropy Figure 3.23 presents polar histograms used to visualize the angular distributions of contact fabric orientation, $P(\theta)$, and the interparticle contact forces, $\bar{f}_n(\theta)$ and $\bar{f}_t(\theta)$ (mean normal force and mean tangential force, respectively). These anisotropy distributions are evaluated at the midpoint of each stage in the loading cycle (i.e., mid-normal loading and mid-shear). From top to bottom, the rows correspond to $P(\theta)$, $\bar{f}_n(\theta)$, and $\bar{f}_t(\theta)$. Reading the figure from left to right, therefore, illustrates the evolution of these anisotropy measures throughout the deformation cycle.

In polar distributions, each bin (shown as solid lines in the figure) represents the value of the distribution for contacts whose orientations fall within a specified angular range. For the contact fabric distribution, $P(\theta)$, the radial magnitude reflects the probability density of contacts oriented in that direction. In contrast, for the force-based distributions, $\bar{f}_n(\theta)$ and $\bar{f}_t(\theta)$, the radial magnitude represents the average force carried by contacts oriented near that direction. An isotropic state would produce a circular distribution, whereas anisotropy appears as elongated lobes indicating preferred orientations. Because the distributions exhibit π-symmetry,

each preferred direction appears as a pair of opposite peaks, corresponding to a single physical axis.

Experiments and simulations of granular materials under shear have consistently shown that contacts, strong normal forces, and tangential forces tend to align along a common compression direction [24, 25, 38, 76]. This tendency can be examined in the data by comparing the dominant anisotropy axis of each distribution with the principal compressive stress axis. The dominant anisotropy axis is the major axis of the Fourier fit (shown as the dash-dotted curve), which represents the principal direction of the anisotropic distribution. The principal compressive stress axis, computed from the macroscopic stress tensor, is shown as a red dashed line. Alignment between these axes indicates that the preferred orientations of contacts and forces coincide with the direction along which the granular assembly transmits compressive stress.

Following this observation, several trends emerge across the loading cycle. During normal loading, the fabric distribution, $P(\theta)$, is nearly circular, indicating an approximately isotropic contact orientation distribution. In the shear-right-forward (SRF) stage, fabric anisotropy develops, manifested by elongated lobes and a rotated distribution towards a preferred direction. We also observe that the dominant anisotropy axis aligns closely with the principal compressive stress axis (within a few degrees), indicating that the contact network begins to organize along the direction of compressive loading. During shear-right-reverse (SRR), the magnitude of fabric anisotropy decreases (shorter radial bins), suggesting partial rearrangement of contacts during reversal. In the following shear-left-forward (SLF) stage, $P(\theta)$ rotates clockwise and shows the largest misalignment between the anisotropy axis and the principal stress axis, indicating that the contact network is reorganizing under the reversed shear direction. Finally, during shear-left-reverse (SLR), the distribution becomes nearly isotropic again, with short radial bins and only weak directional preference.

The mean normal force distribution, $\bar{f}_n(\theta)$, exhibits a clearer preferred orientation than the fabric distribution. During normal loading, two pronounced lobes appear near the vertical loading direction, indicating that compressive forces primarily transmit along contacts aligned with the applied load. In the SRF stage, the distribution shifts and develops a peanut-shaped form, characteristic of anisotropic force transmission. The anisotropy and principal stress axes remain closely aligned, and the largest bins occur near this axis, indicating that strong normal forces preferen-

tially align with the compression direction. During SRR and SLF, however, larger misalignments appear between the anisotropy and principal stress axes, reflecting transient rearrangements of the force network after the shear direction reversed. In particular, the shear-left-forward stage shows the greatest misalignment, suggesting that the contact force network has not yet fully reorganized to the new loading direction. By the SLR stage, the axes become nearly aligned again, indicating partial re-establishment of a preferred load-bearing direction.

The mean tangential force distribution, $\bar{f}_t(\theta)$, follows similar trends to those observed for $\bar{f}_n(\theta)$, although it generally exhibits smaller radial magnitudes. Consequently, the tangential force distribution contributes less strongly to the anisotropic structure of the contact network than the compressive normal forces, which dominate stress transmission within the granular assembly. This observation is consistent with findings in the literature, which indicate that, among the three anisotropy components contributing to macroscopic shear strength –fabric anisotropy, normal force anisotropy, tangential force anisotropy– the tangential force component is the least significant [76, 77]. Since tangential contact forces primarily resist sliding between particles, only small interparticle friction is necessary to stabilize the grain clusters that carry the larger compressive forces. In this sense, tangential contact forces help stabilize force chain structures, whereas the compressive normal forces bear the applied load.

Across all force-based distributions, the SLF stage consistently shows the largest misalignment between the anisotropy axis and principal stress axis, highlighting that shear reversal induces transient restructuring of the contact network.

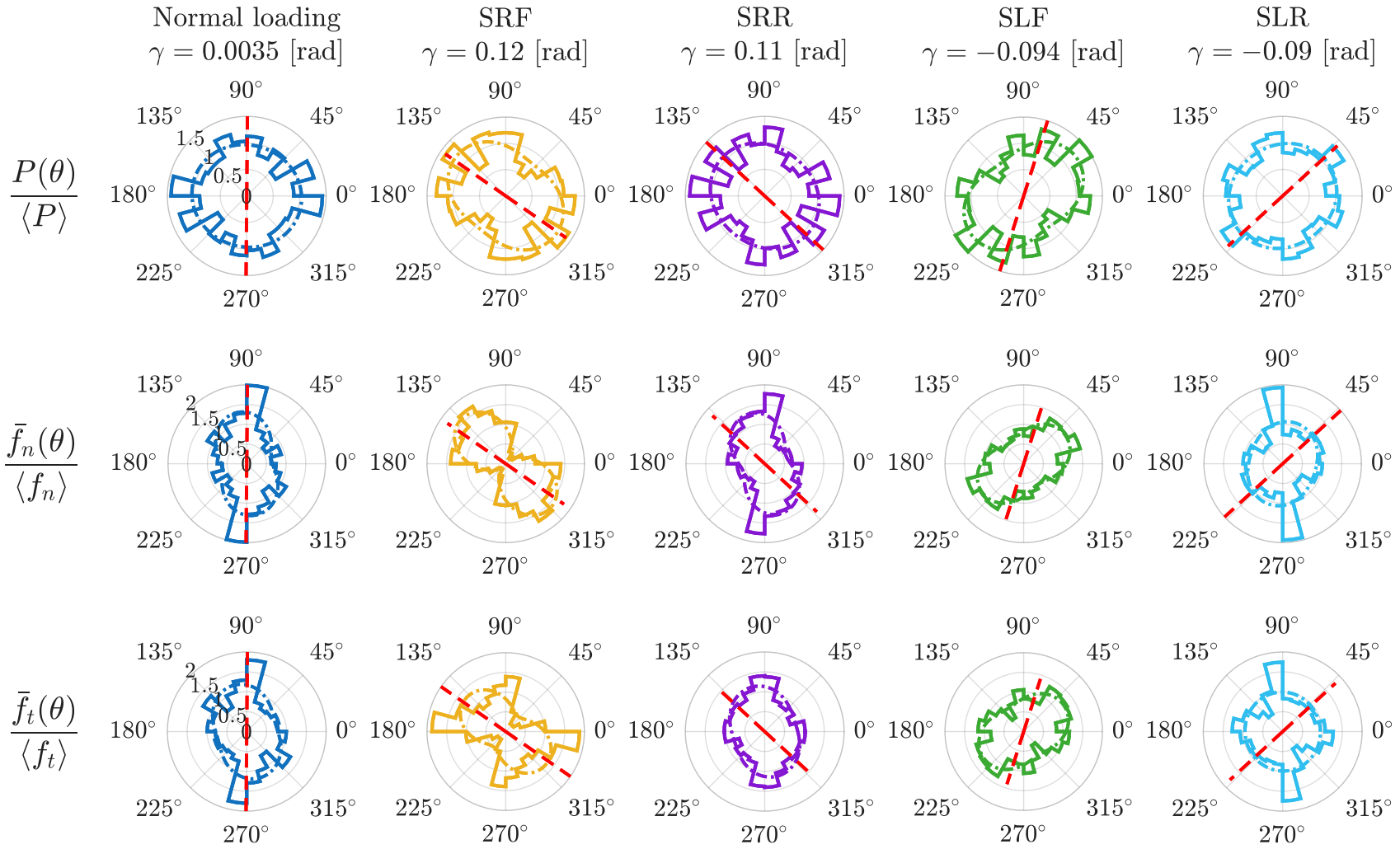


Figure 3.23: Polar histograms showing the normalized angular distributions of contact fabric orientation, $P(\theta)$, the mean normal contact force, $\bar{f}_n(\theta)$, and the mean tangential contact force $\bar{f}_t(\theta)$, at the midpoint of each stage in the loading cycle (i.e., mid-normal loading, and mid-shear). The solid curve shows the distribution, the dash-dotted curve shows the Fourier fit of the distribution, and the red dashed line is the maximum compressive stress axis.

Temporal Evolution of Fabric and Force Anisotropy Magnitudes While the last section qualitatively examined the directional organization of the contact network across discrete snapshots of the cyclic shear deformation, this section provides a quantitative analysis of how these directional structures develop and evolve throughout the loading cycle. Specifically, we examine the fabric anisotropy magnitude (a), the normal force anisotropy magnitude (a_n), and the tangential force anisotropy magnitude (a_t), as functions of shear strain, γ. The evolution of these anisotropy measures provides insight into how the internal structure of the granular assembly reorganizes as shear direction changes during the cycle. The anisotropic magnitudes are obtained from their respective Fourier fit through Eq. (3.8).

The evolution of the fabric and force anisotropy magnitudes during the loading cycle is shown in Figure 3.24. A small initial anisotropy is present even before the shear cell is normally loaded, with all measures having magnitudes of approximately 0.1. During normal loading, the fabric anisotropy, a, remains relatively small and nearly constant, while the force-based anisotropies evolve more strongly. In particular, the normal force anisotropy, a_n, increases rapidly and stabilizes, whereas the tangential force anisotropy, a_t, decreases briefly before increasing and reaching a near constant level. By the end of normal loading, the magnitudes follow the order $a_n > a_t > a$, with typical values of about 0.4, 0.2, and 0.04, respectively.

Once shear begins, all three anisotropy measures increase significantly before approaching a plateau, indicating the rapid development and succeeding stabilization of directional structure within the contact network. The normal force anisotropy remains the dominant contribution, reaching values near 0.72, followed by the tangential force anisotropy (~ 0.4) and the fabric anisotropy (~ 0.2). These trends reflect the strong alignment of load-bearing contacts with the direction of compressive stress as shear deformation progresses.

Upon shear reversal in the SRR stage, the anisotropy magnitudes initially decrease before increasing again toward the end of the stage. This temporary reduction corresponds to a partial breakdown and reorganization of the contact network after the loading direction changed. The decrease is more substantial for the force-based anisotropies, a_n and a_t, than for the fabric anisotropy, a.

By the SLF stage, the magnitudes of the three anisotropy measures become more comparable, oftentimes overlapping. Small fluctuations in a_n and a_t at the beginning of the stage suggest local rearrangements of contact reorientations. The anisotropy measures remain closely grouped in the final shearing stage, with no

single measure dominating, indicating that the granular assembly has reached a reorganized steady structure. When all three curves dip simultaneously, the tangential force component slightly dominates, suggesting enhanced frictional mobilization during rearrangement, likely associated with localized sliding and reformation of force chains.

Overall, the SRF stage exhibits the highest anisotropy magnitude across both fabric- and force-based measures. After the substantial reduction observed during the shear-right-reverse stage, the remaining stages show relatively stable anisotropy levels, indicating that the internal structure of the granular assembly has largely adjusted to the cyclic loading condition.

These results demonstrate that force anisotropy develops more strongly than fabric anisotropy during shear, indicating that the redistribution of contact forces plays a larger role than geometric rearrangement in controlling the evolving stress transmission within the granular assembly.

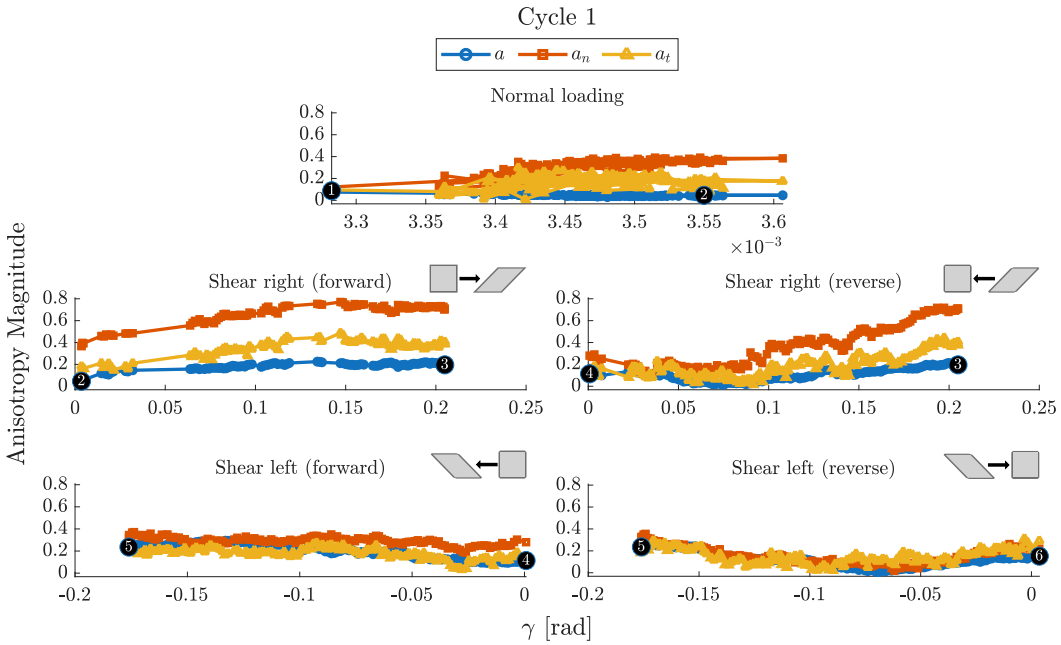


Figure 3.24: Evolution of the fabric anisotropy magnitude, a, mean normal force anisotropy magnitude, a_n, and mean tangential force anisotropy magnitude, a_t, per stage in the loading cycle.

Verification of the Stress-Force-Fabric Relationship The stress-force-fabric (SFF) relationship connects the microstructural fabric and force anisotropy magnitudes to the macroscopic invariant stress ratio through,

$$\frac{\sigma_1 - \sigma_2}{\sigma_1 + \sigma_2} = \frac{\frac{1}{2}(a + a_n + a_t)}{(1 + (aa_n/2))} \tag{3.10}$$

where σ_1 and σ_2 are the major and minor principal stresses, respectively [77]. The left-hand side of Eq. (3.10) is also recognized as q/p, where p is the 2D mean normal stress,

$$p = \frac{\sigma_{11} + \sigma_{22}}{2} = \frac{\sigma_1 - \sigma_2}{2} \,, \tag{3.11}$$

and q is the 2D magnitude of the deviatoric stress,

$$q = \sqrt{\left(\frac{\sigma_{11} - \sigma_{22}}{2}\right)^2 + \sigma_{12}^2} = \frac{\sigma_1 + \sigma_2}{2} \,. \tag{3.12}$$

The ratio q/p is obtained from contact-level data using the Christoffersen equation (Eq. (2.6)) and represents the stress anisotropy within the granular assembly. Since it is composed of the principal stresses, q/p is also invariant under coordinate rotation. This invariant stress ratio should not be confused with the boundary stress ratio, τ/σ_n, which represents the frictional strength of the material. For more clarity, both can be expressed in terms of the internal friction angle of the material, ϕ, as $q/p = \sin\phi$ and $\tau/\sigma_n = \tan\phi$ [78].

Rothenburg and Bathurst simplified the SFF relation (Eq. (3.10)) by neglecting the second-order product in the denominator, $aa_n/2$, after observing from DEM simulations of biaxial compression that this contribution was very small compared to the additive anisotropy terms in the numerator [77]. The resulting simplified stress-force-fabric relation is,

$$\frac{q}{p} = \frac{1}{2}(a + a_n + a_t) \,. \tag{3.13}$$

Figure 3.25 displays the invariant shear stress ratio versus shear strain, where the experimental data are in blue, the full stress-force-fabric results (Eqn. 3.10) are in orange, and the simplified stress-force-fabric results (Eqn. 3.13) are in yellow. During normal loading, the theoretical curves coincide but slightly overpredict the internal stress anisotropy, indicating a small systematic tendency to overpredict q/p. Because the two SFF expressions coincide in this stage, the discrepancy cannot be attributed to the neglected second-order term in the simplified SFF equation.

During shearing, both theoretical equations reproduce the overall petal structure, including the larger shear-right lobe and the smaller shear-left lobe, showing that the anisotropy-based framework captures the primary cyclic trend in the internal stress ratio. However, there are stage-dependent discrepancies. In SRF, both theories overpredict the experimental response, although the full stress-force-fabric expression remains closer to it than the simplified form. In SRR, the two theoretical curves nearly overlap and agree relatively well with the experimental curve, except near the end of the stage. The largest discrepancies occur during the shear-left stages, particularly SLF, where the theory alternates between underpredicting and overpredicting the experimental q/p over much of the stage. These results suggest that anisotropy magnitudes capture the main trends in the evolution of the internal stress state, whereas reversal-related microstructural reorganization and directional effects are not fully accounted for. Moreover, the experimental q/p response appears smoother than the anisotropy-based predictions because q/p is a homogenized macroscopic stress invariant, whereas the theoretical formulations are directly influenced by evolving fabric and contact-force anisotropies that are more sensitive to local microstructural rearrangements during cyclic loading.

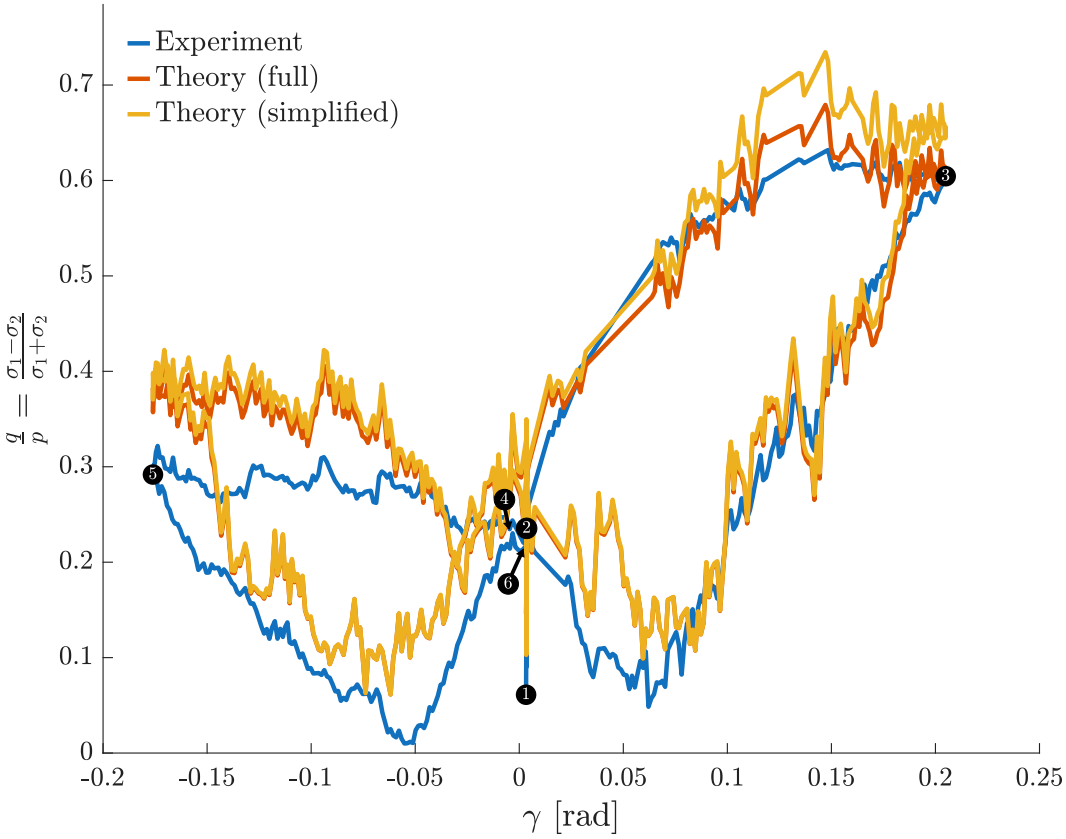


Figure 3.25: Verification of the stress-force-fabric relationship.

We can further examine the effectiveness of the full and simplified stress-force-fabric relationships through scatter plots in which the theoretical prediction is plotted on the x-axis, and the experimental invariant stress ratio, q/p, is plotted on the y-axis, together with a 1:1 reference line (Figure 3.26). Points below the 1:1 line indicate that the experimental q/p is smaller than the theoretical prediction, implying that the theory overpredicts. Conversely, points above the 1:1 line indicate that the experimental q/p exceeds the theoretical prediction, implying that the theory underpredicts.

For both theoretical expressions, most of the data lie between 0.1 and 0.4. Within this dense region, most points lie below the 1:1 line, indicating that both theories generally overpredict the invariant stress ratio. At larger predicted q/p values, roughly 0.4 to 0.75, the data are sparser with most points now lying above the $y = x$ line, indicating a tendency toward underprediction in that regime. Intuitively, this means that at moderate invariant stress ratios, the anisotropy measures predict a stronger internal stress response than is actually mobilized. In contrast, at higher invariant stress ratios, the theory sometimes fails to capture the highest experimentally attained stress states, with the full theory showing only minimal improvement over the simplified theory in this regime. Although the stress-force-fabric relationship is based on monotonic biaxial loading conditions [77], the expressions still perform well for cyclic shear, except when the anisotropy magnitudes are largest or evolving rapidly, such as during the shear-right-forward stage.

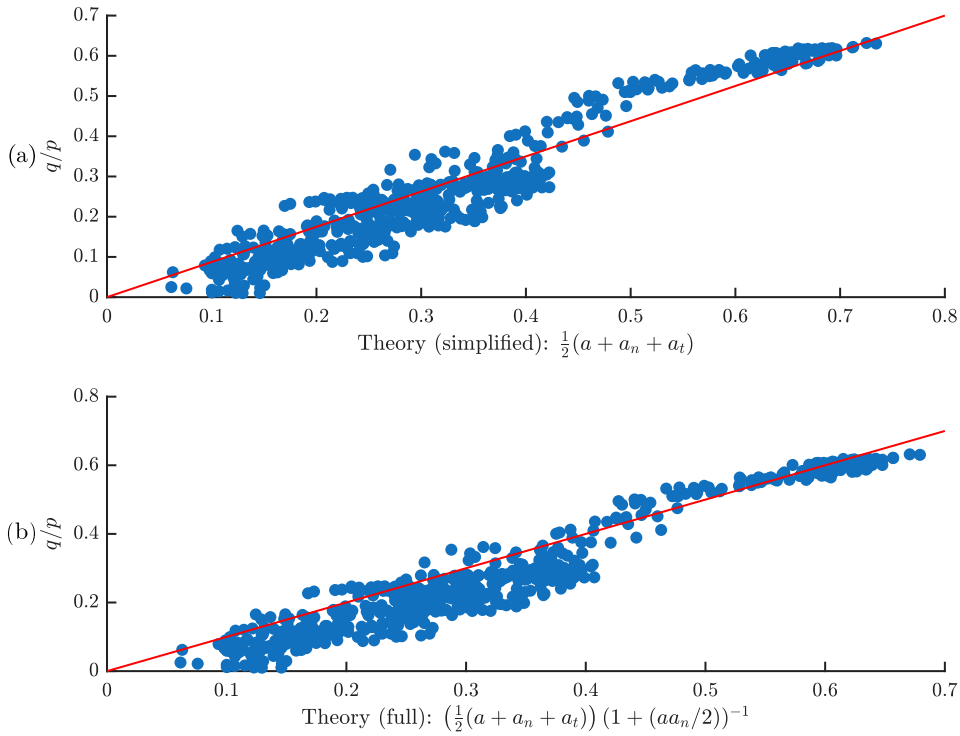


Figure 3.26: Scatter plots comparing the theoretical stress-force-fabric (SFF) relation with the experimental invariant stress ratio, q/p, which indicates internal stress anisotropy. The simplified (a) and full (b) SFF expressions are shown. Points below the red $y = x$ line indicate that the theory overpredicts q/p, and vice versa.

Force Transmission Whereas the stress-force-fabric relation established a micro-to-macro connection between the anisotropy in the contact network and the macroscopic invariant stress ratio, it does not describe how forces are distributed among individual contacts. We can gain further insight into the underlying micromechanics by moving away from averaged quantities (i.e., volume-averaged q/p) and instead examining the statistical distribution of contact forces through probability density functions of the normalized normal and tangential forces, as well as the mobilized friction. Figure 3.27 shows the probability density function (PDF) of the **normal force**, f_n, normalized by the mean normal force, $\langle f_n \rangle$, for each stage in the loading cycle, on a semi-log scale. Contacts with $\frac{f_n}{\langle f_n \rangle} < 1$ are typically associated with weak network forces, while those with $\frac{f_n}{\langle f_n \rangle} > 1$ belong to the strong force network [28].

This distribution reveals two distinct regimes. A very steep decay is observed for very weak forces, approximately $\frac{f_n}{\langle f_n \rangle} \lesssim 0.4$, followed by a more gradual decay for $\frac{f_n}{\langle f_n \rangle} \gtrsim 0.4$. The latter regime spans both moderate and strong forces and follows an

approximately exponential form,

$$P(f_n/< f_n >) \sim \exp\left(-\beta f_n/< f_n >\right) \tag{3.14}$$

where β is a positive constant. The exponential tail is a well-established feature of granular materials and reflects the heterogeneous nature of force transmission [39, 41, 79].

We also observe stage-wise differences. The shear-right-forward (SRF) and shear-left-forward (SLF) stages alternate between higher and lower probabilities in the large force regime, indicating that the distribution of strong forces is not symmetric with respect to the shear direction. This asymmetry reflects path dependence and ongoing reorganization of the force network. The shear-right-reverse (SRR) stage appears to have the most stable behavior (i.e., few large fluctuations), suggesting that the internal structure is more settled, consistent with our observations from the stress-force-fabric relation.

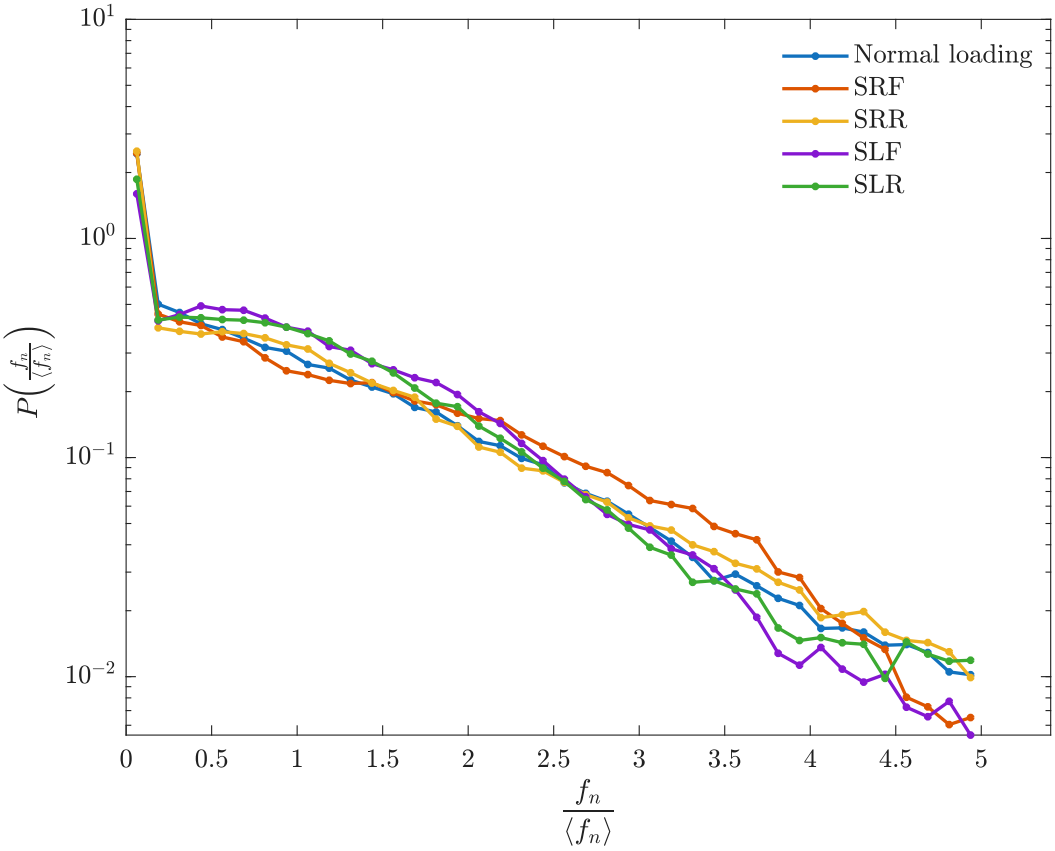


Figure 3.27: Probability density function of the normal force, f_n, normalized by the mean normal force, $\langle f_n \rangle$, for each stage in the loading cycle, on a semi-log scale.

Figure 3.28 shows the PDF of the **tangential force**, $|f_t|$, normalized by the mean normal force for each stage. We observe trends similar to those of the normal force distribution, indicating that shear transmission is strongly coupled to the normal force network. However, the initial slope of the tangential force distribution is much steeper, indicating that most contacts carry very small tangential forces. At higher normalized values, $|f_t|/\langle f_n \rangle \approx 1$, we observe increased variability because a small number of contacts contribute to this regime.

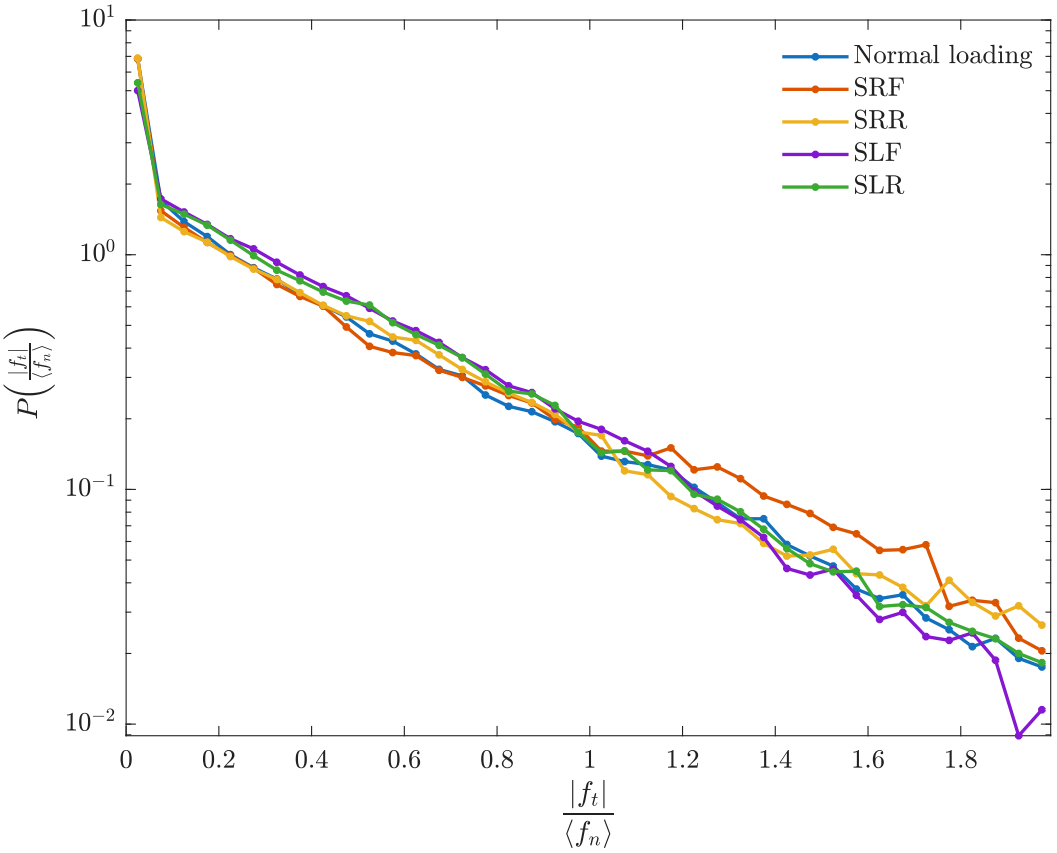


Figure 3.28: Probability density function of the tangential force magnitude, $|f_t|$, normalized by the mean normal force, $\langle f_n \rangle$, for each stage in the loading cycle, on a semi-log scale.

Figure 3.29 shows the PDF of the **mobilized friction**

$$S = |f_t|/\mu f_n \tag{3.15}$$

where μ is the interparticle friction coefficient. This variable reveals how close a contact is to the Coulomb failure criterion (i.e., how much normal stress it can withstand before sliding). Failure occurs when $S = 1$; this is hence the maximum x-limit in the plot. While a small number of contacts exhibit $S > 1$, likely due to

measurement or inversion uncertainty, the vast majority of contacts lie below this limit.

After the initial soft decay, we observe a small peak at low mobilization levels, $S \approx 0.13-0.20$, indicating that most contacts are far from sliding. Beyond this peak, the probability decreases exponentially, showing that highly mobilized contacts are progressively less common. Near $S \approx 1$, we observe a sharp increase, corresponding to contacts approaching the Coulomb limit. These contacts are likely associated with local rearrangements and force chain restructuring events.

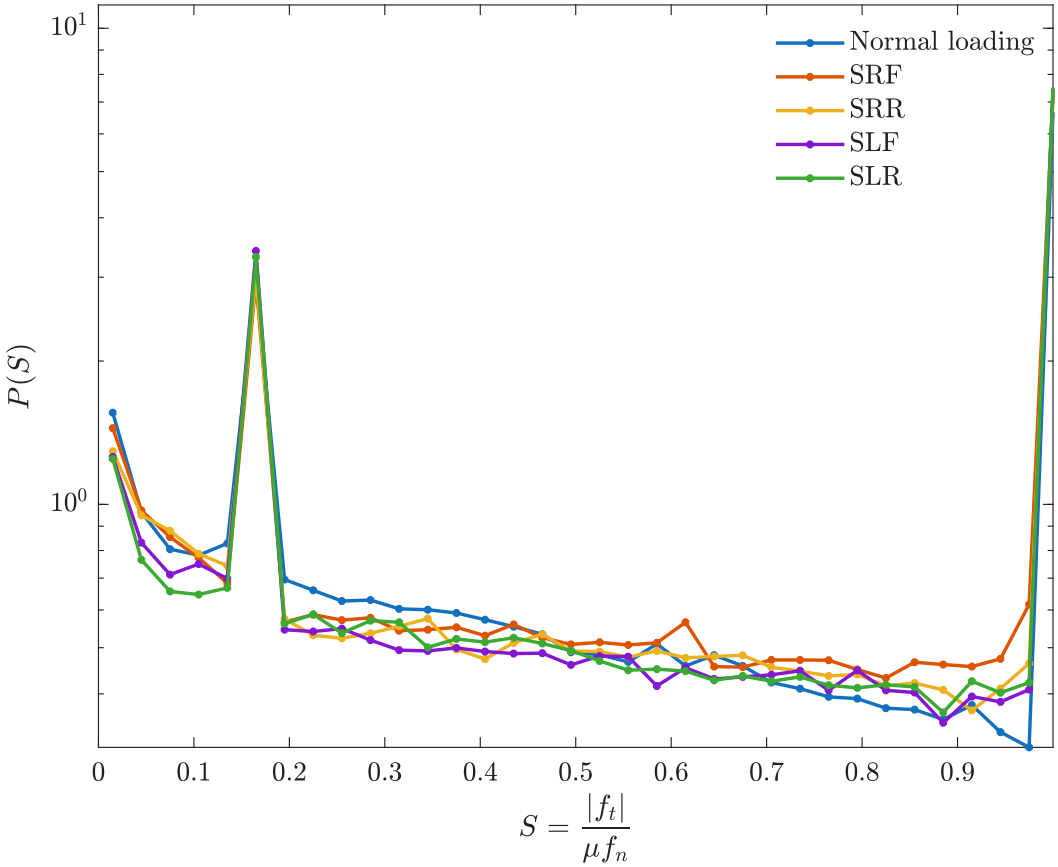


Figure 3.29: Probability density function of the mobilized friction, $S = |f_t|/\mu f_n$, where μ is the interparticle friction coefficient. This variable reveals how close a contact is to sliding (Coulomb failure criterion).

In summary, the PDFs of the normalized normal and tangential contact forces exhibit strong heterogeneity in force transmission, characterized by exponential tails, indicating that a small number of contacts carry forces significantly larger than the mean. This explains why force chains appear as sparse, high-force structures: they correspond to the exponential tail of the force distribution rather than the bulk of contacts.

The mobilized friction distribution further shows that most contacts remain far from sliding, with a smaller subset approaching the Coulomb limit, providing a mechanism for intermittent rearrangement of the force network. These highly mobilized contacts are likely involved in the formation, breakage, and reorientation of force chains observed in the previous sections.

Stage-dependent variations in all three distributions highlight the path-dependent evolution of the contact force network during cyclic shear. In particular, the asymmetry between forward and reverse stages indicates that the force chain structure retains memory of prior loading, leading to directional differences in force transmission and network organization.

3.3.2.5 Grain-Scale Response Summary

Overall, the grain-scale response shows that while the granular assembly maintains a nearly constant level of global connectivity during cyclic shear, its internal structure and force transmission pathways undergo continuous, path-dependent reorganization. The coordination number remains relatively constant, indicating that the total number of contacts is largely preserved. However, the force chain network — which represents the load-bearing subset of contacts – shows significant variability, especially near shear reversals, where existing chains break down and reform in response to changes in the loading direction.

Forward shearing stages, particularly shear-right-forward (SRF), promote the formation of longer, more persistent force chain structures, as evidenced by higher total chain lengths (in terms of the number of grains), larger accumulated network content, and greater participation within the force chain network. Conversely, reverse stages feature decreased chain persistence and more fluctuations, indicating repeated disruption and reorganization of the force chain structure. Although a relatively stable proportion of grains participate in the strong-force network, the way these grains form cohesive force chains depends heavily on the loading direction and deformation history.

This structural evolution is closely tied to the development of anisotropy. Force anisotropy dominates over fabric anisotropy, indicating that changes in force magnitude and direction play a greater role than purely geometric rearrangement in governing stress transmission. The highest anisotropy levels occur during forward shear stages, whereas shear reversals induce a misalignment between the anisotropy and principal stress directions, highlighting temporary restructuring of the contact

network. We analyzed how effectively the stress-force-fabric equation links the anisotropy magnitudes to the invariant stress ratio at the macroscale. We found that it captures the overall cyclic trends in stress evolution, with discrepancies only during periods of rapid structural reorganization or high anisotropy.

At the contact level, force transmission remains highly heterogeneous, with a small subset of contacts bearing disproportionately large forces, as shown by exponential force distributions. Most contacts remain well below the sliding threshold, while a smaller number approach the Coulomb limit, thereby allowing intermittent rearrangement of the force network. The observed asymmetry between forward and reverse stages, across both structural and force-based measures, demonstrates that the granular system retains memory of previous loading, leading to a direction-dependent evolution of force chains and stress transmission pathways.

3.4 Summary

In this chapter, we showed that the response of a granular assembly subjected to a single cycle of simple shear is direction- and history-dependent, governed by the evolving contact network, force chains, and anisotropy. At the macroscale, measured quantities exhibit clear asymmetry between forward and reverse shear, along with incomplete recovery of stress and packing state after one cycle. Despite this irreversibility, the net volumetric strain over the full cycle remains negligible, indicating that substantial internal rearrangements can occur without a significant change in bulk volume.

The grain-scale analysis reveals that this macroscopic behavior arises from the continuous reorganization of the force chain network, rather than from changes in contact connectivity. During periods when the coordination number remains nearly constant, force chains exhibit strong path dependence: forward shear promotes the formation of longer, more persistent structures, whereas reversals cause force chains to break down and reform in the new direction. This cyclic restructuring governs how forces are transmitted throughout the assembly, thereby directly contributing to the observed macroscale asymmetry.

The evolution of anisotropy further highlights the dominance of force transmission over purely geometric effects. Force anisotropy consistently exceeds fabric anisotropy and plays a major role in controlling macroscopic stress response. During shear reversals, temporary misalignment between the anisotropy and principal stress directions reflects rapid internal restructuring and is also associated with increased

fluctuations in the macroscopic measures. The stress-force-fabric relationship captures the overall cyclic trends, but deviates when the assembly rapidly reorganizes, emphasizing the transient nature of the underlying grain-scale mechanisms.

At the contact scale, force transmission remains highly heterogeneous, with a small subset of contacts carrying the majority of the load. These strong contacts form and dissolve directionally, enabling intermittent rearrangement while preserving overall connectivity. This behavior indicates that memory in granular systems is encoded not in the number of contacts but in the organization and persistence of force chains.

Chapter 4

MULTISCALE RESPONSE OF GRANULAR MATERIALS UNDER CYCLIC SIMPLE SHEAR: EFFECTS OF PACKING STATE AND CONFINEMENT

4.1 Introduction

The previous chapter (Chapter 3) examined the response of a granular assembly subjected to a single cycle of simple shear and showed that even one loading cycle produces strongly direction- and history-dependent behavior. Macroscopic irreversibility was linked to the continual reorganization of the internal force network, while grain-scale analyses demonstrated that force transmission, anisotropy, and force chain restructuring govern how shear resistance is mobilized and lost during loading reversals. In particular, this baseline experiment showed that cyclic memory is encoded primarily in the evolving force chain and anisotropic contact structure rather than in the total contact count.

While those results established the fundamental mechanisms at work in a single cycle, they also raise a broader question: how do these same mechanisms evolve when shearing is repeated? A single cycle reveals the onset of structural adaptation. However, it cannot determine whether the contact network progressively stabilizes, whether force chains degrade or strengthen with continued loading, or whether anisotropic structures persist, weaken, or reorganize into new recurrent states. Repeated cyclic loading introduces the possibility of cumulative conditioning, structural fatigue, densification, and evolving stress-transmission efficiency that cannot be resolved from a single-cycle experiment alone.

A second unresolved question concerns the role of the initial state and confinement. The baseline experiment demonstrated how a single granular assembly responds under a fixed packing condition and a normal load, but granular mechanics has long shown that density and confinement can fundamentally alter contact stability, dilatancy, and force-chain development [71, 72]. Dense and loose packings may therefore respond through different grain-scale pathways, while changes in applied normal stress may modify the persistence and intensity of those pathways. Understanding these influences requires a broader experimental matrix than the baseline one-cycle, simple-shear experiment.

Accordingly, this chapter extends the analysis from one cycle to four three-cycle cyclic simple shear experiments spanning two initial packing states (dense and loose) and two levels of applied normal stress. By comparing both the macroscopic and grain-scale responses across these experiments, the chapter seeks to identify which features of cyclic behavior are universal, which depend primarily on packing state, and which are controlled by confinement. In doing so, it builds directly on the mechanistic framework established in the previous chapter and uses repeated cyclic loading to reveal how granular assemblies accumulate history, reorganize internal structure, and evolve under sustained cyclic shear.

The first two experiments involve densely packed granular assemblies subjected to normal stresses of $\sigma_n = -44.1$ kPa (122 lb load) and $\sigma_n = -29.6$ kPa (82 lb load), respectively. The remaining two experiments follow the same loading conditions but with initially loose packings. The dense granular assemblies contain 332 grains (272 interior and 60 boundary-layer grains), while the loose granular assemblies contain 318 grains (258 interior and 60 boundary-layer grains). Only the interior grains are used in the digital image correlation (DIC) and granular element method (GEM) analyses. The initial void ratios are 0.260 (122 lb) and 0.247 (82 lb) for the densely packed experiments, and 0.280 (122 lb) and 0.287 (82 lb) for the loosely packed experiments, reflecting the higher void content of the loose configurations within the same shear volume.

For each experiment, the macroscopic response is evaluated through the evolution of the stress ratio, μ, volumetric strain, ϵ_v, void ratio, e, and dilatancy, β. These measures collectively describe shear resistance, volume change, packing state, and shear-volume coupling under cyclic loading. The macroscopic results reveal how the granular assembly responds to repeated shear, including the development of hysteresis, directional asymmetry, and cycle-dependent behavior.

Following the macroscopic analysis, the grain-scale response is examined to identify the internal mechanisms responsible for these behaviors. In particular, we analyze the evolution of force chains, contact topology, and stress-force-fabric relationships. These grain-scale metrics provide insight into how load is transmitted, how contact networks reorganize during shear reversal, and how particle-level structural evolution gives rise to the observed macroscopic response.

4.2 Experiment # 1: Densely Packed, $\sigma_n = -44.1$ kPa

The first experiment is of a densely packed granular assembly, normally loaded by $\sigma_n = -44.1$ kPa, corresponding to 122 lb (55.3 kg). The dense granular assembly consists of 332 grains total, 60 of which are the boundary PTFE particles that do not contribute to the DIC or GEM analysis. The initial void ratio for the granular assembly is 0.260.

4.2.1 Macroscopic Response

Figure 4.1 shows the macroscopic response of the three-cycle, densely packed experiment under $\sigma_n = -44.1$ kPa. As in Chapter 3, this response is evaluated through the stress ratio, μ, volumetric strain, ϵ_V, void ratio, e, and dilatancy, β, which characterize the assembly's shear resistance, volume change, packing state, and shear-volume coupling under cyclic loading.

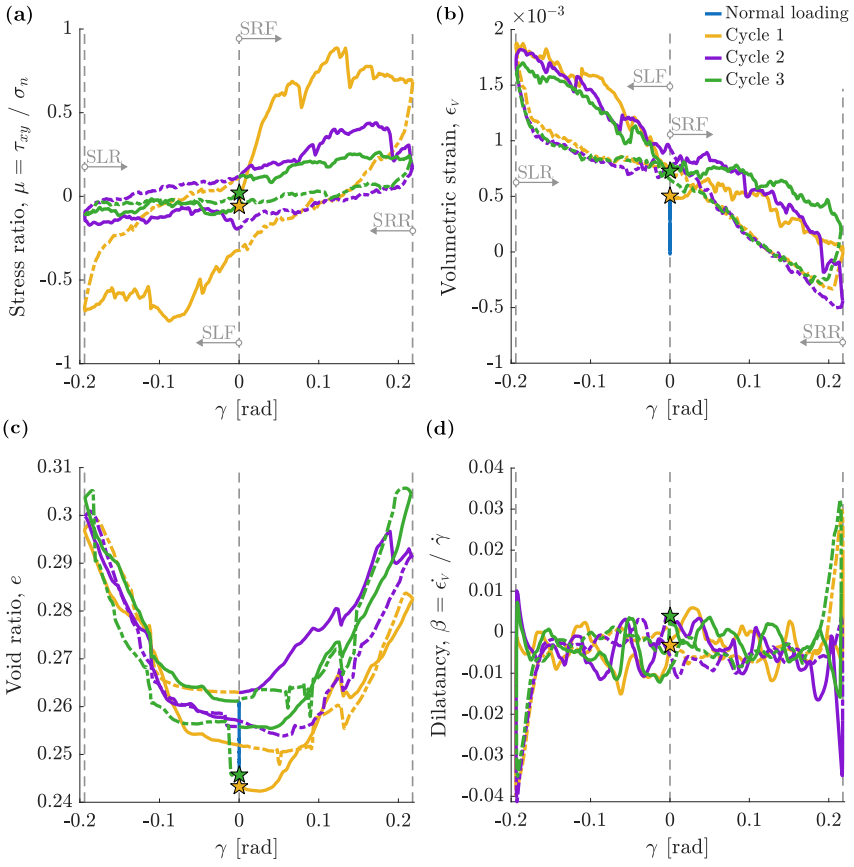


Figure 4.1: Macroscopic response of the three-cycle, densely packed granular assembly under $\sigma_n = -44.1$ kPa: (a) stress ratio, μ; (b) volumetric strain, ϵ_V; (c) void ratio, e; and (d) dilatancy, β, versus shear strain, γ. Solid curves denote forward shearing (SRF, SRR), dash-dotted curves denote reverse shearing (SLF, SLR), and gray vertical dashed lines indicate stage transitions. Yellow and green stars mark the start and end of cyclic loading, respectively.

4.2.1.1 Stress Ratio

Figure 4.1a shows the evolution of the stress ratio, $\mu = \tau_{xy}/\sigma_n$, which reflects the mobilized shear resistance. Two main trends are apparent across all three cycles: (1) the magnitudes of the positive and negative stress ratio peaks decrease with increasing cycle number, and (2) the response remains directionally asymmetrical, with consistently broader shear-right branches than shear-left branches.

The reduction in both μ_{max} and μ_{min} with continued cycling indicates that the granular assembly progressively mobilizes less shear resistance as deformation accumulates. This suggests that repeated shearing weakens or reorganizes the internal load-bearing structure, reducing the granular assembly's ability to sustain large shear stresses in either direction.

As in the one-cycle baseline experiment (Figure 3.9a), the shear-right branches remain broader and more developed than the shear-left branches, indicating that the material response depends not only on the current loading direction, but also on the deformation history. This continued asymmetry across all three cycles suggests that structural memory is retained even as the assembly evolves under cyclic loading.

Another notable feature is the pronounced fluctuation in μ near the end of the shear-right-forward (SRF) stage during cycles 1 and 2. This same fluctuation was also observed in the baseline experiment and likely reflects a major internal restructuring event, such as a sudden rearrangement of contacts or rapid reorganization of the force-transmitting network. In contrast, during cycle 3, the SRF branch becomes much smoother, with μ remaining nearly constant at approximately 0.23 throughout most of the stage. This suggests that by the third cycle, the assembly has transitioned toward a more stable and repeatable response during forward-right shearing.

The reverse-shear response also changes with increasing cycle number. In cycles 1 and 2, the forward and reverse paths remain distinct for both the shear-right and shear-left branches. By cycle 3, the shear-left-forward (SLF) and shear-left-reverse (SLR) paths largely overlap. In addition, the shear-left branch remains close to zero (≈ -0.05). Together, these features suggest that repeated cyclic shearing progressively reorganizes the internal contact network into a directionally-biased load-bearing structure, such that shear resistance is more readily mobilized in the rightward direction than in the leftward direction. Similar links between shear-induced anisotropy, force transmission, and loading-history dependent behavior have been reported in prior granular mechanics studies [10, 39].

4.2.1.2 Volumetric Strain

Figure 4.1b shows the volumetric strain, ϵ_V, which captures the bulk contraction or dilation of the assembly during shearing. Overall, the volumetric response indicates that the granular assembly accommodates cyclic shear through a combination of continued densification, intermittent dilation, and repeated internal restructuring. Although dilation becomes increasingly important during shearing, volumetric compression continues to play an important role throughout the cyclic response.

Following substantial densification during normal loading, cycle 1 initially continues to compress at the onset of SRF, then transitions to gradual dilation. This suggests that the assembly first undergoes additional packing adjustment as particles settle into more stable configurations under the onset of shear. In contrast, cycles 2 and 3 bypass this initial compressive regime and instead dilate immediately after SRF, indicating that the assembly has already been sufficiently restructured by the first cycle such that continued shearing does not promote expansion but rather further compaction.

Among all cycles, cycle 2 exhibits the largest volumetric change during SRF, beginning at the highest ϵ_V and ending at the lowest ϵ_V. Thus, the second cycle involves the strongest volumetric accommodation, likely reflecting substantial internal rearrangement as the assembly continues to evolve away from its initially prepared state. By the third cycle, the SRF response remains strongly dilative, and ϵ_V stays higher than in cycle 1, indicating that continued shearing increasingly requires volumetric expansion of the packing.

As in the baseline experiment, all cycles exhibit rapid decreases in ϵ_V immediately after shear reversal, followed by smoother evolution as the deformation continues. These abrupt drops likely correspond to transient restructuring events in which the previously established contact network becomes incompatible with the reversed loading direction and must reorganize into a new load-bearing configuration. Compared to the baseline response, cycle 2 also exhibits two pronounced rapid dilation events prior to reversal, suggesting that significant internal restructuring may also occur as the assembly approaches mechanically transitional states near reversal.

The hysteretic nature of the volumetric response is further reflected in the self-intersecting forward and reverse paths observed in all three cycles. These intersections indicate that the volumetric state depends not only on the current shear strain, but also on the loading direction and prior deformation history. In addition,

the leftward and rightward branches differ in shape, confirming that the assembly accommodates shear-induced volume change asymmetrically with respect to the loading direction.

Another important asymmetry is that the magnitude of compaction consistently exceeds that of dilation in all cycles. This indicates that although dilation is repeatedly mobilized during shearing, it is never sufficient to offset the total compaction accumulated throughout the loading history. Together, these features suggest that the dense granular assembly evolves towards a strongly path-dependent volumetric response characterized by repeated internal restructuring, directional asymmetry, and a persistent bias toward densification.

4.2.1.3 Dilatancy

Figure 4.1d shows the dilatancy, β, as a function of shear strain, γ. As in the baseline experiment, β is defined with respect to γ, so its sign depends on the shearing direction. Therefore, contraction and dilation are interpreted in conjunction with the evolution of ϵ_v, rather than from the sign of β alone. In this sense, β is most useful for identifying how strongly shear deformation is coupled to volume change throughout the loading cycle. Peaks and extrema in β correspond to periods of intensified internal rearrangement, while smoother near-constant regions indicate more stable deformation. Because $\dot{\gamma} \approx 0$ at shear reversal, the response appears as near-vertical segments at those transition points. To better visualize the evolution, Figure 4.2 shows the dilatancy response separated by shear stage.

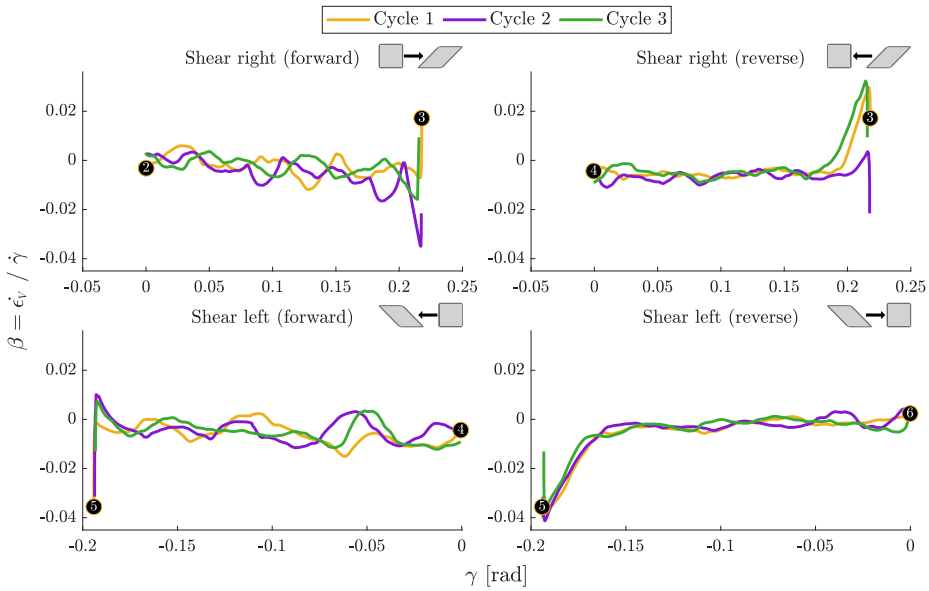


Figure 4.2: Dilatancy evolution per stage for the three-cycle, densely packed granular assembly under $\sigma_n = -44.1$ kPa. Stage markers are shown only for Cycle 1.

Overall, the dilatancy response indicates that the coupling between shear and volumetric deformation is highly stage-dependent and remains directionally asymmetric in all three cycles. One consistent feature is that the reverse-shear stages exhibit noticeably less fluctuation and variability than the forward-shear stages. This smoother reverse-stage behavior corresponds to the near-linear segments observed in the ϵ_V response, suggesting that once the assembly has adjusted to the reversed loading direction, deformation proceeds through a more stable and repeatable volumetric response. In contrast, the stronger fluctuations during forward-shear stages indicate that those stages involve more intermittent internal restructuring and less uniform volumetric accommodation.

Near the end of shear-right-forward (SRF), all three cycles exhibit a pronounced change in β, coinciding with the increasingly dilative behavior observed in ϵ_V. This trend is especially pronounced in cycles 2 and 3, both of which reach a clear minimum, whereas cycle 1 exhibits a comparatively weak response. These extrema suggest that cycles 2 and 3 exhibit substantially stronger shear-volume coupling during forward right-shearing, likely reflecting more intense internal rearrangement as the assembly continues to evolve under repeated loading. The strong β response near the end of SRF is also consistent with earlier-observed fluctuations in the stress ratio, further indicating that this stage is associated with major structural adjustment of the load-bearing contact network.

Immediately after reversal into the shear-right-reverse (SRR) stage, β changes rapidly before transitioning to a smoother, near-steady regime. When interpreted together with ϵ_V, this behavior suggests that the assembly first undergoes a short-lived volumetric adjustment as the previously established contact network becomes incompatible with the reversed loading direction, after which the assembly gradually settles into a more stable deformation mode. Among the three cycles, cycle 2 reaches this stabilized regime the quickest, indicating that the internal structure adjusts more efficiently to the reversal of rightward loading in that cycle.

A similar but opposite trend occurs in the leftward branch. Near the end of shear-left-forward (SLF), all three cycles exhibit a strong β response that coincides with the contractive behavior observed in ϵ_V. Again, later cycles exhibit the strongest extrema, while cycle 1 exhibits a comparatively weak response. Shortly after reversal into the shear-left-reverse (SLR) stage, β again changes rapidly before approaching a weaker and more stable regime, indicating that the assembly undergoes another short-lived restructuring event before re-establishing a more uniform mode of deformation.

Compared to the baseline one-cycle experiment, the present three-cycle response shows that the strongest dilatancy events are redistributed across different stages of the loading cycle. In the baseline, densely packed assembly, both the maximum and minimum β values occurred during the shear-left stages, whereas here the largest extrema occur in later cycles and in different parts of the cycle. This suggests that repeated cyclic loading progressively changes not only the magnitude of shear-volume coupling but also the timing at which that coupling is most strongly activated.

Another important feature is the overall shift in the cycle-scale β response. In the baseline experiment, β began at a small positive value and ended at a larger negative value after one cycle. In contrast, in the present three-cycle experiment, β begins at a small negative value and ends at a small positive value by the end of the third cycle. This shift suggests that repeated cyclic loading alters the balance between contraction- and dilation-dominated deformation throughout the loading history, further supporting the interpretation that the granular assembly evolves toward a reconditioned, history-dependent deformation state.

Finally, when interpreted together with the volumetric strain and stress ratio responses, the strongest β extrema coincide with periods of pronounced volumetric adjustment and changes in shear resistance. This is consistent with the well-established link between dilation, internal rearrangement, and friction mobilization in dense granular materials [31, 71, 72]. In this sense, the dilatancy response provides further evidence that the dense assembly does not simply repeat the same deformation mode from cycle to cycle, but instead progressively evolves in how it couples shear resistance with volumetric response.

4.2.1.4 Void Ratio

Figure 4.1c shows the void ratio, e, which provides a measure of the evolving packing state. Overall, the void ratio indicates that cyclic shearing produces a repeatable yet history-dependent opening and closing of the packing structure, with partial recovery at each cycle but no complete return to the initial state.

Across all cycles, the forward shearing stages are generally associated with a gradual increase in the void ratio, whereas the reverse shearing stages exhibit a gradual decrease. These trends are consistent with the dilation and contraction patterns observed in the volumetric strain response, indicating that the assembly systematically opens during forward shearing and closes during reverse shearing.

A notable feature of the response is that the maximum void ratio for each cycle occurs immediately after shear reversal. This brief increase in e suggests a transient opening of the packing as the previously established contact network becomes mechanically incompatible with the reversed loading direction and must reorganize to support the new shear direction. The fact that these peak void ratio values increase with cycle number indicates that the assembly reaches progressively looser states at reversal as cyclic loading proceeds. By cycle 3, the largest void volumes occur at the onset of shear-right-reverse (SRR) and shear-left-reverse (SLR). This behavior is consistent with the well-known tendency of dense granular materials to expand when sheared [31].

As in the baseline experiment, all three cycles also exhibit a near-constant void ratio toward the end of SRR and into SLF. This suggests a quasi-steady deformation regime in which grain rearrangements continue to accommodate shear without producing substantial net changes in the packing density. Mechanistically, this implies that local dilation and contraction occur in balance, allowing deformation to proceed while maintaining an approximately steady bulk packing state for part of the cycle.

The void ratio response also exhibits clear directional asymmetry and hysteresis. All three cycles show self-intersecting leftward and rightward branches, indicating that the packing state depends not only on the current shear strain but also on the loading path used to reach it. Among the three cycles, cycle 2 exhibits the largest variation in the branch shape, with a broad shear-right loop and an almost collapsed shear-left loop. This suggests that during cycle 2, the packing response is far less reversible in the rightward direction than in the leftward direction, highlighting a strong directional bias in the assembly's structural evolution.

Despite these stage-wise fluctuations, the granular assembly nearly recovers its initial packing state by the end of the third cycle. The final void ratio is only slightly greater than the value at the start of cycle 1, indicating that most of the opening and closing of the packing structure over the loading history is recoverable at the cycle scale. However, the small positive offset in the final void ratio (+0.0024) also indicates that the recovery is incomplete and that the assembly evolves toward a slightly looser terminal configuration than its initial configuration. This same behavior was also observed in the baseline one-cycle dense experiment under the same normal load, suggesting that this residual loosening is a persistent feature of the dense response rather than a consequence of the cycle count alone.

Taken together, these features suggest that cyclic shearing drives repeated but incomplete restructuring of the packing state, such that the assembly repeatedly opens and closes in a directionally dependent manner while gradually evolving toward a slightly altered final configuration.

4.2.1.5 Macroscopic Response Summary

Altogether, the macroscopic response of the three-cycle, densely packed granular assembly under $\sigma_n = -44.1$ kPa (approximately 122 lb or 55.3 kg) indicates that repeated cyclic shearing progressively reconditions the assembly rather than reproducing the same response each cycle. The stress ratio shows reduced shear resistance with increasing cycle count, while persistent asymmetry between the shear-right and shear-left branches indicates that the response remains strongly direction-dependent throughout loading. The volumetric strain and dilatancy responses further show that deformation is accommodated through repeated contraction, dilation, and abrupt internal restructuring, particularly near shear reversals and toward the ends of forward-shearing stages. Although much of the cyclic opening and closing of the packing structure is recoverable over a full cycle, the small residual increase in final void ratio indicates that the assembly does not fully return to its initial state. Overall, repeated cyclic loading drives the dense granular assembly toward a more history-dependent and anisotropic mechanical state, in which shear resistance, volume change, and packing evolution become increasingly conditioned by prior deformation. The following section examines the grain-scale evolution of force chains, anisotropy, and stress transmission underlying this macroscopic behavior.

4.2.2 Grain-scale Response

The macroscale trends (Figure 4.1) suggest an evolving internal structure; we now examine that structure in depth.

4.2.2.1 Coordination Number

The coordination number, Z_c, defined as the average number of contacts per grain, tracks the evolution of the underlying contact network (capturing both strong and weak contacts). Variations in Z_c, therefore, indicate periods of contact creation and loss, offering information on how the granular structure reorganizes during shear, particularly near stage transitions and shear reversals. Figure 4.3 shows the coordination number as a function of shear strain. To better visualize the evolution, Figure 4.4 shows the Z_c response separated by shear stage.

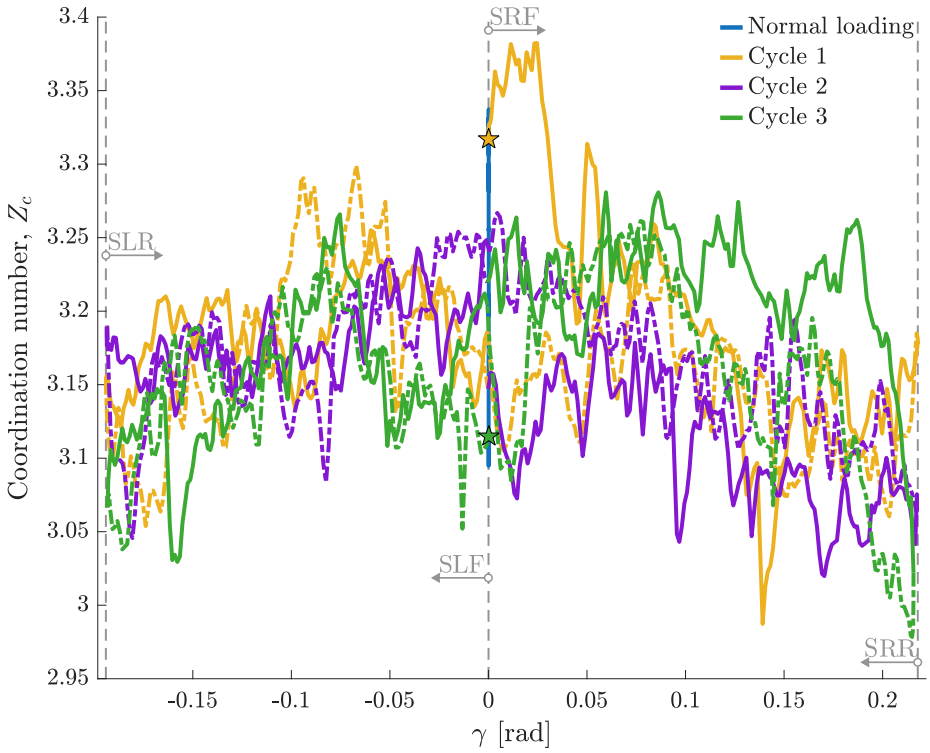


Figure 4.3: Evolution of the coordination number, Z_c, for the dense granular assembly ($\sigma_n = -44.1$ kPa). Z_c is the average number of contacts per particle. Curve style indicates shearing direction (solid: forward, dash-dotted: reverse), gray dashed lines mark stage transitions, and stars mark the start (yellow) and end (green) of cyclic loading.

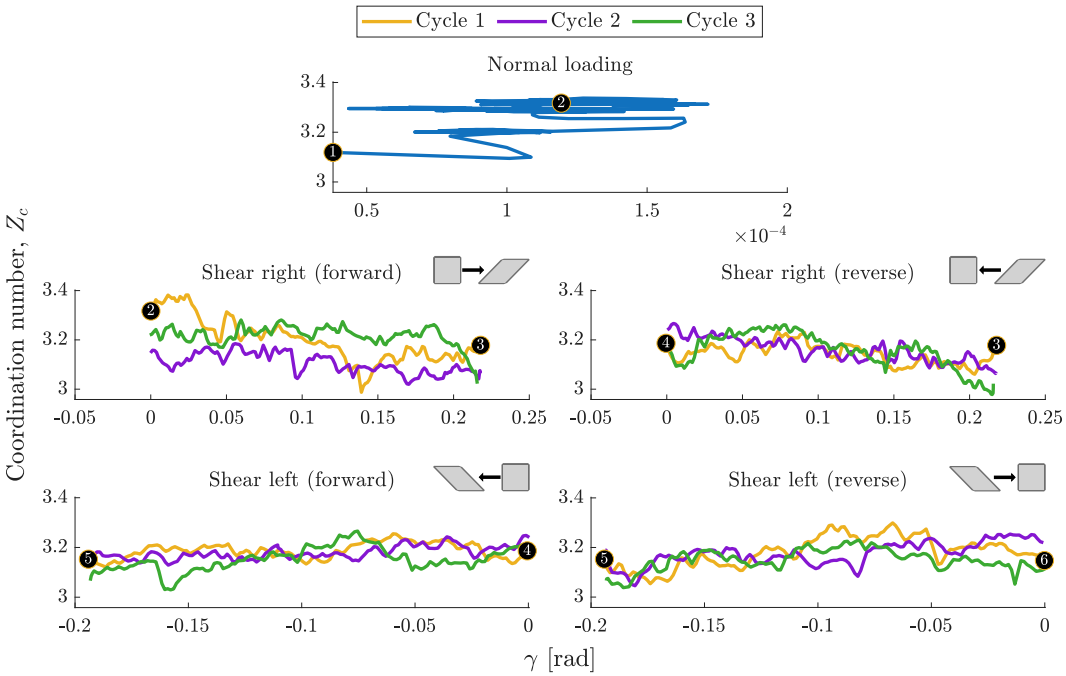


Figure 4.4: Per-stage evolution of the coordination number, Z_c, for the dense granular assembly ($\sigma_n = -44.1$ kPa). Stage markers are shown only for Cycle 1.

As in the baseline one-cycle dense experiment under the same applied normal load, the coordination number increases during normal loading due to contact creation from void collapse under compressive loading. This increase is modest ($\approx$ 3.11 to 3.31) and non-monotonic, reflecting local rearrangements as grains transition toward mechanically stable configurations.

During shear-right-forward (SRF), all cycles exhibit a gradual reduction in Z_c, indicating progressive contact loss as the granular assembly dilates and the contact network reorganizes to accommodate shear. Cycle 1 exhibits the largest fluctuations, including pronounced drops associated with intermittent contact breakage during internal restructuring. In contrast, cycles 2 and 3 evolve more smoothly, suggesting that prior loading history conditions the contact network and lead to more controlled reorganization. The behavior of the first cycle is consistent with that of the baseline experiment, where it also accommodates the largest rearrangements during SRF.

In the shear-right-reverse (SRR) stage, the existing contact network destabilizes and reconfigures to align with the new shear direction. In cycles 1 and 3, this behavior is seen as a net loss in contacts—gradual in cycle 1 and abrupt in cycle 3. In contrast, cycle 2 initially exhibits a transient increase in Z_c, reflecting rapid contact formation, followed by a quasi-steady regime. Hence, cycle 2 promotes a more adaptable network capable of reorganizing without large-scale contact loss.

During shear-left-forward (SLF), all cycles exhibit an overall decrease in Z_c, in contrast to the baseline experiment, where contact formation is instead observed. This suggests that, after multiple cycles, the assembly requires less contact creation to accommodate the new loading direction, consistent with a progressively conditioned structure. Cycle 3 exhibits intermittent bursts of contact formation and loss, reflecting localized rearrangement events, while cycles 1 and 2 evolve more steadily. In particular, cycle 1 shows a stepwise reduction in contacts, indicating incremental restructuring rather than large-scale reorganization.

In the shear-left-reverse (SLR) stage, cycles 1 and 3 follow the baseline experiment trend of an initial drop in Z_c, followed by partial recovery, and ending with a gradual decline; this behavior is consistent with contact disruption followed by partial reformation under reversed shear. In contrast, cycle 2 deviates from this trend, instead showing a net increase in coordination number after the initial recovery, suggesting enhanced contact stabilization.

Across all cycles, both the maximum and minimum coordination numbers occur during SRF in cycle 1, indicating that the most significant contact network restructuring occurs during the initial shear stage. Unlike the baseline experiment, where the extrema occur in different stages, this reflects a front-loaded structural adjustment under repeated loading. Moreover, as in the baseline experiment, the net change in Z_c from the onset to the end of cyclic shear is negative. Hence, the granular assembly experiences cumulative contact loss over cyclic shear, with substantially greater degradation than in the single-cycle case (-0.212 versus -0.003). This highlights the progressive reduction in contact connectivity with repeated cycling under the same applied normal load.

Overall, the coordination number response is strongly history-dependent, with distinct contact evolution under forward and reverse shearing. All cycles exhibit self-intersecting paths, indicating that similar coordination states can be reached through different loading histories. Hence, this demonstrates that the coordination number alone does not uniquely define the internal state of the granular assembly.

4.2.2.2 Force Chain Statistics and Evolution

Although the coordination number provides insight into how the underlying contact network evolves, this section examines how a subset of strong contacts transmits stress through an evolving force chain network. These force chains support the bulk granular medium and allow it to withstand shear stresses [28, 73].

Force chains were identified using the detection procedure introduced in Chapter 3, Section 3.3.2.1, with the same angle $\alpha = 30^\circ$ (for the force chain quasi-linearity metric) and strong-network criteria applied here for consistency. Therefore, we begin the discussion below on the response of the detected force chains.

Number of Detected Force Chains The number of detected force chains as a function of shear strain, γ, is shown in Figure 4.5, and the associated evolution per stage is shown in Figure 4.6. As in the baseline one-cycle experiment, this measure reflects the extent to which the force-bearing skeleton continuously reorganizes during cyclic loading. In general, an increase in the number of detected force chains corresponds to fragmentation of the strong network into shorter load-bearing segments, whereas a decrease indicates coalescence into fewer, more dominant chains.

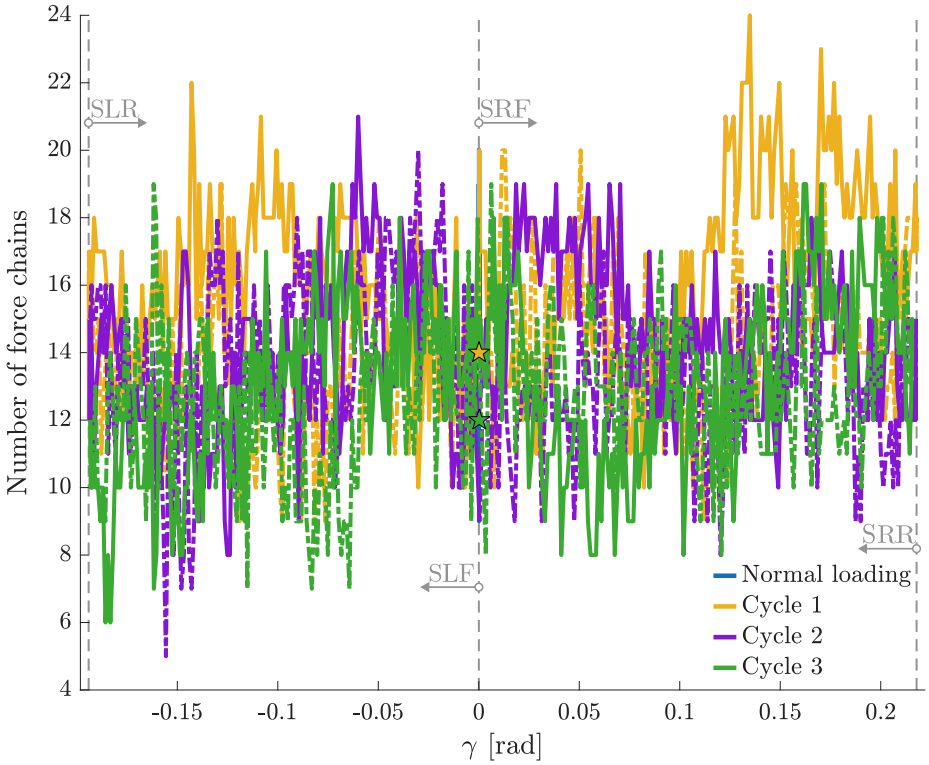


Figure 4.5: Evolution of the detected number of force chains, for the dense granular assembly ($\sigma_n = -44.1$ kPa). Curve style indicates shearing direction (solid: forward, dash-dotted: reverse), gray dashed lines mark stage transitions, and stars mark the start (yellow) and end (green) of cyclic loading.

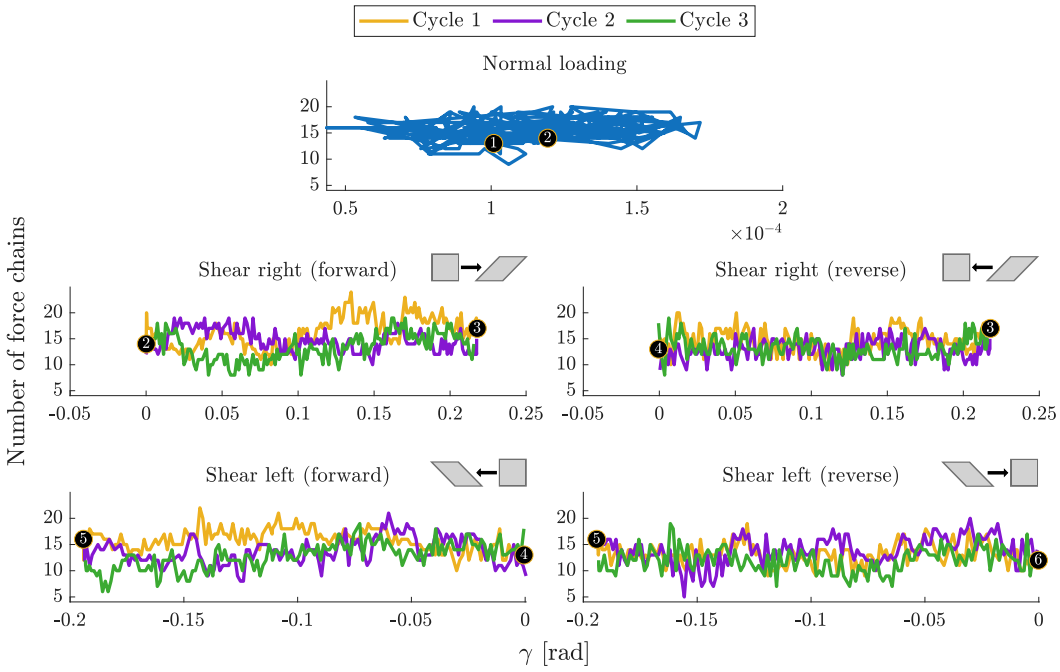


Figure 4.6: Per-stage evolution of the detected number of force chains for the dense granular assembly ($\sigma_n = -44.1$ kPa). Stage markers are shown only for Cycle 1.

During normal loading, the number of detected force chains varies significantly ($\approx 19 - 20$), with a mean value of approximately 16. This variability is consistent with the incremental application of the normal load, during which force chains repeatedly relax, collapse, and reform as the assembly adjusts to each incremental load.

Compared to the baseline one-cycle, densely packed, 122 lb normally loaded experiment, the forward shearing stages exhibit a more irregular, cycle-dependent evolution. During the shear-right-forward (SRF) stage, the baseline initially increased and then stabilized, whereas the three-cycle response shows greater divergence across cycles. Cycle 2 also begins with an increase, but over a shorter strain interval, indicating rapid fragmentation of the strong network. In contrast, cycles 1 and 3 initially lose force chains before gradually reforming them, suggesting early breakdown followed by progressive reorganization. Similarly, during the shear-right-forward (SRF) stage, whereas the baseline experiment exhibited a brief increase followed by stabilization and gradual decline, the three-cycle response remains more internally structured, with cycles 1 and 2 showing extended quasi-steady regimes and cycle 3 exhibiting more late-stage breakdown and reformation fluctuations. Together, these forward stages indicate that repeated cyclic loading does not produce a smoother force chain response, but rather a more history-dependent competition between fragmentation and re-coalescence.

The reverse shearing stages are comparatively more grouped. At the beginning of the shear-right-reverse (SRR) stage, the baseline exhibited a non-monotonic decrease associated with the reorientation of the strong network towards the reversed shear direction. Similarly, in the three-cycle experiment, cycles 1 and 2 also trend downward throughout the stage. The third cycle is the exception, ending with more force chains than it began with. Likewise, during the shear-left-reverse (SLR) stage, all cycles remain variable, but their responses stay relatively close compared to the forward shear stages, and only cycle 3 ends with a net increase in force chain count. This suggests that the reverse-shearing stages produce a more convergent force chain response, despite active local restructuring.

Overall, the largest fluctuations in the number of detected force chains occur during the forward-shearing stages, when the strong network undergoes its most active restructuring. The global maximum occurs in cycle 1 during SRF, and the global minimum occurs in cycle 2 during SLF. Cycle 3 generally remains between the responses of cycles 1 and 2, suggesting that the force chain network becomes

progressively conditioned with cycling, while still remaining substantial history dependence.

Total Force Chain Length The total force chain length, calculated according to Eq. (3.1), is defined as the sum of all detected force chains and is expressed in terms of the number of grains rather than the physical length. Unlike the total number of detected force chains, which only indicates how many are present, this metric also reflects the overall extent of the force chain network. Figure 4.7 shows the total force chain length as a function of shear strain, γ, while Figure 4.8 shows its per-stage evolution.

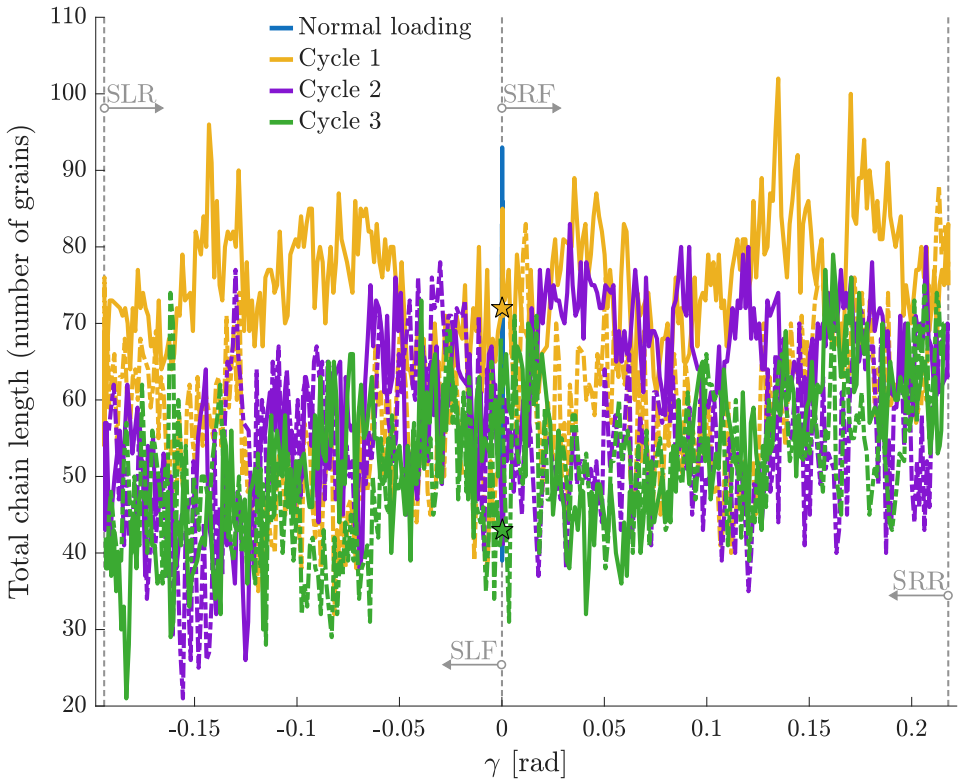


Figure 4.7: Evolution of the total force chain length, in number of grains, for the dense granular assembly ($\sigma_n = -44.1$ kPa). Curve style indicates shearing direction (solid: forward, dash-dotted: reverse), gray dashed lines mark stage transitions, and stars mark the start (yellow) and end (green) of cyclic loading.

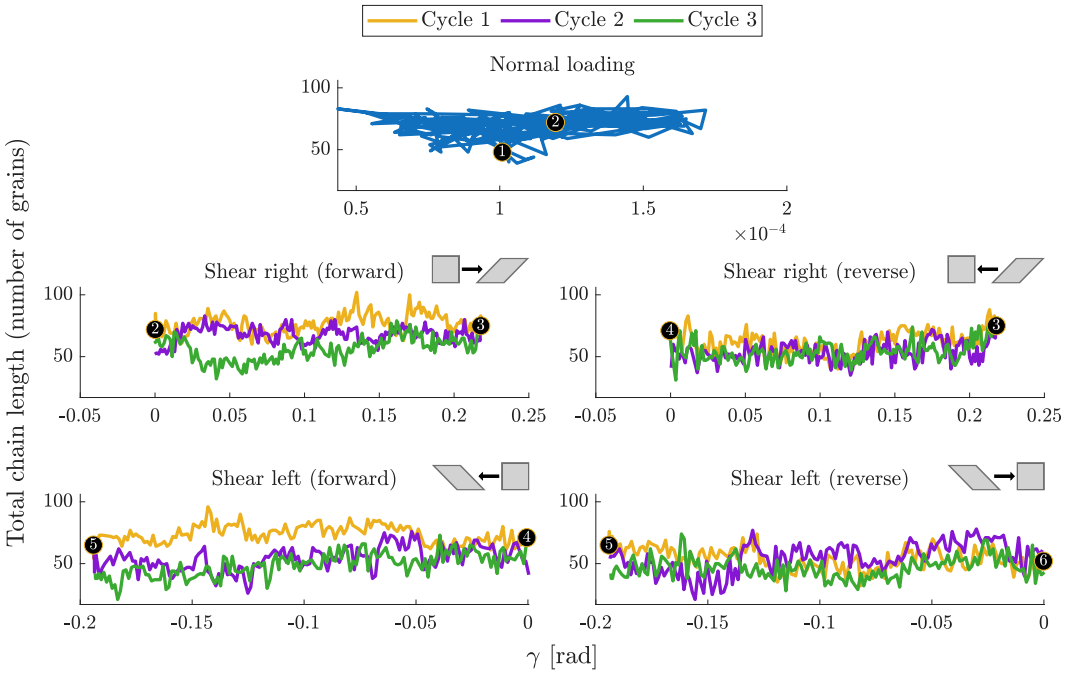


Figure 4.8: Per-stage evolution of the total force chain length, in number of grains, for the dense granular assembly ($\sigma_n = -44.1$ kPa). Stage markers are shown only for Cycle 1.

As in the baseline experiment, the total force chain length plot resembles the plot of the detected number of force chains, indicating that the overall force chain network is governed primarily by changes in the number of force chains, rather than by large shifts in the typical size of individual chains. Thus, the same stage-wise and cycle-wise trends are observed here. However, a notable difference appears in the shear-left-forward (SLF) stage, where cycle 1 separates more clearly from cycles 2 and 3, suggesting that repeated cyclic loading progressively reduces the spatial extent of the strong network, even when its overall structural evolution remains similar.

Accumulated Force Chain Network Content Figure 4.9 shows the normalized area under the curve (AUC) of the total chain length, calculated according to Eq. (3.2). The AUC represents the average sustained force chain network size per unit shear deformation. Intuitively, this metric captures the average extent and persistence of the force chain network per unit deformation.

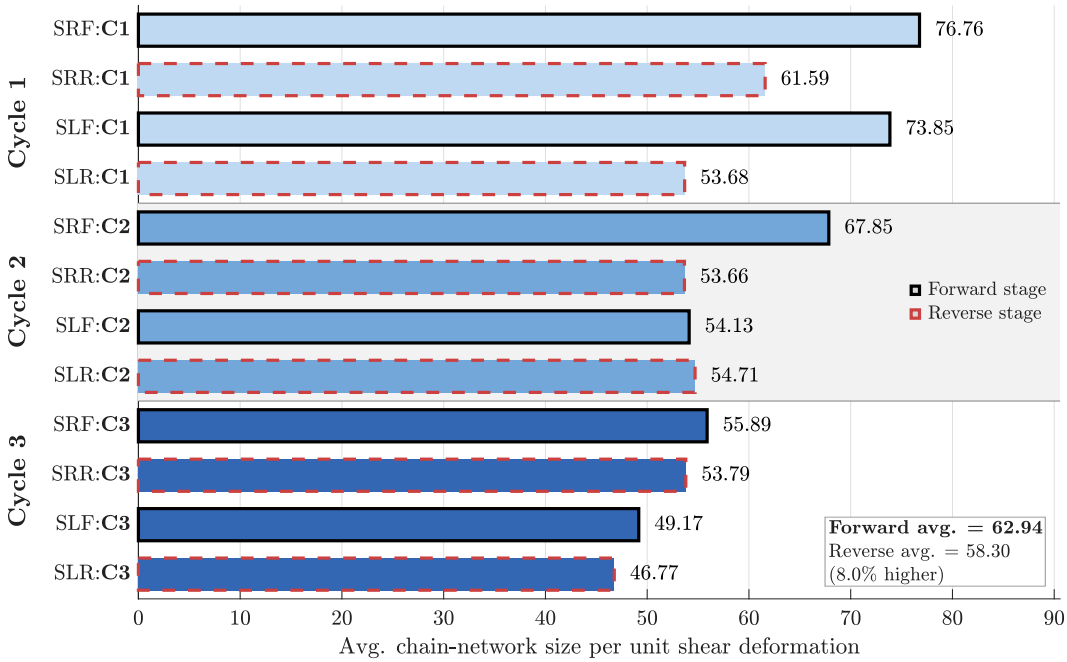


Figure 4.9: Bar chart of the normalized area under the curve (AUC) of the total force chain length for each cycle and shear stage for the dense assembly ($\sigma_n = -44.1$ kPa). The normalized AUC represents the average extent and persistence of the force chain network sustained per unit shear deformation within each stage.

As in the baseline experiment, cycle 1 follows the same overall progression: the shear-right-forward (SRF) stage exhibits the highest normalized AUC, indicating the formation of large and sustained force chain structures, while the following reversal (the shear-right-reverse (SRR) stage) leads to a reduction in AUC, reflecting disruption and reorganization of the existing network. During the shear-left-forward (SLF) stage, the force chain structure partially rebuilds but does not recover to the level reached during SRF, and the final reversal (the shear-left-reverse (SLR)] stage) again reduces the persistence of the force chain network.

In the three-cycle experiment, all cycles exhibit their highest normalized AUC during SRF, confirming that the initial forward-shearing stage consistently mobilizes the most extensive and persistent force chain network. This is followed by a marked reduction in AUC during the shear-left stages, indicating that force chain persistence weakens as the loading direction changes and the network undergoes repeated reorganization. However, the evolution during the shear-left stages differs across cycles. In cycle 2, the force chain partially rebuilds during SLF to a level exceeding that of SRR, and further strengthens during SLR, suggesting that later cycles can reorganize into more persistent load-bearing structures under reversed loading. In contrast, cycle 3 exhibits a monotonic decrease in the normalized AUC with loading

progression, indicating a progressive reduction in the persistence of the force chain network with continued cycling.

Lastly, consistent with the baseline experiment, two key trends emerge. First, the initial forward shearing stage (SRF) produces the most extensive and persistent force chain structures. Second, the forward-shearing stages maintain higher normalized AUC values than the reverse-shearing stages (approximately 8% higher), indicating that the force chains are more effectively mobilized and sustained during forward loading than during reversal. Together, these observations suggest that while the force chain network reorganizes throughout cyclic loading, its ability to sustain extended load-bearing structures diminishes with repeated reversals and continued cycling.

Force Chain Participation Figure 4.10 shows violin plots of the force chain density for each shear stage and cycle, where the chain density is calculated using Eq. (3.3). Because force chain density reflects the fraction of interior grains participating in the force chain network, it provides a normalized measure of the spatial extent of the strong force-bearing skeleton. Unlike the total force chain length, which emphasizes the overall size of the network, the chain density distributions also reveal how stable, variable, or intermittently organized the network is at each loading stage. In a violin plot, the vertical red lines represent the median, and the vertical blue lines represent the lower and upper quartiles (Q1 and Q3). The width at any point on the violin shape indicates the frequency of data at that value. The tails of the violin plot represent extremes of the data distribution. Moreover, the distribution can also have multiple peaks, indicating possible multiple regimes in the data.

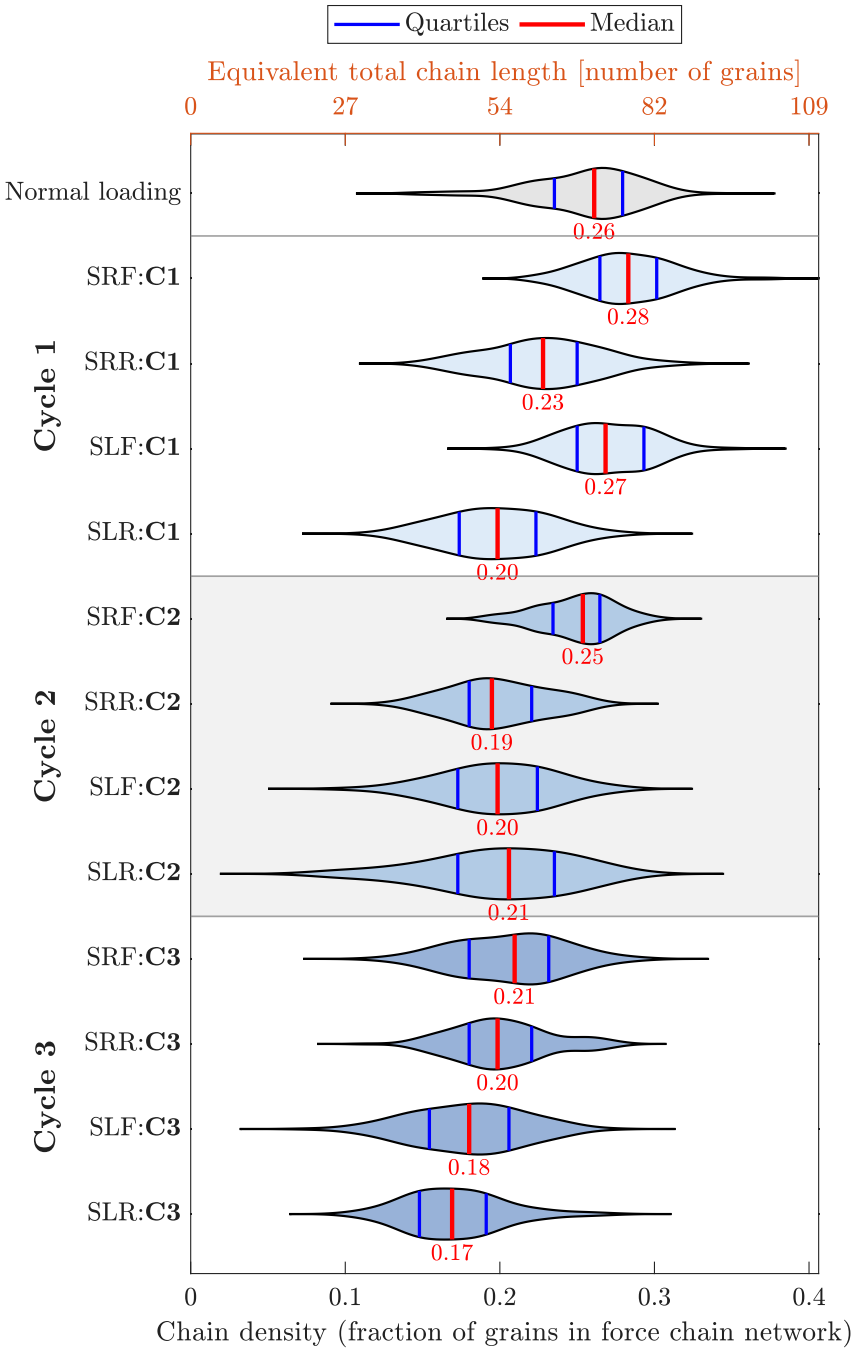


Figure 4.10: Violin plots of the force chain density for each cycle and shear stage for the dense assembly ($\sigma_n = -44.1$ kPa). Force chain density is defined as the fraction of grains participating in the force chain network relative to the total number of interior grains. The bottom x-axis shows the normalized chain density, while the top x-axis shows the equivalent total force chain length in number of grains. The width of each violin indicates the relative frequency of occurrence of a given chain density during that stage.

The normal loading stage has a median chain density of approximately 0.26 and therefore serves as a useful pre-shear reference state. Its distribution shows two preferred participation ranges centered on moderately sized and larger force chain networks, indicating that the confined assembly alternates between two characteristic levels of strong network engagement before the onset of shear.

As in the baseline experiment, the highest median chain density occurs during the shear-right-forward (SRF) stage in cycle 1 (≈ 0.28), indicating that the first forward shear stage mobilizes the largest fraction of grains into the force chain network. This stage also exhibits substantial variability, including occasional high-density states corresponding to very extensive force chain structures. More broadly, cycle 1 in the three-cycle experiment follows the same median chain density ordering as in the baseline one-cycle experiment: it is highest during SRF, drops during the shear-right-forward (SRF) stage, partially recovers during the shear-left-forward (SLF) stage, and reaches its lowest level in the shear-left-reverse (SLR) stage. However, unlike the baseline experiment, the final SLR stage in cycle 1 falls below even the median of the normal loading stage, indicating a greater net reduction in force chain participation after one full cycle of repeated shearing.

The later cycles show a progressive shift toward smaller, less extensive force chain networks. Following the low median chain density of 0.20 at the end of cycle 1, the response partially recovers during SRF in cycle 2 (≈ 0.25). The median chain density then increases gradually through the remaining stages of cycle 2, before decreasing again throughout cycle 3. Further, one notable feature of cycles 2 and 3 is that, from SRR in cycle 2 onward, all stages yield median values lower than those of the first three stages in cycle 1. Particularly, the median chain density decreases by approximately 0.11 from the onset to the end of cyclic shearing, indicating that repeated cycling progressively reduces the fraction of grains participating in the strong force-bearing skeleton.

In addition to changes in the median chain density, several stages exhibit distinctly non-Gaussian, multi-state distributions, indicating that the force chain network does not fluctuate about a single typical configuration. In particular, stages such as SLF in cycle 1 and both shear-right stages in cycles 2 and 3 show either pinching or dual-width distributions, suggesting that the assembly intermittently transitions between different levels of force chain participation within the same shear stage. In contrast, the remaining stages are more nearly Gaussian, indicating a comparatively more uniform strong-network response. A few stages also exhibit long, narrow tails

– most notably SRF in cycle 1 and SLR in cycle 2 – indicating that the granular assembly occasionally accesses unusually large or small force chain networks, even when the typical state is more moderate.

Overall, the chain density violin plots indicate that the largest and most spatially extensive force chain networks are mobilized during the initial forward-shear stage, whereas repeated cyclic loading progressively reduces the typical participation and stability of the strong force-bearing skeleton. Thus, although force chains continue to form throughout the loading history, they increasingly involve a smaller fraction of the assembly and fluctuate between multiple transient structural states.

Strong Network Participation and Strong Network Chain Participation Unlike force chain density, which measures the fraction of all grains participating in force chains, this section distinguishes between (1) the fraction of high-stress grains among all interior grains (Eq. (3.5)) and (2) the fraction of high-stress grains that are organized into force chains (Eq. (3.6)). These metrics define the strong network participation and the strong network chain participation, respectively. Figure 4.11 summarizes the median values for each quantity by loading stage and cycle. Error bars denote one-half of the interquartile range (IQR) centered on the median. Tables of the median and mean absolute deviation (MAD) for each stage are provided in Appendix E.

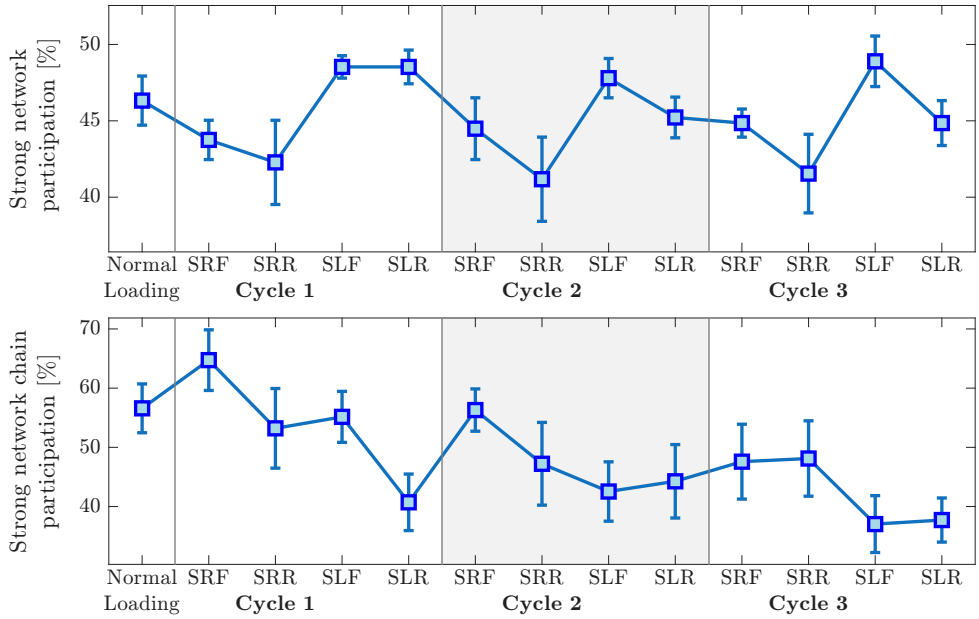


Figure 4.11: Stage-wise medians of the strong network participation [%] (top) and the strong network chain participation [%] (bottom) for each cycle and shear stage for the dense assembly ($\sigma_n = -44.1$ kPa). Error bars represent one-half of the interquartile range, centered about the median.

Across the three-cycle response, the two metrics exhibit notably different behavior. While strong network participation remains relatively stable from stage to stage, strong network chain participation varies more substantially, indicating that repeated cycling affects the organization of the strong network into chain-like structures more than its overall size.

The strong network participation remains within a relatively narrow range overall, with median values between approximately 38% and 51%. Although the stage-wise progression is not monotonic, the response generally evolves through alternating periods of gradual reduction and partial recovery. The global minimum occurs during the shear-right-reverse (SRR) stage in cycle 2, while the maximum occurs during the shear-left-forward (SLF) stage in cycle 3. Despite these fluctuations, the median value at the end of the loading history remains only modestly below that of the normal loading stage, and slightly above that at the onset of shear. Thus, repeated cycling does not strongly alter the overall fraction of grains carrying above-average stress.

In contrast, the strong network chain participation spans a broader median range ($37\% - 64\%$) and exhibits a less regular stage-wise evolution, indicating that the degree to which the strong network organizes into force chains is more sensitive to loading history than the size of the strong network itself. Its global maximum occurs during the shear-right-forward (SRF) stage in cycle 1, while its minimum occurs during SLF in cycle 3. Notably, the minimum chain participation coincides with the maximum strong network participation, showing that a larger strong network does not necessarily imply a more chain-organized one. Instead, the strong force-bearing grains may at times be distributed more diffusely throughout the assembly rather than concentrated into clearly defined force chains.

The variability of the two metrics also differs. The strongest fluctuations generally occur near the reverse-shearing stages, particularly for the chain participation metric, indicating that shear reversal repeatedly disrupts and reforms the organization of strong grains into chain-like structures as the principal stress directions rotate. By comparison, the overall size of the strong network remains more stable, suggesting that cyclic loading affects the internal organization of the strong force-bearing skeleton more than it affects its total population.

In general, these results show that while roughly half of the assembly remains in the strong network throughout cyclic loading, only about 37% – 64% of those strong grains organize into force chains. Including stage-wise variability, this proportion ranges from approximately 33% to 70%. As in the baseline one-cycle experiment, these findings indicate that not all strong grains participate in chain-like load transmission at any given time. This behavior is also consistent with the findings of Peters et al. [73], who observed in a flat indentation test that approximately half of the strong particles belonged to force chains. Despite the very different loading conditions, both results suggest that only a portion of the strong force-bearing population self-organizes into chain-like load-transmitting structures.

Micro-Macro Comparison Next, we compare the stage-wise medians of the macroscopic shear stress and the total force chain length (Figure 4.12).

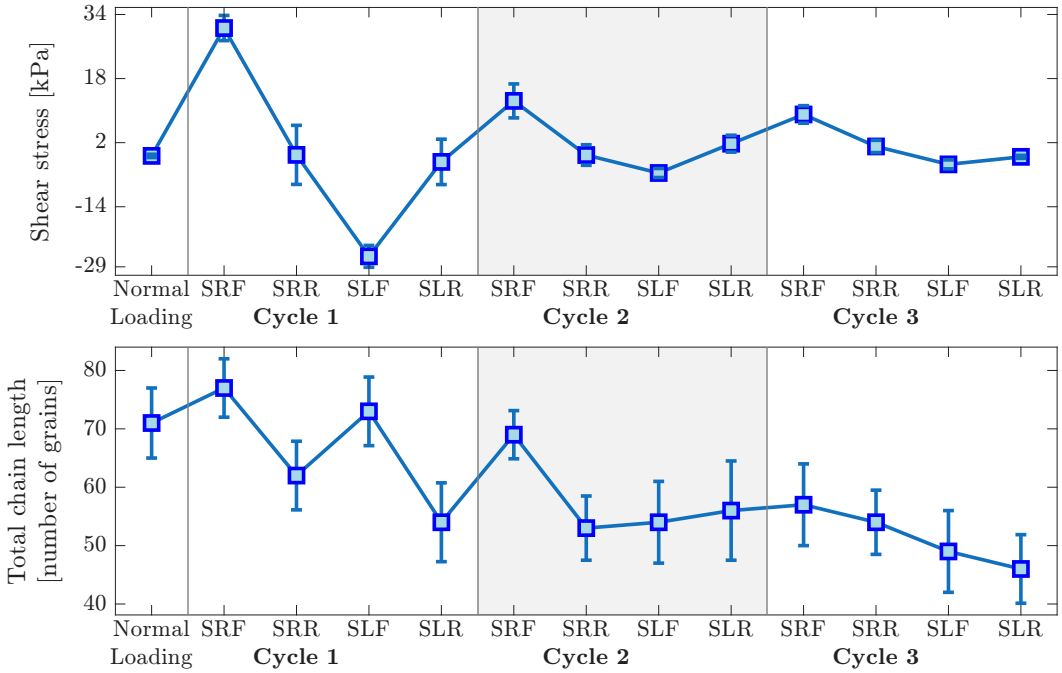


Figure 4.12: Stage-wise medians of the shear stress [kPa] (top) and total chain length [number of grains] (bottom) for each cycle and shear stage for the dense assembly ($\sigma_n = -44.1$ kPa). Error bars represent one-half of the interquartile range, centered about the median.

As in the baseline one-cycle experiment under the same normal stress, cycle 1 of the three-cycle response exhibits the same overall stage-wise progression in both quantities. The median shear stress increases after normal loading, followed by a continued decrease after the shear-right-reverse (SRR) stage through the shear-left-forward (SLF) stage before increasing slightly during the final stage (shear-

left-reverse (SLR)). In contrast, the total force chain length follows an alternating increase-decrease pattern with an overall downward trend. In both the baseline and three-cycle experiments, SRF exhibits the highest median shear stress and the largest force chain network, indicating that the strongest internal resistance to deformation coincides with the most developed force chain structure.

However, beyond this initial correspondence, the relationship between shear stress and total force chain length becomes less direct. As in the baseline experiment, the median total force chain length does not track the median shear stress in a monotonic way throughout the remaining stages, indicating that a larger force chain network does not necessarily produce a higher macroscopic shear stress. Additionally, a more pronounced decoupling between the two quantities is observed in later cycles. Specifically, in cycles 2 and 3, the median shear stress varies over a much narrower range, whereas the total force chain length continues to evolve with moderate-to-large variability. This indicates that repeated cyclic loading reduces the sensitivity of the macroscopic shear stress to changes in the overall size of the force chain network.

Together, these results show that repeated cyclic loading progressively weakens the direct correspondence between the size of the force chain network and the magnitude of the macroscopic shear stress. In other words, a longer force chain network does not necessarily imply a stronger macroscopic response. Rather, the shear stress depends on the overall extent of the force chain network and how effectively that network is configured to transmit load. Factors such as chain connectivity and the magnitude and orientation of contact forces relative to the principal load direction all influence the efficiency with which the force chain skeleton contributes to the bulk shear resistance. This motivates the next section, which examines the anisotropy of the contact and force networks to better understand how the force chain structure contributes to macroscopic stress transmission.

4.2.2.3 Force Chain Structure and Anisotropy

As in the baseline experiment, the following subsections analyze the orientation distributions of both contacts (fabric anisotropy) and interparticle forces (force anisotropy), and their relationships with macroscale quantities through the stress-force-fabric framework. In addition, the probability density functions (PDF) of normalized contact forces are examined to characterize how forces are transmitted through the granular assembly.

Fabric and Force Anisotropy This section uses polar histograms to examine the angular distributions of contact fabric orientation, $P(\theta)$, and the interparticle contact forces, $\bar{f}_n(\theta)$ and $\bar{f}_t(\theta)$ (mean normal force and mean tangential force, respectively). In these plots, the radial magnitude represents the relative frequency or average force associated with a given contact orientation, while the shape and elongation of the distribution indicate the degree of anisotropy. More elongated (lobed) distributions reflect stronger directional bias, whereas more circular distributions indicate a more isotropic response. Detailed interpretation of these polar histograms is provided in Chapter 3, Section 3.3.2.4.

The **contact fabric orientation**, $P(\theta)$, characterizes the directional distribution of contacts within the granular assembly and, therefore, reflects the geometric structure through which forces are transmitted. Figure 4.13 shows the polar distributions of contact orientations for each cycle and loading stage.

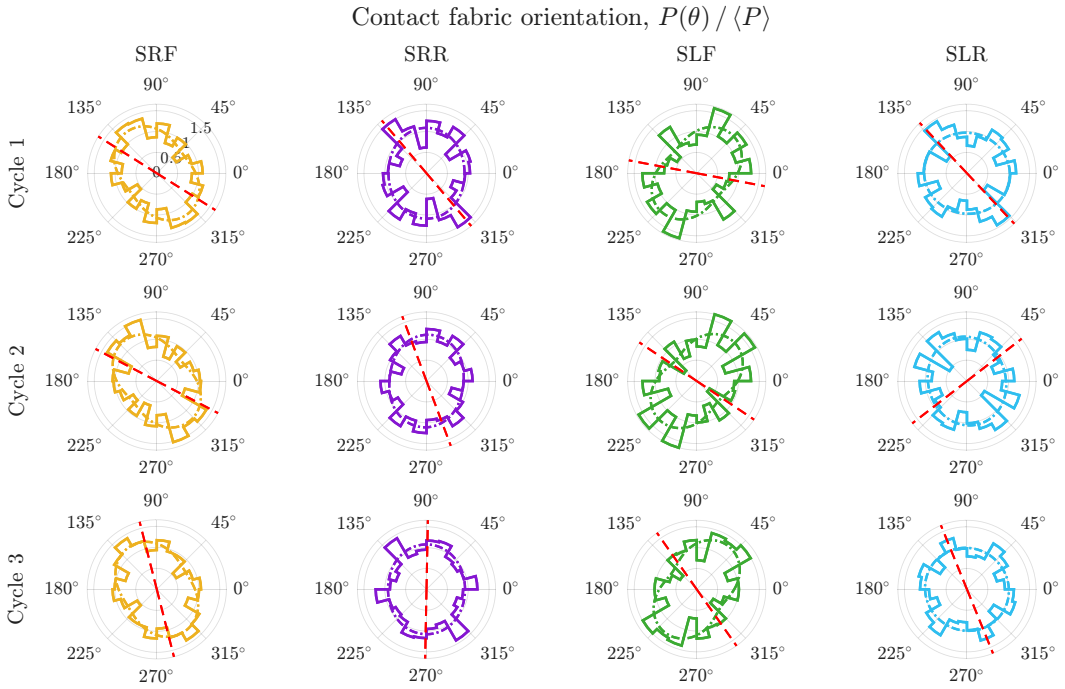


Figure 4.13: Polar histograms of the normalized angular distributions of the contact fabric orientation, $P(\theta)$, arranged by cycle (rows) and midpoint of each shear stage (columns) for the dense assembly ($\sigma_n = -44.1$ kPa). The solid curve represents the distribution, the dash-dotted curve shows its Fourier fit, and the red dashed line denotes the principal compressive stress axis.

Across all cycles, the shear-right-forward (SRF) stage exhibits a clear preferred contact orientation, with elongated lobes aligned approximately along the 125° direction, defining the dominant fabric anisotropy axis. Although this direction

coincides with the location of the longest lobes, it does not necessarily align with the principal compressive stress axis. In fact, we observe a small misalignment between the two axes, with cycles 1 and 2 exhibiting nearly 21° misalignment and cycle 3 slightly less ($\approx$ 18°). Furthermore, while the principal stress direction remains relatively consistent between the first two cycles, it shifts noticeably by cycle 3, accompanied by reduced lobe elongation, suggesting a weaker, reoriented contact structure in later cycles.

Upon shear reversal, in the shear-right-reverse (SRR) stage, the degree of anisotropy decreases across all cycles, as the distributions become more circular. Nevertheless, a preferred orientation persists near the 90° direction, indicating that the contact network retains the directional bias even as it reorganizes. The misalignment between the dominant fabric orientation and the compressive axis decreases with cycle progression, becoming nearly negligible by cycle 3. This indicates that repeated cycling promotes a more consistent alignment between the contact structure and the loading direction during shear reversal, even though the overall anisotropy is reduced.

During the shear-left-forward (SLF) stage, the preferred contact orientation rotates toward the 45° direction, reflecting the change in the loading direction. This stage exhibits the strongest anisotropy across all cycles, with lobes that are more pronounced and elongated than those in other stages. However, unlike SRR, the misalignment between the dominant fabric orientation and the compressive axis does not vary monotonically with cycle count. Instead, the misalignment follows a cycle-dependent ordering, with moderate misalignment in cycle 1 ($\approx$ 58°), increasing further in cycle 3 ($\approx$ 70°), and reaching its largest value in cycle 2 ($\approx$ 81°). This indicates that the contact network becomes less consistently aligned with the principal stress direction during this stage.

In the final stage, the shear-left-reverse (SLR) stage, the contact fabric becomes nearly isotropic in cycles 1 and 3, while cycle 2 retains a modest degree of anisotropy. Overall, the magnitude of contact distributions decreases with increasing cycle count, suggesting a progressive weakening of fabric anisotropy in the later stages of cyclic loading. The orientation of the principal stress axis is also more variable in this stage, and the misalignment between the fabric and the stress directions remains inconsistent, particularly in cycle 2, indicating a less stable structural configuration under repeated shear reversal.

Compared to the baseline one-cycle experiment, cycle 1 exhibits a similar stage-wise behavior, including strong anisotropy during forward shear, reduced anisotropy upon shear reversal, and the largest misalignment during SLF. However, the three-cycle response reveals that repeated loading alters both the magnitude and the alignment of the contact fabric, leading to increased orientation variability and reduced structural coherence in later cycles.

The **mean normal contact force orientation**, $\bar{f}_n(\theta)$, characterizes the directional distribution of compressive forces and, thus, reflects how load is transmitted through the contact network. Figure 4.14 shows the polar distributions of the normalized mean normal contact forces.

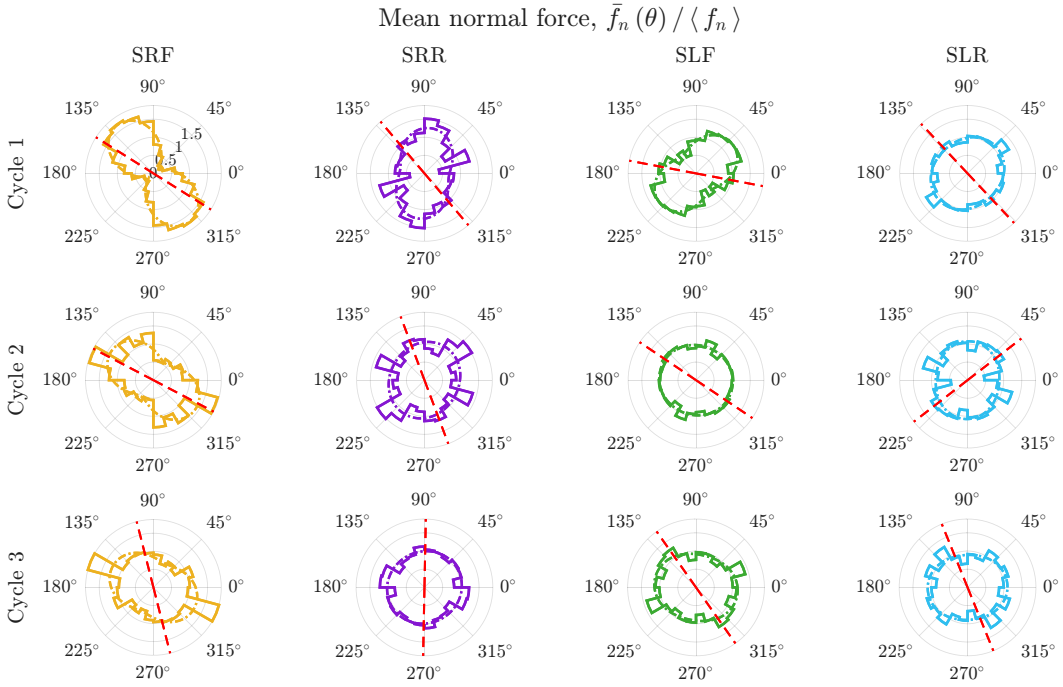


Figure 4.14: Polar histograms of the mean contact normal force, $\bar{f}_n(\theta)$, arranged by cycle (rows) and midpoint of each shear stage (columns) for the dense assembly ($\sigma_n = -44.1$ kPa). The solid curve represents the distribution, the dash-dotted curve shows its Fourier fit, and the red dashed line denotes the principal compressive stress axis.

During SRF, the distribution exhibits a pronounced anisotropic structure consistent with directional force transmission. As in the baseline one-cycle experiment, cycle 1 shows a characteristic peanut-shaped distribution, indicating a strong localization of compressive forces along a preferred direction. In later cycles, the distributions become broader and less elongated, suggesting reduced directional concentration of force transmission, even though distinct lobes remain. The dominant anisotropy

axis remains relatively stable across cycles, while the principal stress direction shifts, leading to a small misalignment in cycles 1 and 2, and a substantially larger misalignment in cycle 3. This indicates that although the preferred direction of force transmission persists, its alignment with the macroscopic stress state becomes less consistent as cycling continues.

Upon shear reversal, in the SRR stage, the distributions become more cycle-dependent. Cycle 1 retains a relatively strong anisotropic structure, while cycles 2 and 3 exhibit reduced anisotropy and more isotropic distributions. Despite variability in the principal stress direction across cycles, the misalignment between the dominant anisotropy axis and the compressive stress axis decreases with cycle progression, suggesting that repeated cycling promotes consistent alignment between force transmission and loading direction during shear reversal, even as the overall anisotropy weakens.

During SLF, cycle 1 exhibits a strongly anisotropic distribution with significant misalignment relative to the compressive stress axis, consistent with the baseline experiment. In contrast, cycles 2 and 3 show weaker anisotropy and more rounded distributions, indicating a less directionally concentrated force network in later cycles. While cycle 2 shows minimal misalignment between the anisotropy and compressive axes, cycle 3 exhibits moderate misalignment, though still reduced compared to cycle 1. These trends suggest that repeated cyclic loading modifies both the magnitude and the alignment of force anisotropy, leading to a more diffuse but more consistently oriented force-transmission structure during this stage.

In the final shear stage (SLR), all cycles exhibit relatively low anisotropy with modest directional bias. Compared to the baseline experiment, the three-cycle response shows greater variability in the alignment between the anisotropy and compressive stress axes, with cycle 1 showing the largest misalignment, and cycle 2 the smallest. Overall, the magnitude of anisotropy in this stage remains limited, indicating that force transmission becomes more distributed and less strongly aligned along a preferred direction under repeated shear reversal.

Across all stages, a general trend emerges in which the mean normal force distributions in cycles 2 and 3 are more circular and less anisotropic than in cycle 1, particularly from SRR through SLF. Hence, repeated cyclic loading leads to a progressive reduction in force anisotropy, even though preferred directions of force transmission remain. Thus, while the contact network continues to support load through directional force chains, the efficiency of this transmission becomes less

strongly concentrated along a single dominant direction.

The **mean tangential contact force orientation**, $\bar{f}_t(\theta)$, characterizes the directional distribution of shear forces at contacts and therefore reflects how shear is transmitted through the granular assembly. Figure 4.15 shows the polar distributions of the normalized mean tangential contact forces for each cycle and loading stage.

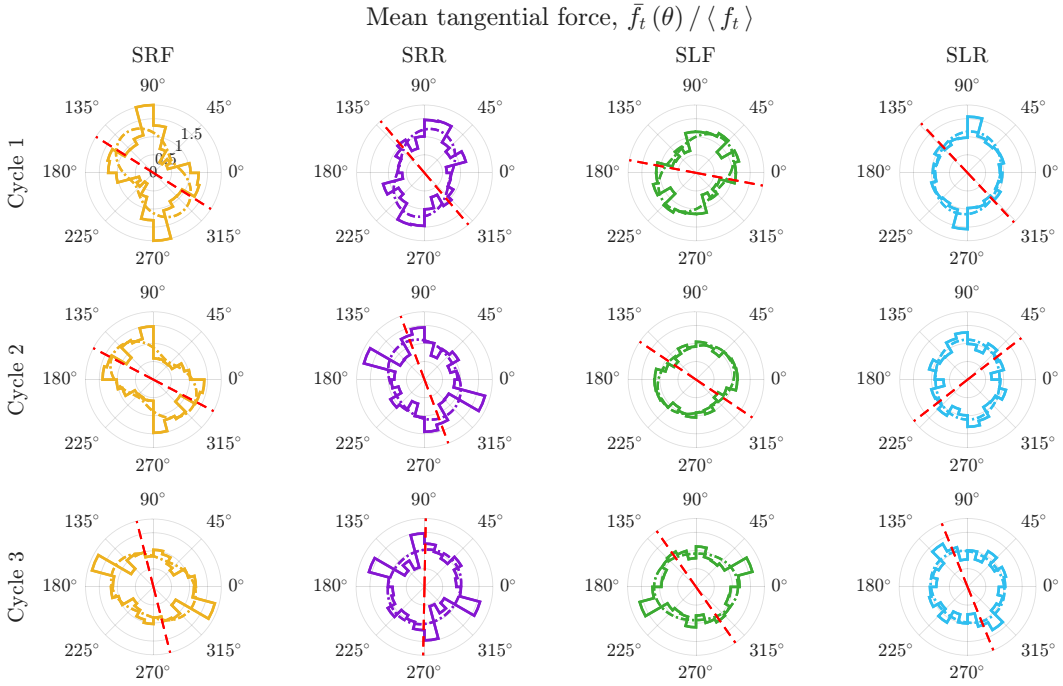


Figure 4.15: Polar histograms of the mean contact tangential force, $\bar{f}_t(\theta)$, arranged by cycle (rows) and midpoint of each shear stage (columns) for the dense assembly ($\sigma_n = -44.1$ kPa). The solid curve represents the distribution, the dash-dotted curve shows its Fourier fit, and the red dashed line denotes the principal compressive stress axis.

Across all cycles, the tangential force distribution exhibits behavior broadly similar to that of the mean contact normal forces, but with notable differences in both orientation and variability. In particular, the shear-left stages (SLF and SLR) during cycles 2 and 3 exhibit comparatively low anisotropy magnitudes and limited variability, indicating that tangential force transmission becomes more diffuse in these stages as cycling continues.

During the SRF stage, cycle 1 exhibits a pronounced anisotropic structure with a broader peanut-shaped distribution and strong lobes aligned near the 95° direction, indicating that concentrated shear transmission along a preferred direction. As in the normal force distributions, the magnitude of anisotropy decreases with increasing cycles, while the dominant orientation remains relatively stable near the

135° direction. Cycles 1 and 2 show close alignment between the tangential force anisotropy axis and the compressive stress direction, while cycle 3 exhibits a larger misalignment, indicating reduced coherence between shear force transmission and the principal load direction in later cycles.

Upon shear reversal (SRR), the tangential force distributions become more variable across cycles. Cycle 1 retains a structure similar to that of the normal force distribution but with a stronger concentration of shear forces over a broader angular range. In contrast, cycle 2 exhibits a more elongated distribution with greater anisotropy, while cycle 3 remains relatively isotropic but with localized bursts of higher force magnitude. Unlike the normal force response, the smallest misalignment between the anisotropy and compressive axes occurs in cycle 2, indicating that the alignment of shear force transmission evolves differently from that of compressive forces under repeated shear reversal.

During SLF, cycle 1 again exhibits strong anisotropy with significant misalignment relative to the compressive axis, consistent with the normal force behavior. However, the preferred orientation of the tangential forces shifts relative to the normal force distribution, indicating that the shear forces are mobilized along different contact directions. In later cycles, the distributions become more organized but less anisotropic overall. Cycle 2 develops a clearer preferred direction, while cycle 3 reflects the dominant orientation observed in the normal force network, suggesting increasing coupling between normal and tangential force transmission as the system evolves.

In the final shear stage (SLR), cycles 1 and 2 retain a preferred direction of tangential force transmission, while cycle 3 becomes more isotropic. Across cycles, the anisotropy axes gradually rotate counterclockwise, consistent with the evolution observed in the normal force distributions. However, the orientations of the tangential and normal force anisotropies differ systematically, typically by several tens of degrees, indicating that shear forces are not transmitted along the same direction as the compressive forces. The degree of misalignment between the tangential force anisotropy and the compressive stress axis is generally moderate, with cycle 3 showing the closest alignment in this stage.

Overall, the tangential force distributions exhibit their strongest anisotropy during SRF, although the peak occurs in cycle 1 rather than in later cycles as observed in the normal forces. Together, these results indicate that while both normal and tangential contact forces contribute to anisotropic load transmission, the orientation

and evolution of shear forces are more variable and less consistently aligned with the principal stress direction. This highlights the distinct role of tangential forces in accommodating shear deformation within the evolving contact network.

Together, the results of the contact fabric and the force anisotropy distributions show that shear resistance is governed not only by the presence of force chains but also by the directional organization of the contact network and the effectiveness with which forces are transmitted along that structure. Although forward shearing stages produce strong anisotropy with aligned contact and force networks, shear reversal leads to reorganization and reduced directional bias. With continued cycling, the contact and force networks become less strongly aligned and more variable in orientation, particularly for the tangential forces. This evolution helps explain the reduced correspondence between force chain extent and macroscopic shear stress observed in the micro-macro comparison.

Temporal Evolution of Fabric and Force Anisotropy Magnitudes While the previous section qualitatively examined the directional organization of the contact and force networks through polar histograms, this section provides a quantitative assessment of how these directional structures evolve throughout cyclic loading. Specifically, we examine the fabric anisotropy magnitude, a, the normal force anisotropy magnitude, a_n, and the tangential force anisotropy magnitude a_t, as functions of shear strain. These measures, obtained from the Fourier fits of the corresponding angular distributions (Eq. (3.8)), quantify the degree of directional bias in the contact geometry and force transmission. Their evolution (Figure 4.16) provides insight into how the internal structure of the granular assembly reorganizes as the loading direction changes across stages and cycles.

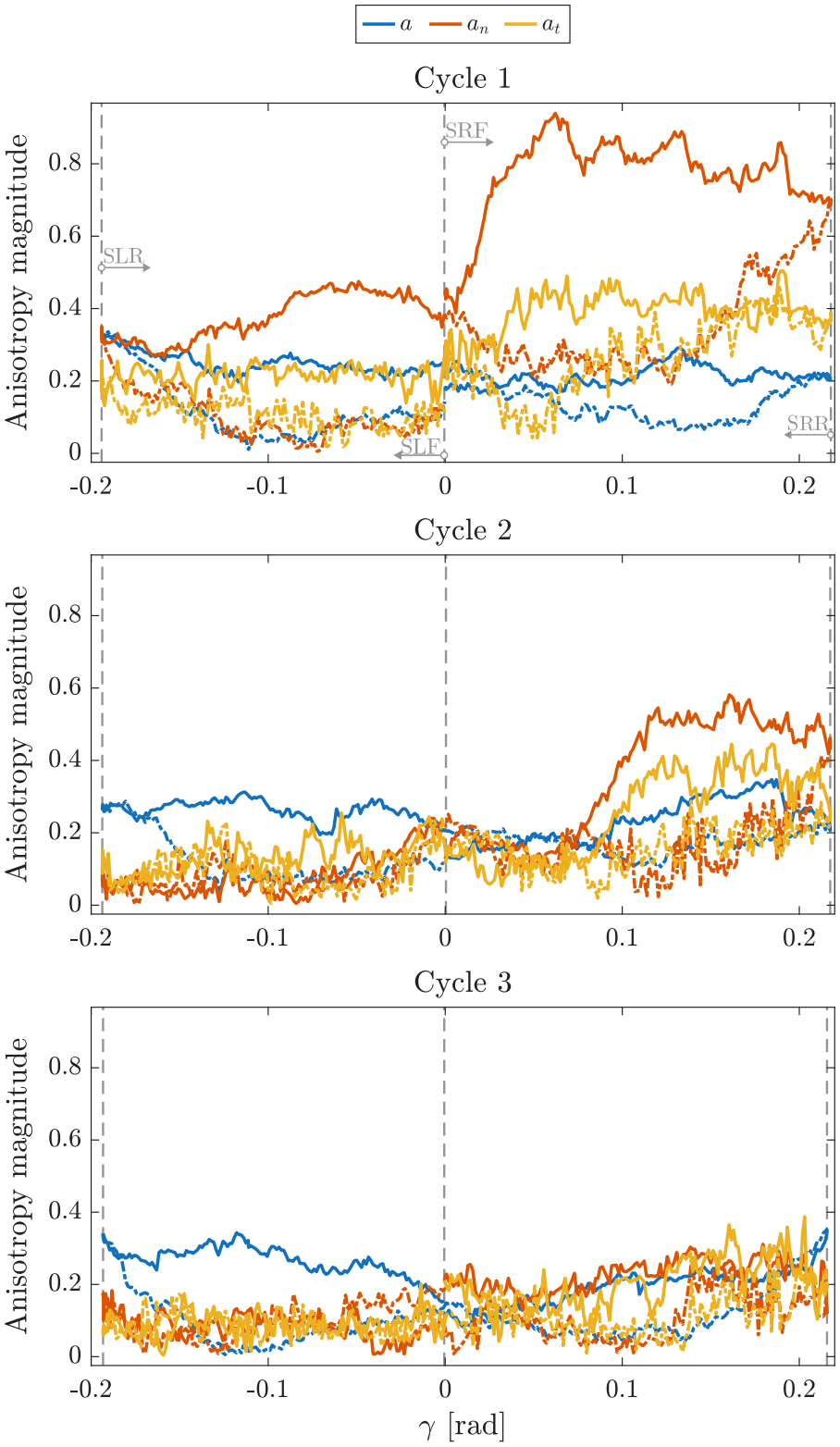


Figure 4.16: Per cycle evolution of the anisotropy magnitudes as functions of shear strain for the dense assembly ($\sigma_n = -44.1$ kPa): fabric anisotropy magnitude, a, and normal and tangential force anisotropy magnitudes, a_n and a_t, respectively. Curve style indicates shearing direction (solid: forward, dash-dotted: reverse), gray dashed lines mark stage transitions.

As in the baseline experiment, all measures begin with relatively low anisotropies, ranging from 0.03 to 0.18. Although not shown in the figure, the fabric anisotropy gradually decreases under normal loading. In contrast, both force anisotropy measures exhibit an overall increasing trend despite significant fluctuations, indicating that directional force transmission begins to develop prior to shearing. Also, consistent with the baseline experiment, a_n exhibits the largest magnitude, while a remains the smallest.

During shear-right-forward (SRF), the force anisotropy magnitudes increase rapidly, particularly in cycle 1, where a_n reaches its peak before gradually decreasing with continued deformation. In later cycles, this response becomes both delayed and significantly weakened, with lower peak magnitudes and extended periods of relatively steady behavior prior to mobilization. By cycle 3, both a_n and a_t are confined to a much narrower range of low values, indicating a substantial reduction in force anisotropy with repeated cycling. Although fluctuations persist, the overall amplitude of variation decreases, suggesting a progressive loss of strong directional force transmission.

Upon shear reversal, in the shear-right-reverse (SRR) stage, the force anisotropy magnitudes reorganize, typically exhibiting a gradual decrease followed by a partial recovery within the stage. This reorganization reflects the force network's adjustment to the new loading direction. However, as cycling progresses, both the magnitude and variability of a_n and a_t diminish, indicating that the force network becomes less responsive and less directionally structured under repeated reversal.

During the shear-left-forward (SLF) stage, the force anisotropy continues to weaken in later cycles. While cycle 1 still exhibits a clear directional response with a moderate magnitude, cycles 2 and 3 show reduced anisotropy, with a_n and a_t becoming comparable in magnitude and, in some cases, nearly overlapping. By the final stage, shear-left-reverse (SLR), all anisotropy measures collapse toward similar low values, indicating that the distinction between fabric and force anisotropy becomes less pronounced as the system evolves.

In contrast to the force anisotropy measures, the fabric anisotropy exhibits a much more stable response across cycles. Although its magnitude remains comparatively small, it retains a consistent stage-wise structure with only minor reductions in amplitude. In particular, a shows gradual variation within each stage and only limited collapse near shear reversal, indicating that the geometric structure of the contact network is more persistent than the force transmission pathways.

Overall, the anisotropy magnitudes show a clear hierarchy and evolution: a_n and a_t initially dominate and exhibit strong directional bias during early cycles, but progressively weaken and converge toward the smaller, more stable fabric anisotropy as cycling continues. This indicates that repeated cyclic loading reduces the strength and variability of directional force transmission, even as the underlying contact structure remains relatively intact. As a result, the granular assembly evolves toward a state in which force transmission is less anisotropic and more uniformly distributed, thereby contributing to the reduced sensitivity of macroscopic shear stress to force chain structure observed in the micro-macro comparison. Moreover, this reduction in anisotropy magnitude is consistent with the observed decrease in strong network organization and force chain persistence in later cycles.

Verification of the Stress-Force-Fabric Relationship The previous section quantified the evolution of the fabric and force anisotropy magnitudes, showing that repeated cyclic loading reduces both the strength and variability of directional force transmission. Although these measures describe how the contact network and force chains are organized, they do not directly indicate how effectively this structure contributes to the macroscopic stress response. To establish this connection, we evaluated the stress-force-fabric (SFF) relationship, which provides a micromechanical framework linking the invariant stress ratio (q/p) to the anisotropy of the contact fabric and force networks. Using the expressions introduced in Chapter 3, Section 3.3.2.4, the theoretical predictions are compared with the experimentally measured q/p response for each cycle (Figure 4.17).

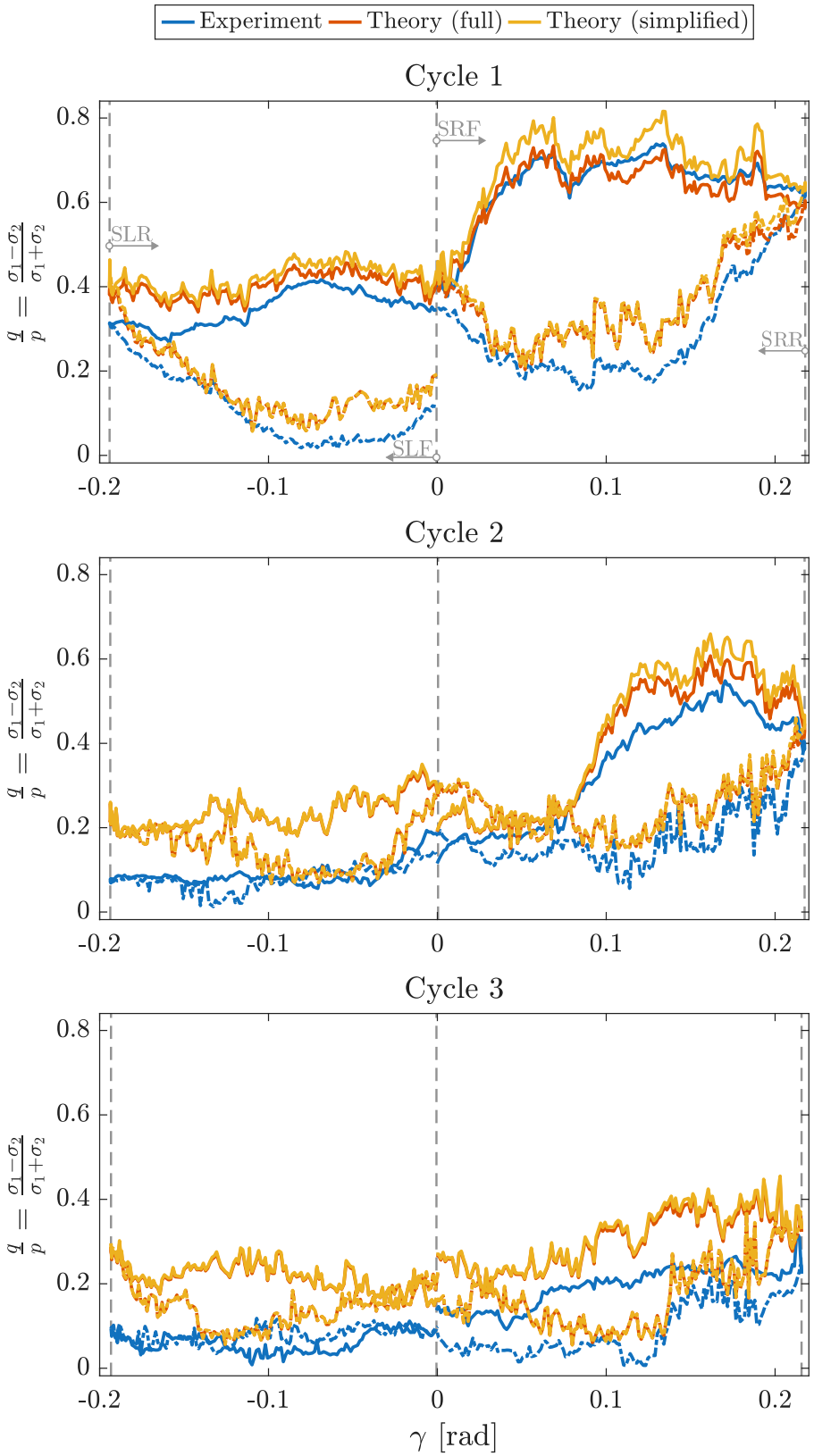


Figure 4.17: Per cycle evolution of the invariant stress ratio, q/p, as a function of shear strain for the dense assembly ($\sigma_n = -44.1$ kPa). The experimental response is compared with the predictions of the full and simplified stress-force-fabric (SFF) relationships. Curve style indicates shearing direction (solid: forward, dash-dotted: reverse), gray dashed lines mark stage transitions.

As in the baseline experiment, the shear-right-forward (SRF) stage is characterized by an overprediction of the experimental response by both theoretical expressions, with the full SFF formulation remaining closest to the data. Similarly, during the shear-left-reverse (SLR) stage, the general trends observed in the baseline experiment are maintained. In contrast, the behavior during the shear-right-reverse (SRR) and shear-left-forward (SLF) stages differs more substantially from the baseline response. In the three-cycle experiment, the theory briefly overpredicts the experimental response at the onset of SRR, but underpredicts it for the remainder of the stage. During SLF, the theoretical predictions consistently overestimate the experimental q/p, unlike the baseline case, where alternating over- and under-predictions were observed.

These discrepancies become more systematic in later cycles. In cycles 2 and 3, the theoretical expressions consistently overpredict the experimental response during forward shearing stages (SRF and SLF), underpredict during SRR, and only briefly match the experimental results during portions of SLR. This indicates that the SFF framework, while capturing the overall structure, becomes less accurate at predicting the response magnitude as cyclic loading progresses.

The evolution of the experimental response provides further insight into these discrepancies. As in the baseline experiment, cycle 1 exhibits a pronounced shear-right petal and a smaller shear-left petal. With continued cycling, the amplitude of the shear-right response decreases, while the shear-left branch weakens more significantly, approaching a nearly collapsed state in cycles 2 and 3. In particular, portions of the shear-right branch in later cycles exhibit temporary collapse before partially reopening, reflecting the transient restructuring of the force network.

Since the theoretical SFF expressions retain a more pronounced and symmetric loop structure, they tend to overpredict the response in stages where the experimental petals collapse, particularly during the shear-left stages. This suggests that the SFF relation does not fully capture the reduction in effective anisotropy and force transmission efficiency that develops with repeated cycling.

Overall, these results indicate that although the SFF framework successfully captures the qualitative structure of the stress response, its predictive accuracy decreases under cyclic loading as the contact and force networks become weaker and less effectively organized. This result highlights the importance of anisotropy magnitude and alignment, as well as their evolution with loading history, in determining the macroscopic stress response.

Force Transmission While the stress-force-fabric (SFF) relationship links anisotropy to the macroscopic state response, it does not fully capture the distribution of forces at the contact level. In particular, the discrepancies between theoretical predictions and the experimental response suggest that changes in the distribution and magnitude of contact forces play an important role in governing bulk behavior. To further investigate these effects, this section examines the probability density functions (PDFs) of the normalized normal and tangential contact forces, as well as the mobilized friction, providing insight into how force transmission evolves across loading stages and cycles.

Figure 4.18 shows the PDFs of the **normalized normal contact force**, $f_n / \langle f_n \rangle$. The PDFs of $f_n / \langle f_n \rangle$ exhibit two distinct regimes across all cycles: a steep decay at low forces followed by a more gradual, approximately exponential decay at higher force levels. This bimodal behavior reflects the well-known separation between weak contacts, which form a background network, and strong contacts, which carry the majority of the load.

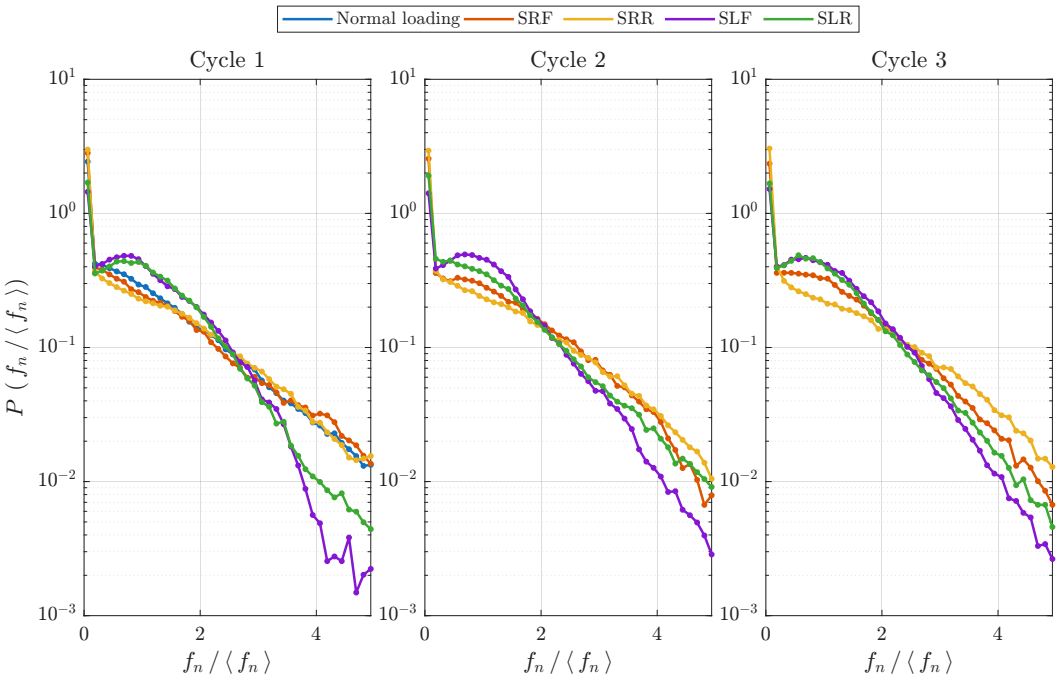


Figure 4.18: Per-cycle evolution of the probability density function (PDF) of the normalized normal contact force, $f_n / \langle f_n \rangle$, for the dense assembly ($\sigma_n = -44.1$ kPa). Each panel shows one loading cycle, with all stages on a semi-log scale.

As in the baseline experiment, the steep decay regime remains largely unchanged, indicating that the population of weak contacts is relatively insensitive to cyclic loading. In contrast, differences emerge in the moderate-to-strong force regime,

where stage-dependent variations become more pronounced. During the shear-right stages, the PDFs remain closely grouped and decay nearly linearly, suggesting a relatively stable distribution of load-bearing contacts. The shear-right-reverse (SRR) stage, in particular, exhibits the most consistent behavior, indicating that force redistribution during reversal is more uniform in this regime.

Clear deviations occur during the shear-left stages, where the shear-left-forward (SLF) and shear-left-reverse (SLR) stages separate from the other stages at higher force levels. This separation indicates that fewer contacts sustain very large forces, suggesting a weaker, more diffuse force chain network during leftward shearing. With increasing cycles, these differences become more pronounced, and by cycle 3, each stage exhibits a more distinct distribution. This progressive separation implies that cyclic loading leads to reorganization of the strong-force network, reducing its coherence and redistributing the load across a broader set of contacts.

Figure 4.19 shows the PDFs of the **normalized tangential contact force**, $f_t / \langle f_n \rangle$. The PDFs of the $f_t / \langle f_n \rangle$ show a similar two-regime behavior, but with a much steeper initial decay; this reflects that most contacts carry relatively small tangential forces, consistent with frictional constraints and intermittent mobilization of shear resistance.

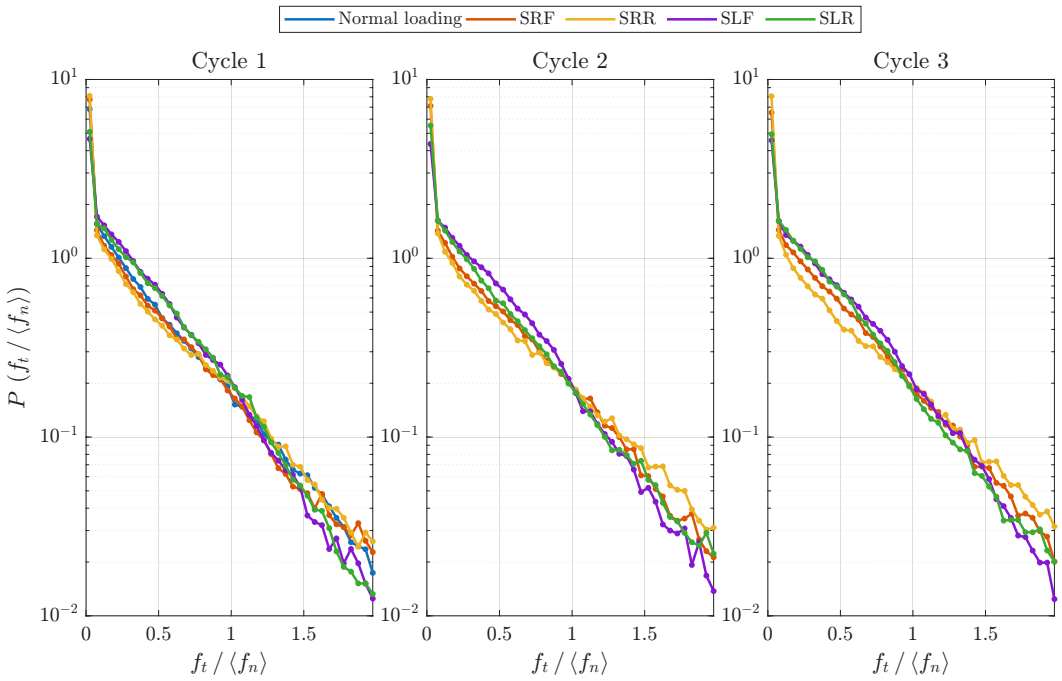


Figure 4.19: Per-cycle evolution of the probability density function (PDF) of the normalized tangential contact force, $f_t / \langle f_n \rangle$, for the dense assembly ($\sigma_n = -44.1$ kPa). Each panel shows one loading cycle, with all stages on a semi-log scale.

In the low-force regime, the shear-left stages consistently exhibit higher probabilities than the shear-right stages, indicating that a larger fraction of contacts participates in low-level shear interactions during leftward loading. Hence, shear-left deformation is accommodated by a broader distribution of weak tangential forces, rather than a concentrated set of strongly mobilized contacts.

At higher force levels, the behavior diverges more clearly. The shear-right stages remain closely grouped with relatively minor fluctuations, while the shear-left stages deviate and attain lower probabilities, indicating fewer contacts carrying large tangential forces. This suggests that shear-right loading promotes a more coherent and concentrated shear force network, whereas shear-left loading leads to a more distributed and less efficient transmission of shear forces.

With increasing cycles, the separation between stages becomes more pronounced, particularly beyond $f_t / \langle f_n \rangle > 1$, where the PDFs spread out and exhibit greater variability. The SRR stage consistently shows the highest probability of very large tangential forces, indicating that shear reversal promotes localized bursts of strong frictional interactions as the contact network reorganizes.

Figure 4.20 shows the PDFs of the **mobilized friction**, $S = |f_t|/\mu f_n$. The PDFs of S further illustrate the distribution of shear resistance across contacts. As in the baseline experiment, the distributions exhibit an initial soft decay, followed by a pronounced peak at low mobilization levels ($S \approx 0.13 - 0.20$), and a gradual decay toward the failure limit at $S = 1$. This behavior indicates that most contacts operate well below their frictional capacity, with only a small fraction approaching failure.

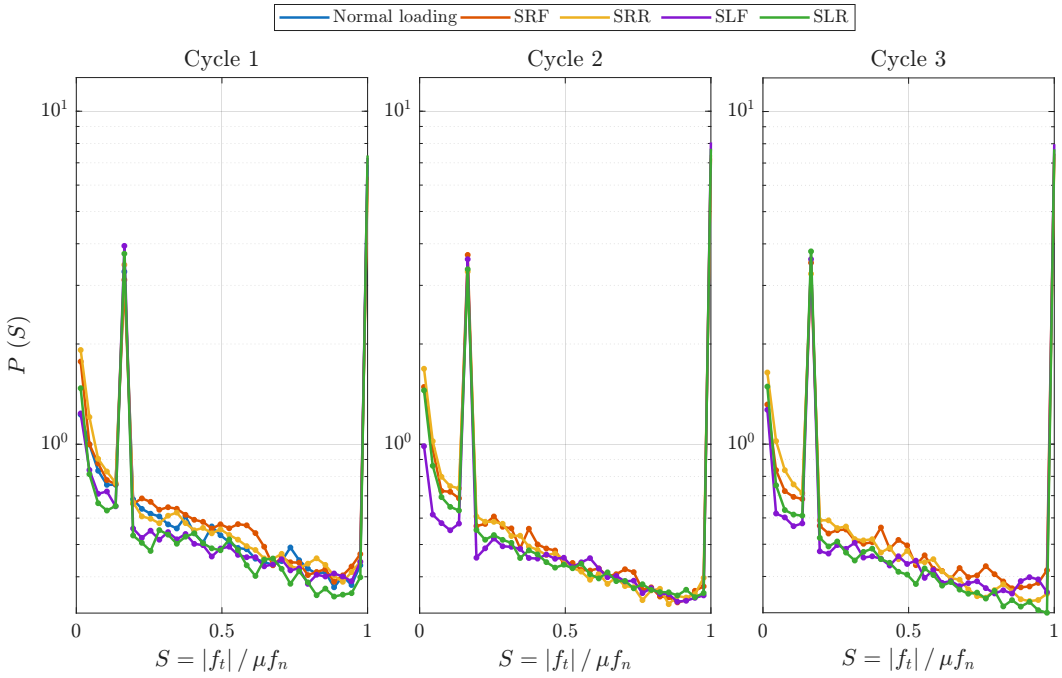


Figure 4.20: Per cycle evolution of the probability density function (PDF) of the mobilized friction, $S = |f_t|/\mu f_n$, for the dense assembly ($\sigma_n = -44.1$ kPa). Each panel shows one loading cycle, with all stages on a semi-log scale. Here, μ is the interparticle friction coefficient, and S indicates the proximity of a contact to sliding (Coulomb failure criterion).

Across all cycles, the position and magnitude of the peak evolve with the loading stage, reflecting changes in the mobilization of frictional resistance. In cycle 1, the peak occurs during SLF, consistent with the strong engagement of frictional contacts during leftward shearing. However, in later cycles, this peak shifts between stages, indicating a redistribution of frictional activity as the system evolves.

As cyclic loading progresses, the distributions become more tightly grouped at some stages and more widely separated at others, suggesting that the system alternates between uniform and localized mobilization of friction. In particular, all stages approach the asymptotic limit at $S = 1$, indicating that a subset of contacts constantly reaches near-failure conditions, even as the overall force network weakens.

In general, the force transmission results show that cyclic loading progressively alters the distribution and mobilization of forces within the granular assembly. The normal force PDFs indicate that, while the population of weak contacts remains largely unchanged, the strong-force network becomes less coherent, with high-force contacts redistributed across stages and cycles. The tangential force distributions further reveal that shear resistance becomes more diffuse, with fewer contacts sus-

taining large tangential forces and greater variability emerging in later cycles. This behavior is reflected in the mobilized friction distributions, which show that most contacts operate well below the sliding limit, while only a small subset approaches failure, with the location and intensity of this subset shifting across stages and cycles. Together, these results indicate that repeated cycling leads to a more distributed and less efficiently organized force-transmission network, thereby providing a mechanistic explanation for the observed reduction in anisotropy and the weakened correspondence between the force chain structure and the macroscopic shear stress.

4.2.2.4 Grain-Scale Response Summary

The grain-scale response of the three-cycle, densely packed granular assembly under $\sigma_n = -44.1$ kPa $\approx$ 122 lb (55.3 kg) reveals a progressive evolution of the contact network, force transmission pathways, and their relationship to the macroscopic behavior. While cycle 1 closely mirrors the baseline one-cycle experiment, subsequent cycles exhibit clear signs of structural conditioning, with reduced variability, weakened anisotropy, and increasingly diffuse force transmission.

The coordination number indicates that cyclic shearing results in a net loss of contacts. Thus, the granular assembly does not fully recover its initial packing configuration after each cycle. This loss of contacts is accompanied by increased fluctuation and stage-dependent restructuring, particularly near shear reversals, where the contact network must reorganize to accommodate changes in loading direction.

The evolution of force chains further reflects this restructuring. Although the overall number and total length of force chains exhibit similar trends to the baseline response, their behavior becomes increasingly variable and less stable with continued cycling. Measures of force chain density and participation indicate that, while a significant fraction of grains continue to carry above-average stress, a smaller and more variable portion of these grains organizes into coherent chain-like structures. This suggests that the strong network persists, but its organization becomes less efficient and more spatially distributed.

The anisotropy analysis reinforces this interpretation. While the contact fabric maintains a relatively stable geometric structure, the magnitudes of force anisotropy – particularly for the normal and tangential forces – decrease significantly with increasing number of cycles. This indicates that the directional bias in force transmission weakens over time, even as the underlying contact network remains largely intact. Moreover, the increasing misalignment among fabric, force, and stress direc-

tions highlights that effective load transmission depends on both the presence and orientation of contacts, as well as the distribution of forces they carry.

The loss of directional coherence is further reflected in the verification of the stress-force-fabric relationship. Although the SFF framework captures the overall structure of the invariant stress response, its predictive accuracy declines in later cycles, particularly as the experimental stress response weakens and becomes less asymmetric. These discrepancies arise because the theoretical formulation does not fully account for the reduced anisotropy and the evolving efficiency of force transmission under repeated loading.

The force transmission results provide direct insight into these changes. Although the population of weak contacts remains largely unchanged, the strong force network becomes less coherent, with high-force contacts redistributed across stages and cycles. Tangential forces, in particular, become more diffuse, indicating that shear resistance is increasingly distributed across a broader set of contacts rather than concentrated along well-defined force chains. The mobilized friction distributions further indicate that most contacts remain well below the failure level, with only a small, shifting subset approaching the sliding limit.

These results collectively demonstrate that repeated cyclic loading drives the granular assembly toward a state characterized by reduced anisotropy, reduced force chain coherence, and more distributed force transmission. Although the contact network continues to support the load, it does so less efficiently, with weaker directional organization and greater variability in force transmission. This evolution provides a mechanistic explanation for the observed macroscopic behavior, including a reduced shear stress response, increased path dependence, and a decreased correspondence between force chain structure and bulk stress.

4.3 Experiment # 2: Densely Packed, $\sigma_n = -29.6$ kPa

The second experiment is a densely packed granular assembly normally loaded to $\sigma_n = -29.6$ kPa, corresponding to 82 lb (37.2 kg). As in the first three-cycle experiment (Section 4.2), the granular assembly consists of 332 grains in total, of which 60 are boundary grains, and 272 are interior grains (these interior grains participate in the DIC and GEM analyses). The initial void ratio for this experiment is 0.247.

4.3.1 Macroscopic Response

Figure 4.1 shows the macroscopic mechanical response of the three-cycle, densely packed experiment, loaded by $\sigma_n = -29.6$ kPa. As previously done, the macroscopic response is evaluated through the evolution of stress ratio, μ, volumetric strain, ϵ_V, void ratio, e, and dilatancy, β, which together characterize the granular assembly's shear resistance, volume change, packing state, and shear-volume coupling under cyclic loading.

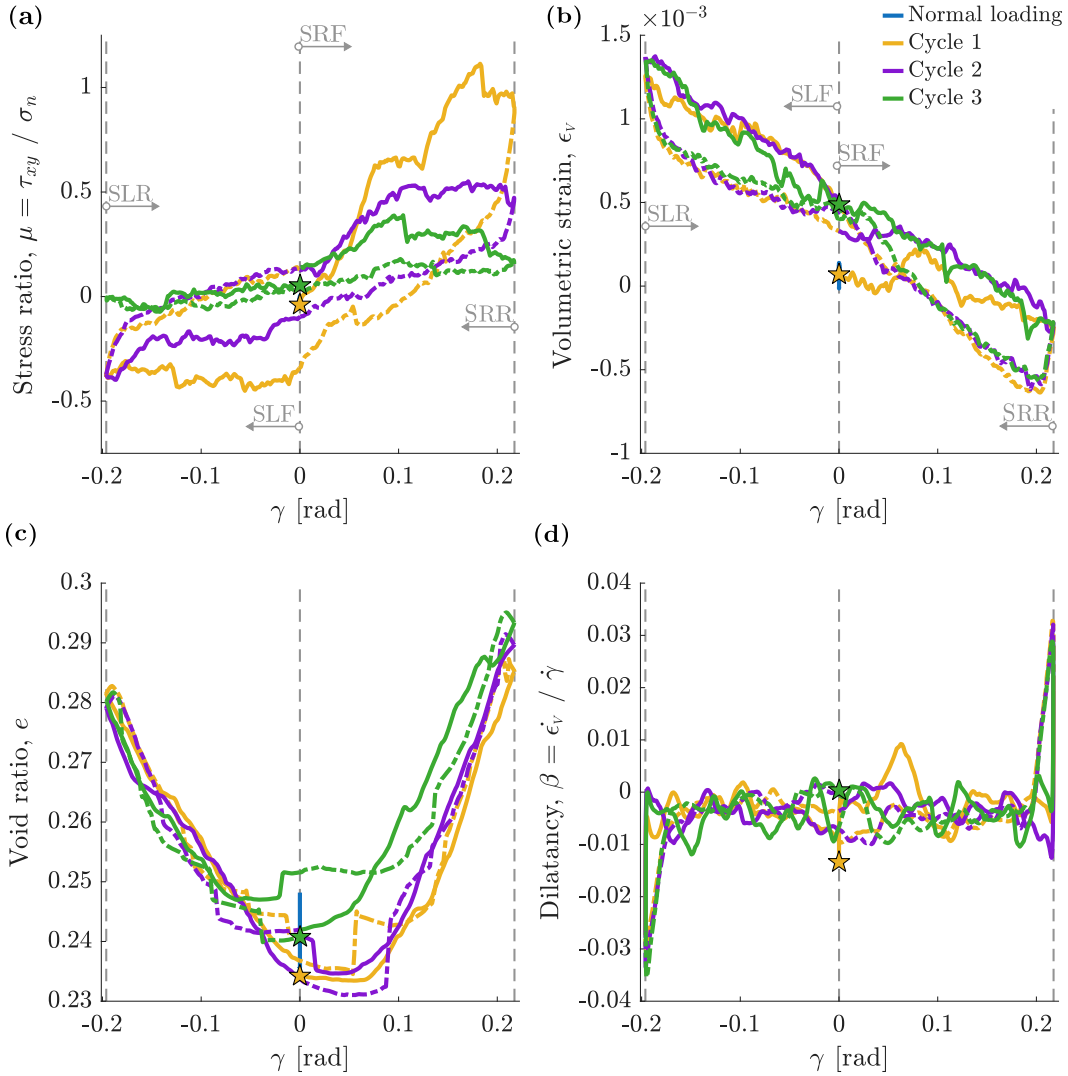


Figure 4.21: Macroscopic behavior of the three-cycle, densely packed granular assembly under $\sigma_n = -29.6$ kPa. (a) Stress ratio, μ, (b) volumetric strain, ϵ_V, (c) void ratio, e, and (d) dilatancy, β, as functions of shear strain, γ. Solid curves indicate forward shearing stages (SRF, SRR), whereas dash-dotted curves indicate reverse shearing stages (SLF, SLR). Furthermore, gray vertical dashed lines indicate shear-stage transitions. The yellow and green stars mark the start and end of the cyclic loading, respectively.

4.3.1.1 Stress Ratio

Figure 4.21a shows the evolution of the stress ratio, μ, as a function of shear strain. In general, the stress ratio response exhibits the same primary features observed in the more highly confined ($\sigma_n = -44.1$ kPa $\approx$ 122 lb) dense experiment, with several important quantitative and qualitative differences. For easier comparison between the two three-cycle, dense experiments, Figure 4.22 shows the μ responses side-by-side.

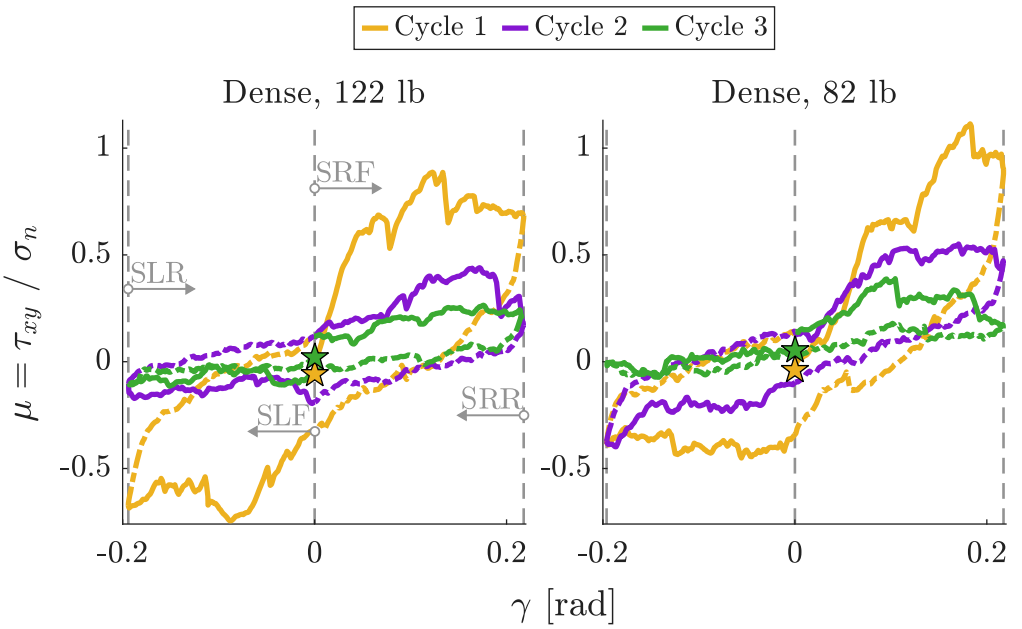


Figure 4.22: Stress ratio evolution for the two three-cycle, dense experiments. Left: higher-confinement ($\sigma_n = -44.1$ kPa $\approx$ 122 lb). Right: lower-confinement ($\sigma_n = -29.6$ kPa $\approx$ 82 lb). Curve style indicates shearing direction (solid: forward, dash-dotted: reverse), gray dashed lines mark stage transitions, and stars mark the start (yellow) and end (green) of cyclic loading.

As in the 122 lb case, two main trends are evident across all cycles: (1) the magnitudes of both the positive and negative stress ratio peaks decrease with increasing cycle number, and (2) the response remains directionally asymmetric, with consistently broader shear-right branches than shear-left branches. However, the stress ratio magnitudes are generally larger in the 82 lb case, particularly for the peak positive values. For example, μ_{max} occurs in cycle 1 for both experiments but reaches approximately 1.11 in the 82 lb case compared to 0.89 in the 122 lb case. This increase in the stress ratio at lower normal stress indicates that the assembly can mobilize greater shear resistance relative to the applied confinement, consistent with reduced confinement allowing more pronounced reorientation of force chains

and mobilization of friction.

Pronounced fluctuations are again observed near the end of the shear-right-forward (SRF), indicating significant internal restructuring during forward shearing. However, unlike the 122 lb case, where these fluctuations were primarily confined to cycles 1 and 2, the 82 lb normally-loaded assembly continues to exhibit similarly strong fluctuations in cycle 3. This persistence suggests that the assembly remains more dynamically active under lower confinement, with less progression toward a stabilized or repeatable response over successive cycles.

The evolution of the reverse-shear response with cycle number is also consistent with the more confined case. In cycles 1 and 2, the forward and reverse paths remain distinct for both the shear-right and shear-left branches, indicating continued hysteresis. By cycle 3, the shear-left-forward (SLF) and shear-left-reverse (SLR) paths largely overlap, and the shear-left branch remains close to zero, indicating that little reverse shear resistance is mobilized in that direction. This suggests that, despite differences in confinement, the dense assembly still evolves toward a strongly direction-dependent state under cyclic loading.

Several additional features distinguish the response from this 82 lb dense experiment from that of the 122 lb dense experiment. In cycle 2, μ shows a sharp decrease near the end of the SLF stage, producing a pronounced dip that was not observed under higher confinement. This drop causes the SLF path to approach the minimum value observed in cycle 1, resulting in a relatively large negative stress ratio magnitude for cycle 2. Similarly, in cycle 1, a local increase in μ is observed near the end of the shear-right-reverse (SRR) stage before gradually decreasing again, a feature not present in the more confined granular assembly. These additional fluctuations suggest that the internal contact network is less stable under lower normal stress and more susceptible to localized rearrangement events.

The overall geometry of the stress ratio loops also shows subtle but important differences when compared to the more highly confined case. In particular, the rightward branch of cycle 1 in the 82 lb experiment is narrower than that observed in the 122 lb experiment. This suggests that under lower confinement, the load-bearing force chain network is less stable and cannot sustain high levels of shear resistance over an extended strain range, leading to more transient, localized mobilization of strength during forward shearing.

Together, these results indicate that lowering the normal stress does not fundamentally change the qualitative cyclic response of the dense assembly, but instead increases its sensitivity to internal restructuring and the magnitude of mobilized shear resistance. Although the 82 lb experiment reaches a higher peak stress ratio than the 122 lb case, the narrower rightward branch in cycle 1 indicates that this resistance is mobilized over a smaller strain range. This suggests that under lower confinement, the load-bearing contact network is less stable and less capable of sustaining high shear resistance during forward shearing. As a result, the assembly retains the strongly path-dependent and directionally asymmetric behavior observed under higher confinement, while exhibiting a more transient and dynamically evolving stress response.

4.3.1.2 Volumetric Strain

Figure 4.21b shows the volumetric strain, ϵ_V, as a function of shear strain for the densely packed granular assembly under $\sigma_n = -29.6\,\text{kPa}$ (approximately 82 lb). Overall, the response exhibits the same primary features observed in the more highly confined 122 lb case, including stage-dependent contraction and dilation, repeated restructuring near reversal, and persistent directional asymmetry. However, under lower normal stress, these features evolve more gradually and remain active later in the loading history, indicating slower volumetric stabilization. Figure 4.23 compares the responses of the 122 lb (left) and 82 lb (right) densely packed experiments.

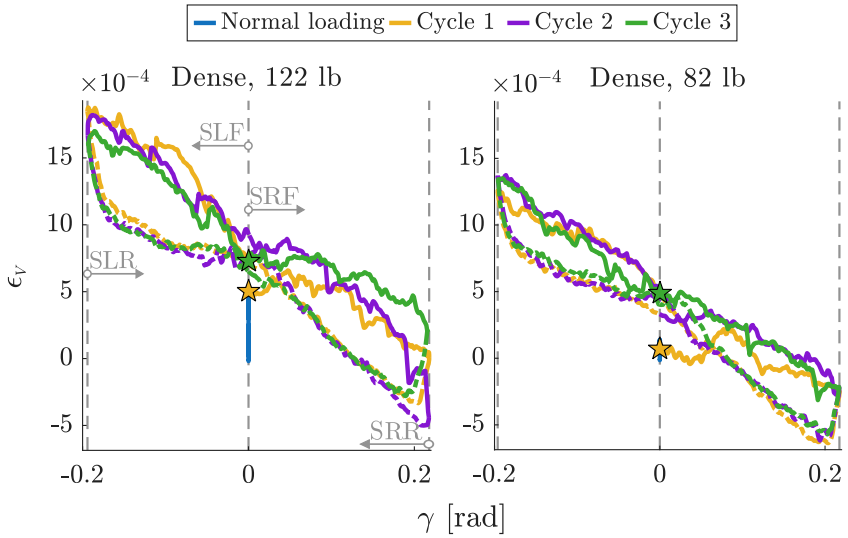


Figure 4.23: Volumetric strain evolution for the two three-cycle, dense experiments. Left: higher-confinement ($\sigma_n = -44.1$ kPa $\approx$ 122 lb). Right: lower-confinement ($\sigma_n = -29.6$ kPa $\approx$ 82 lb). Curve style indicates shearing direction (solid: forward, dash-dotted: reverse), gray dashed lines mark stage transitions, and stars mark the start (yellow) and end (green) of cyclic loading.

The first noticeable difference appears during the normal loading stage. Whereas the 122 lb dense assembly exhibited a monotonic decrease in ϵ_V during normal loading, indicating sustained densification, the 82 lb assembly undergoes only a small initial increase in ϵ_V before partially decreasing again. Additionally, while both dense experiments result in a higher volumetric strain at the end of cycle 3 than at the beginning of cycle 1, the overall ϵ_V change is greater in the 82 lb case than in the more confined assembly. These observations suggest that under lower normal stress, the granular assembly exhibits a less stable, less uniformly consolidating loading response, remaining more susceptible to early rearrangement or partial volumetric relaxation even before cyclic shearing begins.

During cycle 1, the assembly again exhibits an initial compressive regime at the onset of the shear-right-forward (SRF) stage before transitioning to dilation, consistent with the behavior observed in the 122 lb case. However, in the 82 lb case, this initial compressive regime persists over a longer strain interval before dilation begins. This suggests that under lower confinement, the assembly requires more forward shearing before transitioning from packing adjustment to shear-induced expansion. In this sense, the dense experiment still exhibits the same qualitative volumetric mechanism, but the transition into fully dilative behavior is delayed.

The evolution across cycles also differs from that in the more confined case. In the 122 lb experiment, cycle 2 exhibited the clearest and largest volumetric excursion during SRF, beginning at the highest ϵ_V and ending at the lowest ϵ_V. In contrast, in the 82 lb case, the cycle-to-cycle progression is less cleanly ordered: cycle 3 begins at the highest ϵ_V, while cycle 2 reaches the lowest ϵ_V by the end of SRF. In addition, although cycle 3 generally remains above cycle 1 during SRF, it briefly dips below it near the end of the stage. Together, these features suggest that the volumetric response under lower confinement remains more dynamically distributed across later cycles, rather than concentrating its strongest restructuring into cycle 2 as in the 122 lb case.

As in the baseline experiment and the more highly confined dense experiment, all three cycles exhibit rapid decreases in ϵ_V immediately after shear reversal, followed by a smoother evolution as deformation continues. These abrupt drops again suggest transient restructuring events in which the previously established contact network becomes mechanically incompatible with the reversed loading direction and must reorganize into a new load-bearing configuration. However, a notable difference is that the additional pronounced dilation events before shear reversal – previously

observed in cycle 2 of the 122 lb experiment – now shift to cycle 3 in the 82 lb case. This again demonstrates that under lower confinement, major internal restructuring persists later in the loading history, and volumetric response takes longer to settle into a repeatable cyclic pattern.

The overall loop geometry remains strongly asymmetric. All three cycles exhibit self-intersecting forward and reverse paths, indicating that the volumetric state depends not only on the current shear strain but also on the deformation path history. In addition, the reverse stages again exhibit less fluctuation and variability than the forward stages, suggesting that reverse loading is accommodated by smoother and more stable volumetric adjustment. However, a notable difference from the highly confined case is that the 82 lb curves exhibit substantially greater overlap near the stage-reversal regions. Whereas the 122 lb experiment shows clearer cycle separation at these transition points, the 82 lb experiment response tends to pass through more similar volumetric states across the cycles. This suggests that, under reduced normal stress, the assembly more readily revisits similar transition configurations during shear reversal, even if the subsequent stage-wise evolution remains cycle-dependent.

Collectively, these results indicate that reducing the normal stress does not fundamentally change the qualitative volumetric behavior of the dense assembly, but instead delays and prolongs the internal restructuring associated with cyclic shearing. The assembly continues to deform through compaction, dilation, and reversal-driven organization, but under lower confinement, these processes remain active into later cycles rather than stabilizing early in the loading history.

4.3.1.3 Dilatancy

Figure 4.21d shows the dilatancy, β, as a function of shear strain, γ, for the three-cycle, densely packed experiment under a normal load of $\sigma_n = -29.6$ kPa ($\approx$ 82 lb). As in the more highly confined assembly, β is interpreted in conjunction with volumetric strain, ϵ_V, with peaks and extrema corresponding to stages of intensified internal rearrangement and smoother regions indicating more stable deformation. Overall, the dilatancy response retains the same stage-dependent and directionally asymmetric structure observed in the 122 lb case, but with weaker extrema, more gradual evolution, and less distinct cycle-to-cycle differentiation. Figure 4.24 shows the β response of the dense, 122 lb experiment (left) and dense, 82 lb experiment (right). For a cycle-by-cycle comparison of these densely packed experiments, refer to Appendix B, Figure B.1.

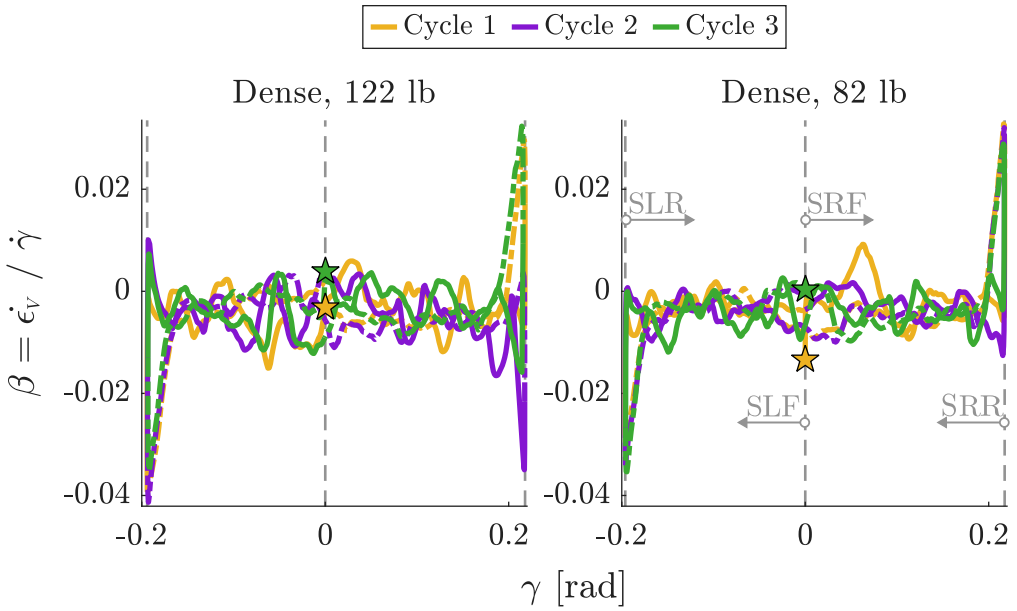


Figure 4.24: Dilatancy evolution for the two three-cycle, dense experiments. Left: higher-confinement ($\sigma_n = -44.1$ kPa $\approx$ 122 lb). Right: lower-confinement ($\sigma_n = -29.6$ kPa $\approx$ 82 lb). Curve style indicates shearing direction (solid: forward, dash-dotted: reverse), gray dashed lines mark stage transitions, and stars mark the start (yellow) and end (green) of cyclic loading.

Across all three cycles, the reverse-shear stages (SLF and SLR) again exhibit less fluctuation and variability than the forward-shear stages (SRF and SRR), corresponding to the smoother, near-linear regimes observed in the ϵ_v response. In contrast, the forward stages continue to exhibit more pronounced fluctuations, suggesting that they are associated with more active internal restructuring. In cycle 1, both experiments exhibit an initial peak in β at the onset of forward shear; however, in the 82 lb case, this peak occurs at a higher magnitude and at a later strain, consistent with the extended initial compression regime observed in ϵ_v under lower confinement.

A key difference from the 122 lb experiment is the reduced strength and clarity of the dilatancy extrema. In the more confined case, all three cycles exhibited a pronounced decrease in β near the end of shear-right-forward (SRF), with cycles 2 and 3 reaching clear minima. In contrast, in the 82 lb experiment, only cycle 2 exhibits a pronounced minimum during SRF, while cycles 1 and 3 show relatively weak deviations from their mean response. Furthermore, the minimum attained by cycle 2 is substantially smaller in magnitude than in the 122 lb case. This indicates that, under reduced normal stress, forward shearing is less effective at mobilizing strong dilation and that the coupling between shear deformation and volumetric

expansion is correspondingly weaker.

Following reversal into the shear-right-reverse (SRR) stage, β again exhibits a rapid transition before settling into a smoother regime. However, unlike the 122 lb case, where cycle 2 stabilized the quickest out of all cycles, all three cycles in the 82 lb case stabilize at approximately the same rate. In addition, cycles 2 and 3 exhibit noticeable fluctuations near the end of SRR, which are also present in the 122 lb experiment but with significantly smaller amplitudes. These features suggest that, under lower confinement, the transition into stable reverse-shear deformation is less sharply differentiated across cycles and remains more dynamically active.

A similar but sign-reversed behavior occurs in the leftward branch. Near the end of the shear-left-forward (SLF) stage, all three cycles exhibit a strong β response corresponding to the contractive behavior in ϵ_v. However, the extrema in cycles 2 and 3 are again significantly weaker than those observed in the 122 lb case. After reversal into the SLR stage, β rapidly adjusts before approaching a weaker, near-steady regime. While the magnitude of the initial SLF extrema remains comparable across cycles in the 82 lb experiment, the corresponding extrema in the 122 lb experiment are generally more pronounced, particularly for cycle 2.

The locations of the maximum and minimum β values also shift under reduced confinement. In the 122 lb experiment, the minimum occurred in cycle 2, and the maximum occurred in cycle 3. In the 82 lb experiment, the minimum occurs in cycle 3 and the maximum in cycle 1. This redistribution of extrema further indicates that the strongest shear-volume coupling is no longer confined to the early cycles but instead remains active and evolves throughout the entire loading history.

Finally, the overall cycle-scale dilatancy evolution shows a larger net change in the 82 lb case than in the 122 lb case. In the 122 lb dense experiment, the granular assembly exhibited a modest shift in β between the start and end of cyclic loading. For the 82 lb dense experiment, β begins at a more negative value and ends at a value closer to zero, resulting in a larger overall change. This suggests that, although the instantaneous coupling between shear and volumetric change is weaker under lower confinement, the cumulative evolution of this coupling over the loading history is more pronounced.

Together, these observations indicate that reducing the normal stress weakens the intensity of shear-volume coupling while simultaneously making its evolution more gradual and more broadly distributed across cycles. The dense assembly continues to

exhibit directionally asymmetric and stage-dependent dilatancy behavior, but under lower confinement, the response becomes less sharply organized, less dominated by early-cycle restructuring, and more persistently influenced by ongoing internal rearrangement.

4.3.1.4 Void Ratio

Figure 4.21c shows the void ratio, e, as a function of shear strain, γ, for the three-cycle, densely packed experiment under a normal load of $\sigma_n = -29.6$ kPa (≈ 82 lb). Overall, the void ratio response exhibits the same primary opening and closing trends observed in the more highly confined dense experiment, but with greater cycle-to-cycle variability, more abrupt restructuring events, and a larger residual loosening by the end of the loading history. Figure 4.25 shows the void ratio evolution of the two differently confined experiments side-by-side.

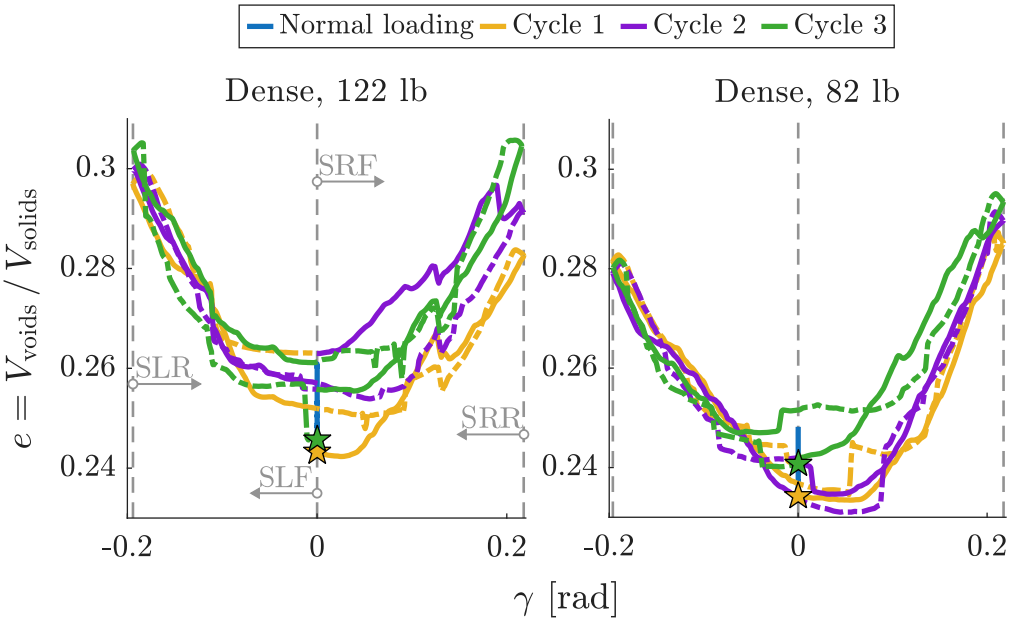


Figure 4.25: Void ratio evolution for the two three-cycle, dense experiments. Left: higher-confinement ($\sigma_n = -44.1$ kPa ≈ 122 lb). Right: lower-confinement ($\sigma_n = -29.6$ kPa ≈ 82 lb). Curve style indicates shearing direction (solid: forward, dash-dotted: reverse), gray dashed lines mark stage transitions, and stars mark the start (yellow) and end (green) of cyclic loading.

As in the 122 lb dense experiment, the forward shearing stages are generally associated with a gradual increase in void ratio, while the reverse stages exhibit a gradual decrease. These trends are consistent with the dilation and contraction observed in the volumetric strain response, indicating that the packing structure continues to open systematically during forward shearing and close during reverse shearing.

Thus, the fundamental cyclic packing mechanism remains unchanged under reduced confinement.

A second consistent feature is that the maximum void ratio in each cycle occurs immediately after shear reversal. This again suggests that the loosest packing states are reached when the previously established contact network becomes mechanically incompatible with the reversed loading direction, necessitating reorganization into a new configuration. However, unlike the 122 lb case, where the peak void ratio values followed a more systematic ordering across cycles, the 82 lb response is less uniform. The ordering of the peak void ratios remains consistent only along the rightward branch (increasing cycles leading to higher e values), whereas in the leftward branch, the cycle ranking rearranges, with cycle 1 reaching the largest peak void ratio and cycle 2 the smallest. This less orderly progression suggests that under lower confinement, the evolution of the packing state becomes more sensitive to local rearrangement history and less consistently organized across cycles.

A particularly notable difference from the 122 lb experiment occurs in the portions of the cycle that previously exhibited near-constant void ratio. In the more highly confined assembly, across all cycles, the void ratio remained nearly constant toward the end of the shear-right-reverse (SRR) stage and into the shear-left-forward (SLF) stage, suggesting a quasi-steady deformation regime. In contrast, in the 82 lb assembly, cycles 1 and 2 exhibit a pronounced staircase-like drop in e near the end of SRR, while cycle 3 exhibits a similar drop at the beginning of SLF. These abrupt decreases suggest that, under lower confinement, the granular assembly is less able to maintain a stable, quasi-steady packing evolution and instead undergoes sudden, localized restructuring events, even within stages that were previously comparatively stable.

Another important directional difference is that the shear-right branch exhibits greater variability and cycle-to-cycle separation, whereas the shear-left branch remains comparatively tighter and less fluctuating. In particular, the three cycles become nearly indistinguishable near the leftward transition between SLF and shear-left-reverse (SLR), while they remain clearly separated near the corresponding rightward transition. This suggests that the assembly more readily visits similar packing states during leftward reversal than during rightward reversal, further emphasizing the directional bias in the evolution of the packing structure under cyclic loading.

Lastly, as in the 122 lb experiment, the final void ratio at the end of the loading history remains greater than the value at the onset of cyclic shear, indicating that the assembly does not fully recover its initial packing state. However, this residual increase is substantially larger in the 82 lb experiment (+0.0065) than in the 122 lb case (+0.0024), indicating that lower confinement results in a more persistently loose final configuration. Hence, although much of the cyclic opening and closing of the packing structure remains recoverable, the assembly exhibits a greater degree of irreversible structural loosening under reduced normal stress.

As a whole, these results indicate that lowering the normal stress does not fundamentally alter the cyclic opening and closing behavior of the dense granular assembly, but instead makes the packing evolution less uniform, more prone to restructuring, and less fully recoverable. Under reduced confinement, the assembly still repeatedly visits similar packing states during cyclic loading, but does so with greater sensitivity to local rearrangement history and with a larger residual e between the end and start of cyclic loading.

4.3.1.5 Macroscopic Response Summary

The macroscopic response of the three-cycle, densely packed granular assembly under $\sigma_n = -29.6$ kPa $\approx$ 82 [lb] indicates that reducing the normal stress does not fundamentally alter the qualitative cyclic behavior of the dense assembly, but instead changes how that behavior develops and persists over the loading history. As in the more highly confined, dense experiment, the response remains strongly path-dependent and directionally asymmetric, with a progressive reduction in the stress ratio peaks, repeated volumetric restructuring near reversals, hysteretic packing evolution, and incomplete recovery of the initial state. However, under lower confinement, the assembly mobilizes higher stress ratios, exhibits more persistent restructuring into later cycles, and shows a less sharply stabilized response throughout the loading history. The volumetric strain and void ratio responses further indicate that the assembly remains more prone to restructuring and less fully recoverable, ultimately evolving toward a final looser packing state than in the 122 lb case. Additionally, the dilatancy response suggests that the strongest shear-volume coupling events are less intense and more gradually distributed across cycles. Overall, these results indicate that lower confinement preserves the same dense granular response mechanisms but makes the assembly less structurally constrained, less rapidly conditioned, and more persistently sensitive to internal rearrangement under cyclic loading.

4.3.2 Grain-Scale Response

The macroscale response (Figure 4.21) suggests a more gradual restructuring of the granular assembly under lower confinement. We now examine this behavior at the grain-scale, focusing on the contact network, force transmission, and their roles in governing the observed behavior.

4.3.2.1 Coordination Number

The coordination number, Z_c, reflects the connectivity of the contact network and provides information on how the granular assembly redistributes contacts under cyclic loading. Figure 4.26 shows the coordination number as a function of shear strain, and Figure 4.27 shows its evolution per stage.

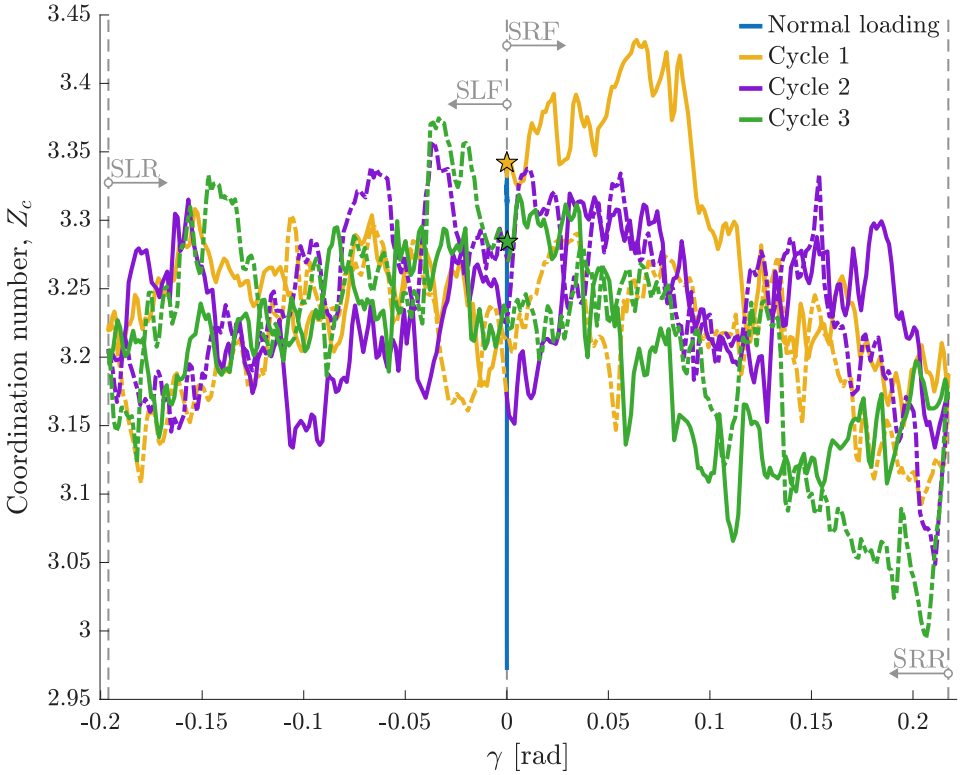


Figure 4.26: Evolution of the coordination number, Z_c, for the dense granular assembly ($\sigma_n = -29.6$ kPa). Z_c is the average number of contacts per particle. Curve style indicates shearing direction (solid: forward, dash-dotted: reverse), gray dashed lines mark stage transitions, and stars mark the start (yellow) and end (green) of cyclic loading.

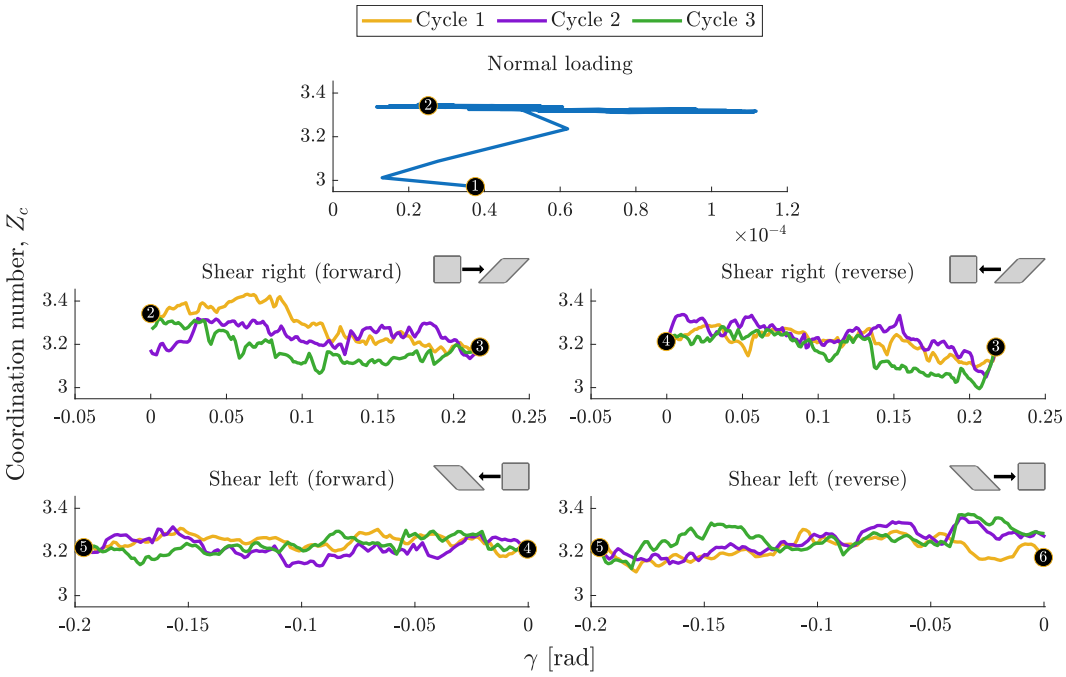


Figure 4.27: Per-stage evolution of the coordination number, Z_c, for the dense granular assembly ($\sigma_n = -29.6$ kPa). Stage markers are shown only for Cycle 1.

Compared to the higher-confinement case ($\sigma_n = -44.1$ kPa), the 82 lb experiment exhibits both a higher minimum and maximum coordination number, as well as a smaller net loss of contacts over the loading history. While both assemblies experience a reduction in Z_c between the onset of shear, the decrease is significantly smaller under lower confinement, indicating that the network remains more stable and less degraded.

During normal loading, Z_c increases more substantially than in the higher-confined case, reflecting greater initial contact formation as the assembly compacts. Upon the onset of shearing (shear-right-reverse (SRR)), all cycles exhibit an overall decreasing trend, consistent with contact loss due to particle rearrangement. However, unlike the 122 lb experiment, cycles 1 and 2 show a brief initial increase, suggesting that under lower confinement, the assembly undergoes additional contact formation before significant rearrangement occurs. In later cycles, this response becomes smoother and more gradual, indicating a more stable but progressively weakening contact network.

Upon shear reversal (shear-right-reverse (SRR)), all cycles initially lose contacts before transitioning to a recovery phase, during which new contacts form as the network reorganizes. A key difference from the higher-confinement case is that the initial contact loss occurs along nearly overlapping paths, indicating a consistent

response across cycles, albeit with different magnitudes. This suggests that under lower confinement, the contact network responds more uniformly to reversal, even though the extent of restructuring varies. However, increased fluctuations – particularly in cycle 3 – indicate that the network becomes more dynamically unstable during this stage compared to the 122 lb experiment.

A similar pattern is observed during the final stage (shear-left-reverse (SLR)), where all cycles initially lose contacts and then partially recover. Unlike the higher-confinement case, where only one cycle retained an increased coordination number, multiple cycles in the 82 lb experiment recovered to higher values by the end of the stage. Thus, under lower confinement, the contact network retains a greater capacity for reformation and recovery following shear reversal. At the same time, the increased variability – especially in cycle 3 – indicates that this recovery is less uniform and more sensitive to local rearrangements.

During the shear-left-forward (SLF) stage, the behavior diverges further from the higher confined case. While cycle 1 exhibits a relatively stable and slightly increasing trend, cycles 2 and 3 show increased fluctuations within a narrow range of Z_c, accompanied by an overall decrease. This suggests that repeated cycling leads to a more localized and intermittent restructuring process, rather than the more uniform contact loss observed in the 122 lb experiment. The persistence of fluctuations near shear reversal, particularly in cycle 3, further highlights the increasing sensitivity of the contact network to loading history.

Overall, the coordination number results show that reducing confinement leads to a more resilient and more dynamically variable contact network. Although the assembly retains a higher level of connectivity and experiences a smaller net loss of contacts, it also exhibits greater fluctuations and less uniform evolution across stages and cycles. This suggests that under lower confinement, the granular assembly accommodates deformation through more distributed and intermittent contact rearrangements, rather than the more systematic and pronounced restructuring observed at higher confinement.

4.3.2.2 Force Chain Statistics and Evolution

Although the coordination number describes the overall connectivity of the contact network, it does not distinguish between contacts that actively carry load and those that form the primarily load-bearing skeleton of the granular assembly. Therefore, this section examines the evolution of detected force chains to provide a deeper

insight into how stress is transmitted and redistributed during cyclic loading.

Number of Detected Force Chains The number of detected force chains reflects the fragmentation and reorganization of the strong force-bearing network under cyclic loading. Figure 4.28 shows the number of force chains as a function of shear strain, γ, and Figure 4.29 shows its evolution per stage.

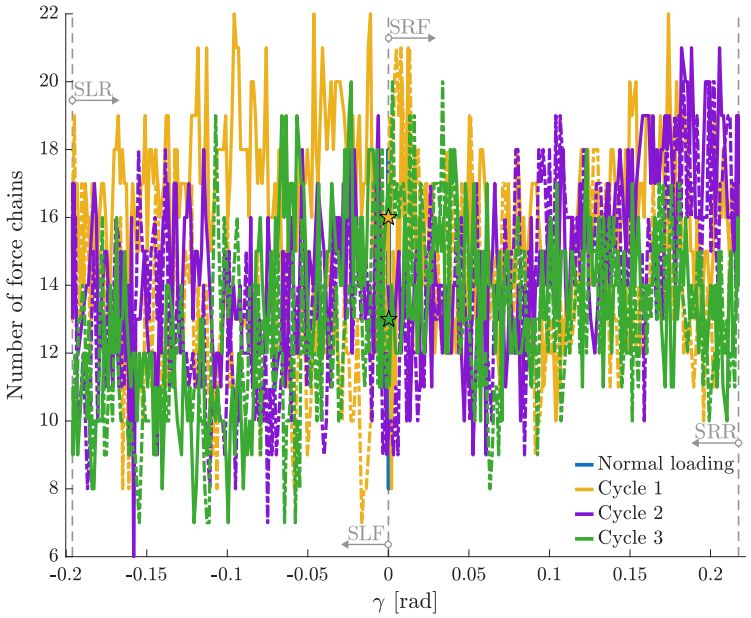


Figure 4.28: Evolution of the detected number of force chains for the dense granular assembly ($\sigma_n = -29.6$ kPa). Curve style indicates shearing direction (solid: forward, dash-dotted: reverse), gray dashed lines mark stage transitions, and stars mark the start (yellow) and end (green) of cyclic loading.

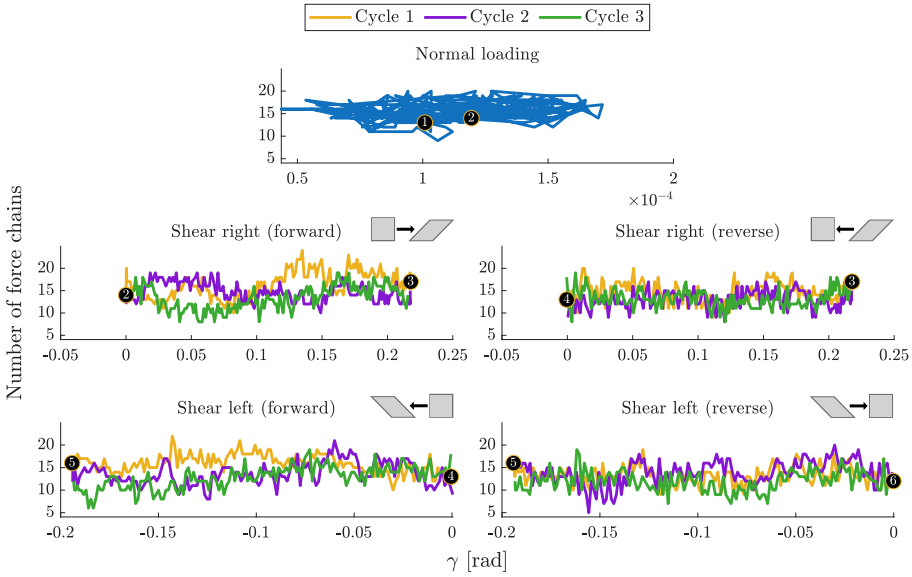


Figure 4.29: Per-stage evolution of the detected number of force chains for the dense granular assembly ($\sigma_n = -29.6$ kPa). Stage markers are shown only for Cycle 1.

Compared to the higher confined experiment, the 82 lb experiment exhibits a higher minimum but a smaller maximum number of force chains, indicating that the strong network is more uniformly distributed but less capable of forming highly concentrated load-bearing structures. In both cases, the maximum occurs during the shear-right-forward (SRF) stage in cycle 1, although under lower confinement, multiple local maxima appear across the shear-right stages, reflecting a more variable response.

During normal loading, the number of force chains increases overall, but with substantial fluctuations as successive load increments are applied. This variability indicates that the strong force network undergoes repeated cycles of formation and relaxation, rather than developing monotonically.

Upon the onset of shearing (SRR), the cycles exhibit greater overlap than in the higher-confinement case, suggesting a more uniform response across cycles. Cycles 2 and 3 show a net increase in force chains, indicating progressive development of the strong network, while cycle 1 initially loses force chains before recovering. Despite these differences, all cycles exhibit an abrupt drop near shear reversal, reflecting the breakdown of existing force chains as the network reorganizes to accommodate the new loading direction.

In the shear-right-reverse (SRR) stage, all cycles initially lose force chains before transitioning to a regime of reformation. Compared to the 122 lb experiment, the responses remain more tightly grouped, indicating a more consistent restructuring process across cycles. However, the evolution becomes increasingly variable, with cycle 2 transitioning from a relatively high to a low force chain count and cycle 3 showing the opposite trend. Overall, the stage is characterized by a net decrease in force chains, suggesting that reversal promotes fragmentation of the strong force network.

In the final stage (shear-left-reverse (SLR)), the behavior diverges further across cycles. Cycles 1 and 2 exhibit a gradual, fluctuating evolution with a net loss of force chains, while cycle 3 shows a more abrupt transition between two quasi-steady states, ultimately ending with a greater number of force chains. Despite these differences, the responses remain within a relatively narrow range, indicating that the strong network is less extreme but more constrained under lower confinement.

During the shear-left-forward (SLF) stage, the 82 lb experiment exhibits greater fluctuations and more distinct cycle-dependent behavior than the higher-confinement

case. In contrast to the shear-right stages, where responses remain largely overlapped, the shear-left stages show increased separation, indicating that the strong force network becomes more sensitive to loading history in these stages.

Overall, the force chain results show that reducing confinement leads to a more distributed but less strongly organized force chain network. Although the system maintains a relatively consistent number of force chains across cycles, these structures are less stable and more prone to fluctuations, reflecting a shift from concentrated, coherent load-bearing pathways to a more intermittent, spatially distributed force-transmission mechanism.

Total Force Chain Length The total force chain length, measured in number of grains, accounts for both the number and size of individual force chains. Figure 4.30 shows the total force chain length as a function of shear strain, while Figure 4.31 shows its per-stage evolution.

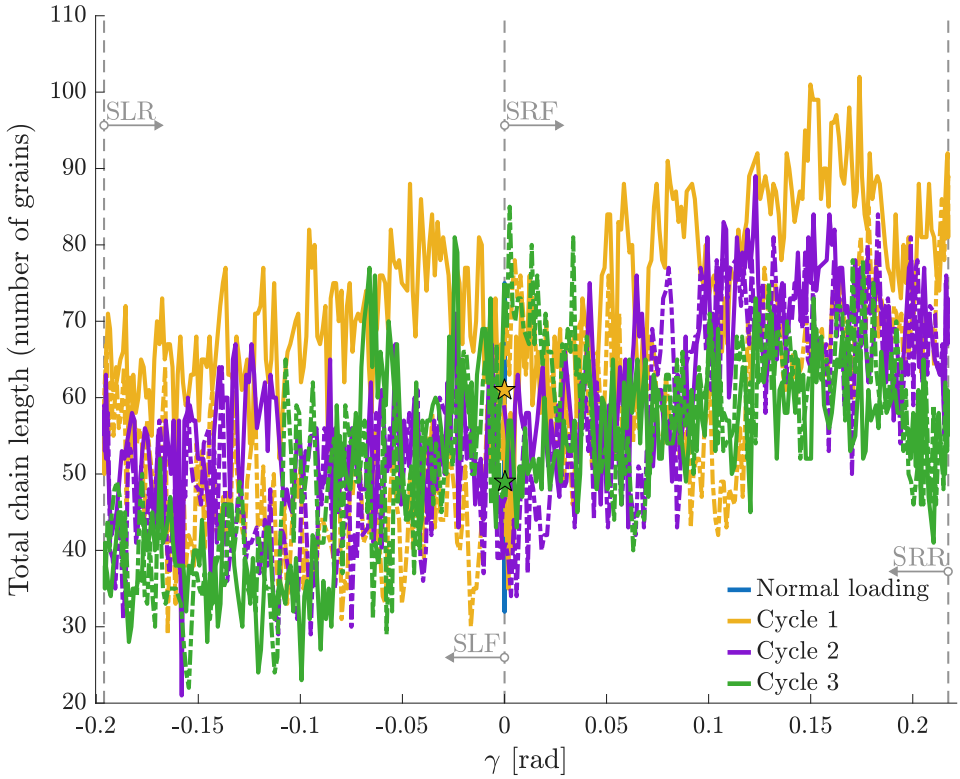


Figure 4.30: Evolution of the total force chain length, in number of grains, for the dense granular assembly ($\sigma_n = -29.6$ kPa). Curve style indicates shearing direction (solid: forward, dash-dotted: reverse), gray dashed lines mark stage transitions, and stars mark the start (yellow) and end (green) of cyclic loading.

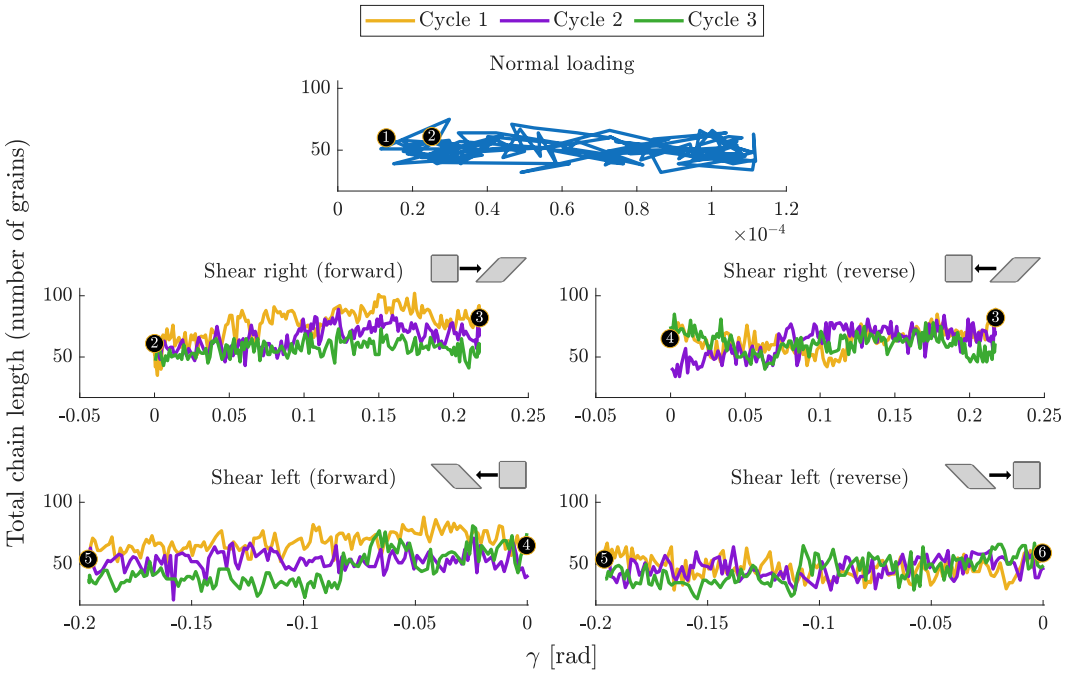


Figure 4.31: Per-stage evolution of the total force chain length, in number of grains, for the dense granular assembly ($\sigma_n = -29.6$ kPa). Stage markers are shown only for Cycle 1.

Overall, the total force chain length exhibits trends broadly similar to those observed for the detected number of force chains. This similarity indicates that the evolution of the strong network is primarily governed by changes in the number of force chains, with only secondary contributions from variations in their individual lengths. However, noticeable differences emerge during the shear-right-forward (SRF) stage. While the number of force chains remains largely overlapped across cycles for much of the stage, the total chain length shows earlier and more pronounced separation. In particular, cycle 1 maintains the largest force chain structure throughout the stage, exhibiting an overall increase in total chain length despite a brief dip near shear reversal. In contrast, later cycles initially evolve together before diverging, with cycle 2 ultimately developing a larger force chain network than cycle 3. Hence, under lower confinement, differences in chain growth and extension become more significant than differences in force chain count alone.

Consistent with the higher-confinement case, both experiments attain a minimum total chain length of approximately 21 grains and a maximum of approximately 102 grains, with the maximum occurring during SRF in cycle 1. However, the overall reduction in force chain length across the loading history is much smaller under lower confinement. While the 122 lb case exhibits a substantial loss of total chain

length, the 82 lb experiment shows only a modest decrease, indicating that the force chain network remains more persistent.

Taken together, these results suggest that reducing the applied normal load leads to a force chain network that is less extreme in its growth but more resilient under repeated cycles. Although the network does not develop as large or concentrated structures, it retains a greater portion of its overall extent, indicating a shift toward a more distributed and sustained load-bearing framework, rather than one dominated by large, highly localized force chains.

Accumulated Force Chain Network Content Figure 4.32 shows the normalized accumulated force chain network content. This metric represents the average size of the force chain network sustained per unit shear deformation and quantifies the persistence of the strong force network across each stage.

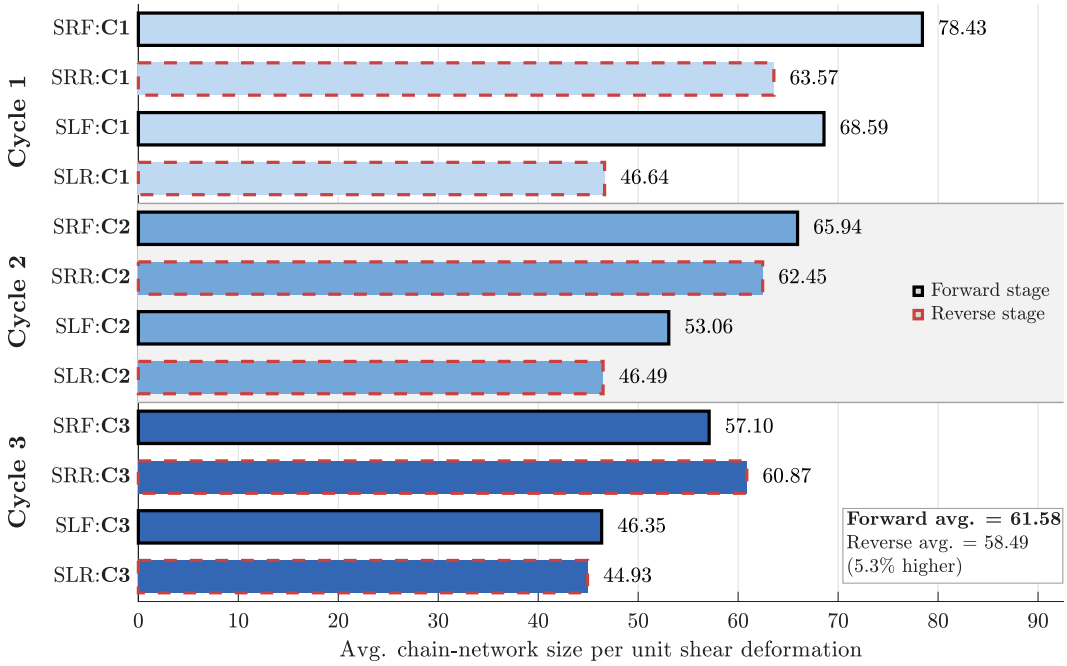


Figure 4.32: Bar chart of the normalized area under the curve (AUC) of the total force chain length for each cycle and shear stage for the dense assembly ($\sigma_n = -29.6\,\text{kPa}$). The normalized AUC represents the average extent and persistence of the force chain network sustained per unit shear deformation within each stage.

As in the higher confined case, the forward-shear stages exhibit a larger average AUC than the reverse-shear stages. However, under lower confinement, this difference is reduced, with the forward stages exceeding the reverse stages by only about 5.3%, indicating a weaker distinction between the loading directions.

In cycle 1, the stage-wise behavior closely follows that of the higher-confinement

case. The AUC reaches its maximum during shear-right-forward (SRF), decreases during shear-right-reverse (SRR), partially recovers during shear-left-forward (SLF), and drops significantly during shear-left-reverse (SLR). This progression reflects the initial development, disruption, and partial reformation of the force chain network as the loading direction evolves.

In contrast, cycle 2 exhibits markedly different behavior. While SRF again produces a recovery in AUC, the magnitude of this recovery is smaller than that observed in the previous cycle. The subsequent stages are characterized by progressive, large decreases in AUC, indicating sustained weakening of the force chain network. This behavior differs in the higher-confinement case, where the AUC evolved more gradually, suggesting that under lower confinement, the network becomes more sensitive to cyclic degradation.

A similar but more pronounced recovery occurs at the transition from cycle 2 to cycle 3, where the AUC increases sharply during SRF. This recovery is significantly larger than that observed under higher confinement, indicating that the network retains a greater capacity for reformation following prior degradation. However, the peak AUC in cycle 3 remains lower than in earlier cycles, reflecting an overall decline in network persistence.

In the 122 lb experiment, cycle 3 was characterized by a monotonic decrease in AUC across stages, indicating continued weakening of the force chain network. Although the 82 lb experiment observes this same behavior during the shear-left stages, a key difference occurs during SRR, where it shows a temporary increase in AUC, attaining a value exceeding that during SRF. This behavior suggests that under lower confinement, the force chain network can undergo localized strengthening during reversal, even as the overall structure continues to degrade.

Overall, the AUC results indicate that reducing confinement leads to a force chain network that is less persistent and more sensitive to cyclic degradation, but also more capable of intermittent recovery and reformation. This behavior reflects a shift from a steadily evolving network under higher confinement to one that exhibits greater variability and episodic restructuring at the grain-scale.

Force Chain Participation The force chain density provides a measure of grains participating in the force chain network and reflects both the extent and organization of the strong force-bearing structure. Figure 4.33 shows violin plots of the force chain density for each shear stage and cycle.

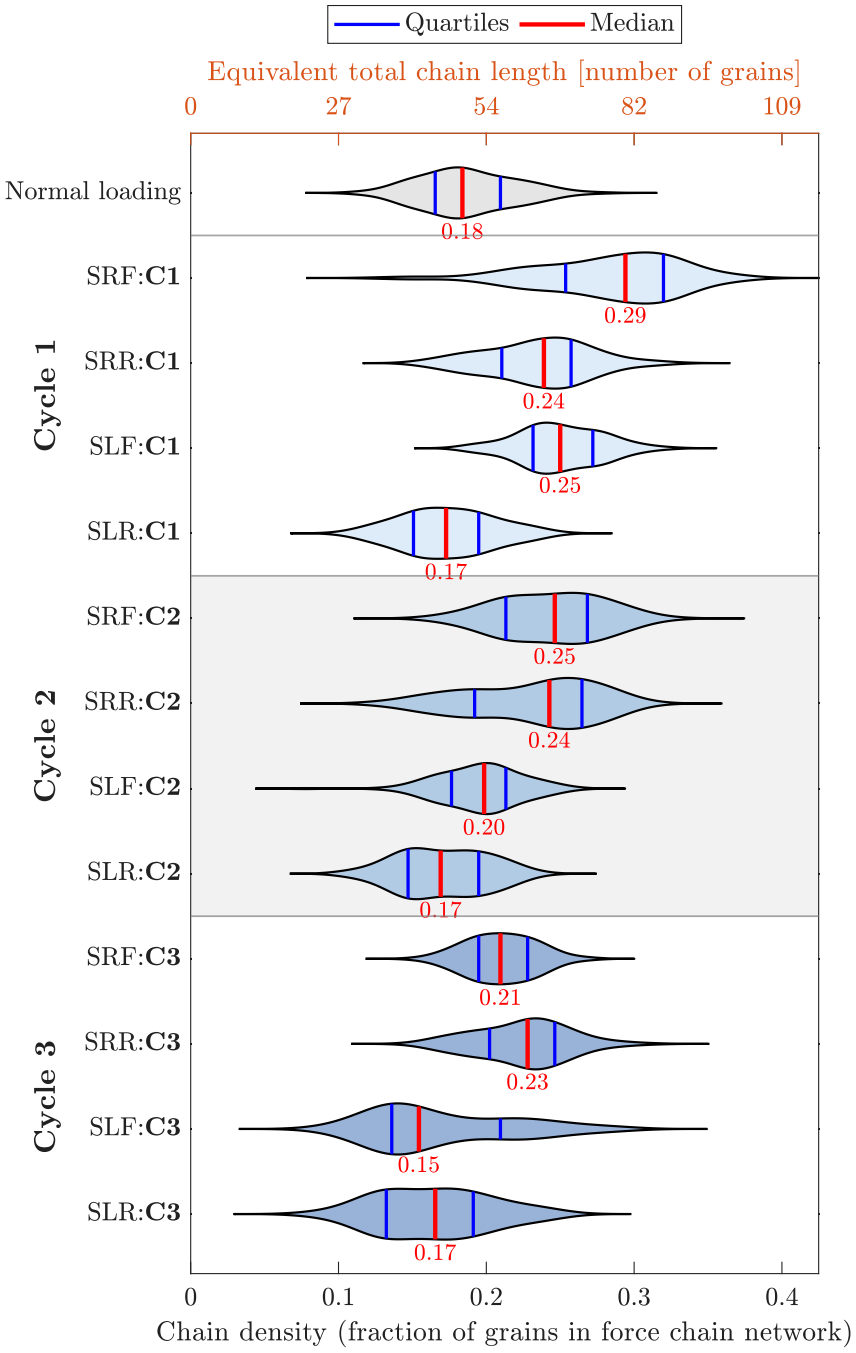


Figure 4.33: Violin plots of the force chain density for each cycle and shear stage for the dense assembly ($\sigma_n = -29.6$ kPa). Force chain density is defined as the fraction of grains participating in the force chain network relative to the total number of interior grains. The bottom x-axis shows the normalized chain density, while the top x-axis shows the equivalent total force chain length in number of grains. The width of each violin indicates the relative frequency of occurrence of a given chain density during that stage.

Compared to the higher-confinement case, the 82 lb experiment exhibits a lower chain density during normal loading, along with a more compact, near-Gaussian distribution. This indicates that under lower confinement, fewer grains initially participate in the force chain network, and the structure is less heterogeneous.

In cycle 1, the evolution of chain density follows the same overall pattern observed in the AUC results, with the shear-right-forward (SRF) stage exhibiting the highest median value. However, the underlying distributions differ markedly from those in the higher-confinement case. In particular, the SRF stage exhibits a more structured distribution, with distinct regions corresponding to moderate-to-large force chain sizes and a pronounced lower tail. This suggests that while the network reaches its largest extent during forward shearing, it remains less uniformly organized, with a broader range of participating structures. In contrast, the subsequent stages exhibit behavior more comparable to the higher-confinement case, though with reduced magnitudes and weaker recovery during shear-left-forward (SLF), resulting in a larger net decrease in chain density over the first cycle.

In cycles 2 and 3, the response diverges significantly from that of the higher-confinement case. During cycle 2, the chain density decreases monotonically across stages, indicating progressive degradation of the force chain network. The distributions become broader and more structured, often displaying multiple preferred ranges of chain sizes rather than a single dominant configuration. This reflects a transition toward a more heterogeneous and distributed force chain network, in which no single characteristic structure dominates.

In cycle 3, the chain density evolution becomes more irregular, following a non-monotonic (zig-zag) pattern across stages. Although small recoveries occur between certain stages, they are outweighed by larger decreases when transitioning between shear directions. The distributions remain structured but increasingly biased toward smaller force chain sizes, indicating that the network continues to fragment and reorganize into less extensive configurations.

Overall, the force chain density results show that at a lower applied normal load, the network is less dense, more heterogeneous, and more dynamically evolving. Compared to the higher-confinement case, the distributions exhibit fewer near-Gaussian shapes and more multimodal structure, indicating that the force chain network does not settle into a single dominant configuration. Instead, it evolves through a combination of fragmentation, partial recovery, and redistribution, consistent with a more intermittent and less efficiently load-bearing system. This behavior is consistent

with the AUC results, which indicate reduced persistence and increased variability of the force chain network under lower confinement.

Strong Network Participation and Strong Network Chain Participation Unlike force chain density, which reflects the fraction of all grains participating in force chains, strong network participation and strong network chain participation distinguish between the size of the strong force network and the degree to which that network organizes into chain-like structures. Figure 4.34 summarizes the stage-wise medians and variability in both measures.

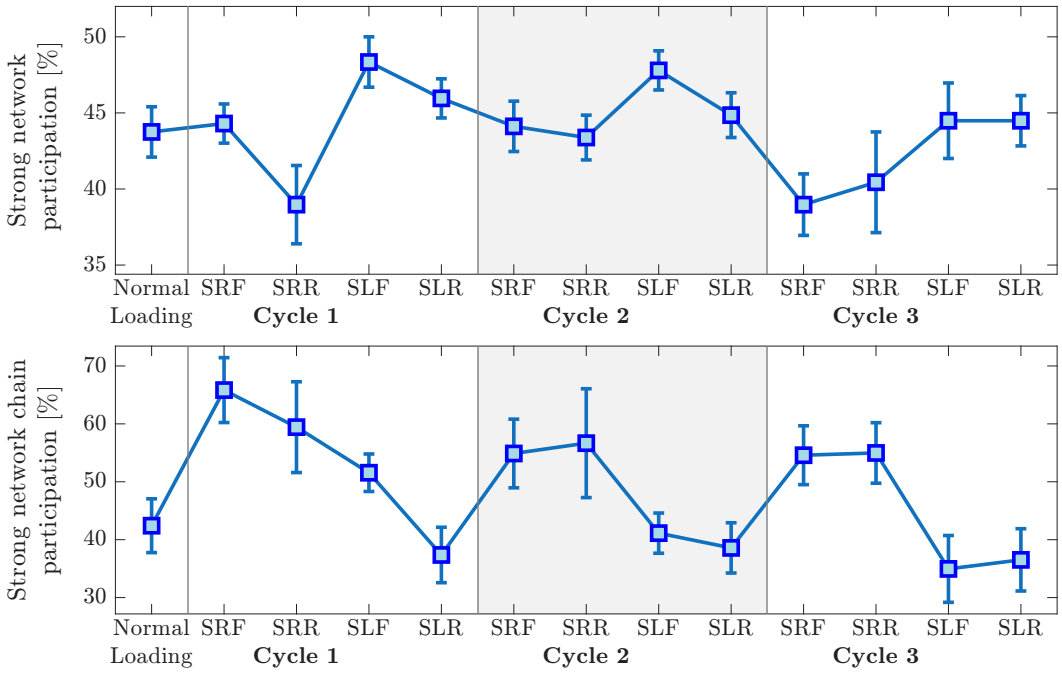


Figure 4.34: Stage-wise medians of the strong network participation [%] (top) and the strong network chain participation [%] (bottom) for each cycle and shear stage for the dense assembly ($\sigma_n = -29.6$ kPa). Error bars represent one-half of the interquartile range, centered about the median.

The **strong network participation**, defined as the fraction of grains carrying above-average stress, exhibits behavior that differs from the higher-confinement case, particularly during early stages of loading. In contrast to the 122 lb experiment, where participation decreases from normal loading to shear-right-forward (SRF), the 82 lb case shows an initial increase, corresponding to a larger portion of the assembly becoming engaged in load-bearing at the onset of shear. However, this increase is followed by a more pronounced decrease during shear-right-reverse (SRR), suggesting that the expanded strong network is less stable and more susceptible to disruption upon shear reversal.

Across subsequent stages, the strong network participation exhibits a combination of partial recovery and gradual decline. While both experiments show similar overall trends in cycle 2, the 82 lb case exhibits a narrower range of values, indicating a more constrained yet less variable strong network. In cycle 3, the response becomes smoother and more stable, with a gradual increase followed by a near steady-state, in contrast to the more fluctuating behavior observed under higher confinement. Despite these differences, the overall range of participation remains comparable across the two experiments, suggesting that the size of the strong network is not significantly reduced under lower confinement but instead evolves more uniformly.

In contrast, the **strong network chain participation**, which measures the fraction of strong grains that are organized into force chains, exhibits markedly different behavior. Although both experiments show an increase from normal loading to SRF, the subsequent evolution diverges. In the 82 lb case, chain participation decreases monotonically throughout cycle 1, indicating that although more grains may carry above-average stress, a smaller fraction organizes into coherent force chain structures. This trend continues in later cycles, where chain participation shows repeated increases during SRR, followed by sharp decreases during shear-left-forward (SLF) and shear-left-reverse (SLR), reflecting a cycle of formation and breakdown of force chain organization.

Compared to the higher-confined case, the strong network chain participation in the 82 lb experiment exhibits greater variability in later cycles, despite attaining both a lower maximum and a lower minimum. This suggests that the organization of the strong network into force chains becomes less stable and more intermittent, even though the overall size of the strong network remains relatively consistent.

In general, these results show that while roughly half of the assembly remains in the strong network throughout cycling, only about $35\% - 66\%$ of those strong grains organize into force chains. Including stage-wise variability, this proportion ranges from approximately 29% to 71%. These values are comparable to those observed under higher confinement; however, the 82 lb experiment exhibits greater variability across stages and cycles, indicating that the organization of the strong network into force chains is less stable and more intermittent under lower confinement. As a result, the load-bearing response is more distributed across many grains, but less effectively concentrated along coherent force chains, consistent with the more diffuse and variable force transmission observed in earlier sections.

Micro-Macro Comparison Next, we compare the stage-wise medians of the macroscopic shear stress and the total force chain length (Figure 4.35). The relationship between macroscopic shear stress and total force chain length provides insight into how the evolving force chain network contributes to bulk resistance. As in the higher-confinement case, the overall stage-wise trends in both quantities are broadly similar, particularly during the early stages of loading.

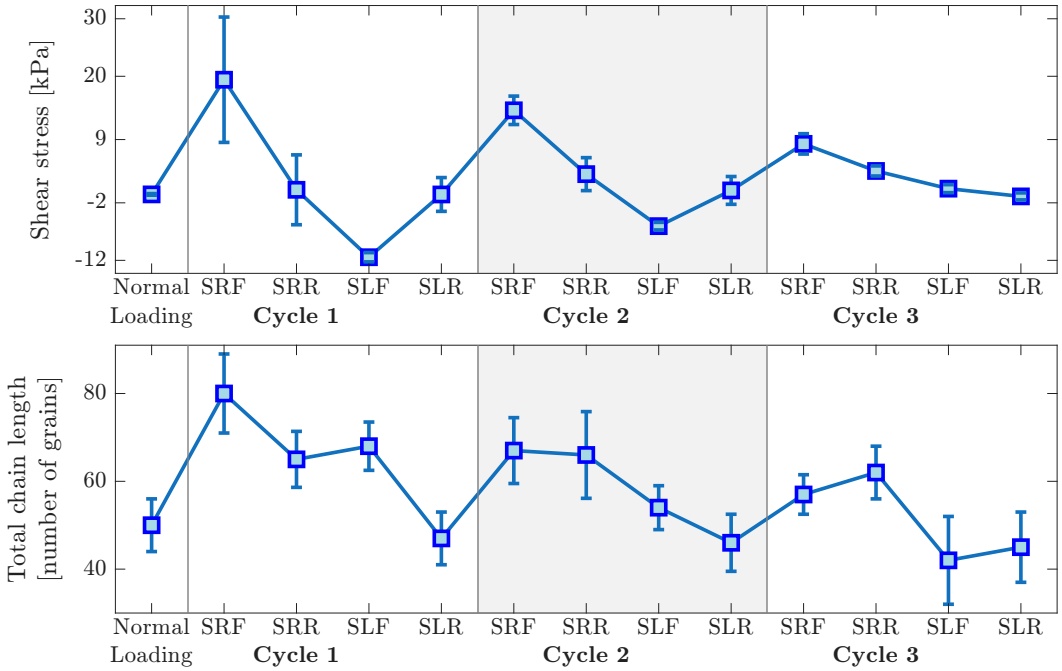


Figure 4.35: Stage-wise medians of the shear stress [kPa] (top) and total chain length [number of grains] (bottom) for each cycle and shear stage for the dense assembly ($\sigma_n = -29.6$ kPa). Error bars represent one-half of the interquartile range, centered about the median.

The shear stress response in the 82 lb experiment follows the same general pattern as in the 122 lb case; it increases during forward shearing and decreases after reversal. However, the overall shear stress range is significantly smaller under lower confinement, and the response exhibits greater variability, particularly during shear-right-forward (SRF), where large fluctuations are observed that are not present in the more confined case. Hence, although the qualitative behavior is preserved, the macroscopic response becomes less stable and more sensitive to local rearrangements under reduced confinement.

The total force chain length exhibits a similar correspondence during the early stages of loading, with both experiments showing comparable trends from normal loading through shear-right-reverse (SRR) in cycle 2. However, important differences

emerge in the magnitude and evolution of the response. Under lower confinement, the increase in force chain length during SRF is significantly more pronounced, indicating rapid initial development of the force chain network. In contrast, subsequent changes are less systematic, with more gradual or irregular variations replacing the more consistent increase-decrease patterns observed under higher confinement.

In later cycles, the divergence between the two experiments becomes more pronounced. Although the 122 lb case exhibits relatively smooth and bounded evolution of the total chain length, the 82 lb experiment shows greater variability over a wider range, with alternating periods of monotonic decrease, recovery, and abrupt drops across stages. This indicates that under lower confinement, the force chain network evolves in a more irregular and less predictable manner, reflecting a greater sensitivity to the cyclic loading history.

Despite these differences, both experiments exhibit alignment between the peak shear stress and maximum force chain length, indicating that the strongest macroscopic resistance still coincides with the most developed force chain network. However, beyond this initial correspondence, the two quantities do not track each other consistently. As in the 122 lb experiment, a larger force chain network does not necessarily yield higher shear stress, particularly in later stages, where variability increases, and the response becomes less organized.

Overall, these results indicate that reducing confinement preserves the general link between force chain development and shear resistance but weakens its consistency. The macroscopic response becomes more variable and less directly tied to the size of the force chain network, reflecting a shift toward less efficient, more distributed force transmission, consistent with reduced organization and increased intermittency observed at the grain-scale.

4.3.2.3 Force Chain Structure and Anisotropy

The following subsections analyze the orientation distributions of both contacts (fabric anisotropy) and interparticle forces (force anisotropy), and their relationships with macroscale quantities through the stress-force-fabric framework. In addition, the probability density functions (PDF) of normalized contact forces are examined to characterize how forces are transmitted through the granular assembly.

Fabric and Force Anisotropy This section uses polar histograms to examine the angular distributions of contact fabric orientation, $P(\theta)$, and the interparticle contact forces, $\bar{f}_n(\theta)$ and $\bar{f}_t(\theta)$ (mean normal and tangential forces, respectively). In these plots, the radial magnitude represents the relative frequency or average force associated with a given contact orientation, while the shape of the distribution reflects the degree of anisotropy. More elongated (lobed) distributions indicate a stronger directional bias, whereas more circular distributions indicate a more isotropic response.

The **contact fabric orientation**, $P(\theta)$, reflects the directional organization of the contact network and provides a geometric basis for force transmission. Compared to the higher-confinement case, the 82 lb experiment exhibits a more cycle-dependent and less consistently aligned fabric structure, particularly with respect to the principal compressive stress direction. Figure 4.36 shows the polar distributions of contact orientations for each cycle and loading stage.

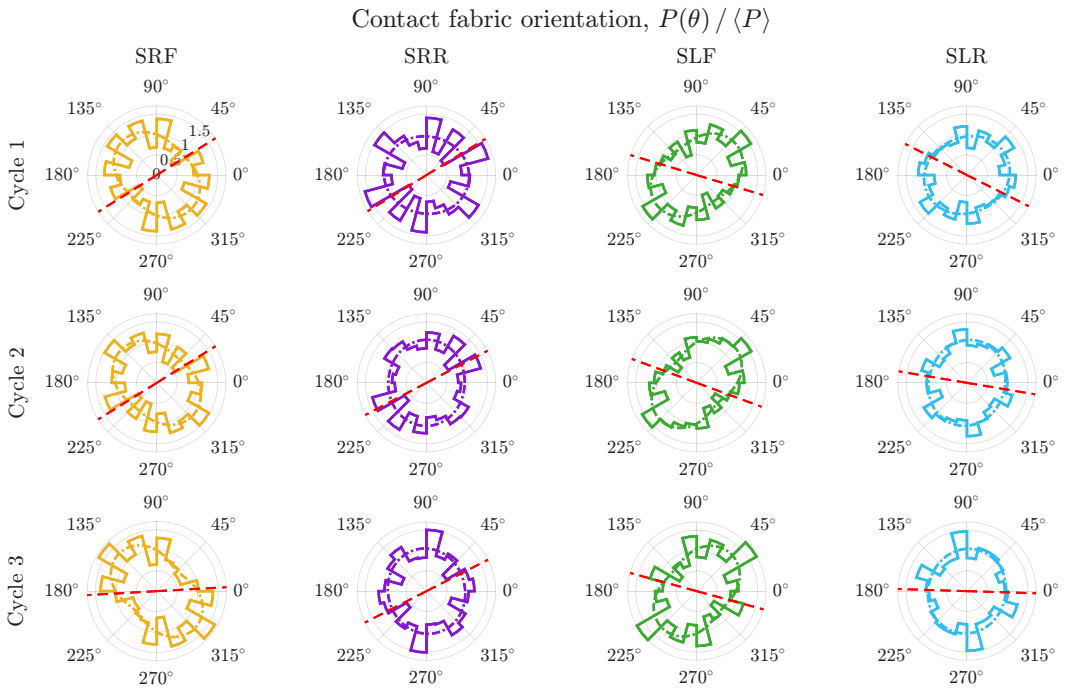


Figure 4.36: Polar histograms of the normalized angular distributions of the contact fabric orientation, $P(\theta)$, arranged by cycle (rows) and midpoint of each shear stage (columns) for the dense assembly ($\sigma_n = -29.6$ kPa). The solid curve represents the distribution, the dash-dotted curve shows its Fourier fit, and the red dashed line denotes the principal compressive stress axis.

During shear-right-forward (SRF), the fabric anisotropy axis in the 82 lb experiment aligns near the 135° direction, in contrast to the ~ 125° alignment observed during higher confinement. Although the anisotropy axis remains relatively consistent across cycles, the compressive axes are significantly larger than in the 122 lb case, with cycles 1 and 2 exhibiting substantial misalignment and cycle 3 showing a more moderate offset. This indicates that, under lower confinement, the contact network remains anisotropic but is less effectively oriented to support the principal loading direction. In addition, the distributions exhibit similarly sized lobes, suggesting a more dispersed, less concentrated contact structure.

During shear reversal (shear-right-reverse (SRR)), the fabric orientation becomes strongly cycle-dependent, in contrast to the more consistent alignment observed under higher confinement. While the compressive axis remains relatively stable across cycles, the anisotropy axis varies significantly, leading to a wide range of misalignment values. In particular, cycle 3 exhibits the largest misalignment, while cycle 1 shows the smallest. Although the distributions retain elongated features, they become more isotropic overall, especially in later cycles, indicating reduced directional coherence of the contact network during reversal.

In shear-left-forward (SLF), the anisotropy and compressive axes remain relatively consistent across cycles in both experiments, resulting in smaller variations in misalignment. As in the 122 lb experiment, cycle 2 exhibits the largest misalignment and cycle 1 the smallest, although the overall magnitude of misalignment is reduced. Despite this alignment, the distributions remain oblong, with cycle 3 exhibiting larger and more frequent lobes, indicating increased structural variability and redistribution of contacts. In contrast, cycle 2 shows reduced variability, suggesting a more stable but less dynamic configuration.

During shear-left-reverse (SLR), the distributions become nearly isotropic across all cycles. However, in contrast to the higher confinement experiment, where the magnitude of the contact distribution decreases with cycling, the 82 lb experiment exhibits an increase in distribution magnitude with cycle count. While cycles 1 and 2 maintain relatively small and less pronounced lobes, cycle 3 develops a more distinct structure with both long and intermediate lobes, indicating renewed anisotropic features despite the overall nearly isotropic shape. This behavior suggests that, under lower confinement, the contact network undergoes progressive reorganization during cyclic loading, allowing contacts to reorient and form a more directionally structured configuration. Unlike the 122 lb experiment, where structural degradation

dominates, the reduced constraints enable the development of anisotropy through rearrangement. However, this increased anisotropy does not indicate improved alignment with the principal stress direction, suggesting that the evolving structure is not optimally configured for efficient load transmission.

The **mean normal force angular distribution**, $\bar{f}_n(\theta)$, reflects how compressive loads are transmitted through the contact network. Compared to the higher-confinement case, the 82 lb experiment exhibits a weaker, more cycle-dependent normal force anisotropy, particularly in the later stages. Figure 4.37 shows the polar distributions of $\bar{f}_n(\theta)$ for each cycle and loading stage.

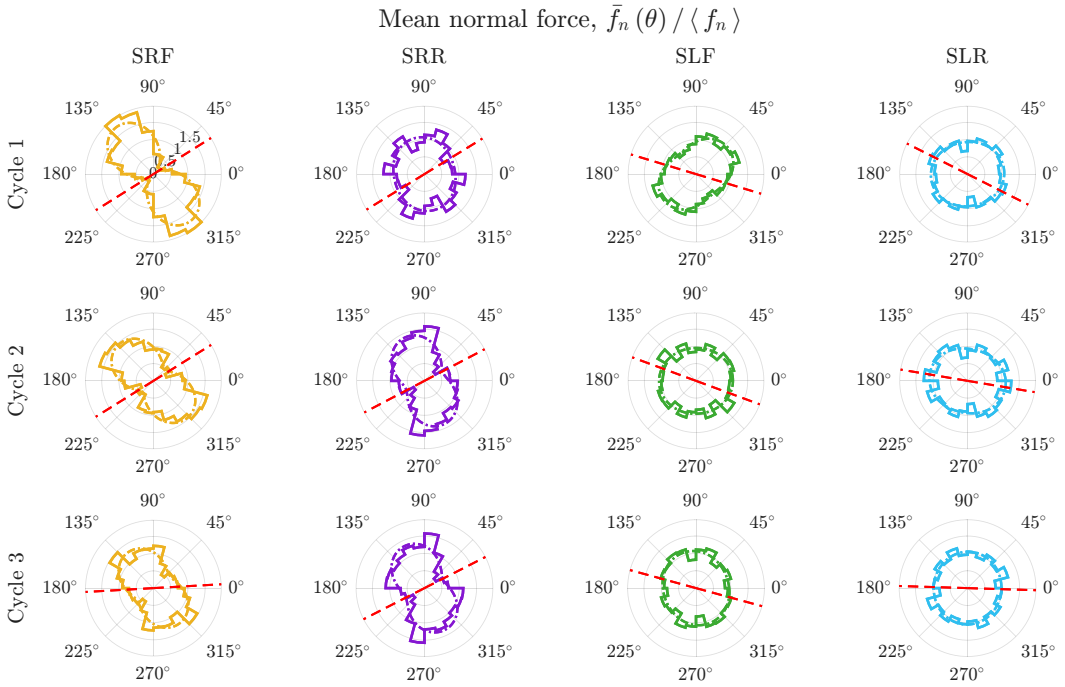


Figure 4.37: Polar histograms of the mean contact normal force, $\bar{f}_n(\theta)$, arranged by cycle (rows) and midpoint of each shear stage (columns) for the dense assembly ($\sigma_n = -29.6$ kPa). The solid curve represents the distribution, the dash-dotted curve shows its Fourier fit, and the red dashed line denotes the principal compressive stress axis.

During SRF, cycle 1 retains the characteristic peanut-shaped distribution observed under higher confinement, but with a larger anisotropy magnitude and clear preference for contacts along the primary load-bearing direction. With increasing cycles, this structure broadens and becomes less pronounced, and the anisotropy magnitude decreases, indicating a progressive weakening of directional force transmission. Although the anisotropy axis remains relatively consistent across cycles, the misalignment with the compressive stress axis decreases slightly, suggesting partial

reorientation of the force network.

During SRR, the behavior differs from that of the higher-confinement case. Instead of approaching isotropy in later cycles, cycles 2 and 3 retain elongated distributions, indicating sustained directional structure. However, the preferred orientations become more complex, with multiple alignment ranges emerging. At the same time, the misalignment between the anisotropy and stress axes increases with cycle count, indicating that although the force network remains anisotropic, it becomes less efficiently aligned with the loading direction.

In SLF, the overall distribution shapes remain similar across cycles, but the orientation of the anisotropy axes becomes more variable, particularly in cycles 2 and 3. This results in a range of misalignment values, with cycle 2 showing the smallest misalignment and cycles 1 and 3 exhibiting larger misalignments. Despite this variability, the magnitude of anisotropy remains relatively modest, indicating that force transmission is directionally structured but not strongly concentrated.

Lastly, during SLR, the distributions become nearly isotropic across all cycles, with very small anisotropy magnitudes confined to a narrow range. Compared with the higher-confinement case, the response is significantly weaker. Furthermore, no systematic increase in anisotropy is observed with cycling. Hence, by the final stage, the normal force network becomes highly diffuse, with only weak directional preferences remaining.

The **mean tangential force distributions**, $\bar{f}_t(\theta)$, provide insight into how shear forces are mobilized across the contact network. As with the normal forces, the 82 lb experiment exhibits a more variable and less coherent anisotropic structure than the higher-confinement case. Figure 4.38 shows the polar distributions of $\bar{f}_t(\theta)$ for each cycle and loading stage.

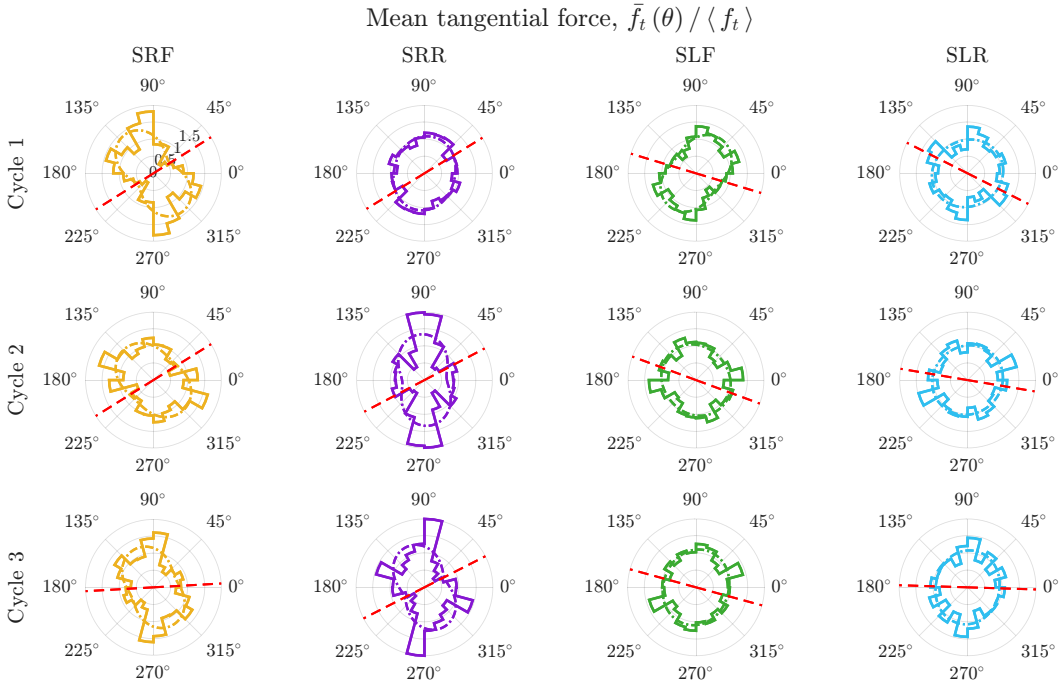


Figure 4.38: Polar histograms of the mean contact tangential force, $\bar{f}_t(\theta)$, arranged by cycle (rows) and midpoint of each shear stage (columns) for the dense assembly ($\sigma_n = -29.6\,\text{kPa}$). The solid curve represents the distribution, the dash-dotted curve shows its Fourier fit, and the red dashed line denotes the principal compressive stress axis.

During SRF, cycle 1 again exhibits a peanut-shaped distribution, though broader than in the 122 lb case, indicating a more diffuse shear force network. In later cycles, the distributions become more elliptical and reduced in magnitude, but exhibit increased variability, with a wider range of preferred orientations. Despite these changes, the anisotropy axes remain broadly aligned with those of the normal force, suggesting that compressive and shear forces still share a common structural framework. The misalignment with the stress axis follows a similar pattern to the higher-confinement case, with cycle 1 showing the largest offset and cycle 3 the smallest.

In the SRR stage, the anisotropy axes shift and the distributions become more variable, particularly in cycles 2 and 3. Although the overall magnitude remains modest, the increasing misalignment with cycle count indicates that the shear force network becomes progressively less aligned with the principal stress direction, even as localized directional features persist.

During SLF, the anisotropy axes exhibit significant shifts relative to the normal force, particularly in later cycles. This results in a wider range of misalignment values, with cycle 2 remaining the most aligned and cycle 3 the least aligned.

The distributions show increased variability, especially in cycle 3, where localized lobes indicate preferred orientations that differ from the dominant loading direction. This suggests that shear resistance becomes increasingly heterogeneous and locally controlled.

Lastly, during SLR, the distributions again approach isotropy, although more pronounced lobes remain than in the higher-confinement case. The anisotropy magnitude increases with cycle count, reaching its highest value in cycle 3, and the misalignment with the stress axis increases correspondingly. This suggests that, under lower confinement, the shear force network undergoes progressive reorganization, developing a directional structure that is not optimally aligned with the applied loading.

Overall, the results on normal and tangential force anisotropy show that reducing confinement leads to force networks that remain anisotropic but become increasingly variable, misaligned, and less efficiently organized. While directional structures persist, they are less consistently aligned with the principal stress direction and are more sensitive to cyclic loading history. This behavior is consistent with the fabric results and helps explain the reduced effectiveness of force transmission and the weakened correspondence between the force chain structure and macroscopic stress.

Temporal Evolution of Fabric and Force Anisotropy Magnitudes While the previous section examined the directional organization of the contact and force networks at discrete stages using polar histograms, we now quantify how these directional structures evolve continuously throughout cyclic loading. Specifically, we examine the evolution of the fabric anisotropic magnitude (a), the normal force anisotropy magnitude (a_n), and the tangential force anisotropy magnitude (a_t) as functions of shear strain (Figure 4.39). These measures provide insight into how the internal structure of the granular assembly develops, reorganizes, and degrades as the loading direction changes.

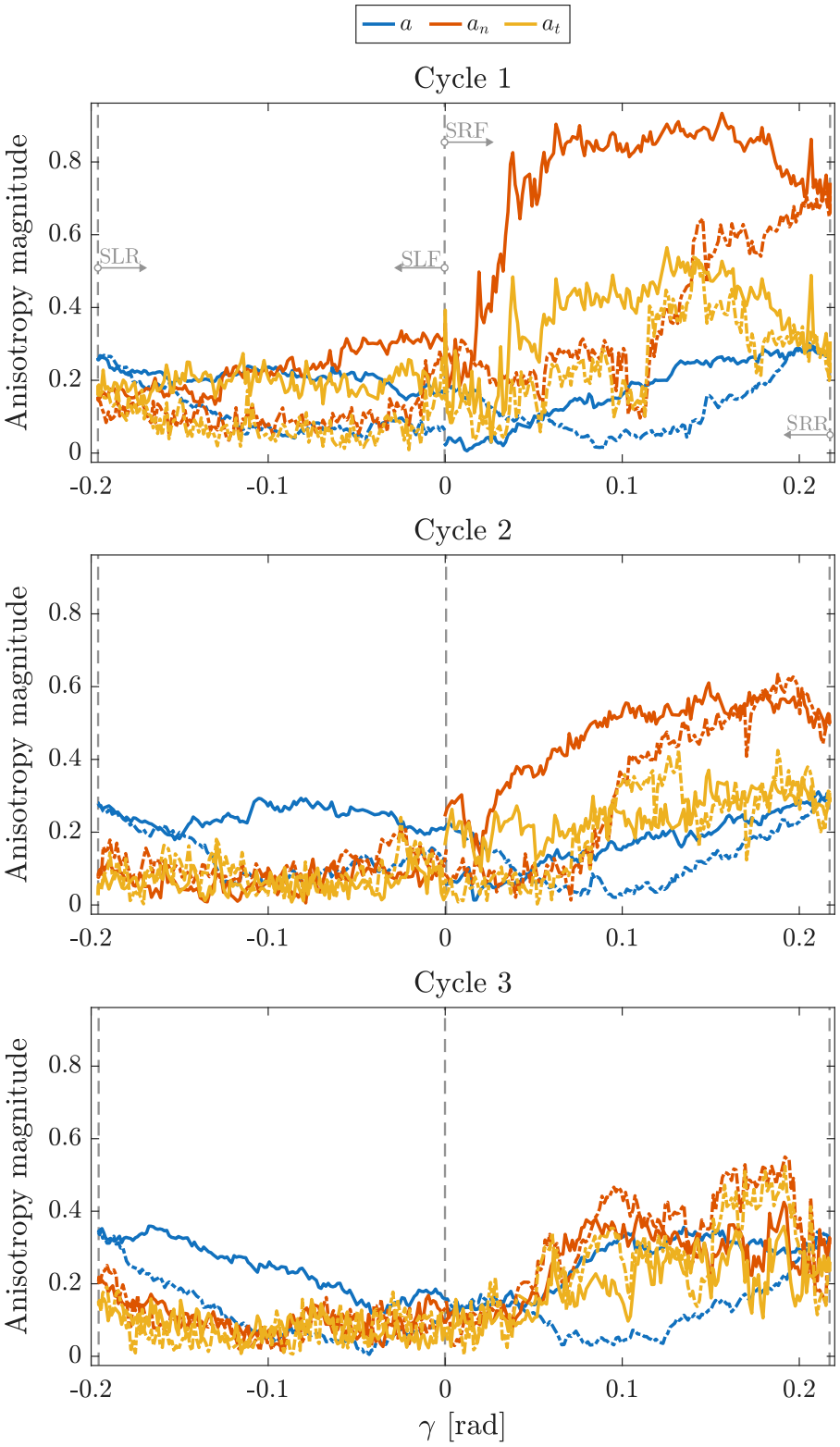


Figure 4.39: Per cycle evolution of the anisotropy magnitudes as functions of shear strain for the dense assembly ($\sigma_n = -29.6$ kPa): fabric anisotropy magnitude, a, and normal and tangential force anisotropy magnitudes, a_n and a_t, respectively. Curve style indicates shearing direction (solid: forward, dash-dotted: reverse), gray dashed lines mark stage transitions.

All anisotropy measures begin at nonzero values, indicating that some degree of directional structure is present even before shearing. During normal loading, all anisotropy measures increase, although the fabric anisotropy increases only slightly in comparison to the force anisotropies. In contrast, under higher confinement, the fabric anisotropy decreased during this stage. This difference suggests that, under lower confinement, the contact network retains sufficient freedom to undergo localized rearrangements that promote mild directional structuring, rather than being driven toward a more uniform configuration under compression.

With the onset of shear (shear-right-forward (SRF)), the evolution of the normal force anisotropy, a_n, reveals a more gradual and irregular buildup of directional structure compared to the higher-confinement case. Rather than exhibiting a rapid increase followed by a steady decline, the 82 lb response develops through a sequence of fluctuations and incremental growth, ultimately reaching its peak near shear reversal. This delayed peak indicates that anisotropy is not established immediately, but instead emerges progressively as the contact network continually reorganizes under deformation.

The initial shear-right-reverse (SRR) evolution also differs between the two confinement levels. In the 122 lb experiment, the a_n response changes rapidly at the onset of reversal and then gradually levels off, whereas in the 82 lb experiment, it begins more gradually before steepening. This behavior suggests that, under lower confinement, the force network reorganizes more progressively during reversal rather than relaxing immediately.

As cyclic loading progresses, the evolution of the force anisotropies, a_n and a_t, becomes increasingly fragmented rather than sustained throughout the loading path. In cycle 1, both measures remain elevated across most of the forward and reverse branches, indicating that the force network maintains a coherent directional structure throughout the cycle. However, by cycle 2, this behavior begins to diverge. The normal force anisotropy still remains elevated over a large portion of the forward-shear path, dropping only near shear reversal, whereas in cycle 3 it is sustained only over limited portions of the stage, primarily midway through right-shear and again near shear reversal.

The tangential force anisotropy, a_t, exhibits a more pronounced version of this behavior. In both cycles 2 and 3, elevated values of a_t occur only in short segments of the loading path, with much of the cycle characterized by weak directional organization. This indicates that shear forces are more sensitive to local rearrangements

and are less able to maintain a consistent orientation as the contact network evolves.

Mechanistically, this transition from sustained to intermittent anisotropy reflects a change in how the force network carries the load. In the first cycle, force chains form and persist over large strain intervals, providing a stable directional framework for stress transmission. However, with continued cycling under lower confinement, these structures become increasingly unstable and are repeatedly disrupted. As a result, directional force transmission is no longer maintained continuously, but instead appears only during brief periods when the network temporarily reorganizes into a favorable configuration. This behavior indicates a growing dependence on loading history and a reduced ability of the system to sustain a coherent load-bearing structure.

Verification of the Stress-Force-Fabric Relationship The evolution of anisotropy magnitudes showed that, under lower confinement, directional structure develops more gradually, becomes increasingly intermittent, and is strongly influenced by loading reversals. These changes in the internal force network have direct implications for macroscopic stress transmission. To examine this connection, we now compare the experimental invariant stress ratio, q/p, with the predictions of the stress-force-fabric (SFF) relationships (Figure 4.40), which link macroscopic stress to the underlying anisotropy of the contact and force networks.

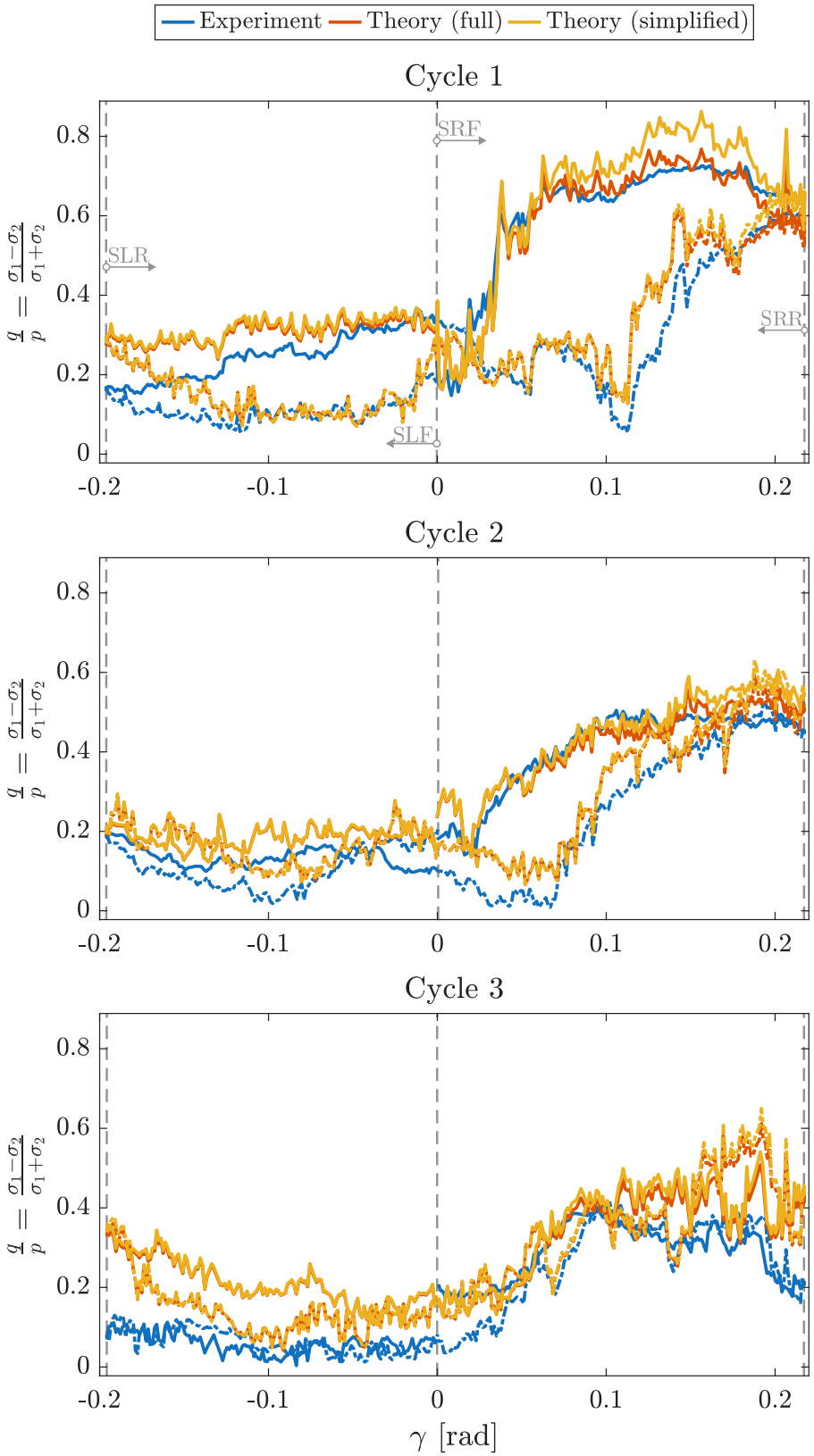


Figure 4.40: Per cycle evolution of the invariant stress ratio, q/p, as a function of shear strain for the dense assembly ($\sigma_n = -29.6$ kPa). The experimental response is compared with the predictions of the full and simplified stress-force-fabric (SFF) relationships. Curve style indicates shearing direction (solid: forward, dash-dotted: reverse), gray dashed lines mark stage transitions.

As in the 122 lb experiment, both SFF formulations capture the overall petal-like structure of the experimental q/p response, indicating that the theory remains effective in representing the general coupling between stress and anisotropy. However, clear stage- and cycle-dependent discrepancies emerge, reflecting the reduced ability of the evolving force network to sustain a consistent relationship between the internal structure and macroscopic stress.

In cycle 1, the deviations between theory and experiment already suggest differences in the development of anisotropy under lower confinement. In shear-right-forward (SRF), during the initial linear regime, the theory slightly underestimates the experimental response, indicating that the measured stress increases more rapidly than predicted from the evolving anisotropy. As shearing progresses, the theory begins to overpredict q/p, implying that, although the directional force structure develops, it is weak, short-lived, or misaligned with the principal stress direction, limiting its contribution to macroscopic stress. This is consistent with the earlier observation that anisotropy develops more gradually and with greater fluctuation, reflecting a force network that is less efficiently organized. As in the 122 lb case, the full SFF formulation provides a closer match than the simplified version, particularly after the initial linear regime, highlighting the importance of capturing the full coupling between fabric and force anisotropies.

As the system transitions into cycle 2, the agreement between theory and experiment becomes more variable. Although there are brief intervals where the SFF predictions align closely with the measured q/p, the response increasingly alternates between under- and overprediction. This behavior indicates that the relationship between anisotropy and stress is no longer stable but instead evolves in a stage-dependent manner. In particular, following the first shear reversal, the theory tends to underpredict, then overpredict, for much of the remaining loading path (from shear-right-reverse (SRR) through shear-left-reverse (SLR)). Mechanistically, this reflects a force network that is continuously reorganizing: although directional structure develops, its orientation and connectivity are not consistently aligned with the principal stress direction, thereby limiting its ability to transmit load efficiently.

This trend becomes more pronounced in cycle 3, where the discrepancy between theory and experiment is amplified. The theoretical response consistently overpredicts the experimental q/p, particularly along the leftward branch, where the predicted curve remains above the measured response with only minimal overlap. This persistent overprediction indicates that the anisotropy in the system is no longer configured

to efficiently contribute to the macroscopic stress. Instead, the force network appears increasingly fragmented and misaligned, consistent with the intermittent and localized anisotropy observed in the previous section.

Throughout the experiment, the magnitude of q/p decreases with increasing cycle count, reflecting a progressive weakening of macroscopic shear resistance. While the rightward branch remains dominant in cycles 1 and 2, the leftward branch progressively diminishes, eventually collapsing by cycle 3. Under lower confinement, this asymmetry becomes more pronounced, with cycle 3 also exhibiting a substantially reduced rightward branch. This behavior mirrors the evolution of anisotropy, in which the directional structure is no longer sustained throughout the full loading path but appears only intermittently.

Consistent with the anisotropy results, the location of the peak q/p changes from forward shearing in cycle 1 to the reversal stages in later cycles. This shift indicates that dominant structural reorganization – and thus the most effective stress transmission – occurs during transitions between loading directions rather than during steady shearing. Additionally, the initial portion of the reversal stage in cycle 1 exhibits a distinct curvature relative to the higher-confinement case, with a more gradual onset of stress change followed by a steeper evolution. This behavior further supports the interpretation that, under lower confinement, the force network adapts to reversal through progressive reorganization rather than immediate reorganization.

Overall, these results demonstrate that while the SFF framework continues to capture the general structure of the stress response, its predictive accuracy diminishes as the cycle count increases under lower confinement. This is not due to a failure of the theoretical form itself, but rather reflects a breakdown in the assumption that anisotropy can be directly and consistently related to macroscopic stress. Instead, the evolving force network becomes increasingly intermittent, misaligned, and history-dependent, reducing the efficiency with which internal structure translates into bulk stress.

Force Transmission The SFF results showed that, under lower confinement, the relationship between internal anisotropy and macroscopic stress becomes increasingly inconsistent, with theory progressively overpredicting the measured response. This breakdown reflects a force network that is less effectively organized for load transmission. To better understand the origin of this behavior, we now examine the distribution of interparticle forces through probability density functions (PDFs) of the normal force, tangential force, and mobilized friction.

Figure 4.41 shows the per-cycle PDFs of the **normalized normal force**, $f_n / \langle f_n \rangle$, with each panel corresponding to a loading cycle and all shear stages included for comparison.

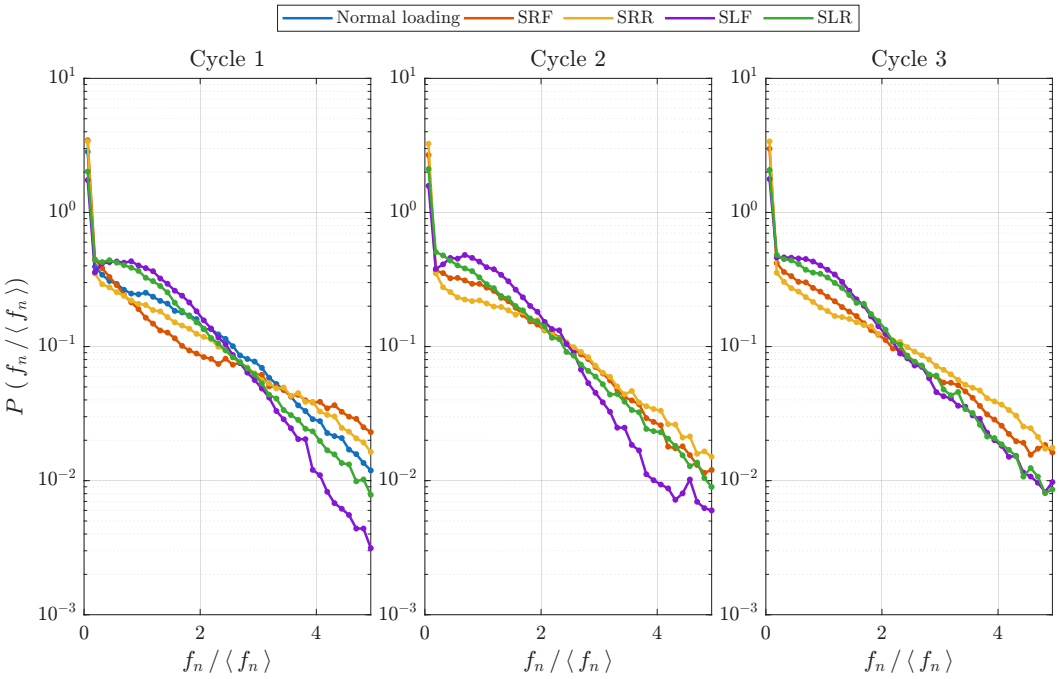


Figure 4.41: Per-cycle evolution of the probability density function (PDF) of the normalized normal contact force, $f_n / \langle f_n \rangle$, for the dense assembly ($\sigma_n = -29.6\,\text{kPa}$). Each panel shows one loading cycle, with all stages on a semi-log scale.

Across all cycles, the distributions retain the characteristic structure observed under higher confinement, with an initial rapid decay followed by a more gradual exponential tail at larger forces. This general form indicates that the system continues to transmit load through a heterogeneous network consisting of many weak contacts and a smaller population of strong load-bearing contacts. However, key differences emerge in how these force populations are organized across stages and cycles.

A notable feature is a bottleneck region, where the stage-dependent distributions converge before diverging again at higher force levels. Under lower confinement, this bottleneck occurs at similar force levels in cycles 1 and 3 as in the higher-confinement case, but shifts to higher normalized forces in cycle 2. This shift suggests that in cycle 2, stronger contacts are required before the force network reorganizes into distinct stage-dependent structures, indicating a temporary redistribution of load toward higher-force contacts.

More broadly, the shear-left stages consistently dominate both the low- and high-force regimes, suggesting that these stages are associated with a broader range of

force magnitudes. Mechanistically, this reflects a force network that is less uniformly organized, with both an increased population of weak contacts and a small number of disproportionately strong contacts carrying load. Under lower confinement, this behavior becomes more pronounced, particularly in cycle 1, where the stage-dependent distributions remain more distinct across the full force range. This suggests that the force network is less constrained and more sensitive to the loading direction, resulting in greater variability in the force distribution.

As cycling progresses, the high-force tails of the distributions become less distinct across stages, particularly in cycle 3, where multiple stages converge toward similar probability levels. This indicates a loss of persistent, stage-dependent force structure at large forces. Instead of maintaining distinct populations of strong contacts, the system exhibits a more uniform but weaker high-force network, consistent with the earlier observation that anisotropy becomes intermittent and less sustained.

Figure 4.42 shows the per-cycle PDFs of the **normalized tangential force**, $f_t\,/\langle f_n\rangle$, again organized by cycle with all shear stages included in each panel.

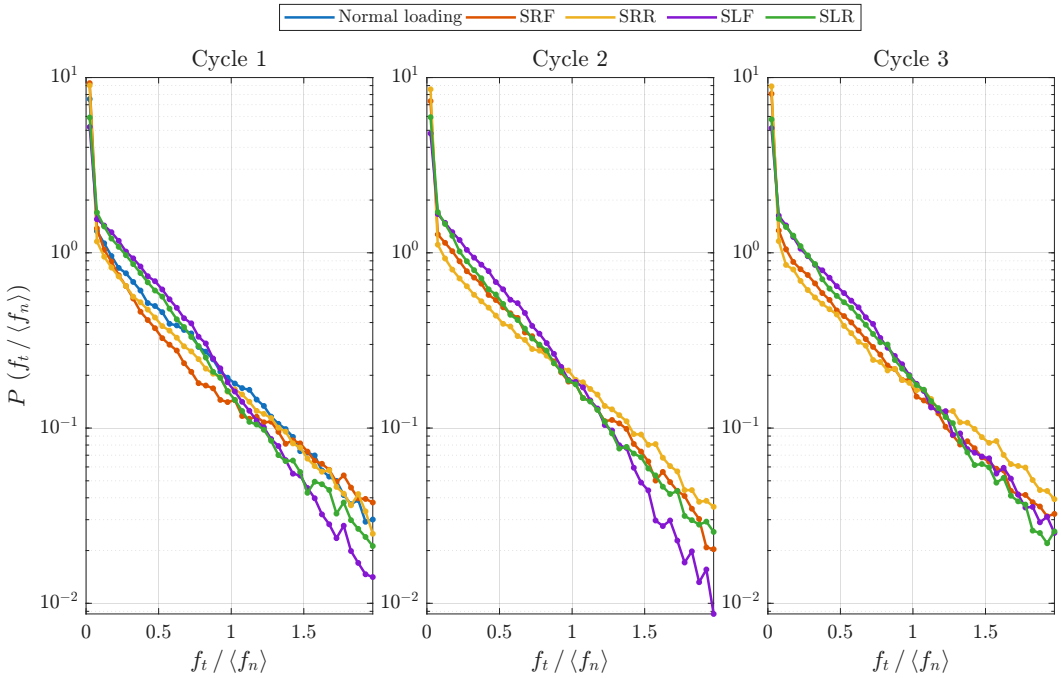


Figure 4.42: Per-cycle evolution of the probability density function (PDF) of the normalized tangential contact force, $f_t\,/\langle f_n\rangle$, for the dense assembly ($\sigma_n = -29.6$ kPa). Each panel shows one loading cycle, with all stages on a semi-log scale.

The tangential force distributions exhibit a similar overall structure to the normal force PDFs, with a steep initial decay followed by an exponential tail. This indicates that shear forces, like normal forces, are distributed across a broad range of contact magnitudes. However, the organization of these forces differs in important ways, particularly under lower confinement.

The bottleneck region in the tangential force PDFs is noticeably narrower under lower confinement, especially in cycles 1 and 3, where the stage-dependent distributions converge only over a limited range of forces. Instead, the force network transitions more rapidly between distinct configurations, reflecting a more dynamic and less stable organization of shear forces.

Prior to the bottleneck, the stage-dependent differences are more pronounced than in the 122 lb experiment, indicating that shear forces are more strongly influenced by loading direction. After the bottleneck, the distributions again diverge, but with greater variability across stages, particularly in cycles 2 and 3. This behavior reflects a tangential force network that is more sensitive to local rearrangements and less capable of sustaining a consistent directional structure, consistent with the earlier observation that a_t is weaker and more intermittent than a_n.

In later cycles, the high-force tails of the tangential force distribution exhibit greater overlap across stages, indicating reduced distinctiveness of strong shear contacts. This suggests that, under repeated loading, the system loses its ability to maintain stage-specific shear force structures, further contributing to the reduced efficiency of stress transmission observed in the SFF results.

Figure 4.43 shows the per-cycle PDFs of the **mobilized friction**, $S = |f_t|/\mu f_n$, with each panel corresponding to a cycle and all shear stages included for comparison.

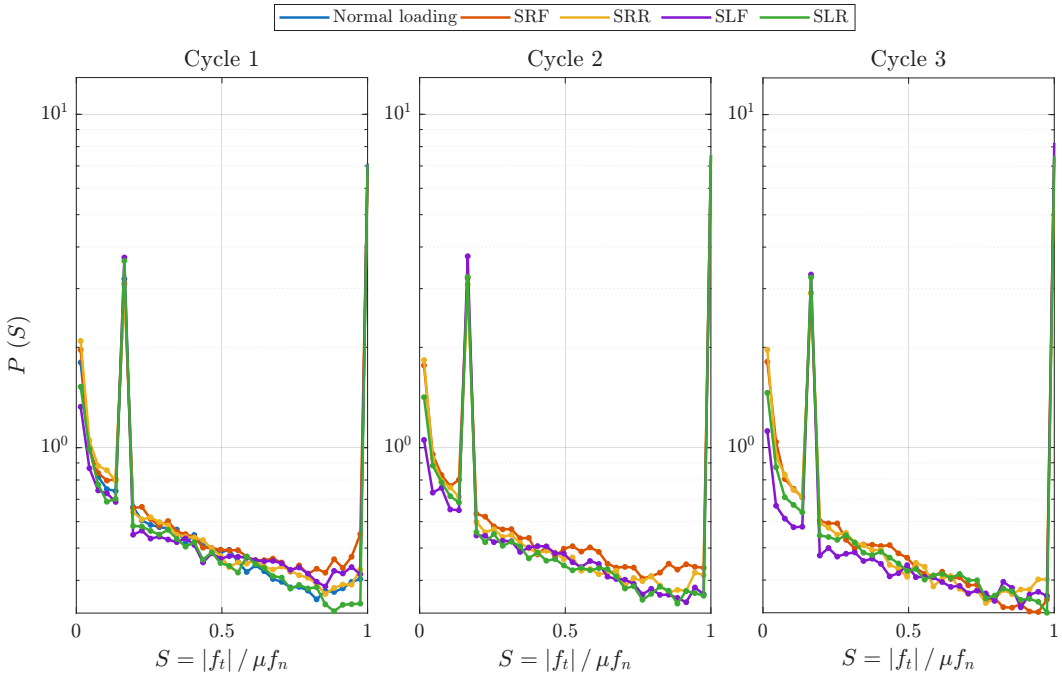


Figure 4.43: Per cycle evolution of the probability density function (PDF) of the mobilized friction, $S = |f_t|/\mu f_n$, for the dense assembly ($\sigma_n = -29.6$ kPa). Each panel shows one loading cycle, with all stages on a semi-log scale. Here, μ is the interparticle friction coefficient, and S indicates the proximity of a contact to sliding (Coulomb failure criterion).

As in the higher-confinement case, the distributions exhibit a soft initial decay followed by a pronounced peak at low mobilization levels and a gradual decay toward the failure limit. This structure reflects a system in which most contacts operate well below the sliding threshold, with only a small fraction approaching failure.

In contrast, under lower confinement, the stage-dependent differences in friction mobilization are significantly reduced, particularly in the early portion of the distribution. In cycle 1, the PDFs remain closely grouped across stages over a broad range of mobilization values, indicating that the degree of frictional engagement is less sensitive to loading direction. This suggests that despite differences in force magnitudes, the contacts exhibit similar levels of mobilization, indicating a more uniform frictional response.

As cycling progresses, the distributions remain tightly clustered over much of the mobilization range, with deviations occurring only at higher S values. In cycle 2, for example, only the SRF stage exhibits a noticeable deviation at moderate mobilization levels, while the remaining stages remain closely aligned. This indicates

that frictional activation becomes more localized, occurring only in specific stages and over limited portions of the loading path.

By cycle 3, the distributions become even more compressed, with reduced variability across stages and a narrower range of PDF values. This collapsed behavior reflects a system in which the range of frictional states is limited, suggesting that contacts are less frequently driven toward higher mobilization levels. This indicates a reduction in the system's ability to develop highly mobilized, load-bearing contacts, consistent with the observed weakening of both anisotropy and macroscopic shear resistance.

4.3.2.4 Grain-Scale Response Summary

The grain-scale response of the three-cycle, densely packed granular assembly under $\sigma_n = -29.6$ kPa $\approx$ 82 lb (37.2 kg) reveals a system that remains structurally organized but becomes progressively less stable and less efficient at transmitting load under cycle shear. Compared to the higher-confinement case, the reduced normal stress allows greater freedom for contact rearrangement, leading to increased variability and a stronger dependence on loading history across all measured quantities.

At the contact level, the coordination number exhibits smaller net changes over the loading history but greater fluctuations within each stage. Although the same general trends are observed – contact loss near shear reversal followed by partial recovery – the lower-confinement experiment shows less consistent behavior across cycles, indicating that contacts are more readily broken and reformed. This reflects a network that is less constrained and more sensitive to local rearrangements.

The force chain network exhibits similar overall trends but with reduced structural persistence. While both experiments show a net loss of force chains and total chain length, the reduction is smaller under lower confinement, and the evolution is less systematic. Rather than following a consistent stage-dependent pattern, the network undergoes continuous reorganization, with overlapping yet distinct responses across cycles. This behavior is further reflected in the chain density and AUC results, which show a broader range of force chain configurations and a weaker distinction between the forward- and reverse-shearing stages.

The strong network results indicate that, although a similar fraction of grains participates in the strong network, the organization of those grains into force chains becomes more variable and less consistent across cycles. This suggests that strong contacts persist, but are less effectively assembled into coherent, load-bearing structures under lower confinement.

The micro-macro comparison further highlights this reduced structural efficiency. While peak shear stress and total chain length still coincide during the first cycle, this correspondence weakens significantly in later cycles. The shear stress evolves within a narrower range, while the force chain network continues to fluctuate, indicating that the effectiveness of stress transmission increasingly depends on network configuration rather than on its overall size.

The anisotropy and SFF results provide a consistent explanation for this behavior. Under lower confinement, anisotropy develops more gradually, becomes increasingly intermittent, and is more strongly influenced by loading reversals. Although directional structure still forms, it is not sustained across the full loading path and is often misaligned with the principal stress direction. As a result, the SFF framework increasingly overpredicts the experimental response, reflecting a reduced ability of the force network to efficiently translate internal structure into macroscopic stress. Consistent with this, the force transmission PDFs show that load becomes more diffusely distributed, with fewer persistent high-force contacts and a more uniform frictional response.

Taken together, these results show that reducing confinement does not eliminate structural organization, but fundamentally alters how that structure evolves and contributes to load transmission. The system transitions from a persistently organized and efficiently aligned force network to one that is continuously reorganized, intermittently expressed, and less effectively coupled to macroscopic stress.

4.4 Experiment # 3: Loosely Packed, $\sigma_n = -44.1$ kPa

The third experiment is a loosely packed granular assembly normally loaded by $\sigma_n = -44.1$ kPa, corresponding to 122 lb (55.3 kg). For a loose packing, the granular assembly consists of 318 grains in total, of which 60 are boundary grains, and 258 are interior grains (these interior grains participate in the DIC and GEM analyses). The initial void ratio for this loosely packed experiment is 0.28.

4.4.1 Macroscopic Response

Figure 4.44 shows the macroscopic mechanical response of the three-cycle, loosely packed experiment, loaded by $\sigma_n = -44.1$ kPa. Once again, the macroscopic response is evaluated through the evolution of stress ratio, μ, volumetric strain, ϵ_v, void ratio, e, and dilatancy, β, which together characterize the granular assembly's shear resistance, volume change, packing state, and shear-volume coupling under cyclic loading.

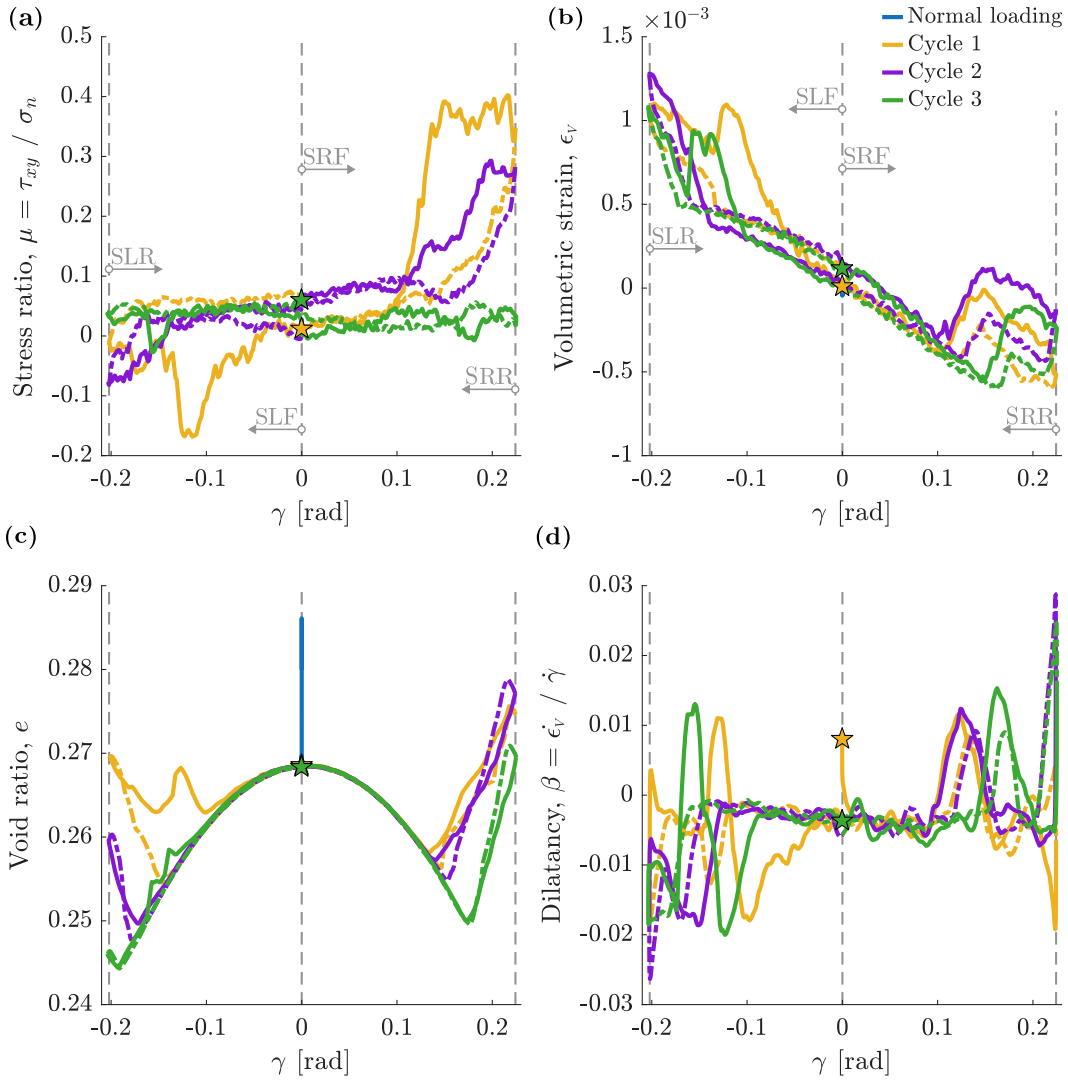


Figure 4.44: Macroscopic behavior of the three-cycle, loosely packed granular assembly under $\sigma_n = -44.1$ kPa. (a) Stress ratio, μ, (b) volumetric strain, ϵ_v, (c) void ratio, e, and (d) dilatancy, β, as functions of shear strain, γ. Solid curves indicate forward shearing stages (SRF, SRR), whereas dash-dotted curves indicate reverse shearing stages (SLF, SLR). Furthermore, gray vertical dashed lines indicate shear-stage transitions. The yellow and green stars mark the start and end of the cyclic loading, respectively.

4.4.1.1 Stress Ratio

Figure 4.44a shows the evolution of the stress ratio, μ, as a function of shear strain, γ, for the three-cycle, loosely packed granular assembly under $\sigma_n = -44.1$ kPa, corresponding to 122 lb. Compared to the corresponding densely packed experiment at the same normal stress (Figure 4.45), the loose assembly exhibits a substantially reduced, more weakly sustained stress ratio response, indicating a diminished ability to form and maintain a load-bearing contact network during cyclic shearing.

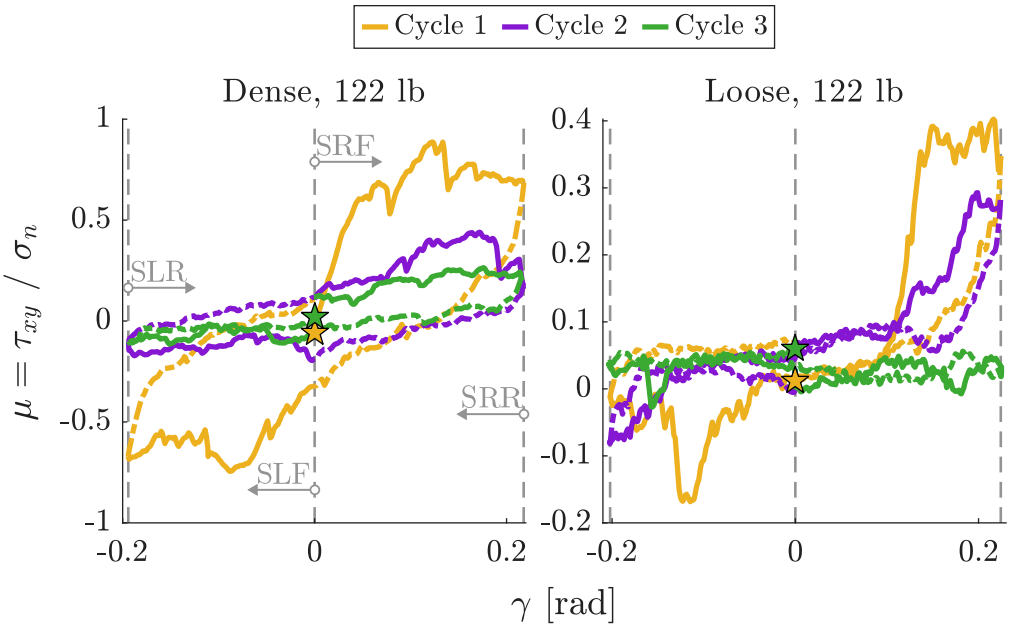


Figure 4.45: Stress ratio evolution for the three-cycle, dense (left) and loose (right) experiments subjected to a normal load of $\sigma_n = -44.1$ kPa. Curve style indicates shearing direction (solid: forward, dash-dotted: reverse), gray dashed lines mark stage transitions, and stars mark the start (yellow) and end (green) of cyclic loading.

Although the same overall trend of decreasing stress ratio peaks with increasing cycle number is preserved, the magnitudes of both the positive and negative extrema are significantly reduced. The maximum μ in the loose assembly is only about 45% of that observed in the dense case, while the minimum magnitude is similarly reduced. This indicates that loosening the initial packing substantially limits friction mobilization and reduces the efficiency of force transmission through the assembly.

A defining feature of the loose response is that appreciable shear resistance is mobilized only over limited portions of the load path. During large parts of both the shear-right and shear-left branches, the stress ratio remains near zero, indicating that the assembly cannot sustain a coherent force chain structure over extended strain intervals. Instead, resistance develops primarily during short segments of the cycle, particularly near stage transitions or during localized growth phases. This behavior contrasts sharply with the dense experiment, in which shear resistance is maintained over a much broader portion of the loading history.

The stage-wise evolution during shear-right-forward (SRF) further illustrates this behavior. In cycle 1, μ gradually increases with minimal fluctuation, suggesting a period of progressive formation of the force chain. This is followed by a rapid increase over a short strain interval, indicating a brief but effective mobilization

of shear resistance before stabilizing. Cycle 2 exhibits a similar but more gradual increase, while cycle 3 remains nearly constant throughout the stage, indicating that by the third cycle, the assembly is largely unable to mobilize meaningful forward shear resistance. This progressive suppression of μ across cycles suggests that repeated loading further degrades the already weak load-bearing structure in a loose assembly.

During the reverse stages, the response remains comparatively smoother and less fluctuating, as also observed in the densely packed experiments. However, this smoothness reflects the absence of strong transmission rather than a stable hysteretic response. The stress ratio evolves gradually with only minor deviations, indicating that reverse shearing is primarily accommodated by particle rearrangement rather than sustained resistance. Similar behavior is observed in both the shear-right-reverse (SRR) and shear-left-reverse (SLR) stages, where μ remains low and only weakly cycle-dependent.

The shear-left-forward stage (SLF) further highlights the instability of the loose response. Cycle 1 exhibits a pronounced drop, followed by partial recovery and large fluctuations, indicating intermittent formation and breakdown of force-transmitting structures. Cycle 2 evolves more gradually, while cycle 3 remains largely unresponsive, again suggesting that the assembly is unable to sustain coherent resistance in later cycles. These differences indicate that a loose packing leads to highly variable and transient force transmission, particularly in the forward-shearing directions.

Collectively, these results indicate that, under the same applied normal stress, reducing the initial packing density fundamentally limits the assembly's ability to develop and sustain a load-bearing contact network. Although the dense assembly maintains shear resistance over extended portions of the cycle, the loose assembly exhibits a highly intermittent response, with resistance mobilized only briefly and degrading rapidly with repeated loading. As a result, the stress ratio loops have become increasingly collapsed, reflecting a transition from sustained force transmission to predominantly rearrangement-driven deformation.

4.4.1.2 Volumetric Strain

Figure 4.44b shows the volumetric strain, ϵ_V, as a function of shear strain, γ, for the three-cycle, loosely packed granular assembly under $\sigma_n = -44.1$ kPa, corresponding to 122 lb. Compared to the corresponding densely packed experiment (Figure 4.46), the loose assembly exhibits a more tightly grouped, lower-amplitude, and more

uniformly evolving volumetric response over much of the loading history. Although the same broad features of dilation, contraction, and reversal-driven restructuring remain present, the volumetric behavior is less strongly differentiated by cycle and appears to be accommodated by a more repeatable, low-amplitude deformation mode. To better visualize the evolution, Figure 4.47 shows the volumetric response of the 122 lb, loosely packed granular assembly separated by shear stage.

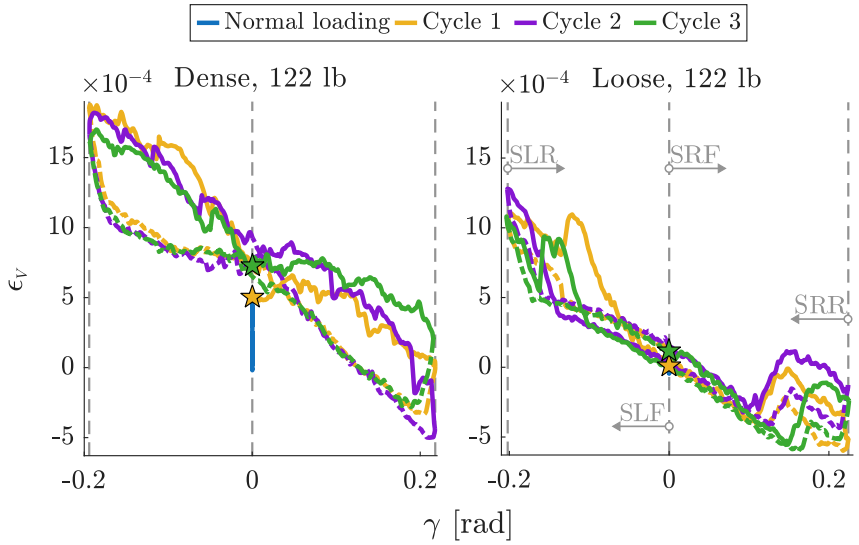


Figure 4.46: Volumetric strain evolution for the three-cycle, dense (left) and loose (right) experiments subjected to a normal load of $\sigma_n = -44.1$ kPa. Curve style indicates shearing direction (solid: forward, dash-dotted: reverse), gray dashed lines mark stage transitions, and stars mark the start (yellow) and end (green) of cyclic loading.

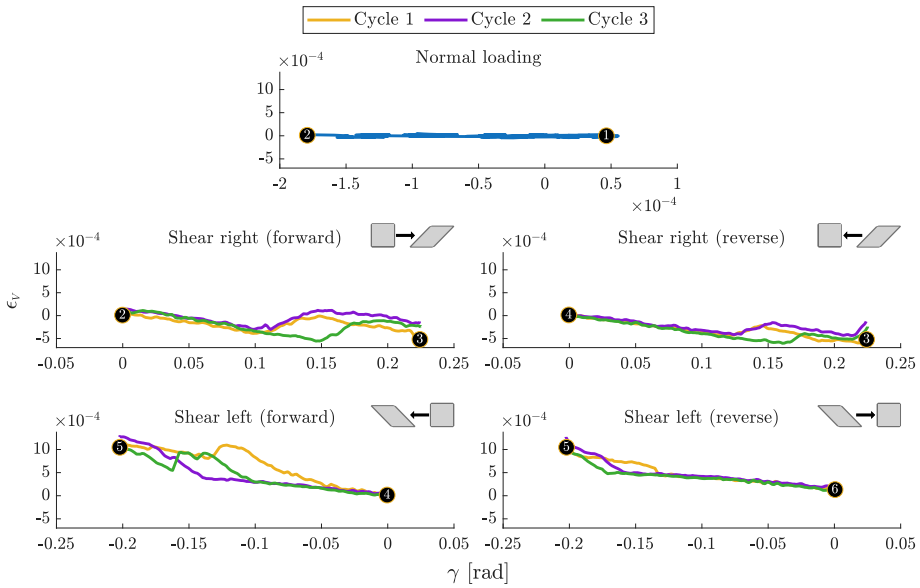


Figure 4.47: Volumetric strain evolution per stage for the three-cycle, loosely packed, assembly under $\sigma_n = -44.1$ kPa. Stage markers are shown only for Cycle 1.

The first noticeable difference occurs during the normal loading stage. Whereas the dense 122 lb experiment exhibited sustained compaction during normal loading, the loose experiment alternated rapidly between compaction and dilation regimes before ending at a slightly compressed state by the end of normal loading. This indicates that the loose assembly does not undergo monotonic consolidation under the applied normal stress, but instead experiences early rearrangement and partial structural relaxation even before cyclic shearing begins. As a result, the assembly enters the cyclic loading phase from a less-stably consolidated initial state than that of the densely packed assembly.

During the shear-right-forward (SRF) stage, all three cycles initially exhibit a similar and nearly linear decrease in ϵ_v, indicating a common dilative response in the early part of the stage. This behavior contrasts with the dense assembly, in which cycle 1 initially compacted before transitioning to dilation, while cycles 2 and 3 dilated immediately. In the loose assembly, all three cycles instead follow a closely grouped, relatively stable initial path, suggesting that early rightward shearing is accommodated by a common volumetric deformation mode that is only weakly dependent on cycle number. However, near the latter portion of SRF, each cycle undergoes a localized compaction-dilation fluctuation, indicating a temporary departure from this otherwise uniform response. Cycles 1 and 2 experience this fluctuation at nearly the same strain level, whereas cycle 3 exhibits it closer to the end of the stage.

Following reversal into the shear-right-reverse (SRR) stage, the assembly exhibits a largely shared volumetric evolution across cycles. Cycle 1 initially compacts, first gradually and then more rapidly, before undergoing a short dilative burst and then returning to a stable compaction regime for the remainder of the stage. Cycles 2 and 3 follow a similar overall pattern, although they initially dilate before transitioning into the same steady compaction response. Importantly, during the latter portion of SRR, all three cycles become nearly indistinguishable, indicating that SRR drives the loose assembly toward a highly repeatable volumetric state regardless of prior cycle history.

A similar convergence is observed in the shear-left-reverse (SLR) stage. Following shear direction reversal, cycles 2 and 3 begin by dilating before entering a gradual and stable dilative regime, while cycle 1 transitions more slowly into the same response over a longer strain interval. This again suggests that under loose-packing conditions, much of the volumetric response is governed by a shared, quasi-steady deformation mode rather than by strongly cycle-specific restructuring.

The shear left-forward (SLF) stage is the main exception to this otherwise tightly grouped behavior. At the beginning of this stage, all three cycles continue to compact gradually, but eventually depart from this common path through a large localized fluctuation. In cycles 1 and 3, this takes the form of a pronounced compaction-dilation event, whereas cycle 2 instead transitions into a more rapid compaction regime without a comparable rebound. Hence, although the loose assembly exhibits a relatively uniform volumetric response over much of the loading history, the left-forward stage remains especially sensitive to localized structural adjustment and retains the greatest cycle-to-cycle variability.

The ϵ_V response still exhibits directional asymmetry and hysteresis, but much of the central portion of the loading path remains tightly compressed and highly overlapped across cycles. This suggests that the loose assembly repeatedly revisits similar volumetric states over larger portions of the loading history, even as localized restructuring events intermittently disrupt that otherwise uniform response. In addition, we still observe multiple self-intersecting paths, indicating that the volumetric state remains path-dependent despite strong cycle overlap.

As in the dense 122 lb experiment, the final volumetric state remains more compacted than at the onset of cyclic shearing, although the net difference is smaller in the loose 122 lb experiment. Moreover, the magnitude of compaction still consistently exceeds that of dilation across all cycles, indicating that the assembly retains an overall compressive bias despite its looser initial state. However, the extrema in ϵ_V are substantially smaller than in the densely packed experiment, showing that loosening the initial packing suppresses the magnitude of volumetric restructuring even though the same broad stage-dependent mechanisms remain active.

Altogether, these results indicate that the loosely packed, 122 lb experiment accommodates cyclic deformation through a much more uniform and tightly grouped volumetric response than the corresponding densely packed, 122 lb experiment. Rather than exhibiting strongly cycle-differentiated volumetric evolution throughout the loading path, the loose assembly repeatedly returns to similar quasi-steady states, departing from them only during localized restructuring events. Thus, under loose packing conditions, this suggests that much of the deformation is accommodated by repeatable rearrangement rather than by sustained, cycle-dependent structural evolution.

4.4.1.3 Dilatancy

Figure 4.44d shows the dilatancy, β, as a function of shear strain, γ, for the loosely packed experiment under $\sigma_n = -44.1$ kPa (approximately 122 lb). Dilatancy is interpreted alongside the volumetric strain, ϵ_V, where peaks and extrema correspond to intensified internal rearrangement and smoother regions indicate more stable deformation. Compared with the corresponding dense experiment (Figure 4.48), the loose assembly exhibits a more localized and intermittent response, with most of the loading path characterized by weak shear-volume coupling. Figure 4.49 provides a clearer stage-by-stage view of the dilatancy response.

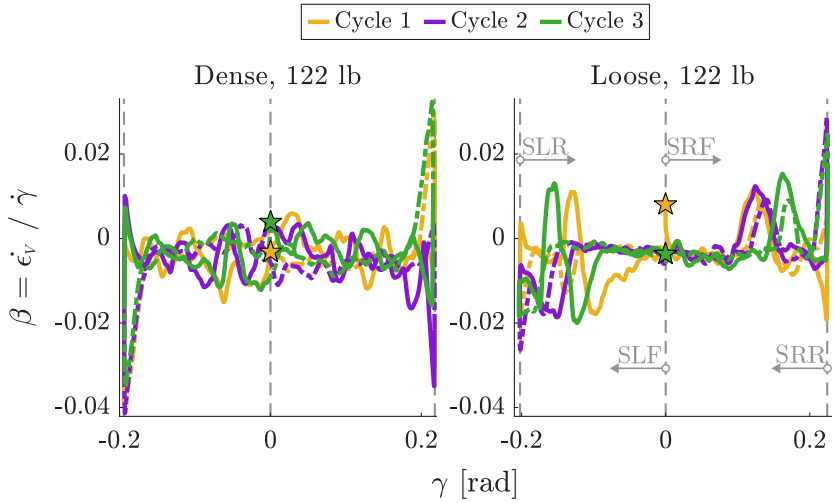


Figure 4.48: Void ratio evolution for the three-cycle, dense (left) and loose (right) experiments subjected to a normal load of $\sigma_n = -44.1$ kPa. Curve style indicates shearing direction (solid: forward, dash-dotted: reverse), gray dashed lines mark stage transitions, and stars mark the start (yellow) and end (green) of cyclic loading.

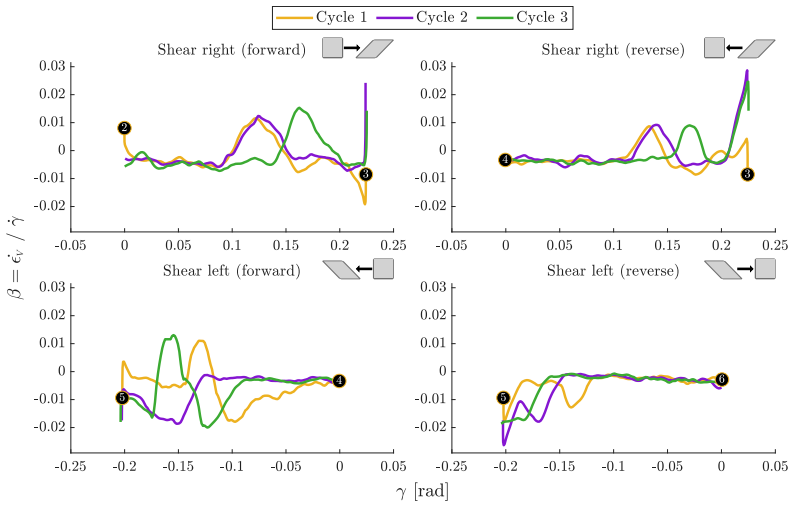


Figure 4.49: Dilatancy per stage for the three-cycle, loosely packed, assembly under $\sigma_n = -44.1$ kPa. Stage markers are shown only for Cycle 1.

During the shear-right-forward (SRF) stage, all three cycles exhibit a gradual decrease in β during the initial portion of the stage, consistent with the early-stage dilative response observed in ϵ_V. During this interval, the curves remain tightly grouped, indicating a shared deformation mode with relatively weak coupling. As the cycles depart from this common path and undergo localized compaction-dilation fluctuations, β exhibits corresponding peaks. These peaks occur in the same sequence as the deviations observed in ϵ_V, confirming that the strongest shear-volume coupling is activated only during these localized restructuring events rather than throughout the stage.

Following reversal into the shear-right-reverse (SRR) stage, all cycles exhibit a rapid drop in β before transitioning into a tightly grouped, nearly stable regime. This sharp change corresponds to the rapid compaction observed in ϵ_V immediately after reversal and reflects a brief but significant restructuring of the contact network. The magnitude of this drop varies by cycle, with cycles 2 and 3 exhibiting stronger responses than cycle 1, but all cycles quickly converge toward a common, weakly varying state. A secondary fluctuation occurs shortly thereafter, corresponding to a brief dilative adjustment before the response stabilizes again. Overall, the SRR stage is characterized by a short-lived burst of strong coupling followed by a predominantly low-coupling regime.

A similar but sign-reversed pattern is observed in the shear-left-reverse (SLR) stage. Following reversal, β increases rapidly as the assembly dilates, with cycles 1 and 2 responding more abruptly and with greater fluctuation than cycle 3. In contrast, cycle 3 evolves more gradually, indicating a smoother adjustment of the packing structure. Despite these initial differences, all cycles again converge to a tightly grouped, stable regime in which β varies only weakly with strain. This behavior reinforces the observation that strong shear-volume coupling in the loose assembly is confined primarily to short intervals near shear reversal, while the remainder of the deformation is accommodated through a more uniform rearrangement.

Consistent with the volumetric response, much of the central portion of the loading path exhibits tightly overlapped β curves across all cycles. This indicates that for large portions of the cycle, the loose assembly deforms with minimal variation in the shear-volume coupling and repeatedly follows a common, quasi-steady deformation path. In contrast, the largest fluctuations in dilatancy occur leading up to and following shear reversal, when the contact network undergoes the most abrupt structural changes.

The dilatancy response also retains directional asymmetry and hysteresis. The maximum β occurs in the right branch during SRR, while the minimum occurs in the left branch during SLR, consistent with the dense 122 lb experiment. However, the loose assembly exhibits greater variability in β near the transition regions, with higher-amplitude fluctuations leading up to reversal. This indicates that, although the overall coupling is weaker, the restructuring events themselves can be more irregular and less constrained under loose packing conditions.

Lastly, there is a notable difference in the overall shift in dilatancy over the loading history. Whereas the dense assembly began at a negative β and ended at a slightly positive value, the loose assembly began at a positive β and ended at a slightly negative value. This shift reflects a reversal in the dominant volumetric mechanism: rather than transitioning to a dilation-dominated state, the loose assembly evolves toward a compaction-dominated response under cyclic loading.

Collectively, these results indicate that the loose 122 lb experiment exhibits a dilatancy response that is weak for most of the loading path and strongly activated only during localized restructuring events near reversal. Unlike the 122 lb dense experiment, where shear-volume coupling is more sustained and cycle-dependent, the loose assembly primarily governs deformation by rearrangement with minimal volumetric coupling, except during brief restructuring events.

4.4.1.4 Void Ratio

Figure 4.44c shows the void ratio, e, as a function of shear strain, γ, for the three-cycle, loosely packed experiment under $\sigma_n = -44.1$ kPa (approximately 122 lb). Compared to the corresponding densely packed experiment (Figure 4.50), the void ratio response of the loose assembly exhibits a fundamentally different evolution, characterized by a reversal in the direction of volumetric change during forward and reverse shearing, strong convergence to a shared path across cycles, and a net densification over the loading history.

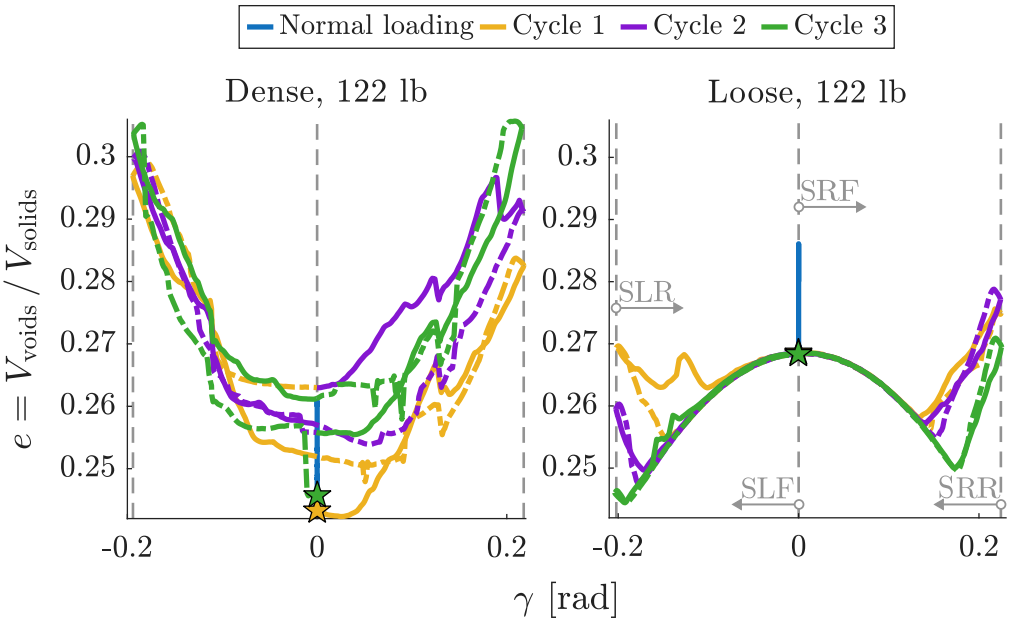


Figure 4.50: Void ratio evolution for the three-cycle, dense (left) and loose (right) experiments subjected to a normal load of $\sigma_n = -44.1$ kPa. Curve style indicates shearing direction (solid: forward, dash-dotted: reverse), gray dashed lines mark stage transitions, and stars mark the start (yellow) and end (green) of cyclic loading.

A primary distinction from the dense assembly is that the relationship between shear direction and volumetric change is reversed. Whereas in the dense case, forward shearing was associated with dilation and reverse shearing with contraction, the loose assembly exhibits the opposite trend: away from the immediate vicinity of reversal points, forward shearing generally results in a gradual decrease in void ratio, while reverse shearing produces an increase. This indicates that the loose assembly accommodates shear primarily through progressive compaction under forward loading and partial dilation under reversal, reflecting a fundamentally different packing response mechanism than in the dense case.

Another defining feature of the loose response is the strong convergence of all three cycles onto nearly the same void ratio path over most of the loading history. Away from the immediate vicinity of shear reversal, the cycles become nearly indistinguishable, indicating that the packing state repeatedly returns to a common structural trajectory that is largely independent of cycle number. Deviations between cycles are confined primarily to short intervals near the ends and beginning of stages – specifically near the end of shear-right-forward (SRF), the start of shear-right-reverse (SRR), the end of shear-left-forward (SLF), and the start of shear-left-reverse (SLR) – showing that most of the cycle-to-cycle differences arise mainly

during transient restructuring events rather than during the bulk of the deformation.

This convergence is especially evident in the third cycle, which exhibits the most complete overlap and remains nearly indistinguishable over most of the loading path except immediately before and after shear reversal. Cycle 2 also exhibits extended intervals of nearly identical evolution, while cycle 1 shows the greatest departure from this shared path. Thus, the loose assembly undergoes its strongest structural adjustment earlier in the loading history before progressively converging toward a more retracing and cycle-insensitive response in later cycles. In this respect, the loose assembly does not continue to evolve into distinct packing states from cycle to cycle, but instead increasingly revisits previously established ones.

The stage-wise evolution (Figure 4.51) further supports this interpretation. In both the rightward and leftward branches, the assembly repeatedly departs from and then returns to previously traversed void ratio paths, indicating that most of the packing evolution is governed by a shared compaction-dilation trajectory. The largest deviations from this common path occur near shear reversal, where the contact network is forced to reorganize more abruptly. Even then, the response rapidly returns to the same underlying structural path, showing that the loose assembly repeatedly rejoins similar packing states after each localized restructuring event. Furthermore, though maxima still occur immediately after shear reversal, consistent with the moment of greatest structural incompatibility, their ordering across cycles is not systematic, suggesting that the cycle history still influences the response, but only within these localized transition intervals.

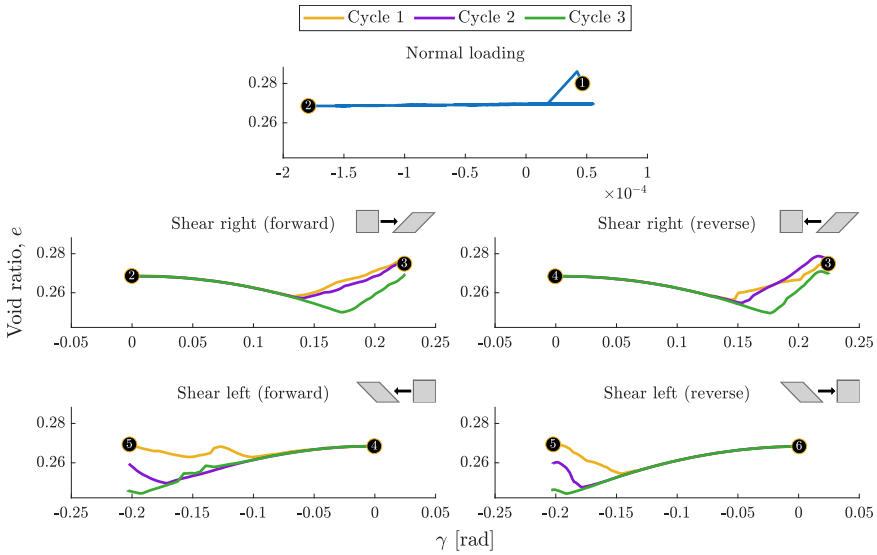


Figure 4.51: Void ratio evolution per stage for the three-cycle, loosely packed, assembly under $\sigma_n = -44.1$ kPa. Stage markers are shown only for Cycle 1.

An important final distinction is that, unlike the dense assembly, the loose assembly evolves toward a more compacted final state. The void ratio at the end of the loading history is lower than at the onset of cyclic shear, indicating net densification under repeated loading. Although this change is modest relative to the full range of the void ratio evolution, it contrasts directly with the dense case, in which the assembly became slightly looser. Interestingly, while the loose experiment reaches a lower maximum e than the dense experiment, the minimum e attained in the two cases is nearly the same. This suggests that both instances can compact toward a similar lower-bound packing state under cyclic loading, but the loose assembly is less able to reopen or dilate away from that compacted configuration once shear is applied. Together, these observations indicate that cyclic shearing progressively drives the loose packing toward a more stable and compact configuration.

In summary, these results indicate that the loose 122 lb experiment accommodates deformation through a highly repeatable, path-retracing packing response, in which most of the loading history is governed by a shared, compaction-dominated trajectory. Unlike the dense 122 lb experiment, where the packing evolution is strongly cycle-dependent and distributed throughout the stages, the loose assembly concentrates its restructuring near shear reversal and repeatedly returns to previously visited packing states. Ultimately, this suggests that under loose packing conditions, deformation is governed primarily by gradual rearrangement and progressive densification rather than by sustained, cycle-dependent structural evolution.

4.4.1.5 Macroscopic Response Summary

The collective macroscopic response of the three-cycle, loosely packed assembly under $\sigma_n = -44.1$ kPa (approximately 22 lb) differs fundamentally from that of the corresponding densely packed assembly, despite being subjected to the same normal stress. Whereas the dense assembly developed sustained shear resistance, directionally differentiated volumetric evolution, and a progressively looser final packing state, the loose assembly exhibits a much weaker and more intermittent stress ratio, a tightly grouped and largely repeatable volumetric response, and net densification over the loading history. Throughout much of the cycle, the loose assembly repeatedly revisits similar volumetric and packing states, with most cycle-to-cycle variability confined to short intervals near shear reversal. In addition, the dilatancy response indicates that shear-volume coupling is weak over most of the loading path and becomes significant only during localized restructuring events. Overall, these results suggest that the loose assembly accommodates cyclic shear

primarily through gradual rearrangement, path retracing, and progressive structural consolidation rather than through sustained, cycle-dependent force transmission and dilation-dominated response observed in the dense assembly. Thus, at the same confinement level, the initial packing state exerts a first-order control on the macroscopic deformation mechanism. This distinction is consistent with classical and modern granular mechanics, in which dense granular media tend to dilate and mobilize greater peak shear resistance, while loose granular media tend to contract and evolve toward more compact states under shear. In particular, the strong dependence of shear strength, dilatancy, and packing state is well established in the work of Rowe and Bolton, while more recent micromechanical and cyclic-shear studies similarly show that the granular response under repeated loading strongly depends on the evolving packing state and reorganization of the contact network [11, 71, 72, 80].

4.4.2 Grain-Scale Response

The macroscale response (Figure 4.44) indicates that the loose granular assembly undergoes continuous, extensive restructuring under cyclic loading, with the internal force-bearing structure remaining highly dynamic. We now investigate this behavior at the grain-scale.

4.4.2.1 Coordination Number

The coordination number, Z_c, tracks the evolution of the contact network by measuring the average number of contacts per grain. Variations in Z_c reflect periods of contact creation and loss, providing insight into how the granular structure reorganizes during shear. Figure 4.52 shows its evolution with shear strain, while Figure 4.53 presents the stage-wise response.

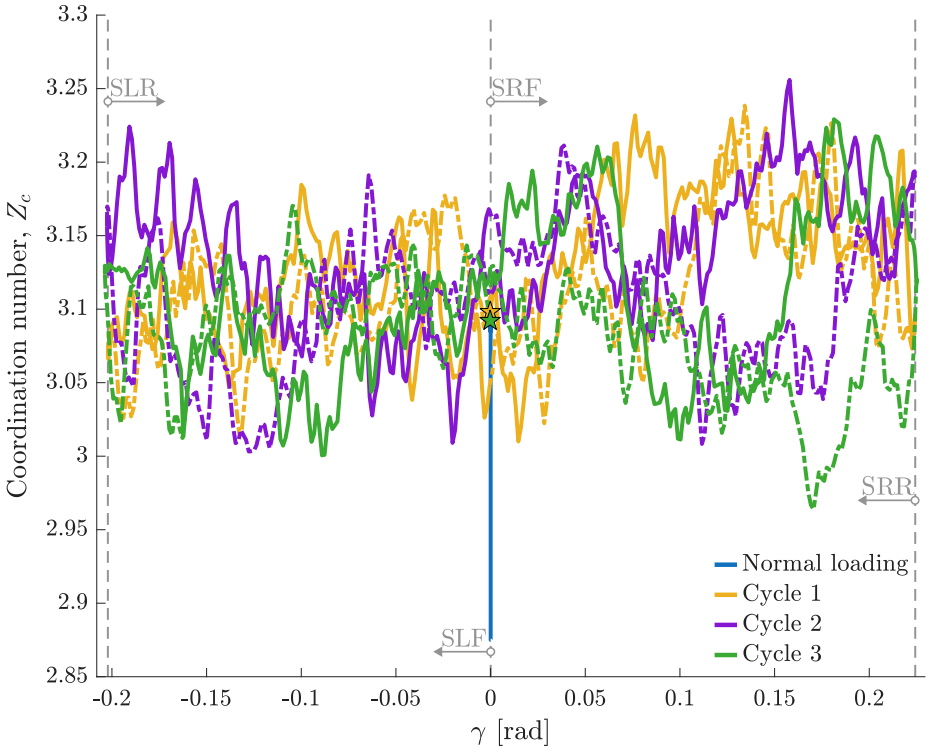


Figure 4.52: Evolution of the coordination number, Z_c, for the loose granular assembly ($\sigma_n = -44.1$ kPa). Z_c is the average number of contacts per particle. Curve style indicates shearing direction (solid: forward, dash-dotted: reverse), gray dashed lines mark stage transitions, and stars mark the start (yellow) and end (green) of cyclic loading.

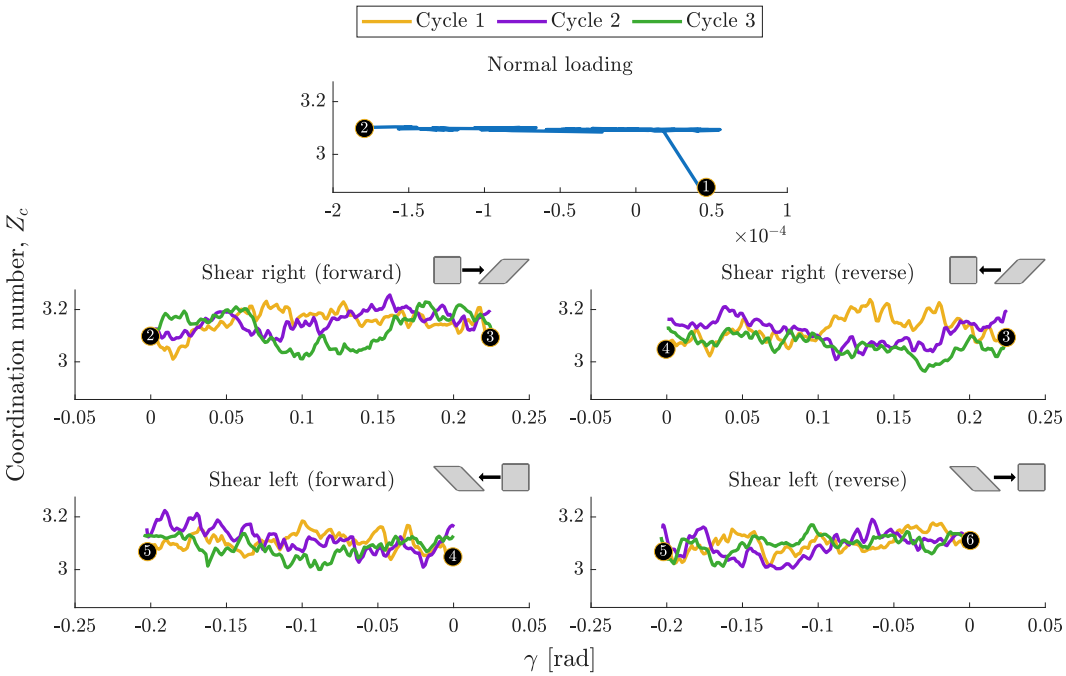


Figure 4.53: Per-stage evolution of the coordination number, Z_c, for the loose granular assembly ($\sigma_n = -44.1$ kPa). Stage markers are shown only for Cycle 1.

The coordination number response of the 122 lb loose assembly reflects a system that undergoes more constrained variations in contact connectivity, despite continuous rearrangement under cyclic shear. Compared with the dense assembly, the overall increase in Z_c under normal loading is nearly identical. However, the net change from the onset to the end of shear is substantially smaller in the loose assembly, indicating that, although contacts are continuously formed and broken, the system maintains a more stable average level of connectivity over the full loading history.

This difference is also reflected in the extrema of the coordination number. While the dense assembly reaches both its maximum and minimum values during the first cycle, the loose assembly exhibits a delayed evolution, with the maximum occurring in cycle 2 and the minimum in cycle 3. Although the minimum values are comparable between the two systems, the reduced maximum in the loose assembly indicates that it is less capable of forming highly connected configurations, consistent with a more open packing structure.

The stage-wise evolution further highlights the role of confinement and packing structure. During shear-right-forward (SRF), Z_c does not evolve monotonically, but instead exhibits a sequence of local rearrangements. In cycle 1, this appears as an initial loss of contacts followed by recovery and gradual decline, whereas in later cycles the response becomes more segmented, with periods of relatively steady coordination interspersed with brief reorganization events. This behavior suggests that a looser packing leads to contact formation and breakage occurring in a more distributed and less synchronized manner.

Upon shear reversal (shear-right-reverse (SRR)), all cycles exhibit rapid adjustments in coordination number, reflecting the disruption of the existing contact network and the formation of a new one aligned with the reversed loading direction. However, unlike the dense assembly, where contact loss dominates this stage, the loose assembly shows a more balanced response, with both decreases and subsequent recoveries occurring within the same stage. In particular, later cycles exhibit partial recovery of contacts by the end of SRR, indicating that the system can more readily reorganize without sustaining a net loss of connectivity.

The shear-left stages (shear-left-forward (SLF) and shear-left-reverse (SLR)) exhibit comparatively more stable behavior, with all cycles evolving within a narrower range of Z_c values. This tighter grouping indicates that, once the system has adapted to the reversed loading direction, the contact network fluctuates within a constrained band of configurations. Notably, the response in these stages is less sensitive to

cycle number than in the shear-right stages, suggesting that the system reaches a more repeatable structural state during leftward shearing.

Overall, the evolution of the coordination number in the loose assembly is characterized by smaller amplitude variations and a more confined range of values than in the dense case. This is reflected in the shape of the response, which forms a more rectangular envelope rather than the crescent-like structure observed under higher density. Mechanistically, this indicates that the loose assembly undergoes continuous but moderate contact rearrangements, without the large-scale formation and loss of contacts exhibited in the dense granular assembly. As a result, the contact network remains more stable on average, even though it is locally dynamic throughout the loading history.

4.4.2.2 Force Chain Statistics and Evolution

While the coordination number describes how the overall network evolves, it does not distinguish which contacts are actively transmitting load. We now focus on the subset of strong contacts that organize into force chains, which form the primary load-bearing structure within the granular assembly. Examining the evolution of these force chains provides insight into how stress is redistributed and sustained during cyclic shear.

Number of Detected Force Chains We begin by examining the number of detected force chains, which reflects how the load-bearing structure forms, breaks, and reorganizes throughout the loading history. The number of force chains as a function of shear strain is shown in Figure 4.54, and the associated per-stage evolution per stage is shown in Figure 4.55.

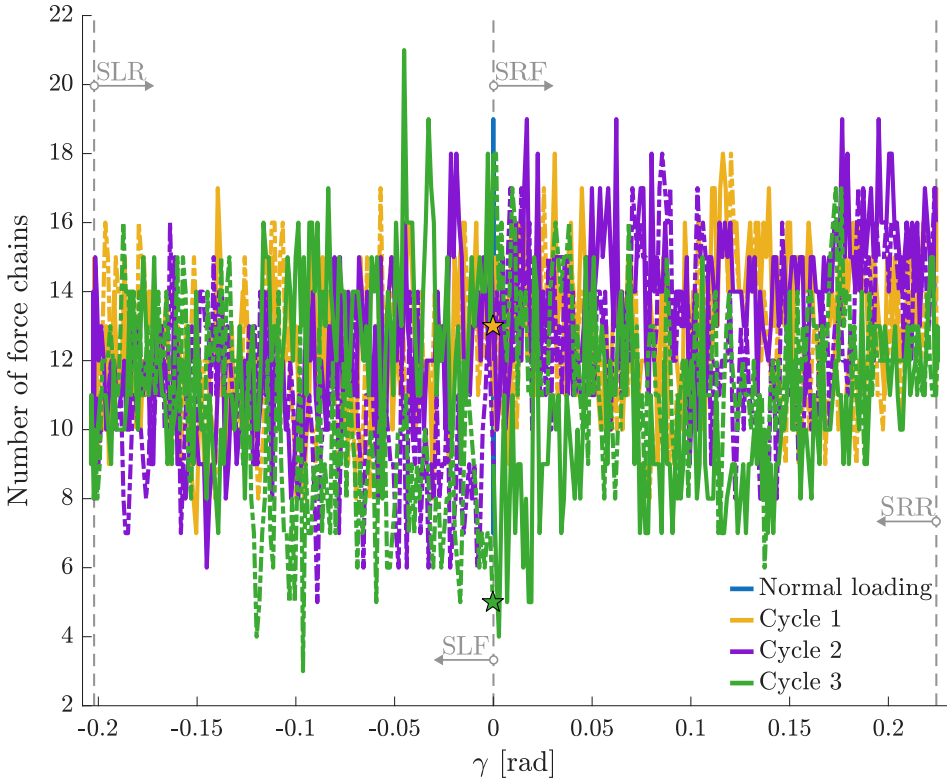


Figure 4.54: Evolution of the detected number of force chains, for the loose granular assembly ($\sigma_n = -44.1$ kPa). Curve style indicates shearing direction (solid: forward, dash-dotted: reverse), gray dashed lines mark stage transitions, and stars mark the start (yellow) and end (green) of cyclic loading.

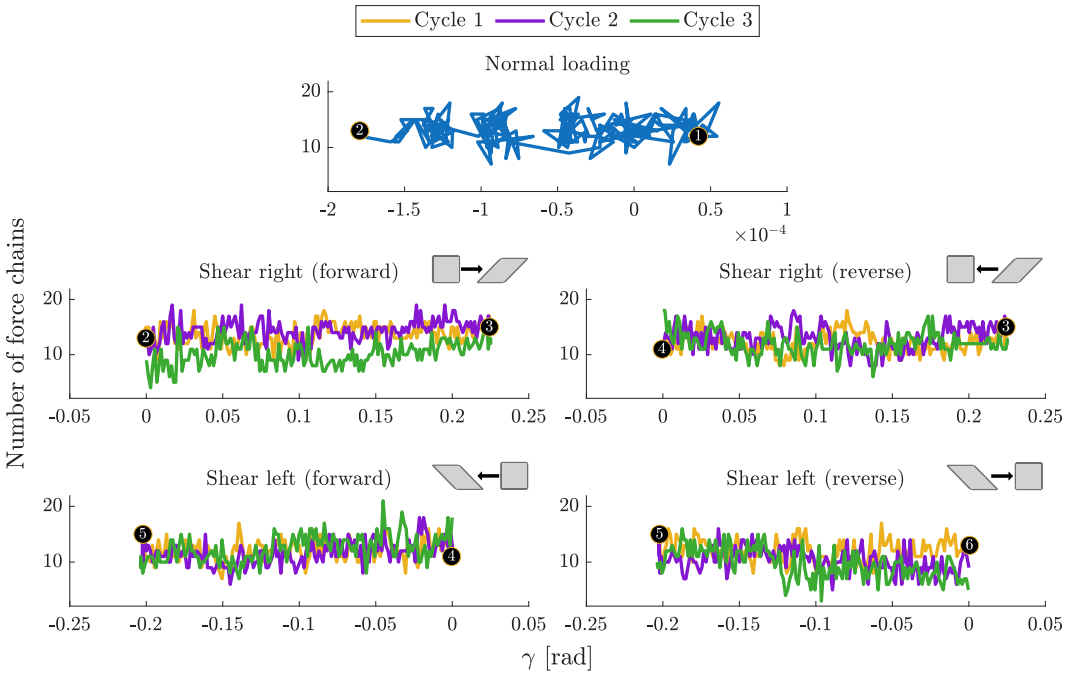


Figure 4.55: Per-stage evolution of the detected number of force chains for the loose granular assembly ($\sigma_n = -44.1$ kPa). Stage markers are shown only for Cycle 1.

During normal loading, the number of force chains fluctuates significantly, ranging from approximately 7 to 19, with an average of around 13. Unlike the dense granular assembly, the loose system exhibits clear groupings associated with each load increment, separated by relaxation periods; this indicates that force chains form in discrete bursts as contacts are progressively engaged under compression, followed by short intervals of redistribution as the system relaxes. Mechanistically, this reflects a more heterogeneous accumulation of the load-bearing structure, in which chains form and reorganize incrementally rather than evolve smoothly.

The onset of shear (shear-right-forward (SRF)) leads to an initial drop in the number of force chains, with the magnitude of this drop increasing with the cycle count; this reflects the breakdown of force chains incompatible with the imposed shear direction. Following this initial disruption, all cycles exhibit a gradual increase in the number of force chains, indicating the formation of new load-bearing structures aligned with the shear direction.

Compared to the dense assembly, the loose response is more stable and exhibits greater overlap between cycles, particularly for cycles 1 and 2 beyond mid-stage. Rather than exhibiting large, irregular fluctuations, cycle 1 transitions between two near-steady regimes, indicating that the system alternates between distinct yet stable force chain configurations. Additionally, no single cycle consistently dominates; instead, cycles 1 and 2 compete for the highest number of force chains throughout SRF. This suggests that under loose packing, the force chain network is less rigidly organized and more sensitive to local rearrangements, allowing multiple configurations to maintain comparable load levels.

During shear reversal (shear-right-reverse (SRR)), the evolution of force chains reflects a redistribution of load as the assembly adapts to the new loading direction. Cycles 1 and 2 begin with a relatively high number of force chains and gradually lose chains over the course of the stage, indicating the progressive breakdown of the existing load-bearing structure. In contrast, cycle 3 begins with fewer force chains, but gains more chains over the course of the stage, ultimately reaching the highest values. This behavior, also observed in the dense assembly, reflects a shift in when the system forms its load-bearing structure, with later cycles rebuilding chains during reversal rather than during forward shearing.

Across all cycles, the beginning and end of SRR are characterized by near-steady regimes, whereas the middle portion exhibits greater variability. This behavior suggests that the system transitions between relatively stable configurations, with more

active reorganization occurring as the network adjusts to the reversed loading direction. Compared to the dense case, the fluctuations are more contained, indicating that the force chain network reorganizes more gradually under the same confinement but with a looser packing.

The shear-left stages exhibit a more structured and, in some cases, more tightly grouped response than the forward-shear stages. In particular, shear-left-forward (SLF) shows the strongest overlap across cycles, indicating that the force chain network converges toward a similar configuration once the system has adapted to the reversed loading direction. This contrasts with the dense assembly, where forward-shear stages exhibited the greatest overlap, highlighting a shift in where structural consistency occurs.

During shear-left-reverse (SLR), the evolution begins with an initial steady regime across cycles, followed by a gradual decrease and subsequent recovery in the number of force chains. While cycles 2 and 3 exhibit pronounced fluctuations early in the stage, cycle 1 remains relatively stable until a distinct drop near mid-stage, after which it transitions to a lower chain-count regime. Notably, all cycles transition from a higher- to a lower-force chain regime, indicating a redistribution of load-bearing structures as the system progresses through the stage.

Despite these transitions, the overall evolution in the loose assembly is more stable than in the dense case, with fewer large fluctuations and more sustained periods of steady behavior. This indicates that although force chains continue to form and break, the system maintains a more consistent load-bearing structure throughout the loading history.

Over the full loading history, the loose assembly exhibits a net loss of approximately 8 force chains, compared to only 2 in the dense assembly, indicating a greater cumulative degradation of the load-bearing structure. The minimum and maximum number of force chains occur during cycle 3, with values of approximately 3 and 21, respectively. In contrast, the dense assembly reached its maximum in cycle 1 and its minimum in cycle 2.

Despite this shift in the timing of extrema, the overall pattern remains consistent: the maximum number of force chains is still associated with forward shearing, while the minimum occurs during reverse-shear stages. Thus, forward shearing continues to promote the formation of load-bearing chains, while reversal leads to their breakdown. However, the redistribution of these extrema across cycles suggests that the

timing of force chain formation and destruction becomes increasingly influenced by the loading history rather than being tied to a single stage.

Overall, the evolution of the number of force chains in the 122 lb loosely packed assembly reflects a network that is more stable in its instantaneous behavior, but undergoes greater cumulative change over time. Compared to the dense case, the force chain structure is less dominated by large, abrupt reorganizations and instead evolves through more gradual, cycle-dependent adjustments, indicating a more distributed and adaptive mode of stress transmission.

Total Force Chain Length Next, we examine the total force chain length, which quantifies the size of the force chain network (in terms of the number of grains) and provides insight into how far stresses are transmitted through connected grain clusters. Figure 4.56 shows the total force chain length as a function of shear strain, γ, while Figure 4.57 shows its per-stage evolution. In general, the total chain length closely follows the number of detected force chains, indicating that the formation and loss of load-bearing paths are broadly consistent with changes in overall network size. However, key stage-wise differences reveal how chain structure evolves beyond simple changes in count.

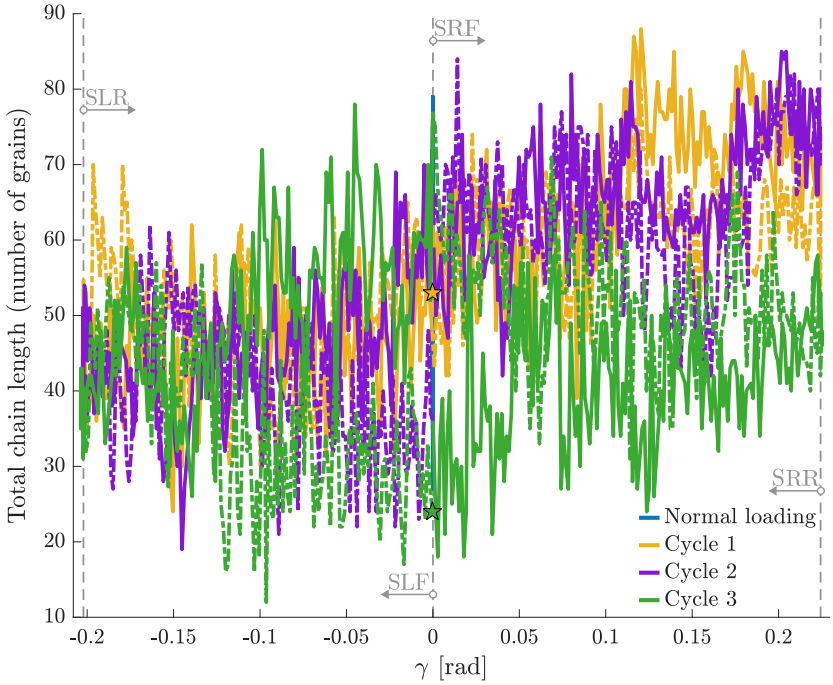


Figure 4.56: Evolution of the total force chain length, in number of grains, for the loose granular assembly ($\sigma_n = -44.1$ kPa). Curve style indicates shearing direction (solid: forward, dash-dotted: reverse), gray dashed lines mark stage transitions, and stars mark the start (yellow) and end (green) of cyclic loading.

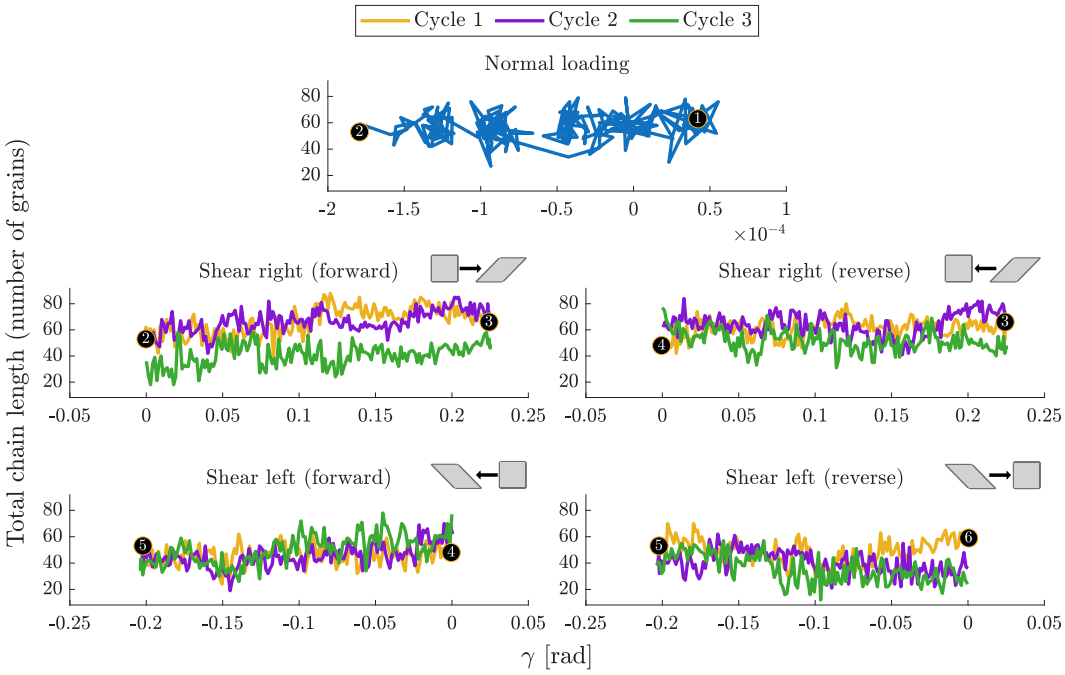


Figure 4.57: Per-stage evolution of the total force chain length, in number of grains, for the loose granular assembly ($\sigma_n = -44.1$ kPa). Stage markers are shown only for Cycle 1.

During normal loading, the total chain length decreases, in contrast to the increase observed in the number of force chains. Thus, although more chains are formed, they are shorter on average, indicating that the load-bearing structure becomes increasingly fragmented with each added load increment. The total chain length ranges from approximately 27 to 79 grains, with most values centered around 53. This suggests that compression promotes the formation of multiple short, localized force chains rather than a few long, system-spanning structures, resulting in a more distributed but less connected load-bearing network.

During forward shearing, the total chain length shows a clearer separation between cycles than the number of force chains. In particular, the cycle 3 response shifts downward, exhibiting the shortest chain lengths in this stage, while cycles 1 and 2 remain closely grouped. This indicates that although there are a comparable number of chains, those in cycle 3 are shorter and less developed. The brief divergence between cycles 1 and 2 near mid-stage further suggests that small differences in local rearrangements can influence how far force chains extend, even when their total number remains similar. Overall, this behavior reflects a reduced ability in later cycles to sustain extended load-bearing structures under shear.

The difference between cycles becomes more pronounced during shear reversal (shear-right-reverse (SRR)). Unlike the number of force chains, which shows significant overlap, the total chain length exhibits more distinct behavior across cycles, with cycle 2 having the largest force chain length and cycle 3 the smallest. While the number of chains may remain similar, their connectivity and spatial extent differ significantly. This suggests that reversal disrupts longer chains more effectively in later cycles, leading to shorter, more localized force transmission pathways. As a result, cycle 3 remains dominated by shorter chains for most of SRR.

During shear-left-forward (SLF), the evolution of the total chain length closely mirrors that of the number of force chains, indicating that both the number and size of the load-bearing structures evolve in a consistent manner. Minor differences are observed at the beginning of the stage, where cycles 2 and 3 exhibit less pronounced fluctuations, suggesting a more stable reorganization of the force chain network in these cycles.

In contrast, the shear-left-reverse (SLR) stage shows a less tightly grouped response than observed in the number of force chains. Near the end of the stage, cycle 1 exhibits a clearer upward shift relative to cycles 2 and 3, indicating that it sustains longer chains while the later cycles remain confined to shorter structures. This suggests that although the number of chains may be similar, the ability to maintain extended load-bearing paths becomes increasingly dependent on the cycle during this stage.

Lastly, compared to the 122 lb dense experiment, the loose assembly reaches significantly smaller extrema in total chain length, with a minimum of approximately 12 grains and a maximum of 88 grains, compared to 21 and 102 grains, respectively. Despite these differences, both packings exhibit the same net loss of 29 grains in the total chain length from the onset to the end of cyclic shear. Hence, while the loose assembly forms smaller, more fragmented force chain structures at any given stage, the cumulative degradation of the load-bearing network over the full loading history is comparable to that of the dense assembly. This suggests that stress transmission in the loose granular assembly becomes more localized, with shorter chains carrying load over smaller distances, even though the overall reduction in load-bearing capacity follows a similar trend.

Accumulated Force Chain Network Content While the number and length of force chains describe the structure of the load-bearing network, they do not directly quantify how effectively that structure transmits stress. To address this, we examine the normalized area under the force chain length curve (Figure 4.58), which quantifies the overall persistence and effectiveness of the force chain network across each stage.

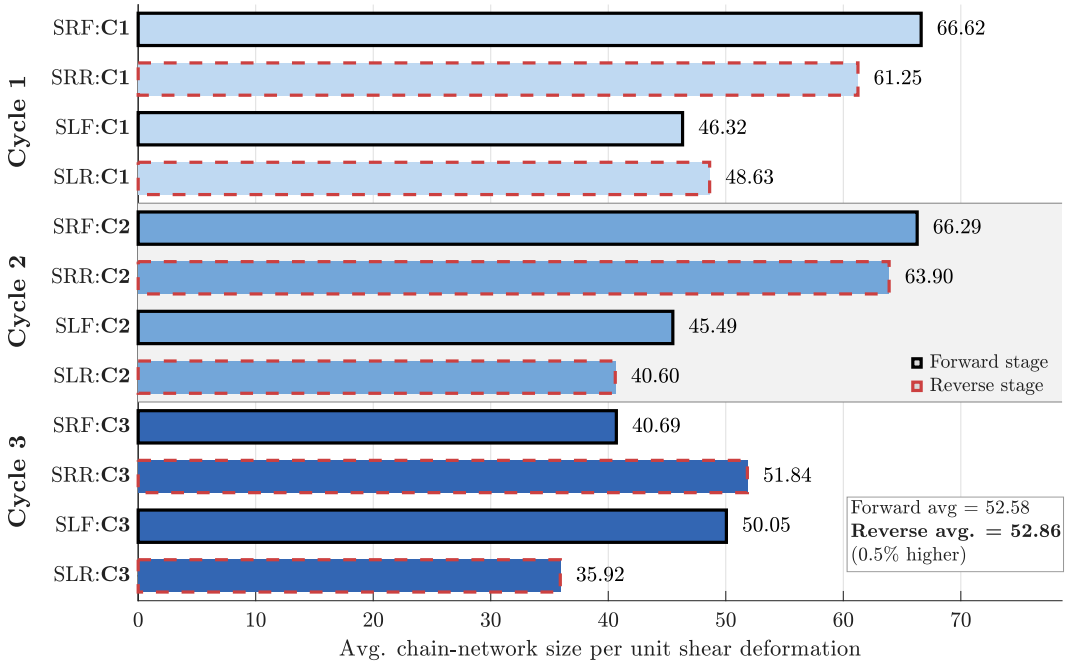


Figure 4.58: Bar chart of the normalized area under the curve (AUC) of the total force chain length for each cycle and shear stage for the loose assembly ($\sigma_n = -44.1$ kPa). The normalized AUC represents the average extent and persistence of the force chain network sustained per unit shear deformation within each stage.

In cycle 1, the loose assembly exhibits a more gradual, less extreme redistribution of the load-bearing structure than in the dense case. The drop in the area under the curve (AUC) from shear-right-forward (SRF) to shear-right-reverse (SRR) is significantly smaller, indicating that shear reversal does not disrupt the force chain network as strongly. However, unlike the dense assembly – where partial recovery occurs during shear-left-forward (SLF) – the loose system continues to lose structural efficiency during this stage. A slight recovery is observed in shear-left-reverse (SLR), resulting in a higher AUC than in SLF. This behavior suggests that, under loose packing, the force chain network is less abruptly disrupted by reversal but also less capable of rapidly rebuilding into an efficient load-bearing configuration immediately afterward.

In cycle 2, the AUC during SRF recovers to a value close to that of cycle 1, indicating that the system can still reestablish a comparable level of load-bearing structure at the start of the cycle. However, the AUC declines for the remainder of the cycle, reflecting a progressive loss of structural efficiency. Notably, shear reversal events (SRF $\rightarrow$ SRR and SLF $\rightarrow$ SRR) produces a much larger drop. This indicates that the most significant restructuring is not associated with the reversal itself, but with the subsequent reorganization into the new loading direction. In contrast to the dense assembly, where the later stages showed a more consistent trend, the SRR-SLR portion of cycle 2 in the loose assembly exhibits a slight monotonic increase, suggesting a gradual stabilization of the force chain network as the new configuration begins to form.

By cycle 3, the system shows a reduced ability to recover its load-bearing structure during SRF, with only a minimal increase in AUC relative to the end of the previous cycle. However, unlike the dense assembly, the AUC increases substantially during SRR, reaching values that exceed those observed in the shear-left stages of earlier cycles. This indicates that, in later cycles, the system forms more effective load-bearing structures during reversal rather than during forward shearing. Following this increase, the AUC decreases monotonically through the shear-left stages, with only a minor drop between SRR and SLF but a more pronounced decrease from SLF to SLR. This behavior contrasts with the dense case, where cycle 3 exhibited a steady, monotonic decrease, highlighting a fundamental shift in the timing at which the system is most effective at transmitting stress.

Overall, the loose assembly exhibits a more balanced distribution of structural efficiency between forward and reverse shear stages. On average, the reverse stages attain a slightly higher AUC than the forward stages, although the difference is small ($\approx 0.5\%$). This contrasts with the dense assembly, where forward shearing produced significantly higher AUC values. Hence, under loose packing, the force chain network is less strongly aligned with the primary loading direction and instead redistributes load more evenly throughout the cycle. As a result, stress transmission becomes less stage-dependent and more influenced by the cumulative history of rearrangements, consistent with the more stable yet less coordinated force chain structures observed previously.

Force Chain Participation Figure 4.59 shows violin plots of the force chain density for each shear stage and cycle. These distributions capture both the typical participation level and the variability in force chain structure across grains. In each

violin plot, the red line denotes the median and the blue lines denote the lower and upper quartiles (Q1 and Q3). The width at any value indicates the relative frequency of the data, while the tails represent the extremes of the distribution. Multiple peaks may also occur, indicating possible distinct regimes within the data.

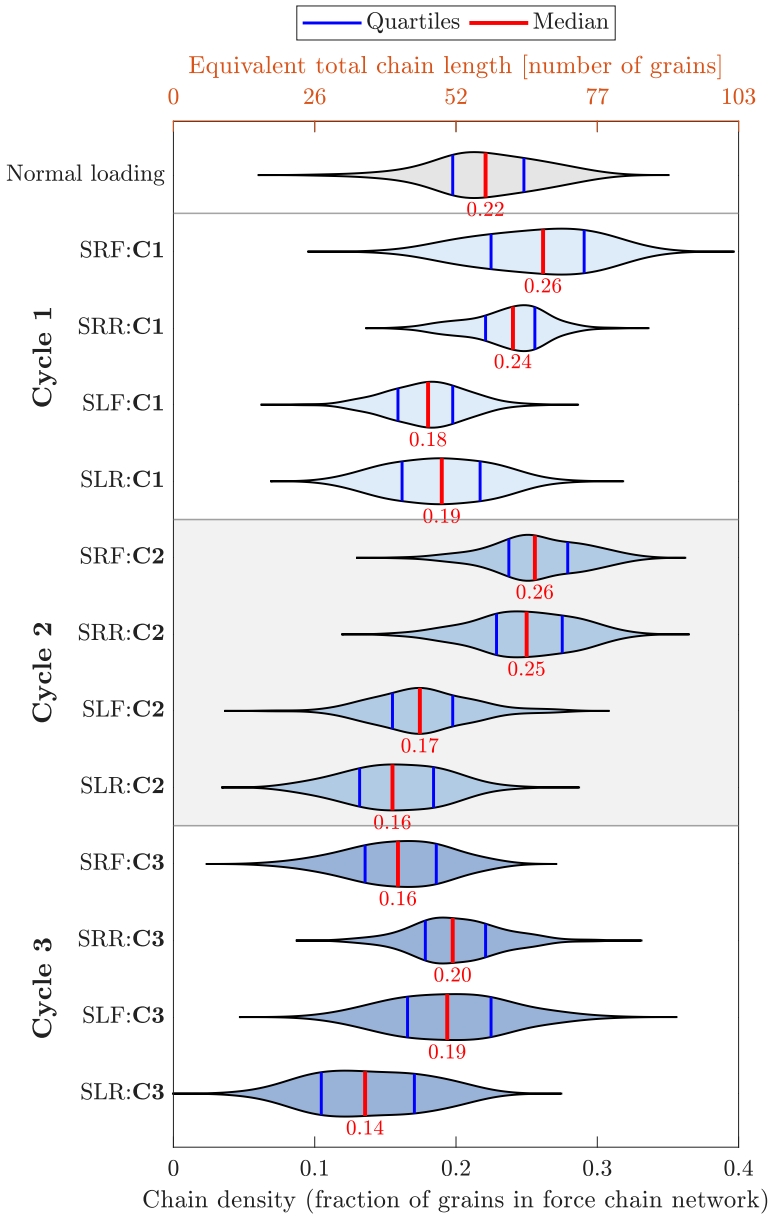


Figure 4.59: Violin plots of the force chain density for each cycle and shear stage for the loose assembly ($\sigma_n = -44.1$ kPa). Force chain density is defined as the fraction of grains participating in the force chain network relative to the total number of interior grains. The bottom x-axis shows the normalized chain density, while the top x-axis shows the equivalent total force chain length in number of grains. The width of each violin indicates the relative frequency of occurrence of a given chain density during that stage.

During normal loading, the chain density distribution exhibits a single dominant participation range, in contrast to the bimodal structure observed in the dense assembly. The median chain density is also lower (0.22 versus 0.26), indicating that fewer grains participate in the force chain network on average. At the same time, the distribution spans a wider range of values, with a long lower tail and a broader but shorter upper tail. This suggests that the loose assembly supports a more heterogeneous load-bearing structure, in which participation is spread across a wider range of chain sizes, but lacks the distinct separation between weakly and strongly connected regions seen under denser packing.

In cycle 1, the chain density exhibits a larger increase from normal loading to shear-right-forward (SRF) than in the dense assembly, indicating that the loose assembly initially builds force chain structure more readily. From SRF to shear-left-forward (SLF), the median chain density then decreases monotonically before slightly recovering in shear-left-reverse (SLR), indicating a gradual reduction in the extent of load-bearing structures followed by partial stabilization.

The SRF stage exhibits the widest distribution and achieves the highest chain densities, reflecting the formation of large, well-developed force chain structures during forward shearing. In contrast, shear-right-reverse (SRR) shows the narrowest range and a more confined participation band, indicating that reversal suppresses the formation of extended structures. Moreover, the shear-left stages exhibit more Gaussian-like distributions with shorter tails, suggesting a more uniform participation of grains in the force chain network.

In cycle 2, the chain density initially recovers from the end of cycle 1 but then decreases monotonically across the stages, indicating a progressive weakening of the force chain network. The largest decrease occurs during the transition from SRR to SLF, indicating that the most significant weakening of the force chain network occurs not at the moment of shear reversal itself, but during the subsequent adjustment within the reversed loading direction.

The distribution shapes further highlight this behavior. The shear-right stages exhibit broader, slightly bimodal-like distributions, indicating the coexistence of different force chain sizes, while the shear-left stages remain more Gaussian, reflecting a more uniform but weaker network. Notably, the shear-right stages maintain higher chain density ranges than the shear-left stages, indicating that forward shearing continues to promote more extensive force chain participation, even though the overall network weakens through the cycle.

In cycle 3, the chain density begins at a level similar to the end of cycle 2, indicating limited recovery between cycles. Unlike the dense assembly, which shows a monotonic decrease, the loose system exhibits a non-monotonic evolution, with an increase from SRF to SRR followed by a decrease through the remaining stages. This behavior suggests that in later cycles, the system forms more extensive force chain structures during reversal than during forward shearing, consistent with the shift observed in the AUC response.

The distribution widths further reflect this transition. SLF exhibits the widest range of chain densities, indicating strong variability in how the network reorganizes, while SRR remains more constrained. Hence, although reversal initiates the formation of new structures, the full variability in participation emerges during the subsequent adjustment stage.

Overall, both dense and loose assemblies exhibit a similar net loss in chain density over the loading history. However, the loose assembly attains both lower minimum and maximum chain densities, indicating that its force chain network is consistently less extensive. Mechanistically, this reflects a shift toward more localized and distributed stress transmission, where fewer grains participate in large, connected structures. Instead of forming strong, system-spanning chains, the loose assembly distributes the load across smaller, more variable clusters, resulting in a broader but less cohesive force chain network.

Strong Network Participation and Strong Network Chain Participation While the previous section examined how broadly force chains are distributed across the assembly, it does not distinguish whether those participating grains belong to the strong force network. We therefore now examine the fraction of grains carrying above-average load (strong network participation), as well as the fraction of those strong grains that organize into force chains (strong network participation in force chains). Together, these measures provide insight into how effectively the load-bearing portion of the assembly is mobilized during cyclic shear. Figure 4.60 summarizes the stage-wise medians and variability in both measures.

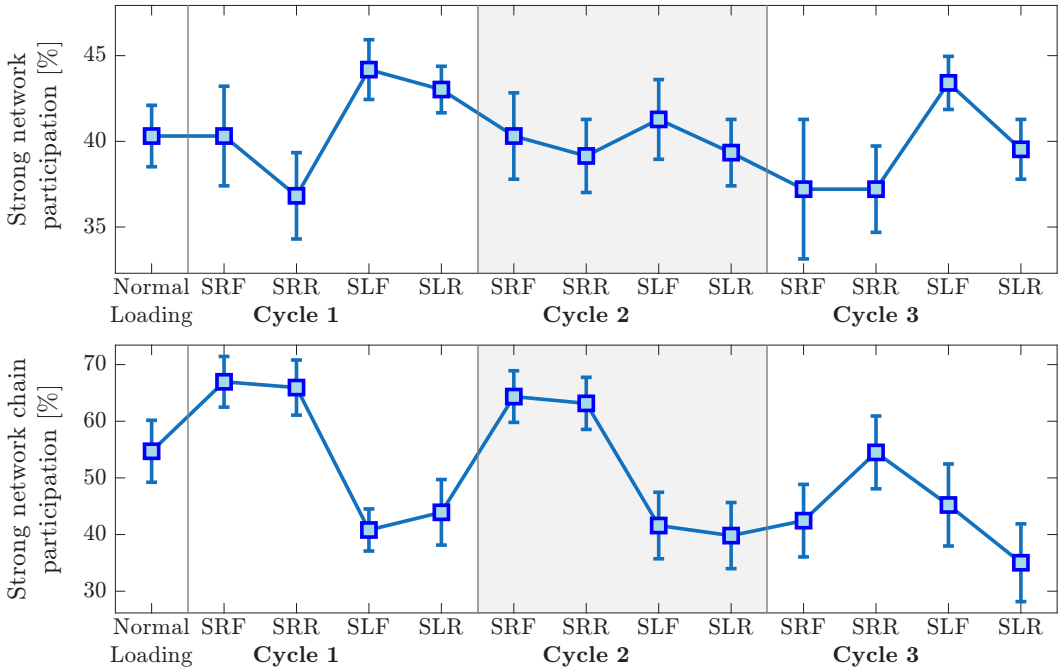


Figure 4.60: Stage-wise medians of the strong network participation [%] (top) and the strong network chain participation [%] (bottom) for each cycle and shear stage for the loose assembly ($\sigma_n = -44.1$ kPa). Error bars represent one-half of the interquartile range, centered about the median.

The **strong network participation** remains comparatively stable throughout the loading history, indicating that a persistent subset of the assembly continues to carry above-average forces even under repeated shearing. Median values remain within a narrow range of approximately 36.8% to 44.2% (34.3% to 45.9% including variability), demonstrating that cyclic loading does not eliminate the strong network, but instead redistributes which grains participate in it.

The most pronounced weakening occurs during the immediate reversal stage, shear-right-reverse (SRR), where the strong-network participation reaches its minimum. This suggests that reversing the loading direction disrupts the previously established stress-bearing skeleton, temporarily reducing the number of grains capable of sustaining elevated loads. In contrast, participation reaches a maximum during shear-left-forward (SLF), indicating that continued shearing in the reversed direction allows a renewed strong contact framework to develop once the system has had time to reorganize.

As cycling progresses, the same broad pattern persists, but with reduced magnitude. The fluctuations observed in cycle 1 weaken in cycle 2, whereas cycle 3 exhibits a more variable shear-left response. This indicates that repeated loading progressively

reduces the strong network's sensitivity to individual loading stages while increasing the heterogeneity of rearrangements in later cycles.

Compared with the dense assembly, the loose system evolves more smoothly and within a smaller range of values, indicating a more gradual redistribution of load-bearing responsibility among grains. However, the net reduction from the onset to the end of shear is larger than in the dense case, suggesting that although the strong network changes less abruptly, it experiences greater cumulative weakening over repeated cycles.

The **strong network chain participation** measures how effectively the strong grains organize into force chains. The median strong network chain participation spans approximately 35% to 67% (41.7% to 71.4% including variability), indicating that only a subset of strong grains contributes to coherent load-bearing chains at any given stage.

Participation is highest during SRF of cycle 1, showing that forward shearing initially promotes the alignment of strong grains into efficient stress-transmitting chains. Thereafter, the response generally weakens through the loading history, with the minimum occurring during shear-left-reverse (SLR) of cycle 3. This progressive decline indicates that repeated shearing reduces the ability of strong grains to remain organized within persistent force chain structures, even when those grains continue to carry elevated forces.

Unlike the comparatively stable, strong network participation, this metric exhibits sharper stage-to-stage drops, particularly during continued shearing in the reversed direction. This shows that the organization of strong grains into chains is more sensitive to the loading history than the mere presence of strong grains. In other words, strong contacts persist longer than the structural coherence of the force chain network they form.

Compared with the dense assembly, the loose assembly reaches a slightly higher upper bound but undergoes more pronounced reduction between stages, especially during cycles 1 and 2. This suggests that loose packing can effectively mobilize strong grains into chains, but those chains are less stable and more easily disrupted during subsequent deformation. The larger net loss from the onset to the end of shear further supports the conclusion that chain organization deteriorates more substantially in the loose assembly. In general, these results show that while roughly 40% of the assembly remains in the strong network throughout cyclic loading, only

about 35% to 67% of those strong grains organize into detectable force chains.

Micro-Macro Comparison The preceding sections examined how the internal load-bearing network evolves at the grain-scale. We now compare these structural changes with the macroscopic shear stress response to evaluate how effectively the evolving force chain network translates internal organization into bulk resistance. This comparison is particularly useful for identifying when grain-scale strengthening and macroscopic strengthening remain coupled, and when they begin to diverge. Hence, we examine the stage-wise medians of the macroscopic shear stress and the total force chain length (Figure 4.61).

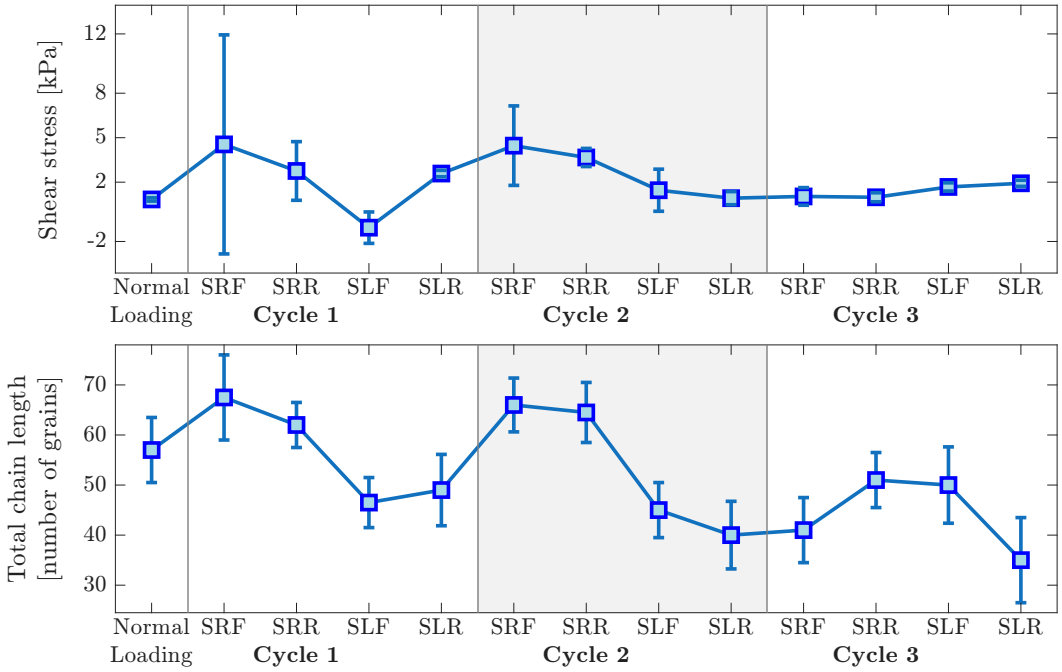


Figure 4.61: Stage-wise medians of the shear stress [kPa] (top) and total chain length [number of grains] (bottom) for each cycle and shear stage for the loose assembly ($\sigma_n = -44.1$ kPa). Error bars represent one-half of the interquartile range, centered about the median.

Compared with the 122 lb dense assembly, the loose assembly exhibits a substantially weaker **shear stress** response throughout the loading history, remaining within a narrow range of approximately -1.1 to 4.5 kPa, far below that of the dense assembly. Even the weakened later-cycle response of the dense assembly exceeds that of the loose case. This indicates that the looser packing is less capable of converting contact forces into sustained bulk shear resistance, because fewer contacts are organized into stable, system-spanning load-bearing structures.

Despite this reduced magnitude, the loose assembly initially follows the same stage-wise evolution as in the dense case. From normal loading to shear-right-forward (SRF), the shear stress increases, reflecting the mobilization of shear resistance as force chains align with the imposed loading direction. From SRF of cycle 1 through shear-left-forward (SLF) of cycle 2, the shear stress then decreases progressively, before remaining nearly constant through most of cycle 3. Thus, the most pronounced stress changes occur early in the loading history, whereas later cycles exhibit little additional strengthening or weakening. The near-zero variability throughout cycle 3 further suggests that the system approaches a mechanically exhausted state in which repeated shearing produces minimal new resistance.

The **total chain length** closely tracks the shear stress response throughout most of the loading history, indicating that macroscopic resistance remains strongly linked to the size of the force chain network. When longer chains are present, the assembly sustains greater shear stress; when the network contracts, the bulk response weakens. This agreement persists through shear-right-reverse (SRR) of cycle 3, demonstrating that force chain extent remains the dominant control on stress transmission over most stages.

A notable decoupling emerges during the final cycle. In cycle 3, the total chain length increases from SRF to SRR, then decreases gradually through SLF, before dropping sharply in shear-left-reverse (SLR), whereas the shear stress remains nearly constant throughout. This indicates that continued restructuring of the internal force network no longer produces a proportional macroscopic response. In other words, the system still reorganizes internally, but these rearrangements become mechanically inefficient and contribute little additional bulk strength.

Compared with the dense assembly, the loose system weakens through a more gradual reduction in chain length rather than the sharper increase-decrease fluctuations observed in the dense experiment. This suggests that stress transmission in the loose assembly degrades through the gradual fragmentation of the force chain skeleton rather than through abrupt network collapse. Whereas the dense case reached a near-steady structural state from SRR of cycle 2 onward, the loose system instead exhibits a late-cycle buildup in chain length followed by a sharp terminal drop, indicating that internal restructuring continues longer but ultimately fails to sustain shear resistance.

Overall, the micro-macro comparison shows that the loose assembly maintains a clear relationship between the force chain structure and the bulk stress during

the early and intermediate stages of loading. However, with continued cycling, this coupling weakens: the force network continues to reorganize, but its ability to generate macroscopic shear resistance diminishes substantially. Thus, repeated loading does not eliminate internal structure, but progressively reduces the efficiency with which that structure carries load.

4.4.2.3 Force Chain Structure and Anisotropy

The following subsections analyze the orientation distributions of both contacts (fabric anisotropy) and interparticle forces (force anisotropy), and their relationships with macroscale quantities through the stress-force-fabric framework. In addition, the probability density functions (PDF) of normalized contact forces are examined to characterize how forces are transmitted through the granular assembly.

Fabric and Force Anisotropy Polar histograms are used to examine the angular distributions of contact fabric orientation, $P(\theta)$, and the mean interparticle forces, $\bar{f}_n(\theta)$ and $\bar{f}_t(\theta)$. As in the previous sections, the radial magnitude represents the relative frequency or average force associated with a given orientation, while the shape of the distribution reflects the degree of anisotropy. In the loosely packed assemblies, these distributions tend to exhibit greater variability and less persistent directional structure, reflecting the more dynamic and intermittent nature of force transmission.

The **contact fabric** of the loose assembly remains anisotropic throughout most loading stages, indicating that repeated shearing continually reorganizes the contact network into preferred orientations rather than driving it toward a fully random structure (Figure 4.62). Compared with the dense assembly, the principal anisotropy directions are often similar, but the associated stress-axis orientations differ substantially. This suggests that loose packing preserves comparable geometric contact patterns while redistributing the forces carried by those contacts differently.

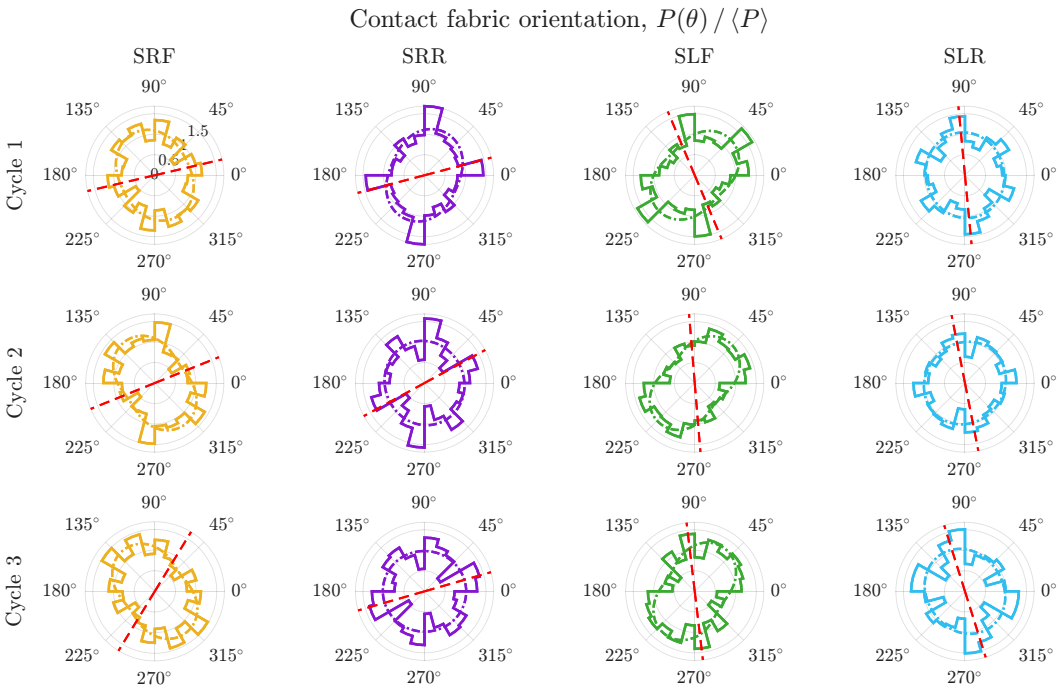


Figure 4.62: Polar histograms of the normalized angular distributions of the contact fabric orientation, $P(\theta)$, arranged by cycle (rows) and midpoint of each shear stage (columns) for the loose assembly ($\sigma_n = -44.1$ kPa). The solid curve represents the distribution, the dash-dotted curve shows its Fourier fit, and the red dashed line denotes the principal compressive stress axis.

During the shear-right stages, shear-right-forward (SRF) and shear-right-reverse (SRR), the fabric response becomes increasingly cycle-dependent. In SRF, the anisotropy magnitude is strongest in the middle cycle and weakest in cycle 1, while cycle 3 exhibits the smallest misalignment with the principal stress direction. This indicates that repeated loading gradually improves directional compatibility between the contact network and the imposed stress state, even when the overall fabric strength does not increase monotonically. In SRR, the anisotropy magnitude increases with cycle count, while later cycles become more rounded in shape. This suggests that reversal promotes a more evenly distributed contact arrangement, but one that still retains a measurable preferred orientation.

The shear-left stages, shear-left-forward (SLF) and shear-left-reverse (SLR), exhibit a different mode of organization. During SLF, the misalignment between fabric and stress axes decreases monotonically with cycle count, indicating progressive adaptation of the contact network to the reversed loading direction. In contrast, SLR shows no clear monotonic trend in misalignment, suggesting that once the reversed structure is established, subsequent reloading yields more localized, cycle-

specific rearrangements rather than systematic directional evolution. Overall, the loose assembly exhibits a fabric response that is persistent but more dynamically reoriented than in the dense case.

The **mean normal force distributions** remain strongly directional throughout the loading history, especially during the shear-right stages, where characteristic peanut-shaped responses indicate concentrated compressive load transfer along preferred orientations (Figure 4.63). Compared with the dense assembly, the loose system retains the same general structure but exhibits weaker, more cycle-dependent anisotropy in later cycles. This suggests that loose packing can still develop directional compressive force chains, but these structures become less persistent as cyclic history accumulates.

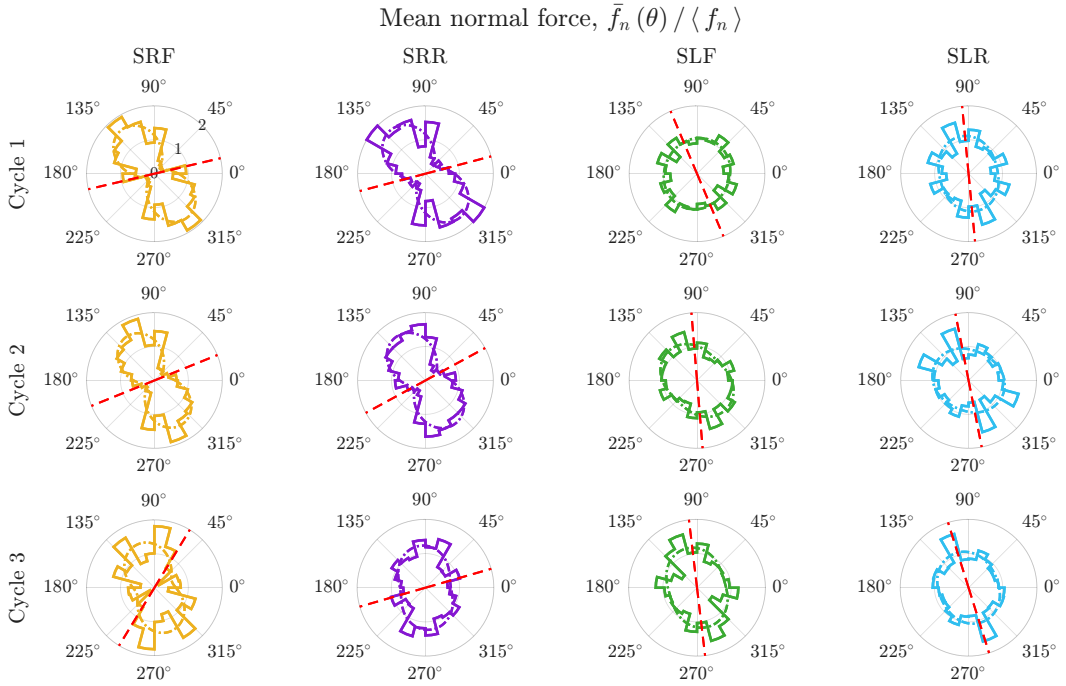


Figure 4.63: Polar histograms of the mean contact normal force, $\bar{f}_n(\theta)$, arranged by cycle (rows) and midpoint of each shear stage (columns) for the loose assembly ($\sigma_n = -44.1$ kPa). The solid curve represents the distribution, the dash-dotted curve shows its Fourier fit, and the red dashed line denotes the principal compressive stress axis.

During both SRF and SRR, the f_n anisotropy magnitude generally decreases with cycle count. This progressive weakening indicates that repeated loading reduces the system's ability to sustain strongly concentrated compressive pathways. At the same time, cycle 3 often exhibits smaller misalignment with the stress axis than earlier cycles, implying that although the force network weakens, it becomes

more efficiently oriented relative to the applied loading. In other words, later cycles produce fewer dominant force paths, but those that remain are better aligned mechanically.

The shear-left stages show a more mixed response. In SLF, cycle 1 becomes nearly isotropic, while later cycles retain an elliptical structure, indicating that reversal initially disrupts directional normal force transmission before new preferred pathways emerge. During SLR, anisotropy increases with cycle count, and the principal lobes align closely with the stress axis in cycles 1 and 3. This suggests that continued shearing in the reversed direction allows compressive contacts to reassemble into efficiently aligned load-bearing paths, particularly in the later stages of deformation.

The **mean tangential force** response broadly follows the directional trends of the normal force network, indicating that frictional forces develop on the same dominant contact network that carries compression (Figure 4.64).

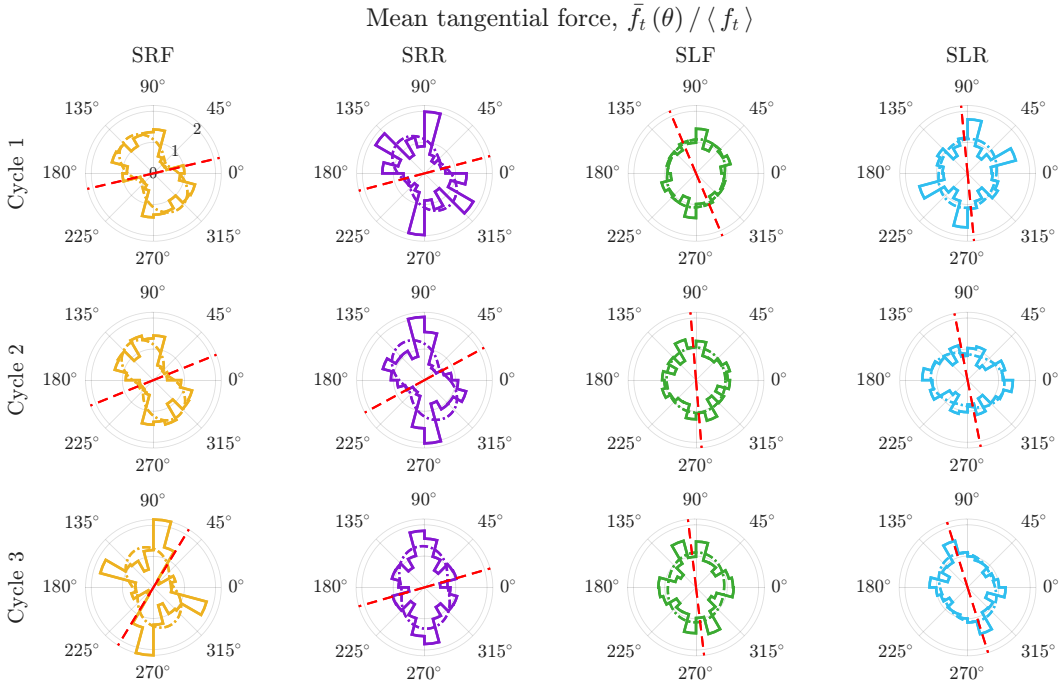


Figure 4.64: Polar histograms of the mean contact tangential force, $\bar{f}_t(\theta)$, arranged by cycle (rows) and midpoint of each shear stage (columns) for the loose assembly ($\sigma_n = -44.1$ kPa). The solid curve represents the distribution, the dash-dotted curve shows its Fourier fit, and the red dashed line denotes the principal compressive stress axis.

In the shear-right stages, the anisotropy axes of $\bar{f}_t(\theta)$ remain nearly aligned with those of $\bar{f}_n(\theta)$, showing that normal and tangential forces are cooperatively mobilized along common structural pathways. However, unlike the normal force response, tangential anisotropy can strengthen with cycle count during SRF, with cycle 3 exhibiting the strongest directional frictional response. This indicates that although compressive force chains weaken with repeated loading, the surviving contacts may mobilize larger frictional forces to maintain resistance. In this sense, friction increasingly compensates for the loss of strong anisotropy in the normal force.

During SLF, the f_t distributions become nearly isotropic and considerably weaker, indicating that frictional resistance is temporarily dispersed following reversal. Yet in some cycles, the tangential anisotropy aligns almost perfectly with the principal stress direction despite small magnitudes. This suggests that even weak frictional networks can become geometrically efficient. By SLR, the tangential force response again resembles the normal force structure, although typically with weaker magnitudes in later cycles. Overall, frictional forces remain strongly history-dependent and appear more sensitive to local rearrangements than normal forces.

Taken together, the fabric and force anisotropy results show that the 122 lb loose assembly maintains a persistent directional internal structure throughout cyclic loading, but the mechanism of stress transmission evolves with cycle history. Early cycles rely more strongly on concentrated normal force pathways, whereas later cycles exhibit weaker compressive anisotropy but, in some stages, stronger frictional organization. Thus, repeated shearing does not erase anisotropy; instead, it shifts the load transfer balance from dominant compressive chains to a more distributed, frictionally assisted network.

Temporal Evolution of Fabric and Force Anisotropy Magnitudes The polar histograms identified the preferred orientations of contacts and contact forces at selected stages in the loading history. We now examine how the magnitude of these anisotropies evolves continuously with shear strain (Figure 4.65). These responses reveal whether the contact network is directional and when that directional structure strengthens, weakens, collapses, or reorganizes during cyclic loading.

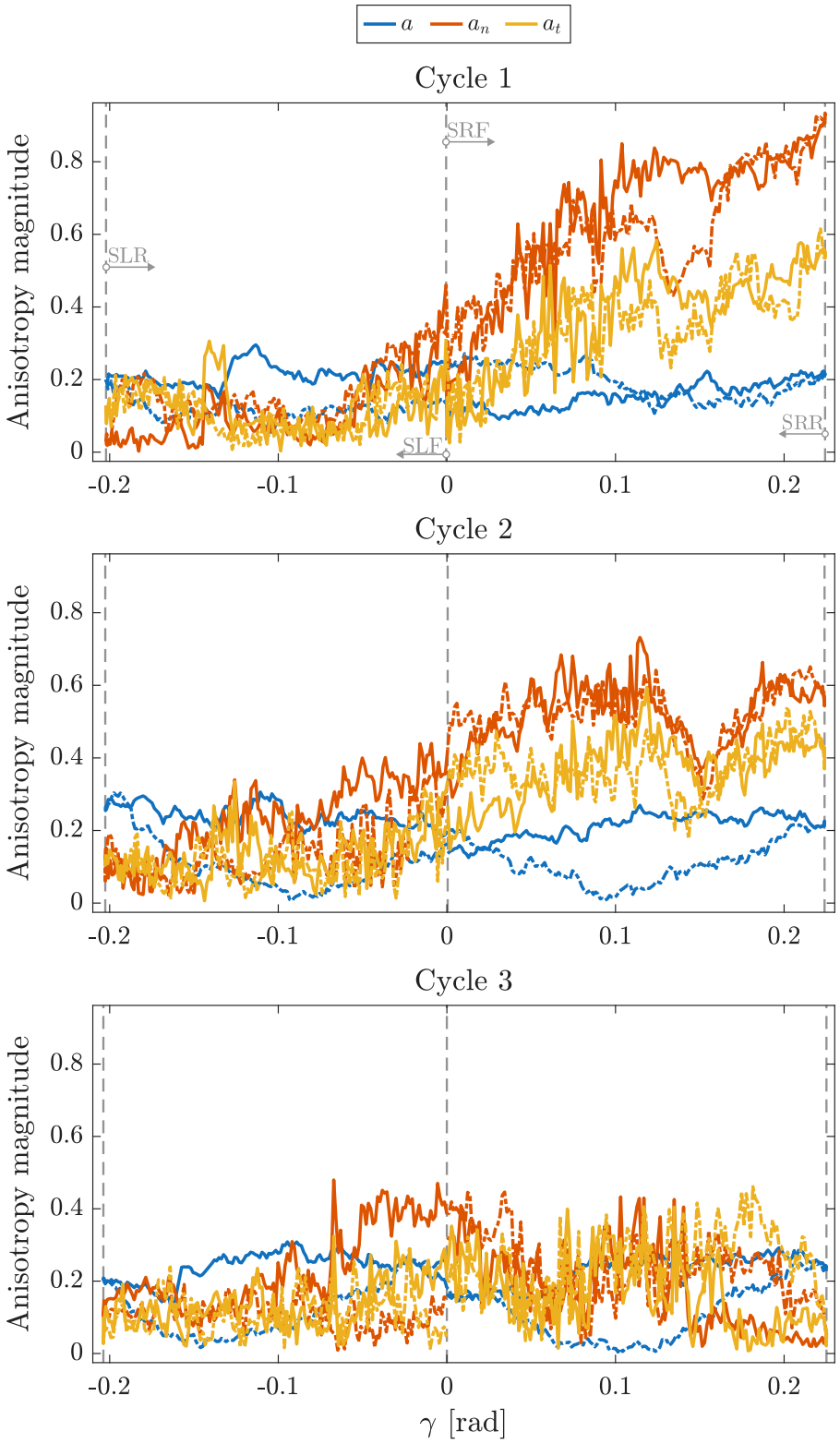


Figure 4.65: Per cycle evolution of the anisotropy magnitudes as functions of shear strain for the loose assembly ($\sigma_n = -44.1$ kPa): fabric anisotropy magnitude, a, and normal and tangential force anisotropy magnitudes, a_n and a_t, respectively. Curve style indicates shearing direction (solid: forward, dash-dotted: reverse), gray dashed lines mark stage transitions.

The **normal force anisotropy**, a_n, exhibits the strongest response of the three measures during the early cycles, indicating that bulk resistance is initially governed primarily by directional compressive force chains. In cycles 1 and 2, the right- and left-shear branches retain a positively sloped petal structure, showing that anisotropy strengthens systematically with shear deformation before weakening near reversal. However, the branches are partially collapsed over portions of the cycle, especially near the outer strain limits, indicating intervals in which directional force transmission weakens or remains nearly unchanged despite continued deformation.

Pronounced departures occur near reversal, particularly during shear-right-reverse (SRR), where temporary widening of the branch indicates rapid disruption and rebuilding of compressive load paths as the system adapts to the reversed loading direction. By cycle 3, the earlier petal structure largely disappears. Instead of a smooth strengthening-weakening pattern, the response becomes localized near shear reversal, while much of the cycle remains weak or nearly collapsed. This indicates that repeated loading progressively reduces the granular assembly's ability to sustain persistent directional normal force chains, concentrating restructuring into brief transitional intervals rather than throughout the entire loading path.

Compared to the 122 lb dense assembly, the loose experiment reaches a similar peak a_n, but a lower minimum value. Thus, the loose packing can still momentarily generate strong compressive anisotropy, yet it spends more of the cycle in the weakened states and exhibits a more history-dependent evolution.

The **tangential force anisotropy**, a_t, broadly mirrors the evolution of a_n, confirming that frictional forces are mobilized along the same dominant contact network that carries compression. However, a_t remains smaller in magnitude, indicating that friction acts as a secondary contributor to directional stress transmission rather than the primary one.

In cycles 1 and 2, the same general petal structure persists on the shear-left side, showing that frictional anisotropy is less sustained during continued reversed loading. Localized widening near reversal again marks brief periods of intensified mobilization of friction as contacts adjust. By cycle 3, most of the response collapses, except for a narrow but taller region near shear reversal, indicating that frictional resistance is increasingly concentrated in short-lived episodes rather than maintained steadily through the cycle.

Relative to the dense assembly, the loose assembly reaches a higher peak a_t despite weaker average behavior. This suggests that although frictional anisotropy is less persistent, certain transient rearrangements in the loose packing can strongly mobilize tangential forces when contact reorientation is most active.

Unlike the force anisotropies, the **fabric anisotropy**, a, evolves over a much narrower range, indicating that the geometric contact network remains comparatively stable even while the forces carried by that network fluctuate strongly. In cycle 1, the response forms a thin, nearly collapsed strip, suggesting that the contact network changes only modestly despite ongoing force redistribution. Thus, substantial variations in stress transmission can occur without equally large changes in contact geometry.

By cycles 2 and 3, the response develops broader butterfly-like structures, indicating more active cyclic reorientation of the contact network. In these later cycles, the forward-shear stages generally strengthen a, while the reverse stages initially weaken it before partial recovery. Mechanistically, this implies that repeated loading progressively imprints a reversible directional memory into the contact network: contacts weaken during reversal, then re-form along preferred orientations as shearing continues.

Compared with the dense experiment, the loose assembly exhibits lower minimum and maximum a values. This suggests that a loosely packed system reorganizes more readily but develops a weaker, more persistent geometric bias than the denser system.

The results from the three anisotropy measures show that, in the loose assembly, directional stress transmission is initially dominated by normal force anisotropy, with tangential anisotropy providing a smaller but coupled contribution, whereas fabric anisotropy evolves more gradually. In the early cycles, the force anisotropies clearly exceed the fabric anisotropy during shear-right loading, indicating that strong directional forces develop more rapidly than the contact geometry itself. However, by cycle 3, the right-shear branches of a_n and a_t weaken substantially and approach each other, showing that compressive and frictional anisotropy both diminish with cyclic history.

In contrast, the shear-left branches of a_n and a_t remain low throughout all cycles and often approach the magnitude of a. This indicates that once the loading direction has been reversed, the assembly relies less on strong directional force chains and more

on the residual geometric organization of the contact network. Overall, repeated shearing does not eliminate anisotropy but shifts the system from force-dominated directional strengthening to a weaker, more geometry-controlled response.

Verification of the Stress-Force-Fabric Relationship The anisotropy magnitude results identified how the contact network and contact forces evolve directionally during cyclic loading. We now test how effectively those internal anisotropies predict the bulk invariant stress ratio through the stress-force-fabric (SFF) relation. This comparison (Figure 4.66) is important because it assesses whether the measured grain-scale organization remains sufficient to explain the macroscopic shear response, or whether additional mechanisms emerge as the cyclic history accumulates.

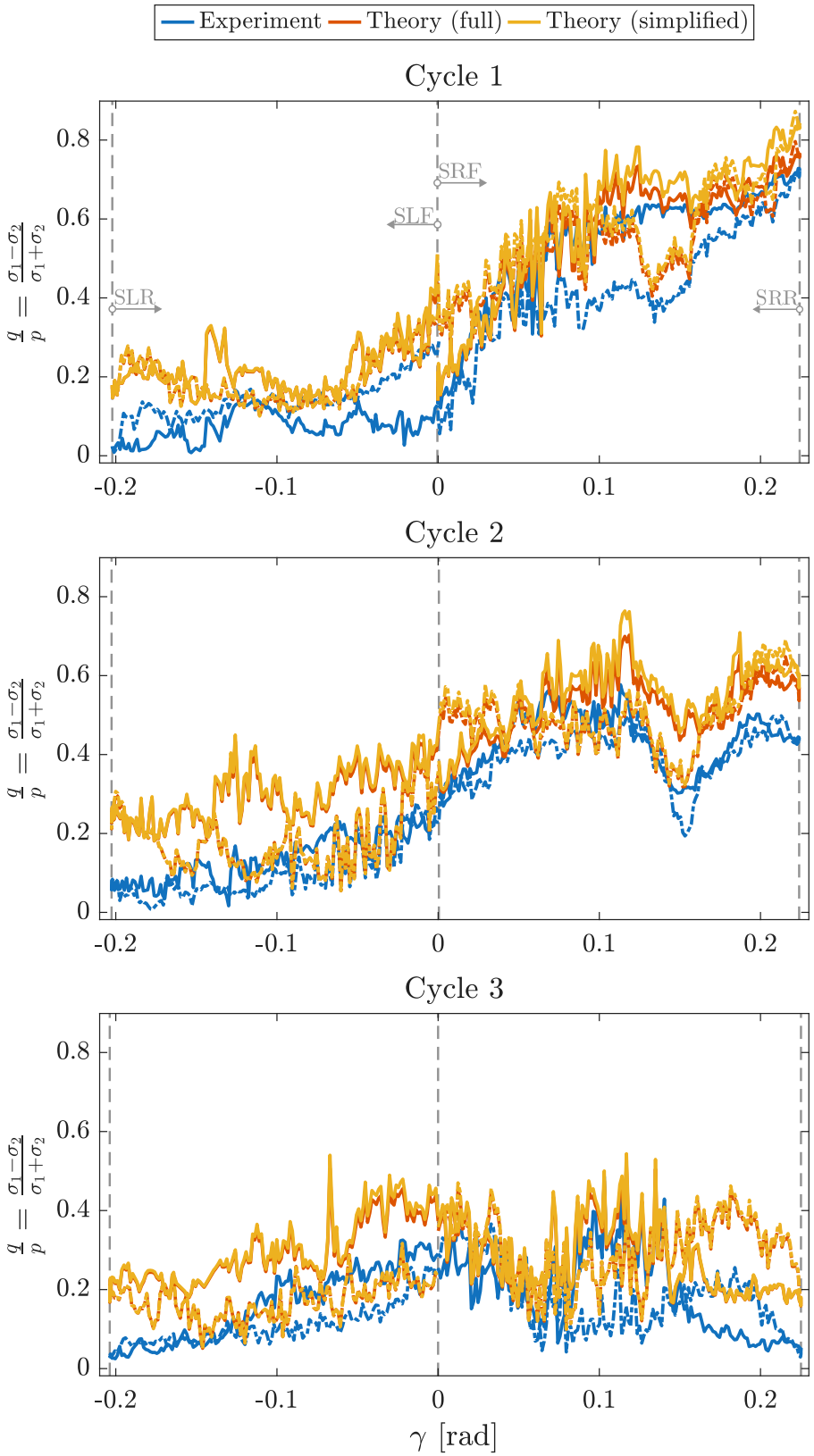


Figure 4.66: Per cycle evolution of the invariant stress ratio, q/p, as a function of shear strain for the loose assembly ($\sigma_n = -44.1$ kPa). The experimental response is compared with the predictions of the full and simplified stress-force-fabric (SFF) relationships. Curve style indicates shearing direction (solid: forward, dash-dotted: reverse), gray dashed lines mark stage transitions.

Interestingly, the experimental q/p evolution closely resembles the response of the normal force anisotropy magnitude, a_n, indicating that bulk shear resistance remains strongly linked to directional compressive force transmission. However, the experimental response is smoother and exhibits fewer collapsed regions than a_n, showing that macroscopic stress integrates many local fluctuations into a more continuous bulk signal.

In most stages, the full SFF expression tracks the experimental q/p more closely than the simplified relation, particularly during shear-right loading. This indicates that retaining the full coupling between the fabric, normal, and tangential force anisotropies remains important even in the loose assembly. Although the simplified form captures the broad trends, it neglects interactions that become relevant when the internal force network is weak, evolving, or partially misaligned.

In cycle 1, both theoretical expressions reproduce the initial linear increase in q/p during shear-right-forward (SRF), showing that the early mobilization of shear strength is well described by the measured anisotropies. Past mid-stage, however, both theories begin to overpredict the response, though the full SFF relation remains closer to the experimental data. This suggests that once deformation progresses, the internal anisotropy continues to strengthen more rapidly than the bulk stress can be mobilized.

During shear-right-reverse (SRR), the theory again overestimates the measured response, indicating that reversal weakens the macroscopic resistance more than anisotropy alone predicts. The discrepancy becomes largest in the shear-left stages, where both shear-left-forward (SLF) and most of shear-left-reverse (SLR) are substantially overpredicted. This implies that once the loading direction has reversed, the directional structure may still exist, but it is less effective at generating shear stress than the theoretical relation assumes.

By cycle 2, the theory overpredicts the entire SRF stage, though agreement remains reasonable in the first half before deviation widens. In contrast, agreement improves during the latter portion of SRR, indicating that some stages of reversed loading are more consistent with the measured anisotropy state than those under forward loading.

The largest discrepancies again occur during SLF, where theoretical values substantially exceed the measured q/p. This indicates that the contact and force anisotropies persist, but their efficiency in producing macroscopic shear resistance declines. Dur-

ing SLR, agreement improves with distance from shear reversal, suggesting that once the reversed structure stabilizes, the SFF framework regains partial predictive power.

In cycle 3, the same broad behavior continues. The SRF stage resembles cycle 2, with systematic overprediction throughout. During SRR, the theory overpredicts the entire stage, indicating that the remaining anisotropic structure no longer translates efficiently into shear resistance. The shear-left stages also mirror the cycle 2 response, with strong overprediction in SLF and only limited agreement in portions of SLR. This persistent mismatch in the later cycles suggests that repeated loading progressively weakens the coupling between directional grain-scale structures and the bulk stress response. Anisotropy remains measurable, but the mechanical effectiveness diminishes.

Despite the loose and dense assemblies exhibiting very different anisotropy petal structures, both systems display the same broad shear-left behavior: SLF strongly overpredicts the experimental q/p, while SLR remains overpredicted through most of the stage. This commonality suggests that the greatest limitations of the SFF framework arise not from packing density alone but from the mechanics of reversed loading itself. Under reversal, the internal structure may remain anisotropic, yet contacts can be less stable, mobilized less efficiently, or intermittently slip. As a result, measured anisotropy overstates the actual load-bearing capacity of the granular assembly.

Overall, the SFF results show that anisotropy-based theory captures the general evolution of shear strength in the loose assembly, particularly during the early forward-shear stages where structure and stress remain strongly coupled. However, repeated cycling and reversed loading progressively reduce that coupling. The contact network continues to exhibit measurable fabric and force anisotropy, but these directional features become increasingly ineffective at producing macroscopic shear resistance. Thus, the primary limitation in later cycles is not the disappearance of anisotropy, but the declining efficiency with which the anisotropic structure is converted into bulk strength.

Force Transmission The SFF analysis evaluated how grain-scale anisotropy translates into bulk shear resistance. We now examine the underlying contact force distributions directly through the probability density functions (PDFs) of normalized normal force, tangential force, and friction mobilization. These distributions reveal how load is shared between weak and strong contacts and how that force-transmission structure evolves under cyclic loading.

Figure 4.67 shows the per-cycle PDFs of the **normalized normal force**, $f_n / \langle f_n \rangle$, with each panel corresponding to a loading cycle and all shear stages included for comparison.

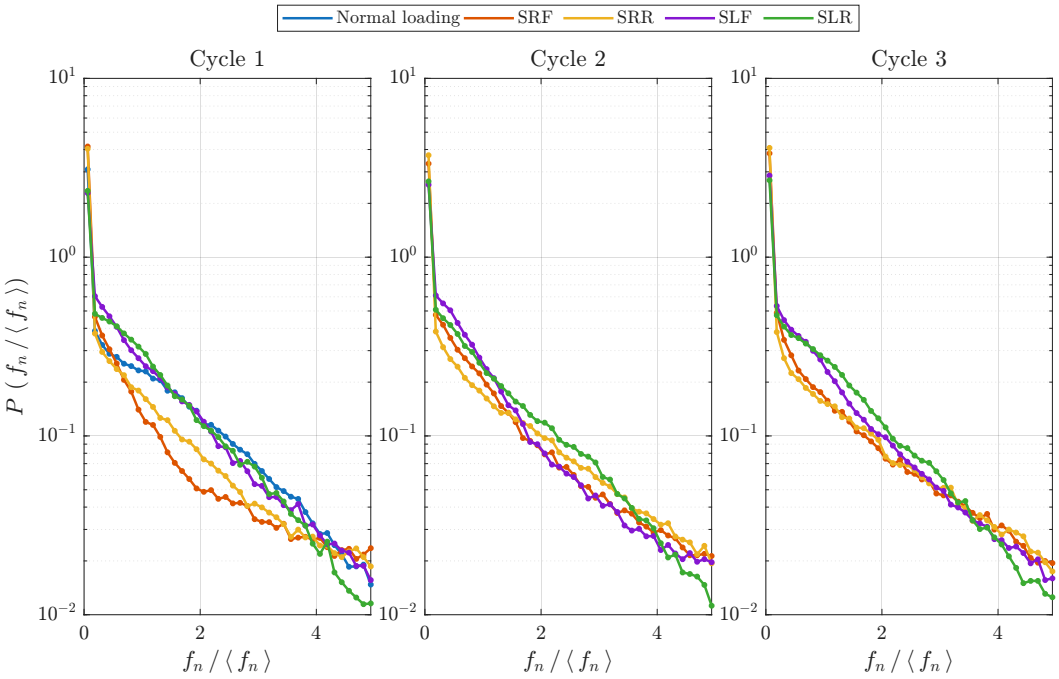


Figure 4.67: Per-cycle evolution of the probability density function (PDF) of the normalized normal contact force, $f_n / \langle f_n \rangle$, for the loose assembly ($\sigma_n = -44.1$ kPa). Each panel shows one loading cycle, with all stages on a semi-log scale.

As in the dense assembly, the normal force PDFs exhibit two characteristic regimes: an initial steep decay associated with the many weak contacts that stabilize the packing, followed by a slower tail decay associated with the smaller population of strong load-bearing contacts. This bimodal-like structure confirms that stress transmission remains partitioned between a weak-contact phase and a strong force chain phase.

Compared with the dense experiment, the loose assembly exhibits less tightly grouped stage responses after the weak-force regime, indicating that the population of strong contacts is more sensitive to loading stage and cycle history. In cycle 1, the shear-right stages, shear-right-forward (SRF) and shear-right-reverse (SRR), diverge early and only reconverge in the highest-force tail, while the shear-left stages, shear-left-forward (SLF) and shear-left-reverse (SLR), remain more linear and less strongly separated. This suggests that forward shearing initially reorganizes strong compressive contacts more actively, whereas the reversed stages distribute force more uniformly.

By cycle 2, the stages remain largely distinct through the intermediate-force range, and only move closer together at high force levels. This indicates that repeated loading increases stage dependence in maintaining strong contacts. In cycle 3, however, the shear-right stages become more closely grouped, while all stages partially converge in the upper-force range before separating again. This suggests that later cycling drives the system toward a more common strong-contact structure, although residual stage-specific differences remain.

Across all cycles, the ordering of the shear-left stages reverses from moderate to high force levels: stages that initially contain more moderately strong contacts end with fewer extreme contacts. Mechanistically, this indicates that some loading stages support many intermediate-force contacts but are less effective at concentrating load into the strongest force chains.

Figure 4.68 shows the per-cycle PDFs of the **normalized tangential force**, $f_t / \langle f_n \rangle$, again organized by cycle with all shear stages included in each panel.

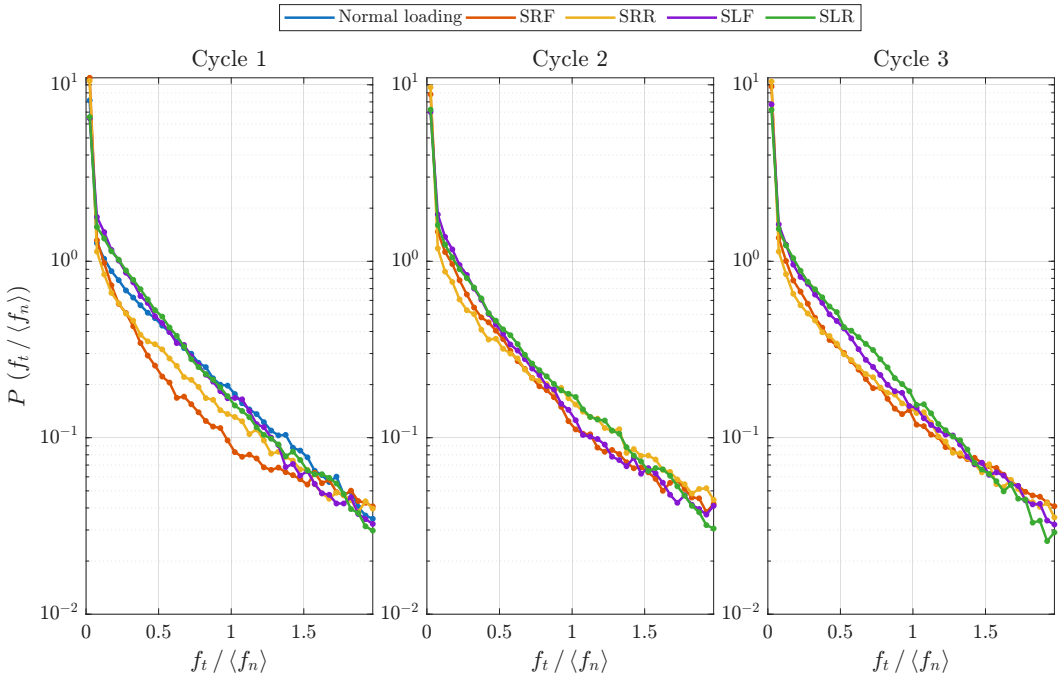


Figure 4.68: Per-cycle evolution of the probability density function (PDF) of the normalized tangential contact force, $f_t / \langle f_n \rangle$, for the loose assembly ($\sigma_n = -44.1$ kPa). Each panel shows one loading cycle, with all stages on a semi-log scale.

The tangential force PDFs show a more grouped response than the normal force PDFs, indicating that frictional load sharing is less stage-sensitive than compressive force transmission. In cycle 1, the shear-right stages remain closely grouped, as do the shear-left stages, with all stages converging in the high-force tail. This suggests

that although tangential forces redistribute during normal loading, extreme frictional forces are constrained by similar contact-level limits across stages.

In cycles 2 and 3, the distributions develop repeated convergence and divergence regions, indicating transitions between common and stage-specific frictional states. The forward and reverse stages often form paired groupings before merging again at larger force levels. This behavior implies that friction mobilization is strongly controlled by contact orientation and slip history, but remains bounded by a common frictional capacity.

Compared with the dense assembly, the loose system exhibits a narrower spread in the high-force regime, particularly in later cycles. Thus, while the dense experiment develops more differentiated extreme tangential forces, the loose packing distributes frictional resistance more evenly among contacts. This is consistent with a more diffuse and less chain-dominated load-bearing network.

Figure 4.69 shows the per-cycle PDFs of the **mobilized friction**, $S = |f_t|/\mu f_n$, with each panel corresponding to a cycle and all shear stages included for comparison.

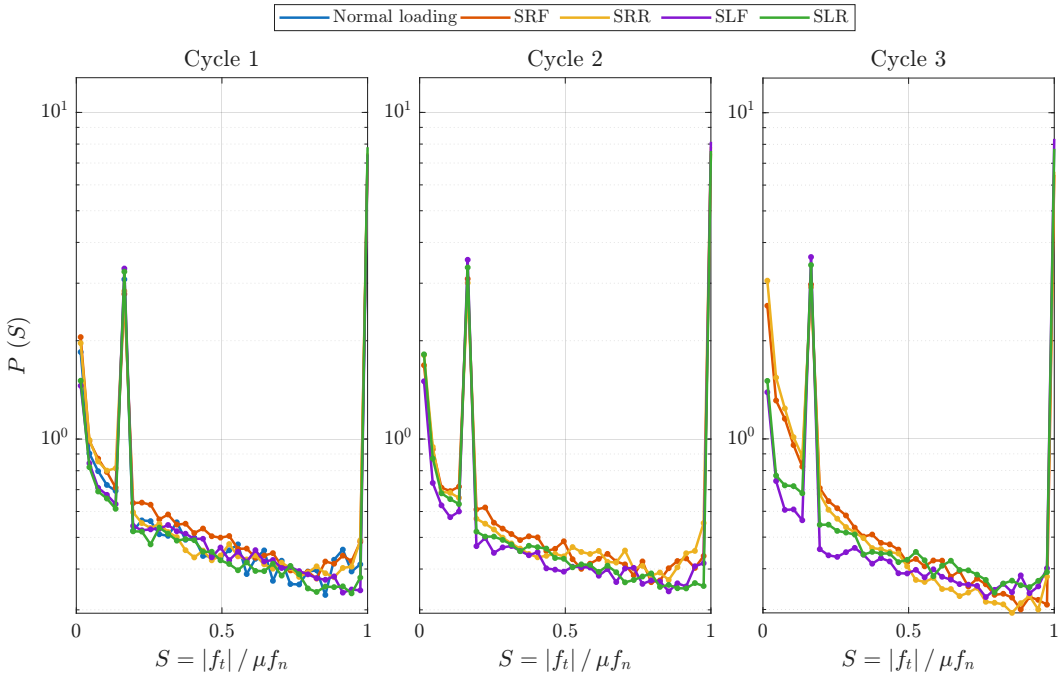


Figure 4.69: Per cycle evolution of the probability density function (PDF) of the mobilized friction, $S = |f_t|/\mu f_n$, for the loose assembly ($\sigma_n = -44.1$ kPa). Each panel shows one loading cycle, with all stages on a semi-log scale. Here, μ is the interparticle friction coefficient, and S indicates the proximity of a contact to sliding (Coulomb failure criterion).

As in the dense assembly, the friction mobilization PDFs exhibit four characteristic regimes: an initial gradual decay, a pronounced intermediate fluctuation, a subsequent linear decay, and finally a sharp rise as $S \rightarrow 1$, where contacts approach the Coulomb sliding limit. This recurring structure indicates that contacts pass through consistent states of weak frictional loading, partial mobilization, and near-failure regardless of packing condition.

In cycle 1, the loose assembly shows more tightly grouped stage responses than the dense case, indicating that frictional demand is initially distributed more uniformly across loading stages. However, by cycle 2, the high-S regime becomes more strongly separated between stages, whereas the dense case remained nearly collapsed. This indicates that repeated cycling causes stage-dependent differences in how close contacts approach slip.

In cycle 3, the shear-right stages begin with substantially higher low-S PDF values than in the dense assembly, indicating a larger population of lightly mobilized contacts. After the intermediate fluctuation, the initially separated stages converge near $S \approx 0.4$ and remain grouped through the remainder of the range. This suggests that despite different early-cycle contact states, the later-cycle network evolves toward a common friction mobilization state once moderate slip demand is reached. Moreover, one notable late-cycle feature is that SRF begins with a relatively high probability but ends with the lowest probability near failure. This indicates that forward shearing in the final cycle involves many lightly mobilized contacts but relatively few capable of sustaining loads near the sliding limit.

Altogether, the force-transmission PDFs show that the 122 lb loose assembly retains the same bimodal stress-sharing structure observed in the dense case: many weak contacts support stability, while a smaller subset of strong contacts carries most of the load. However, the loose packing exhibits a more stage-dependent variation in the strong normal force tail, a narrower spread of extreme tangential forces, and increasingly differentiated friction mobilization with cycling. These trends indicate that repeated loading makes force chains less persistent and more sensitive to loading direction. Therefore, stress transmission becomes more distributed and less concentrated into stable, dominant load paths. In the loose assembly, load is carried by a broader population of transient contacts rather than by a smaller number of persistent, strong force chains.

4.4.2.4 Grain-Scale Response Summary

The grain-scale response of the three-cycle, loosely packed granular assembly under $\sigma_n = -44.1$ kPa $\approx$ 122 lb (55.3 kg) exhibits a load-bearing network that remains active throughout cyclic loading, but progressively becomes less coherent, less directional, and less efficient at transmitting stress. Compared with the dense assembly subjected to the same σ_n, the loose packing generally evolves more smoothly and with fewer abrupt structural reorganizations, yet it undergoes greater cumulative degradation of its internal force chain structure over the full loading history.

The contact network remains comparatively stable, with the coordination number varying over a narrower range than in the dense case. This indicates that cyclic loading does not strongly alter the total number of contacts, but instead reorganizes how those contacts participate in load transfer. The extrema of the coordination number shift to later stages of the loading history, indicating that the most significant contact restructuring is delayed relative to the dense assembly and occurs after the system has adjusted to the reversed loading directions.

The force chain network reflects this gradual but persistent reorganization. Although the number of detected force chains remains relatively stable across many stages, the total chain length and chain density decline overall, indicating that the assembly increasingly supports the load through shorter, more fragmented chains. Thus, repeated shearing progressively reduces the spatial extent and connectivity of load-bearing paths. Compared with the dense experiment, the loose assembly forms smaller force chain structures and exhibits a broader distribution of participation, consistent with a more diffuse stress-transmission network.

The strong force network also persists throughout the loading history, with roughly $37\% - 44\%$ of grains belonging to it at most stages. However, only about $35\% - 67\%$ of those strong grains organize into detectable force chains. This demonstrates that many grains continue to carry above-average forces even after repeated loading, but an increasingly smaller fraction of them participate in coherent chain structures. Consequently, degradation occurs more through loss of organization than through disappearance of strong contacts.

Directional measures further show that anisotropy is retained but progressively weakened. In the early cycles, normal force anisotropy dominates the response, indicating that shear resistance is initially carried by strongly oriented compressive force chains, with tangential anisotropy providing a secondary contribution. By

later cycles, both force anisotropies weaken substantially, while fabric anisotropy remains measurable. This indicates that repeated loading erodes directional force transmission more rapidly than it erodes the underlying contact geometry, leaving behind a weaker but persistent structural memory.

The micro-macro comparisons support this interpretation. Early in the loading history, the total chain length and anisotropy measures closely track the bulk shear-stress response, indicating strong coupling between internal structure and macroscopic resistance. However, in later cycles, the force network continues to reorganize while the shear stress changes only minimally. Thus, the internal structure remains active, but becomes increasingly ineffective at generating additional bulk strength.

The force-transmission PDFs reinforce these conclusions. The assembly retains the same weak-contact/strong-contact partition observed in denser packings, but the strong-force tails become more stage-dependent and less persistent with cycling. Extreme tangential forces are distributed more narrowly, while friction mobilization becomes increasingly sensitive to loading history. Together, these trends indicate that stress is carried less through stable dominant chains and more through a broader population of transient contacts.

Overall, the 122 lb loose assembly demonstrates that cyclic loading gradually transforms the grain-scale structure. The contact network, strong network, and anisotropic organization all persist, yet their ability to assemble into long-lived, directionally efficient force chains diminishes with repeated shear. As a result, the assembly evolves toward a more distributed, history-dependent, and mechanically weaker mode of stress transmission.

4.5 Experiment # 4: Loosely Packed, $\sigma_n = -29.6$ kPa

The fourth experiment is a loosely packed granular assembly normally loaded by $\sigma_n = -29.6$ kPa, corresponding to 82 lb (37.2 kg). For a loose packing, the granular assembly consists of 318 grains in total, of which 60 are boundary grains, and 258 are interior grains (these interior grains participate in the DIC and GEM analyses). The initial void ratio for this loosely packed experiment is 0.287.

4.5.1 Macroscopic Response

Figure 4.70 shows the macroscopic mechanical response of the three-cycle, loosely packed experiment, loaded by $\sigma_n = -29.6$ kPa. As done for all experiments, the macroscopic response is evaluated through the evolution of stress ratio, μ, volumetric strain, ϵ_V, void ratio, e, and dilatancy, β, which together characterize the granular assembly's shear resistance, volume change, packing state, and shear-volume coupling under cyclic loading.

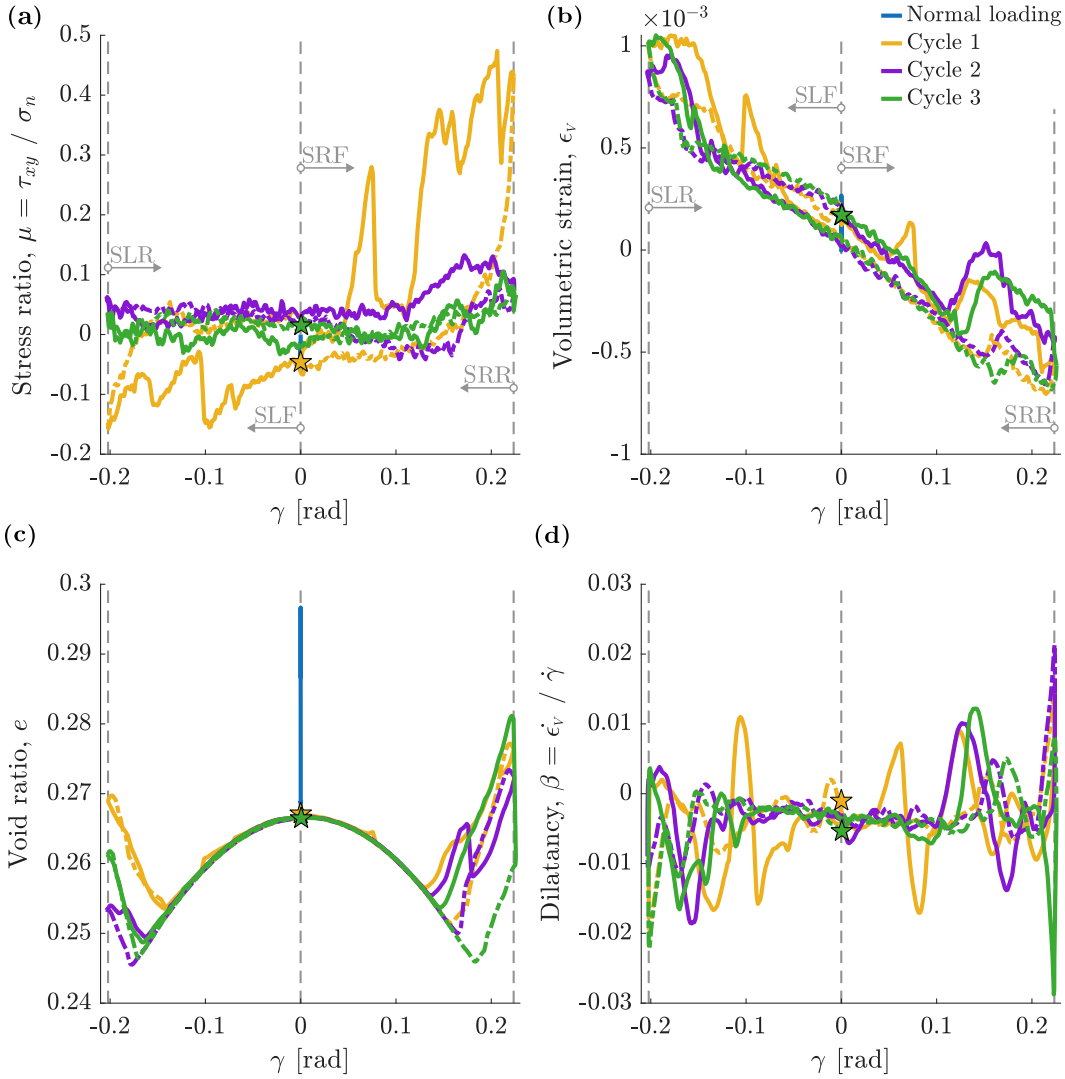


Figure 4.70: Macroscopic behavior of the three-cycle, loosely packed granular assembly under $\sigma_n = -44.1$ kPa. (a) Stress ratio, μ, (b) volumetric strain, ϵ_V, (c) void ratio, e, and (d) dilatancy, β, as functions of shear strain, γ. Solid curves indicate forward shearing stages (SRF, SRR), whereas dash-dotted curves indicate reverse shearing stages (SLF, SLR). Furthermore, gray vertical dashed lines indicate shear-stage transitions. The yellow and green stars mark the start and end of the cyclic loading, respectively.

4.5.1.1 Stress Ratio

Figure 4.70a shows the evolution of the stress ratio, μ, as a function of shear strain, γ, for the three-cycle, loosely packed granular assembly under $\sigma_n = -29.6$ kPa, corresponding to 82 lb. Compared to the corresponding loose experiment under higher confinement (Figure 4.71), the overall stress ratio response remains qualitatively similar: much of the loading history is characterized by low or near-zero stress ratio, and appreciable shear resistance is mobilized only over limited portions of the cycle. Thus, reducing the normal stress does not fundamentally alter the weak and stage-localized nature of force transmission in the loose assembly.

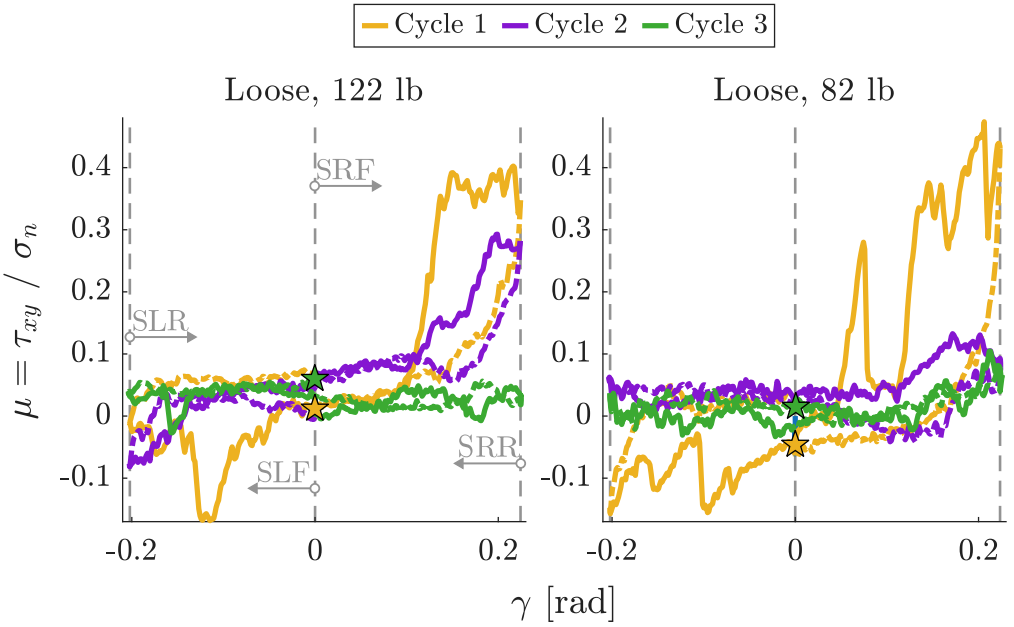


Figure 4.71: Stress ratio evolution for the two three-cycle, loose experiments subjected to a normal load of $\sigma_n = -29.6$ kPa. Curve style indicates shearing direction (solid: forward, dash-dotted: reverse), gray dashed lines mark stage transitions, and stars mark the start (yellow) and end (green) of cyclic loading.

The main difference between the more- and less-confined loose experiments is that the 82-lb assembly exhibits a more unstable early-cycle response. In particular, cycle 1 mobilizes the strongest shear resistance, but does so through a more fluctuating and irregular evolution, especially during shear-right-forward (SRF) and shear-left-forward (SLF), where multiple restructuring events are observed. In contrast, cycles 2 and 3 remain comparatively weak throughout most of the loading history, with cycle 2 showing particularly limited mobilization of resistance and cycle 3 remaining largely collapsed, except for a modest increase near the end of SRF. These trends suggest that under lower confinement, the loose assembly can still briefly mobilize a

load-bearing contact structure, but that structure is more intermittent and less stable than in the corresponding 122 lb loose experiment.

Another notable feature is that the reverse-shear stages remain weak and tightly grouped across all three cycles. Compared to the 122 lb loose experiment, the shear-right-reverse (SRR) and shear-left-reverse (SLR) responses exhibit greater overlap and less sustained cycle-to-cycle separation once the initial transition has passed. Thus, under reduced confinement, reverse shearing is accommodated by a more uniform, weakly mobilized frictional response rather than by persistent hysteretic force transmission.

As in the 122 lb loose experiment, cycle 1 exhibits the greatest variability and reaches the maximum and minimum stress ratio values, while large portions of the loading history remain close to $\mu \approx 0$. Both loose experiments also end at a slightly higher stress ratio than at the onset of cyclic shearing, although the net increase is larger in the 82 lb case. Taken together, these results indicate that lowering the normal stress in the loose assembly does not change the basic stress-transmission mechanism, but instead makes the response more weakly sustained, more tightly grouped in later cycles, and more susceptible to intermittent restructuring during early-cycle shear mobilization.

4.5.1.2 Volumetric Strain

Figure 4.70b shows the volumetric strain, ϵ_v, as a function of shear strain for the three-cycle, loosely packed granular assembly under $\sigma_n = -29.6$ kPa, corresponding to 82 lb. Overall, the volumetric response is highly similar to that of the more highly confined loose experiment, indicating that reducing the normal stress does not fundamentally alter the compaction-dominated volumetric deformation mechanism of the loose assembly. Instead, the lower-confinement response appears even more tightly grouped and shows weak evolution across cycles. For an easier comparison between both loosely packed experiments, Figure 4.72 shows the ϵ_v evolution of the 122 lb case (left) and the 82 lb case (right).

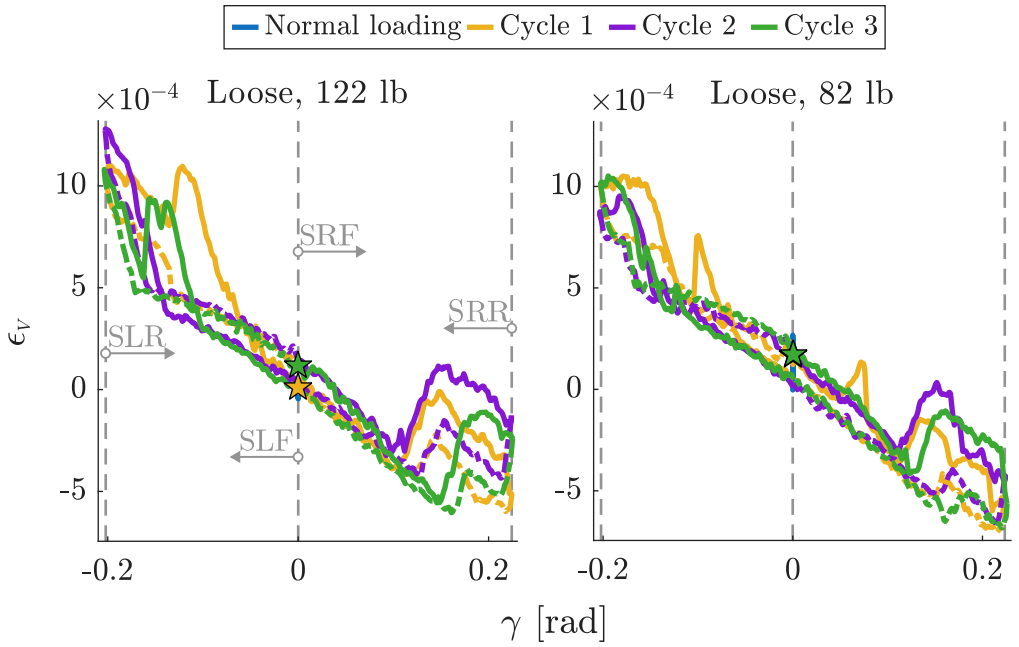


Figure 4.72: Volumetric strain evolution for the two three-cycle, loose experiments subjected to a normal load of $\sigma_n = -29.6$ kPa. Curve style indicates shearing direction (solid: forward, dash-dotted: reverse), gray dashed lines mark stage transitions, and stars mark the start (yellow) and end (green) of cyclic loading.

As in the 122 lb loose experiment, the normal loading stage exhibits alternating compaction and dilative adjustments before settling into a slightly more compacted state, indicating that the loose assembly undergoes early rearrangement rather than monotonic consolidation under applied normal stress. During cyclic shearing, the stage-wise evolution remains largely unchanged; that is, the cycles stay tightly grouped over much of the loading history, and the main departures from this shared path occur only during localized restructuring events near stage transitions.

The strongest similarities are observed in the reverse shear stages, where the response is nearly identical to that of the 122 lb loose assembly. In both shear-right-reverse (SRR) and shear-left-reverse (SLR), the cycles remain tightly grouped and quickly return to common quasi-steady deformation paths following brief transition-induced fluctuations. The main difference is that, under lower confinement, these grouped regimes persist over slightly larger portions of the strain history, indicating that the response is even more uniformly accommodated across cycles.

The forward shearing stages also remain broadly similar, but with slightly greater stabilization in the later cycles. In shear-right-forward (SRF) and shear-left-forward (SLF), cycle 1 still exhibits the strongest localized fluctuations, while cycles 2 and 3 remain more tightly grouped and evolve more gradually. Compared to the 122 lb

loose experiment, cycles 2 and 3 remain close to one another over a larger fraction of the shear stage, particularly in SLF, again indicating that the lower-confinement assembly more readily revisits shared volumetric states rather than evolving along strongly cycle-specific paths.

As in the more highly confined loose assembly, the ϵ_V response retains directionally asymmetry, hysteresis, and multiple self-intersections, indicating that the volumetric state remains path-dependent despite the strong overlap between cycles. The final volumetric state also remains more compacted than at the onset of cyclic shear, and the magnitude of compaction continues to exceed that of dilation across all stages. However, the overall change in ϵ_V from the start to the end of the cyclic loading is smaller than in the 122 lb loose case, indicating that although the same volumetric mechanism remains active, its cumulative expression is more muted under reduced confinement.

Together, these results indicate that lowering the normal stress in the assembly does not fundamentally change the volumetric deformation mode, but instead makes the response more tightly grouped, more repeatable, and slightly less cumulative over the loading history. The 82 lb loose assembly, therefore, appears to accommodate cyclic shear through the same compaction-dominated and path-retracting volumetric mechanism observed in the 122 lb loose assembly, but through a weaker evolving form.

4.5.1.3 Dilatancy

Figure 4.70d shows the dilatancy, β, as a function of shear strain, γ, for the three-cycle, loosely packed experiment under $\sigma_n = -29.6$ kPa (approximately 82 lb). The dilatancy is interpreted in conjunction with the volumetric strain, ϵ_V, with peaks and extrema corresponding to periods of intensified internal rearrangement and smoother regions indicating more stable deformation. In general, the dilatancy response remains qualitatively similar to the corresponding more highly confined experiment (Figure 4.73): the shear-volume coupling is weak over most of the loading history and becomes significant only during localized restructuring events near stage transitions. Thus, reducing the normal stress does not fundamentally alter the localized nature of dilatancy in the loose assembly. For a cycle-by-cycle comparison of these densely packed experiments, refer to Appendix B, Figure B.2.

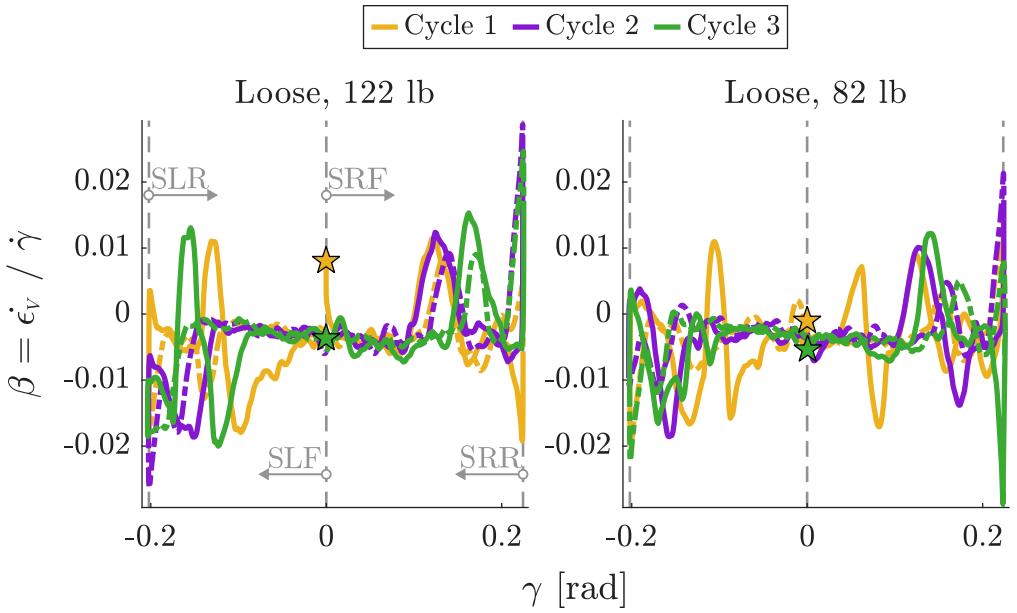


Figure 4.73: Dilatancy evolution for the two three-cycle, loose experiments subjected to a normal load of $\sigma_n = -29.6$ kPa. Curve style indicates shearing direction (solid: forward, dash-dotted: reverse), gray dashed lines mark stage transitions, and stars mark the start (yellow) and end (green) of cyclic loading.

The primary difference is that the lower-confined response is more irregular and less stable, particularly during the forward-shearing stages. In the shear-right-forward (SRF) stage, all cycles initially exhibit a short, tightly grouped regime before diverging through localized fluctuations, with cycle 1 again showing the strongest and earliest deviations. Compared to the 122 lb case, these fluctuations are more chaotic, with β frequently alternating in sign, indicating repeated formation and collapse of weakly developed contact structures. Cycles 2 and 3 remain more gradual and delayed in their response, but still exhibit localized restructuring events later in the stage.

The reverse-shear stages retain their characteristic tightly grouped behavior. In both shear-right-reverse (SRR) and shear-left-reverse (SLR), all cycles undergo a rapid transition immediately after shear reversal, followed by a near-steady regime in which β varies only weakly. Compared to the forward stages, these regimes remain more clustered and less variable, indicating that reverse shear is still accommodated through relatively uniform rearrangement. However, in the 82 lb case, the initial transitions and secondary fluctuations are somewhat more irregular, and cycle 1 remains less stable than cycles 2 and 3 even within these otherwise grouped responses.

As in the more highly confined loose experiment, the central portion of the loading path exhibits strongly overlapped β curves across all cycles, indicating that most of the deformation occurs with minimal variation in shear-volume coupling. The strongest coupling remains confined to short intervals near reversal, consistent with the localized restructuring events observed in the volumetric strain response.

A final distinction is that the overall dilatancy evolution is weaker compared to the 122 lb loose experiment. The dilatancy begins near zero and ends at a small negative value, resulting in a significantly smaller net change over the loading history. Hence, although the same localized coupling mechanisms remain active, their cumulative effect is reduced under lower confinement.

Collectively, these results indicate that lowering the normal stress in the loose assembly does not change the fundamentally weak and localized nature of dilatancy, but results in a response that is more irregular, less stable in early-cycle shear, and less cumulative over the loading history.

4.5.1.4 Void Ratio

Figure 4.70c shows the void ratio, e, as a function of shear strain for the loosely packed experiment under $\sigma_n = -29.6\,\text{kPa}$ ($\approx$ 82 lb). Overall, the response remains highly consistent with that of the more highly confined loose experiment (Figure 4.74), indicating that reducing the normal stress does not fundamentally alter the packing-state evolution of the loose assembly. Instead, the 82 lb experiment exhibits the same path-retracing, compaction-dominated behavior, but with slightly greater irregularity and somewhat larger net densification over the loading history.

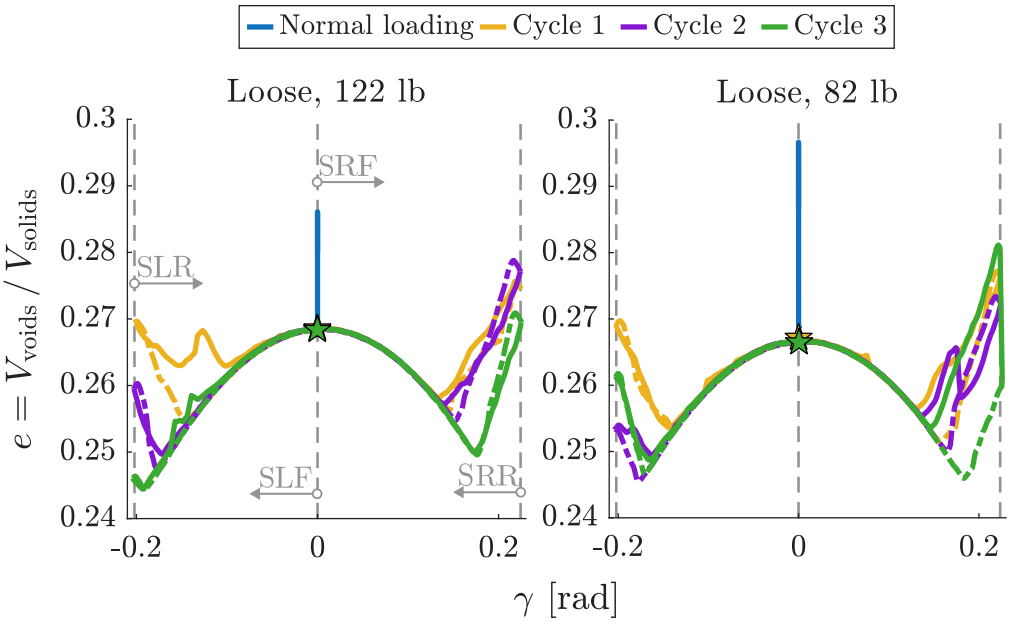


Figure 4.74: Void ratio evolution for the two three-cycle, loose experiments subjected to a normal load of $\sigma_n = -29.6$ kPa. Curve style indicates shearing direction (solid: forward, dash-dotted: reverse), gray dashed lines mark stage transitions, and stars mark the start (yellow) and end (green) of cyclic loading.

As in the 122 lb loose case, forward shearing generally produces a gradual decrease in void ratio over most of the loading path, while reverse shearing produces an increase. Away from the immediate vicinity of shear reversal, the cycles again become indistinguishable, indicating that the packing state repeatedly returns to a common structural trajectory that is only weakly dependent on cycle number. Thus, the strong path-retracing behavior observed in the more highly confined loose experiment is preserved under lower confinement.

The main differences are localized and relatively minor. In the 82 lb assembly, small additional fluctuations appear near the ends of some forward stages, and the normal loading response takes slightly longer to settle to a stable value, indicating somewhat greater structural irregularity under reduced confinement. Even so, the reverse-shear stages remain especially similar between the two loose experiments, with strongly overlapping responses and only limited cycle-to-cycle separation.

A final important similarity is that the 82 lb loose experiment, like its more confined counterpart, evolves toward a more compacted final state. The void ratio at the end of the loading history remains lower than at the onset of cyclic shear, indicating net densification under repeated loading. The magnitude of this net densification is slightly larger than in the 122 lb loose case, suggesting that lower confinement

leads to a somewhat greater cumulative structural consolidation, even though the overall packing-state evolution remains governed by the same shared and retracing deformation path.

Altogether, these results indicate that lowering the normal stress in the loose assembly does not change the fundamental packing-state response under cyclic shear. Rather, the granular assembly continues to evolve through a strongly path-dependent and compaction-dominated mechanism, while exhibiting slightly greater irregularity and slightly stronger net densification under reduced confinement.

4.5.1.5 Macroscopic Response Summary

In total, the macroscopic response of the three-cycle, loosely packed assembly under $\sigma_n = -29.6$ kPa (approximately 82 lb) remains highly consistent with that of the corresponding 122 lb loose assembly, indicating that reducing the normal stress does not fundamentally change the dominant deformation mechanisms of the loose packing. In both loose experiments, the stress ratio remains weak over much of the loading history, the volumetric strain and void ratio responses exhibit strong path retracing and cycle overlap, and the dilatancy response is largely confined to short-lived restructuring events near stage transitions. However, compared to the more highly confined assembly, the 82 lb assembly exhibits a more weakly sustained and more irregular stress ratio response, slightly greater structural irregularity during volumetric strain and void ratio evolution, and a modestly larger net densification over the loading history. Overall, these results suggest that under loose-packing conditions, the governing deformation mechanism is largely preserved as confinement is reduced, but its macroscopic expression becomes weaker, less stable, and slightly more compaction-dominated.

4.5.2 Grain-Scale Response

The macroscale response (Figure 4.70) reflects progressive but highly variable restructuring within the loosely packed granular assembly under lower confinement. We now examine this evolution at the grain-scale.

4.5.2.1 Coordination Number

The coordination number, Z_c, measures the average number of contacts per grain. Variations in Z_c reflect periods of contact creation and loss, providing insight into how the granular structure reorganizes during shear. Figure 4.75 shows its evolution with shear strain, while Figure 4.76 presents the stage-wise response.

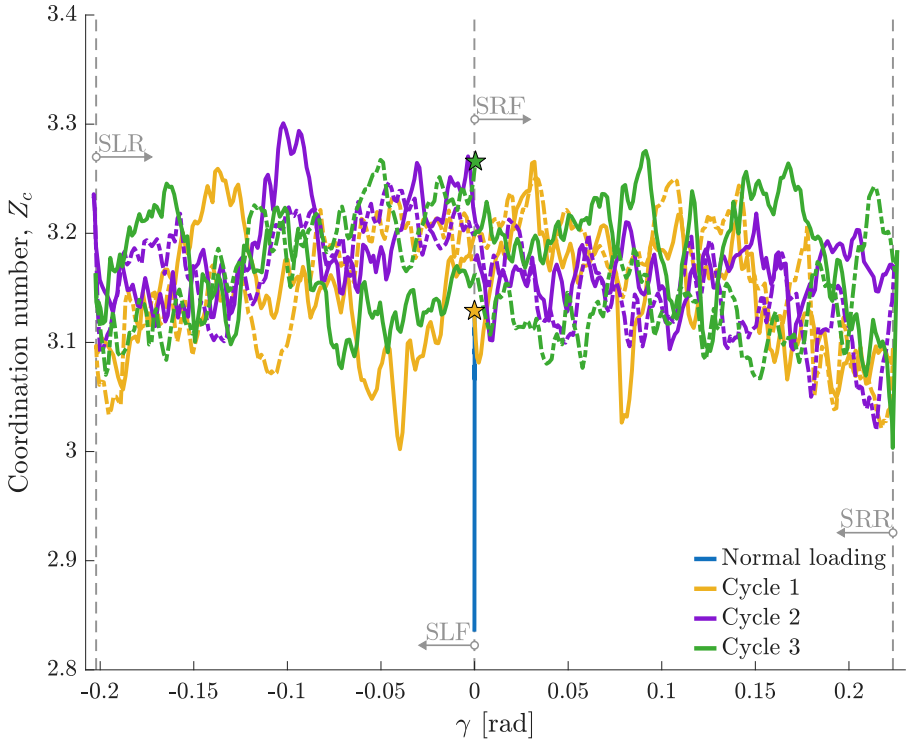


Figure 4.75: Evolution of the coordination number, Z_c, for the loose granular assembly ($\sigma_n = -29.6$ kPa). Z_c is the average number of contacts per particle. Curve style indicates shearing direction (solid: forward, dash-dotted: reverse), gray dashed lines mark stage transitions, and stars mark the start (yellow) and end (green) of cyclic loading.

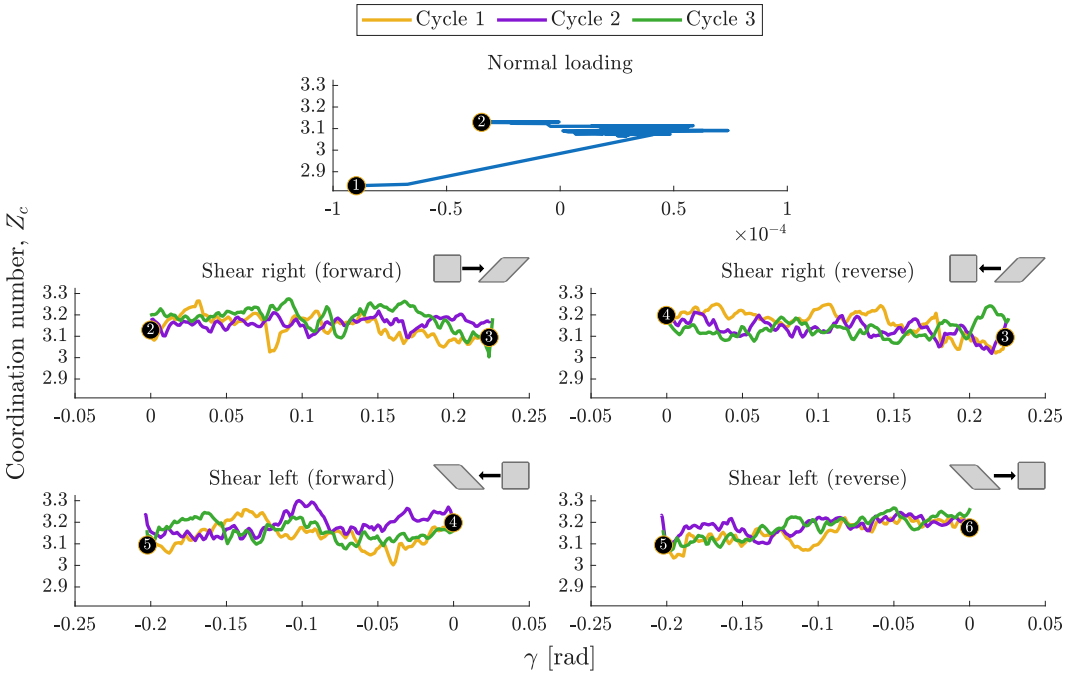


Figure 4.76: Per-stage evolution of the coordination number, Z_c, for the loose granular assembly ($\sigma_n = -29.6$ kPa). Stage markers are shown only for Cycle 1.

During shear-right-forward (SRF), all cycles exhibit a more stable and confined Z_c evolution compared to the 122 lb loose experiment. The response remains within a relatively narrow range, with cycle 2 showing the least variability. This indicates that contact formation and loss are more balanced, preventing large fluctuations in connectivity. Under lower confinement, the grains can rearrange more freely, allowing the system to accommodate deformation through gradual adjustments rather than large-scale contact breakage. As a result, the sharp restructuring observed under higher confinement is replaced by a smoother, more distributed evolution of the contact network. Although local rearrangements are still present – particularly in cycle 1, where a rapid initial drop and recovery occur – they happen over shorter timescales and with a smaller amplitude.

The differences between confinement levels become more pronounced during shear reversal (shear-right-reverse (SRR)). In the 122 lb experiment, SRR is characterized by a consistent loss of contacts as the existing network becomes incompatible with the reversed loading direction. In contrast, the 82 lb case exhibits a more complex response, particularly in cycle 3, where an initial increase-decrease fluctuation replaces the immediate drop in coordination number. This behavior indicates that reversal does not simply break contacts but instead triggers rapid local reorganization. Rather than undergoing a uniform loss of connectivity, the system redistributes contacts as it adapts to the new loading direction. Following this initial adjustment, all cycles exhibit a gradual increase in Z_c, reflecting the formation of new contacts aligned with the reversed shear. However, the rate of this increase diminishes with cycle count, suggesting that the network becomes progressively less responsive to reversal as prior rearrangements accumulate.

The most significant restructuring occurs during the shear-left stages, particularly in the shear-left-forward (SLF) stage. During this stage, the coordination number evolves through alternating regimes of contact creation and loss as the network reorganizes into a new configuration. In particular, the system transitions between relatively well-connected and weakly connected states within the same stage, indicating that structural reorganization is most active during this period. Furthermore, unlike the higher-confinement case, where extrema were associated with forward shearing, the 82 lb response shows that the system continues to adjust and rebuild its contact network well after shear reversal.

Following this period of active restructuring, the response in shear-left-reverse (SLR) becomes more consistent across cycles. All cycles exhibit an initial drop in

coordination number, followed by a rapid recovery to a nearly steady regime, then a secondary decrease, before gradually increasing for the remainder of the stage. The magnitude of the secondary drop becomes progressively weaker in later cycles. This indicates that while the system still undergoes contact disruption after the steady regime, the extent of this disruption diminishes with cycling, suggesting that the contact network becomes increasingly stable and less susceptible to large-scale rearrangement.

The structure of the shear branches further highlights how Z_c evolves under reduced confinement. In the 82 lb case, the rightward and leftward branches exhibit more collapsed behavior in certain cycles, particularly in cycle 2, where both branches remain confined to a narrow range of Z_c. This indicates that contact connectivity varies little throughout the loading path, reflecting a more balanced exchange between contact formation and loss. However, this behavior is not uniform across cycles. In cycle 1, the rightward branch is more compressed, in contrast to the 122 lb case, where the leftward branch was nearly collapsed. By cycle 3, both branches exhibit a broader spread, indicating a partial recovery of connectivity variability. These changes suggest that the evolution of the contact structure becomes increasingly cycle-dependent, with the balance between contact formation and loss shifting as the system accumulates deformation history.

Overall, the evolution of the coordination number reflects a system in which contact connectivity is continuously reorganized yet remains relatively stable in magnitude. Compared to the 122 lb loose experiment, the response exhibits fewer extreme fluctuations and a more balanced exchange between contact formation and loss. Hence, reducing the applied normal load shifts the dominant restructuring from forward shearing to post-reversal stages, in which the system reorganizes into new contact configurations. As a result, the contact network becomes more history-dependent, with its evolution governed less by individual loading stages and more by the cumulative effects of cyclic rearrangement.

4.5.2.2 Force Chain Statistics and Evolution

While the coordination number describes how many contacts exist within the assembly, it does not identify which of those contacts actively transmit load. We therefore now examine the evolving force chain network, formed by subsets of strong contacts that carry the majority of the stress. The number of detected force chains provides a first measure of how the load-bearing skeleton forms, fragments, and reorganizes during cyclic shear.

Number of Detected Force Chains The number of force chains as a function of shear strain is shown in Figure 4.77, and the associated per-stage evolution per stage is shown in Figure 4.78.

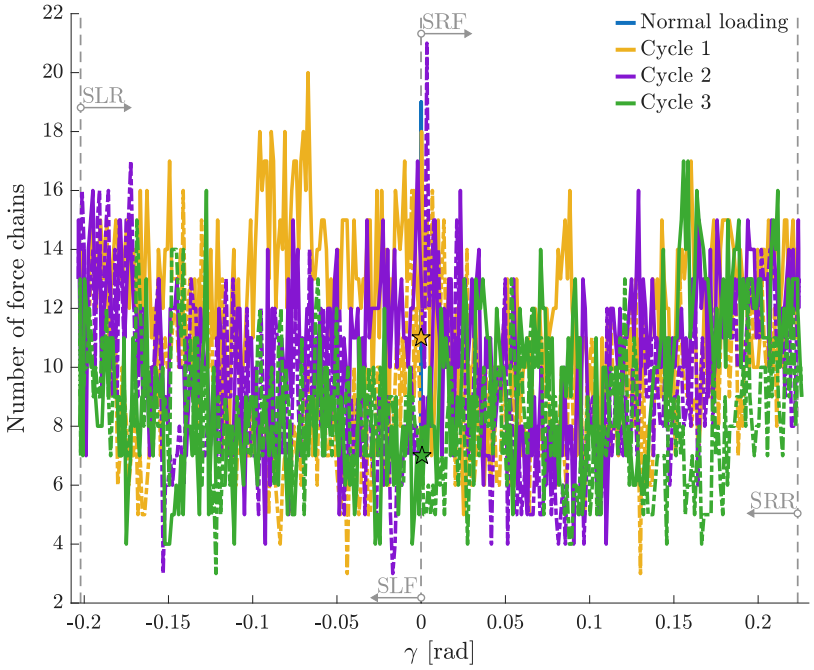


Figure 4.77: Evolution of the detected number of force chains, for the loose granular assembly ($\sigma_n = -29.6$ kPa). Curve style indicates shearing direction (solid: forward, dash-dotted: reverse), gray dashed lines mark stage transitions, and stars mark the start (yellow) and end (green) of cyclic loading.

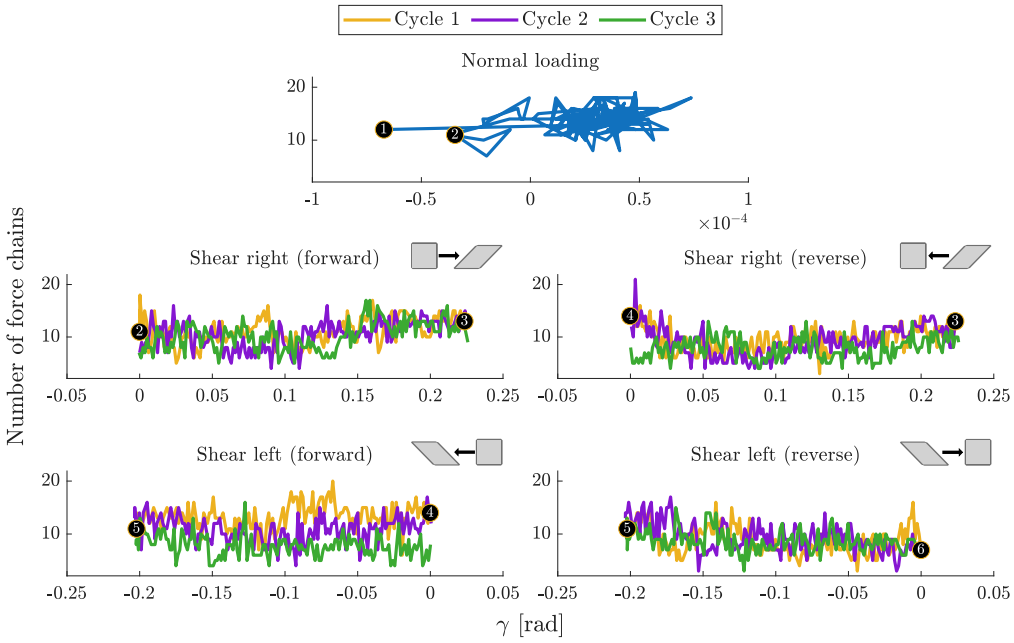


Figure 4.78: Per-stage evolution of the detected number of force chains for the loose granular assembly ($\sigma_n = -29.6$ kPa). Stage markers are shown only for Cycle 1.

During normal loading, the 82 lb loose assembly exhibits a slight net loss in detected force chains, in contrast to the gain observed under higher confinement. Rather than forming discrete bursts associated with each load increment, the response appears as one continuously fluctuating population ranging from approximately 7 to 19 chains. This suggests that, under lower confinement, compression does not progressively consolidate the load-bearing skeleton. Instead, weak confinement allows frequent local rearrangements that repeatedly create and destroy short-lived force chains, producing a more diffuse and unstable pre-shear structure.

As in the 122 lb loose assembly, all cycles show an overall increase in force chains during shear-right-forward (SRF), indicating that continued deformation promotes the formation of load-bearing paths aligned with the imposed shear direction. However, the cycle responses are more differentiated under lower confinement. Cycles 1 and 2 exhibit an initial drop at the onset of shear, reflecting the breakdown of force chains inherited from normal loading. In contrast, cycle 3 increases immediately, suggesting that the network in later loading history is already predisposed toward the new loading direction and can strengthen without first undergoing significant disruption. After this onset response, cycles 1 and 2 evolve through alternating gradual decreases and increases, while cycle 3 transitions between two relatively steady regimes: a low chain count and then a higher one. By the end of the stage, all cycles converge closely. Thus, although lower confinement produces more varied early-stage restructuring, the assembly still evolves toward a common load-bearing state as shearing progresses.

The shear-right-reverse (SRR) stage exhibits one of the clearest departures from the 122 lb loose response. Under higher confinement, cycles 1 and 2 lost chains while cycle 3 gained chains over the stage. Here, cycle 1 gains chains overall, cycle 2 remains nearly unchanged, and cycle 3 loses chains. This inversion suggests that lower confinement alters how the existing force network responds to reversal. Rather than uniformly destabilizing earlier-cycle chains, reversal can promote new chain formation in some cycles while weakening others. In effect, the response becomes more dependent on the inherited internal state than on the loading stage alone. Variability also increases with cycle count, indicating that repeated loading progressively amplifies the force chain network's sensitivity to local rearrangements. Near the end of the stage, cycle 2 exhibits a pronounced increase–decrease fluctuation, whereas cycles 1 and 3 remain comparatively steady, showing that the later-cycle network can reorganize abruptly even when the average chain count changes little.

During shear-left-forward (SLF), the cycles become more clearly separated than in the higher-confinement case. Cycle 1 sustains the largest number of force chains through most of the stage, while cycle 3 consistently exhibits the fewest. However, near the end of the stage, cycle 2 overtakes the others, indicating a delayed strengthening of the load-bearing skeleton. Cycles 1 and 2 transition between higher- and lower-chain-count regimes, whereas cycle 3 evolves more steadily, though it still shows intermittent fluctuations. Leading into shear reversal, the later cycles exhibit a buildup of force chains followed by a sharp drop, while cycle 1 remains more gradual. Hence, under lower confinement, some cycles accumulate unstable force structures that collapse near reversal, whereas others reorganize more continuously.

Compared to the other shear stages, the shear-left-reverse (SLR) response is the most tightly grouped, indicating that continued shear in the reverse direction drives the cycles toward a more common structural state. All cycles trend downward overall, showing a net loss of force chains through the stage. Although the later portions of the stage are similar, the initial responses differ from cycle to cycle. Cycle 1 gradually decreases, partially recovers, and then settles into a steady regime. Cycles 2 and 3 instead begin with near-steady behavior, then decrease, and partially recover. A notable late-stage peak in cycle 1, absent under higher confinement, suggests that lower confinement permits a brief final reorganization before the stage ends.

Despite the stage-wise differences, both the 122 lb and 82 lb loose assemblies reach nearly the same minimum and maximum number of force chains. However, the lower-confinement system experiences a smaller net loss over the full loading history (approximately -4 chains compared with -8 under higher confinement). This indicates that reducing confinement does not substantially alter the attainable range of force chain populations, but it does improve their cumulative persistence. Rather than undergoing sustained degradation, the weaker confinement promotes a more continuously reconfiguring network in which chains are repeatedly created and destroyed, allowing the total population to be maintained more effectively over time.

Total Force Chain Length Although the number of detected force chains indicates the number of load-bearing structures, the total chain length reflects their overall spatial extent and connectivity. Therefore, this metric distinguishes whether the assembly carries the load through many short chains or through fewer, more developed force chain networks. Figure 4.79 shows the total force chain length as a function of shear strain, while Figure 4.80 shows its per-stage evolution.

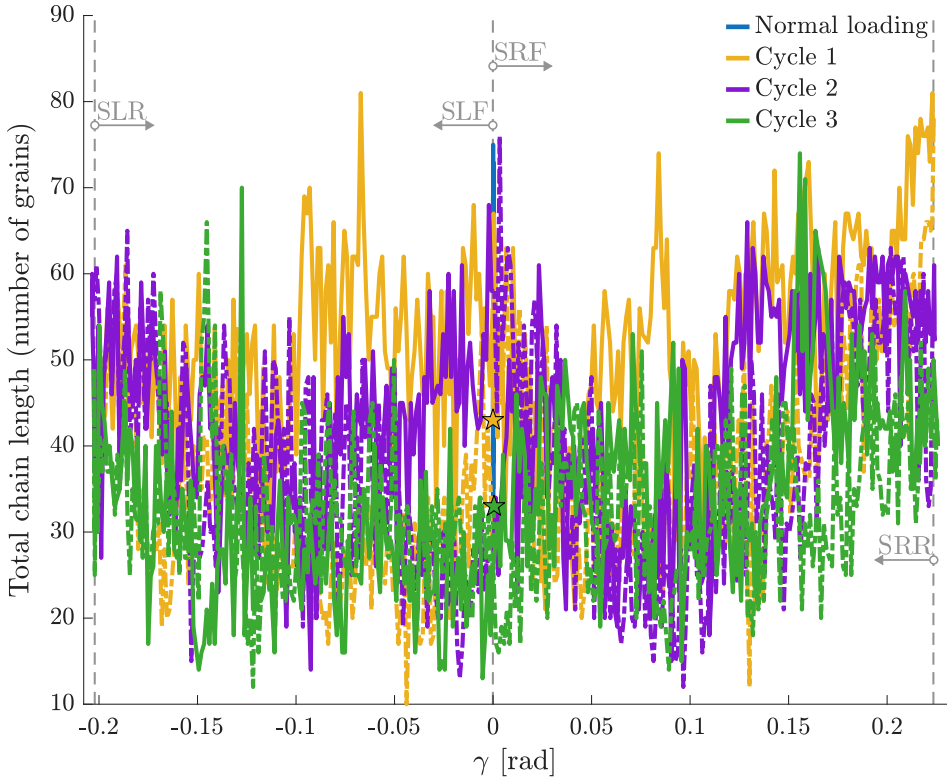


Figure 4.79: Evolution of the total force chain length, in number of grains, for the loose granular assembly ($\sigma_n = -29.6$ kPa). Curve style indicates shearing direction (solid: forward, dash-dotted: reverse), gray dashed lines mark stage transitions, and stars mark the start (yellow) and end (green) of cyclic loading.

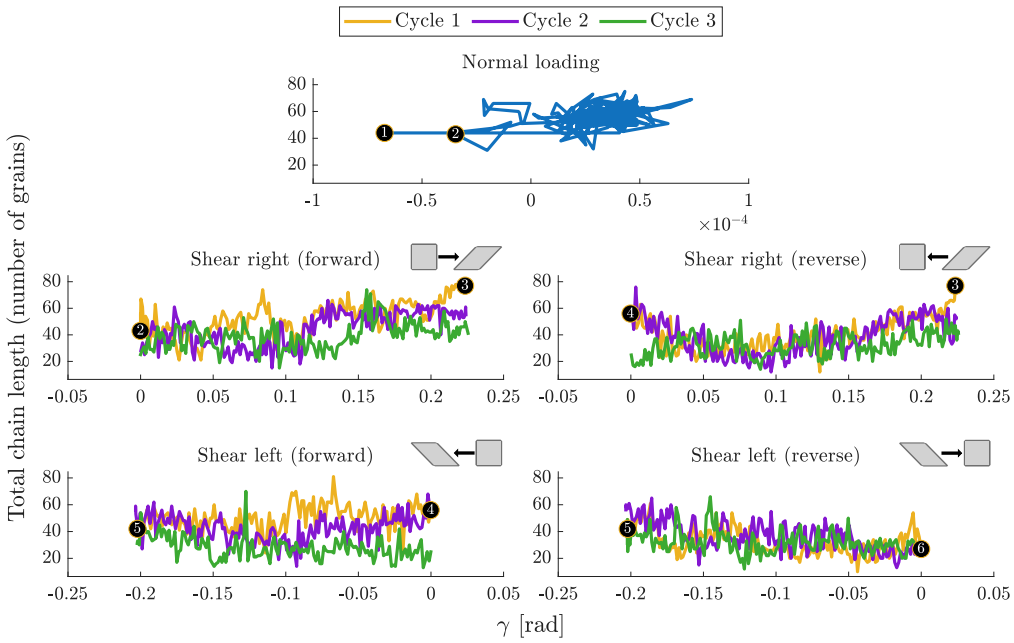


Figure 4.80: Per-stage evolution of the total force chain length, in number of grains, for the loose granular assembly ($\sigma_n = -29.6$ kPa). Stage markers are shown only for Cycle 1.

Consistent with the force chain count, the total chain length decreases slightly during normal loading, dropping from approximately 44 to 43 grains. The response again appears as a single broad, fluctuating burst rather than discrete growth events, with chain sizes ranging from roughly 31 to 75 grains. This indicates that added confinement does not progressively form longer, more connected chains. Instead, local rearrangements repeatedly fragment and rebuild the network, leaving the overall extent of the force chain nearly unchanged prior to shear.

During the first half of shear-right-forward (SRF), the total chain length closely follows the same upward trend observed in the number of force chains, indicating that new force chains are initially accompanied by expanding network connectivity. However, beyond mid-stage, cycle 3 diverges sharply downward while cycles 1 and 2 continue to strengthen. By the end of SRF, the cycles are clearly separated in the order cycle 1 > cycle 2 > cycle 3, suggesting that although all cycles can generate additional force chains during forward shear, later-cycle structures become progressively less able to sustain long, connected pathways. In other words, chain formation persists, but chain growth becomes less efficient with cyclic history.

During shear-right-reverse (SRR), cycles 1 and 3 initially respond differently before converging into the same tightly grouped behavior seen in the chain-count response. Cycle 1 begins with the largest total chain length, while cycle 3 initially drops below the others. This indicates that reversal first acts on inherited network geometry: stronger cycle 1 structures begin longer but contract more quickly, whereas the weaker cycle 3 structure starts already diminished. Once this inherited memory is erased, all cycles evolve toward a common reversal-state network with a similar total extent.

The shear-left-forward (SLF) response remains broadly similar to the detected force chain count behavior, showing that changes in the number of chains and their total extent remain strongly coupled during this stage. Cycle 3 generally maintains the smallest force chain structure, except for one brief spike, where it momentarily becomes the largest. Cycle 1 sustains the largest chain network for most of the stage, before cycle 2 overtakes near the end. This delayed takeover suggests that some cycles gradually strengthen through continued reversed loading, while others rely more on structures inherited from the previous stage.

During shear-left-reverse (SLR), cycle 3 exhibits the same fluctuations observed in the chain count response, but with a larger amplitude in total chain length. Thus, the same creation–loss events involve greater changes in network connectivity than

in chain number alone. Mechanistically, this means that fluctuations during this stage are driven less by the simple gain or loss of individual chains and more by the merging, extension, fragmentation, or shortening of chains. The network's topology is more dynamic than the raw population count suggests.

Relative to the higher-confined loose assembly, the 82 lb loose system attains both a lower minimum and lower maximum total chain length (10 versus 12 grains, and 81 versus 88 grains, respectively). Thus, reduced confinement limits both the minimum and maximum attainable force chain extents, resulting in a generally smaller force chain skeleton. More importantly, the lower confinement assembly loses far less total chain length over the loading history, decreasing by only about 10 grains compared with 29 grains under higher confinement. Thus, although the network is smaller overall, it is more persistent and less prone to cumulative structural degradation. Another notable difference appears in the branch geometry of the cyclic response. Under higher confinement, the shear-right branch tends to support longer chains than the shear-left branch, producing a positively sloped loop. In contrast, the 82 lb system exhibits a more symmetric, wide U-shaped response. This suggests that lower confinement reduces directional asymmetry, allowing similar force chain extents to develop in both shear directions.

Overall, the total chain length results show that reducing confinement does not eliminate force chain development, but it produces a smaller, more symmetric, and more continuously reorganizing network. The assembly carries a load through shorter, connected pathways than the 122 lb loose case does, yet those pathways degrade less severely with repeated cycling. Thus, lower confinement weakens the maximum connectivity of the force chain skeleton but improves its long-term persistence by promoting continual restructuring rather than progressive collapse.

Accumulated Force Chain Network Content While the total chain length measures the instantaneous size of the force chain network, the normalized AUC provides a stage-wise measure of how sustained that network is at each loading branch (Figure 4.81). Hence, larger AUC values indicate that force chain structures remain more developed over the course of a stage, whereas smaller values indicate more fragmented or short-lived load-bearing organization.

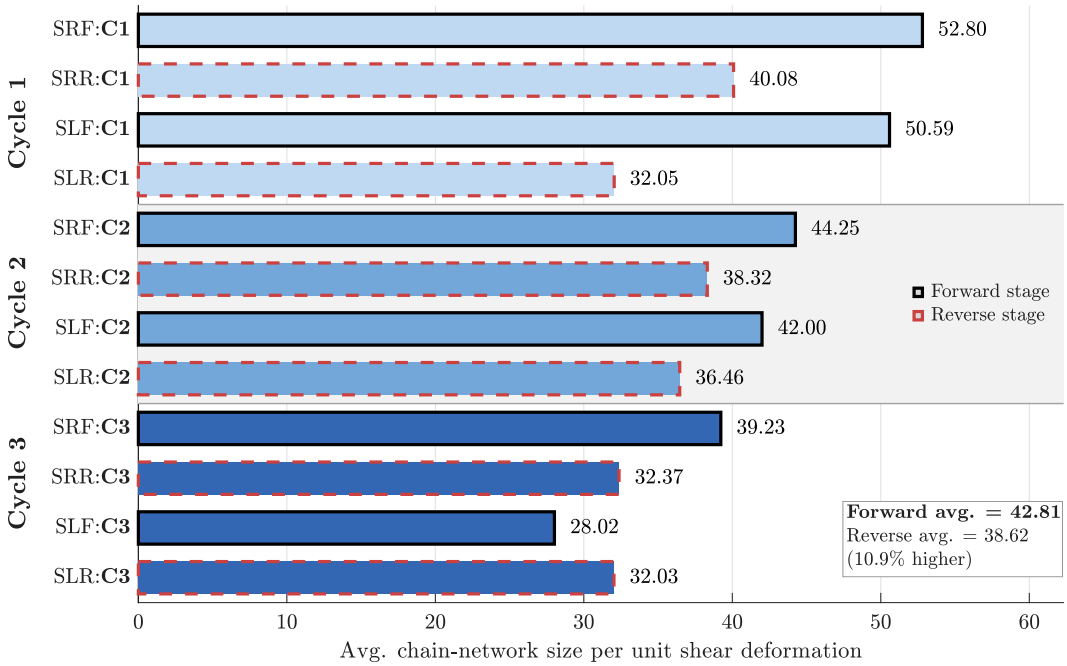


Figure 4.81: Bar chart of the normalized area under the curve (AUC) of the total force chain length for each cycle and shear stage for the loose assembly ($\sigma_n = -29.6$ kPa). The normalized AUC represents the average extent and persistence of the force chain network sustained per unit shear deformation within each stage.

Unlike the 122 lb loose assembly, cycles 1 and 2 of the 82 lb loose system follow the same stage sequence: high AUC during shear-right-forward (SRF), a decrease in shear-right-reverse (SRR), recovery to a larger value in shear-left-forward (SLF), and then a final drop to the minimum value in shear-left-reverse (SLR). This recurring pattern suggests that forward shearing initially promotes sustained force chain development; reversal weakens that structure; continued shearing in the reversed direction allows partial rebuilding; and the final reversal stage again disrupts the network. However, under lower confinement, the cycle 2 response is substantially weaker than that of cycle 1. In particular, the drops during reversal and the subsequent recovery are much smaller, indicating that repeated loading reduces the assembly's ability to both lose and regain force chain connectivity. Hence, the network becomes less responsive and less structurally dynamic after the first cycle.

From SLR of cycle 2 to SRF of cycle 3, the AUC shows a stronger recovery than under higher confinement. Hence, lower confinement allows the force chain network to rebuild more effectively between cycles, likely because weaker confinement permits easier rearrangement and reassembly of contacts. Furthermore, unlike the monotonic decline observed under higher confinement, the remainder of cycle 3 does not continue to weaken steadily. Instead, the AUC partially recovers again

during SLR, reaching a value only slightly below that of SRR, suggesting that the final cycle retains some capacity for structural renewal, even after repeated loading.

Throughout the loading history, the net reduction in AUC is smaller under lower confinement (approximately 21 compared to 31). Thus, although the 82 lb loose assembly develops a smaller force chain network overall, it experiences less cumulative degradation of that network. Another key difference is the directional bias. In the 82 lb system, the forward-shear stages attain an average AUC approximately 10.9% greater than the reverse stages, while the higher-confined loose assembly showed only a marginal forward-stage advantage. This indicates that reducing confinement enhances the contrast between loading directions: forward shearing becomes substantially more effective at sustaining force chain structure than reversed loading.

Overall, the AUC results show that the 82 lb loose assembly supports a smaller but more recoverable force chain network than the 122 lb loose case. Repeated loading weakens the response after cycle 1, yet the network retains a greater ability to rebuild between cycles and suffers less long-term structural loss. Thus, lower confinement reduces the maximum persistence of force chains within individual stages, but increases their capacity for renewal under continued cyclic loading.

Force Chain Participation The AUC quantified the cumulative persistence of force chain structure within each stage. Now, we examine the chain density violin plots (Figure 4.82) to show how widely the force chain structure is distributed across the assembly and to reveal whether load-bearing participation is concentrated within a narrow subset of grains or spread more uniformly across a range of possible chain sizes. In a violin plot, the vertical red lines represent the median, and the vertical blue lines represent the lower and upper quartiles (Q1 and Q3). The width at any point on the violin shape indicates the frequency of data at that value. The tails of the violin plot represent extremes of the data distribution. Moreover, the distribution can also have multiple peaks, indicating possible multiple regimes in the data.

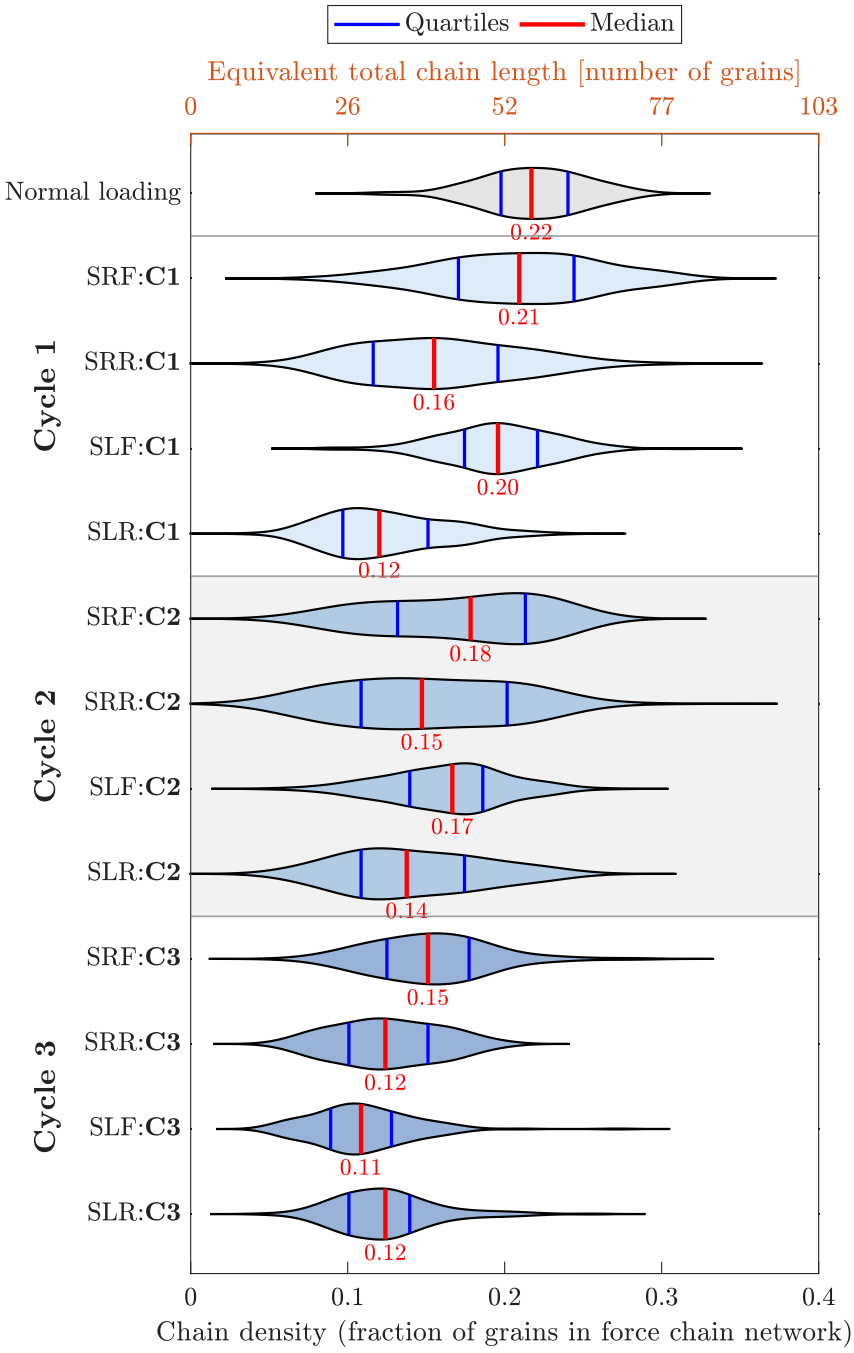


Figure 4.82: Violin plots of the force chain density for each cycle and shear stage for the loose assembly ($\sigma_n = -29.6$ kPa). Force chain density is defined as the fraction of grains participating in the force chain network relative to the total number of interior grains. The bottom x-axis shows the normalized chain density, while the top x-axis shows the equivalent total force chain length in number of grains. The width of each violin indicates the relative frequency of occurrence of a given chain density during that stage.

During normal loading, the 82 lb loose assembly has a median chain density of approximately 0.22, matching that of the 122 lb loose assembly. However, the distribution is more Gaussian, and the lower tail is shorter, indicating that although the average force chain participation remains unchanged, the lower-confinement assembly exhibits a more uniform initial network with fewer extremely sparse chain states. From normal loading to shear-right-forward (SRF) of cycle 1, the median chain density decreases slightly, indicating that the onset of shear initially disrupts the preexisting force chain network rather than immediately strengthening it. The shear-right stages remain broadly Gaussian, but SRF is centered around medium-sized chain structures, whereas shear-right-reverse (SRR) shifts toward smaller-to-medium structures. Moreover, the long upper tail of SRR shows that reversal can still intermittently generate larger force-chain structures even though most of the network remains modest in size. In contrast, the shear-left stages are weaker overall. shear-left-forward (SLF) partially recovers to a value slightly below SRF, while shear-left-reverse (SLR) decreases further and develops two preferred participation ranges. This suggests that continued reversed loading fragments the network into competing small- and medium-sized structural states rather than sustaining a single dominant chain scale.

Entering cycle 2, the median chain density rises sharply from SLR of Cycle 1 to SRF, indicating substantial rebuilding of the force chain network between cycles. This strong recovery, also observed in the 122 lb loose assembly, suggests that unloading from the prior cycle leaves the packing in a state favorable for forming new chains. The shear-right stages again exhibit a mild bimodal structure, but now span the widest density ranges of the loading history, extending to approximately 0.35 in SRF and 0.37 in SRR. This indicates the coexistence between smaller transient chains and larger sustained structures. The more uniform center of the SRR violin plot further suggests that reversal redistributes participation more evenly across chain sizes than forward shearing does. The shear-left stages become more Gaussian. Although SLF is left-skewed while SLR is right-skewed, implying asymmetric reorganization before and after the final reversal. One stage trends toward contraction into smaller networks, while the other permits renewed growth into larger structures.

Cycle 3 exhibits only weak recovery entering SRF, indicating diminished inter-cycle rebuilding relative to cycle 2. Thereafter, the median chain density decreases through SLF before partially recovering in SLR, suggesting that the later-cycle network remains active but is less capable of sustained growth. All stage distributions

are approximately Gaussian and concentrated within small- to medium-chain densities, indicating that repeated loading has shifted the assembly toward more modest, uniform force chain structures. Even the SLF violin plot, which exhibits the longest upper tail, has the bulk of its distribution confined to relatively modest chain densities. Lastly, within cycle 3, SRF exhibits the broadest central distribution. More generally, the shear-right stages display Gaussian distributions broader than those of the shear-left stages, indicating greater variability in force chain participation during rightward shearing. In contrast, the narrower shear-left distributions suggest a more concentrated, repeatable response once loading continues in the reversed direction.

Relative to the 122 lb loose system, both the minimum and maximum chain densities are smaller in the 82 lb case (0.038 versus 0.046, and 0.314 versus 0.341, respectively), even though both experiments attain their maximum during cycle 1. Thus, reducing confinement lowers both the lowest and the highest attainable levels of force chain participation. More importantly, the net loss in chain density from the onset to the end of shear is much smaller under lower confinement (approximately -0.039 versus -0.11). This indicates that although the 82 lb loose assembly supports smaller force-chain structures overall, those structures degrade less severely over repeated cycling.

Overall, the chain density results show that lower confinement yields a force chain network with a smaller magnitude but a broader range of accessible structural states. The assembly repeatedly transitions between small- and medium-sized chain structures rather than concentrating load in the largest networks observed under higher confinement. Repeated loading, therefore, weakens peak force chain participation, but it also reduces cumulative structural loss. In the 82 lb loose assembly, stress transmission becomes more distributed, more recoverable, and less dependent on maintaining large dominant chain structures.

Strong Network Participation and Strong Network Chain Participation The chain density results showed that force chain structures are widely distributed throughout the assembly. We now distinguish whether those participating grains belong to the load-bearing strong network. Accordingly, we examine both the fraction of grains carrying above-average forces (strong network participation) and the fraction of those strong grains that organize into force chains (strong network chain participation). Together, these metrics reveal how efficiently the stress-bearing portion of the loose assembly remains structured under reduced confinement. Figure 4.83 summarizes the stage-wise medians and variability in both measures.

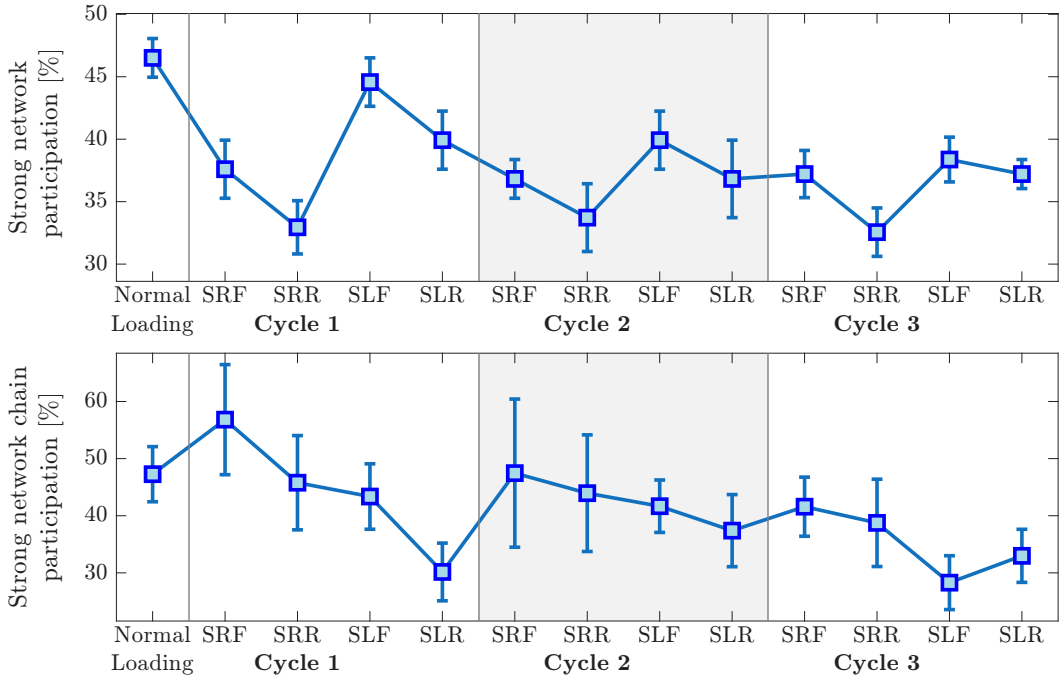


Figure 4.83: Stage-wise medians of the strong network participation [%] (top) and the strong network chain participation [%] (bottom) for each cycle and shear stage for the loose assembly ($\sigma_n = -29.6$ kPa). Error bars represent one-half of the interquartile range, centered about the median.

During normal loading, the **strong network participation** median begins at 46.5%, the highest value of the entire loading history, and notably above the 40.3% observed in the 122 lb loose experiment. At the onset of shear (shear-right-forward (SRF)), the strong network participation drops by approximately 8.9%, suggesting that the contact network formed under normal compression is highly sensitive to shear. Thereafter, the response alternates between weakening and recovery rather than following a smooth monotonic trend.

Excluding the normal loading stage, median values remain within a moderate range of approximately 32.6% to 44.6% (30.6% to 46.5% including variability). The minimum occurs during shear-right-reverse (SRR) of cycle 3, whereas the largest stage-to-stage rebound occurs during shear-left-forward (SLF) of cycle 1. This recurring pattern suggests that reversals into the shear-right direction tend to disrupt the established strong contact framework, while continued shearing in the opposite direction allows a renewed load-bearing structure to emerge.

As cycling progresses, the response becomes increasingly irregular. Cycle 2 shows only modest recovery during SLF, while cycle 3 exhibits the sharpest stage-to-stage fluctuations, particularly across the SRF → SRR reversal and the subsequent SRR → SLF transition. This indicates that repeated loading does not stabilize the strong network, but instead promotes a fragile structure that is first disrupted during reversal and then continues to reorganize as the assembly adapts to the new loading direction.

Compared with the 122 lb loose response, the 82 lb assembly exhibits greater fluctuations despite occupying a similar overall range. The larger net reduction from the onset to the end of cyclic shear further indicates that lower confinement leads to greater cumulative weakening of the population of grains carrying above-average forces.

The **strong network chain participation** measures how effectively those strong grains organize into coherent force chains. Median values range from approximately 28.3% to 56.8% (23.6% to 66.5% including variability), indicating that only a subset of strong grains participates in chain-like load transfer at any given stage.

Participation increases from normal loading to SRF, where the global maximum occurs in cycle 1. Hence, the initial forward shearing motion promotes the rapid alignment of strong grains into efficient stress-transmitting chains, even as the overall number of strong grains declines. Subsequently, the response progressively weakens throughout the remainder of cycle 1, reaching a minimum by SLR.

Cycles 2 and 3 follow the same broad pattern of partial recovery at SRF followed by gradual decline, but with smaller amplitudes than cycle 1. This suggests that much of the major structural reorganization occurs during the first cycle, after which the remaining chain network evolves more incrementally. Variability is also greatest during the SRF stages of cycles 1 and 2, indicating that forward shearing is the most susceptible stage to intermittent chain formation and collapse.

Unlike strong network participation, this metric exhibits larger directional changes from stage to stage, confirming that the organization of strong grains into chains is more sensitive to loading history than the mere presence of strong grains. In other words, strong contacts may persist, while the coherent chain structures they form are repeatedly rearranged.

In contrast to the higher-confinement experiment, the 82 lb system occupies a narrower range of chain participation values and experiences a much smaller net decline from the onset to the end of shear. Thus, lower confinement reduces the total

number of strong grains, but those that remain retain a relatively consistent tendency to organize into force chains once the first cycle restructuring has occurred.

In general, these results show that while roughly 33% to 45% of the assembly remains in the strong network during cyclic shear, only about 28% to 57% of those strong grains organize into detectable force chains. Relative to the 122 lb loose experiment, this indicates that lowering confinement does not greatly change the overall size of the strong network, but it does reduce the extent to which those strong grains assemble into coherent force-chain structures.

Micro-Macro Comparison In this section, we examine the stage-wise medians of the macroscopic shear stress and the total force chain length (Figure 4.84). Examining these quantities together assesses how effectively the evolving force chain network translates internal organization into bulk resistance.

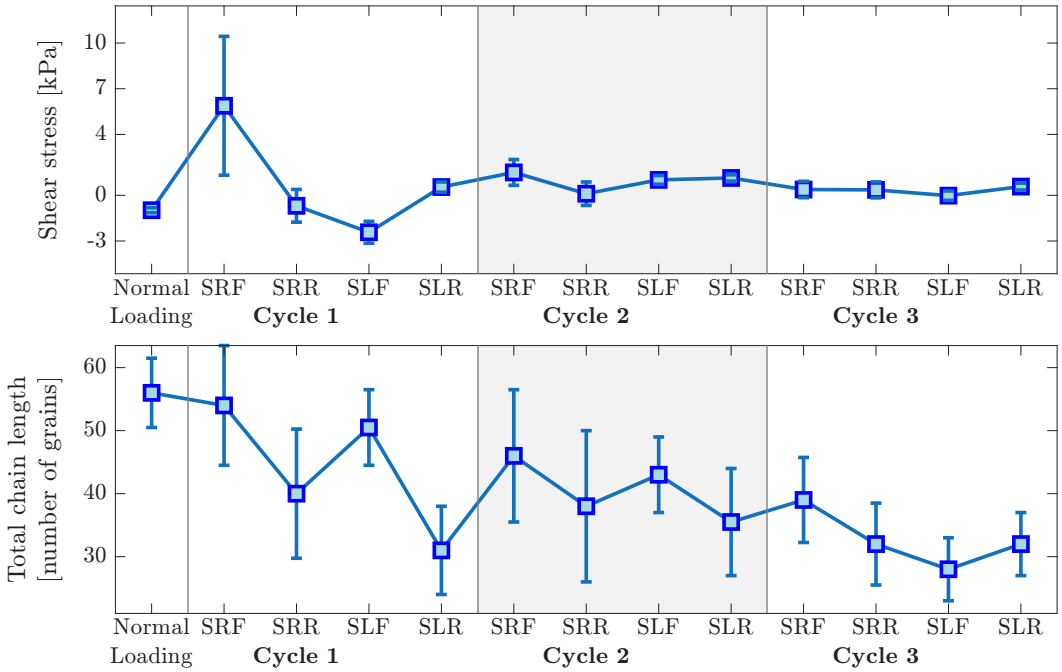


Figure 4.84: Stage-wise medians of the shear stress [kPa] (top) and total chain length [number of grains] (bottom) for each cycle and shear stage for the loose assembly ($\sigma_n = -29.6$ kPa). Error bars represent one-half of the interquartile range, centered about the median.

The median **shear stress** remains within approximately -0.021 to 5.88 kPa (-0.33 to 10.43 kPa including variability), indicating that reduced confinement limits the assembly's ability to maintain bulk shear resistance. From normal loading to shear-right-reverse (SRR) in cycle 1, the shear stress undergoes a sharp increase-decrease fluctuation, ultimately ending only slightly above its median value during normal

loading. This suggests that shear resistance is rapidly mobilized at the onset of shear, but much of that strength is lost during the first shear reversal as the contact network reorganizes.

From SRR of cycle 1 through shear-right-forward (SRF) of cycle 2, the shear stress weakens gradually before partially recovering. Afterward, cycles 2 and 3 remain nearly constant within a narrow range, indicating that the most significant shear stress evolution occurs early in the loading history. The maximum median shear stress occurs during SRF of cycle 1, whereas the minimum occurs during shear-left-forward (SLF) of cycle 3. As in the higher confined case, SRF also exhibits the greatest variability, indicating that the initial forward-shear stage remains the most mechanically unstable portion of the response.

The **total chain length** follows many of the same broad trends, indicating that macroscopic stress remains closely tied to the extent of the force-chain network. From normal loading to SRR in cycle 1, the total chain length decreases monotonically, indicating progressive contraction of the initially compressed force chain network during the first loading sequence.

Thereafter, the response generally follows a repeating increase-decrease pattern through SRR in cycle 3, with progressively smaller amplitudes in later cycles. This suggests that most large-scale restructuring of the force chain network occurs during cycle 1, while later cycles involve more modest internal adjustments. In cycle 3, the pattern weakens further, as the total chain length continues decreasing from SRR to SLF before recovering slightly during SLR.

Excluding the normal loading stage, the maximum total chain length occurs during SRF in cycle 1, and the minimum during SLF in cycle 3, which matches the locations of the shear stress extrema. This agreement indicates that the strongest and weakest bulk states correspond to the most and least extensive force chain networks, respectively. Overall, the median total chain length remains within approximately 32 to 56 grains (27 to 61.5, including variability).

Compared with the 122 lb loose assembly, the 82 lb case evolves within a narrower range of both shear stress and chain length. The lower confined system, therefore, preserves the same qualitative coupling between the force chain structure and the bulk stress, but at a reduced intensity. Both confinement levels reach their maximum during SRF in cycle 1, confirming that early forward shearing is the most effective stage for mobilizing stress and expanding the force-chain network. The

main difference between the two loose experiments is that the lower-confined assembly evolves more smoothly, whereas the higher-confined assembly exhibits sharper stage-to-stage structural adjustments. Hence, stronger confinement promotes more abrupt reorganization of load-bearing contacts, while lower confinement favors a weaker but more gradual redistribution of force paths.

Overall, the micro–macro comparison shows that the 82 lb loose assembly retains a clear relationship between force chain extent and macroscopic shear stress, particularly during cycle 1 when both quantities undergo their largest changes. With continued cycling, this coupling weakens as both responses settle into narrow ranges. Thus, repeated loading does not eliminate internal structure but progressively drives the granular assembly toward a mechanically stabilized state, in which further contact network rearrangements generate only limited additional shear resistance.

4.5.2.3 Force Chain Structure and Anisotropy

The following subsections analyze the orientation distributions of both contacts (fabric anisotropy) and interparticle forces (force anisotropy), and their relationships with macroscale quantities through the stress-force-fabric framework. In addition, the probability density functions (PDF) of normalized contact forces are examined to characterize how forces are transmitted through the granular assembly.

Fabric and Force Anisotropy Polar histograms are used to examine the angular distributions of contact fabric orientation, $P(\theta)$, and the mean interparticle forces, $\bar{f}_n(\theta)$ and $\bar{f}_t(\theta)$. As in previous sections, the radial magnitude represents the relative frequency or average force at a given orientation, while the shape of the distribution reflects the degree of anisotropy. In loosely packed assemblies under lower confinement, these distributions tend to show greater variability and weaker directional persistence, reflecting a more dynamic and less stable force-transmission network.

The **contact fabric**, $P(\theta)$, of the 82 lb loose assembly remains anisotropic throughout nearly all shear stages, indicating that repeated loading continues to organize the contact network into preferred orientations rather than driving it toward a random state (Figure 4.85). As in the 122 lb loose case, directional structure is retained across the loading history; however, under lower confinement, the anisotropy magnitudes are generally weaker, while the principal fabric directions often remain comparable. The main distinction is that the orientations of the associated principal stress axes shift more substantially, producing different patterns of fabric–stress alignment.

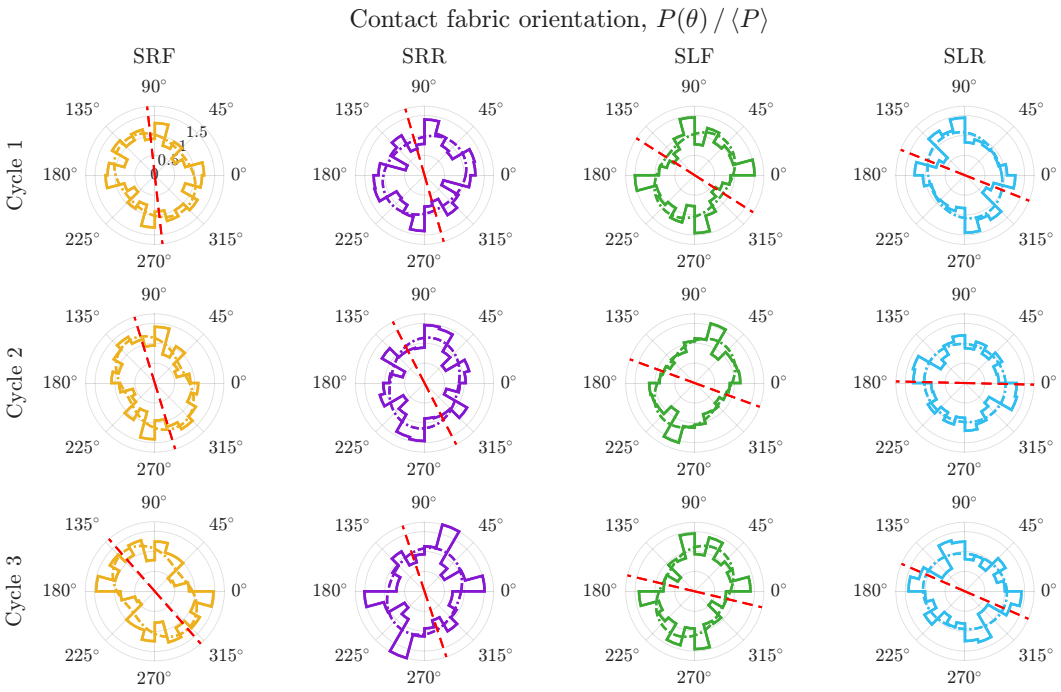


Figure 4.85: Polar histograms of the normalized angular distributions of the contact fabric orientation, $P(\theta)$, arranged by cycle (rows) and midpoint of each shear stage (columns) for the loose assembly ($\sigma_n = -29.6$ kPa). The solid curve represents the distribution, the dash-dotted curve shows its Fourier fit, and the red dashed line denotes the principal compressive stress axis.

During the shear-right stages, shear-right-forward (SRF) and shear-right-reverse (SRR), the lower confined assembly exhibits stronger cycle dependence than the 122 lb case. In SRF, the misalignment between the fabric anisotropy and principal stress axes decreases markedly with cycle count, reaching near alignment by cycle 3. In contrast, the more highly confined assembly retains larger offsets at the same stage. In SRR, the 82 lb assembly preserves elongated anisotropic shapes, whereas the 122 lb case approaches near-isotropic states in later cycles. This indicates that lower confinement weakens the fabric response, but allows directional memory of the contact arrangement to persist more strongly during reversal stages.

During the shear-left stages, shear-right-forward (SRF) and shear-left-reverse (SLR), $P(\theta)$ remains persistent but undergoes stage-dependent reorientation. SLF generally exhibits greater fabric–stress misalignment than in the 122 lb assembly, whereas SLR shows improved alignment in later cycles. Thus, the reversed loading direction does not erase anisotropic structure, but instead changes how effectively that structure aligns with the evolving stress field. Overall, compared with the higher confined loose assembly, the 82 lb system exhibits a weaker but more persistent

fabric response: stronger confinement produces sharper anisotropy, whereas lower confinement favors continued reorientation and longer directional memory.

The **mean normal force network**, $\bar{f}_n(\theta)$, also remains anisotropic throughout all stages (Figure 4.86), but with simpler and less concentrated distributions than in the 122 lb loose assembly. Characteristic peanut-shaped responses become less persistent under lower confinement, especially in later cycles where elliptical distributions are more common. In contrast, the higher confined assembly more frequently maintains sharply defined peanut-shaped forms during the shear-right stages. This suggests that reduced confinement weakens focused compression force chains and promotes more distributed normal-force transmission.

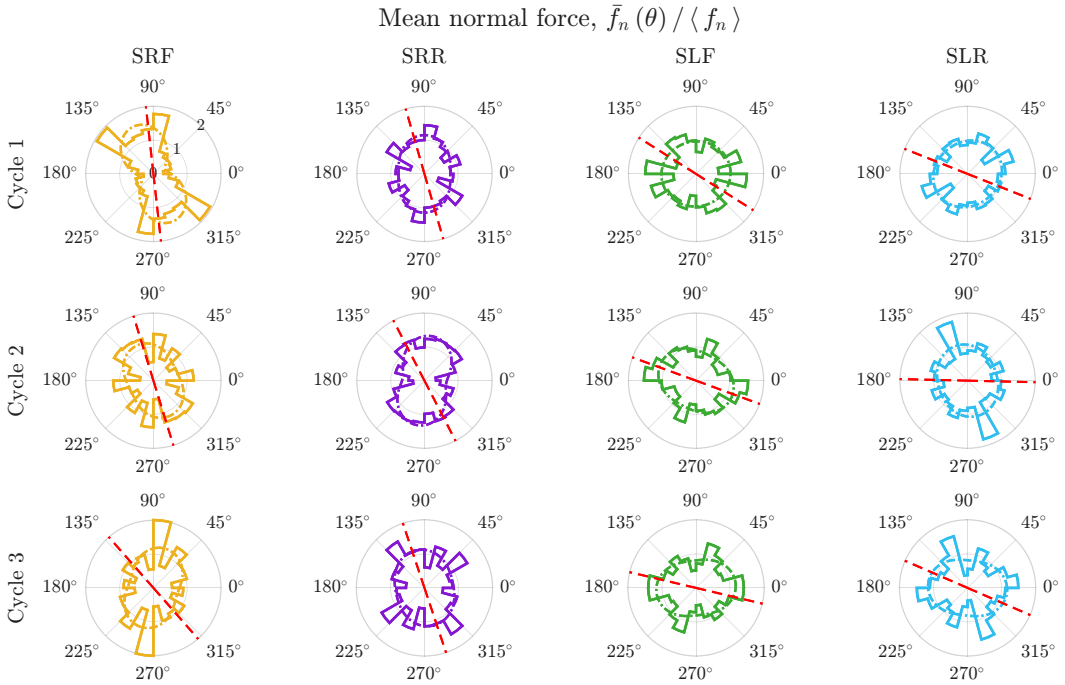


Figure 4.86: Polar histograms of the mean contact normal force, $\bar{f}_n(\theta)$, arranged by cycle (rows) and midpoint of each shear stage (columns) for the loose assembly ($\sigma_n = -29.6\,\text{kPa}$). The solid curve represents the distribution, the dash-dotted curve shows its Fourier fit, and the red dashed line denotes the principal compressive stress axis.

Across most stages, the normal force anisotropy axis is more closely aligned with the compressive stress axis than in the higher confined case. Thus, although the anisotropy magnitude is often reduced, the dominant normal-force pathways tend to orient more efficiently with the imposed loading direction. The cycle dependence remains pronounced, but without a single monotonic trend. Instead, $\bar{f}_n(\theta)$ alternates between diffuse and concentrated states depending on the loading direction and the

cycle history. Relative to the 122 lb loose assembly, the 82 lb loose system therefore trades force concentration for improved directional efficiency.

The **mean tangential force network**, $\bar{f}_t(\theta)$, broadly mirrors the normal force response (Figure 4.87), but at consistently smaller magnitudes and with greater stage-to-stage variability. In both confinement levels, the preferred tangential directions generally align with those of the normal force network, indicating that frictional resistance develops along many of the same dominant contact pathways. However, under lower confinement, the tangential distributions are more often rounded or weakly anisotropic, showing that frictional resistance is mobilized across a broader range of contact orientations than in the 122 lb assembly.

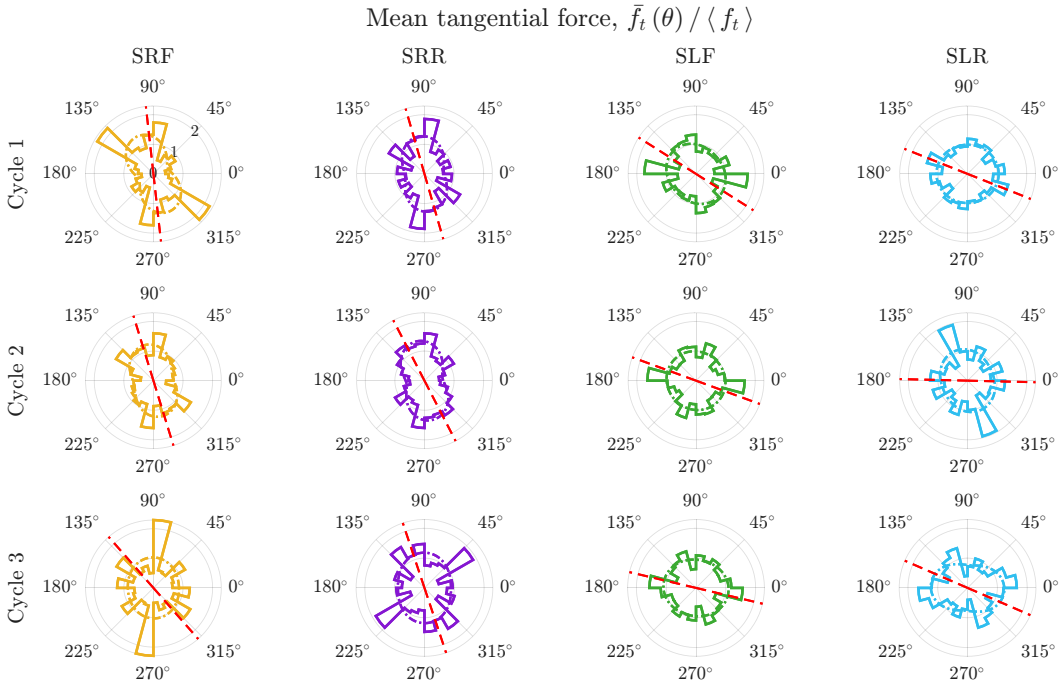


Figure 4.87: Polar histograms of the mean contact tangential force, $\bar{f}_t(\theta)$, arranged by cycle (rows) and midpoint of each shear stage (columns) for the loose assembly ($\sigma_n = -29.6\,\text{kPa}$). The solid curve represents the distribution, the dash-dotted curve shows its Fourier fit, and the red dashed line denotes the principal compressive stress axis.

Despite this greater variability, the coupling between $\bar{f}_t(\theta)$ and $\bar{f}_n(\theta)$ remains strong. Both components generally concentrate within the same preferred orientation ranges, although there are selective deviations. In cycle 1, the tangential response develops an additional preferred sector near 140° to 165°, not emphasized in the normal force response. Moreover, the dominant lobe is strongest in the tangential component during cycle 2, but strongest in the normal force component during cycle 3. This

indicates that while normal and frictional forces typically share common load paths, their relative importance changes with cyclic history. Hence, lower confinement results in a weaker but more spatially distributed mobilization of friction.

Together, the fabric and force anisotropy results show that lowering confinement does not eliminate directional organization within the assembly. Instead, it shifts the system toward weaker but more persistent anisotropic states. Contact and force networks remain directionally structured, while their principal anisotropy axes often align more closely with the evolving stress field than in the 122 lb loose assembly. Thus, reduced confinement weakens the magnitude of anisotropy but can improve directional efficiency, broaden load-transmission pathways, and preserve structural memory under cyclic loading.

Temporal Evolution of Fabric and Force Anisotropy Magnitudes The polar histograms identified the preferred orientations of contacts and contact forces at selected stages in the loading history. Now we examine how the magnitudes of the fabric and contact force anisotropies evolve continuously with shear strain (Figure 4.88). These responses reveal whether the contact network is directional and when that directional structure strengthens, weakens, collapses, or reorganizes during cyclic loading.

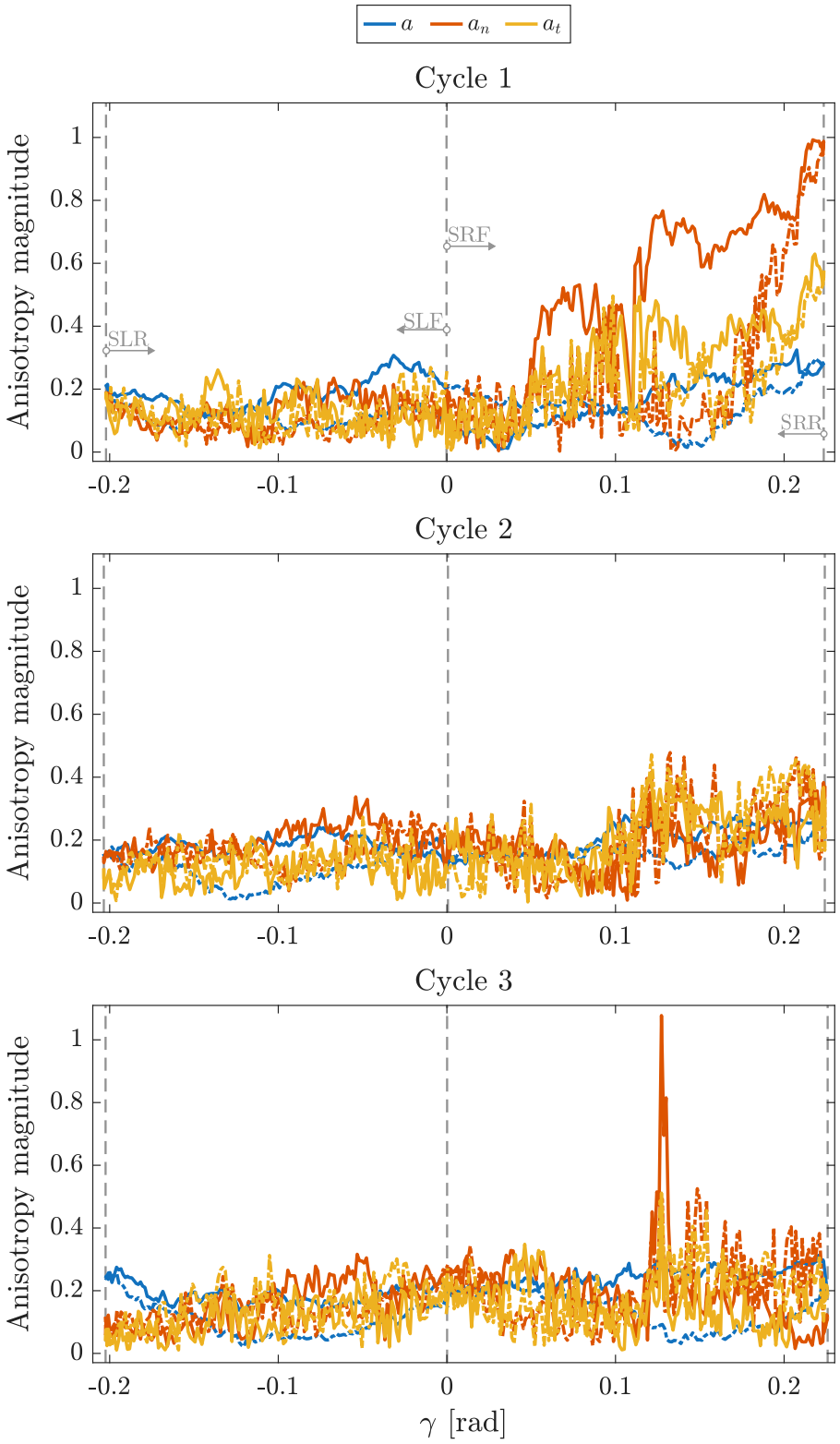


Figure 4.88: Per cycle evolution of the anisotropy magnitudes as functions of shear strain for the loose assembly ($\sigma_n = -29.6$ kPa): fabric anisotropy magnitude, a, and normal and tangential force anisotropy magnitudes, a_n and a_t, respectively. Curve style indicates shearing direction (solid: forward, dash-dotted: reverse), gray dashed lines mark stage transitions.

The temporal evolution of the anisotropy magnitudes reveals that lowering confinement alters the cyclic loop geometry more strongly than it changes their overall ordering. In the 122 lb loose assembly, the normal and tangential force anisotropies, a_n and a_t, developed wider and more positively sloped loops with broadened central regions and collapsed ends during cycles 1 and 2. In contrast, the 82 lb loose assembly exhibits left and right branches that remain near-zero-slope over much of the loading history. This flatter structure indicates that reduced confinement suppresses sustained anisotropic growth during continued shearing, confining the response to narrower, more compact trajectories. Hence, the force network is less able to strengthen progressively along a loading branch and instead adjusts through smaller, incremental redistributions of load.

For **the normal force anisotropy**, a_n, cycle 1 still increases during shear-right-forward (SRF), but with pronounced fluctuations that are not present under higher confinement. These oscillations suggest intermittent formation and collapse of dominant compression pathways as the initially loose contact network seeks stable load-bearing alignments. Upon reversal, the SRF and shear-right-reverse (SRR) paths briefly overlap before the SRR path drops sharply, confining the remainder of the cycle to a narrow low-magnitude band. This abrupt collapse implies that the force chains formed during SRF are more fragile under lower confinement and rapidly dismantled upon shear reversal. The same compressed structure persists into cycle 2, where the broader evolution observed in the 122 lb assembly is replaced by evolution largely restricted to the narrow region established during the first reversal. This suggests that once the strongest directional chains are lost, subsequent cycles are accommodated by the repeated reuse of a weaker but already conditioned contact framework rather than by renewed large-scale chain growth.

By cycle 3, the stage-wise trends remain distinct, although both right and left petals are substantially collapsed. A pronounced fluctuation during SRF yields the global maximum, indicating that even after partial stabilization, the assembly can still undergo short-lived episodes of rapid force chain concentration when local contacts temporarily align favorably. Overall, relative to the higher-confined case, the 82 lb assembly exhibits a more constrained but intermittently sharper a_n response, with slightly larger extrema. Thus, lower confinement reduces sustained normal force anisotropy while preserving the possibility of transient force surges.

The **tangential force anisotropy**, a_t, follows the same broad behavior as a_n, confirming that frictional anisotropy remains strongly coupled to the normal-force network.

Compared with the 122 lb assembly, the shear-left branches are more collapsed across all cycles, while the downward deviation during SRR of cycle 1 is more pronounced. The enlarged loop area near the first rightward reversal suggests stronger transient frictional mobilization and release as contacts slide, detach, and reform under the new loading direction. In contrast, the large late-cycle loop area observed near SRR in the 122 lb assembly becomes much smaller under lower confinement, implying that repeated cycling under weaker confinement reduces the capacity for frictional stresses to accumulate before reversal. Cycle 3 again exhibits the same fluctuation seen in a_n, but at a reduced magnitude. Thus, friction responds to the same structural events as in the normal force network, but with lower intensity.

The **fabric anisotropy magnitude**, a, remains the most structurally stable of the three measures and broadly retains the same loop architecture observed in the 122 lb assembly. However, the petal geometry changes appreciably. In cycle 1, the central collapsed portion rotates into a negatively sloped segment rather than remaining flat, indicating that contact anisotropy progressively relaxes during branch transfer instead of being temporarily preserved. This behavior is consistent with easier grain rolling and contact rearrangement under lower confinement, which promotes faster reorientation of the contact network [27]. During SRR, the loop opens downward, creating a larger non-zero region than under higher confinement, suggesting a longer-lived transitional state in which the previous contact alignment has weakened before a new reversed fabric structure is established.

In cycle 2, the central collapse extends over a longer strain interval, while the surrounding petals shorten, especially along the shear-right branch. This indicates that a larger portion of the loading cycle is now accommodated without major restructuring, suggesting progressive cyclic adaptation and a shakedown-like tendency toward reduced internal rearrangement [81]. By cycle 3, the central region simplifies into a near-linear collapsed segment rather than the L-shaped form observed previously, while the shear-left branch narrows substantially. These changes suggest that abrupt structural transitions are replaced by smoother, more incremental reorientation of contacts. Despite this more compact geometry, both the minimum and maximum a values slightly exceed those of the 122 lb assembly, indicating that weaker confinement reduces the duration of strong fabric states more than their attainable amplitude.

As in the 122 lb loose assembly, the shear-right loops of a_n and a_t dominate over a during cycle 1, indicating that force anisotropy responds more strongly than contact geometry during the first mobilization of shear resistance. A key difference emerges in cycles 2 and 3, where a_n, a_t, and a become comparable in magnitude and frequently overlap, suggesting that, after the initial cycle, the force and contact networks evolve more coordinately under lower confinement. The main exception is the large fluctuation in a_n during SRF in cycle 3, indicating that the normal force network can still abruptly reorganize even after the broader system has stabilized.

Together, these results show that reducing confinement compresses the anisotropy-magnitude loops into flatter, more overlapping structures while preserving their fundamental stage sequence. Relative to the 122 lb loose assembly, the 82 lb loose assembly exhibits less sustained directional strengthening, faster collapse of previously formed anisotropic states during reversal, and earlier convergence toward a mechanically conditioned response. Thus, reduced confinement shifts the assembly from a strongly differentiated, anisotropic evolution toward a more compact and coordinated cyclic state, in which subsequent deformation is increasingly accommodated by modest contact adjustments rather than by repeated large-scale rebuilding of the internal network.

Verification of the Stress-Force-Fabric Relationship The previous section identified how the contact network and contact forces evolve directionally during cyclic loading. This section now uses the stress-force-fabric (SFF) relation to test how effectively those internal anisotropies predict the bulk invariant stress ratio. This comparison (Figure 4.89) is important for assessing whether the measured grain-scale organization remains sufficient to explain the macroscopic shear response, or whether additional mechanisms emerge as the cyclic history accumulates.

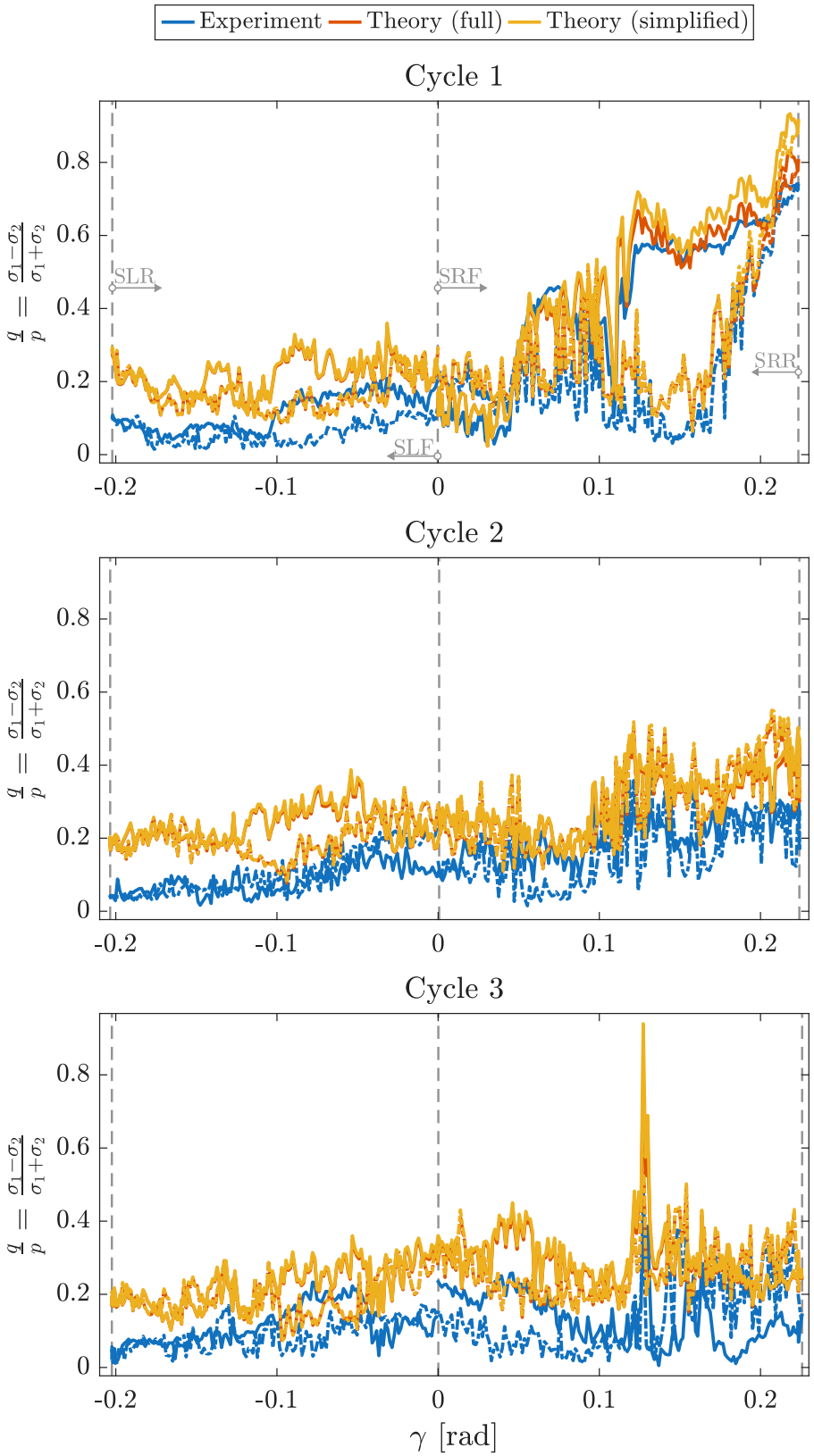


Figure 4.89: Per cycle evolution of the invariant stress ratio, q/p, as a function of shear strain for the loose assembly ($\sigma_n = -29.6$ kPa). The experimental response is compared with the predictions of the full and simplified stress-force-fabric (SFF) relationships. Curve style indicates shearing direction (solid: forward, dash-dotted: reverse), gray dashed lines mark stage transitions.

The SFF relation reproduces the overall cyclic structure of the 82 lb loose assembly reasonably well, but its agreement with the experimental q/p response is weaker than in the 122 lb loose case. As in the higher confined assembly, the experimental q/p evolution closely resembles that of a_n, including the pronounced fluctuations that distinguish this lower confinement response. This confirms that normal force anisotropy remains the dominant internal contributor to the invariant stress ratio. At the same time, the theory captures the broad per-cycle loop geometry more successfully than the finer local variations, especially once the response begins to fluctuate or collapse into narrow branches.

A persistent asymmetry remains between the shear-right and shear-left stages. As in the 122 lb loose assembly, the shear-left branches are where the theory performs worst: shear-left-forward (SLF) substantially overestimates the experiment, while shear-left-reverse (SLR) also overpredicts for most of the stage, only approaching the experimental response over brief intervals. This repeated left-branch bias suggests that once the assembly has adapted to the reversed loading direction, the measured stress ratio is reduced more strongly than would be expected from the magnitudes of fabric and force anisotropy alone. In other words, under leftward shearing, the internal anisotropic structure remains present, but its efficiency in generating macroscopic stress appears lower than predicted by the SFF relation.

During cycle 1, the theory performs best early in shear-right-forward (SRF), where it follows the initial steady regime and subsequent gradual increase reasonably well. However, once the experimental q/p begins to decrease through a series of fluctuations, the theoretical response shifts into clear overprediction. Even so, the full theoretical expression remains closer to the experimental response than the simplified relation, consistent with the behavior observed in the 122 lb loose assembly. During shear-right-reverse (SRR), the theory again overestimates q/p, but the deviation is smaller while the experimental response continues to decrease. Once q/p settles into a more stable low-magnitude regime, the mismatch becomes more apparent, with only brief intervals of good agreement near the end of the stage. This suggests that the theory captures the onset of anisotropy mobilization more effectively than the later-stage weakened response that follows reversal.

In cycle 2, the same broad pattern persists but with less sustained agreement. The theory overestimates the experimental response throughout SRF, just as it does throughout SLF. Relative to the 122 lb loose assembly, the main difference is that the 82 lb loose system exhibits fewer portions of partial agreement during the shear-

right stages. Under higher confinement, the theory still tracked the experimental response reasonably well during part of SRF and improved later in SRR, whereas under lower confinement, the deviation becomes established earlier and persists more continuously. This indicates that reduced confinement weakens the extent to which the measured anisotropies translate into macroscopic stress, even when the broad loop shape remains similar.

By cycle 3, the separation between theory and experiment becomes even more pronounced. Both SRF and SLF lie well above the experimental q/p, with only very limited intervals of overlap, primarily near the end of SLF. Compared with the 122 lb loose assembly, the later-cycle divergence is therefore stronger and more persistent under lower confinement, suggesting that repeated cycling progressively reduces the stress-carrying efficiency of the anisotropic contact structure. Thus, although the force and fabric anisotropies remain sufficient to reproduce the overall loop form, they increasingly overstate the amount of bulk shear resistance that the assembly can actually mobilize.

Overall, the 82 lb loose assembly retains the same qualitative stress-force-fabric trends observed in the 122 lb loose case: the full expression outperforms the simplified relation, the experimental invariant stress ratio continues to track the normal-force anisotropy, and the largest discrepancies remain concentrated in the shear-left stages. The principal difference is that, under lower confinement, intervals of agreement are shorter and the later-cycle overprediction is more pronounced. Thus, while the underlying stress–force–fabric coupling remains intact, the anisotropic contact structure becomes less effective at converting internal directional organization into macroscopic shear resistance.

Force Transmission The SFF analysis evaluated how grain-scale anisotropy translates into bulk shear resistance. Next, we examine the underlying contact force distributions using probability density functions (PDFs) for the normalized normal and tangential forces, and friction mobilization. These distributions reveal how load is shared between weak and strong contacts and how that force-transmission structure evolves under cyclic loading.

Figure 4.90 shows the per-cycle PDFs of the **normalized normal force**, $f_n / \langle f_n \rangle$, with each panel corresponding to a loading cycle and all shear stages included for comparison.

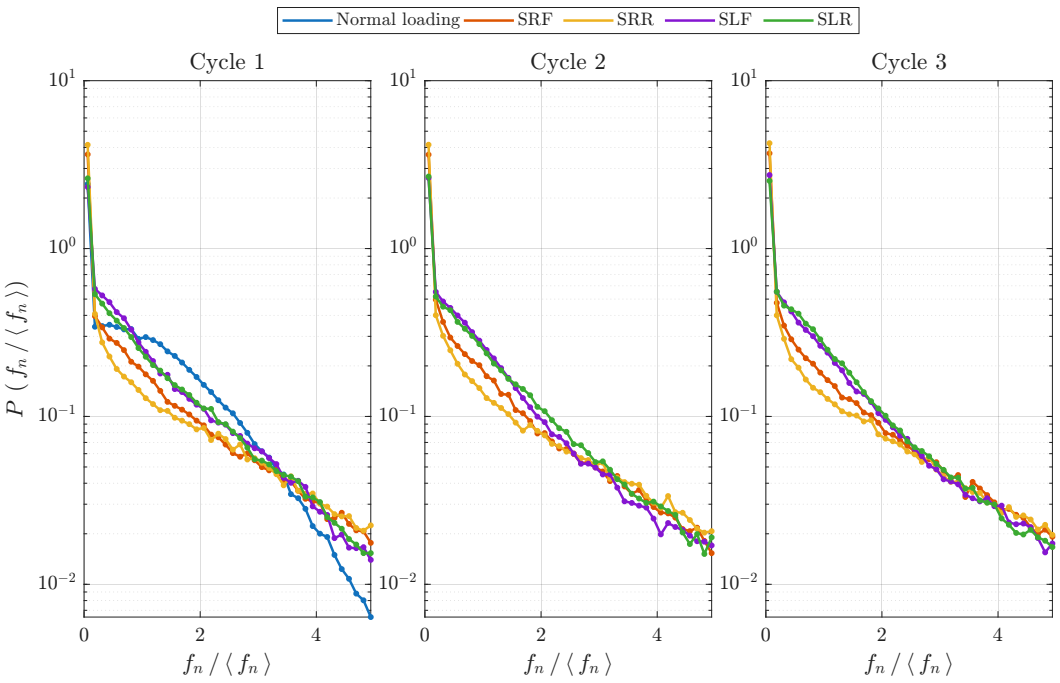


Figure 4.90: Per-cycle evolution of the probability density function (PDF) of the normalized normal contact force, $f_n\ /\langle f_n\rangle$, for the loose assembly ($\sigma_n = -29.6$ kPa). Each panel shows one loading cycle, with all stages on a semi-log scale.

As in the 122 lb case, the normal force PDFs preserve the same broad two-regime structure: an initial steep decay followed by a more gradual tail response. This indicates that the assembly still comprises a large population of common, low-force contacts and a smaller population of stronger, load-bearing contacts. However, under lower confinement, the stage responses are more tightly grouped, with earlier convergences and weaker systematic ordering across the strong-force tail.

The normal force PDFs also remain stage-dependent across all cycles, but the 82 lb loose assembly exhibits noticeably less divergence among stages than the 122 lb case. In cycle 1, after the initial steep decay, the shear-right stages no longer separate strongly from the remaining stages and all responses converge earlier, around $f_n\ /\langle f_n\rangle \approx 3.5$. Under higher confinement, these stage distinctions persisted to larger normalized forces. This earlier convergence suggests that reduced confinement limits the persistence of highly concentrated f_n chains, thereby making the strongest contacts more statistically similar across loading stages.

At intermediate-to-high forces, the 82 lb assembly still develops directional grouping, with shear-right stages tending toward higher PDF values and shear-left stages toward lower values, indicating that loading direction continues to influence the strongest normal force contacts, although less sharply than in the 122 lb assembly.

The normal loading stage is also more variable under lower confinement, briefly dominating the moderate-force regime before decaying to the lowest tail probabilities. This suggests that the pre-sheared loose contact network contains a broader spread of moderate contacts, but lacks the sustained high-force pathways that develop during shear.

Cycles 2 and 3 reinforce the same trend. Stage responses remain more tightly grouped, with the shear-left stages frequently overlapping and the high-force tails showing less separation than under higher confinement. Unlike the 122 lb assembly, there is no consistent ordering of the stages, with some beginning with the highest PDFs and others ending with the lowest. Thus, reducing confinement weakens the hierarchy of f_n transmission, replacing strongly differentiated stage responses with a more blended, adaptive contact-force distribution.

Figure 4.91 shows the per-cycle PDFs of the **normalized tangential force**, $f_t\,/\langle f_n\rangle$, again organized by cycle with all shear stages included in each panel.

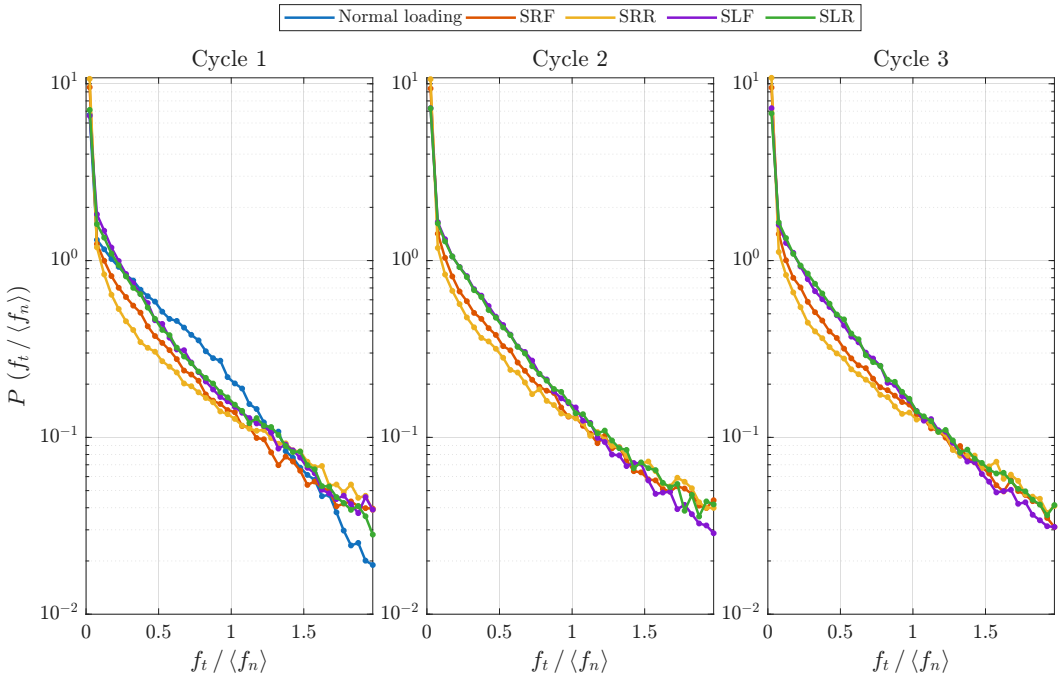


Figure 4.91: Per-cycle evolution of the probability density function (PDF) of the normalized tangential contact force, $f_t\,/\langle f_n\rangle$, for the loose assembly ($\sigma_n = -29.6$ kPa). Each panel shows one loading cycle, with all stages on a semi-log scale.

The tangential force PDFs show a similar but even stronger tendency toward convergence. In cycle 1, the normal loading stage again exhibits the most variable behavior, dominating much of the force range before ending with the lowest tail probabilities. Beyond the initial decay regime, the shear-left stages remain tightly grouped, while

the shear-right stages are more distinct, but the overall spread is narrower than in the 122 lb loose experiment. As in the higher confined case, all stages converge and remain closely grouped in the larger-force regime.

Cycles 2 and 3 continue this behavior. The same bottleneck structure observed in the 122 lb assembly is retained, with stages beginning separately, converging over an intermediate force range, and diverging again at the tail. However, in the 82 lb assembly, the converged region occurs later and is more sustained. This indicates that under lower confinement, tangential-force mobilization becomes more uniform across stages over a wider portion of the force spectrum.

At the highest normalized tangential forces, some stage-specific deviations remain, particularly fluctuations in shear-right-reverse (SRR) and occasional instability in shear-left-reverse (SLR). Nevertheless, unlike the 122 lb assembly, no persistent stage ordering develops across cycles, again suggesting that reduced confinement weakens the preferential concentration of frictional resistance into specific loading branches and instead distributes tangential force transmission more broadly across the contact network.

Figure 4.92 shows the per-cycle PDFs of the **mobilized friction**, $S = |f_t|/\mu f_n$, with each panel corresponding to a cycle and all shear stages included for comparison.

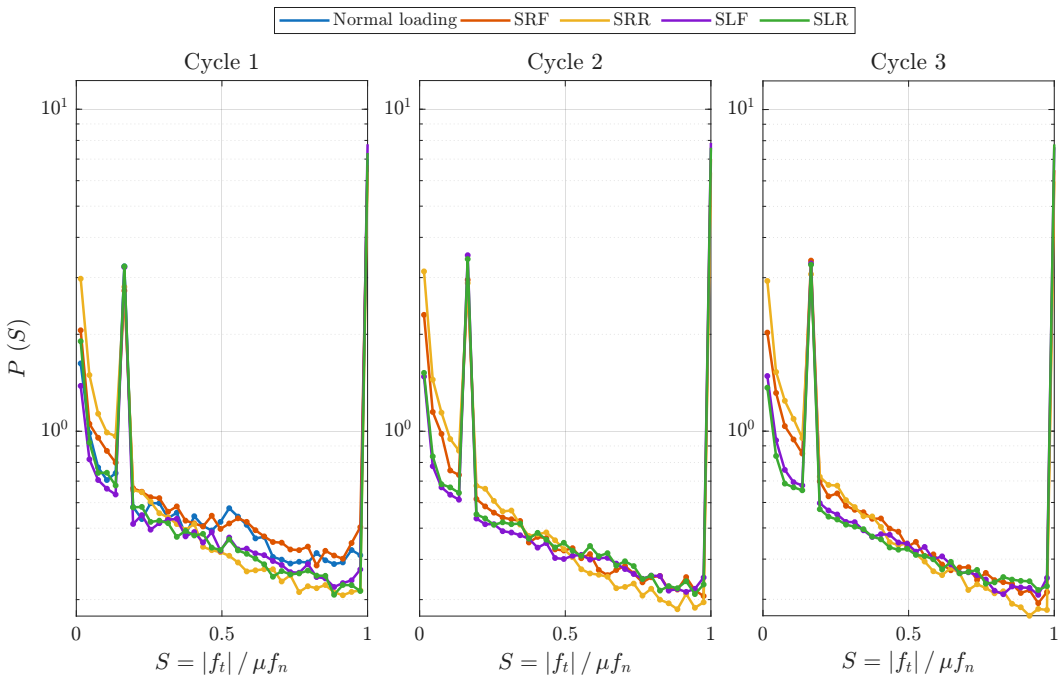


Figure 4.92: Per cycle evolution of the probability density function (PDF) of the mobilized friction, $S = |f_t|/\mu f_n$, for the loose assembly ($\sigma_n = -29.6$ kPa). Each panel shows one loading cycle, with all stages on a semi-log scale. Here, μ is the interparticle friction coefficient, and S indicates the proximity of a contact to sliding (Coulomb failure criterion).

The friction mobilization PDFs retain the same characteristic structure observed in the 122 lb loose assembly: an initial gradual decay, a pronounced increase–decrease fluctuation, a subsequent near-linear decay, and a sharp rise as contacts approach the failure envelope at $S = 1$. The persistence of this pattern across both confinement levels indicates that the basic mechanisms of frictional activation and near-slip contact populations remain robust.

The main differences lie in the relative grouping and decay rates. In cycle 1, stage responses become more distinct during the early decay regime, but remain tightly grouped after the fluctuation until larger S values. In cycles 2 and 3, the shear-right stages begin at substantially higher PDF values than in the 122 lb assembly, indicating a larger population of lightly mobilized right-shear contacts under reduced confinement. After the fluctuation, the stage responses remain more tightly grouped overall, though SRR develops downward deviations at high mobilization levels.

Another important trend is that the final linear decay regime steepens with cycle count in the 82 lb assembly, whereas it remained more consistent under higher confinement. This suggests that repeated cycling progressively reduces the population

of moderately mobilized contacts under lower confinement, leaving a sharper separation between low-mobilization contacts and those nearing slip. In addition, the peak of the pronounced fluctuation is lower than in the 122 lb assembly, especially in cycle 3, indicating weaker transient frictional mobilization as cycling progresses.

Overall, the PDF results show that reducing confinement does not eliminate the characteristic force-transmission signatures of the loose assembly, but it does cause the stage responses to become more tightly grouped and statistically similar. Strong-force tails converge earlier, tangential force distributions remain grouped over broader force ranges, and friction mobilization responses become more uniform after transient fluctuations. Relative to the 122 lb loose assembly, the 82 lb system therefore transmits load through a less hierarchical and more distributed contact force network. Strong contacts and highly mobilized frictional states still emerge, but they are less persistently tied to specific shear stages.

4.5.2.4 Grain-Scale Response Summary

The grain-scale response of the three-cycle, loosely packed granular assembly under $\sigma_n = -29.6$ kPa $\approx$ 82 lb (37.2 kg) exhibits a load-bearing network that remains active throughout cyclic loading, but reorganizes in a more distributed, adaptive, and mechanically coordinated manner than in the 122 lb loose assembly. Compared with the higher-confined loose case, reducing the applied normal load weakens force concentration and directional strengthening, yet promotes smoother structural evolution, stronger overlap among grain-scale measures, and greater persistence of contact network memory across cycles.

The contact network remains comparatively stable, with the coordination number evolving within a relatively narrow range and with fewer extreme fluctuations than in the 122 lb loose assembly. This indicates that cyclic loading does not substantially alter the total number of contacts but instead redistributes connectivity via a more balanced exchange between contact formation and loss. Unlike the higher confined case, where restructuring was concentrated in forward shearing, the most active reorganization now occurs after shear reversal, particularly during shear-left stages. Thus, lowering confinement shifts the dominant contact adjustment to later portions of the loading cycle, where the system rebuilds connectivity as it adapts to the reversed loading direction.

The force chain network reflects this same balance between persistence and redistribution. Force chains remain present throughout the loading history, but their structural measures evolve within narrower ranges than in the 122 lb case. Chain density and total chain length still fluctuate with loading stage, although the changes are less abrupt and more tightly grouped across cycles. This indicates that repeated shearing does not strongly destroy the force chain skeleton but instead modifies it through incremental shortening, re-linking, and redistribution of load-bearing paths. Relative to the higher-confined case, the 82 lb loose assembly therefore carries stress through smaller but more persistent force chain structures that reorganize without large-scale collapse.

The strong force network also remains robust. Roughly one-third to nearly one-half of the grains continue to belong to the strong network throughout cyclic loading, demonstrating that a substantial fraction of the assembly persistently carries above-average forces. However, only a portion of those strong grains organize into detectable force chains, and this participation becomes increasingly dependent on the loading stage. Compared with the 122 lb loose assembly, the lower confined case shows greater fluctuation in the strong network participation but a narrower range in chain participation. This indicates that reducing confinement does not remove strong contact, but instead changes how selectively those contacts assemble into coherent stress-transmitting chains. As a result, load-bearing responsibility is shared more broadly, even when the chain organization remains intermittent.

Directional measure further shows that anisotropy is retained but expressed differently under lower confinement. The contact fabric and the normal and tangential force anisotropies all remain measurable throughout the loading history, confirming that cyclic shearing continues to organize the internal structure into preferred directions. However, unlike the 122 lb case, the anisotropy magnitudes are generally weaker, their cyclic loops are flatter and more compact, and the different anisotropy magnitudes overlap more strongly after the first cycle. Hence, lowering the confinement reduces sustained directional strengthening while promoting a more synchronized evolution of the contact and force networks. Therefore, structural memory persists but in a weaker and more coordinated manner.

The micro-macro comparisons support this interpretation. The bulk invariant stress ratio continues to resemble the normal force anisotropy, and the stress-force-fabric relation still reproduces the broad cyclic loop structure. However, the periods of close agreement shorten, and later-cycle overprediction becomes more pronounced

than in the 122 lb loose assembly. Thus, the same internal anisotropic structure generates less macroscopic shear resistance under lower confinement. Put simply, the contact and force networks remain directionally organized, but become less efficient at converting that organization into bulk strength.

The force transmission PDFs reinforce these conclusions. The assembly retains the same weak- and strong-contact partition observed under higher confinement, although the stage responses become more tightly grouped and the strong-force tails converge earlier. The tangential force distributions remain clustered over broader force ranges, while the friction mobilization responses become more uniform after transient fluctuations. Together, these trends indicate that stress is transmitted through a less hierarchical, more statistically similar contact force network, in which strong contacts still emerge but are less consistently associated with specific loading stages.

Overall, the 82 lb loose assembly demonstrates that reducing confinement does not eliminate the grain-scale structures responsible for shear resistance. The contact network, force chain, strong network, and anisotropic organization all persist, but they evolve toward a more distributed and mechanically coordinated state. Compared with the 122 lb loose assembly, stress transmission becomes less concentrated, less directionally amplified, and less efficient, but more adaptable and more strongly governed by cumulative cyclic history than by any single loading stage.

4.6 Macroscopic Response Across Experiments: Influence of Packing State and Normal Stress

Taken together, the four three-cycle experiments reveal that both the initial packing state and the applied normal stress influence the macroscopic response of the granular assembly in fundamentally different ways. The most significant distinction arises from the initial packing condition: at a given normal stress, the densely and loosely packed granular assemblies do not simply exhibit different response magnitudes; instead, they deform through qualitatively different mechanisms. In contrast, changing the applied normal stress within a packing state primarily modifies the intensity, stability, and cumulative extent of the response rather than its overall form. Refer to Appendix C for figures showing the response of each macroscopic variable with all combinations of applied normal stress and initial packing state.

The densely packed assemblies exhibit stronger and more persistent mobilization of shear resistance, more clearly separated hysteretic branches, and more cycle-

dependent volumetric and packing evolution. In both dense experiments, the stress ratio response is characterized by pronounced directional asymmetry, broader shear-right branches, and decreasing peak magnitudes as the cycle number increases, indicating progressive weakening of the load-bearing structure under repeated shear. The corresponding volumetric and dilatancy responses also show stronger cycle-to-cycle differentiation, more persistent branch separation, and more clearly sustained dilation-driven behavior. This distinction between dense and loose granular packing states is consistent with established granular mechanics, in which denser packings generally mobilize greater peak shear resistance and stronger dilation under shear [71, 72].

In contrast, the loosely packed granular assemblies exhibit a fundamentally different style of deformation. In both loose experiments, the stress ratio remains near zero over large portions of the loading history, indicating that the assembly generally cannot sustain a strong load-bearing contact structure except over localized intervals. The volumetric strain, void ratio, and dilatancy responses instead reveal highly repeatable, path-retracing behavior, in which much of the loading history is governed by strongly overlapping cycles and shared deformation paths. Unlike the dense assemblies, the loose assemblies do not continue evolving toward increasingly distinct cycle-specific states. Instead, they repeatedly return to previously visited structural and volumetric configurations, with most of the cycle-to-cycle differences concentrated near reversal and other short-lived restructuring events. Both loose experiments also evolve toward more compacted final states, indicating progressive densification under repeated loading. This compaction-dominated conditioning under cyclic shear is also consistent with previous granular shear experiments [82].

These comparisons indicate that the effect of packing state is not simply to strengthen or weaken the response, but to alter the dominant deformation mechanism itself. Dense granular assemblies accommodate cyclic shear through stronger force transmission, more sustained dilation, and more persistent cycle-dependent structural evolution, whereas loose assemblies deform primarily through gradual rearrangement, localized restructuring, and progressive structural consolidation. On this basis, the dense and loose granular assemblies represent mechanically distinct cyclic-shear regimes rather than two different magnitudes of the same response.

The role of the normal stress is more subtle. Within each packing condition, reducing the applied normal stress does not fundamentally change the macroscopic response type, but instead alters the strength and stability of that response. In

the dense assemblies, lower confinement tends to reduce the persistence and separation of the hysteretic response while preserving the same general asymmetric and dilation-associated behavior. In the loose assemblies, lower confinement preserves the same path-retracing and compaction-dominated response but yields more weakly sustained and more irregular stress ratio and dilatancy responses, while also slightly increasing net densification. Thus, the normal stress primarily regulates the expression of the response, whereas the packing state governs its form. This interpretation is also consistent with classical stress-dilatancy and density-dependent strength frameworks for granular materials [71, 72].

One last unifying observation across all four experiments is that the most pronounced restructuring events tend to occur either near shear reversal or at the ends of the forward-shearing stages. These intervals are consistently associated with abrupt changes in stress ratio, volumetric strain, dilatancy, and void ratio, indicating that they correspond to transient reorganization or the internal contact network as the assembly transitions between loading directions or approaches mechanically unstable states. In contrast, the reverse shearing stages are generally smoother, more tightly grouped, and less variable, suggesting that once the assembly has reorganized after shear reversal, deformation is often accommodated by more stable, repeatable grain-scale adjustment.

Overall, the macroscopic response demonstrates that initial packing exerts first-order control over the cyclic deformation mechanism of the granular assembly, while normal stress primarily governs the degree to which that mechanism is mobilized, sustained, and stabilized.

4.7 Grain-Scale Response Across Experiments: Influence of Packing State and Normal Stress

Taken together, the four three-cycle experiments reveal that the initial packing state and applied normal stress govern the grain-scale response in fundamentally different ways. The dominant control is the packing condition. At a given normal stress, the densely and loosely packed granular assemblies do not merely differ in response magnitude; they evolve through distinct internal load-transfer mechanisms. In contrast, changing the applied normal stress within a packing state primarily modifies the intensity, persistence, and efficiency of those mechanisms rather than their essential form. This mirrors the trends observed in the macroscopic response, in which packing state controls the deformation mode, while confinement regulates

its expression. Refer to Appendix D for figures showing the response of most grain-scale metrics with all combinations of applied normal stress and initial packing state.

The densely packed assemblies develop stronger and more coherent internal load-bearing structures. In both dense experiments, the coordination number, force chain measures, and anisotropy metrics indicate that cyclic shear initially mobilizes a well-organized contact and force network capable of efficiently transmitting load. These assemblies sustain longer, more directional force chains, stronger anisotropy in normal- and tangential-force components, and clearer correspondence between grain-scale structure and bulk shear stress. However, repeated cycling progressively weakens this organization. Force anisotropy declines, force transmission becomes more diffuse, and the predictive accuracy of the stress–force–fabric relation deteriorates in later cycles. Thus, repeated loading gradually degrades the coherence and directional effectiveness of the initial, highly efficient internal structure of densely packed granular assemblies.

The loosely packed assemblies exhibit a different mode of grain-scale evolution. In both loose experiments, the contact network remains comparatively stable in magnitude, but the force-bearing structure is less concentrated and more distributed than in the dense cases. Force chains persist throughout the loading history, yet they are shorter, more fragmented, and more strongly reorganized by loading stage. A substantial fraction of grains continue to carry above-average forces, but a smaller portion of those grains assemble into coherent chain-like structures. Likewise, anisotropy remains measurable, yet it is generally weaker, more compact, and less effective at generating macroscopic shear resistance. These results indicate that loose assemblies transmit load through broader, more adaptive contact force networks rather than through dominant, system-spanning directional chains.

Therefore, the contrast between dense and loose states reflects a fundamental difference in how load is carried during cyclic shear, rather than a simple difference in response magnitude. Dense packings begin with a stronger, more coherent internal load-bearing network of contacts and force chains, so cyclic loading primarily weakens the system by gradually breaking down that initially efficient structure. Loose packings, by contrast, begin with a more diffuse network that carries load less selectively, so cyclic loading acts mainly through continued rearrangement, redistribution of forces, and progressive compaction into more stable configurations. Thus, the dense and loose assemblies represent two distinct grain-scale cyclic-shear

regimes: one governed by the degradation of an initially strong structure, and the other by the conditioning of a more distributed structure.

The role of normal stress is more subtle. Within each packing state, reducing confinement does not fundamentally change the type of grain-scale organization that develops; rather, it alters its strength, stability, and persistence. In the dense experiments, lower confinement preserves the same tendency toward organized force transmission, but increases variability, weakens anisotropy, and reduces the sustained correspondence between force chains and shear stress. The internal network remains structured, yet becomes more intermittent and less efficient. In the loose assemblies, lower confinement preserves the same distributed and adaptive character, but further weakens force concentration, tightens the grouping of probability density responses, and shortens the intervals over which anisotropy successfully predicts macroscopic stress. Thus, confinement primarily regulates the degree to which the existing grain-scale mechanism is expressed.

One unifying observation across all four experiments is that the most pronounced grain-scale restructuring occurs near shear reversal or during forward-shearing stages. These intervals are repeatedly associated with abrupt changes in coordination number, force chain organization, anisotropy magnitude, and stress–force–fabric agreement, indicating rapid reconfiguration of the internal load-bearing network as the assembly adapts to changes in the loading direction. In contrast, many reverse-shearing intervals are smoother and more repeatable, suggesting that once the network has reorganized after reversal, subsequent deformation is often accommodated through more stable incremental adjustments.

Overall, the grain-scale response demonstrates that the packing state exerts first-order control over the internal stress-transmission mechanism, while normal stress primarily determines how strongly, efficiently, and persistently that mechanism is mobilized. Dense assemblies favor concentrated, directional, and initially efficient load-bearing structures that degrade with cycling. Loose assemblies favor distributed, adaptive, and history-dependent load-sharing structures that remain active but less effective throughout cyclic shear. These grain-scale distinctions provide the mechanistic foundation for the contrasting macroscopic responses observed across the four experiments.

4.8 Summary

This chapter examined the macroscopic and grain-scale behavior of granular media subjected to three-cycle simple shear, with emphasis on how initial packing state and applied normal stress govern the response. Across all four experiments, the results show that packing state exerts dominant control over the deformation mechanism, while confinement primarily regulates its strength, persistence, and stability. Therefore, densely- and loosely packed assemblies do not behave as stronger and weaker versions of the same material state; rather, they evolve through fundamentally different cyclic-shear modes.

At the macroscopic scale, the densely packed assemblies developed stronger shear resistance, more pronounced hysteresis, clearer directional asymmetry, and more persistent cycle-to-cycle differentiation. Their responses are characterized by sustained dilation-driven behavior and progressively weakening, yet still organized, shear branches. In contrast, the loose assemblies exhibited near-zero stress ratios over large portions of the loading history, strong path retracing in volumetric and void ratio measures, and progressive densification with repeated cycling. Rather than evolving toward increasingly distinct cycle-specific states, the loose assemblies repeatedly returned to previously visited deformation paths, with most restructuring concentrated near shear reversals and other localized transition intervals.

The grain-scale results provide the mechanistic basis for these macroscopic differences. Dense assemblies initially formed stronger, more coherent contact-force skeletons, with longer force chains, greater anisotropy, and clearer coupling between the internal structure and bulk stress. Repeated cycling progressively degraded this organization: force anisotropy weakened, force chains became less coherent, and force transmission grew more diffuse. Thus, the macroscopic weakening observed in dense packings corresponds to the gradual deterioration of an initially efficient load-bearing structure.

Loose assemblies exhibited a different internal response. Their contact networks remained comparatively stable in magnitude, while load transmission occurred through shorter, more fragmented, and more distributed force chains. A substantial fraction of grains continued to carry above-average forces, yet fewer of those grains organized into persistent chain-like structures. Although anisotropy remained measurable, it was generally weaker and less effective at generating macroscopic stress. Thus, repeated cycling conditioned the loose systems primarily through continual rearrangement, redistribution of load, and progressive compaction rather than

through degradation of a previously strong internal skeleton.

The effect of normal stress was more subtle but consistent across packing states. Reducing confinement did not fundamentally change the form of the response, but weakened its expression. In dense assemblies, lower confinement increased variability, reduced the persistence of anisotropy, and weakened the correspondence between grain-scale structure and shear stress. In loose assemblies, lower confinement further suppressed force concentration, tightened the grouping of probability density responses, and reduced the efficiency with which internal anisotropy generated bulk resistance. Hence, confinement controls how strongly the governing grain-scale mechanism is mobilized, while the packing state determines which mechanism it is.

Overall, these findings demonstrate that the macroscopic response of granular media under cyclic shear is rooted in the evolving efficiency of grain-scale stress transmission. Dense systems resist by initially forming strong, directional structures that degrade under repeated loading, whereas loose systems deform through adaptive, less-concentrated networks that reorganize and compact over time. By linking bulk behavior to contact topology, force chain evolution, anisotropy, and stress-force-fabric relations, this chapter established a mechanistic framework for understanding how granular materials accumulate history, weaken, and reorganize under repeated cyclic shear.

Chapter 5

CONCLUSIONS AND FUTURE WORK

5.1 Summary of Research Objectives

This thesis investigated the multiscale behavior of dry, cohesionless granular materials subjected to quasi-static cyclic simple shear loading through laboratory experiments coupled with the Granular Element Method (GEM), a force-inference framework for estimating interparticle contact forces.

The primary objectives of this thesis were:

1. To develop and implement an experimental framework for controlled cyclic simple shear loading by upgrading an existing simple shear apparatus.
2. To determine how grain-scale mechanisms – including force chain evolution, contact network reorganization, and anisotropy development – govern the macroscopic cyclic response of granular materials.
3. To evaluate how repeated loading, packing density, and normal confinement influence the multiscale behavior of granular assemblies under cyclic shear.

Chapters 3 and Chapters 4 demonstrate that these objectives were achieved through combined methodological developments and experimental results. Collectively, these results reveal several important findings regarding the cyclic behavior of granular materials, summarized in the following section.

5.2 Major Findings

Across the baseline one-cycle experiment and the four three-cycle experiments, the results consistently show that the macroscopic response of granular materials under cyclic shear is governed by the evolving organization, efficiency, and persistence of grain-scale force transmission. Although bulk measures such as stress ratio, volumetric strain, and void ratio capture the assembly's external response, the underlying mechanisms are rooted in the development and reorganization of contacts, force chains, and anisotropy under loading.

5.2.1 Cyclic Simple Shear Produces Directional and History-Dependent Response

A primary finding of this thesis is that cyclic simple shear does not retrace a reversible mechanical path. In the one-cycle baseline experiment, forward and reverse shearing stages followed different mechanical paths, resulting in clear asymmetry in the stress ratio, volumetric strain, and packing evolution. The granular assembly did not fully recover its initial stress state or initial void ratio after one cycle, indicating irreversible internal rearrangement and memory of previous loading. However, the net volumetric strain over the full cycle remained nearly zero, demonstrating that substantial grain-scale restructuring can occur without a large overall change in volume. These results highlight the importance of examining internal mechanics rather than relying solely on bulk deformation measures.

5.2.2 Macroscopic Behavior is Governed by Evolving Grain-scale Force Transmission

The grain-scale analyses showed that cyclic memory is stored primarily in the evolving structure of the internal force network rather than in the total number of contacts. Throughout the one-cycle experiment, the coordination number remained relatively stable, indicating that the contact network retained a similar overall level of connectivity. In contrast, the force chain network underwent continuous path-dependent reorganization. Forward shearing promoted longer, more coherent, and more persistent load-bearing force chains, whereas shear reversals caused these structures to weaken, dissolve, and reform in new directions. These observations indicate that granular memory is encoded in how the interparticle contacts organize to transmit load.

5.2.3 Packing State Controls the Dominant Cyclic Deformation Mechanism

Across the three-cycle experiments, the initial packing state was found to exert dominant control over the cyclic deformation mechanism.

Densely packed assemblies exhibited greater shear resistance, more pronounced hysteresis, greater anisotropy, and longer force chains that efficiently transmitted load across the granular assembly. However, repeated cycling progressively weakened this initially efficient structure. Force chains became less coherent, anisotropy declined, and the correspondence between grain-scale structure and bulk stress weakened with increasing cycles. Thus, dense systems resisted loading through a strong, directional internal force chain network that gradually degraded under

repeated shear.

Loosely packed assemblies exhibited a fundamentally different response. Rather than forming dominant system-spanning load-bearing force chains, loose packings transmitted load through shorter, more fragmented, and more distributed force networks. Their macroscopic stress ratio remained near zero over substantial portions of the loading history, while volumetric and packing measures showed strong path retracing and progressive densification. Instead of degrading from an initially strong structure, loose systems evolved primarily through continued rearrangement, load redistribution, and conditioning toward more stable packed configurations. These findings demonstrate that dense and loose granular assemblies exhibit fundamentally different cyclic responses, rather than stronger and weaker forms of the same response.

Unlike packing density, the applied normal stress influenced the mechanical response more subtly. Within a given packing state, reducing confinement did not fundamentally change the governing deformation mechanism. Instead, it weakened the expression of that mechanism by reducing force concentration, increasing variability, shortening the persistence of anisotropic structures, and weakening the relationship between internal force organization and bulk shear resistance. In this sense, packing state controlled the form of the cyclic response, whereas normal stress controlled how strongly and how stably that response was mobilized.

5.2.4 Force Chains and Anisotropy as Effective Internal Descriptors

Another important finding is that anisotropy provides a key link between grain-scale structure and macroscopic resistance. In the experiments presented here, force anisotropy consistently exceeded fabric anisotropy, indicating that the directional distribution of contact forces played a larger role than contact geometry alone in governing shear strength. During forward shearing, anisotropy became stronger and more aligned with the principal stress directions, coinciding with greater shear resistance. In contrast, shear reversals caused the anisotropy and the principal stress axes to temporarily misalign, reflecting the rapid restructuring of the internal force chain network. These transitional periods were also associated with increased fluctuations in the macroscopic response, demonstrating the sensitivity of the bulk behavior to internal structural changes.

5.2.5 Multiscale Experimental Methods Provide New Insight into Cyclic Behavior

A further major finding of this thesis is that force chain detection coupled with experimentally inferred GEM contact force networks can provide direct, physically meaningful descriptors of cyclic granular behavior. Metrics such as total force chain length, persistence of the force chain network, and strong-force membership were shown to evolve systematically with the loading stage, packing state, and confinement. These measures helped explain macroscopic weakening, directional asymmetry, and cyclic memory in ways that bulk quantities alone could not. While force chain algorithms are common in DEM studies and photoelastic experiments, their application here to experimentally inferred force networks under cyclic simple shear demonstrates the broader utility of combining GEM with force chain and contact network analyses.

5.2.6 Summary

Overall, the results of this thesis show that the evolving efficiency of grain-scale stress transmission controls the cyclic behavior of granular materials. Densely packed assemblies resist through initially strong directional structures that deteriorate under repeated loading, whereas loosely packed systems deform through adaptive, distributed networks that reorganize and compact over time. By linking bulk response to contact connectivity, force chain evolution, anisotropy, and contact force heterogeneity, this work provides a mechanistic framework for understanding how granular materials accumulate history, weaken, and reorganize under repeated cyclic shear.

5.3 Thesis Contributions

The principal contributions of this thesis are summarized below.

5.3.1 Development of a Cyclic Simple Shear Framework

An experimental framework was developed for conducting controlled quasi-static simple shear tests on two-dimensional granular assemblies. Specifically, the existing apparatus was upgraded with a microcontroller for programmable motion control, the image acquisition framework was adapted to handle large volumes of high-resolution images, and new data processing methods were developed to quantify macroscopic and grain-scale responses.

5.3.2 Application of GEM to Cyclic Loading

The Granular Element Method (GEM) was applied to cyclic simple shear experiments to estimate the evolution of interparticle contact forces over repeated loading cycles. This extends the use of GEM beyond monotonic simple shear studies and demonstrates its effectiveness in cyclic granular mechanics.

5.3.3 Experimental Force Chain Characterization from Inferred Contact Forces

The experimentally inferred contact force networks from GEM were used to characterize the evolution of force chain structure and contact network organization under cyclic simple shear loading. These analyses quantified metrics such as total force chain length, persistence of the force chain network, and strong-force membership.

In contrast, force chain studies are performed more commonly using simulated datasets, particularly DEM-generated assemblies or recent machine-learning-based synthetic data [74, 83]. Although force chains have also been characterized using photoelasticity experiments, these methods remain constrained by requirements on particle materials and simplified grain geometries [84, 85]. The present work demonstrates that GEM provides a practical experimental pathway for quantitative force chain analysis in two-dimensional, opaque granular materials with arbitrary grain shapes.

5.3.4 Multiscale Linkage Between Internal Structure and Bulk Response

This thesis established direct relationships between the macroscopic cyclic response and grain-scale quantities, including coordination number, force chain organization, anisotropy, and contact force distributions. These results help explain how internal structural evolution governs the response of the bulk granular assembly.

5.3.5 Multiscale Insight into the Role of Packing State and Confinement

This thesis provided multiscale insights into how the initial packing state and the applied normal stress influence the mechanical behavior under cyclic simple shear. The results showed that the packing state primarily governs the form of the response, whereas the normal stress mainly regulates its strength, persistence, and stability. It was also shown that densely and loosely packed granular assemblies evolve through different internal load-transfer behaviors under repeated shear.

5.3.6 Creation of a Multiscale Experimental Dataset

This thesis produced a combined macroscopic and grain-scale experimental dataset for granular materials subjected to cyclic simple shear loading. The dataset includes bulk response measures, inferred contact forces, force chain metrics, anisotropy measures, and contact network statistics across multiple packing states and confinement levels. These results provide a useful reference for future validation of DEM, LS-DEM, constitutive, and data-driven models.

5.4 Limitations on the Present Study

While the results of this thesis provide useful insight into the cyclic behavior of granular materials, several limitations of the present experimental framework should be acknowledged.

5.4.1 Two-Dimensional Experimental Representation

The current apparatus is limited to two-dimensional analog granular assemblies. Two-dimensional systems are especially valuable for direct visualization, image-based tracking, and grain-scale force inference, making them well-suited for controlled multiscale experiments. However, the present results arise from a planar system and therefore do not fully capture the out-of-plane constraints, contact topologies, and kinematic freedoms present in natural three-dimensional granular materials.

It should be noted that this limitation applies to the current experimental configuration rather than to the Granular Element Method itself, which has been extended to three-dimensional systems in recent work [53].

5.4.2 Data Acquisition and Tracking Demands

Because the granular assembly is composed of many discrete particles, each grain requires its own area of interest (AOI) for the DIC analysis. Under cyclic shear, grains undergo rapid rearrangements, making fully automated frame-to-frame tracking difficult. As a result, many grains must be tracked manually to achieve successful correlation between deformed images.

For experiments involving hundreds of grains over large image sequences, this process becomes time-intensive and generates substantial data volumes. The resulting full-field displacement and strain data must then be processed further to recover the inputs required for GEM. Consequently, the current workflow requires significant user effort, processing time, and computational resources, motivating future

improvements in automated tracking and parallelized post-processing.

5.4.3 Motion Control Precision

The experimental apparatus uses a velocity-based control system rather than a closed-loop position control system. While this setup is sufficient for conducting quasi-static cyclic simple shear tests, it limits the precision with which repeated displacement amplitudes can be imposed over many cycles.

Cyclic loading was applied using timing-based motion control (e.g., shear right for a prescribed duration). This approach does not fully account for mechanical effects such as backlash, compliance, or minor drive losses that can accumulate during repeated cycling. As a result, the imposed shear range varied slightly with increasing cycle number.

5.4.4 Finite Experimental Scope

The present study focused on a baseline one-cycle test and a set of three-cycle experiments at selected packing states and confinement levels. While this scope was sufficient to identify clear trends in cyclic response, a larger parameter space involving many more cycles, wider cyclic shear amplitudes, varied particle shapes, and a larger range of normal confinement levels would further strengthen the generality of the conclusions.

5.4.5 Force Inference Uncertainty

As with any inverse method, GEM relies on measured kinematic and geometric inputs. Uncertainty in image acquisition, particle tracking, strain measurements, or contact detection can propagate into the inferred contact force estimates. Although care was taken to ensure that inferred force solutions were consistent with measured geometry, contact locations, and governing mechanical constraints, these uncertainties should be considered when interpreting local force quantities.

5.4.6 Summary

These limitations do not diminish the value of the present findings, but rather define the current boundaries of the experimental framework. At the same time, they identify clear opportunities for future improvements in experimental apparatus control, automation, computational efficiency, and experimental realism.

5.5 Future Work

The remainder of this thesis identifies several opportunities to extend the present experimental framework and deepen the understanding of granular materials under cyclic loading.

5.5.1 Improved Motion Control

Although the existing experimental apparatus uses a closed-loop velocity controller, the controller should be upgraded to include closed-loop position control as well. This would improve repeatability across experiments by precisely controlling the shear strain rate and the prescribed displacement ranges.

5.5.2 Automated Tracking and Computational Efficiency

Further development of automated grain-tracking methods would significantly reduce the manual effort required for large image sequences. In addition, optimizing and parallelizing the post-processing workflow would improve computational efficiency for the DIC and GEM analyses.

5.5.3 Additional Cyclic Loading Experiments with Varying Parameters

Future experiments involving larger cycle counts, wider cyclic shear amplitudes, and different loading paths (e.g., asymmetric loading sequences and varying shear strain rates) would help characterize long-term conditioning, ratcheting, and progressive structural evolution.

5.5.4 Broader Material Conditions

Future studies could vary particle shape, interparticle friction coefficient, and grain stiffness to investigate the effects on the mechanical behavior of cyclically sheared granular media. Adjusting these properties would allow the samples to represent a wider range of granular materials better.

5.5.5 Model Validation and Multi-Scale Modeling

The combined experimental and GEM dataset developed in this thesis provides a foundation for future validation of DEM and LS-DEM models for granular materials under cyclic loading. Once validated at the grain, meso, and macroscales, such physics-based models may be applied with greater confidence to a broader range of granular systems, including vehicle-terrain interaction, repeated-load geotechnical problems, and other relevant engineering applications.

5.5.6 Closing Remark

The continued integration of controlled experiments, force-inference techniques, and computational modeling will advance a more predictive, multiscale understanding of granular materials under loading.

BIBLIOGRAPHY

[1] Jacques Duran. “Introduction”. In: *Sands, Powders, and Grains: An Introduction to the Physics of Granular Materials*. Ed. by Jacques Duran. Partially Ordered Systems. New York, NY: Springer, 2000, pp. 1–18. ISBN: 978-1-4612-0499-2. DOI: 10.1007/978-1-4612-0499-2_1.

[2] Heinrich M. Jaeger, Sidney R. Nagel, and Robert P. Behringer. “Granular solids, liquids, and gases”. In: *Reviews of Modern Physics* 68.4 (Oct. 1, 1996), pp. 1259–1273. DOI: 10.1103/RevModPhys.68.1259.

[3] Japan National Committee on Earthquake Engineering. “Niigata Earthquake, 1964”. In: *Proceedings of the 3rd World Conference on Earthquake Engineering*. Vol. III. New Zealand, 1965, s.78–s.105.

[4] Torsten Wichtmann and Theodor Triantafyllidis. “Behaviour of Granular Soils Under Environmentally Induced Cyclic Loads”. In: *Mechanical Behaviour of Soils Under Environmentally Induced Cyclic Loads*. Ed. by Claudio Di Prisco and David Muir Wood. CISM Courses and Lectures. Vienna: Springer, 2012, pp. 1–136. ISBN: 978-3-7091-1068-3. DOI: 10.1007/978-3-7091-1068-3_1.

[5] Knut H. Andersen. “Bearing capacity under cyclic loading â€” offshore, along the coast, and on land.” In: *Canadian Geotechnical Journal* 46.5 (May 2009), pp. 513–535. ISSN: 0008-3674. DOI: 10.1139/T09-003.

[6] Antonio Recuero et al. “A high-fidelity approach for vehicle mobility simulation: Nonlinear finite element tires operating on granular material”. In: *Journal of Terramechanics* 72 (Aug. 1, 2017), pp. 39–54. ISSN: 0022-4898. DOI: 10.1016/j.jterra.2017.04.002.

[7] NASA/JPL-Caltech. *Spirit Close to "Troy," Sol 1871*. NASA Jet Propulsion Laboratory (JPL). July 16, 2009. URL: https://www.jpl.nasa.gov/images/pia12140-spirit-close-to-troy-sol-1871/ (visited on 05/07/2026).

[8] U.S. Marine Corps. *A U.S. Marine guides the driver of a Humvee through a river in Khowst Province, Afghanistan*. Mar. 28, 2005.

[9] NASA/JPL-Caltech. *NASA's Hibernating Mars Rover May Not Call Home*. NASA Jet Propulsion Laboratory (JPL). Feb. 26, 2010. URL: https://www.jpl.nasa.gov/news/nasas-hibernating-mars-rover-may-not-call-home/.

[10] Minyun Hu et al. “Stress-induced anisotropy in sand under cyclic loading”. In: *Granular Matter* 12.5 (Oct. 1, 2010), pp. 469–476. ISSN: 1434-7636. DOI: 10.1007/s10035-010-0206-7.

[11] Ming Yang et al. “Evolution of granular materials under isochoric cyclic simple shearing”. In: *Physical Review E* 103.3 (Mar. 18, 2021), p. 032904. ISSN: 2470-0045, 2470-0053. DOI: 10.1103/PhysRevE.103.032904.

[12] Karl Terzaghi. “Erdbaumechanik auf BodenphysikalischenGrundlagen”. In: (1925).

[13] John Nelson et al. “Oedometer Testing”. In: *Foundation Engineering for Expansive Soils*. John Wiley & Sons, Ltd, 2015, pp. 127–151. ISBN: 978-1-118-99609-6. DOI: 10.1002/9781118996096.ch6.

[14] Yao Li. “Test Granular Materials Failure Using Bi-Directional Simple Shear Apparatus: A Review”. In: *Applied Sciences* 8.7 (July 2018). Number: 7, p. 1140. ISSN: 2076-3417. DOI: 10.3390/app8071140.

[15] A. Sayao and Y. P. Vaid. “A Critical Assessment of Stress Nonuniformities in Hollow Cylinder Test Specimens”. In: *Soils and Foundations* 31.1 (Mar. 1, 1991), pp. 60–72. ISSN: 0038-0806. DOI: 10.3208/sandf1972.31.60.

[16] Peter Dunlop and J.M. Duncan. “Behavior of Soils in Simple Shear Tests”. In: *7th International Conference on Soil Mechanics and Foundation Engineering*. Mexico: International Society for Soil Mechanics and Geotechnical Engineering (ISSMGE), 1969.

[17] Muniram Budhu. “Nonuniformities imposed by simple shear apparatus”. In: *Canadian Geotechnical Journal* 21.1 (Feb. 1984). DOI: 10.1139/t84-010.

[18] Timo Volz. *Landslide aftermath*. Unsplash. May 18, 2021. URL: https://unsplash.com/photos/brown-and-white-concrete-building-on-hill-PM_TgUfDRvM.

[19] Ryan C. Hurley and José E. Andrade. “Friction in inertial granular flows: competition between dilation and grain-scale dissipation rates”. In: *Granular Matter* 17.3 (June 1, 2015), pp. 287–295. ISSN: 1434-7636. DOI: 10.1007/s10035-015-0564-2.

[20] Colin Thornton. “Quasi-static Deformation”. In: *Granular Dynamics, Contact Mechanics and Particle System Simulations: A DEM study*. Ed. by Colin Thornton. Vol. 24. Particle Technology Series. Cham: Springer International Publishing, 2015, pp. 147–195. ISBN: 978-3-319-18711-2. DOI: 10.1007/978-3-319-18711-2_8.

[21] Osborne Reynolds. “LVII. On the dilatancy of media composed of rigid particles in contact. With experimental illustrations”. In: *The London, Edinburgh, and Dublin Philosophical Magazine and Journal of Science* 20.127 (1885), pp. 469–481. DOI: 10.1080/14786448508627791.

[22] Colin Thornton. “Theoretical Background”. In: *Granular Dynamics, Contact Mechanics and Particle System Simulations: A DEM study*. Ed. by Colin Thornton. Vol. 24. Particle Technology Series. Cham: Springer International

Publishing, 2015, pp. 13–25. ISBN: 978-3-319-18711-2. DOI: 10.1007/978-3-319-18711-2_2.

[23] Marte Gutierrez and Abdalsalam Muftah. “Micro-mechanical Observations of Strain Localization in Granular Soils During Simple Shear Loading”. In: *Bifurcation and Degradation of Geomaterials in the New Millennium*. Ed. by Kam-Tim Chau and Jidong Zhao. Springer Series in Geomechanics and Geoengineering. Cham: Springer International Publishing, 2015, pp. 27–32. ISBN: 978-3-319-13506-9. DOI: 10.1007/978-3-319-13506-9_5.

[24] P. A. Cundall and O. D. L. Strack. “A discrete numerical model for granular assemblies”. In: *Geotechnique* (Mar. 1979). DOI: 10.1680/geot.1979.29.1.47.

[25] Masanobu Oda and Junichi Konishi. “Microscopic Deformation Mechanism of Granular Material in Simple Shear”. In: *Soils and Foundations* 14.4 (Dec. 1, 1974), pp. 25–38. ISSN: 0038-0806. DOI: 10.3208/sandf1972.14.4_25.

[26] Matthew R. Kuhn. “Structured deformation in granular materials”. In: *Mechanics of Materials* 31.6 (June 1, 1999), pp. 407–429. ISSN: 0167-6636. DOI: 10.1016/S0167-6636(99)00010-1.

[27] Matthew R Kuhn and Katalin Bagi. “Contact rolling and deformation in granular media”. In: *International Journal of Solids and Structures*. Granular Mechanics 41.21 (Oct. 1, 2004), pp. 5793–5820. ISSN: 0020-7683. DOI: 10.1016/j.ijsolstr.2004.05.066.

[28] Farhang Radjai et al. “Bimodal Character of Stress Transmission in Granular Packings”. In: *Physical Review Letters* 80.1 (Jan. 5, 1998), pp. 61–64. DOI: 10.1103/PhysRevLett.80.61.

[29] Masanobu Oda. “Initial Fabrics and their Relations to Mechanical Properties of Granular Material”. In: *Soils and Foundations* 12.1 (Mar. 1, 1972), pp. 17–36. ISSN: 0038-0806. DOI: 10.3208/sandf1960.12.17.

[30] L. Rothenburg and R. J. Bathurst. “Micromechanical features of granular assemblies with planar elliptical particles”. In: *Geotechnique* 42.1 (Mar. 1992), pp. 79–95. ISSN: 0016-8505. DOI: 10.1680/geot.1992.42.1.79.

[31] Andrew Schofield and Peter Wroth. *Critical state soil mechanics*. Vol. 310. London: McGraw-hill, 1968.

[32] David Muir Wood. *Soil behaviour and critical state soil mechanics*. Cambridge University Press, 1990. 462 pp. ISBN: 978-0-521-33782-3 0-521-33782-8.

[33] A. F. Bower and K. L. Johnson. “Shakedown, Residual Stress and Plastic Flow in Repeated Wheel-Rail Contact”. In: *Rail Quality and Maintenance for Modern Railway Operation: International Conference on Rail Quality and Maintenance for Modern Railway Operation Delft June 1992*. Ed. by J. J. Kalker, D. F. Cannon, and O. Orringer. Dordrecht: Springer Netherlands,

1993, pp. 239–249. ISBN: 978-94-015-8151-6. DOI: 10.1007/978-94-015-8151-6_19.

[34] X. S. Li and Y. F. Dafalias. "Dilatancy for cohesionless soils". In: *Geotechnique* 50.4 (Aug. 1, 2000), pp. 449–460. ISSN: 0016-8505. DOI: 10.1680/geot.2000.50.4.449.

[35] J. Park and J. C. Santamarina. "Sand response to a large number of loading cycles under zero-lateral-strain conditions: evolution of void ratio and small-strain stiffness". In: *Geotechnique* 69.6 (June 2019), pp. 501–513. ISSN: 0016-8505, 1751-7656. DOI: 10.1680/jgeot.17.P.124.

[36] Md Mahmud Sazzad and Kiichi Suzuki. "Effect of Interparticle Friction on the Cyclic Behavior of Granular Materials Using 2D DEM". In: *Journal of Geotechnical and Geoenvironmental Engineering* 137.5 (May 1, 2011), pp. 545–549. ISSN: 1943-5606. DOI: 10.1061/(ASCE)GT.1943-5606.0000441.

[37] Liang Cui et al. "Macro- and micro-mechanics of granular soil in asymmetric cyclic loadings encountered by offshore wind turbine foundations". In: *Granular Matter* 21.3 (July 20, 2019), p. 73. ISSN: 1434-7636. DOI: 10.1007/s10035-019-0924-4.

[38] A. Drescher and G. de Josselin de Jong. "Photoelastic verification of a mechanical model for the flow of a granular material". In: *Journal of the Mechanics and Physics of Solids* 20.5 (Oct. 1, 1972), pp. 337–340. ISSN: 0022-5096. DOI: 10.1016/0022-5096(72)90029-4.

[39] T. S. Majmudar and R. P. Behringer. "Contact force measurements and stress-induced anisotropy in granular materials". In: *Nature* 435.7045 (June 2005), pp. 1079–1082. ISSN: 1476-4687. DOI: 10.1038/nature03805.

[40] José E. Andrade et al. "Granular element method for computational particle mechanics". In: *Computer Methods in Applied Mechanics and Engineering* 241-244 (Oct. 1, 2012), pp. 262–274. ISSN: 0045-7825. DOI: 10.1016/j.cma.2012.06.012.

[41] Farhang Radjai et al. "Force Distributions in Dense Two-Dimensional Granular Systems". In: *Physical Review Letters* 77.2 (July 8, 1996), pp. 274–277. DOI: 10.1103/PhysRevLett.77.274.

[42] Amy L. Rechenmacher. "Grain-scale processes governing shear band initiation and evolution in sands". In: *Journal of the Mechanics and Physics of Solids* 54.1 (Jan. 1, 2006), pp. 22–45. ISSN: 0022-5096. DOI: 10.1016/j.jmps.2005.08.009.

[43] Reid Kawamoto et al. "All you need is shape: Predicting shear banding in sand with LS-DEM". In: *Journal of the Mechanics and Physics of Solids* 111 (Feb. 1, 2018), pp. 375–392. ISSN: 0022-5096. DOI: 10.1016/j.jmps.2017.10.003.

[44] Michael A. Michael A., Jean-José Orteu, and Hubert W. Schreier. "Digital Image Correlation (DIC)". In: *Image Correlation for Shape, Motion and Deformation Measurements: Basic Concepts,Theory and Applications*. Ed. by Hubert Schreier, Jean-José Orteu, and Michael A. Sutton. Boston, MA: Springer US, 2009, pp. 1–37. ISBN: 978-0-387-78747-3. DOI: 10.1007/978-0-387-78747-3_5.

[45] S.A. Hall et al. "Discrete and Continuum analysis of localised deformation in sand using X-ray CT and Volumetric Digital Image Correlation". In: *Geotechnique* 60.5 (May 2010), pp. 315–322. DOI: 10.1680/geot.2010.60.5.315.

[46] V. Cnudde and M. N. Boone. "High-resolution X-ray computed tomography in geosciences: A review of the current technology and applications". In: *Earth-Science Reviews* 123 (Aug. 1, 2013), pp. 1–17. ISSN: 0012-8252. DOI: 10.1016/j.earscirev.2013.04.003.

[47] Carmine Senatore et al. "Design and implementation of a particle image velocimetry method for analysis of running gear–soil interaction". In: *Journal of Terramechanics* 50.5 (Oct. 1, 2013), pp. 311–326. ISSN: 0022-4898. DOI: 10.1016/j.jterra.2013.09.004.

[48] Siavash Amirrahmat et al. "3D Experimental Measurements of Evolution of Force Chains in Natural Silica Sand". In: *Journal of Geotechnical and Geoenvironmental Engineering* 146.5 (May 1, 2020), p. 04020027. ISSN: 1943-5606. DOI: 10.1061/(ASCE)GT.1943-5606.0002241.

[49] Karen E. Daniels, Jonathan E. Kollmer, and James G. Puckett. "Photoelastic force measurements in granular materials". In: *Review of Scientific Instruments* 88.5 (May 26, 2017), p. 051808. ISSN: 0034-6748. DOI: 10.1063/1.4983049.

[50] Aghil Abed Zadeh et al. "Enlightening force chains: a review of photoelasticimetry in granular matter". In: *Granular Matter* 21.4 (Aug. 22, 2019), p. 83. ISSN: 1434-7636. DOI: 10.1007/s10035-019-0942-2.

[51] Ryan Hurley et al. "Extracting inter-particle forces in opaque granular materials: Beyond photoelasticity". In: *Journal of the Mechanics and Physics of Solids* 63 (Feb. 1, 2014), pp. 154–166. ISSN: 0022-5096. DOI: 10.1016/j.jmps.2013.09.013.

[52] R.C. Hurley et al. "Dynamic Inter-Particle Force Inference in Granular Materials: Method and Application". In: *Experimental Mechanics* 56.2 (Feb. 1, 2016), pp. 217–229. ISSN: 1741-2765. DOI: 10.1007/s11340-015-0063-8.

[53] Sohanjit Ghosh, Mohmad M. Thakur, and Ryan C. Hurley. "Quantifying 3D time-resolved kinematics and kinetics during rapid granular compaction, Part I: Quasistatic and dynamic deformation regimes". In: *Journal of the Mechanics and Physics of Solids* 191 (Oct. 1, 2024), p. 105765. ISSN: 0022-5096. DOI: 10.1016/j.jmps.2024.105765.

[54] Liuchi Li, Eloïse Marteau, and José E. Andrade. "Capturing the inter-particle force distribution in granular material using LS-DEM". In: *Granular Matter* 21.3 (May 17, 2019), p. 43. ISSN: 1434-7636. DOI: 10.1007/s10035-019-0893-7.

[55] Eloïse Marteau and José E. Andrade. "An Experimental Study of the Effect of Particle Shape on Force Transmission and Mobilized Strength of Granular Materials". In: *Journal of Applied Mechanics* 88.11 (Nov. 1, 2021), p. 111009. ISSN: 0021-8936, 1528-9036. DOI: 10.1115/1.4051818.

[56] Eloïse Marteau. "Laboratory Studies of Granular Materials Under Shear: From Avalanches to Force Chains". PhD thesis. California Institute of Technology, 2018. DOI: 10.7907/FKM0-P754.

[57] J. Christoffersen, M. M. Mehrabadi, and S. Nemat-Nasser. "A Micromechanical Description of Granular Material Behavior". In: *Journal of Applied Mechanics* 48.2 (June 1, 1981), pp. 339–344. ISSN: 0021-8936. DOI: 10.1115/1.3157619.

[58] CVX Research, Inc. *CVX: Matlab Software for Disciplined Convex Programming, version 2.0*. Aug. 2012. URL: https://cvxr.com/cvx (visited on 04/21/2026).

[59] M. Grant and S. Boyd. "Graph Implementations for Nonsmooth Convex Programs". In: *Recent Advances in Learning and Control*. Ed. by V. Blondel, S. Boyd, and H. Kimura. Lecture Notes in Control and Information Sciences. Springer-Verlag Limited, 2008, pp. 95–110.

[60] José Andrade, Randel Lindemann, and Karl Iagnemma. *XTerramechanics: Integrated Simulations of Planetary Surface Missions*. California Institute of Technology, Apr. 2, 2012.

[61] Keng-Wit Lim et al. "Multiscale characterization and modeling of granular materials through a computational mechanics avatar: a case study with experiment". In: *Acta Geotechnica* 11.2 (Apr. 2016), pp. 243–253. ISSN: 18611125. DOI: 10.1007/s11440-015-0405-9.

[62] M. E. Cates et al. "Jamming, Force Chains, and Fragile Matter". In: *Physical Review Letters* 81.9 (Aug. 31, 1998), pp. 1841–1844. DOI: 10.1103/PhysRevLett.81.1841.

[63] Eloïse Marteau and José E. Andrade. "A novel experimental device for investigating the multiscale behavior of granular materials under shear". In: *Granular Matter* 19.4 (Oct. 7, 2017), p. 77. ISSN: 1434-7636. DOI: 10.1007/s10035-017-0766-x.

[64] Allied Vision. *Prosilica GT 4905 Data Sheet*. July 18, 2022.

[65] Hajxme Matsuoka. "A Microscopic Study on Shear Mechanism of Granular Materials". In: *Soils and Foundations* 14.1 (Mar. 1974), pp. 29–43. ISSN: 00380806. DOI: 10.3208/sandf1972.14.29.

[66] F. Calvetti, G. Combe, and J. Lanier. "Experimental micromechanical analysis of a 2D granular material: relation between structure evolution and loading path". In: *Mechanics of Cohesive-frictional Materials* 2.2 (1997), pp. 121–163. ISSN: 1099-1484. DOI: 10.1002/(SICI)1099-1484(199704)2:2<121::AID-CFM27>3.0.CO;2-2.

[67] Correlated Solutions, Inc. *Vic-2D Software Manual*. Version 6.2.

[68] Correlated Solutions, Inc. *Resolution and Accuracy*. 2020. URL: https://correlated.kayako.com/article/32-resolution-and-accuracy.

[69] Rory Bigger et al. *A Good Practices Guide for Digital Image Correlation*. Edition: 1. International Digital Image Correlation Society, Oct. 24, 2018. DOI: 10.32720/idics/gpg.ed1/print.format.

[70] K. H. Roscoe, A. N. Schofield, and C. P. Wroth. "On The Yielding of Soils". In: *Geotechnique* 8.1 (Mar. 1, 1958), pp. 22–53. ISSN: 0016-8505. DOI: 10.1680/geot.1958.8.1.22.

[71] M. D. Bolton. "The strength and dilatancy of sands". In: *Geotechnique* 36.1 (Mar. 1, 1986), pp. 65–78. ISSN: 0016-8505. DOI: 10.1680/geot.1986.36.1.65.

[72] P. W. Rowe. "The stress-dilatancy relation for static equilibrium of an assembly of particles in contact". In: *Proceedings of the Royal Society of London. A. Mathematical and Physical Sciences* 269.1339 (Oct. 9, 1962), pp. 500–527. ISSN: 0080-4630. DOI: 10.1098/rspa.1962.0193.

[73] J. F. Peters et al. "Characterization of force chains in granular material". In: *Physical Review E* 72.4 (Oct. 21, 2005), p. 041307. DOI: 10.1103/PhysRevE.72.041307.

[74] Omid Ejtehadi et al. "Force-chain finder: A software tool for the recursive detection of force-chains in granular materials via minor principal stress". In: *Computer Physics Communications* 297 (Apr. 1, 2024), p. 109070. ISSN: 0010-4655. DOI: 10.1016/j.cpc.2023.109070.

[75] Chandima N. P. G. Arachchige and Luke A. Prendergast. "Confidence intervals for median absolute deviations". In: *Communications in Statistics - Simulation and Computation* 55.1 (Jan. 2, 2026), pp. 13–22. ISSN: 0361-0918. DOI: 10.1080/03610918.2024.2376198.

[76] C. Thornton and D. J. Barnes. "Computer simulated deformation of compact granular assemblies". In: *Acta Mechanica* 64.1 (Dec. 1, 1986), pp. 45–61. ISSN: 1619-6937. DOI: 10.1007/BF01180097.

[77] L. Rothenburg and R. J. Bathurst. "Analytical study of induced anisotropy in idealized granular materials". In: *Geotechnique* 39.4 (Dec. 1, 1989), pp. 601–614. ISSN: 0016-8505. DOI: 10.1680/geot.1989.39.4.601.

[78] Farhang Radjai and Emilien Azéma. “Shear strength of granular materials”. In: *European Journal of Environmental and Civil Engineering* 13.2 (Feb. 1, 2009). _eprint: https://doi.org/10.1080/19648189.2009.9693100, pp. 203–218. ISSN: 1964-8189. DOI: 10.1080/19648189.2009.9693100.

[79] Daniel M. Mueth, Heinrich M. Jaeger, and Sidney R. Nagel. “Force distribution in a granular medium”. In: *Physical Review E* 57.3 (Mar. 1, 1998), pp. 3164–3169. DOI: 10.1103/PhysRevE.57.3164.

[80] N. P. Kruyt and L. Rothenburg. “A micromechanical study of dilatancy of granular materials”. In: *Journal of the Mechanics and Physics of Solids* 95 (Oct. 1, 2016), pp. 411–427. ISSN: 0022-5096. DOI: 10.1016/j.jmps.2016.01.019.

[81] Wonjun Cha, Junghee Park, and J. Carlos Santamarina. “Long-Term Response of Sand Subjected to Repetitive Simple Shear Loading: Shakedown, Ratcheting, and Terminal Void Ratio”. In: *Journal of Geotechnical and Geoenvironmental Engineering* 149.6 (June 1, 2023), p. 04023028. DOI: 10.1061/JGGEFK.GTENG-10814.

[82] M. Nicolas, P. Duru, and O. Pouliquen. “Compaction of a granular material under cyclic shear”. In: *The European Physical Journal E* 3.4 (Dec. 2000), pp. 309–314. ISSN: 12928941. DOI: 10.1007/s101890070001. arXiv: cond-mat/0006252.

[83] Rituparno Mandal, Corneel Casert, and Peter Sollich. “Robust prediction of force chains in jammed solids using graph neural networks”. In: *Nature Communications* 13 (July 30, 2022), p. 4424. ISSN: 2041-1723. DOI: 10.1038/s41467-022-31732-3.

[84] Qingfa Chen et al. “Automatic extraction method of force chain information and its application in the flow photoelastic experiment of granular matter”. In: *Particuology* 83 (Dec. 1, 2023), pp. 142–155. ISSN: 1674-2001. DOI: 10.1016/j.partic.2023.02.017.

[85] Enlin Long, Qingfa Chen, and Jun Liu. “Characteristics of force chains in the flow of photoelastic particles under a barrier”. In: *Particulate Science and Technology* 42.3 (Apr. 2, 2024), pp. 495–506. ISSN: 0272-6351. DOI: 10.1080/02726351.2023.2263380.

Appendix A

FORCE CHAIN DETECTION ALGORITHM: α SELECTION

An α sweep analysis was performed to determine the best choice of angular tolerance to use in the force chain detection algorithm. This parameter was selected once from the baseline experiment in Chapter 3, and used across all experiments in the thesis for consistency. Four values, $\alpha = 20°, 25°, 30°$, and $35°$, were evaluated using three representative frames from the shear cycle (Figure A.1): (1) a mid-stage frame: Img 176 (about halfway through the forward shear right stage), (2) the strongest force chain frame: Img 210, and (3) a near-reversal shear frame: Img 549 (near the transition from shear left-forward to shear left-reverse). For each frame, we examined the following algorithm outputs: the number of force chains, the mean force chain length, the accepted edge angles, and the degree of a grain (see Tables A.1,A.2,A.3).

The accepted edge angle, θ, represents the angular misalignment between neighboring force vectors. The α parameter defines the maximum allowable misalignment: $\theta \leq \alpha$. Thus, smaller values of θ signify more strongly aligned contacts and more linear force transmission.

The degree of a grain is defined as the number of accepted chain edges attached to it. A degree of 1 is a grain at the end of a force chain, a degree of 2 is a grain that is in the interior of a linear chain, and a degree of 3 is a grain that is a junction between different load paths (also called a branch point). While physically meaningful branching can occur in granular materials, excessive branching introduced only after relaxing the angular tolerance may indicate over-connection of the force chain network [73, 74].

Across all three frames, the results were stable in the sense that increasing α consistently increased the number of accepted edges, the number of force chains, and the mean force chain length. This behavior is expected, since larger α values relax the alignment criterion and allow more contacts to be incorporated into the force chain network. However, the $\alpha = 20°$ and $\alpha = 25°$ values were too restrictive, resulting in underconnected, fragmented force chains. At another extreme, $\alpha = 35°$, created artificial force chain branching in Img 176 and Img 549, whereas no branching was observed at $\alpha = 30°$. Also at $\alpha = 35°$, the maximum accepted edge angle approached the full tolerance angle, indicating the acceptance of increasingly

misaligned contacts into the force chain network.

Based on these observations, $\alpha = 30°$ was selected as the optimal angular tolerance. This value maximizes chain continuity, achieving a tight angular distribution of permitted contacts aligned with the most compressive principal stress vectors.

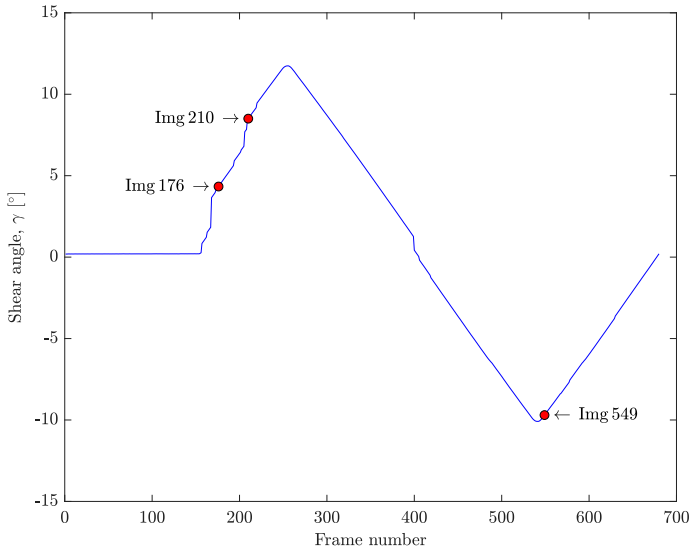


Figure A.1: Three frames analyzed for α selection from the densely-packed, -44.1 [kPa] normally loaded, $N = 1$ cyclic simple shear experiment.

Output	**α= 20°**	**α= 25°**	**α= 30°**	**α= 35°**
No. of FCs	9	14	16	17
Mean FC length	3.33	3.93	4.44	4.82
Accepted edge angles	median = 12.7° max = 19.8°	median = 12.5° max = 23.4°	median = 14.4° max = 29.5°	median = 14.6° max = 34.1°
Accepted edge degree stats	max = 2 grains with deg ≥ 3 : 0	max = 2 grains with ≥ 3 : 0	max = 2 grain with ≥ 3 : 0	max = 3 grain with ≥ 3 : 2

Table A.1: Mid-stage frame (Img 176).

Output	**α= 20°**	**α= 25°**	**α= 30°**	**α= 35°**
No. of FCs	9	14	14	13
Mean FC length	3.33	4.29	5.07	6.15
Accepted edge angles	median = 8.7° max = 19.2°	median = 9.9° max = 24.2°	median = 13.6° max = 28.7°	median = 15.5° max =34.3 °
Accepted edge degree stats	max = 2 grains with deg ≥ 3 : 0	max = 2 grains with ≥ 3 : 0	max = 2 grain with ≥ 3 : 0	max = 2 grain with ≥ 3 : 0

Table A.2: Strongest force chain frame (Img 210).

Output	**α= 20°**	**α= 25°**	**α= 30°**	**α= 35°**
No. of FCs	4	8	13	14
Mean FC length	4.00	4.38	5.00	5.21
Accepted edge angles	median = 6.7° max = 14.4°	median = 7.3° max = 20.6°	median = 12.1° max = 28.1°	median = 12.4° max =33.3 °
Accepted edge degree stats	max = 2 grains with deg ≥ 3 : 0	max = 2 grains with ≥ 3 : 0	max = 2 grain with ≥ 3 : 0	max = 3 grain with ≥ 3 : 1

Table A.3: Near shear-reversal frame (Img 549).

Appendix B

THREE-CYCLE EXPERIMENTS: DILATANCY PER CYCLE

B.1 Densely Packed Granular Assembly

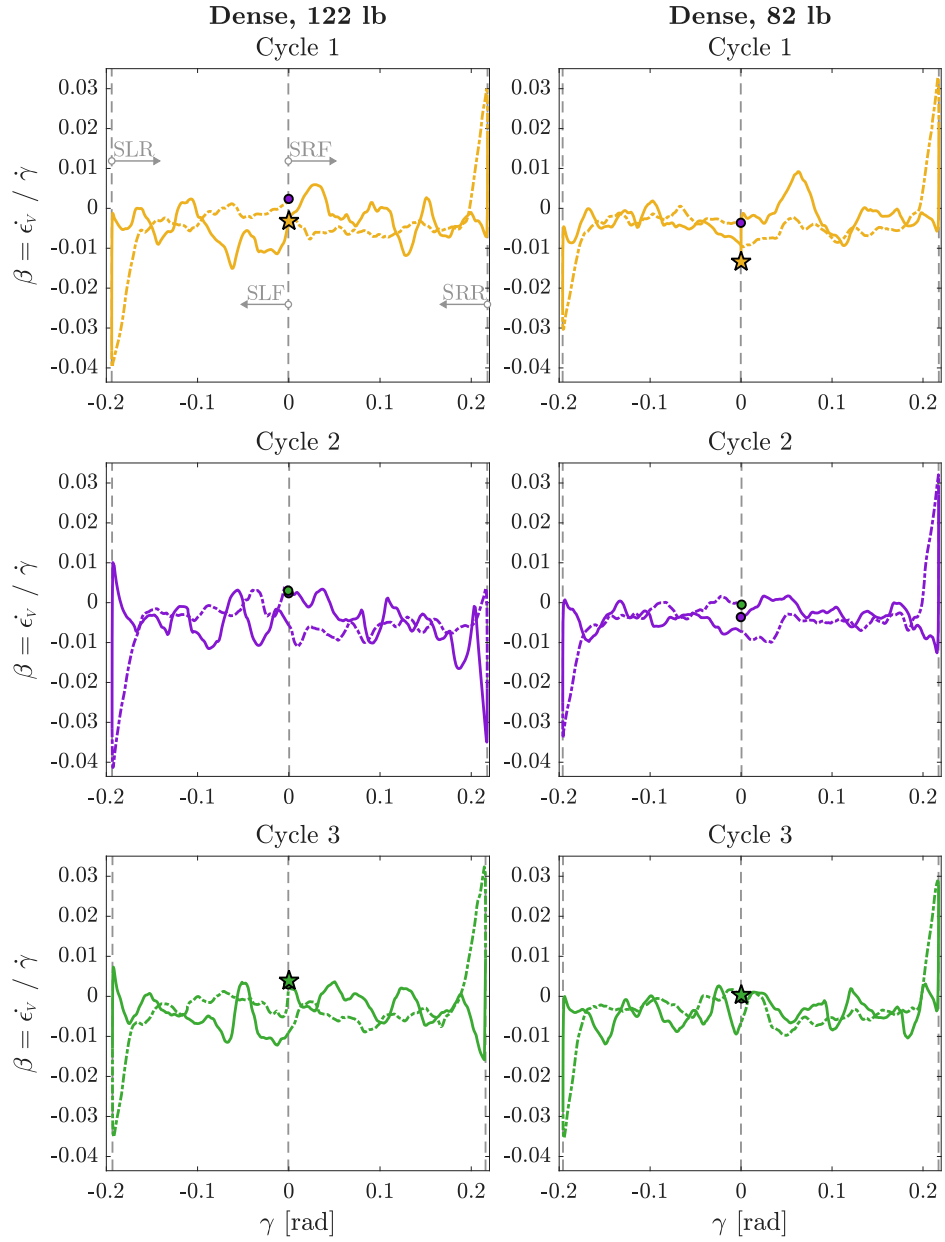


Figure B.1: Dilatancy evolution per cycle for the three-cycle, dense experiments. Left column: higher-confinement ($\sigma_n = -44.1$ kPa $\approx$ 122 lb). Right column: lower-confinement ($\sigma_n = -29.6$ kPa $\approx$ 82 lb). Curve style indicates shearing direction (solid: forward, dash-dotted: reverse), gray dashed lines mark stage transitions, stars mark the start (orange) and end (green) of cyclic loading, and filled circles indicate where cycles connect.

B.2 Loosely Packed Granular Assembly

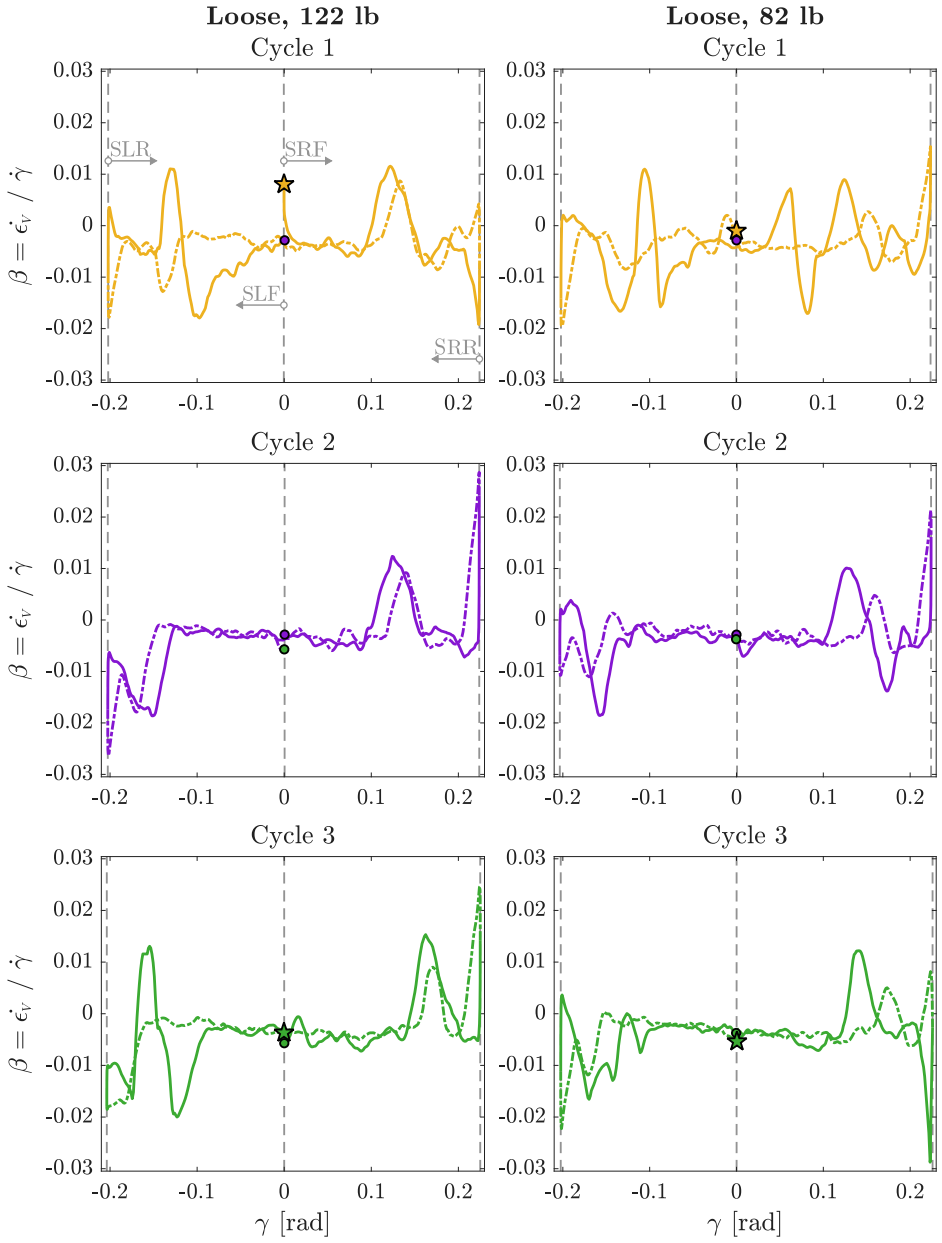


Figure B.2: Dilatancy evolution per cycle for the three-cycle, loose experiments. Left column: higher-confinement ($\sigma_n = -44.1$ kPa $\approx$ 122 lb). Right column: lower-confinement ($\sigma_n = -29.6$ kPa $\approx$ 82 lb). Curve style indicates shearing direction (solid: forward, dash-dotted: reverse), gray dashed lines mark stage transitions, stars mark the start (orange) and end (green) of cyclic loading, and filled circles indicate where cycles connect.

Appendix C

THREE-CYCLE EXPERIMENTS: MACROSCOPIC COMPARISON PLOTS

C.1 Stress Ratio

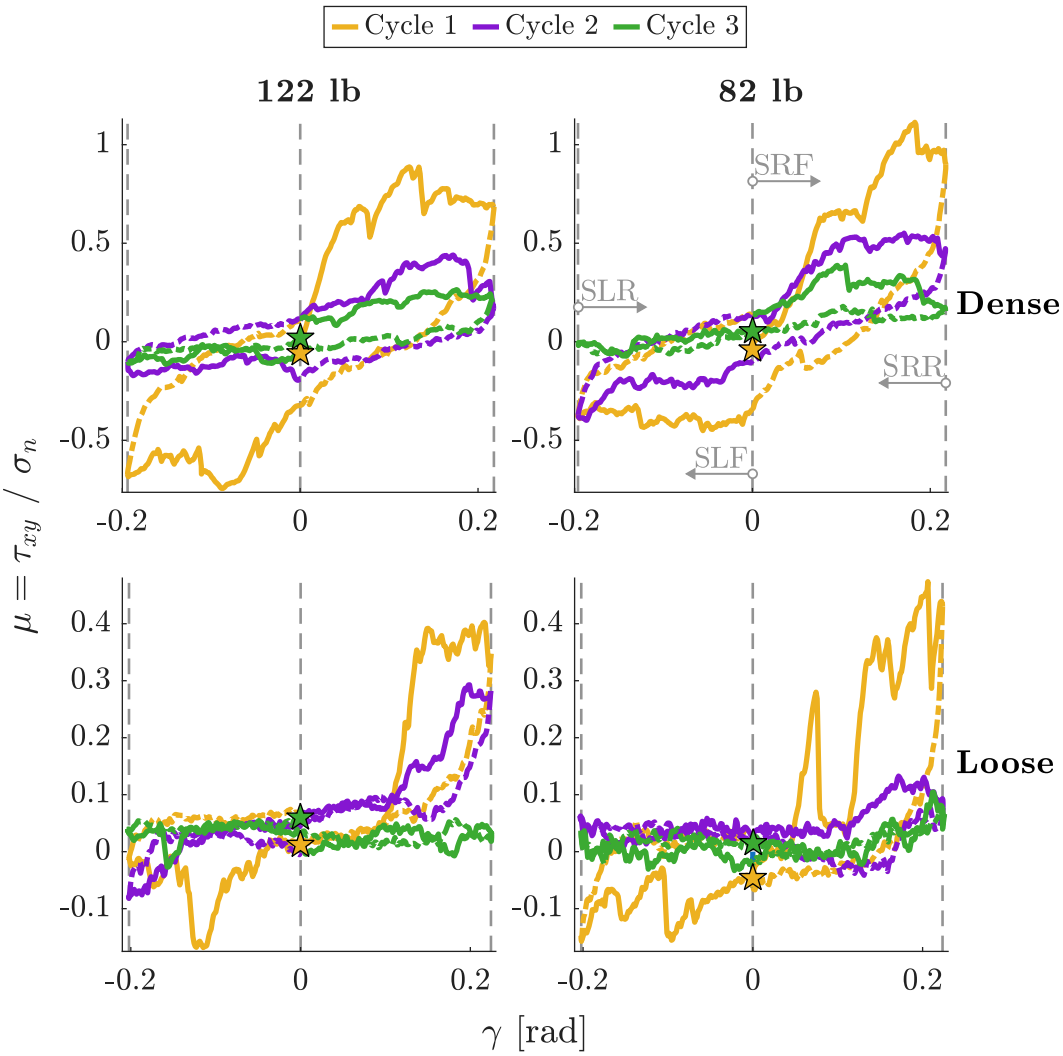


Figure C.1: Stress ratio evolution for the three-cycle experiments. Columns indicate the applied normal stress: (left) $\sigma_n = -44.1$ kPa $\approx$ 122 lb, and (right) $\sigma_n = -29.6$ kPa $\approx$ 82 lb. Rows indicate (top) densely packed and (bottom) loosely packed granular assemblies. Curve style indicates shearing direction (solid: forward, dash-dotted: reverse), gray dashed lines mark stage transitions, and stars mark the start (yellow) and end (green) of cyclic loading.

C.2 Volumetric Strain

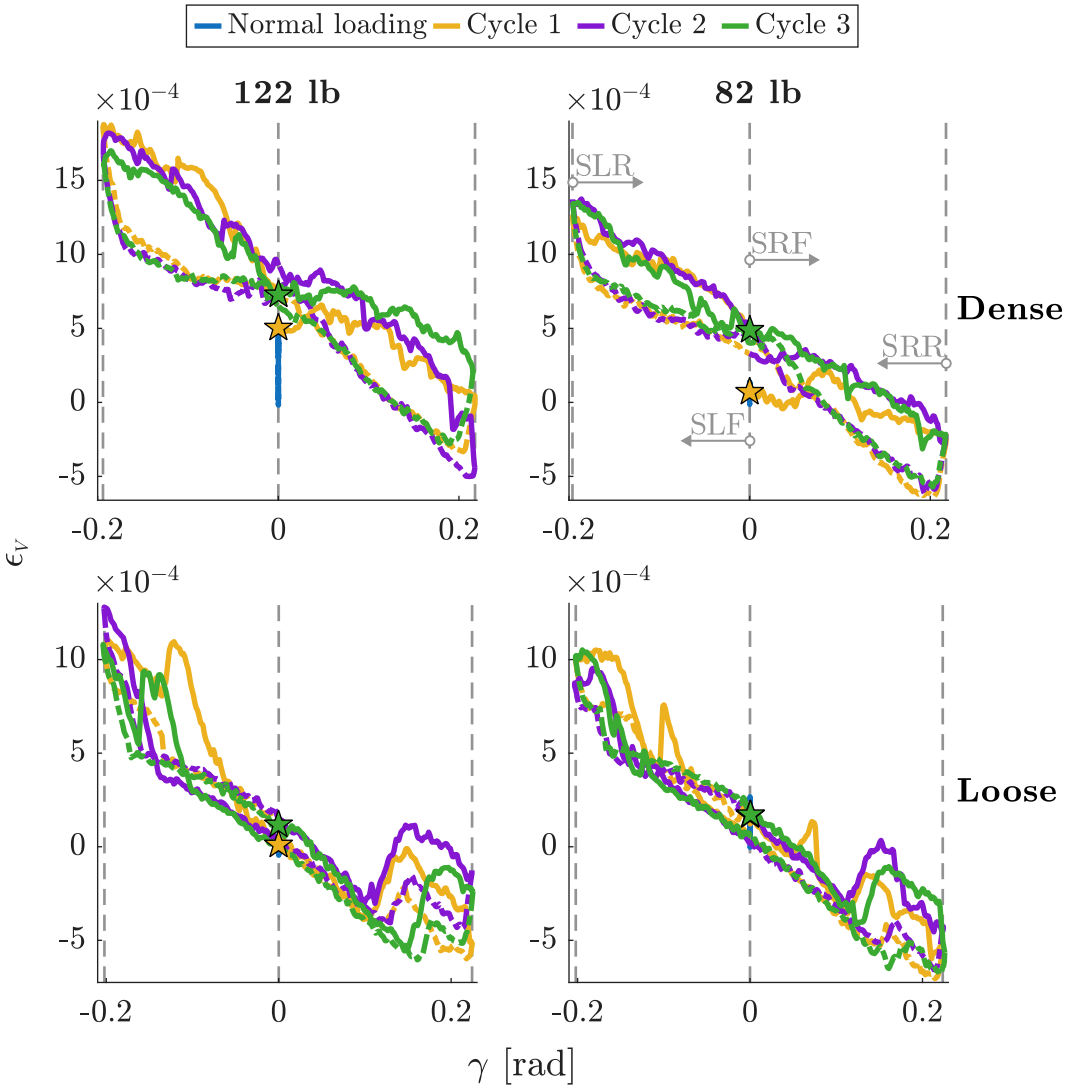


Figure C.2: Volumetric strain evolution for the three-cycle experiments. Columns indicate the applied normal stress: (left) $\sigma_n = -44.1$ kPa $\approx$ 122 lb, and (right) $\sigma_n = -29.6$ kPa $\approx$ 82 lb. Rows indicate (top) densely packed and (bottom) loosely packed granular assemblies. Curve style indicates shearing direction (solid: forward, dash-dotted: reverse), gray dashed lines mark stage transitions, and stars mark the start (yellow) and end (green) of cyclic loading.

C.3 Dilatancy

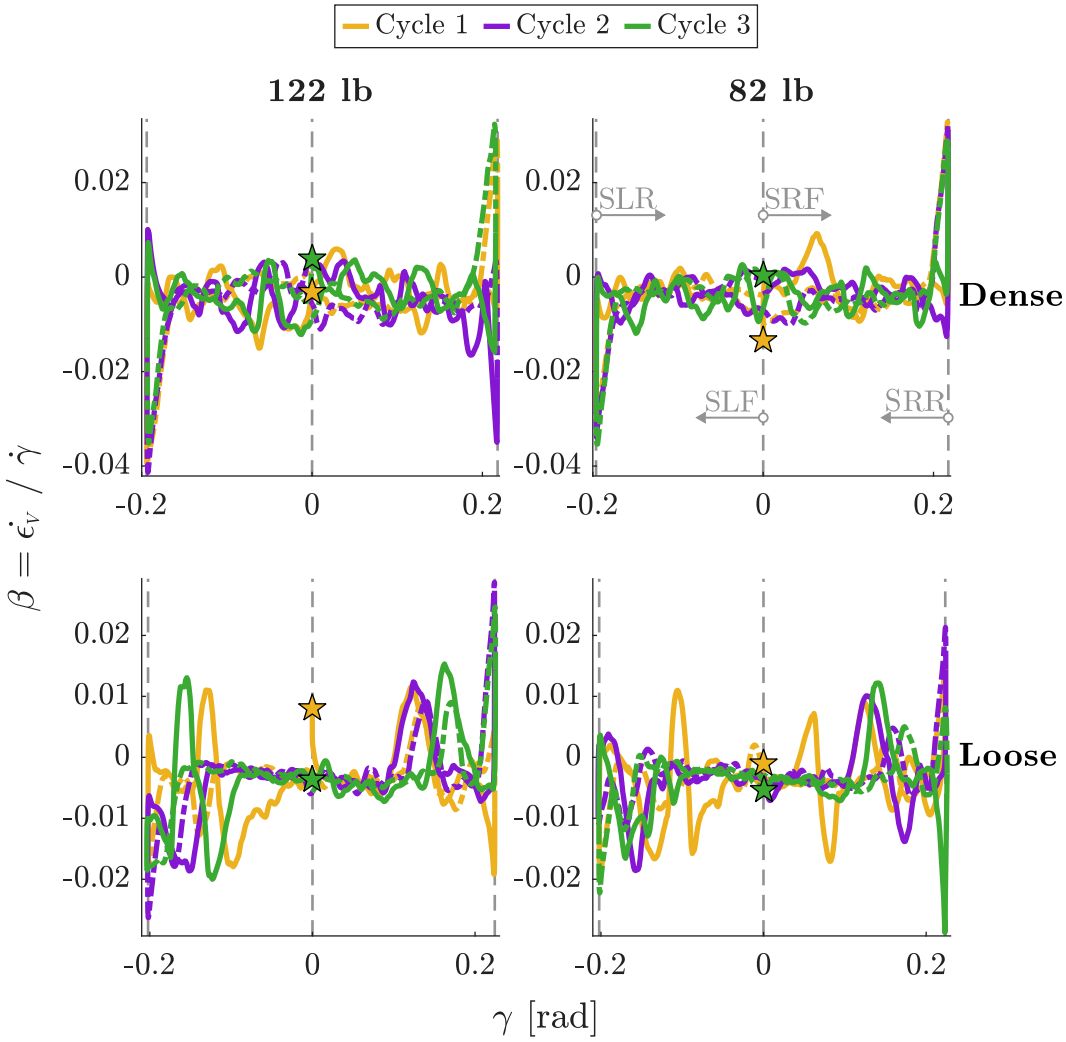


Figure C.3: Dilatancy evolution for the three-cycle experiments. Columns indicate the applied normal stress: (left) $\sigma_n = -44.1$ kPa $\approx$ 122 lb, and (right) $\sigma_n = -29.6$ kPa $\approx$ 82 lb. Rows indicate (top) densely packed and (bottom) loosely packed granular assemblies. Curve style indicates shearing direction (solid: forward, dash-dotted: reverse), gray dashed lines mark stage transitions, and stars mark the start (yellow) and end (green) of cyclic loading.

C.4 Void Ratio

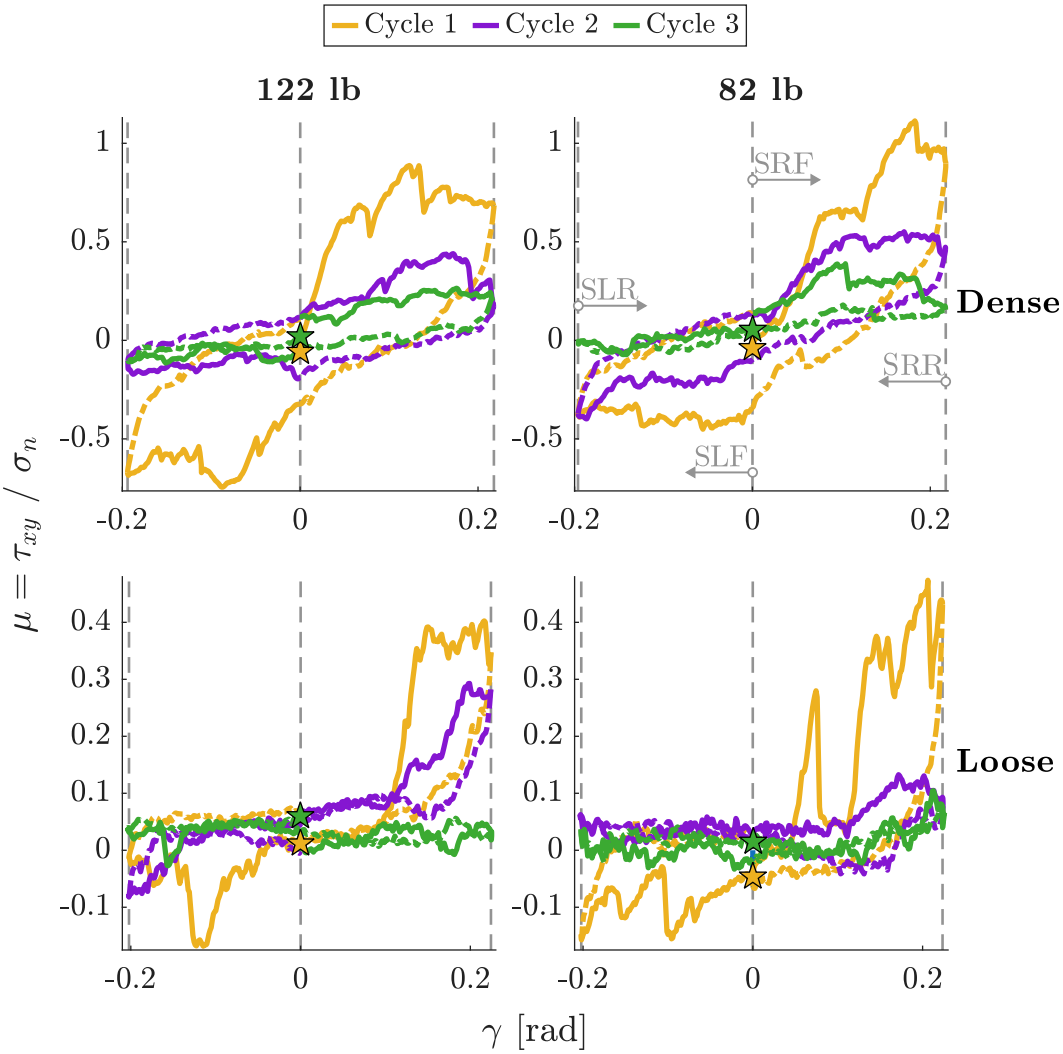


Figure C.4: Void ratio evolution for the three-cycle experiments. Columns indicate the applied normal stress: (left) $\sigma_n = -44.1$ kPa $\approx$ 122 lb, and (right) $\sigma_n = -29.6$ kPa $\approx$ 82 lb. Rows indicate (top) densely packed and (bottom) loosely packed granular assemblies. Curve style indicates shearing direction (solid: forward, dash-dotted: reverse), gray dashed lines mark stage transitions, and stars mark the start (yellow) and end (green) of cyclic loading.

Appendix D

THREE-CYCLE EXPERIMENTS: GRAIN-SCALE COMPARISON PLOTS

D.1 Coordination Number

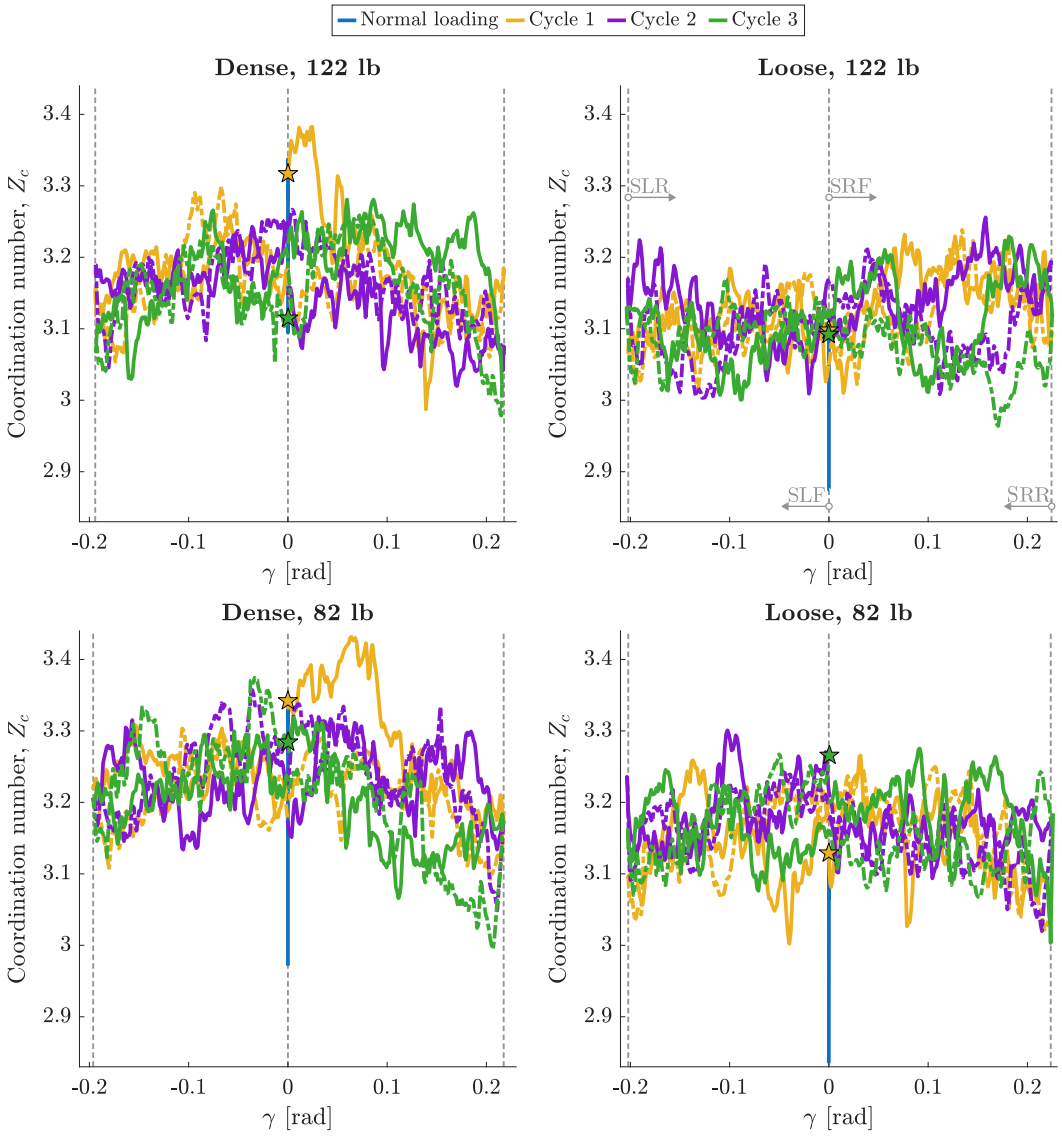


Figure D.1: Coordination number evolution for the three-cycle experiments. Columns indicate (left) densely packed and (right) loosely packed granular assemblies. Rows indicate the applied normal stress: (top) $\sigma_n = -44.1$ kPa ≈ 122 lb, and (bottom) $\sigma_n = -29.6$ kPa ≈ 82 lb. Curve style indicates shearing direction (solid: forward, dash-dotted: reverse), gray dashed lines mark stage transitions, and stars mark the start (yellow) and end (green) of cyclic loading.

D.2 The Number of Detected Force Chains

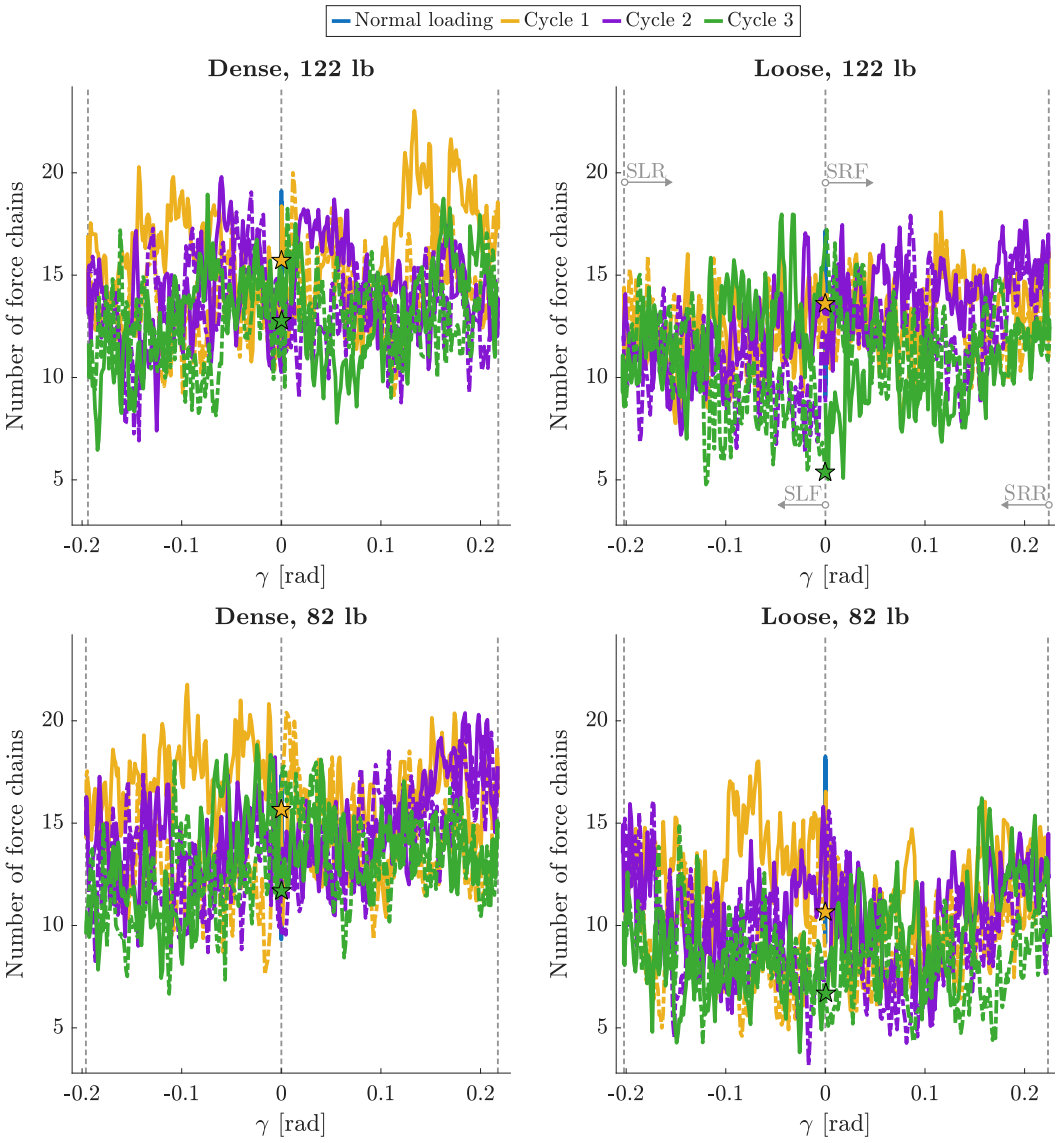
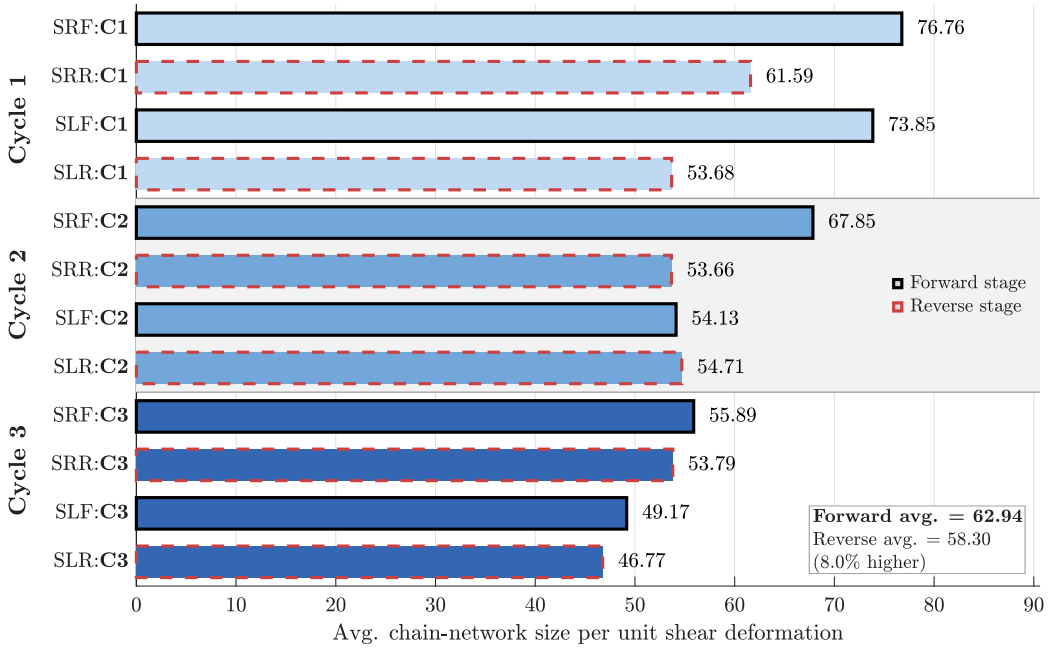


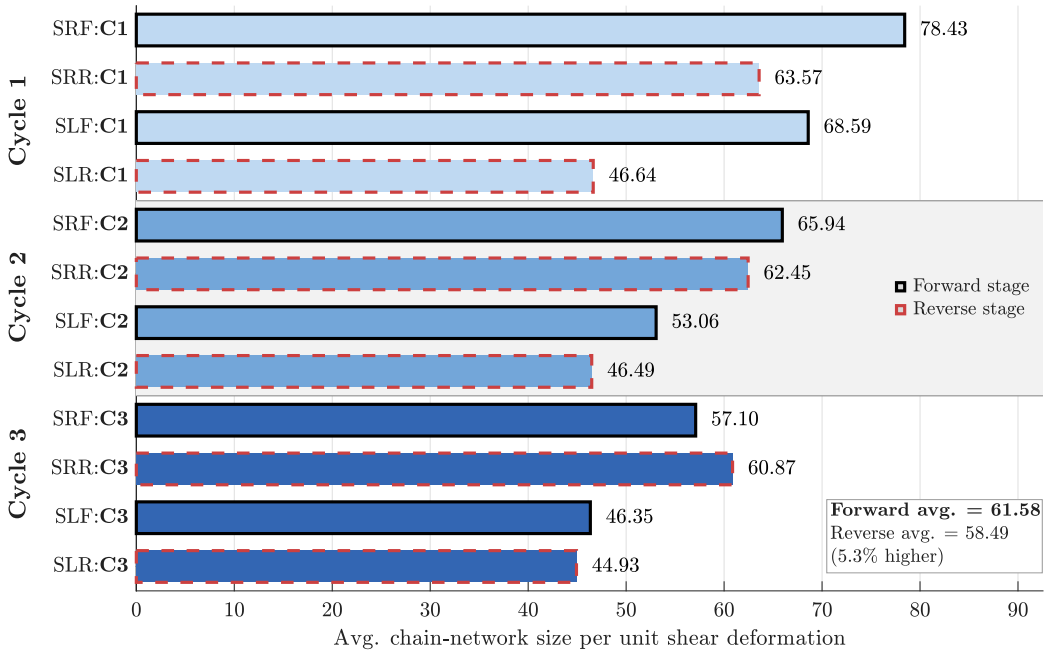
Figure D.2: Number of force chains evolution for the three-cycle experiments. Columns indicate (left) densely packed and (right) loosely packed granular assemblies. Rows indicate the applied normal stress: (top) $\sigma_n = -44.1$ kPa $\approx$ 122 lb, and (bottom) $\sigma_n = -29.6$ kPa $\approx$ 82 lb. Curve style indicates shearing direction (solid: forward, dash-dotted: reverse), gray dashed lines mark stage transitions, and stars mark the start (yellow) and end (green) of cyclic loading.

D.3 Accumulated Force Chain Network Content

D.3.0.1 Densely Packed



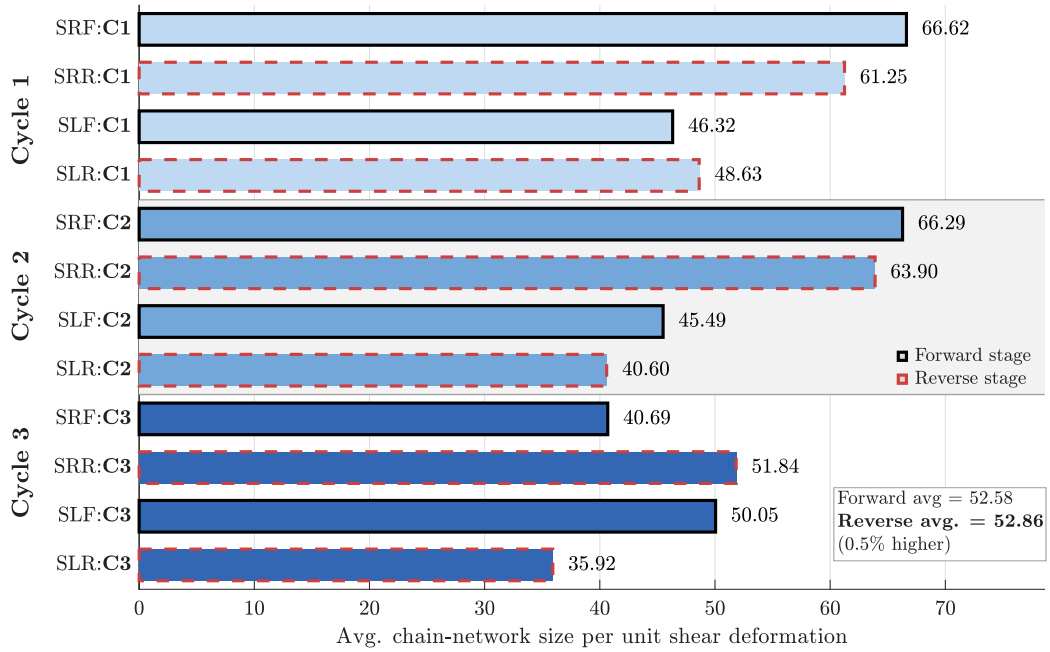
(a)



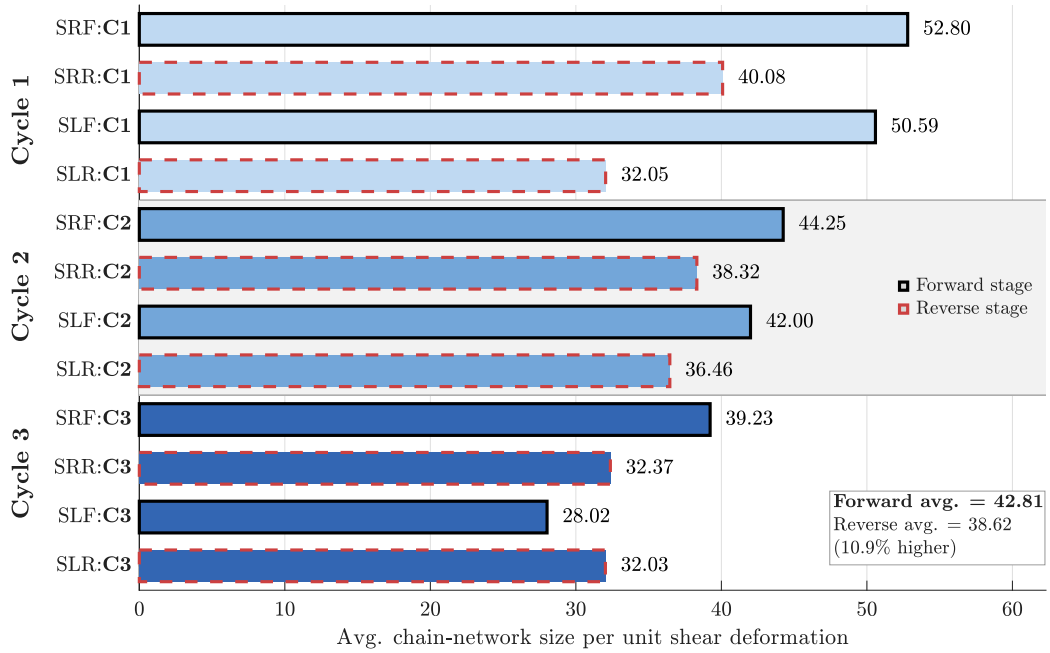
(b)

Figure D.3: Bar chart of the normalized area under the curve (AUC) of the total force chain length for each cycle and shear stage for the dense assembly. (a) Higher confinement ($\sigma_n = -44.1$ kPa), and (b) lower confinement ($\sigma_n = -29.6$ kPa $\approx$ 82 lb) . The normalized AUC represents the average extent and persistence of the force chain network sustained per unit shear deformation within each stage.

D.3.0.2 Loosely Packed



(a)



(b)

Figure D.4: Bar chart of the normalized area under the curve (AUC) of the total force chain length for each cycle and shear stage for the loose assembly. (a) Higher confinement ($\sigma_n = -44.1$ kPa), and (b) lower confinement ($\sigma_n = -29.6$ kPa $\approx$ 82 lb) . The normalized AUC represents the average extent and persistence of the force chain network sustained per unit shear deformation within each stage.

D.4 Force Chain Participation

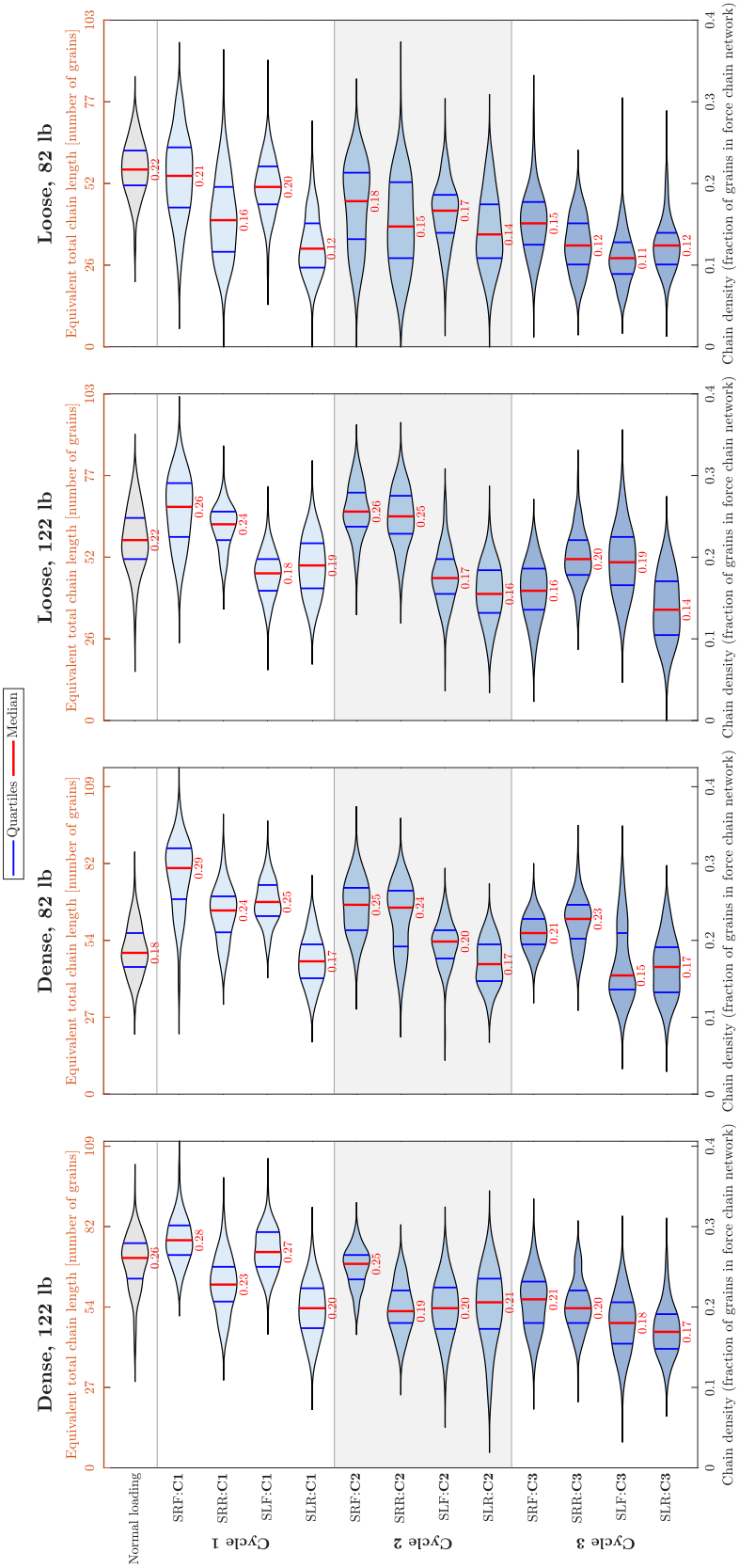


Figure D.5: Violin plots of the force chain density for each cycle and shear stage. Force chain density is defined as the fraction of grains participating in the force chain network relative to the total number of interior grains. The bottom x-axis shows the normalized chain density, while the top x-axis shows the equivalent total force chain length in number of grains. The width of each violin indicates the relative frequency of occurrence of a given chain density during that stage.

D.5 Strong Network Participation and Strong Network Chain Participation

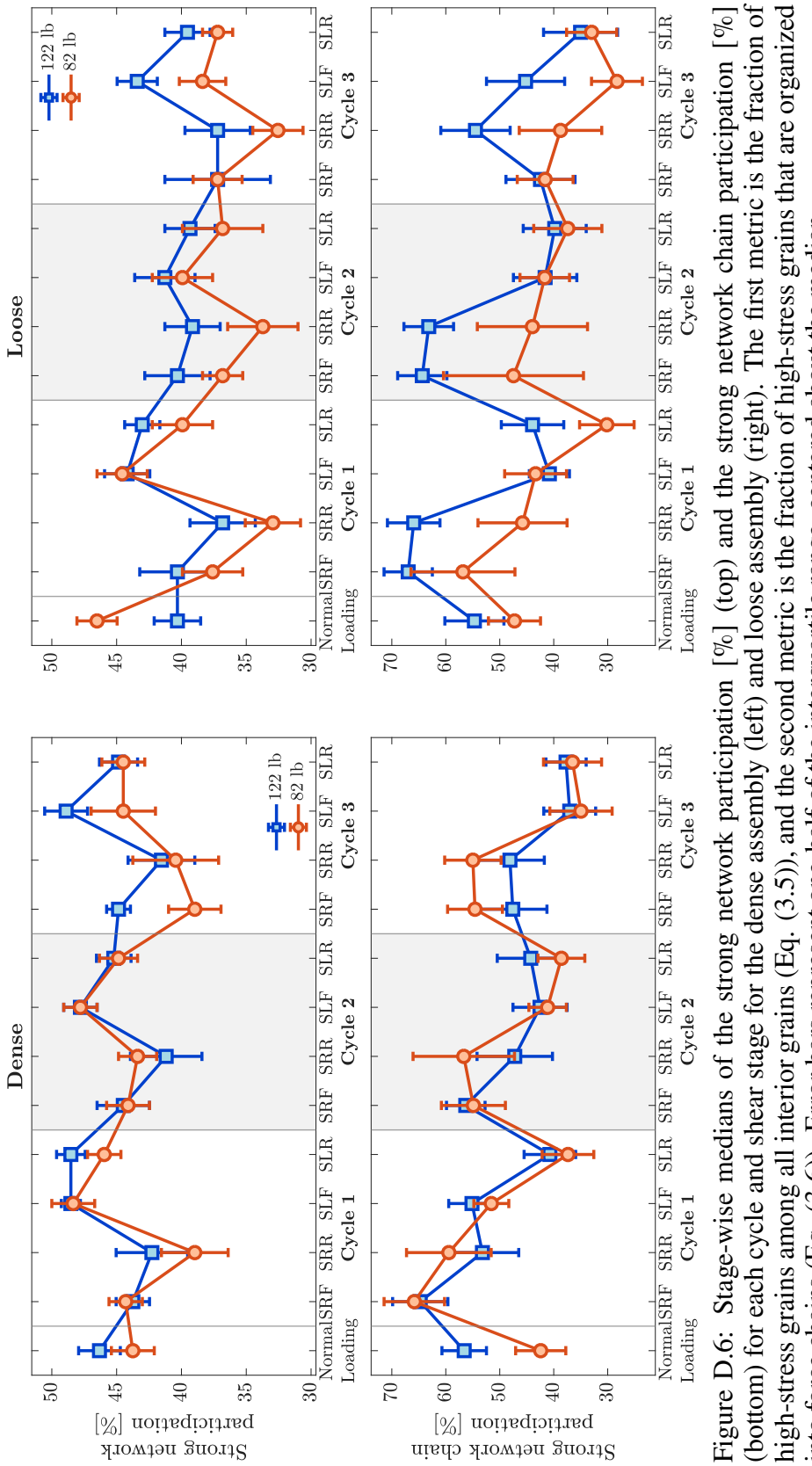


Figure D.6: Stage-wise medians of the strong network participation [%] (top) and the strong network chain participation [%] (bottom) for each cycle and shear stage for the dense assembly (left) and loose assembly (right). The first metric is the fraction of high-stress grains among all interior grains (Eq. (3.5)), and the second metric is the fraction of high-stress grains that are organized into force chains (Eq. (3.6)). Error bars represent one-half of the interquartile range, centered about the median.

D.6 Micro-Macro Comparison

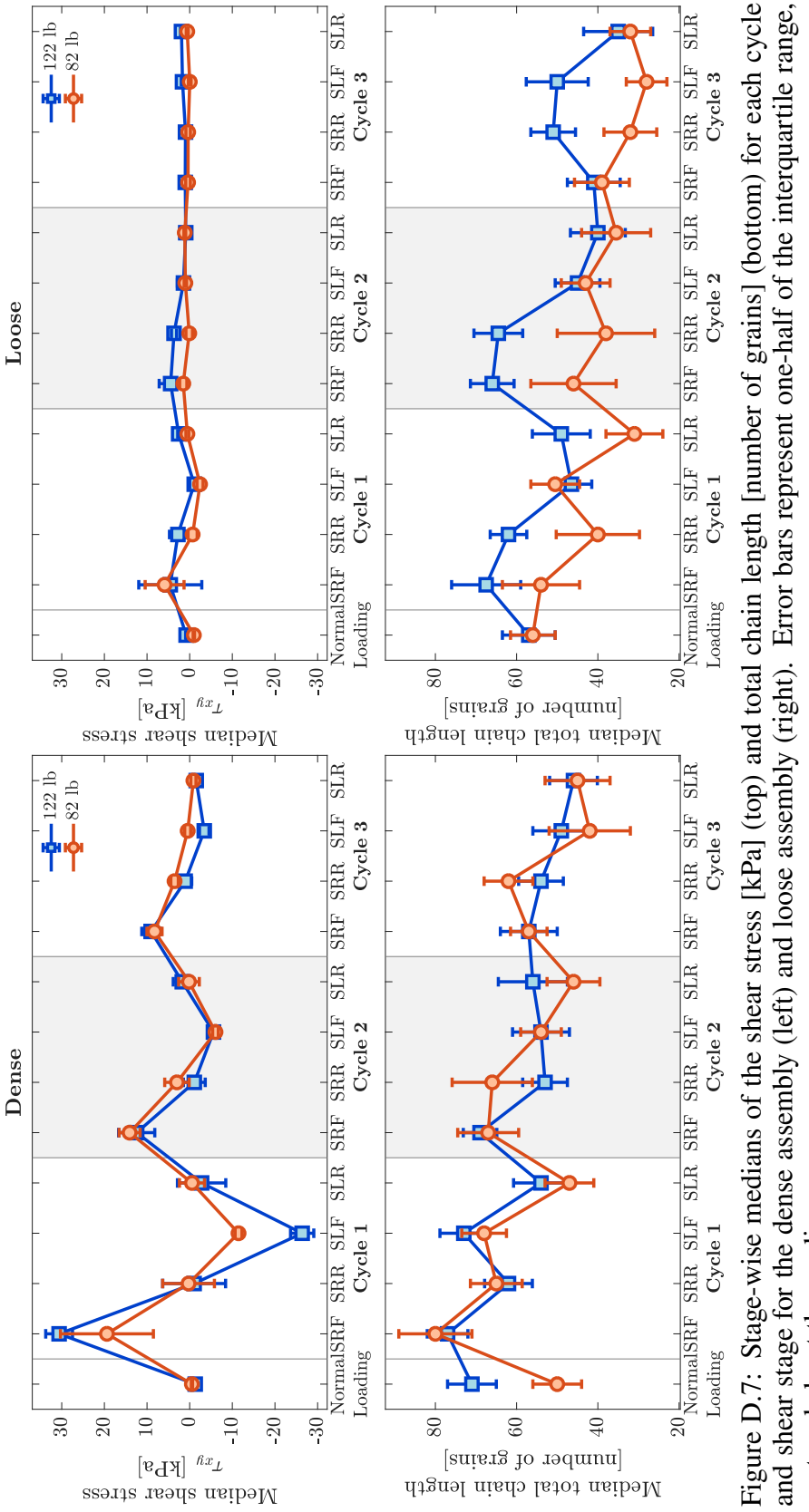


Figure D.7: Stage-wise medians of the shear stress [kPa] (top) and total chain length [number of grains] (bottom) for each cycle and shear stage for the dense assembly (left) and loose assembly (right). Error bars represent one-half of the interquartile range, centered about the median.

D.7 Temporal Evolution of Fabric and Force Anisotropy Magnitudes

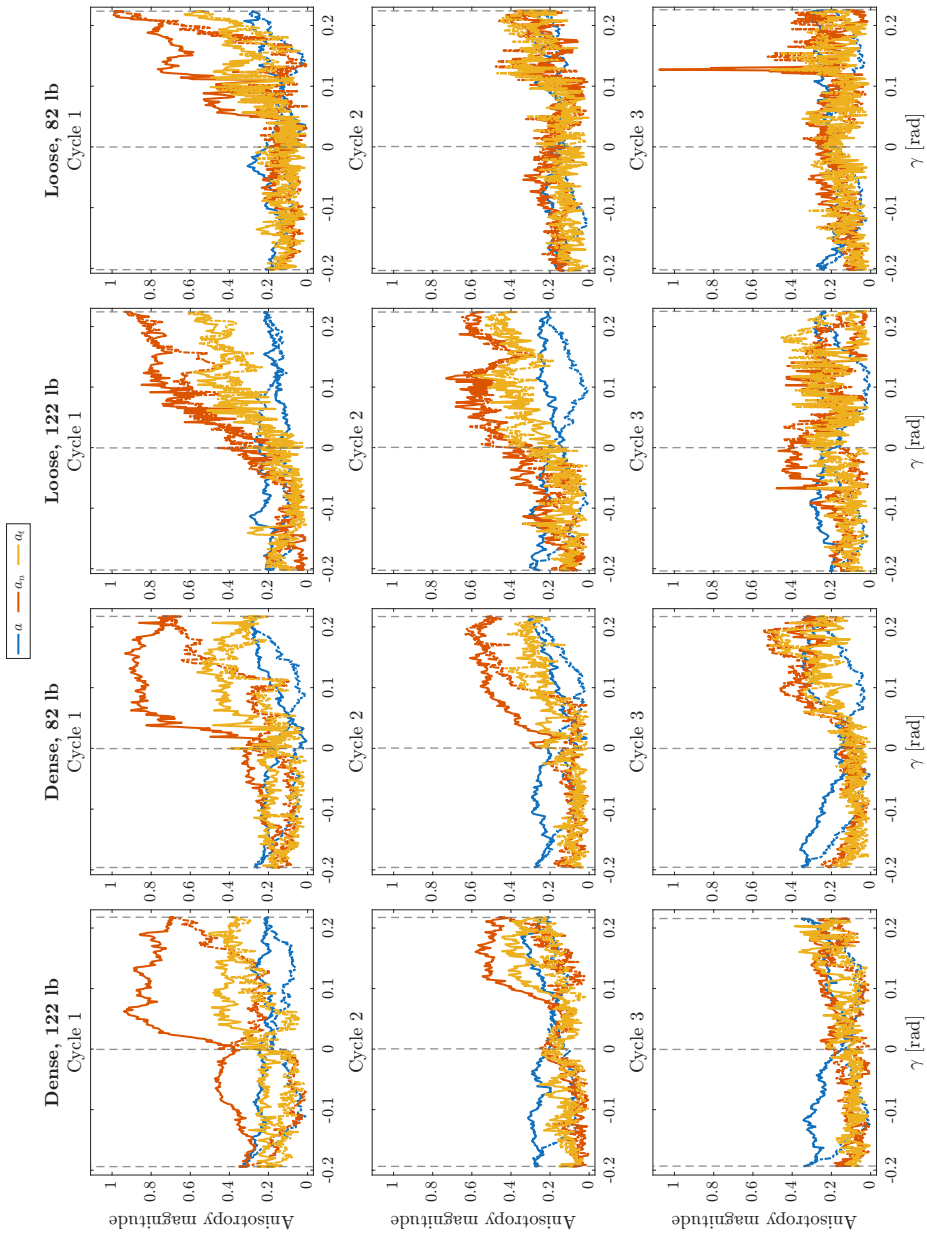


Figure D.8: Per cycle evolution of the anisotropy magnitudes as functions of shear strain: fabric anisotropy magnitude, a, and normal and tangential force anisotropy magnitudes, a_n and a_t, respectively. Curve style indicates shearing direction (solid: forward, dash-dotted: reverse), gray dashed lines mark stage transitions.

D.8 Verification of the Stress-Force-Fabric Relationship

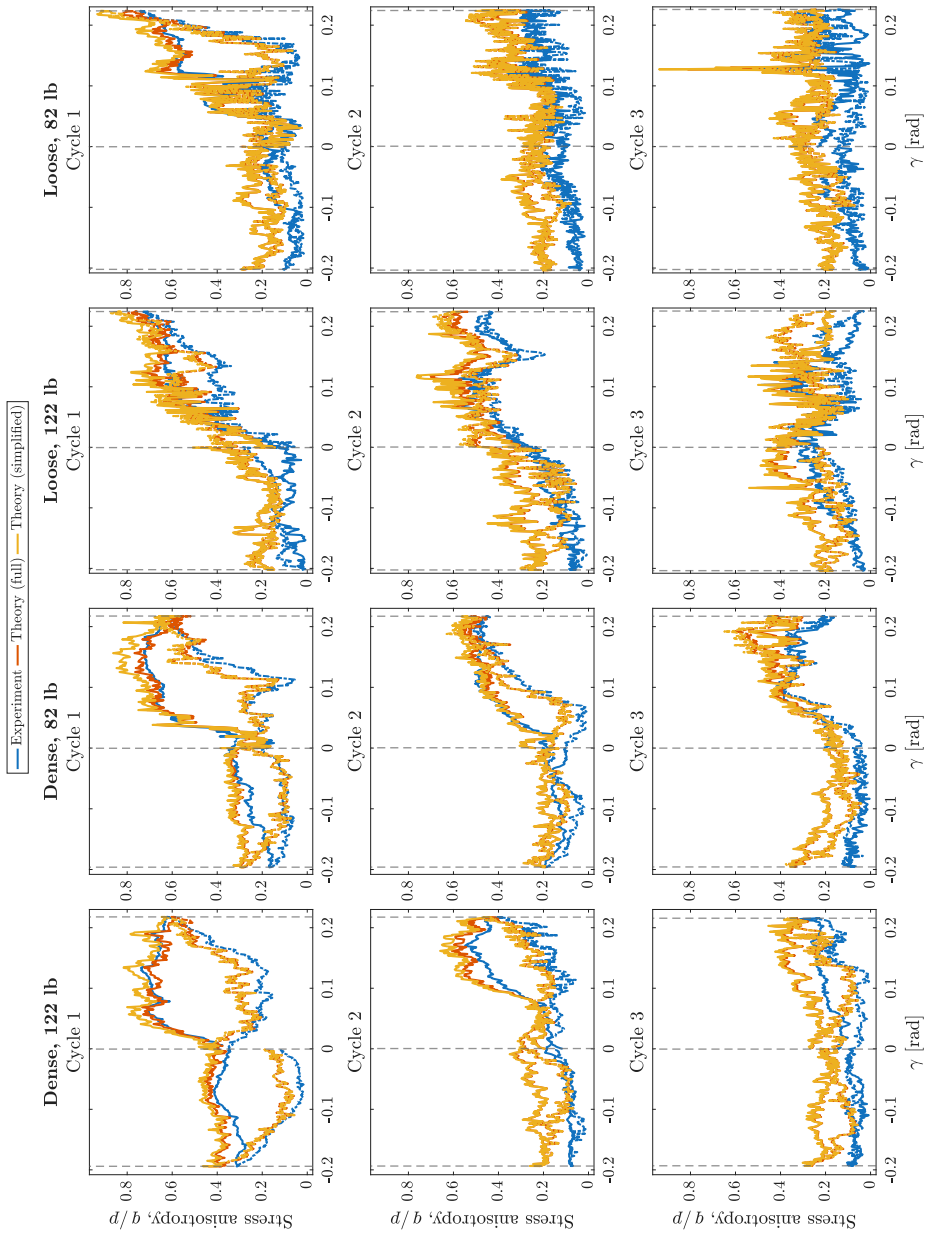
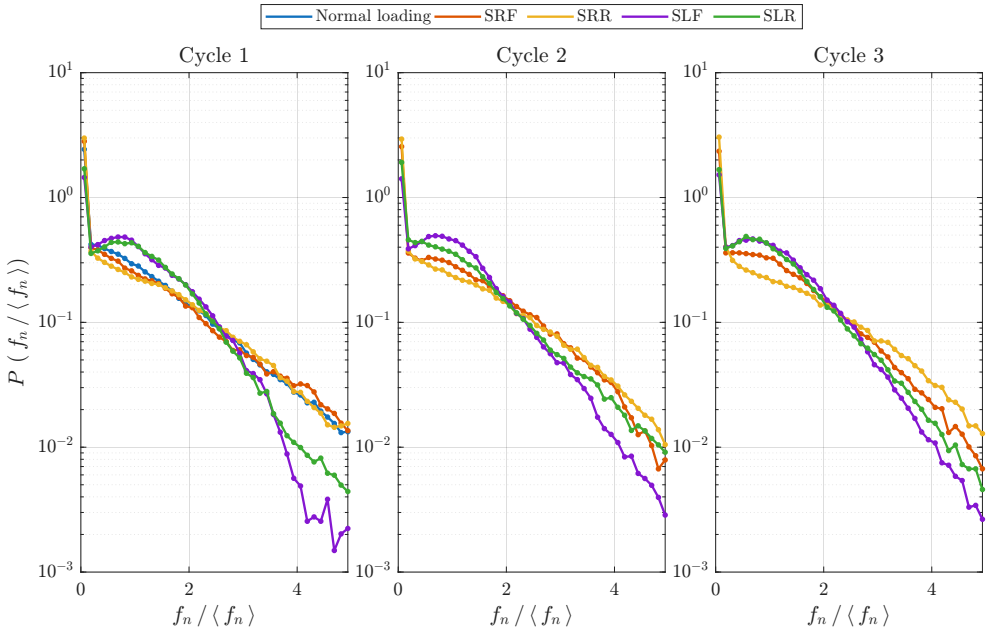


Figure D.9: Per cycle evolution of the invariant stress ratio, q/p, as a function of shear strain. The experimental response is compared with the predictions of the full and simplified stress-force-fabric (SFF) relationships (Eqs. (3.10) and (3.13)). Curve style indicates shearing direction (solid: forward, dash-dotted: reverse), gray dashed lines mark stage transitions.

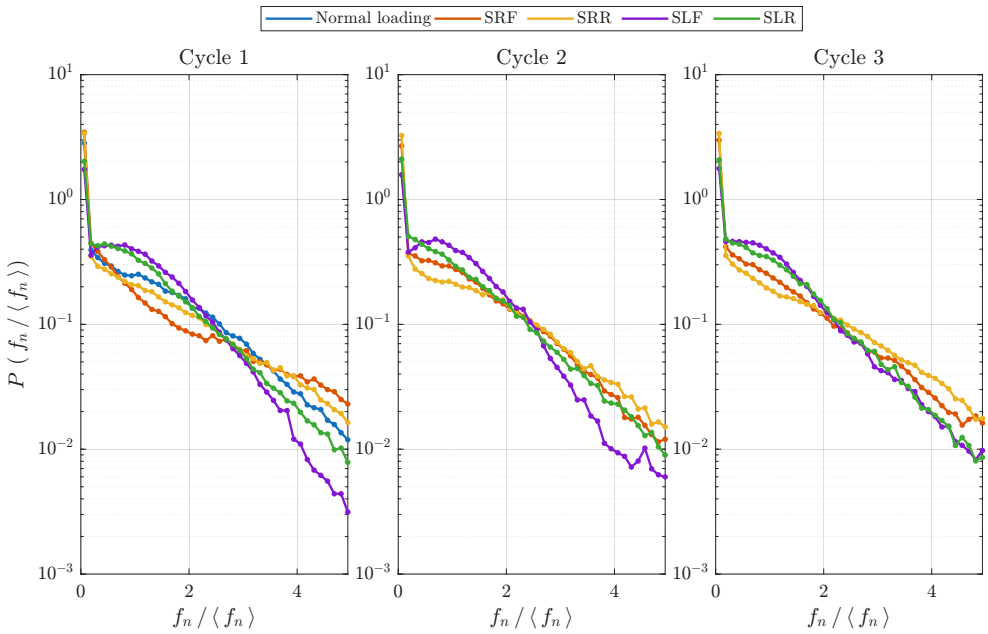
D.9 Force Transmission

D.9.0.1 Normalized Normal Contact Force

Densely Packed



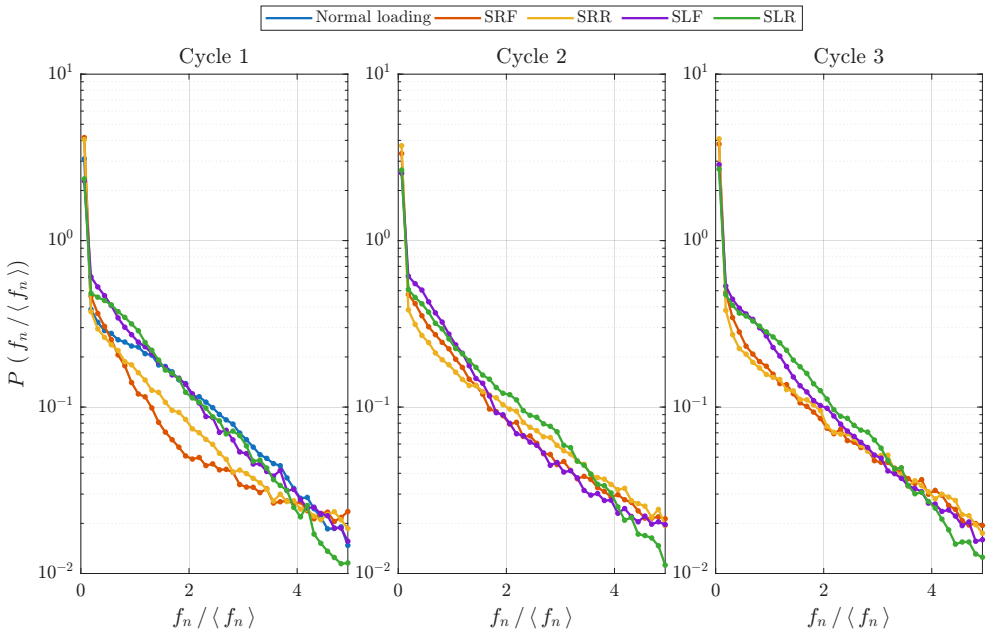
(a)



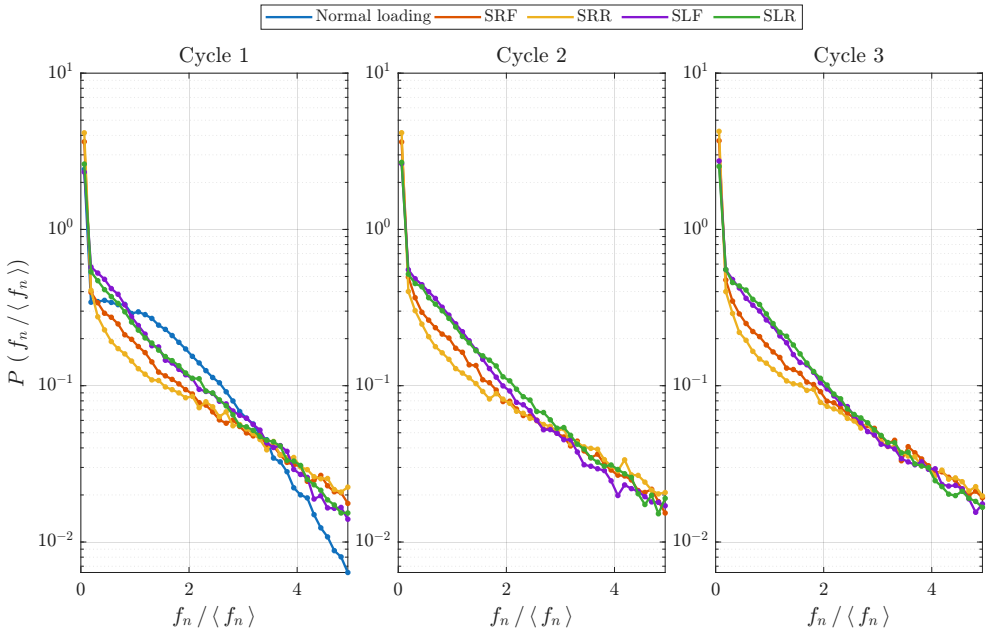
(b)

Figure D.10: Probability density functions (PDFs) of the normalized normal contact force, $f_n\,/\langle f_n\rangle$, for the dense assembly, where each panel shows one loading cycle, with all stages on a semi-log scale. (a) Higher confinement ($\sigma_n = -44.1$ kPa $\approx$ 122 lb load), and (b) lower confinement ($\sigma_n = -29.6$ kPa $\approx$ 82 lb load).

Loosely Packed



(a)

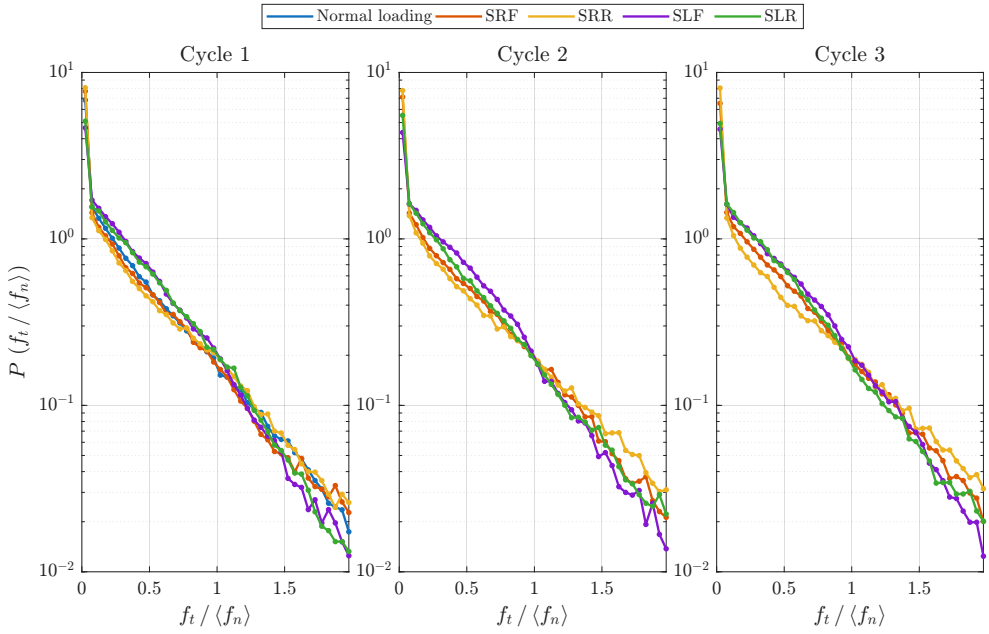


(b)

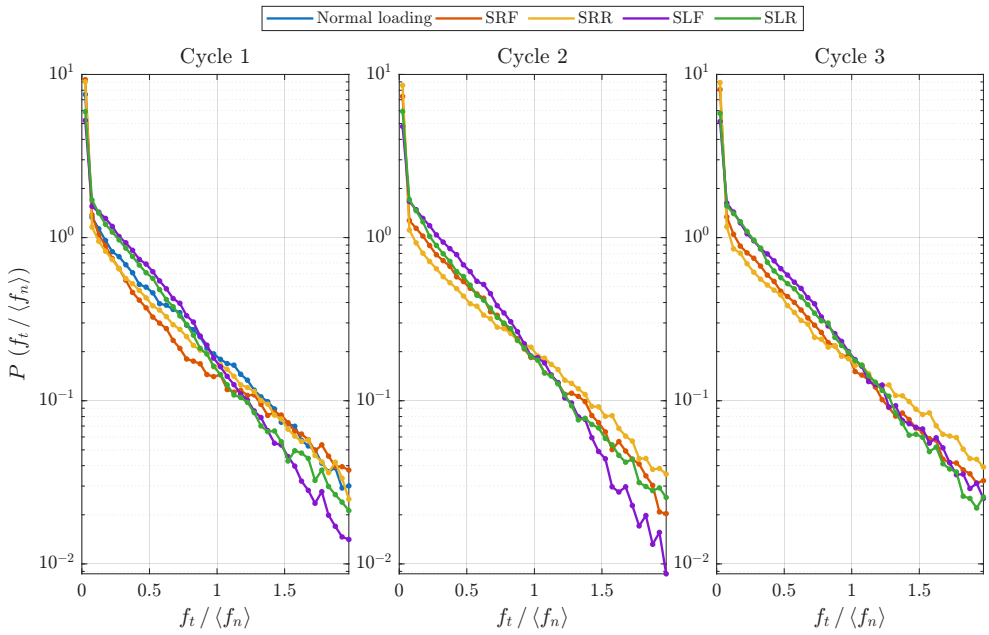
Figure D.11: Probability density functions (PDFs) of the normalized normal contact force, $f_n / \langle f_n \rangle$, for the loose assembly, where each panel shows one loading cycle, with all stages on a semi-log scale. (a) Higher confinement ($\sigma_n = -44.1$ kPa $\approx$ 122 lb load), and (b) lower confinement ($\sigma_n = -29.6$ kPa $\approx$ 82 lb load)..

D.9.0.2 Normalized Tangential Contact Force

Densely Packed



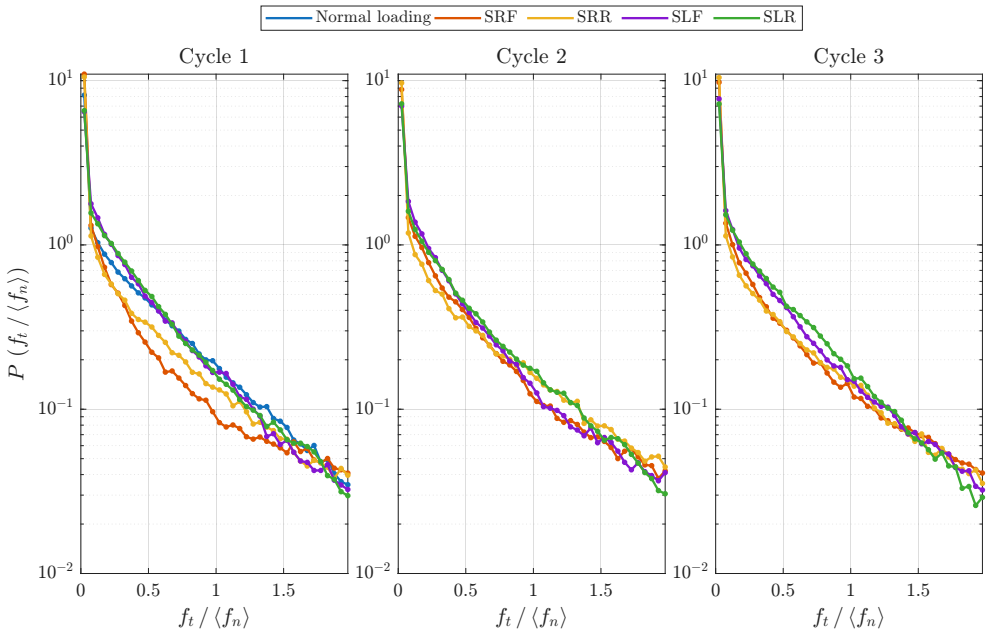
(a)



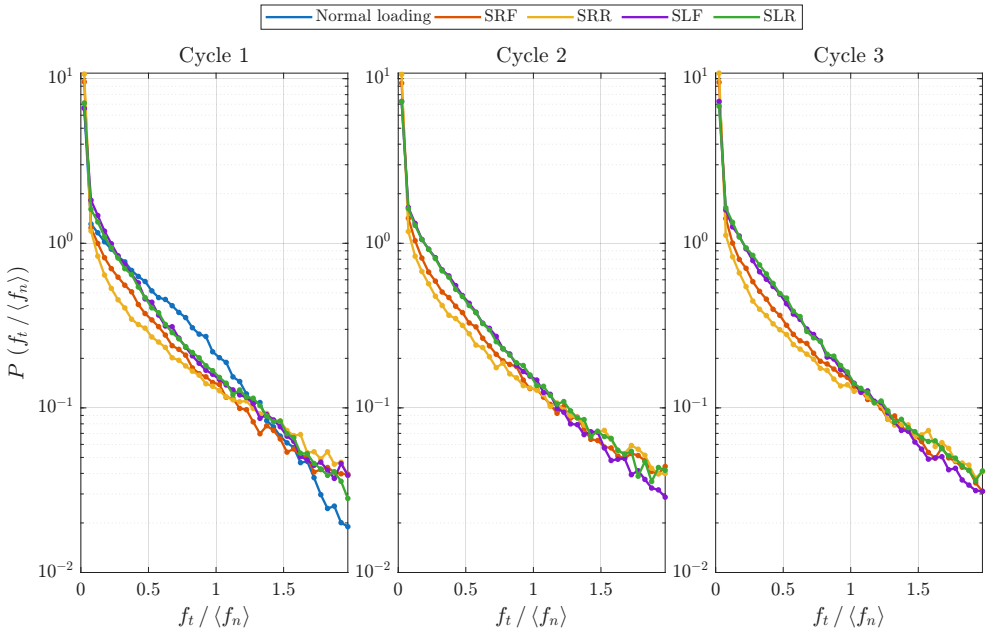
(b)

Figure D.12: Probability density functions (PDFs) of the normalized tangential contact force, $f_t\ /\langle f_n \rangle$, for the dense assembly, where each panel shows one loading cycle, with all stages on a semi-log scale. (a) Higher confinement ($\sigma_n = -44.1$ kPa $\approx$ 122 lb load), and (b) lower confinement ($\sigma_n = -29.6$ kPa $\approx$ 82 lb load).

Loosely Packed



(a)

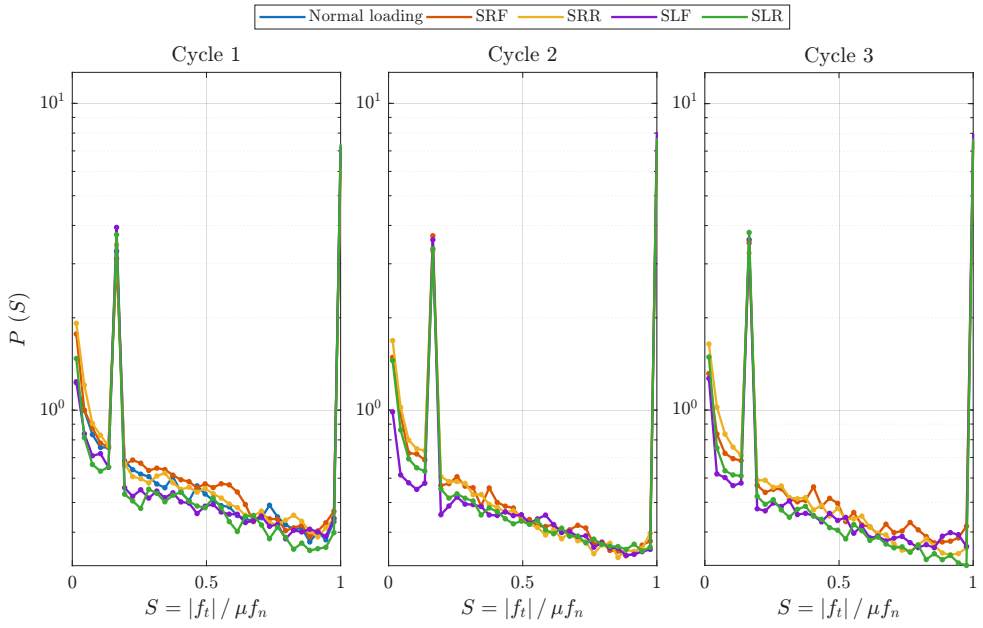


(b)

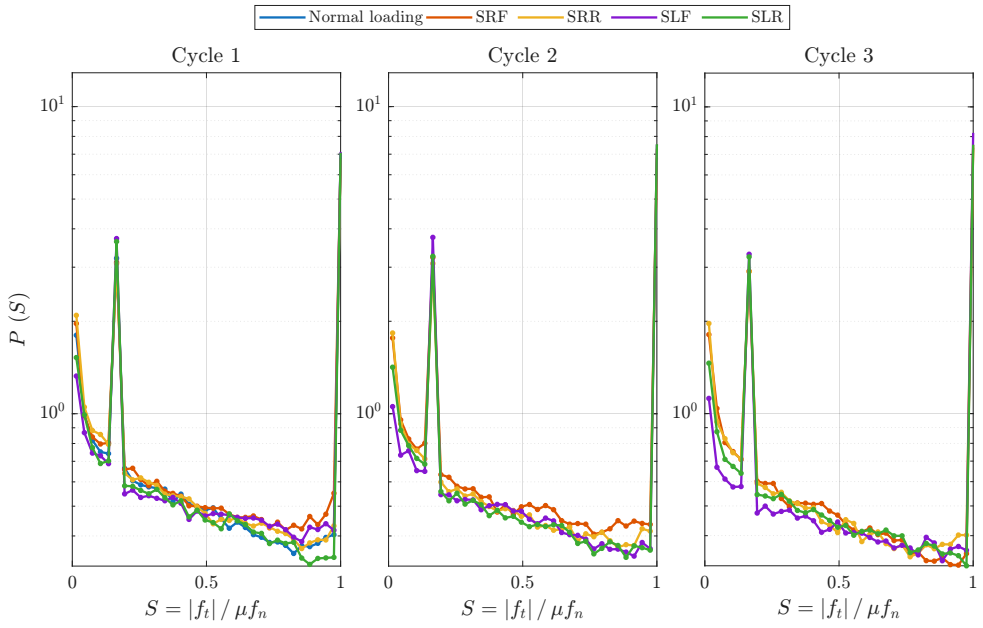
Figure D.13: Probability density functions (PDFs) of the normalized tangential contact force, $f_t\ /\langle f_n \rangle$, for the loose assembly, where each panel shows one loading cycle, with all stages on a semi-log scale. (a) Higher confinement ($\sigma_n = -44.1$ kPa $\approx$ 122 lb load), and (b) lower confinement ($\sigma_n = -29.6$ kPa $\approx$ 82 lb load).

D.9.0.3 Mobilized Friction

Densely Packed



(a)



(b)

Figure D.14: Probability density functions (PDFs) of the mobilized friction, $S = |f_t|/\mu f_n$, for the dense assembly, where each panel shows one loading cycle, with all stages on a semi-log scale. Here, μ is the interparticle friction coefficient, and S indicates the proximity of a contact to sliding (Coulomb failure criterion). (a) Higher confinement ($\sigma_n = -44.1$ kPa $\approx$ 122 lb load), and (b) lower confinement ($\sigma_n = -29.6$ kPa $\approx$ 82 lb load).

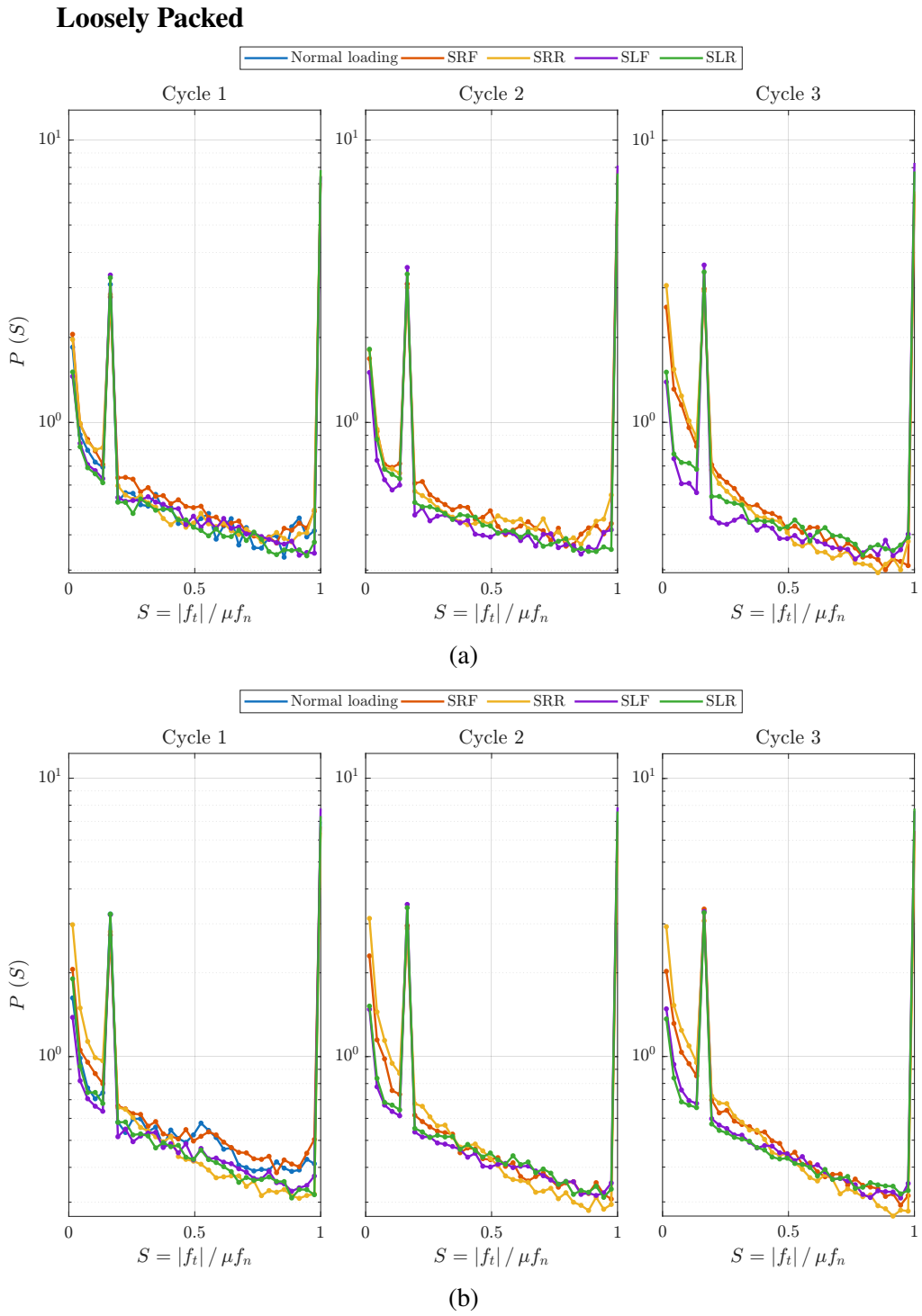


Figure D.15: Probability density functions (PDFs) of the mobilized friction, $S = |f_t|/\mu f_n$, for the loose assembly, where each panel shows one loading cycle, with all stages on a semi-log scale. Here, μ is the interparticle friction coefficient, and S indicates the proximity of a contact to sliding (Coulomb failure criterion). (a) Higher confinement ($\sigma_n = -44.1$ kPa $\approx$ 122 lb load), and (b) lower confinement ($\sigma_n = -29.6$ kPa $\approx$ 82 lb load).

Appendix E

THREE-CYCLE EXPERIMENTS: STRONG NETWORK PARTICIPATION AND STRONG NETWORK CHAIN PARTICIPATION STATISTICS TABLES

The statistical measures used in each table are the median and the mean absolute deviation (MAD). MAD is a robust measure of statistical variability resistant to outliers and skewed data. Smaller MAD values indicate less variability, while larger values indicate more variability [75].

E.1 Experiment # 1: Densely Packed, $\sigma_n = -44.1$ kPa

Table E.1: Percentage of strong network grains: median and MAD

Cycle Stage	Median (%)	MAD (%)
Normal loading	46.32	1.47
Shear right (forward):C1	43.75	1.47
Shear right (reverse):C1	42.28	2.21
Shear left (forward):C1	48.53	0.74
Shear left (reverse):C1	48.53	1.10
Shear right (forward):C2	44.49	1.84
Shear right (reverse):C2	41.18	2.94
Shear left (forward):C2	47.79	1.10
Shear left (reverse):C2	45.22	1.47
Shear right (forward):C3	44.85	1.10
Shear right (reverse):C3	41.54	2.57
Shear left (forward):C3	48.90	1.47
Shear left (reverse):C3	44.85	1.47

Table E.2: Percentage of strong network grains in force chains: median and MAD

Cycle Stage	Median (%)	MAD (%)
Normal loading	56.59	4.25
Shear right (forward):C1	64.73	5.05
Shear right (reverse):C1	53.21	6.75
Shear left (forward):C1	55.15	4.37
Shear left (reverse):C1	40.71	4.74
Shear right (forward):C2	56.30	3.55
Shear right (reverse):C2	47.22	5.30
Shear left (forward):C2	42.54	4.31
Shear left (reverse):C2	44.26	6.05
Shear right (forward):C3	47.58	5.65
Shear right (reverse):C3	48.11	6.22
Shear left (forward):C3	37.04	4.75
Shear left (reverse):C3	37.72	3.74

E.2 Experiment # 2: Densely Packed, $\sigma_n = -29.6$ kPa

Table E.3: Percentage of strong network grains: median and MAD

Cycle Stage	Median (%)	MAD (%)
Normal loading	43.75	1.84
Shear right (forward):C1	44.30	1.29
Shear right (reverse):C1	38.97	2.21
Shear left (forward):C1	48.35	1.65
Shear left (reverse):C1	45.96	1.10
Shear right (forward):C2	44.12	1.47
Shear right (reverse):C2	43.38	1.47
Shear left (forward):C2	47.79	1.47
Shear left (reverse):C2	44.85	1.47
Shear right (forward):C3	38.97	1.84
Shear right (reverse):C3	40.44	2.94
Shear left (forward):C3	44.49	2.21
Shear left (reverse):C3	44.49	1.84

Table E.4: Percentage of strong network grains in force chains: median and MAD

Cycle Stage	Median (%)	MAD (%)
Normal loading	42.41	4.59
Shear right (forward):C1	65.83	5.43
Shear right (reverse):C1	59.43	7.77
Shear left (forward):C1	51.56	3.18
Shear left (reverse):C1	37.36	4.79
Shear right (forward):C2	54.89	6.34
Shear right (reverse):C2	56.67	7.27
Shear left (forward):C2	41.13	3.40
Shear left (reverse):C2	38.58	4.47
Shear right (forward):C3	54.59	4.72
Shear right (reverse):C3	54.98	5.56
Shear left (forward):C3	34.95	5.25
Shear left (reverse):C3	36.52	5.45

E.3 Experiment # 3: Loosely Packed, $\sigma_n = -44.1$ kPa

Table E.5: % of strong network grains median and mean absolute deviation (MAD)

Cycle Stage	Median (%)	MAD (%)
Normal loading	40.31	1.94
Shear right (forward):C1	40.31	2.33
Shear right (reverse):C1	36.82	2.52
Shear left (forward):C1	44.19	1.55
Shear left (reverse):C1	43.02	1.55
Shear right (forward):C2	40.31	2.71
Shear right (reverse):C2	39.15	1.94
Shear left (forward):C2	41.28	2.52
Shear left (reverse):C2	39.34	1.74
Shear right (forward):C3	37.21	3.88
Shear right (reverse):C3	37.21	2.71
Shear left (forward):C3	43.41	1.55
Shear left (reverse):C3	39.54	1.55

Table E.6: % of strong network grains in force chains median and MAD

Cycle Stage	Median (%)	MAD (%)
Normal loading	54.70	5.59
Shear right (forward):C1	66.96	4.32
Shear right (reverse):C1	65.95	4.84
Shear left (forward):C1	40.81	3.70
Shear left (reverse):C1	43.93	6.07
Shear right (forward):C2	64.36	4.45
Shear right (reverse):C2	63.16	4.52
Shear left (forward):C2	41.60	5.10
Shear left (reverse):C2	39.82	5.77
Shear right (forward):C3	42.45	6.38
Shear right (reverse):C3	54.50	6.13
Shear left (forward):C3	45.22	7.12
Shear left (reverse):C3	35.03	6.86

E.4 Experiment # 4: Loosely Packed, $\sigma_n = -29.6$ kPa

Table E.7: % of strong network grains median and mean absolute deviation (MAD)

Cycle Stage	Median (%)	MAD (%)
Normal loading	46.51	1.55
Shear right (forward):C1	37.60	1.94
Shear right (reverse):C1	32.95	2.33
Shear left (forward):C1	44.57	1.94
Shear left (reverse):C1	39.92	2.33
Shear right (forward):C2	36.82	1.94
Shear right (reverse):C2	33.72	2.71
Shear left (forward):C2	39.92	2.33
Shear left (reverse):C2	36.82	3.10
Shear right (forward):C3	37.21	1.94
Shear right (reverse):C3	32.56	1.94
Shear left (forward):C3	38.37	1.94
Shear left (reverse):C3	37.21	1.16

Table E.8: % of strong network grains in force chains median and MAD

Cycle Stage	Median (%)	MAD (%)
Normal loading	47.27	4.54
Shear right (forward):C1	56.82	9.45
Shear right (reverse):C1	45.78	8.37
Shear left (forward):C1	43.36	5.11
Shear left (reverse):C1	30.16	5.04
Shear right (forward):C2	47.46	12.22
Shear right (reverse):C2	43.95	10.19
Shear left (forward):C2	41.67	4.51
Shear left (reverse):C2	37.39	6.18
Shear right (forward):C3	41.58	5.41
Shear right (reverse):C3	38.75	7.68
Shear left (forward):C3	28.28	4.72
Shear left (reverse):C3	32.98	4.66